Design and Optimization of Physical Waveform-Diverse and Spatially-Diverse Radar Emissions

By

Patrick M. McCormick

Submitted to the graduate degree program in Department of Electrical Engineering and Computer Science and the Graduate Faculty of the University of Kansas in partial fulfillment of the requirements for the degree of Doctorate of Philosophy.

Committee members

Shannon D. Blunt, Chairperson

Christopher Allen

James Stiles

Alessandro Salandrino

Emily Arnold

Date defended: May 10, 2018

The Dissertation Committee for Patrick M. McCormick certifies
that this is the approved version of the following dissertation :

Design and Optimization of Physical Waveform-Diverse and Spatially-Diverse Radar Emissions

Shannon D. Blunt, Chairperson

Date approved: May 10, 2018

~~~~~~~~~~~~
For my wife.
~~~~~~~~~~~~

Abstract

With the advancement of arbitrary waveform generation techniques, new radar transmission modes can be designed via precise control of the waveform's time-domain signal structure. The finer degree of emission control for a waveform (or multiple waveforms via a digital array) presents an opportunity to reduce ambiguities in the estimation of parameters within the radar backscatter. While this freedom opens the door to new emission capabilities, one must still consider the practical attributes for radar waveform design. Constraints such as constant amplitude (to maintain sufficient power efficiency) and continuous phase (for spectral containment) are still considered prerequisites for high-powered radar waveforms. These criteria are also applicable to the design of multiple waveforms emitted from an antenna array in a multiple-input multiple-output (MIMO) mode.

In this work, three spatially-diverse radar emission design methods are introduced that provide constant amplitude, spectrally-contained waveforms implemented via a digital array radar (DAR). The first design method, denoted as spatial modulation, designs the radar waveforms via a polyphase-coded frequency-modulated (PCFM) framework to steer the coherent mainbeam of the emission within a pulse. The second design method is an iterative scheme to generate waveforms that achieve a desired wideband and/or widebeam radar emission. However, a wideband and widebeam emission can place a portion of the emitted energy into what is known as the 'invisible' space of the array, which is related to the storage of reactive power that can damage a radar transmitter. The proposed design method purposefully avoids this space and a quantity denoted as the Fractional Reactive Power (FRP) is defined

to assess the quality of the result. The third design method produces simultaneous radar and communications beams in separate spatial directions while maintaining constant modulus by leveraging the orthogonal complement of the emitted directions. This orthogonal energy defines a trade-space between power efficiency gained from constraining waveforms to be constant amplitude and power efficiency lost by emitting energy in undesired directions.

The design of FM waveforms via traditional gradient-based optimization methods is also considered. A waveform model is proposed that is a generalization of the PCFM implementation, denoted as coded-FM (CFM), which defines the phase of the waveform via a summation of weighted, predefined basis functions. Therefore, gradient-based methods can be used to minimize a given cost function with respect to a finite set of optimizable parameters. A generalized integrated sidelobe level (GISL) metric is used as the optimization cost function to minimize the correlation range sidelobes of the radar waveform. System specific waveform optimization is explored by incorporating the linear models of three different loopback configurations into the GISL metric to match the optimized waveforms to the particular systems.

Contents

List of Figures

Chapter 1

Introduction

The implementation of radar has changed considerably since its discovery in the early 1900s, however the mechanism in which radar operates has not. The radar is still bound by the same laws that govern electromagnetic (EM) propagation. Thus we are bound by the advances in radar technology which in turns leads to new theory and experimentation of contemporary radar practices. In the past two decades, the advancement of arbitrary waveform technology has spurred research into waveform diversity and its applications [1–5]. The breadth of this research touches on spectral coexistence issues [6–8] which can entail interference management between radar and communications signals [9, 10] or cooperative spectrum sharing among users of the electromagnetic spectrum [11–13]. The variability of arbitrary waveform generation has also extend to antenna array transmission to generate spatially-diverse emissions such as the frequency diverse array (FDA) [14, 15] and multiple-input multiple-out (MIMO) radar [16–21].

The intersection between waveform diversity and spatial diversity is the the fully digital array radar (DAR) [20], which utilizes independent hardware and waveform generation for each antenna element in the array to achieve adaptable transmit and receive capabilities. With the cost and size reduction of digital processing nodes [22], the DAR is the future trend for array technology [22, 23]. The DAR concept enables the execution of multiple simultaneous radar functions by having the system flexibility to allow the radar to operate in many different modes (e.g. traditional focused beam, MIMO mode, multiple beams, etc.). Also, the DAR provides the means to operate radar and communications functions in a space-division multiplexed mode through formation of two simultaneous focused beams [24, 25]. The concurrent operation of multiple functions via a DAR also alleviates timing requirements that constrain multi-function radars that execute

functions sequentially by having better time-energy management of the available resources of the array [20, 26–28]. The capabilities of this systems structure have applications in cognitive sensing as the digital-at-every-element concept provides a flexible illumination capability combined with a receive structure that retains a digital copy of the individually captured signals thus providing maximum information to the cognitive system [29].

The wave of research into waveform and spatially diverse transmissions is driven by the desire to attain better radar performance or functionality than what previously could be achieved. Greater performance and functionality implies a higher level of radar sensitivity (e.g. a higher dynamic range of estimated scattering powers). From a waveform/emission design standpoint, there are many practical issues of concern in the implementation of waveform and spatially diverse systems that could limit the fidelity achieved in the radar signal processor. Signal distortions in the radio frequency (RF) chains, both linear and nonlinear, can limit the sensitivity of the radar function through an increased sidelobe response of the waveform's autocorrelation function. If the waveform is not spectrally contained, bandlimiting within the radar transmitter can alter the time-domain envelope of the waveform [3]. And for antenna arrays, mutual coupling can effect the signal structure of a spatially-diverse transmission [30].

From a waveform design perspective, there are three methods of limiting the deleterious effects of the hardware distortion: 1) the waveform(s) can be predistorted such that the desired response is achieved after the distortion has taken place [31–37]; 2) choose a waveform/emission structure that is robust to the detrimental distortion effects (e.g. constant amplitude and spectrally contained) and 3) optimize the waveform with the system distortion incorporated into the design process. In this work, methods 2 and 3 are discussed within the context of waveform diverse and spatially diverse radar while preserving the pragmatic attributes of radar waveforms necessary for implementation. In high powered radar systems, it is still considered a requirement that the waveform be constant amplitude due to operation of the transmit amplifier in the saturation region which could significantly distort a waveform that is amplitude modulated (AM). In addition, the waveform must be spectrally contained as to 1) not interfere with proximate users of the EM

spectrum, and 2) avoid distortion due to band-limiting effects in the radar transmitter [3, 38]. These two waveform constraints, constant modulus and spectral containment, are a running theme throughout this work and were a catalyst for the reasoning behind the architecture of the waveform design/optimization methods that are presented.

The main goal of this work is to setup/describe practical models for waveform optimization/design (including frequency depending antenna patterns, mutual coupling, hardware distortion models, robust waveform attributes, etc.). The majority of the waveform design/optimization methods described throughout this work are *system considerate*, meaning the model of the waveform/transmission is chosen such that it would be robust to nonlinear effects for general high power applications, i.e. constant amplitude and spectrally contained [3]. In Chapter 5, *system specific* optimization is considered by incorporating RF distortion modeling into the cost function to account for the specific distortions of components, while maintaining a *system considerate* waveform model to be robust against errors that might be present in the distortion model. For this work, all methods of modeling reality are not considered and less are eventually applied to waveform design/optimization, though it is the hope of the author that the presented work sets the stage for the future work needed in system inclusive waveform/emission optimization.

In Chapter 2, an overview of standard radar processing and implementation is provided. Four sections are included that cover different stages within a standard radar system: the waveform, the transmission, the scattering and reception, and radar digital signal processing. This material lays out a mathematical and conceptual foundation to the problem of practical waveform design that is persistent throughout this work. The overview includes topics such as transmitter distortion and fast-time Doppler effects that can effect the modulation structure of the waveform. It is shown that the frequency modulated (FM) waveform provides the largest degree of robustness to nonlinear transmit distortion effects present in high power radar transmitters thus are the chosen waveform structure used throughout this work.

Chapter 3 is on the analysis of spatially-diverse transmissions, specifically on the improved spatial resolution from operating in a MIMO mode and the effects of mutual coupling in uniform

linear arrays (ULAs). The theorized improvement in spatial resolution when implementing a (non-distributed) MIMO radar transmission mode is typically derived using the *virtual array* concept which makes the assumption of orthogonality between the signals [39, 40]. Here, a *angle-delay ambiguity function* is defined for a narrowband ULA that can be defined as the product between two separable functions: *beam factor* and the *diversity factor*. The beam factor corresponds to the traditional spatial resolution that is achieved given a certain array geometry while the diversity factor illustrates the improvement in angle resolution solely due to waveform diversity in the spatial dimension when operating in a MIMO mode. The mutual coupling of a uniform linear array is defined from both a circuit and scattering points of view. The closed-form models of the self and mutual impedances of between dipole antennas is utilized to characterize two arrays: one with half-wavelength spacing and one with quarter-wavelength spacing. For a broadside impedance match, the scan impedance variation [41] and resulting reflected/coupled energy is characterized for these two arrays. For arrays with spacing less than half-wavelength, an array excitation can place energy into what is known as the *invisible space* which corresponds to low radiation resistance and high reactance. Because wide scan arrays are typically matched at broadside, excitations that produce significant energy in these directions exhibit large reflected/coupled energy. For traditional omnidirectional MIMO beampatterns, this presents an emission design issue as energy is inevitably present in the excitations [42, 43]. A term denoted *Fractional Reactive Power* (FRP) is defined that quantifies the amount of energy in this invisible space and is shown to well approximate the reflected/coupled power in a spatially-diverse transmission mode for the quarter-wavelength array.

Chapter 4, entitled *Waveform Design for Physical Spatially-Diverse Transmission*, consists of three spatially-diverse emission modes each requiring the DAR framework. The first-mode is a implementation of a coherent beam that is steered within the pulse around a center look direction. By using the polyphase-coded FM (PCFM) framework to realize the spatially modulated emission [38, 44], the resulting waveforms are guaranteed to be constant amplitude and spectrally contained thus robust to hardware distortion effects. It is shown that similar resolution capabilities (as theorized with the MIMO virtual array) can also be achieved using this method while still

maintaining a semi-focused transmit beampattern. The second emission mode designs a wideband emission that jointly adheres to a desired spatial distribution and spectral shape that grants the ability for a simultaneous multifunction radar capability. Because of the wideband nature of the array, the warping of the beampattern over frequency may place energy in the invisible over a certain range of frequencies, however the proposed method inherently avoids this region by placing energy only in desired spatial regions known as "beamlets". The final spatially-diverse emission develops and analyzes an optimization scheme to generate an emission that simultaneously emits multiple transmit beams to perform radar and communications functions on a single array while constrained to have constant amplitude waveforms. In this section, the method is experimentally validated on the Air Force Research Lab (AFRL) BEEMER (Baseband-digital at Every Element MIMO Experimental Radar) MIMO system.

In Chapter 5, gradient-based optimization methods are implemented to minimize the autocorrelation sidelobe response of FM waveforms. The ability to apply discrete optimization techniques to continuous-time waveform is admitted via a basis representation where the phase function of the waveform is defined using a finite summation of scaled basis functions. This waveform model, denoted as the coded-FM (CFM), is therefore entirely defined using a finite set of optimizable parameters. The sidelobes of the autocorrelation are minimized according to a metric defined as the generalized integrated sidelobe metric (GISL) which takes the q-norm ratio of the correlation sidelobes to the correlation mainlobe, thus encapsulating the traditional autocorrelation metrics: peak sidelobe level (PSL) and integrated sidelobe level (ISL). In Section 5.2, the nonlinear conjugate gradient (NLCG) descent method is used to minimize the GISL cost function when using the PCFM basis. Within this section it is shown that the expected sidelobe floor (which is typically thought to be a function of the waveform time-bandwidth product) is actually a function of the sampled bandwidth and is largely independent of the time-bandwidth product. In Section 5.3, a quasi-Newton approach is used to minimize the GISL cost function for a waveform model using the Legendre polynomial basis. The GISL metric for this case uses a modified correlation function (in place of the autocorrelation) that takes into account the discrete-time nature of the

matched filter and the continuous-time nature of the emission. A linear model for three different loopback hardware chains is estimated and incorporated into the the optimization cost function to predict and account for the RF distortion imparted to the signal structure in a loopback setting. It is found that, through inclusion of the linear model, the captured signal can be accurately predicted to a high degree thus the deleterious effects caused by hardware distortions are instead leveraged during the design of the waveform, thus demonstrating the benefits of system specific waveform design to achieve higher radar sensitivity.

Chapter 2

Background and Radar Modeling

This chapter serves as a extensive background on waveform definitions, waveform analysis, and factors that contribute to waveform distortion. Note that the topics included in this section are by no means comprehensive, though provide a foundation of knowledge for the following chapters in this work. This chapter is broken up into four main portions: *The Waveform*, *The Transmission*, *The Scattering and Reception*, and *Radar Digital Signal Processing* (DSP); each stage analytically defining how the modulation structure of the waveform is carried/modeled throughout. Because of this, only a single pulse scenario is considered throughout this chapter though all aspects discussed can be extrapolated to multiple pulse scenarios. In Section 2.1, the radar waveform is analytically defined and multiple examples of common waveform archetypes are presented. Section 2.2 defines the transmitter model and defines both linear and nonlinear waveforms distortions and under what conditions they may be present. The scattering and reception of electromagnetic (EM) energy is discussed in Section 2.3, and the chapter is concluded in Section 2.4 where radar DSP examined. Note that not every aspect in this chapter is used throughout this work, but is included for completeness.

2.1 The Waveform

The waveform generated and transmitted by the radar represents how the electromagnetic energy emitted into free space is modulated. A single waveform can be expressed in two different representations: *passband* and *complex-baseband* (sometimes referred to as *complex-envelope*). The passband representation describes a waveform whose spectral content is centered around some

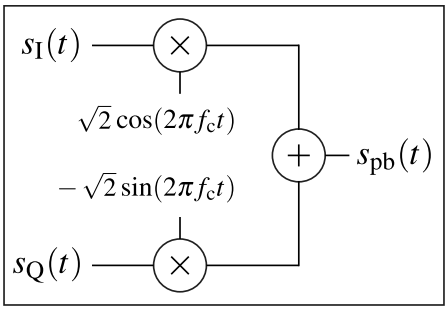

Figure 2.1: Simple model for up-conversion of waveform $s(t)$.

center frequency f_{c} and is expressed using a real-valued continuous function $s_{\mathrm{pb}}(t)$ which is a function of continuous time t. The complex-baseband representation of a waveform is independent of a center frequency by defining the center of the spectral content around 0 Hz through a complex-valued waveform representation denoted as $s(t) = s_{\mathrm{I}}(t) + js_{\mathrm{Q}}(t)$ where $s_{\mathrm{I}}(t)$ and $s_{\mathrm{Q}}(t)$ are the in-phase and quadrature portions of the waveform, respectively, and $j = \sqrt{-1}$ is the imaginary number. Therefore, $s_{\mathrm{I}}(t) = \Re\{s(t)\}$ and $s_{\mathrm{Q}}(t) = \Im\{s(t)\}$ where $\Re\{\bullet\}$ and $\Im\{\bullet\}$ extract the real and imaginary values of the signal, respectively. The complex-valued signal cannot by itself be emitted and must be up-converted to a center frequency (either using local oscillators or with digital up-conversion) as shown in Figure 2.1. Therefore the passband and complex-baseband representations are related as

$$\begin{aligned} s_{\mathrm{pb}}(t) &= \sqrt{2}\Re\left\{s(t)\exp(j2\pi f_{\mathrm{c}}t)\right\} \\ &= \sqrt{2}s_{\mathrm{I}}(t)\cos(2\pi f_{\mathrm{c}}t) - \sqrt{2}s_{\mathrm{Q}}(t)\sin(2\pi f_{\mathrm{c}}t), \end{aligned} \tag{2.1}$$

where the $\sqrt{2}$ scaling maintains equal energy between $s(t)$ and $s_{\mathrm{pb}}(t)$ and

$$\exp(jx) = e^{jx} = \cos(x) + j\sin(x), \tag{2.2}$$

for real-valued number x where $e = 2.71828\ldots$ is Euler's number. Figure 2.2 illustrates the difference in frequency content between the baseband signal $s(t)$ (centered around 0 Hz) and passband signal $s_{\mathrm{pb}}(t)$ (centered around f_{c}). Here, the complex-baseband representation of the waveform $s(t)$ is adopted as the majority of the methods described in this work do not require an

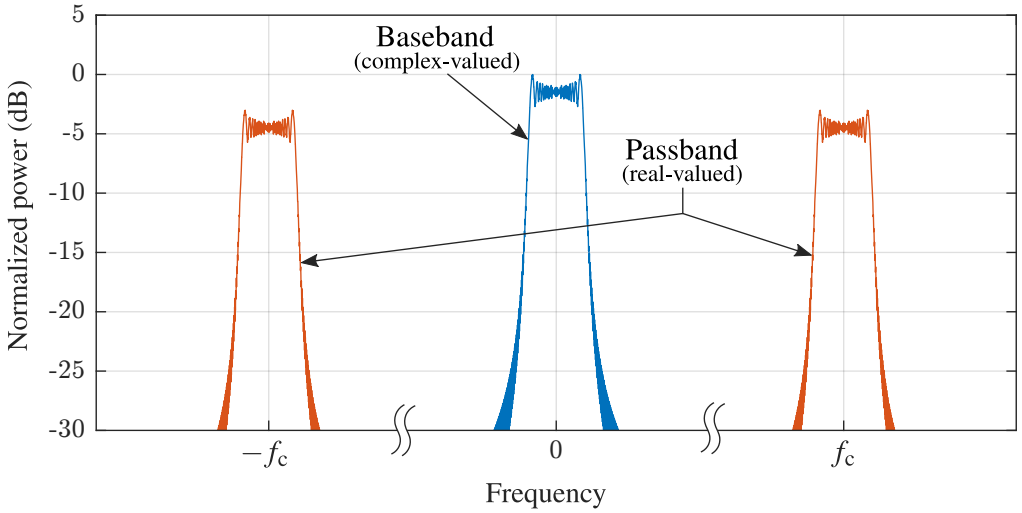

Figure 2.2: Representation of the frequency content of baseband signal $s(t)$ (complex-valued) and passband signal $s_{\text{pb}}(t)$ (real-valued).

absolute center frequency to be defined. Both waveform models ($s(t)$ and $s_{\text{pb}}(t)$) are considered unitless quantities as they do not necessarily pertain to a physical absolute voltage/current.

2.1.1 Baseband Definition

The complex-baseband waveform can be represented as

$$s(t) = u(t)e^{j\psi(t)} \tag{2.3}$$

where $u(t)$ is the positive, real-valued, amplitude envelope and $\psi(t)$ is the phase function. Using this notation, the passband waveform from (2.1) can be written as

$$\begin{aligned} s_{\text{pb}}(t) &= \sqrt{2}\Re\left\{u(t)\exp\left(j\cdot\left(2\pi f_c t + \psi(t)\right)\right)\right\} \\ &= \sqrt{2}u(t)\cos\left(2\pi f_c t + \psi(t)\right) \\ &= \sqrt{2}u(t)\cos\left(\psi_{\text{pb}}(t)\right), \end{aligned} \tag{2.4}$$

where

$$\psi_{\text{pb}}(t) = 2\pi f_{\text{c}} t + \psi(t) \tag{2.5}$$

is the passband phase function.

The waveform can be either continuous-wave (CW) which transmits continuously or pulsed where the waveform is of finite duration and transmitted periodically. For this work only the pulsed operation is considered. For pulse duration T, define $u(t)$ over the interval $t \in [0, T]$ and $u(t) = 0$ for $t \notin [0, T]$, therefore $\psi(t)$ must be defined over $t \in [0, T]$ and is undefined outside this interval. Thus, the total *analytical* energy in the pulsed waveform $s(t)$ can be defined as

$$\mathcal{E}_{\text{s}}^{\text{a}} = \left\| s(t) \right\|_2^2 \tag{2.6}$$

where $\left\| s(t) \right\|_2^2$ is the squared l^2-norm of continuous signal $s(t)$. The squared l^2-norm of arbitrary signal $a(x)$ is defined as[1]

$$\left\| a(x) \right\|_2^2 \triangleq \int_{-\infty}^{\infty} |a(x)|^2 dx < \infty. \tag{2.7}$$

Thus the squared l^2-norm of finite duration waveform $s(t)$ can be represented as

$$\begin{aligned} \left\| s(t) \right\|_2^2 &= \int_{-\infty}^{\infty} |s(t)|^2 dt \\ &= \int_{0}^{T} |s(t)|^2 dt \\ &= \int_{0}^{T} \big(u(t)\big)^2 dt. \end{aligned} \tag{2.8}$$

The superscript $(\bullet)^{\text{a}}$ in (2.6) indicates that the energy is *analytical* and not a *physical* energy (e.g. an energy in Joules)[2] thus is considered unitless. Likewise, the average analytical power is defined

[1] For function with 2 or more dependent variables, the l^2 norm is integrated over time t or frequency f.

[2] In Section 2.2, a physical definition of the transmitted energy is provided.

as the $\mathcal{E}_{\mathrm{s}}^{\mathrm{a}}$ normalized by the pulse duration,

$$\mathcal{P}_{\mathrm{s}}^{\mathrm{a}} = \frac{1}{T}\left\|s(t)\right\|_2^2. \tag{2.9}$$

The spectral response of the pulsed waveform $s(t)$ as a function of continuous frequency f is observed via the Fourier transform $\mathcal{F}\{\bullet\}$,

$$\begin{aligned} S(f) &= \mathcal{F}\{s(t)\} \\ &= \int_{-\infty}^{\infty} s(t)e^{-j2\pi ft}dt \\ &= \int_{0}^{T} s(t)e^{-j2\pi ft}dt, \end{aligned} \tag{2.10}$$

which can be represented by real, positive-valued frequency-domain envelope $U(f)$ and phase function $\Psi(f)$ similar to (2.3) as

$$S(f) = U(f)e^{j\Psi(f)}. \tag{2.11}$$

Likewise, the spectral response of the passband waveform $s_{\mathrm{pb}}(t)$ is

$$S_{\mathrm{pb}}(f) = \int_{0}^{T} s_{\mathrm{pb}}(t)e^{-j2\pi ft}dt, \tag{2.12}$$

where (2.10) and (2.12) are related as

$$S_{\mathrm{pb}}(f) = \frac{1}{\sqrt{2}}\left(S(f-f_{\mathrm{c}}) + S^*(f+f_{\mathrm{c}})\right). \tag{2.13}$$

Applying Parseval's identity [45], the squared-magnitude of $S(f)$ and $S_{\mathrm{pb}}(f)$ have the same total (analytical) energy (from (2.6)) as the waveforms in time,

$$\mathcal{E}_{\mathrm{s}}^{\mathrm{a}} = \left\|s(t)\right\|_2^2 = \left\|S(f)\right\|_2^2 = \left\|s_{\mathrm{pb}}(t)\right\|_2^2 = \left\|S_{\mathrm{pb}}(f)\right\|_2^2, \tag{2.14}$$

and is related to the average analytical power from (2.9) as

$$\mathcal{P}_{\mathrm{s}}^{\mathrm{a}} = \frac{1}{T}\left\|s(t)\right\|_2^2 = \frac{1}{T}\left\|S(f)\right\|_2^2 = \frac{1}{T}\left\|s_{\mathrm{pb}}(t)\right\|_2^2 = \frac{1}{T}\left\|S_{\mathrm{pb}}(f)\right\|_2^2. \tag{2.15}$$

Therefore, $\frac{1}{T}|S(f)|^2$ represents the average power contribution per unit frequency. For notational convenience, the pulse duration normalization $\frac{1}{T}$ is dropped and $|S(f)|^2$ is referred to as the *power spectrum*[3]. The power spectrum is typically represented in decibel scale where

$$|S(f)|^2\ (\mathrm{dB}) = 10\log_{10}\left\{|S(f)|^2\right\}. \tag{2.16}$$

2.1.2 Types of Waveforms

The most basic pulse radar waveform is the rectangular-windowed sinusoid (sometimes referred to as a *simple pulse*). For pulse duration T, the complex-baseband representation of a simple pulse is defined over $t \in [0, T]$ with phase function $\psi_{\mathrm{sp}}(t) = 0$ and amplitude envelope $u_{\mathrm{sp}}(t) = 1$ for $t \in [0, T]$ and $u_{\mathrm{sp}}(t) = 0$ for $t \notin [0, T]$. Using this type of pulse, the expected range resolution ΔR of the probed environment after processing is

$$[\Delta R]_{\mathrm{sp}} = \frac{cT}{2}. \tag{2.17}$$

where $c = 2.99792... \times 10^8$ meters per second is the speed of light in free space. For this work only free space propagation is considered.

Observing (2.17), the only means to improve range resolution using the simple pulse is to reduce the pulse duration. However, the process of reducing the pulse duration also results in a reduction of the total emitted energy limiting the maximum range that can be observed. Therefore, to keep constant total energy the amplitude of the simple pulse must be increased. For example, if we want a reduction of range resolution by two we must shorten the pulse duration by half, and to maintain constant energy we must increase the pulse amplitude by $\sqrt{2}$ (since energy is

[3] In the literature $|S(f)|^2$ is also referred to as the *energy spectral density* [46]. However, to stay consistent with existing publications on radar waveforms, $|S(f)|^2$ is referred to as the *power spectrum* [5].

proportional to the square of the amplitude). This boost in pulse amplitude may not be feasible for physical systems since the power supplied to the radar is finite thus directly limits the achievable radar resolution of a simple pulse.

The bandwidth B of the simple pulse is approximately equal to the inverse of the pulse duration $B \approx 1/T$. Therefore the time-bandwidth product of the pulse (which is considered to be the dimensionality of the pulse) is approximately unity, $BT \approx 1$. By modulating the pulse, either through the amplitude envelope $u(t)$ or phase function $\psi(t)$, the bandwidth of the waveform can be increased independently from the pulse duration. Waveforms with $BT > 1$ are referred to as *pulse compression* waveforms as the pulse duration can be "compressed" into a peak of receive via matched filter processing. The range resolution of a pulse compression waveform is determined by the waveform *bandwidth* as opposed to the pulse duration as

$$[\Delta R]_{\text{pc}} \approx \frac{c}{2B}. \tag{2.18}$$

which can designated without affecting the energy requirements of the radar.

A pulse compression waveform whose modulation is entirely defined via a *continuous* phase function $\psi(t)$ is known as a *frequency modulated* (FM) waveform. For this type of waveform, the amplitude envelope $u(t)$ is typically defined as a rectangular window thus constant amplitude (sometimes referred to as constant envelope or constant modulus). This amplitude design is inherently power efficient as the waveforms can be passed through a high power amplifier (HPA) operating in saturation with low distortion [3]. The property of continuous phase implies that the FM waveform is inherently spectrally contained because it is differentiable with respect to time as

$$\begin{aligned} f_{\text{pb}}(t) &= \frac{1}{2\pi}\frac{d}{dt}\psi_{\text{pb}}(t) \\ &= f_{\text{c}} + \frac{1}{2\pi}\frac{d}{dt}\psi(t) \\ &= f_{\text{c}} + f(t). \end{aligned} \tag{2.19}$$

where

$$f(t) = \frac{1}{2\pi}\frac{d}{dt}\psi(t) \tag{2.20}$$

is the baseband instantaneous frequency and $f_{\text{pb}}(t)$ is the passband instantaneous frequency of the FM waveform. The phase function $\psi(t)$ is related to the instantaneous frequency $f(t)$ through the integral

$$\psi(t) = 2\pi \int_0^t f(\zeta)d\zeta + \psi_0, \tag{2.21}$$

where ψ_0 is the initial phase offset of the waveform, $\psi(0) = \psi_0$.

2.1.2.1 Phase-Coded Pulse

Before discussing different types of FM waveforms, the phase-coded pulse is introduced which is defined entirely by a sequence of N_{c} phase values $\{\psi_0, \psi_1, \ldots, \psi_{N_{\text{c}}-1}\}$. The original phase-coded waveforms were binary thus ψ_n could only take on values $\{0, \pi\}$ though have been extended for polyphase constellations and continuous phase values [5]. The baseband phase-coded waveform is constructed by forming an impulse train of N_{c} complex exponentials each having the phase of the sequence, $\sum_{n=0}^{N_{\text{c}}-1} \delta(t - nT_{\text{c}})e^{j\psi_n}$, where

$$\delta(t) = \begin{cases} 1 & \text{for } t = 0 \\ 0 & \text{otherwise} \end{cases} \tag{2.22}$$

is the impulse function. The impulses are spaced evenly over the pulse duration, separated by duration T_{c} defined as

$$T_{\text{c}} = \frac{T}{N_{\text{c}}}. \tag{2.23}$$

The final stage is a convolution of the weighted impulse train with a shaping filter $w_{\text{c}}(t)$ to form the complex-baseband, time-domain waveform $s_{\text{code}}(t)$ (not necessarily continuous),

$$
\begin{aligned}
s_{\text{code}}(t) &= w_{\text{c}}(t) * \sum_{n=0}^{N_{\text{c}}-1} \delta(t - nT_{\text{c}}) e^{j\psi_n} \\
&= \sum_{n=0}^{N_{\text{c}}-1} w_{\text{c}}(t - nT_{\text{c}}) e^{j\psi_n},
\end{aligned}
\tag{2.24}
$$

where $*$ represents a convolution which for arbitrary signals $a(t)$ and $b(t)$ is equal to

$$
a(t) * b(t) = \int_{-\infty}^{\infty} a(\zeta) b(t - \zeta) d\zeta = \int_{-\infty}^{\infty} a(t - \zeta) b(\zeta) d\zeta. \tag{2.25}
$$

In the frequency domain, the convolution becomes a multiplication of the respective spectrums, $A(f)$ and $B(f)$,

$$
\mathcal{F}\{a(t) * b(t)\} = A(f) B(f). \tag{2.26}
$$

Therefore, the Fourier transform of (2.24) is expressed as

$$
S_{\text{code}}(f) = W_{\text{c}}(f) \bar{S}_{\text{code}}(f), \tag{2.27}
$$

where

$$
\bar{S}_{\text{code}}(f) = \sum_{n=0}^{N_{\text{c}}-1} e^{j\psi_n} e^{-j2\pi f T_{\text{c}} n} \tag{2.28}
$$

is the discrete-time Fourier transform (DTFT) of the phase-coded, complex exponential sequence $\{e^{j\psi_0}, e^{j\psi_1}, \ldots, e^{j\psi_{N_{\text{c}}-1}}\}$. The spectrum in (2.28) is periodic and exists for all frequency, thus the spectral containment of the waveform $s_{\text{code}}(t)$ is entirely controlled via the shaping filter $w_{\text{c}}(t)$ (similar to time domain communications signals carrying information [47]). There are two schools of thought in choosing the function for shaping filter $w_{\text{c}}(t)$: 1) maintaining constant amplitude for saturated amplifier implementation (thus a rectangular function is used), and 2) choosing $w_{\text{c}}(t)$ such that the spectral content of $s_{\text{code}}(t)$ is contained.

The rectangular function (RECT) for $w_{\text{c}}(t)$ is defined as

$$w_{\mathrm{c}}^{\mathrm{r}}(t) = \begin{cases} 1 & \text{for } 0 \le t < T_{\mathrm{c}} \\ 0 & \text{otherwise} \end{cases} . \tag{2.29}$$

The spectral content for this shaping filter is

$$W_{\mathrm{c}}^{\mathrm{r}}(f) = \mathrm{sinc}\left(\pi f T_{\mathrm{c}}\right) e^{-j\pi f T_{\mathrm{c}}} \tag{2.30}$$

where

$$\mathrm{sinc}(x) = \begin{cases} 1 & \text{for } x = 0 \\ \dfrac{\sin x}{x} & \text{otherwise} \end{cases} \tag{2.31}$$

is the sinc-function. To illustrate how to contain the code spectrum[4], the square-root raised cosine (SRRC) filter (denoted $w_{\mathrm{c}}^{\mathrm{s}}(t)$) is used with duration $10T_{\mathrm{c}}$ and roll-off factor of 0.5 shown in Figure 2.3. Figure 2.4 shows the power spectrums $|W_{\mathrm{c}}(f)|^2$ for both the rectangular (blue) and SRRC (red) shaping filters. The cost of constraining the waveform to be constant amplitude has produced large lobes in frequency outside of the band of interest that contain a considerable amount of the waveform energy. It is assumed that on receive the waveform is low-pass filtered and sampled at the code rate $f_{\mathrm{s}} = 1/T_{\mathrm{c}}$ which corresponds to the energy contained between normalized frequencies $fT_{\mathrm{c}} = \pm 0.5$ in Figure 2.4. The DTFT waveform spectrum $\bar{S}_{\mathrm{code}}(f)$ is approximately flat for many well known codes [5], thus the total energy of the filter minus the energy between $fT_{\mathrm{c}} = \pm 0.5$ represents the approximate waveform energy lost during receive processing. For the rectangular filter, normalizing this lost energy by the total filter energy yields

$$\frac{\displaystyle\int_{-\infty}^{\infty} |W_{\mathrm{c}}^{\mathrm{r}}(f)|^2 df - \int_{-0.5T_{\mathrm{c}}}^{0.5T_{\mathrm{c}}} |W_{\mathrm{c}}^{\mathrm{r}}(f)|^2 df}{\displaystyle\int_{-\infty}^{\infty} |W_{\mathrm{c}}^{\mathrm{r}}(f)|^2 df} = 0.2263. \tag{2.32}$$

[4]Many different filters may be used to constrain the spectral footprint. The SRRC function is only one such filter.

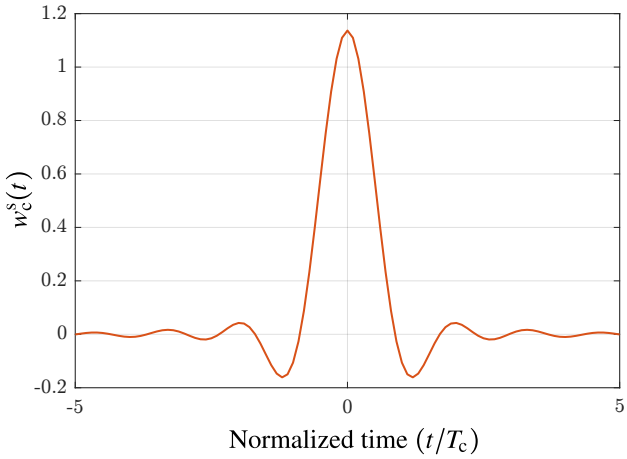

Figure 2.3: Square-root raised-cosine (SRRC) shaping filtering with duration $10T_c$ and roll-off factor of 0.5.

Therefore, the approximate lost energy when using the rectangular shaping filter is 22.63% of the total waveform energy (-1.11 dB). An argument could be made for capturing the entirety of the mainlobe (90% of the energy) for processing. Though, in this case, the captured signal would deviate from the model of the phase sequence from which the waveform was derived. The captured signal would be twice the sampling frequency of the phase code, and, if the code was designed based on some optimality condition, would likely deviate from the expected response.

The phase function of rectangular filtered phase-coded waveform is discontinuous thus does not have a well defined instantaneous frequency $f(t)$. If one were to try and define an instantaneous frequency for this function, it would only take on the three values $\{-\infty, 0, \infty\}$ which no doubt is a contributor to the waveforms large spectral footprint. The instantaneous phase jumps cannot not be achieved by a physical radar transmitter due to a finite bandwidth of the RF components in the transmit chain [3]. This *bandlimiting* takes the form of "dips" in the time envelope of $s_{\text{code}}(t)$ that are dependent on the angle between successive phase code values (more detail in Section 2.2.2).

The out-of-band energy for the rectangular shaping filter is troublesome when considering where in the transmission process it should be dissipated. One extreme case is that all of the energy is reflected and dissipated in the resistive elements of the transmit chain, which for high-powered radar applications $(\sim 10\text{ kW} - 1\text{ MW peak power})$ could result in multiple kilowatts of power to dissipate. The other extreme is to radiate the out-of-band energy into free-space though the

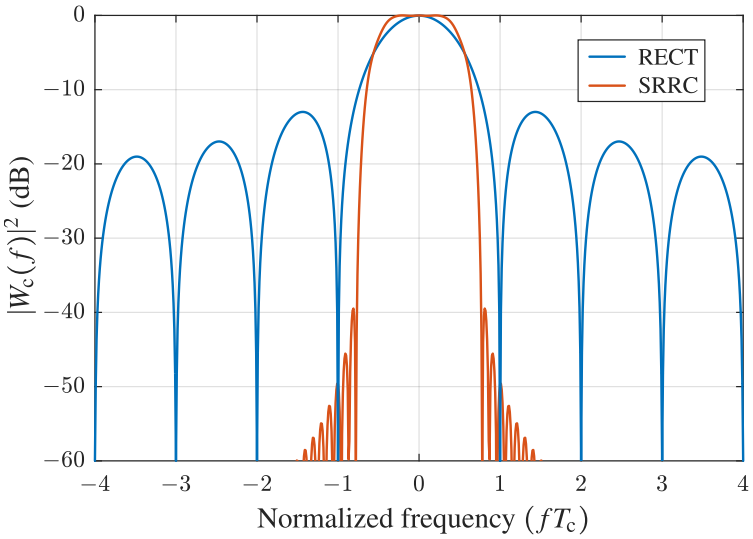

Figure 2.4: Spectrum envelopes $|W_c(f)|^2$ (in dB) versus normalized frequency (fT_c) for rectangular shaping filter $w_c^r(t)$ (blue) and square-root raised cosine shaping filter $w_c^s(t)$ (red).

radar emission is then liable to interfere with adjacent users within the spectrum (e.g. compliance with the radar spectrum engineering criteria (RSEC) mask [48]). In reality, a combination of the two extremes is responsible for the dissipation of the out-of-band energy, though the thought experiment presents an interesting obstacle when considering implementation of these types of waveforms in a high-power radar system.

The spectrum of the SSRC filter in Figure 2.4 (red) displays a much more contained response compared to the rectangular filter. This precise management of the spectrum comes at the cost of an amplitude modulated time envelope of the phase-coded waveform. Figure 2.5 shows the time domain amplitude of a length $N_c = 150$ P4-code whose phase sequence is defined as [5]

$$\psi_{\text{P4},n} = \pi \frac{n^2}{N_c} - \pi n \tag{2.33}$$

for $n \in \{0, 1, \ldots, N_c - 1\}$. The envelope oscillates at the beginning at ends of the pulse where the angle between successive phase code values is the highest. The high amount of amplitude modulation on this waveform prevents high-power amplifier implementation without incurring significant distortion effects (e.g. amplitude compression, intermodulation products, spectral

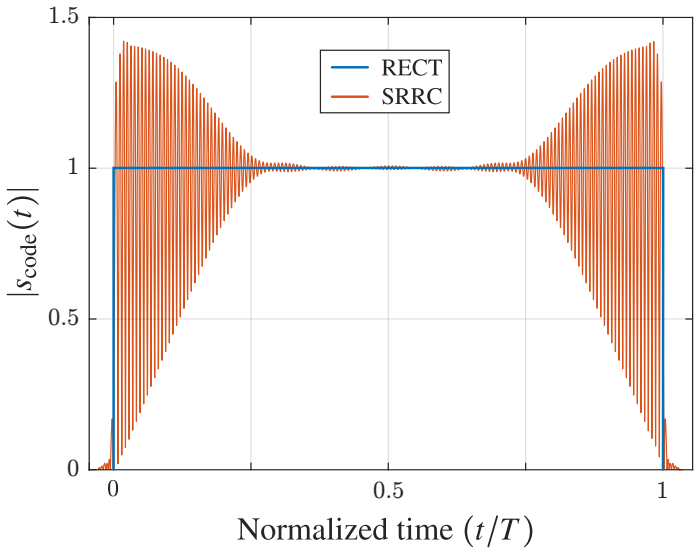

Figure 2.5: Amplitude $|s_{\text{code}}(t)|$ versus normalized time (t/T) for rectangular shaping filter $w_{\text{c}}^{\text{r}}(t)$ (blue) and square-root raised cosine shaping filter $w_{\text{c}}^{\text{s}}(t)$ (red).

regrowth [37]). However, the SRRC-filtered phased-code could be suitable for class-A amplifier applications (i.e. low-power radar) where the requirements of the envelope structure are less stringent. In Section 2.2.2, the bandlimiting effect for a rectangular filtered P4 code is shown to be similar in amplitude shape to that of the SRRC-filtered P4 code.

The fact that the phase-coded waveform is defined via a discrete set of parameters does not inherently produce the ill-effects when considering the signal for high-power radar applications. In fact, a coded structure can be beneficial when optimizing waveforms with respect to a specified cost function (Chapter 5). The culprit is in the how the waveform is modeled, i.e. the conversion from the discrete sequence to the time-domain waveform structure. The code-to-waveform conversion model defined in (2.24) in not generally suitable for high power radar waveform design/optimization as it can only produce waveforms with a large spectral footprint at constant amplitude. In Section 2.1.2.4 another generalized code-to-waveform model is presented that produces FM waveforms whose phase function is continuous thus does not exhibit the spectral broadening of the rectangular-filtered phase-coded waveform.

2.1.2.2 Linear Frequency Modulated Waveform

The most well-known FM waveform is the linear frequency modulated (LFM) waveform which is defined by a linear instantaneous frequency progression over the pulse duration which can either be an increasing (an "up-chirped" LFM) or decreasing (a "down-chirped" LFM) function in time [49]. For bandwidth B, the baseband instantaneous frequencies of the complex-baseband up-chirped and down-chirped LFM waveforms defined over $t \in [0, T]$ are

$$f_{\mathrm{LFM}}(t) = \pm\left(-\tfrac{B}{2} + \tfrac{B}{T}t\right) \tag{2.34}$$

where $(\pm)$ defines the type of LFM ($(+)$ for up-chirp, $(-)$ for down-chirp). Thus, the phase function of the LFM is defined as

$$\begin{aligned} \psi_{\mathrm{LFM}}(t) &= 2\pi \int_0^t f_{\mathrm{LFM}}(\zeta)\, d\zeta + \psi_0 \\ &= \pm 2\pi \cdot \left(-\tfrac{B}{2}t + \tfrac{B}{2T}t^2\right) + \psi_0, \end{aligned} \tag{2.35}$$

where $(\cdot)$ indicates the expressions to the left and right are multiplied and not the function '$\pi(\bullet)$'. Thus, the complex-baseband representation of the LFM waveform is defined as

$$s_{\mathrm{LFM}}(t) = u(t) \exp\left(\pm j \cdot \left(2\pi \cdot \left(-\tfrac{B}{2}t + \tfrac{B}{2T}t^2\right) + \psi_0\right)\right) \tag{2.36}$$

for $t \in [0, T]$. Note that the amplitude envelope $u(t)$ is generally considered to be a rectangular window (constant amplitude) over the duration of the pulse though some tapering can be applied (e.g. a Tukey shading) to control the spectral roll-off properties.

The linear frequency sweep of the instantaneous frequency $f_{\mathrm{LFM}}(t)$ implies that the frequency content of the LFM waveform $S_{\mathrm{LFM}}(f)$ should have an equal power distribution over $\pm 0.5B$ (i.e. a rectangular spectrum). However, the power spectrum $|S_{\mathrm{LFM}}(f)|^2$ only approximates a rectangular window due to finite dimensionality of the waveform. The product of the pulse duration T and bandwidth B defines the dimensionality of the waveform. As this quantity is increased, the better

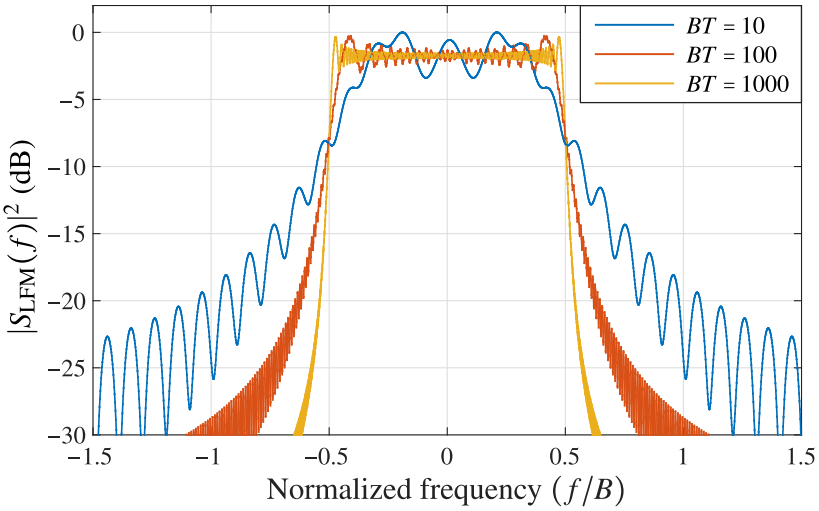

Figure 2.6: Baseband power spectra $|S_{\mathrm{LFM}}(f)|^2$ (in dB) for LFM waveforms of time-bandwidths $BT = 10$ (blue), $BT = 100$ (red), and $BT = 1000$ (yellow).

the approximation of the rectangular spectral shape. To illustrate this effect, Figure 2.6 shows the LFM power spectra $|S_{\mathrm{LFM}}(f)|^2$ for time-bandwidth products $BT \in \{10, 100, 1000\}$. Because the LFM waveform is ubiquitous in radar culture it is used as a baseline case for many of the emission implementations and optimization methods throughout this work.

2.1.2.3 Nonlinear Frequency Modulated Waveform

The LFM waveform is the simplest FM waveform to generate though has undesirable qualities in the estimation of scattering amplitudes. On receive, the received energy is compressed into a peak through a process known as pulse compression (discussed in more detail in Section 2.1.4). The compression response in range is related to the inverse-Fourier transform of the power spectrum $|S(f)|^2$, thus for the LFM would produce a sinc-like response in time of the compressed pulse. The high sidelobe level of the LFM compression response is undesirable as it create ambiguities in time (range) that may mask targets offset in range with a lower power scattering. To alleviate this problem one could taper the waveform in the time domain (non-rectangular amplitude envelope $u(t)$) which is undesirable as it precludes the use of highly efficient amplifiers operating in the saturation region [5]. Shaping of the spectral content (i.e. "spectral tapering") on receive can also be employed though this process removes the received signal energy thus decreasing the

signal-to-noise ratio of profile estimate [5]. The nonlinear FM (NLFM) waveform is designed to spectrally shape the waveform content (as would occur with spectral tapering) without the SNR loss associated with time-envelope or spectral tapering.

The nonlinear FM (NLFM) waveform encompasses the remainder of FM waveforms having nonlinear instantaneous frequency $f(t)$. Thus, the NLFM does not have a strict definition except for the prerequisite of being FM in structure and nonlinear in instantaneous frequency. The traditional method of designing NLFM waveforms is via the *principle of stationary phase* (POSP) [5, 50, 51] which can form the phase function $\psi(t)$ given a time-domain amplitude function $u(t)$ and ideal (desired) frequency-domain envelope $U_{\mathrm{d}}(f)$ for $U_{\mathrm{d}}(f) \geq 0$.

The waveform $s(t)$ can be written in terms of the spectral content $S(f)$ through the inverse Fourier transform, and by using (2.11) can be written as

$$\begin{aligned} s(t) &= \int_{-\infty}^{\infty} S(f) e^{j2\pi ft} df \\ &\approx \int_{-\infty}^{\infty} U_{\mathrm{d}}(f) e^{j(\Psi(f)+2\pi ft)} df. \end{aligned} \tag{2.37}$$

The stationary point in the phase of the integrand is found when

$$\frac{d}{df}\big(\Psi(f) + 2\pi ft\big) = 0. \tag{2.38}$$

Assuming only a single stationary point at $f = \bar{f}$, the solution to (2.38) is expressed as

$$2\pi t = -\Psi'\big(\bar{f}\big), \tag{2.39}$$

where $\Psi'(f) = \frac{d}{df}\Psi(f)$. In [50], is it shown that the amplitude envelope $u(t)$ and desired spectral envelope $U_{\mathrm{d}}(f)$ are related as[5]

[5]Refer to [5, 50] for more information pertaining to the derivation of the POSP for NLFM waveform design.

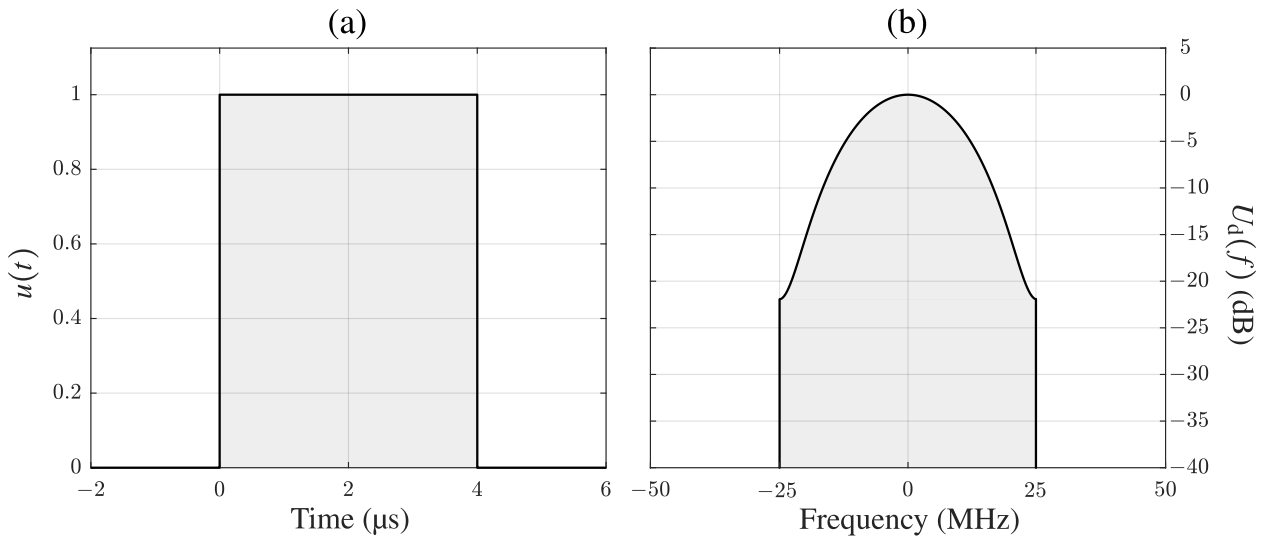

Figure 2.7: NLFM (a) amplitude envelope $u(t)$ of duration $T = 4$ μs and (b) desired spectral window (Hamming) (in dB) for POSP waveform formation.

$$\int_{\infty}^{t} \big(u(\zeta)\big)^2 d\zeta = \int_{-\infty}^{\bar{f}} \big(U_{\mathrm{d}}(\eta)\big)^2 d\eta. \tag{2.40}$$

Defining the left-hand side of the relationship as

$$\mathcal{C}(t) = \int_{\infty}^{t} \big(u(\zeta)\big)^2 d\zeta \tag{2.41}$$

and the right-hand side as

$$\mathcal{D}\big(\bar{f}\big) = \int_{-\infty}^{\bar{f}} \big(U_{\mathrm{d}}(\eta)\big)^2 d\eta, \tag{2.42}$$

the POSP-formed NLFM instantaneous frequency can be defined as

$$f_{\mathrm{POSP}}(t) = \mathcal{D}^{-1}\big(\mathcal{C}(t)\big). \tag{2.43}$$

where $\mathcal{D}^{-1}(\bullet)$ is the inverse function of $\mathcal{D}(\bullet)$. Therefore, the phase function $\psi_{\mathrm{POSP}}(t)$ is found via (2.21), completing the formation of NLFM waveform $s(t) = u(t)\exp\big(j\psi_{\mathrm{POSP}}(t)\big)$.

Figures 2.7(a,b) show an example of a time-domain envelope $u(t)$ and desired frequency-

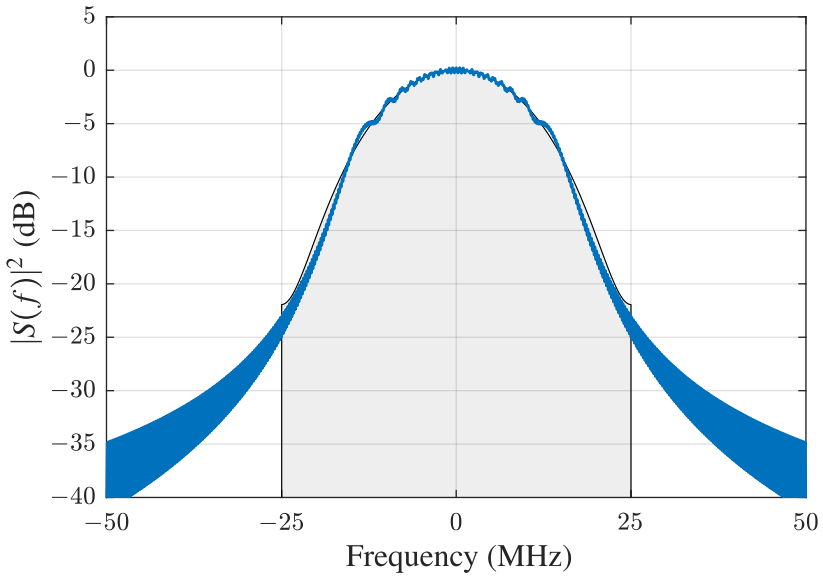

Figure 2.8: NLFM power spectrum $|S(f)|^2$ (in dB) designed via POSP for Hamming spectral window (shown in gray) and rectangular time envelope with duration $T = 4$ µs.

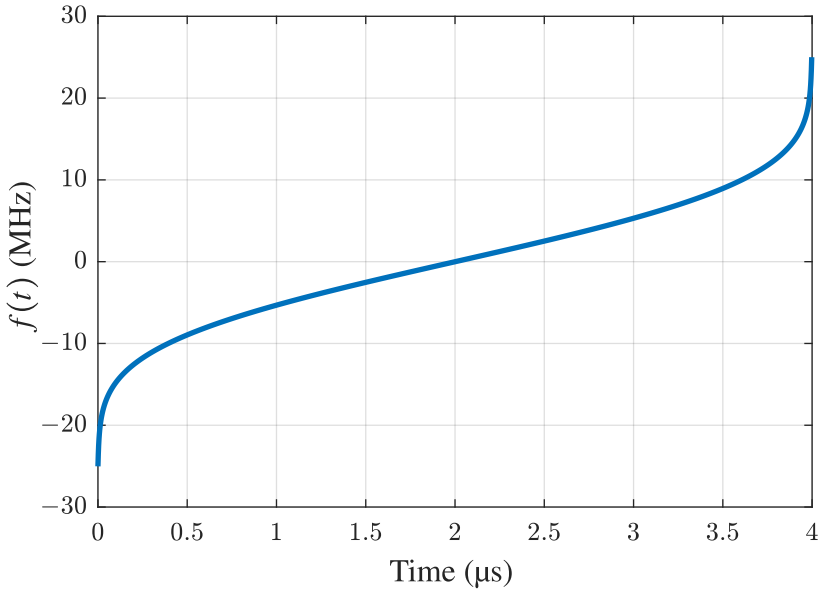

Figure 2.9: Instantaneous frequency $f(t)$ (in MHz) for NLFM waveform designed via POSP for Hamming spectral window and rectangular time envelope with duration $T = 4$ µs.

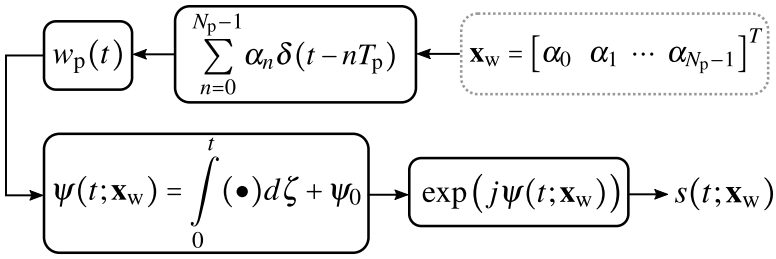

Figure 2.10: Implementation of polyphase-coded FM waveforms

domain envelope $U_{\mathrm{d}}(f)$, respectively. The amplitude envelope in this case is the typical rectangular window with pulse duration set to $T = 4$ µs. The desired spectral window is a Hamming window defined over $f \in [-25, 25]$ MHz and $U_{\mathrm{d}}(f) = 0$ for $f \notin [-25, 25]$ MHz. The NLFM power spectrum designed via the POSP formulation for these initializations in shown in Figure 2.8. Note that the spectrum only approximates the desired window, however this approximation is improved with increasing time-bandwidth product[6]. The NLFM instantaneous frequency is shown in Figure 2.9. The amount of time the instantaneous frequency "spends" around a particular frequency directly relates to the power level of $|S(f)|^2$ at that frequency. Thus the large slopes at the beginning and ends of $f(t)$ produce the tapered structure of the NLFM power spectrum.

2.1.2.4 Polyphase-coded Frequency Modulated Waveform

The Polyphase-Coded FM (PCFM) waveform implementation arises from Continuous Phase Modulation (CPM) used in communications which is employed for aeronautical telemetry [52], deep-space communications [53], and the Bluetooth™ wireless standard [54]. The CPM implementation produces continuous, constant-amplitude waveforms that are power efficient and spectrally well-contained [38]. This waveform framework was originally designed to convert phase codes (Section 2.1.2.1) into FM waveforms (thus the namesake). The successive difference between a phase code sequence produces a discrete sequence of N_{p} parameters $\mathbf{x}_{\mathrm{w}} = [\alpha_0 \quad \alpha_1 \cdots \alpha_{N_{\mathrm{p}}-1}]^T$ (for $(\bullet)^T$ the transpose operation) that represent piecewise instantaneous angular frequencies.

[6]This property is reminiscent of the LFM rectangular spectral approximation. In fact, for a rectangular windowed desired spectral envelope the POSP formulation produces an LFM waveform.

The PCFM implementation (shown in Figure 2.10) forms a length N_p impulse train with time separation T_p, where the nth impulse is weighted by α_n for $n \in \{0, 1, \ldots, N_\mathrm{p}-1\}$ and

$$T_\mathrm{p} = \frac{T}{N_\mathrm{p}}. \tag{2.44}$$

The weighted impulse train is then convolved with the rectangular shaping filter[7]

$$w_\mathrm{p}(t) = \begin{cases} \frac{1}{T_\mathrm{p}} & \text{for } 0 < t \leq T_\mathrm{p} \\ 0 & \text{otherwise} \end{cases}. \tag{2.45}$$

The filtered impulse train is then integrated to form the continuous phase function, $\psi(t; \mathbf{x}_\mathrm{w})$ which can be simplified to the form

$$\begin{aligned} \psi(t; \mathbf{x}_\mathrm{w}) &= \int_0^t w_\mathrm{p}(\zeta) * \sum_{n=0}^{N_\mathrm{p}-1} \alpha_n \delta(\zeta - nT_\mathrm{p}) d\zeta + \psi_0 \\ &= \int_0^t \sum_{n=0}^{N_\mathrm{p}-1} \alpha_n w_\mathrm{p}(\zeta - nT_\mathrm{p}) d\zeta + \psi_0 \\ &= \sum_{n=0}^{N_\mathrm{p}-1} \alpha_n \int_0^t w_\mathrm{p}(\zeta - nT_\mathrm{p}) d\zeta + \psi_0 \\ &= \sum_{n=0}^{N_\mathrm{p}-1} \alpha_n h_n(t) + \psi_0 \end{aligned} \tag{2.46}$$

defined over $t \in [0, T]$ for pulse duration $T = N_\mathrm{p} T_\mathrm{p}$, where

$$h_n(t) = \int_0^t w_\mathrm{p}(\zeta - nT_\mathrm{p}) d\zeta \tag{2.47}$$

is the nth PCFM basis function[8]. Figure 2.11 displays the time-shifted ramp structure of the nth PCFM basis function $h_n(t)$ and time-shifted shaping function $w_\mathrm{p}\left(t - nT_\mathrm{p}\right)$. The summation of

[7] For CPM systems, the shaping filter $w_\mathrm{p}(t)$ can be any function that integrates to a specified constant [47], however in this work only a rectangular function defined over duration T_p that integrates to unity is considered.

[8] In Chapter 5, the functions $h_n(t)$ for $n \in \{0, 1, \ldots, N_\mathrm{p}-1\}$ from (2.47) are generalized to any set of basis functions of which the PCFM basis set is one example.

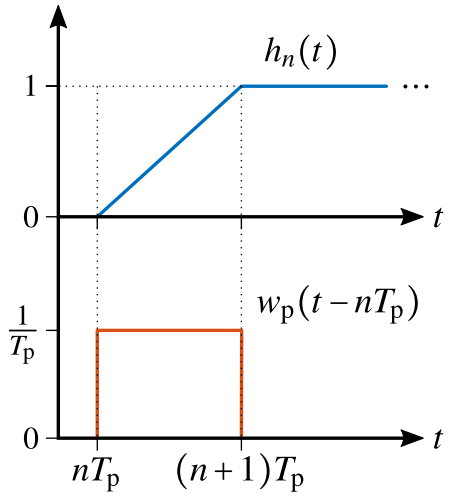

Figure 2.11: Illustration of the nth PCFM basis function $h_n(t)$ and time-shifted shaping function $w_p(t-nT_p)$.

basis functions in (2.46) equates to a piecewise linear phase function. Thus, the continuous FM waveform $s(t;\mathbf{x}_w)$ is

$$\begin{aligned} s(t;\mathbf{x}_w) &= u(t)\exp\left(j\psi(t;\mathbf{x}_w)\right) \\ &= u(t)\exp\left(j\cdot\left(\sum_{n=0}^{N_p-1}\alpha_n h_n(t)+\psi_0\right)\right) \end{aligned} \tag{2.48}$$

for $t\in[0,T]$ and $s(t;\mathbf{x}_w)=0$ for $t\notin[0,T]$. The amplitude envelope $u(t)$ is included for generality however is typically assumed to be unit amplitude $\left(u(t)=1\right)$ to maintain power efficiency (discussed further in Section 2.2.2). Using (2.20), the instantaneous frequency of the PCFM waveform can be represented as

$$f(t;\mathbf{x}_w)=\frac{1}{2\pi}\sum_{n=1}^{N_p}\alpha_n w_p(t-nT_p). \tag{2.49}$$

Note that for any instant in time the instantaneous frequency is defined using only one of the parameters α_n for $n\in\{0,1,\ldots,N_p-1\}$ $\left(\text{i.e. } f(t)=\frac{1}{2\pi}\frac{\alpha_n}{T_p} \text{ for } nT_p<t\le(n+1)T_p\right)$.

In Chapter 5, this code-to-FM waveform framework is generalized to include any arbitrary basis such that the values contained in $\mathbf{x}_w$ are no longer associated with instantaneous frequency values. This new general waveform structure, entitled Coded-FM (or CFM), allows for the phase

function of the FM waveform to be comprised of any chosen basis with the PCFM waveform being a single subset of the CFM waveform.

2.1.3 Bandwidth

To this point the bandwidth B has been presented as a generic bandwidth with no set definition. However, because we are considering waveforms of finite pulse duration, the spectral content of the waveform theoretically extends over the entirety of the electromagnetic spectrum. While defining the bandwidth as infinite might be technically correct, it would also be meaningless. In reality, the spectral footprint of the waveform beyond a certain frequency range will be attenuated to a point where one can define an effective bandwidth. The guidelines for defining this frequency range are different depending on the application of the waveform. For this reason, there are many interpretations of bandwidth considered in practice.

The definition of bandwidth used in the LFM definition from (2.36) is the *analytical bandwidth* which will now be denoted as B_{a} and defined as

$$B_{\mathrm{a}} = \max_t \{f(t)\} - \min_t \{f(t)\}. \tag{2.50}$$

While this bandwidth definition is informative for the LFM waveform, it is not sufficient to describe the spectral behavior of other FM waveforms (particularly as a function of frequency). Because the instantaneous frequency of the LFM waveform is a linear function, one would expect the baseband spectral response to be flat over the analytical bandwidth B_{a}. However, for more complicated instantaneous frequency functions the allocation of power in the frequency domain is not so obvious thus requiring a more thorough analysis.

The two remaining bandwidth definitions considered here are derived from the power spectrum $|S(f)|^2$: one based on power beneath maximum spectral power and one based on percentage of average power. The *3 dB bandwidth* (or *half-power bandwidth*), denoted $B_{3\mathrm{dB}}$, defines the frequency range when the power spectrum drops by half its maximum. If $|S(f)|^2$ is unimodal

(or general shape approximates unimodal) there are two frequencies that meet this criteria: a frequency greater than the maximum point (denoted f^{hi}) and a frequency less than the maximum point (denoted f^{lo}). These frequencies can be found by solving the equation

$$\frac{|S(f)|^2}{\max\limits_f \{|S(f)|^2\}} = 0.5. \tag{2.51}$$

Thus the 3 dB bandwidth is defined as

$$B_{3\text{dB}} = f^{\text{hi}} - f^{\text{lo}}. \tag{2.52}$$

Alternatively, bandwidth can be defined as containing a certain percentage of the average power. Here, the 98% average power (for short 98% power) bandwidth is considered and can be found by solving

$$\int_{-B_{98\%}/2}^{B_{98\%}/2} |S(f)|^2 df = 0.98 \int_{-\infty}^{\infty} |S(f)|^2 df \tag{2.53}$$

for $B_{98\%}$, the 98% power bandwidth.

The time-bandwidth product of a waveform is a common measure of the waveform dimensionality and is defined simply as the product of the waveform bandwidth and the waveform pulse duration. However, depending on the spectral content of a waveform, the bandwidth can vary considerably based on which definition is used. In general, the time-bandwidth product (denoted BT) is defined according to the 3 dB bandwidth of the waveform,

$$BT = B_{3\text{dB}} T. \tag{2.54}$$

The range resolution (discussed further in Section 2.1.4) is dependent on 3 dB bandwidth of the waveform thus is a natural choice for defining the waveform dimensionality. Although, if either of the bandwidths B_{a} or $B_{98\%}$ are more suited for describing the waveform bandwidth for a certain design, it is perfectly valid to define the waveform dimensionality based on these

quantities. Thus, we can define the analytical time-bandwidth as $B_{\mathrm{a}}T$ and the 98% time-bandwidth as $B_{98\%}T$. However, the short-hand definition of time-bandwidth 'BT' is designated for the 3 dB time-bandwidth, $B_{3\mathrm{dB}}T$.

The ratio of the waveform bandwidth to the passband center frequency, called the *fractional bandwidth*, provides a metric on the width of the waveform's spectral occupancy relative to its 'average' frequency. Similar to the time-bandwidth product, the fractional bandwidth is a function of chosen bandwidth definition. Thus, three fractional bandwidths can be defined using the three bandwidth interpretations as

$$[\%\mathrm{BW}]_{\mathrm{a}} = \frac{B_{\mathrm{a}}}{f_{\mathrm{c}}}, \tag{2.55}$$

for the analytical bandwidth B_{a},

$$[\%\mathrm{BW}]_{3\mathrm{dB}} = \frac{B_{3\mathrm{dB}}}{f_{\mathrm{c}}}, \tag{2.56}$$

for the 3 dB bandwidth $B_{3\mathrm{dB}}$, and

$$[\%\mathrm{BW}]_{98\%} = \frac{B_{98\%}}{f_{\mathrm{c}}}, \tag{2.57}$$

for the 98% bandwidth $B_{98\%}$, where $0 \leq \%\mathrm{BW} \leq 2$. A radar waveform is considered narrowband for $[\%\mathrm{BW}]_{3\mathrm{dB}} < 1\%$, wideband for $1\% \leq [\%\mathrm{BW}]_{3\mathrm{dB}} < 25\%$, and ultra-wideband (UWB) for $[\%\mathrm{BW}]_{3\mathrm{dB}} \geq 25\%$ [55].

To illustrate the difference in these bandwidth definitions, the power spectra for an up-chirped LFM and nonlinear FM (NLFM) waveform are generated each having a rectangular amplitude envelope $u(t)$ and the same analytical bandwidths B_{a} and pulse duration T whose product is the analytical time-bandwidth, $B_{\mathrm{a}}T = 200$. Figure 2.12 shows the instantaneous frequencies $f(t)$ for the LFM and NLFM waveforms. The NLFM waveform is the same that was described in Figures 2.8 and 2.9. The LFM instantaneous frequency response is linearly increasing while the NLFM response forms a "sideways-S" curve shape which produces a less ambiguous pulse compressed

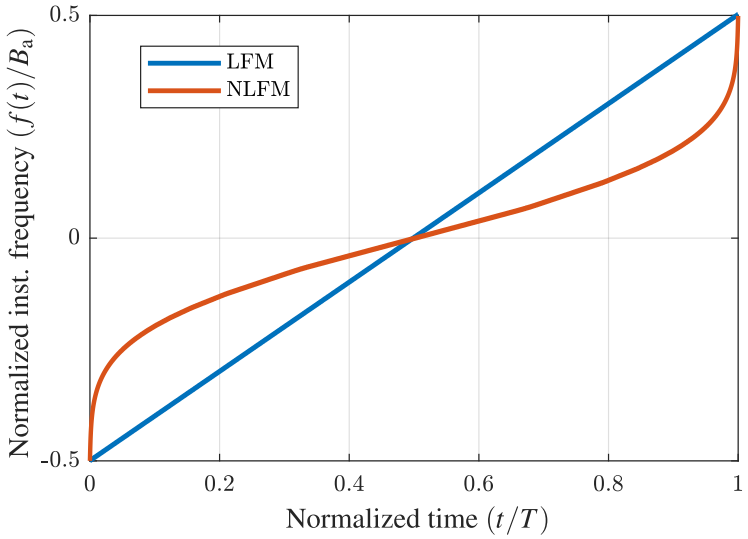

Figure 2.12: Normalized instantaneous frequency $(f(t)/B_a)$ versus normalized time (t/T) for LFM (blue) and NLFM (red).

response (discussed in Section 2.1.4).

Figure 2.13 displays the bandwidths B_{3dB}, $B_{98\%}$, and B_a on the power spectra $|S(f)|^2$ of the LFM and NLFM waveforms. The approximately flat spectrum of the LFM waveform, shown in Figure 2.13(a), results in nearly identical bandwidths for all three definitions with B_{3dB} and $B_{98\%}$ being 94.6% and 98% of the B_a, respectively[9]. The power spectrum for the NLFM waveform (Figure 2.13(b)) follows a Gaussian-like shape where B_{3dB} and $B_{98\%}$ are now 34.3% and 66% of B_a, respectively. The time-bandwidth products for these two waveforms are $[B_{3dB}T]_{LFM} = 189.2$ for the LFM waveform and $[B_{3dB}T]_{NLFM} = 68.6$ for the NLFM waveform (~2.76 times less than the LFM) even though these two waveform have identical analytical time-bandwidth products. The disparity between these bandwidth definitions indicates that for non-LFM waveforms a single bandwidth definition may not sufficient to fully describe the spectral behavior of the waveform.

[9]Because the three definitions are nearly identical for the LFM, the distinction between the bandwidth definitions is typically not discussed.

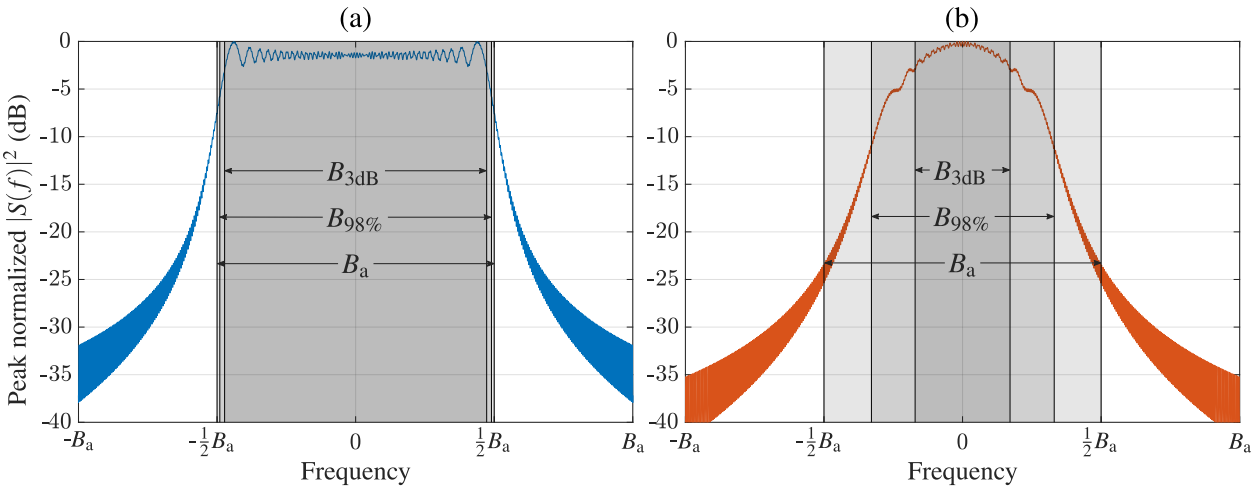

Figure 2.13: Bandwidths $B_{3\text{dB}}$, $B_{98\%}$, and B_{a} illustrated on the power spectra $|S(f)|^2$ (in dB) versus normalized frequency (f/B_{a}) for (a) LFM and (b) NLFM.

2.1.4 Pulse Compression

In the radar receiver, the scattered returns are filtered to increase the signal-to-noise ratio (SNR) of the raw signal and, if a pulse compression waveform is used, compress the scattered pulse into a peak with range resolution defined in (2.18). A rise in SNR amounts to increased detection probability and estimation performance during processing. The filter that maximizes the SNR is called the *matched filter* which is derived from of the waveform $s(t)$. In Section 2.4.2, a derivation is provided (for discretized signals) that proves that the matched filter is the only filter that maximizes the SNR post-correlation. If the noise is assumed to be white and stationary (which is typically the case) the optimal filter for maximization of the SNR is the waveform itself,

$$w_{\text{MF}}(t) = \gamma s(t), \tag{2.58}$$

scaled with some arbitrary constant γ. Thus expected matched filter output $\chi_{\text{a}}(\tau)$ for $s(t)$ (as a function of continuous delay τ) takes the form of the correlation function,

$$\begin{aligned}\chi_{\mathrm{a}}(\tau) &= \int_0^T w_{\mathrm{MF}}^*(t-\tau)s(t)dt \\ &= \gamma \int_0^T s^*(t-\tau)s(t)dt,\end{aligned} \tag{2.59}$$

where $(\bullet)^*$ is the complex-conjugate, which for a complex variable $x = \Re\{x\} + j\Im\{x\}$, is defined as

$$x^* = \Re\{x\} - j\Im\{x\}. \tag{2.60}$$

Therefore, the correlation operation of a waveform with itself (known as the *autocorrelation*) represents the nominal expected response of an isolated scatter in the absence of noise and interference, thus is a standard tool to rate the performance of a waveform. It is useful to scale (2.59) such that the peak is unity ($\chi_{\mathrm{a}}(0) = 1$), thus (2.58) is normalized by the analytical energy $\mathcal{E}_{\mathrm{s}}^{\mathrm{a}}$ as

$$\begin{aligned}w_{\mathrm{MF}}(t) &= \frac{1}{\mathcal{E}_{\mathrm{s}}^{\mathrm{a}}} s(t) \\ &= \frac{s(t)}{\left\| s(t) \right\|_2^2}.\end{aligned} \tag{2.61}$$

Therefore, the autocorrelation function of complex-baseband waveform $s(t)$ is defined as

$$\chi_{\mathrm{a}}(\tau) = \frac{1}{\left\| s(t) \right\|_2^2} \int_0^T s^*(t-\tau)s(t)dt, \tag{2.62}$$

which is related to the power spectrum $|S(f)|^2$ through the inverse Fourier transform as

$$\chi_{\mathrm{a}}(\tau) = \frac{1}{\left\| s(t) \right\|_2^2} \int_{-\infty}^{\infty} |S(f)|^2 \exp(-j2\pi f\tau)df. \tag{2.63}$$

Only finite duration waveforms are considered therefore the autocorrelation function extends over delays $-T < \tau < T$ and is zero outside of these limits.

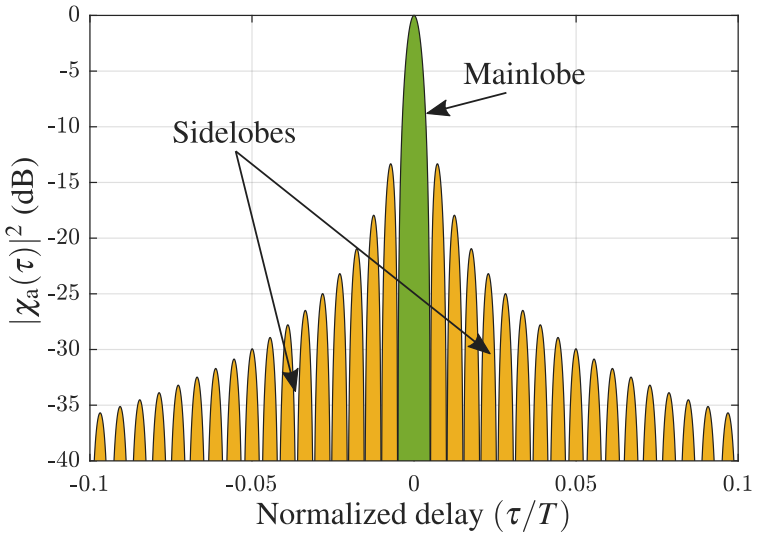

Figure 2.14: Illustration of mainlobe (green) and sidelobes (yellow) for autocorrelation response $|\chi_a(\tau)|^2$ of LFM waveform for normalized delays $\tau/T \in (-0.1\ 0.1)$.

The autocorrelation processing from (2.62) compresses most (but not all) of the energy into a duration $\tau \in [-\Delta\tau\ \Delta\tau]$ of $\chi_a(\tau)$ where $\Delta\tau << T$. This region is called the *mainlobe* of the autocorrelation where $\Delta\tau$ is the peak-to-null width of the mainlobe. The remaining energy contained in the autocorrelation function is manifested in a sidelobe structure that extends from $\Delta\tau < |\tau| < T$ in $\chi_a(\tau)$. Figure 2.14 illustrates the mainlobe (green) and sidelobes (yellow) of a portion of the autocorrelation function for the LFM waveform whose power spectrum is displayed in Figure 2.13(a). The characterization of the sidelobes of $|\chi_a(\tau)|^2$ is significant as the peaks could mask the mainlobe response of a smaller scattering target offset in delay (range).

The quality of a given waveform is generally determined via some measure of its autocorrelation [3], with the most well-known being peak sidelobe level (PSL) which is the ratio of the peak sidelobe level to the peak of the mainlobe defined as

$$\text{PSL} = \max_{\tau}\left\{\frac{|\chi_a(\tau)|^2}{|\chi_a(0)|^2}\right\} \quad \text{for } \tau \in [\Delta\tau, T] \tag{2.64}$$

and integrated sidelobe level (ISL) which is the ratio of energy in the sidelobe to energy in the mainlobe defined as

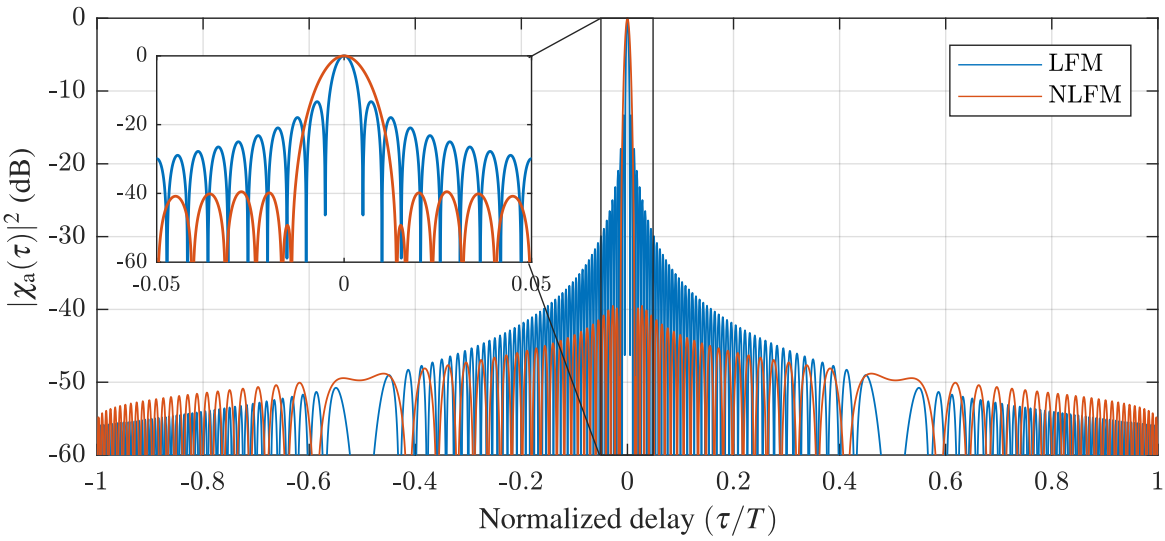

Figure 2.15: Autocorrelation response $|\chi_a(\tau)|^2$ for LFM (blue) and NLFM (red) waveforms.

$$\text{ISL} = \frac{\displaystyle\int_{-T}^{-\Delta\tau} |\chi_a(\tau)|^2 dt + \int_{\Delta\tau}^{T} |\chi_a(\tau)|^2 dt}{\displaystyle\int_{-\Delta\tau}^{\Delta\tau} |\chi_a(\tau)|^2 dt}. \tag{2.65}$$

The lower the quantities are in (2.64) and (2.65), the more desirable the autocorrelation response.

Figure 2.15 shows the squared-magnitude (in dB) of the autocorrelation responses for the LFM (blue) and NLFM (red) waveforms whose power spectra are displayed in Figure 2.13. The PSL (in dB) of the autocorrelation of the NLFM waveform is ~−39.5 dB while the PSL of the LFM autocorrelation is ~−13.2 dB. The ISL for the NLFM waveform is ~−26.7 dB while the ISL of the LFM is ~−9.7 dB. The approximate rectangular shape of the LFM power spectrum results in a sinc-like structure in the time-domain while the lower sidelobe response of the NLFM waveform can be attributed to the rounded spectral shape from Figure 2.13(b).

The peak-to-null width of the autocorrelation function in range is known as the *Rayleigh resolution* defined as ΔR [56]. For two-way free-space propagation, this resolution is related to the peak-to-null duration $\Delta\tau$ as

$$\Delta R = \frac{c\Delta\tau}{2}. \tag{2.66}$$

The peak-to-null mainlobe width $\Delta\tau$ of the autocorrelation is approximately equal to the inverse of the 3 dB bandwidth $B_{3\text{dB}}$ as

$$\Delta\tau \approx \frac{1}{B_{3\text{dB}}}. \tag{2.67}$$

Inserting (2.67) into (2.66), the dependence of the range resolution on the waveform 3 dB bandwidth from (2.18) is revealed as

$$\Delta R \approx \frac{c}{2B_{3\text{dB}}}. \tag{2.68}$$

Note the similarity between (2.66) and the range resolution of a simple pulse from (2.17). The range resolution is decreased by a factor of $T/\Delta\tau$ (known as the *pulse compression ratio*) which represents the improvement in resolution due to modulation of the pulse. Using (2.67), the pulse compression ratio $T/\Delta\tau$ is approximately equal to the time-bandwidth product,

$$\frac{T}{\Delta\tau} \approx B_{3\text{dB}}T = BT. \tag{2.69}$$

Figure 2.16 shows the autocorrelation mainlobes of the LFM (blue) and NLFM (red) versus normalized delay τ/T. In each figure, the normalized peak-to-null width $\Delta\tau/T$ is displayed (the inverse of the pulse compression ratio $T/\Delta\tau$). The normalized peak-to-null mainlobe duration for the LFM and NLFM waveforms is $[\Delta\tau/T]_{\text{LFM}} = 0.00502$ and $[\Delta\tau/T]_{\text{NLFM}} = 0.01405$. From (2.69), $\Delta\tau/T$ is approximately equal to the inverse of the time-bandwidth product $[B_{3\text{dB}}T]^{-1}$. Therefore, according to the measured normalized peak-to-null mainlobe widths the time-bandwidths of the waveforms should be $[BT]_{\text{LFM}} \approx 199$ for LFM and $[BT]_{\text{NLFM}} \approx 71.2$ for NLFM. In Section 2.1.3, the time-bandwidths for the example LFM and NLFM waveforms were calculated using the actual 3 dB bandwidth measurements as $[BT]_{\text{LFM}} = 189.2$ and $[BT]_{\text{NLFM}} = 68.6$, respectively.

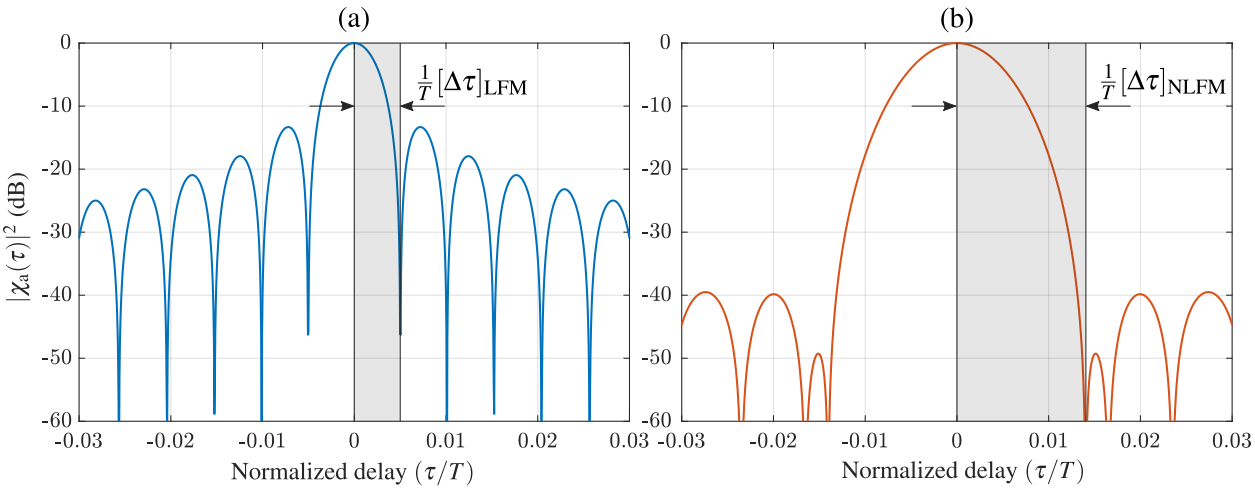

Figure 2.16: Rayleigh range resolution ΔR of autocorrelation response $|\chi_{\text{a}}(\tau)|^2$ for (a) LFM and (b) NLFM.

This approximate relationship is helpful in Chapter 5 where optimization methods are used to design waveforms of approximate time-bandwidth products by fixing the normalized peak-to-null autocorrelation mainlobe widths within the optimization process.

2.1.5 Delay-Doppler Ambiguity Function

A scatterer moving at some radial velocity v with respect to a monostatic radar[10] will impart a Doppler shift of the center frequency of the passband waveform $s_{\text{pb}}(t)$ by some amount

$$f_{\text{D}} = \frac{2v}{c} f_{\text{c}}, \tag{2.70}$$

known as the *Doppler frequency*[11], where $v > 0$ represents a scatterer moving towards the radar. Assuming the passband waveform model $s_{\text{pb}}(t)$ from (2.4) is the reflected signal, the Doppler shifted waveform model can be expressed as

[10] A monostatic radar is one whose transmitter and receiver are collocated and operate using the same antenna via a circulator or transmit/receive (T/R) switch.

[11] The derivation of the Doppler frequency f_{D} from the radial velocity v is shown in Section 2.3.3.

$$
\begin{aligned}
s_{\mathrm{pb}}(t, f_{\mathrm{D}}) &= \sqrt{2}u(t)\cos\left(2\pi\cdot(f_{\mathrm{c}}+\tfrac{2v}{c}f_{\mathrm{c}})t+\psi(t)\right) \\
&= \sqrt{2}u(t)\cos\left(2\pi\cdot(f_{\mathrm{c}}+f_{\mathrm{D}})t+\psi(t)\right) \\
&= \sqrt{2}u(t)\cos\left(2\pi f_{\mathrm{c}}t+\psi(t)+2\pi f_{\mathrm{D}}t\right) \\
&= \sqrt{2}u(t)\cos\left(\psi_{\mathrm{pb}}(t)+\psi_{\mathrm{D}}(t)\right),
\end{aligned}
\tag{2.71}
$$

where

$$
\psi_{\mathrm{D}}(t) = 2\pi f_{\mathrm{D}}t \tag{2.72}
$$

is the Doppler phase function. The term $\psi_{\mathrm{D}}(t)$ distorts the phase of waveform $s_{\mathrm{pb}}(t)$ and, depending on the size of the product $f_{\mathrm{D}}T$ and modulation of the waveform via $u(t)$ and $\psi(t)$, may significantly affect the correlation response during receive processing.

Define the complex-baseband representation of (2.71) as

$$
\begin{aligned}
s(t, f_{\mathrm{D}}) &= u(t)e^{j\psi(t)}e^{j\psi_{\mathrm{D}}(t)} \\
&= s(t)e^{j\psi_{\mathrm{D}}(t)}.
\end{aligned}
\tag{2.73}
$$

The expected distortion can be predicted by correlating (2.73) with the non-Doppler-shifted copy of the baseband waveform $s(t)$ (from (2.3)) as

$$
\begin{aligned}
\chi_{\mathrm{D}}(\tau, f_{\mathrm{D}}) &= \frac{1}{\|s(t)\|_2^2}\int_0^T s^*(t-\tau)s(t, f_{\mathrm{D}})dt \\
&= \frac{1}{\|s(t)\|_2^2}\int_0^T s^*(t-\tau)s(t)e^{j\psi_{\mathrm{D}}(t)}dt \\
&= \frac{1}{\|s(t)\|_2^2}\int_0^T s^*(t-\tau)s(t)e^{j2\pi f_{\mathrm{D}}t}dt.
\end{aligned}
\tag{2.74}
$$

The expression in (2.74) is referred to as the *delay-Doppler ambiguity function* and is equivalent the the autocorrelation function from (2.62) when $f_{\mathrm{D}} = 0$,

$$\chi_{\mathrm{D}}(\tau, f_{\mathrm{D}} = 0) = \chi_{\mathrm{a}}(\tau). \tag{2.75}$$

The delay-Doppler ambiguity function has a maximum at

$$|\chi_{\mathrm{D}}(0,0)| = 1 \geq |\chi_{\mathrm{D}}(\tau, f_{\mathrm{D}})|, \tag{2.76}$$

and has constant energy,

$$\int_{-\infty}^{\infty}\int_{-\infty}^{\infty} |\chi_{\mathrm{D}}(\tau, f_{\mathrm{D}})|^2 d\tau df_{\mathrm{D}} = \text{constant}. \tag{2.77}$$

Refer to [5] for proofs of these properties.

For pulse duration T, the Doppler phase term $\psi_{\mathrm{D}}(t)$ from (2.72) rotates $2\pi f_{\mathrm{D}} T$ radians during the pulse. The sensitivity of $s(t)$ to this Doppler shift is dependent on its specific modulation of the waveform. For example, consider the LFM and NLFM waveforms defined in Section 2.1.3. The delay-Doppler ambiguity response for the LFM and NLFM waveforms as a function of normalized delay (τ/T) and normalized Doppler $(f_{\mathrm{D}}/B_{\mathrm{a}})$ are shown in Figures 2.17 and 2.18, respectively. As the Doppler frequency increases, both waveforms retain a high correlation with the non-Doppler-shifted waveform $s(t)$. The high correlation is depicted by the ridges that are formed across the delay-Doppler space. These ridges indicate that these waveforms are *Doppler tolerant* because the correlation response degrades gracefully with increasing Doppler shift. The sidelobe structure of the LFM waveform stay relatively constant when Doppler shifted, however the NFLM waveform experiences an increased sidelobe level off of the zero-Doppler cut (a well-known drawback to NLFM waveforms [57, 58]).

An example of a waveform that is not Doppler tolerant is an FM noise waveform. One such waveform is the pseudo-random optimized FM (PRO-FM) waveform which is optimized using an alternating projections approach to generate a pulsed, constant amplitude waveform whose spectral content closely matches a desired spectral mask [59] (PRO-FM has also been demonstrated for an FM continuous-wave (FMCW) implementation [60, 61]). Consider a PRO-FM noise waveform

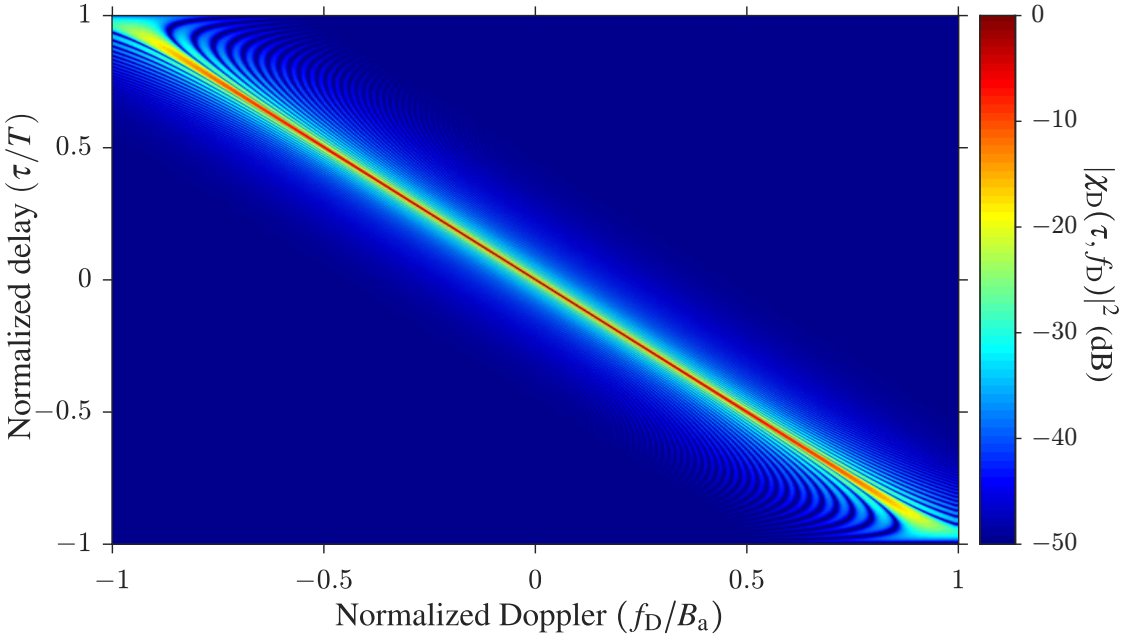

Figure 2.17: Ambiguity function $|\chi_D(\tau, f_D)|^2$ (in dB) via (2.74) versus normalized delay (τ/T) and normalized Doppler (f_D/B_a) of LFM waveform with analytical time-bandwdith $B_aT = 200$.

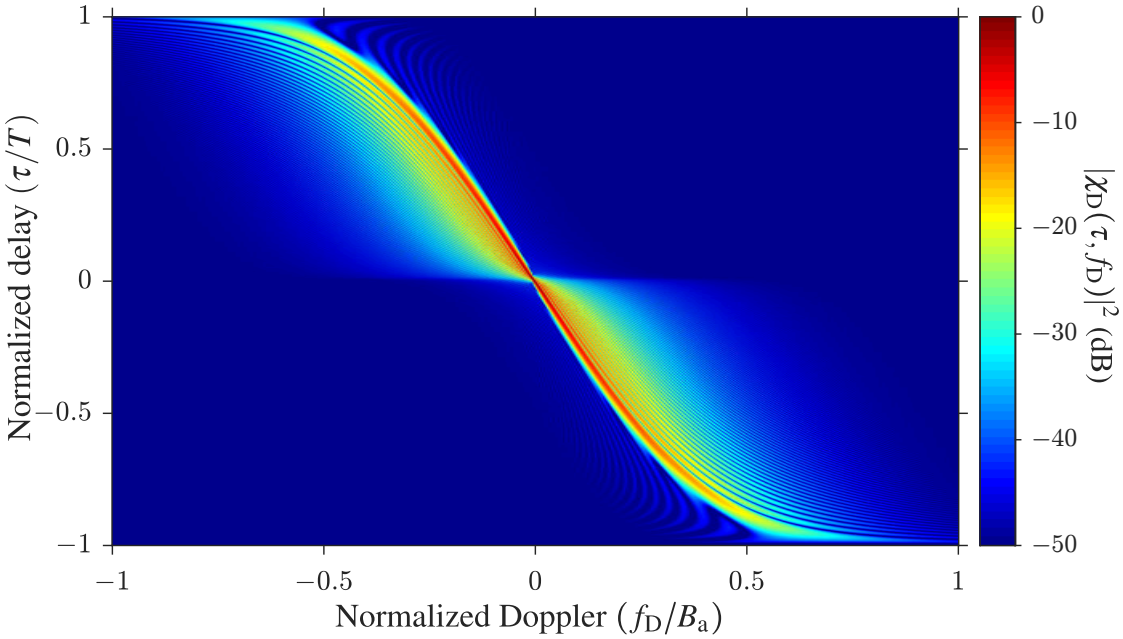

Figure 2.18: Ambiguity function $|\chi_D(\tau, f_D)|^2$ (in dB) via (2.74) versus normalized delay (τ/T) and normalized Doppler (f_D/B_a) of an NLFM waveform with analytical time-bandwdith $B_aT = 200$.

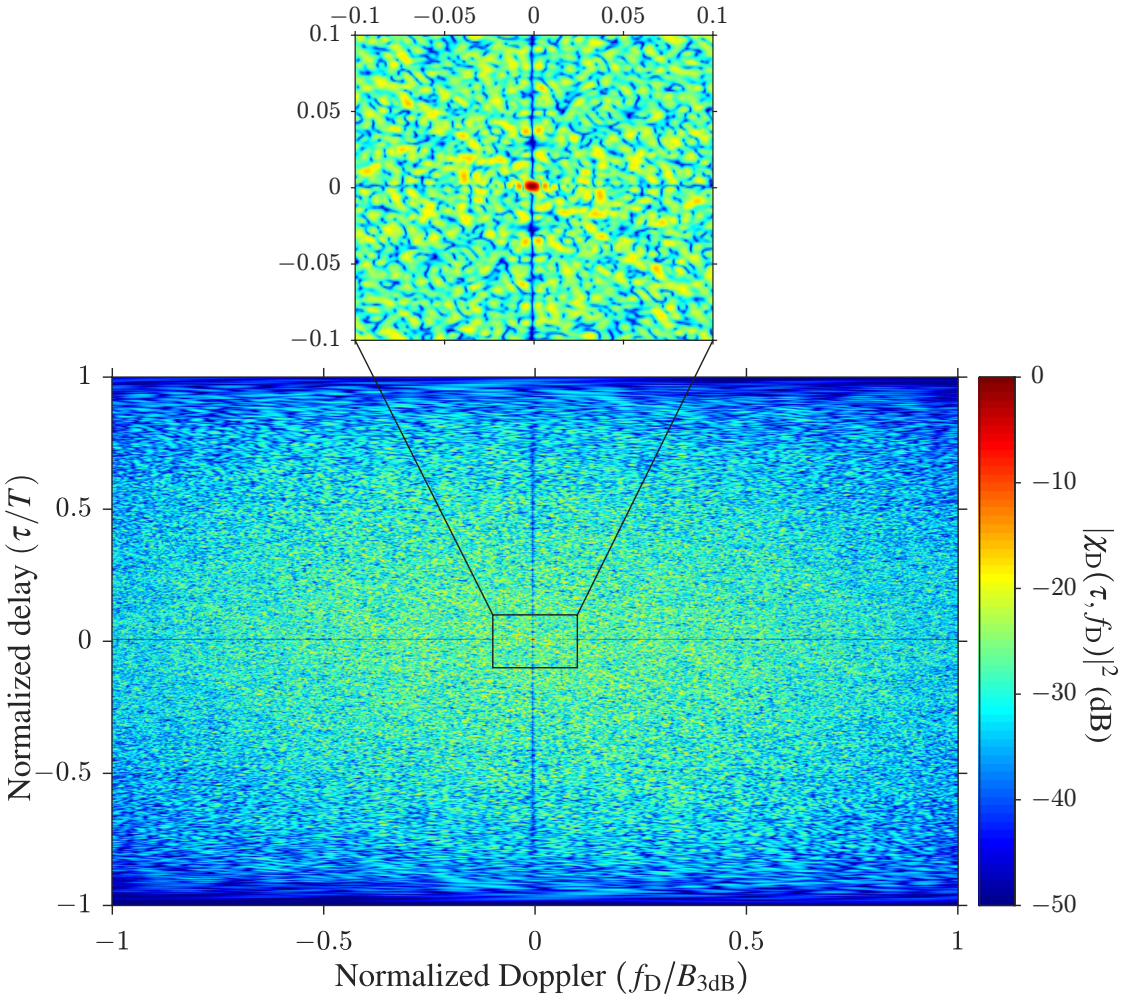

Figure 2.19: Ambiguity function $|\chi_{\mathrm{D}}(\tau, f_{\mathrm{D}})|^2$ (in dB) via (2.74) versus normalized delay (τ/T) and normalized Doppler $(f_{\mathrm{D}}/B_{3\mathrm{dB}})$ of an FM noise waveform with time-bandwdith $BT = 200$.

with time-bandwidth $BT = 200$ matched to a Gaussian spectral template. Figure 2.19 shows the ambiguity function $|\chi_{\mathrm{D}}(\tau, f_{\mathrm{D}})|^2$ (in dB) for this waveform. Note how the peak correlation response at $\chi_{\mathrm{D}}(0,0)$ drops off significantly with increasing Doppler shift. Therefore a target moving off zero Doppler that highly correlates with the LFM and NLFM may not correlate with the FM noise waveform. This effect can be lessened by incorporating a bank of filters on receive each of them matched to a different Doppler shifted version of the waveform.

2.2 The Transmission

A radar waveform can be created via digital-to-analog conversion (DAC) techniques (e.g. arbitrary waveform generator (AWG), direct digital synthesizer (DDS)) or analog waveform generation techniques (e.g. swept/CW local oscillators (LO), amplified thermal noise). The complexity of the waveforms design/optimized in this work require precise control of the amplitude and phase functions of the waveform currently not feasible for analog-only waveform generation. Therefore, we will limit our discussion to analytical waveform designs and DAC waveform implementation. Therefore, the pulsed complex-baseband waveform $s(t)$ can be realized at passband via either analog or digital up-conversion (see (2.1)). The digital method would require a DAC with a high enough sampling rate to adequately represent the waveform at the center frequency.

Once generated, the continuous passband signal $s_{\mathrm{pb}}(t)$ is then sent through amplification and filtering stages and subsequently transmitted into free-space through an antenna designed for the proper band and polarization[12]. A majority of the transmit chain of RF components can be characterized via their frequency response thus can be modeled as a linear time-invariant (LTI) system. However, to maximize power efficiency of the transmission, the waveform is typically sent through a high-powered amplifier (HPA) operating in saturation which is a nonlinear system which cannot be fully characterized via a frequency response. Therefore, the analytical waveform $s(t)$ can experience significant distortion if not properly designed. However, if the waveform

[12]This simple description of a radar transmit chain does not do justice to the complexities of (and ongoing research into) radar transmitters [56]. Though this distilled description allows for a general mindfulness of transmitter effects when designing/optimizing radar emissions.

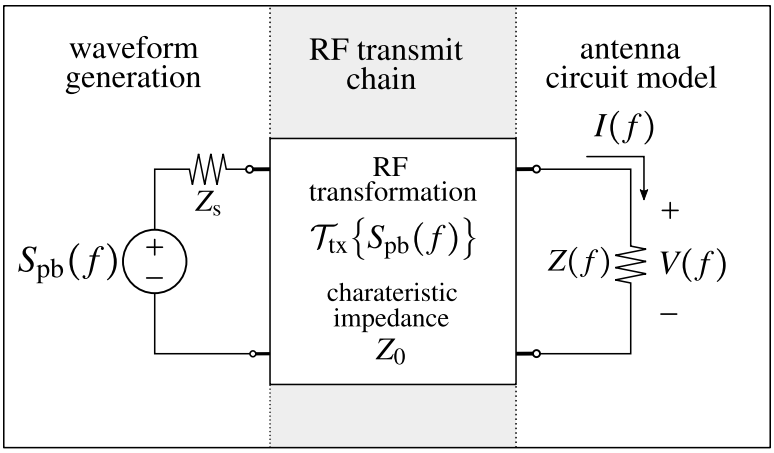

Figure 2.20: Equivalent circuit model of the radar transmitter.

is FM (i.e. constant envelope and spectrally contained) the nonlinear distortion imparted onto waveform is reduced thus is the standard choice for high-power applications. In Section 2.2.2, an in-depth analysis is provided to illustrate exactly why the FM waveform is suited for high-powered amplification.

2.2.1 Equivalent Circuit Model

Figure 2.20 displays an equivalent circuit of the transmission process, where Z_s is the source impedance, $Z(f)$ is the frequency-dependent antenna terminal impedance, Z_0 is the characteristic impedance of the transmission line, $V(f)$ and $I(f)$ are the antenna terminal voltage and current as a function of freqeuncy, and $\mathcal{T}_{tx}\{S_{pb}(f)\}$ is transformation (linear and/or nonlinear) of the waveform $S_{pb}(f)$ inflicted by the RF chain. The circuit model is implemented in the frequency domain to capture the frequency-dependent effects of the system[13]. It is assumed that Z_s and Z_0 have a flat frequency response over some chosen definition of the waveform bandwidth (see Section 2.1.3) and are real-valued and equal (matched source),

$$\Re\{Z_s\} = \Re\{Z_0\} \tag{2.78}$$

[13]Note that transient responses of the system are assumed to be negligible, though it may be possible to rework the circuit model in Figure 2.20 within the Laplace-domain to capture these effects.

and

$$\Im\{Z_s\} = \Im\{Z_0\} = 0. \tag{2.79}$$

Thus the transmission line is lossless and there is no reflected energy at the source. The antenna impedance $Z(f)$ is not assumed to be a matched load thus the reflection coefficient at the antenna terminals as a function of frequency is defined as

$$\Gamma(f) = \frac{Z(f) - Z_s}{Z(f) + Z_s} \tag{2.80}$$

which can assume the values, $0 \leq |\Gamma(f)| \leq 1$. Note that this is a system parameter and is not dependent on the excitation $S_{pb}(f)$. The reflection coefficient can also be defined in terms of forward (towards the antenna) and backward (away from the antenna) traveling wavefronts as

$$\Gamma(f) = \frac{V^-(f)}{V^+(f)}, \tag{2.81}$$

where $V^+(f)$ and $V^-(f)$ are the Fourier transform of the forward and backward traveling waves ($V^+(t)$ and $V^-(t)$) at the antenna terminals. It is assumed that any reflected energy at the antenna terminals gets dissipated in the source impedance and/or resistive components of the RF chain. The reflection coefficient in (2.81) (sometimes referred to as the $\mathcal{S}_{11}$ scattering parameter) is measured using a network analyzer. Another variant called *return loss* discards the phase information of (2.81) and focuses on the magnitude squared. The return loss is typically measured in decibels and is a positive quantity defined as

$$\mathrm{RL}(f) = -10\log_{10}|\Gamma(f)|^2. \tag{2.82}$$

All three quantities describe the radiation efficiency of an antenna. A return loss of 10 dB or higher ($|\Gamma(f)| \leq \sqrt{0.1}$) is typically considered satisfactory. In Section 3.2 we will return to the scattering parameter formulation to describe the mutual coupling between antenna elements in an array.

The spectral content forward traveling wave is defined as the RF transformation of ideal waveform spectral content $S_{\text{pb}}(f)$,

$$V^{+}(f) = \mathcal{T}_{\text{tx}}\{S_{\text{pb}}(f)\}, \tag{2.83}$$

which transforms the unitless signal $S_{\text{pb}}(f)$ into a voltage. The operator $\mathcal{T}_{\text{tx}}\{\bullet\}$ can include linear effects (e.g. filtering, gain, attenuation, dispersion) and/or nonlinear effects (e.g. harmonics, intermodulation products, compression, waveform generation nonlinearities[14], and memory effects). Rearranging (2.81), the spectral content of the backward traveling wave is defined as

$$V^{-}(f) = \Gamma(f)\, V^{+}(f). \tag{2.84}$$

The voltage and current at the antenna terminals can then be found as a combination of the forward and backward traveling wavefronts (also at the antenna terminals) as[15]

$$\begin{aligned} V(f) &= V^{+}(f) + V^{-}(f) \\ &= V^{+}(f)\big(1 + \Gamma(f)\big) \end{aligned} \tag{2.85}$$

and

$$\begin{aligned} I(f) &= \frac{V^{+}(f) - V^{-}(f)}{Z_0} \\ &= \frac{V^{+}(f)}{Z_0}\big(1 - \Gamma(f)\big). \end{aligned} \tag{2.86}$$

2.2.1.1 Time-Domain Representation

Taking the inverse-Fourier transform of the reflection coefficient $\Gamma(f)$,

$$\Gamma(t) = \mathcal{F}^{-1}\{\Gamma(f)\}, \tag{2.87}$$

[14]Even though $\mathcal{T}_{\text{tx}}\{\bullet\}$ is defined as the RF chain distortion, the waveform generation distortion effects are also included to simplify the model.

[15]Note the expressions (2.80) – (2.86) are only true at the antenna terminals and are not generally true throughout the RF chain.

the backward traveling wave (in the time domain) can be expressed via convolution of the foward traveling wave ($V^+(t) = \mathcal{F}^{-1}\{V^+(f)\}$) and the time-domain reflection coefficient,

$$V^-(t) = V^+(t) * \Gamma(t). \tag{2.88}$$

Note that the signals $\Gamma(t)$, $V^+(t)$, and $V^-(t)$ are all real-valued signals as their corresponding spectrums are conjugate symmetric (i.e. $\Gamma(-f) = \Gamma^*(f)$) which has a real-valued time-domain response (i.e. all signals are represented at passband). Note that this must be true as the impedance variation with frequency $Z(f)$ is derived from physical measurements and $V^+(f)$ and $V^-(f)$ are derived from $S_{\text{pb}}(f)$ which is the Fourier transform of real-valued signal $s_{\text{pb}}(t)$. Using $V^-(t)$ and $V^+(t)$, the expression in antenna terminal voltage and current in the time-domain can be represented as

$$\begin{aligned} V(t) &= V^+(t) + V^-(t) \\ &= V^+(t) + V^+(t) * \Gamma(t) \\ &= V^+(t) * \big(\delta(t) + \Gamma(t)\big) \end{aligned} \tag{2.89}$$

and

$$\begin{aligned} I(t) &= \frac{V^+(t) - V^-(t)}{Z_0} \\ &= \frac{V^+(t)}{Z_0} * \big(\delta(t) - \Gamma(t)\big). \end{aligned} \tag{2.90}$$

Through inspection it can be seen that (2.89) and (2.85) and (2.90) and (2.86) are Fourier transform pairs. Because the analysis is performed at passband, $V(t)$ and $I(t)$ are both real-valued signals oscillating at center frequency f_{c}. Therefore, it is useful to define $V(t)$, $I(t)$, $V^+(t)$, and $V^-(t)$ in terms of their respective complex-valued envelopes, $V_{\text{e}}(t)$, $I_{\text{e}}(t)$, $V_{\text{e}}^+(t)$, and $V_{\text{e}}^-(t)$, as

$$V(t) = \Re\{V_{\text{e}}(t)e^{j2\pi f_{\text{c}}t}\}, \tag{2.91}$$

$$I(t) = \Re\left\{I_{\mathrm{e}}(t)e^{j2\pi f_c t}\right\}, \tag{2.92}$$

$$V^{+}(t) = \Re\left\{V_{\mathrm{e}}^{+}(t)e^{j2\pi f_c t}\right\}, \tag{2.93}$$

and

$$V^{-}(t) = \Re\left\{V_{\mathrm{e}}^{-}(t)e^{j2\pi f_c t}\right\}. \tag{2.94}$$

The complex envelopes are related as

$$V_{\mathrm{e}}(t) = V_{\mathrm{e}}^{+}(t) + V_{\mathrm{e}}^{-}(t) \tag{2.95}$$

and

$$I_{\mathrm{e}}(t) = \frac{V_{\mathrm{e}}^{+}(t) - V_{\mathrm{e}}^{-}(t)}{Z_0}. \tag{2.96}$$

To avoid confusion between the signals in the time and frequency domains, below is a list of the Fourier transform pairs between the two domains[16]:

$$\Gamma(t) \overset{\mathcal{F}}{\longleftrightarrow} \Gamma(f)$$

$$V(t) \overset{\mathcal{F}}{\longleftrightarrow} V(f)$$

$$I(t) \overset{\mathcal{F}}{\longleftrightarrow} I(f)$$

$$V^{+}(t) \overset{\mathcal{F}}{\longleftrightarrow} V^{+}(f)$$

$$V^{-}(t) \overset{\mathcal{F}}{\longleftrightarrow} V^{-}(f)$$

[16]The functions $\Gamma(t)$, $V(t)$, $I(t)$, $V^{+}(t)$, and $V^{-}(t)$ are all real-valued (passband) expressions.

2.2.1.2 Instantaneous Powers, Average Powers, and Energies

The instantaneous dissipated power (in Watts) in the antenna is found by taking the product of the terminal voltage $V(t)$ and the terminal current (recall these are both real-valued signals). This power represents the transmitted into free-space though also includes ohmic losses within the antenna. Here, it is assumed that *all* of the dissipated power is converted into transmitted power (zero ohmic losses in the antenna), therefore the instantaneous dissipated energy is equivalent to the instantaneous transmitted energy defined as

$$\mathcal{P}_{\text{tx}}(t) = V(t)I(t). \tag{2.97}$$

Using (2.89), (2.90), (2.93), and (2.94), the instantaneous power $\mathcal{P}_{\text{tx}}(t)$ can be written in terms of the complex-envelopes of the forward and backward traveling voltages as

$$\begin{aligned}\mathcal{P}_{\text{tx}}(t) &= \tfrac{1}{Z_0}\left(\left(V^{+}(t)\right)^2 - \left(V^{-}(t)\right)^2\right) \\ &= \frac{|V_{\text{e}}^{+}(t)|^2 - |V_{\text{e}}^{-}(t)|^2}{2Z_0} + \Re\left\{\frac{\left(V_{\text{e}}^{+}(t)\right)^2 - \left(V_{\text{e}}^{-}(t)\right)^2}{2Z_0} e^{j4\pi f_{\text{c}} t}\right\}.\end{aligned} \tag{2.98}$$

The first term in (2.98) is the slowly varying transmitted power typically associated with the *average* transmitted power. The second term is a oscillating factor at twice the center frequency $2f_{\text{c}}$.

The power *incident* on the antenna terminals (sometimes referred to as the available power) is dictated by the forward traveling voltage $V^{+}(t)$ and the characteristic impedance of the RF chain Z_0,

$$\begin{aligned}\mathcal{P}_{\text{tx}}^{+}(t) &= \frac{|V^{+}(t)|^2}{Z_0} \\ &= \frac{|V_{\text{e}}^{+}(t)|^2}{2Z_0} + \Re\left\{\frac{\left(V_{\text{e}}^{+}(t)\right)^2}{2Z_0} e^{j4\pi f_{\text{c}} t}\right\}.\end{aligned} \tag{2.99}$$

The terms in (2.99) comprise half of the terms for (2.98). The other half are the *reflected* power terms that make up the instaneous reflected power $\mathcal{P}_{\text{tx}}^{-}(t)$ defined as the difference between the

incident and transmit

$$\begin{aligned}\mathcal{P}_{\text{tx}}^{-}(t) &= \mathcal{P}_{\text{tx}}^{+}(t) - \mathcal{P}_{\text{tx}}(t) \\ &= \frac{|V^{-}(t)|^2}{Z_0}\end{aligned} \tag{2.100}$$

which is equal to the instantaneous power of the backward traveling voltage (towards the generator). In terms of the complex envelopes, $\mathcal{P}_{\text{tx}}^{-}(t)$ is expressed as

$$\begin{aligned}\mathcal{P}_{\text{tx}}^{-}(t) &= \frac{|V^{-}(t)|^2}{Z_0} \\ &= \frac{|V_{\text{e}}^{-}(t)|^2}{2Z_0} + \Re\left\{\frac{(V_{\text{e}}^{-}(t))^2}{2Z_0} e^{j4\pi f_c t}\right\}.\end{aligned} \tag{2.101}$$

The total transmitted energy (in Joules) for a single pulse can be found though a simple integration of the instantaneous transmitted power,

$$\begin{aligned}\mathcal{E}_{\text{tx}} &= \int_{-\infty}^{\infty} \mathcal{P}_{\text{tx}}(t)dt \\ &= \frac{\left\|V^{+}(t)\right\|_2^2 - \left\|V^{-}(t)\right\|_2^2}{Z_0} \\ &= \frac{\left\|V_{\text{e}}^{+}(t)\right\|_2^2 - \left\|V_{\text{e}}^{-}(t)\right\|_2^2}{2Z_0}.\end{aligned} \tag{2.102}$$

Note that the second term from (2.98) disappears due to the oscillation between positive and negative powers[17]. Likewise, the total incident and reflected energies for a single pulse are found via integration of (2.99) and (2.101), respectively, as

[17]Note that the "negative" power from the oscillating term just reduces the total instantaneous power $\overline{\mathcal{P}}_{\text{tx}}(t)$ when combined with the first term preventing the instantaneous power from becoming negative which would break conservation of energy.

$$\begin{aligned}\mathcal{E}_{\text{tx}}^{+} &= \int_{-\infty}^{\infty} \mathcal{P}_{\text{tx}}^{+}(t)dt \\ &= \frac{\left\|V^{+}(t)\right\|_2^2}{Z_0} \\ &= \frac{\left\|V_{\text{e}}^{+}(t)\right\|_2^2}{2Z_0}\end{aligned} \tag{2.103}$$

and

$$\begin{aligned}\mathcal{E}_{\text{tx}}^{-} &= \int_{-\infty}^{\infty} \mathcal{P}_{\text{tx}}^{-}(t)dt \\ &= \frac{\left\|V^{-}(t)\right\|_2^2}{Z_0} \\ &= \frac{\left\|V_{\text{e}}^{-}(t)\right\|_2^2}{2Z_0}.\end{aligned} \tag{2.104}$$

Just as in (2.102), the oscillating term disappears leaving the integration of the power in the slowly varying envelopes, $V_{\text{e}}^{+}(t)$ and $V_{\text{e}}^{-}(t)$. The transmitted power (during transmission of the pulse) is found by averaging the energy over the pulse duration as

$$\begin{aligned}\mathcal{P}_{\text{tx}} &= \frac{\mathcal{E}_{\text{tx}}}{T} \\ &= \frac{\left\|V^{+}(t)\right\|_2^2 - \left\|V^{-}(t)\right\|_2^2}{Z_0 T} \\ &= \frac{\left\|V_{\text{e}}^{+}(t)\right\|_2^2 - \left\|V_{\text{e}}^{-}(t)\right\|_2^2}{2Z_0 T}.\end{aligned} \tag{2.105}$$

The corresponding incident and reflected average powers are respectively defined as

$$\begin{aligned}\mathcal{P}_{\text{tx}}^{+} &= \frac{\mathcal{E}_{\text{tx}}^{+}}{T} \\ &= \frac{\left\|V^{+}(t)\right\|_2^2}{Z_0 T} \\ &= \frac{\left\|V_{\text{e}}^{+}(t)\right\|_2^2}{2Z_0 T}\end{aligned} \tag{2.106}$$

and

$$\begin{aligned}\mathcal{P}_{\text{tx}}^{-} &= \frac{\mathcal{E}_{\text{tx}}^{-}}{T} \\ &= \frac{\left\|V^{-}(t)\right\|_2^2}{Z_0 T} \\ &= \frac{\left\|V_{\text{e}}^{-}(t)\right\|_2^2}{2Z_0 T}.\end{aligned} \tag{2.107}$$

It is also useful to define the spectral powers per unit frequency for the transmitted, incident, and reflected signals as

$$\bar{\mathcal{P}}_{\text{tx}}(f) = \frac{|V^{+}(f)|^2\left(1-|\Gamma(f)|^2\right)}{Z_0}, \tag{2.108}$$

$$\bar{\mathcal{P}}_{\text{tx}}^{+}(f) = \frac{|V^{+}(f)|^2}{Z_0}, \tag{2.109}$$

and

$$\bar{\mathcal{P}}_{\text{tx}}^{-}(f) = \frac{|\Gamma(f)|^2|V^{+}(f)|^2}{Z_0}. \tag{2.110}$$

Note that these representations of power are <u>not</u> the Fourier transform of the instantaneous powers $\mathcal{P}_{\text{tx}}(t)$, $\mathcal{P}_{\text{tx}}^{+}(t)$, and $\mathcal{P}_{\text{tx}}^{-}(t)$, thus are demarcated by the bar, $\bar{\bullet}$. However, like the instantaneous signals, the total energies can be obtained by integrating the signals over their domain (in this case frequency), (i.e. $\mathcal{E}_{\text{tx}} = \left\|\bar{\mathcal{P}}_{\text{tx}}(f)\right\|_2^2$). The power spectrums (2.108) – (2.110) represent the time-harmonic average powers for frequency f. This form is useful when defining the spectral power per unit frequency.

2.2.2 Transmit Chain Distortion

It is important to design the analytical waveform model $s(t)$ (and/or $s_{\text{pb}}(t)$) in such a way that the forward traveling voltage $V^{+}(t)$ is a desired response. One way you can do this is by modeling the

entirety of the RF transmit chain such that $V^+(t)$ can be predicted from the waveform model $s_{\text{pb}}(t)$. If the desired signal is known, $s_{\text{pb}}(t)$ can be *predistorted* such that $V^+(t)$ is the desired response after the modeled distortion occurs [31–34]. However, depending on the linearity of the amplifier, accuracy/sensitivity of the amplifier model, and signal structure of $s(t)$, predistortion may not recreate the signal with the fidelity required to achieve the desired radar performance. Though predistortion techniques using the memory polynomial model have been shown to highly linearize non-constant amplitude radar waveforms [31–33][18]. Another method of designing waveforms is to not try and compensate for the distortion, but choose a waveform model that is known to be robust to nonlinear effects in RF transmit chains (i.e. FM waveforms). By imposing the restrictions of constant amplitude amplitude $u(t)$ and continuous-time phase function $\psi(t)$, the waveform can be designed such that linear distortions (e.g. bandlimiting) or nonlinear distortions (e.g. harmonics, intermodulation products) do minimal harm to the signal structure of of the ideal waveform.

2.2.2.1 Linear Distortion

The ideal RF transmitter transformation $\mathcal{T}_{\text{tx}}\{\bullet\}$ from (2.83) is a scaled and delay-shifted copy of the waveform. In the frequency-domain, this ideal transformation (assuming zero propagation delay within the transmit chain) is depicted as,

$$V^+(f) = w_1 S_{\text{pb}}(f), \qquad \textit{(ideal model)} \tag{2.111}$$

where w_1 is a real-valued scalar that transforms the unitless signal $S_{\text{pb}}(f)$ into a voltage. This transformation model captures only scaling (gain/attenuation) and time-shifting of the passband signal. Generalizing the model from (2.111), assume only *linear* properties are present in the RF transmit chain. Linear effects include but are not limited to filtering, dispersion, and linear-region amplification. Like any linear model, it can be described via a frequency response (denoted $W_{\text{tx}}(f)$ in this case) which, when applied to the ideal waveform $S_{\text{pb}}(f)$, produces the expected response

[18] Specifically, the compensation effect that is discussed is "open-loop" predistortion. Closed-loop distortion compensation through a hardware-in-the-loop or transmitter-in-the-loop configuration has been shown to be more effective as the compensation does not rely on a model though is high in complexity [34, 62, 63].

of the system model,

$$V^{+}(f) = W_{\text{tx}}(f)S_{\text{pb}}(f). \qquad \textit{(linear-only model)} \tag{2.112}$$

The linear distortion model is a simple tool that can capture many of the distortions in an RF transmit chain. However, that does not mean it cannot impart significant distortion onto the waveform via *bandlimiting*.

A simple experiment was conducted to compare the linear distortions imparted to a rectangular-filtered P4 coded signal of length $N_{\text{c}} = 150$ (generated using the method from Section 2.1.2.1) and an LFM waveform of time-bandwidth product $BT = 150$. Both signals were realized at a center frequency of $f_{\text{c}} = 1.85$ GHz at a duration of $T = 1$ µs. A Tektronix AWG70002A arbitrary waveform generator operating at 15 GHz DAC sampling rate was used to generate the P4 coded signal and a Tektronix DPO70404C oscilloscope captured the loopback signal directly at passband (no analog down-conversion)[19] at a sampling rate of 25 GHz. The signal was digitally down-converted to complex-baseband and resampled to a sampled rate of 1.5 GHz (×10 the approximate 3 dB bandwidth). Two simple loopback configurations were employed: a direct connection using a Pasternack PE300-36 3 ft cable, and an in-line 300 MHz K&L customized band-pass filter centered 1.85 GHz connected using two PE300-36 cables.

Figure 2.21 shows the power spectra and time envelopes for the ideal P4 coded signal response and both loopback configurations. Recall that a rectangular-filtered P4 code ideally has a constant time envelope as shown in Figure 2.21(b). For the directly connected loopback configuration (Figures 2.21(c,d)), the time envelopes oscillates due to bandlimiting even with 1.5 GHz of sampled bandwdith. If the sidelobes of the spectrum are filtered out using the 300 MHz bandpass filter centered at 1.85 GHz (Figures 2.21(e,f)), the ringing in the envelope becomes exaggerated and starts to resemble the envelope of the SRRC-filtered P4 coded signal from Figure 2.4. Note that the in-band content of the P4 code ($\pm$75 MHz) is effectively unaltered in these tests (compared to the ideal), thus the loopback captures can still be processed without issue (as long as no aliasing

[19] More on down-conversion in Section 2.3.

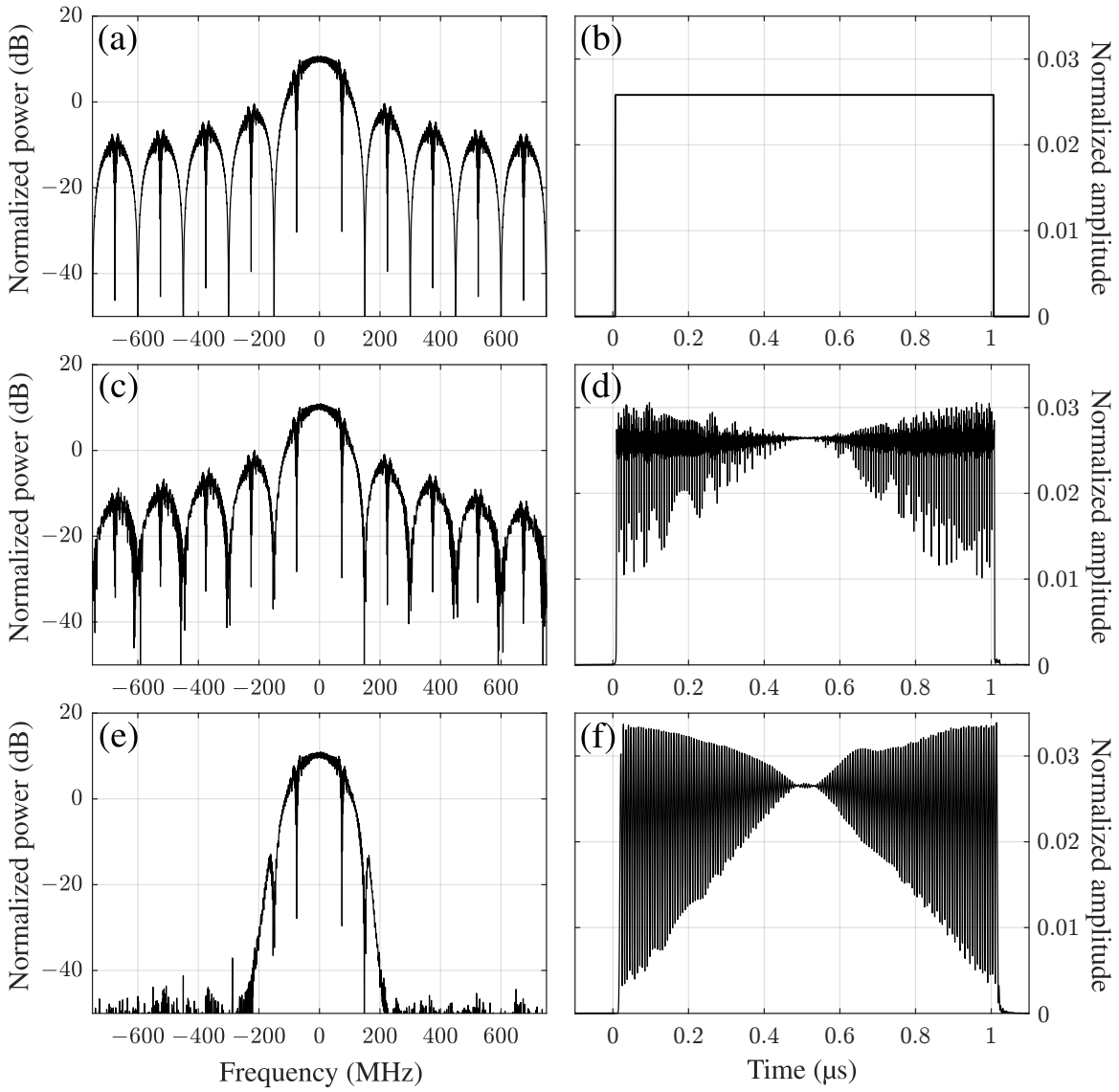

Figure 2.21: Linear distortion due to bandlimiting/filtering in loopback configuration for rectangular filtered P4 code: (a) ideal power spectrum, (b) ideal time envelope, (c) loopback with direct connection power spectrum, (d) loopback with direct connection time envelope, (e) loopback with filter power spectrum, and (f) loopback with filter time envelope. Darkened areas are fine oscillations.

occurs during sampling). However, the ringing that occurs due to bandlimiting in amplitude could theoretically exacerbate nonlinear distortions caused by the HPA if the linear distortion is imparted to the signal prior to amplification.

The ringing in amplitude is caused by the massive increase in instantaneous bandwidth[20] at the phase transitions of the phase-coded pulse. The system cannot handle this explosion in bandwidth, thus the signal becomes bandlimited causing the ringing in the envelope. In [3], the authors liken the behavior to a vector rotating around a unit circle in the complex plane. For a constant amplitude waveform, the length (amplitude) of the vector is constant and the phase of the vector rotates according to the phase function $\psi(t)$. For a coded-waveform, the instantaneous jump in phase causes the vector to jump *through* the unit circle causing a reduction in length (amplitude) of the vector due to the bandwidth limitations of the system.

Figure 2.21 shows the power spectra and time envelopes for the ideal LFM waveform response and both loopback configurations. The LFM does not have the issue of rapid increase in instantaneous bandwidth thus the envelope of both loopback captures do not have ringing in amplitude as seen in the P4 coded case. Both loopback captures have a small variation in amplitude most likely caused by non-flat frequency response of the system though the envelopes remain similar to that of the ideal LFM waveform. Therefore, it can be understood that spectral containment of a waveform allows for bandlimiting/filtering to occur without drastically altering the signal structure in time.

2.2.2.2 Nonlinear Distortion

In high power radar systems, along with linear distortion, there exists significant nonlinearities which cannot be modeled using the linear filter $W_{\text{tx}}(f)$. The nonlinearities are mostly generated within the transmitter HPA, however LO nonlinearities are also present[21] [64]. The HPA nonlinearities include harmonics, intermodulation distortion (IMD), AM/AM, AM/PM, and long/short-term

[20] Recall from Section 2.1.2.1 that the instantaneous frequency of a rectangular filtered phase-coded waveform can only take on the values $\{-\infty, 0, \infty\}$.

[21] The LO nonlinearities are assumed to be much smaller than the amplifier distortions thus are not considered in this work.

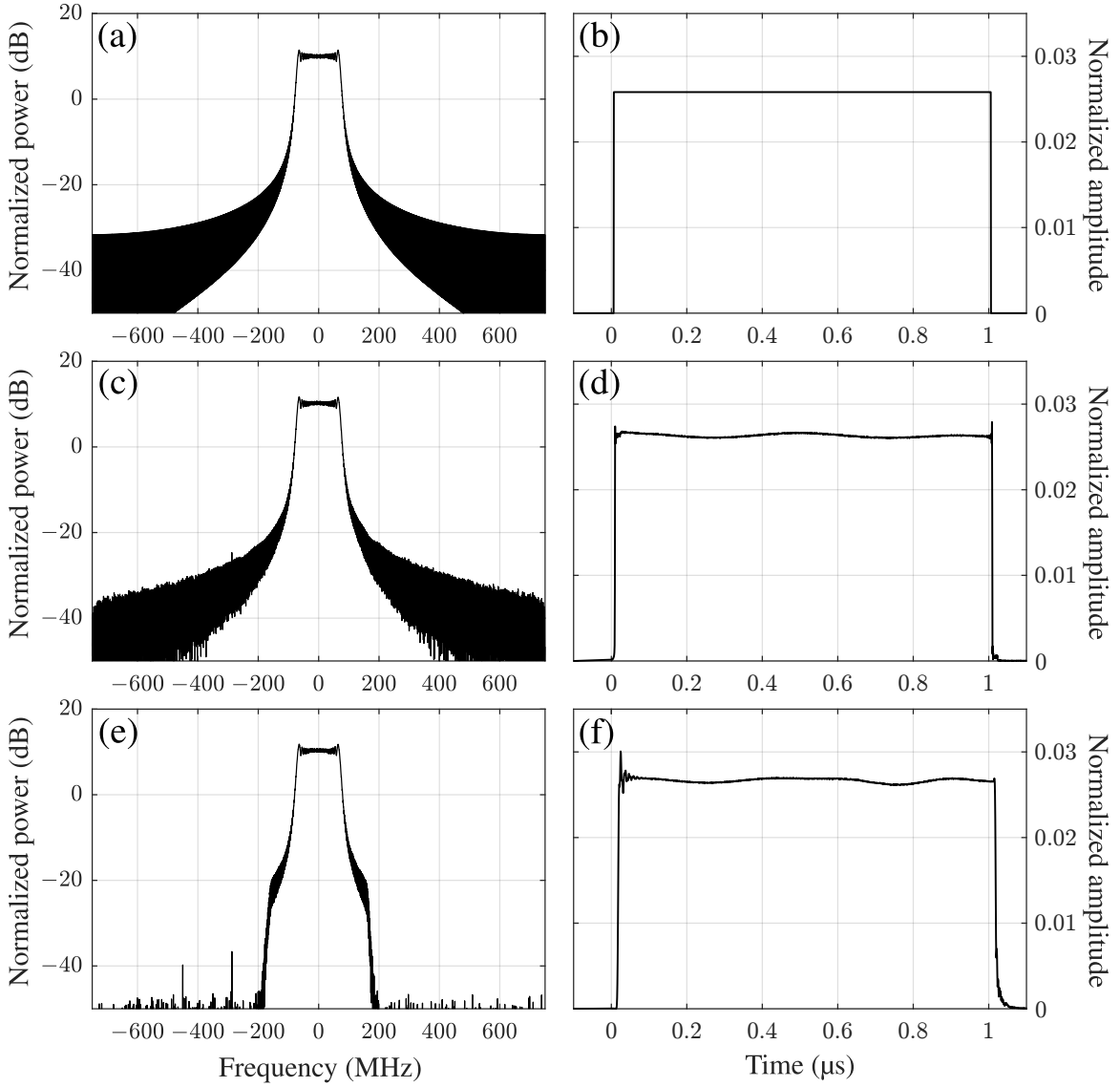

Figure 2.22: Linear distortion due to bandlimiting/filtering in loopback configuration for LFM: (a) ideal power spectrum, (b) ideal time envelope, (c) loopback with direct connection power spectrum, (d) loopback with direct connection time envelope, (e) loopback with filter power spectrum, and (f) loopback with filter time envelope. Darkened areas are fine oscillations.

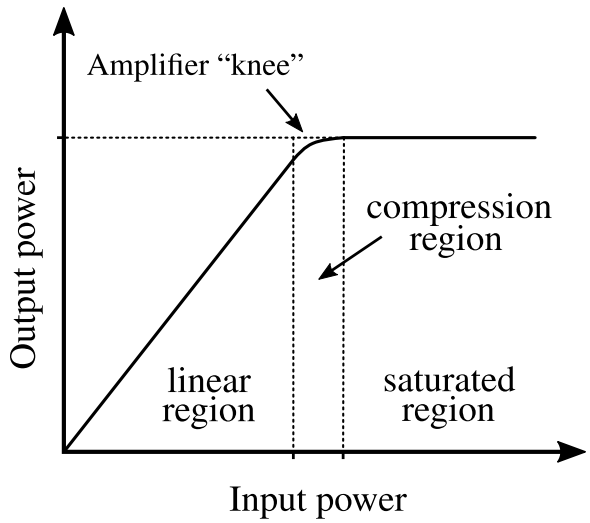

Figure 2.23: Output power versus input power gain curve for a typical amplifier.

memory effects [36, 65–67][22]. Harmonic distortion produces harmonic copies of the waveform at multiples of the center frequency (and bandwidth). IMD occurs when the frequency components of a non-tonal signal interact within the amplifier. IMD is the source of spectral regrowth that occurs to either side and within the waveform band [68]. The distortions AM/AM and AM/PM occur during signal compression and describe the process of converting amplitude modulation (AM) of the signal into to either a distorted amplitude modulation (from amplifier saturation) or phase modulation (PM) at the output of the amplifier (another source of spectral regrowth) [34]. When the output of an HPA is dependent on the signal conditions prior to its arrival, the amplifier is said to have “memory” which is most difficult nonlinearity to model [34]. Amplifier memory can occur in two different time scales: short-term memory, where the input signals are dependent on time scales relative to carrier period $(1/f_c)$ caused by transients in reactive elements of amplifier; and long-term memory, where the input signals are dependent on time scales relative to the signal's envelope (i.e. pulse width for radar) typically attributed to thermal effects within the device [67].

The input versus output power of an amplifier (shown in Figure 2.23) can be characterized by three distinct regions: 1) the linear region, where the output signal is a scaled copy of the input; 2) the compression region, where the output signal begins to compress the peaks of the sinusoid

[22] In some texts (e.g. [64]), IMD is used generally to describe the entirety of the nonlinear distortion effects within an amplifier.

causing nonlinear distortions (also known as the "knee" of the amplifier); and 3) the saturation region, the most power efficient region of the amplifier, where an increase in input amplitude does not result in an increase in output amplitude and severe nonlinear distortions can occur to clipping of the inputted signal[23]. It is typical practice in high power radar systems to operate in the saturation region of the HPA where high amplifier efficiency is required to necessitate sufficient energy-on-target to meet a minimum detectable signal (MDS) on receive [3, 5, 69]. Unfortunately, the nonlinear amplifier distortions are exasperated by operating in the saturation region of the HPA [66, 68][24].

Methods of modeling high-power amplifier nonlinear distortion (with memory)[25] include but are not limited to the Volterra, Wiener, Hammerstein, Wiener-Hammerstein, memory polynomial, and neural network models [66, 68, 70]. Some of these models produce very accurate results though can be quite complex to implement. One particular model that is a good trade-off between complexity and performance is the Wiener-Hammerstein model (Figure 2.24) which has been shown to accurately predict the nonlinear behavior of both traveling-wave tube (TWT) and solid-state (transistor-based) power amplifiers [68]. The model is comprised of two linear distortion stages denoted as $W_{\mathrm{A}}^{\mathrm{i}}(f)$ and $W_{\mathrm{A}}^{\mathrm{o}}(f)$, respectively, and a memoryless nonlinear distortion stage denoted as $\mathcal{T}_{\mathrm{A}}\{\bullet\}$ (e.g. the power series model [64, 68]). Thus for a system with multiple amplification stages, the model in Figure 2.24 can be cascaded multiple times (or connected in parallel) to model the system nonlinearities.

The nonlinear amplification model can be tied back to the transmit chain distortion model $\mathcal{T}_{\mathrm{tx}}\{\bullet\}$ from (2.83) which converts the ideal passband spectral content $S_{\mathrm{pb}}(f)$ into the forward traveling wavefront incident on the antenna $V^{+}(f)$. If we assume that only a single amplifier stage is present in the transmit chain, the nonlinear distortion model for $\mathcal{T}_{\mathrm{tx}}\{\bullet\}$ can be built as shown in

[23]Note that these operating modes for some amplifiers may not be as distinct as presented in Figure 2.23. For example, some traveling-wave tube (TWT) amplifiers may have some slight nonlinearity over the "linear" region [68].

[24]These nonlinear effects can be reduced through "amplifier backoff" (typically administered in communication systems with AM) where the input power is reduced until the maximum waveform instantaneous power is near the knee of the amplifier where a trade-off between nonlinear distortion and linearity is researched [36, 65, 68], though this region is not consider here.

[25]Note that there are two types of memory effects: long-term and short term memory.

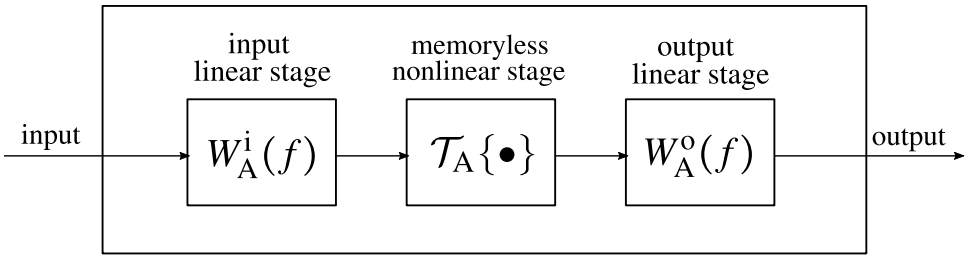

Figure 2.24: The Wiener-Hammerstein model for characterizing an HPA with nonlinear distortion effects (including memory) [68].

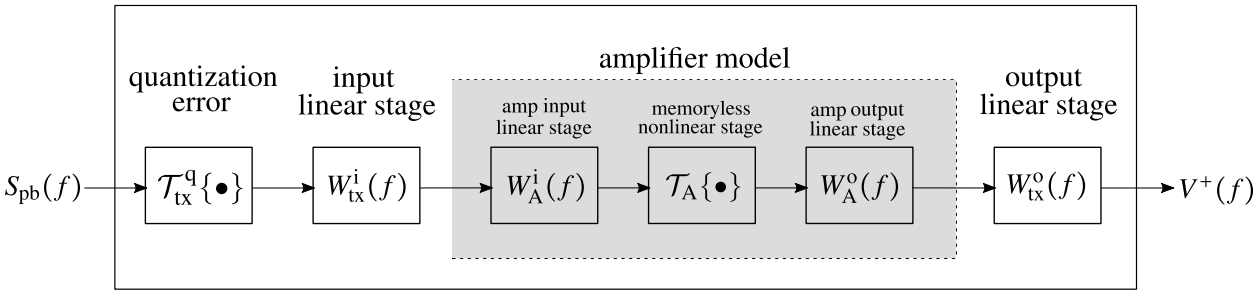

Figure 2.25: Transmit distortion model $\mathcal{T}_{\mathrm{tx}}\{\bullet\}$ (frequency-domain) for single amplifier transmitter.

Figure 2.25, where $\mathcal{T}_{\mathrm{tx}}^{\mathrm{q}}\{\bullet\}$ is a nonlinear transformation representing DAC quantization (and any other nonlinearities) in the waveform generation[26], $W_{\mathrm{tx}}^{\mathrm{i}}(f)$ is the linear model of the RF chain prior to the amplifier, and $W_{\mathrm{tx}}^{\mathrm{o}}(f)$ is the linear model for the RF chain after the amplifier. The amplifier model for the single stage amplification is placed between the input and output linear models of the RF chain. In Figure 2.25, the Wiener-Hammerstein model is implemented though any nonlinear system representing the amplifier can be used. Thus, the transformation in (2.83) can be expressed analytically as

$$V^{+}(f) = \mathcal{T}_{\mathrm{tx}}\left\{S_{\mathrm{pb}}(f)\right\} = W_{\mathrm{tx}}^{\mathrm{o}}(f)W_{\mathrm{A}}^{\mathrm{o}}(f)\,\mathcal{T}_{\mathrm{A}}\left\{W_{\mathrm{A}}^{\mathrm{i}}(f)W_{\mathrm{tx}}^{\mathrm{i}}(f)\,\mathcal{T}_{\mathrm{tx}}^{\mathrm{q}}\left\{S_{\mathrm{pb}}(f)\right\}\right\}. \tag{2.113}$$

The nonlinear distortion that is most significant is in-band and near-band, therefore the discussion will be limited to these topics. The nonlinear distortion of the HPA also creates products at multiples the center frequency of the inputted signal though are not considered here

[26]The DAC nonlinear transformation $\mathcal{T}_{\mathrm{tx}}^{\mathrm{q}}\{\bullet\}$ represents quantization of the waveform, images of the waveform at Nyquist zones of the transmitter sampling rate, harmonic generation, and intermodulation products. While these distortions will affect the signal structure of the waveform, the major source of distortion is the HPA which is the focus of the analysis within this section.

as it does not overlap the spectrum of the fundamental signal thus can be filtered out via *harmonic termination/shorting* [34, 36, 71]. In-band distortions may alter the modulation structure of the inputted signal while near-band distortion are difficult to filter out due to the vicinity to the signal band. The sources of these types of distortions are IMD, AM/AM, and AM/PM. Because these distortions occur (or are worsened) during compression of the signal, spectral regrowth is not typically a problem for linear systems. One method of characterizing this distortion is through the *memoryless* power series model [64,66,68,72] which is a summation of the fundamental (inputted) signal with high order components of the same signal. Because this model is memoryless, it can be used as the transformation stage of the Wiener-Hammerstein model $\mathcal{T}_{\mathrm{A}}\{\bullet\}$ shown in Figure 2.24. Assuming the distortion prior to this memoryless model is small, the *power series model* can be defined using analytical waveform $S_{\mathrm{pb}}(f)$ as

$$\mathcal{T}_{\mathrm{A}}\left\{S_{\mathrm{pb}}(f)\right\} = w_1 S_{\mathrm{pb}}(f) + w_2\left(S_{\mathrm{pb}}(f) * S_{\mathrm{pb}}(f)\right) + w_3\left(S_{\mathrm{pb}}(f) * S_{\mathrm{pb}}(f) * S_{\mathrm{pb}}(f)\right) + \cdots \qquad (2.114)$$

where w_i is the real-valued amplitude of the ith order component[27].

For example, the fundamental through fifth-order products[28] for an LFM with bandwidth B_{a} = 500 MHz and pulse duration T = 300 ns at a center frequency of f_{c} = 2 GHz is shown in Figure 2.26. The even-order products create harmonics at even multiples of the center frequency (and bandwidth) while the odd-order products create the harmonics at odd multiples. Note that the spectral content at the center frequency is either low in energy (even-order products) or similar in shape to LFM fundamental. In fact, the spectral content that appears in the fundamental frequency (for the odd-order product) is indistinguishable from the fundamental itself. Recall that the memoryless nonlinear distortion is a superposition of the fundamental waveform with scaled copies of the higher order products, thus the in-band spectral content of the LFM waveform will be largely unaltered no matter the combination of the products. This lack of distortion in the

[27]Note that the convolutions in (2.114) are multiplications in the time domain.

[28]The spectra in Figure 2.26 are normalized to have equal energy. Typically the higher-order terms will be less than the fundamental depedning on the signal structure and how hard the amplifier is driven into saturation.

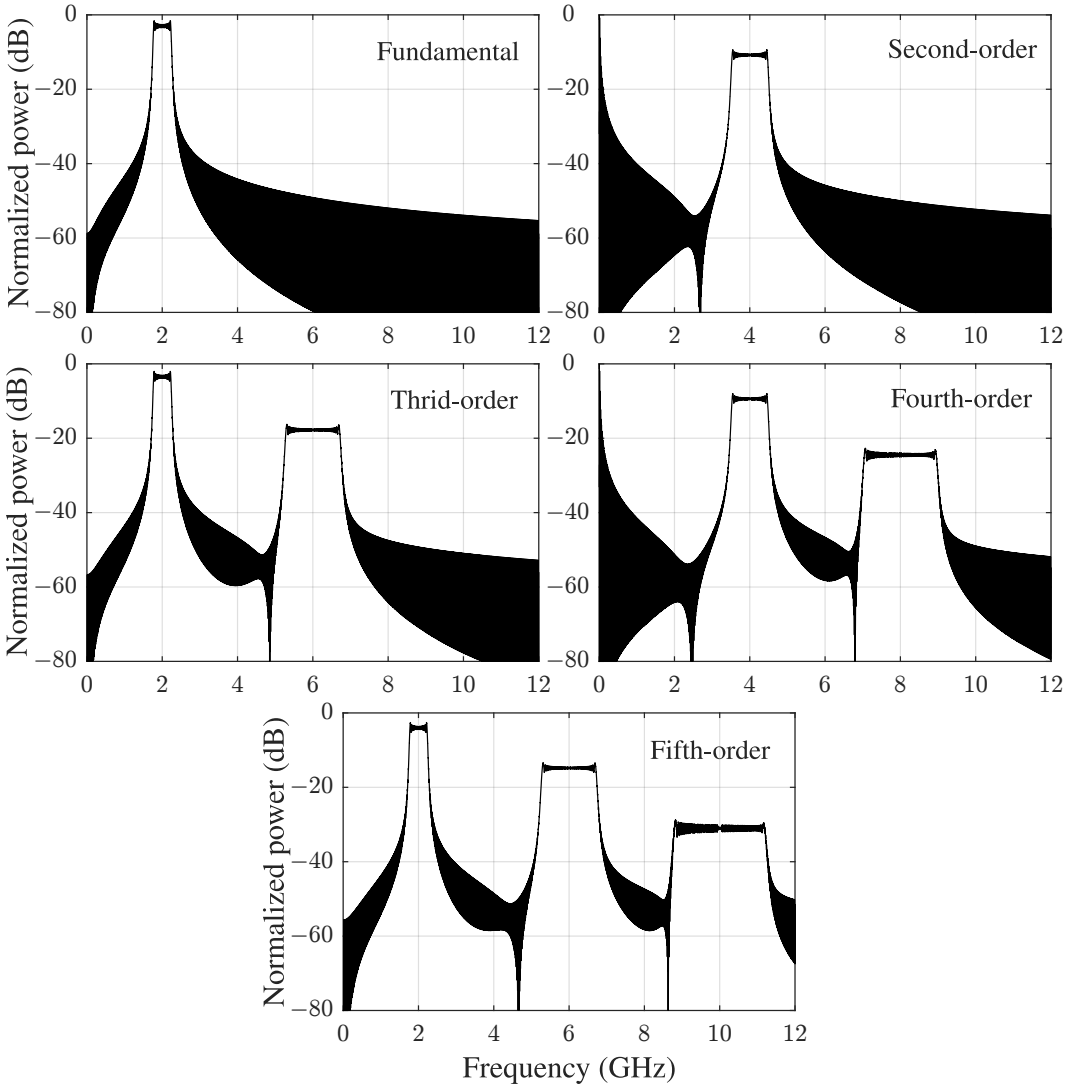

Figure 2.26: Fundamental through fifth-order terms of the power series nonlinear distortion model for LFM of bandwidth B_{a} = 500 MHz, pulse duration T = 300 ns, and center frequency f_{c} = 2 GHz.

fundamental frequency band is a feature of the LFM being constant amplitude.

The property of low nonlinear distortion for constant amplitude waveforms can be proven simple trigonometry. Using the passband waveform model of $s_{\text{pb}}(t)$ from (2.4), the third-order term (in the time domain) can be written as

$$\begin{aligned}\left(s_{\text{pb}}(t)\right)^3 &= \left(u(t)\cos\left(2\pi f_{\text{c}}t + \psi(t)\right)\right)^3 \qquad \textit{(Third-order product)} \\ &= \left(u(t)\right)^3\left(\tfrac{3}{4}\cos\left(2\pi f_{\text{c}}t + \psi(t)\right) + \tfrac{1}{4}\cos\left(2\pi(3f_{\text{c}})t + 3\psi(t)\right)\right).\end{aligned} \tag{2.115}$$

Thus if $u(t)$ is designed to be constant amplitude, the signal structure of the fundamental cosine term $\cos\left(2\pi f_{\text{c}}t + \psi(t)\right)$ remains undistorted (similar analyses can be performed for all odd-order products). Therefore it can be understood that the overall impact that the HPA nonlinearity has on the in-band content of a waveform is dependent on its signal structure, namely the amount of amplitude variation in the signal envelope. Quantitatively, this fluctuation in signal amplitude is characterized by the ratio of the peak instantaneous power to the signal average power, also known as the *peak-to-average power ratio* (PAPR), defined as[29]

$$\text{PAPR} = \frac{\max\limits_{t}\left\{|s(t)|^2\right\}}{\frac{1}{T}\left\|s(t)\right\|_2^2} = \frac{\max\limits_{t}\left\{|u(t)|^2\right\}}{\frac{1}{T}\left\|u(t)\right\|_2^2}, \tag{2.116}$$

for PAPR ≥ 1. Thus a waveform having unity PAPR $(\text{PAPR} = 1)$ implicitly means the waveform is robust to nonlinear effects in HPAs.

Take for an example the non-constant amplitude waveform discussed in Section 2.1.2.1 which is an SRRC-filtered P4 code with $N_{\text{c}} = 150$ phase code values. The phase code is implemented at the same pulse duration and center frequency as the LFM $(f_{\text{c}} = 2$ GHz and $T = 300$ ns$)$. The amplitude envelope for this waveform (shown in Figure 2.5) has a PAPR of 2.15 (or 3.33 dB), thus will not exhibit the same low in-band distortion property as the LFM waveform (as shown by the $(u(t))^3$ term in the third-order product example (2.115). Figure 2.27 displays the fundamental through fifth order products for the SRRC-filtered P4 code. For the odd-order products, the in-

[29]Note the PAPR is occasionally defined with respect to the passband signal $s_{\text{pb}}(t)$, thus would have a minimum of $\sqrt{2}$.

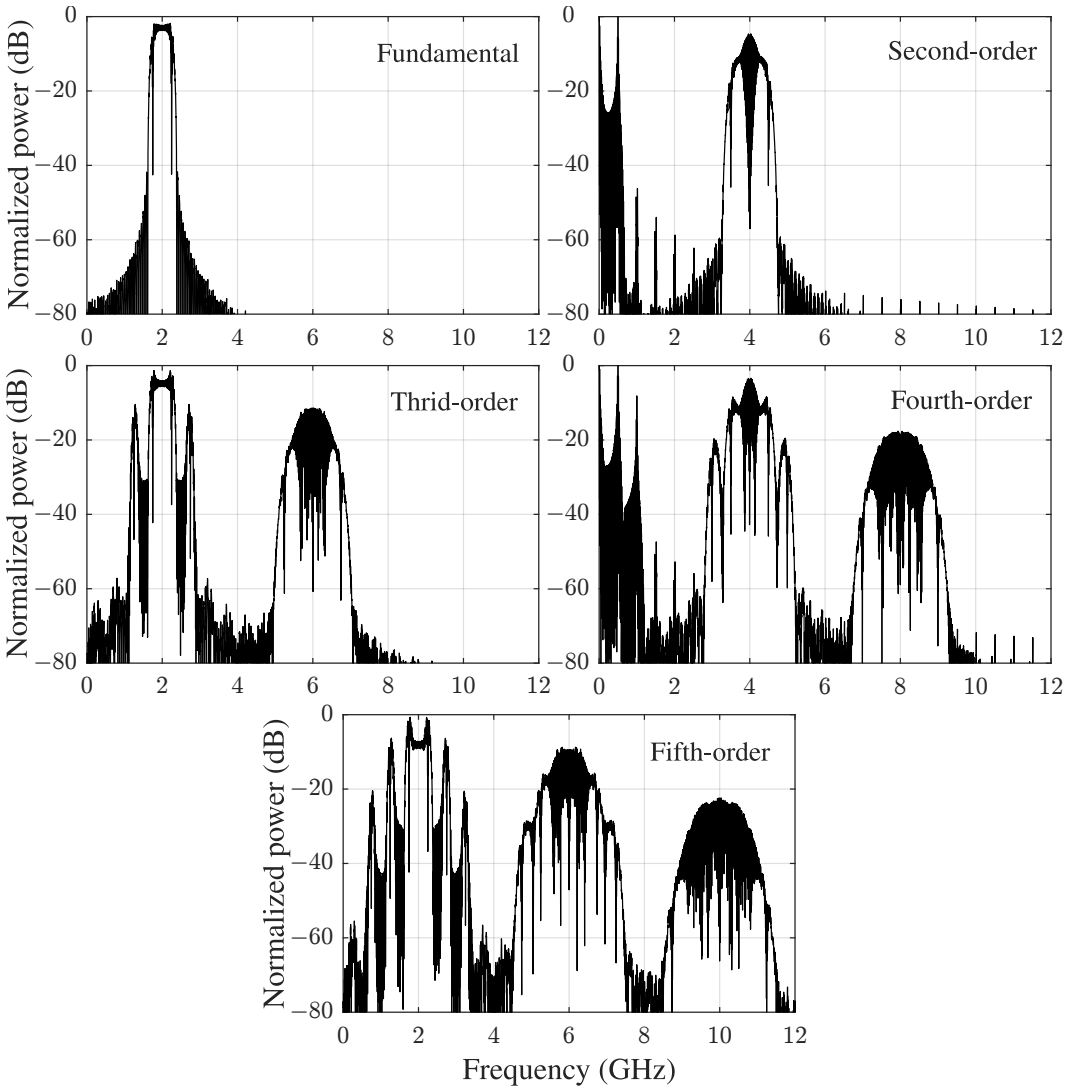

Figure 2.27: Fundamental through fifth-order terms of the power series nonlinear distortion model for SRRC-filtered P4 code of $N_c = 150$ code values, pulse duration $T = 300$ ns, and center frequency $f_c = 2$ GHz.

band spectral content starts to distort compared to the fundamental and large spikes of energy form in the near-band frequencies around the fundamental. This growth in spectral energy around the fundamental band is called *spectral regrowth* [37, 64, 66, 68] which is not present for the constant amplitude LFM higher-order analysis in Figure 2.26. This spectral regrowth can only be lowered by reducing the nonlinearities within the amplifier by through either power back-off [37, 68] to the linear region of the amplifier or a predistortion method that attempts to linearize the nonlinear distortion [31–34]. To achieve the same amount of transmitted power as the LFM waveform with power back-off would require an amplifier with enough "head-room" to operate in the linear region (e.g. for this scenario, you would need a 215 W amplifier instead of a 100 W amplifie to achieve the same output energy as the LFM). Linearization of the a compressed/saturated amplifier can be employed though waveform predistortion of the signal or feedforward/feedback techniques which rely of systems architectures though typically only works in for slightly compressed (signals i.e. operating in the knee of the amplifier operating region) [34–37].

The distortion characteristics (both linear and nonlinear) of constant amplitude FM waveforms make it an attractive candidate for high power radar applications. The spectral containment of an FM waveform minimizes distortions due to bandlimiting that would occur in a radar transmitter. Likewise, the constant amplitude structure of an FM waveform has very little in-band and near-band distortions (i.e. spectral regrowth) that occur due to non-linear effects within the HPA. Therefore, if the FM waveform is designed properly, the in-band content of the forward voltage incident on the transmitting antenna $V^+(f)$ is approximately proportional to the ideal waveform $S_{\text{pb}}(f)$,

$$V^+(f) \approx w_1 S_{\text{pb}}(f), \quad \textit{(constant amplitude)} \tag{2.117}$$

where w_1 is the amount of amplitude gain imparted to the fundamental spectrum. The convenience of this assumption greatly simplifies analysis and optimization of FM waveforms. Though the constraints of constant amplitude and spectrally contained impose a hard restriction during the waveform design. Also, as sensitivity increases, as does the need for higher model fidelity.

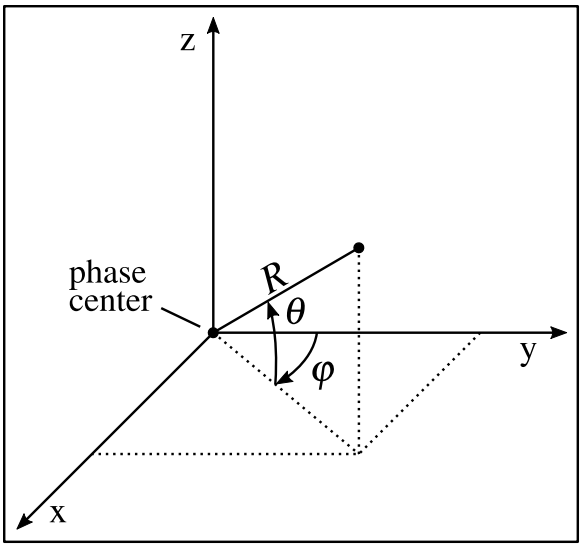

Figure 2.28: Spatial geometry of free-space propagation.

In Chapter 5 it is shown that greater waveform performance (in terms of correlation sidelobe level) can be achieved by considering a *system specific* design that employs both a highly robust waveform model (i.e. FM) with the linear model of a simple loopback scenario. This waveform design method is akin to predistortion though the waveform is optimized along side the distortion model. The optimization problem is designed to try and limit the sensitivity of the optimized waveform performance to model errors by not combining high volatile waveforms (i.e. susceptible to transmitter distortion) with complex transmitter models.

2.2.3 Geometry and Emitted Fields

Once transmitted, the pulsed electromagnetic (EM) energy travels in free space at the speed of light on a vector pointed away from the radar transmitter and illuminates a desired region in space. Figure 2.28 shows the geometry of the free-space where φ is measured as the angle off the y-axis in the xy-plane and θ is the angle measured off the xy-plane. The phase center of the antenna is located at the origin therefore R is the distance (in meters) from the antenna.

Assuming the electric-field is polarized in the θ dimension, the far-field electric and magnetic field spectral contents with respect to the forward voltage $V^{+}(f)$ can be written as

$$\vec{\mathscr{E}}(R,\theta,\varphi;f) = \sqrt{\frac{\eta}{Z_0}}\frac{e^{-j\frac{2\pi f}{c}R}}{R\sqrt{4\pi}}F(f,\theta,\varphi)V^{+}(f)\,\vec{a}_{\theta} \quad [\text{V/m/Hz}] \tag{2.118}$$

and

$$\vec{\mathscr{H}}(R,\theta,\varphi;f) = \frac{1}{\eta}\left(\vec{\mathscr{E}}(R,\theta,\varphi;f)\bullet\vec{a}_{\theta}\right)\vec{a}_{\varphi} \quad [\text{A/m/Hz}], \tag{2.119}$$

where $\bullet$ is the dot product, $\eta \approx 120\pi\ \Omega$ is the intrinsic impedance of free space, $F(f,\theta,\varphi)$ is the frequency-dependent antenna pattern in the domainant polarization (θ in this case), and $\vec{a}_{\theta}$ and $\vec{a}_{\varphi}$ are the unit vectors in the θ and φ dimensions, respectively. In this configuration, the antenna pattern $F(f,\theta,\varphi)$ is calculated via an S_{21} scattering parameter measurement in an anechoic chamber over all angles and frequencies of interest. The pattern is corrected for spherical spreading losses and normalized by the total *incident* power on the antenna thus would include losses due impedance mismatch variation with frequency. The scaling term $\sqrt{\frac{\eta}{Z_0}}$ is a convenient factor when comparing the squared-amplitude of the antenna pattern $|F(f,\theta,\varphi)|^2$ to the reflection coefficient $|\Gamma(f)|^2$ (relationship shown later in section). The inverse-Fourier transform of (2.118) and (2.119) produces the real-valued instantaneous fields expressed as

$$\vec{\mathscr{E}}(R,\theta,\varphi;t) = \sqrt{\frac{\eta}{Z_0}}\frac{F(t,\theta,\varphi)}{R\sqrt{4\pi}} * V^{+}\left(t-\tfrac{R}{c}\right)\vec{a}_{\theta} \quad [\text{V/m}] \tag{2.120}$$

and

$$\vec{\mathscr{H}}(R,\theta,\varphi;t) = \frac{1}{\eta}\left(\vec{\mathscr{E}}(R,\theta,\varphi;t)\bullet\vec{a}_{\theta}\right)\vec{a}_{\varphi} \quad [\text{A/m}]. \tag{2.121}$$

Taking the cross-product of the fields yields the instantaneous Poynting vector,

$$\begin{aligned}\vec{\mathscr{P}}(R,\theta,\varphi;t) &= \vec{\mathscr{E}}(R,\theta,\varphi;t)\times\vec{\mathscr{H}}(R,\theta,\varphi;t)\\ &= \frac{1}{Z_0}\frac{1}{4\pi R^2}\left(F(t,\theta,\varphi) * V^{+}\left(t-\tfrac{R}{c}\right)\right)^2\vec{a}_{R} \quad [\text{W/m}^2].\end{aligned} \tag{2.122}$$

The radiation intensity of the emission is found by taking the dot product of (2.122) with $\vec{a}_R$ and

removing the dependence on range,

$$\mathscr{U}(t,\theta,\varphi) = \frac{1}{4\pi Z_0}\Big(F(t,\theta,\varphi) * V^+(t)\Big)^2 \quad [\text{W/unit solid angle}]. \tag{2.123}$$

The total emitted energy can be found by integrating (2.123) over all space and time. Assuming no ohmic losses within the antenna, this energy is equivalent to the energy dissipated in the antenna load model ((2.102) in Section 2.2.1). Therefore, (2.102) can be expressed in terms of $V^+(f)$ and $F(f,\theta,\varphi)$ as[30]

$$\begin{aligned}\mathcal{E}_{\text{tx}} &= \int_{-\infty}^{\infty}\int_{0}^{2\pi}\int_{-\pi/2}^{\pi/2} \mathscr{U}(t,\theta,\varphi)\cos\theta\, d\theta\, d\varphi\, dt \\ &= \frac{1}{4\pi Z_0}\int_{-\infty}^{\infty}|V^+(f)|^2 \int_{0}^{2\pi}\int_{-\pi/2}^{\pi/2}|F(f,\theta,\varphi)|^2\cos\theta\, d\theta\, d\varphi\, df.\end{aligned} \tag{2.124}$$

For better comparison, (2.102) can be rewritten in terms of $V^+(f)$ and $\Gamma(f)$ as

$$\mathcal{E}_{\text{tx}} = \frac{1}{Z_0}\int_{-\infty}^{\infty}|V^+(f)|^2\big(1-|\Gamma(f)|^2\big)df. \tag{2.125}$$

The equivalence between the energies dissipated in the transmit chain and the energy transmitted implies that the average transmitted power $\mathcal{P}_{\text{tx}}$ is also equivalent in both domains given the definition of (2.105). Also note that because $F(f,\theta,\varphi)$ and $\Gamma(f)$ are derived off of time-harmonic measurements, we can make the conclusion that the antenna pattern is related to the reflection coefficient as

$$\frac{1}{4\pi}\int_{0}^{2\pi}\int_{-\pi/2}^{\pi/2}|F(f,\theta,\varphi)|^2\cos\theta\, d\theta\, d\varphi = 1-|\Gamma(f)|^2. \tag{2.126}$$

The directivity of the antenna describes the power distribution in space relative to an isotropic radiator. Because we are assuming a lossless antenna, the directivity is equivalent to the gain of

[30]The derivation of (2.124) is provided in Appendix A.1.

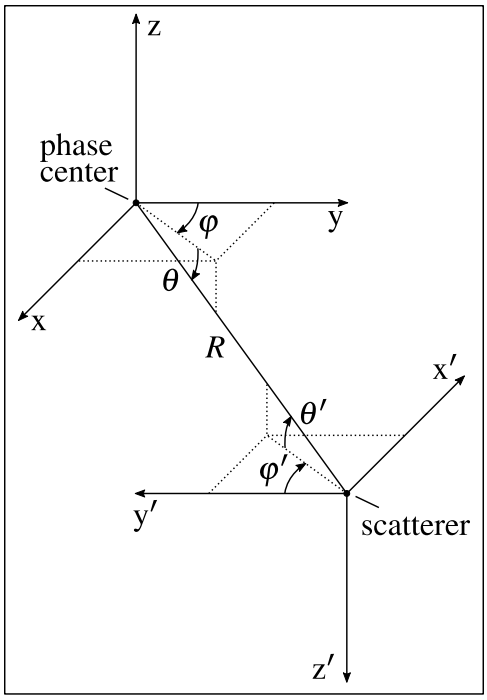

Figure 2.29: Relationship between antenna and scatterer geometry.

the antenna. Thus, the gain (and directivity) can be defined in terms of $F(f,\varphi,\phi)$ as [73]

$$\begin{aligned}\mathcal{G}(f,\theta,\varphi) &= 4\pi \frac{|F(f,\theta,\varphi)|^2}{\int_0^{2\pi}\int_{-\pi/2}^{\pi/2} |F(f,\theta,\varphi)|^2 \cos\theta d\theta d\varphi} \\ &= \frac{|F(f,\theta,\varphi)|^2}{1-|\Gamma(f)|^2}.\end{aligned} \tag{2.127}$$

The *effective* gain is defined as the gain multiplied by the reflection mismatch efficiency [73],

$$\begin{aligned}\mathcal{G}_{\mathrm{e}}(f,\theta,\varphi) &= \mathcal{G}(f,\theta,\varphi)\left(1-|\Gamma(f)|^2\right) \\ &= |F(f,\theta,\varphi)|^2.\end{aligned} \tag{2.128}$$

2.3 The Scattering and Reception

After transmission, the emitted energy scatters off the illuminated scene. Once the energy is scattered, the continuum of scatterers can be modeled as individual sources of energy. The fields

scattered from a single scatterer at range R (for a single polarization) can be defined as[31]

$$\vec{\mathscr{E}}^{\mathrm{s}}(R',\theta',\varphi';f) = \Upsilon(f,\theta',\varphi')\left(\vec{\mathscr{E}}(R,\theta,\varphi;f)\bullet\vec{a}_{\theta}\right)\frac{e^{-j\frac{2\pi f}{c}R'}}{R'\sqrt{4\pi}}\vec{a}_{\theta'}, \tag{2.129}$$

where R' is the range *from* the scatterer, φ' and θ' are the transformed coordinates, and $\Upsilon(f,\theta',\varphi')$ is the complex-valued *effective length* of the scatterer (in meters) which captures the incident field and scatters the energy irregularly in space and frequency. The chosen transformed scattering coordinates axes for the scattered field are shown in Figure 2.29. There are an infinite number of ways to define the coordinate axes. However, for a monostatic (or quasi-monostatic[32]) system, a portion of the scattered energy reflects back to the collocated receive antenna from the direction it was transmitted (known as *backscatter*). Thus, this orientation is chosen because $\varphi' = \varphi$ and $\theta' = \theta$ corresponds to a backscattered trajectory.

The incident field at the monostatic receiver for the single scatterer at range R corresponds to (2.129) when $R' = R$, $\varphi' = \varphi$, and $\theta' = \theta$, thus can be expressed as[33]

$$\vec{\mathscr{E}}^{\mathrm{s}}(R'=R,\theta'=\theta,\varphi'=\varphi;f) = \sqrt{\frac{\eta}{Z_0}}\frac{e^{-j\frac{4\pi f}{c}R}}{4\pi R^2}\Upsilon(f,\theta,\varphi)F(f,\theta,\varphi)V^{+}(f)\,\vec{a}_{\theta'}. \quad \textit{(single scatterer)} \tag{2.130}$$

Taking the magnitude-squared of this incident field yields the incident power density per unit frequency for this single scatterer scenario as

$$\begin{aligned}\bar{\mathcal{P}}^{\mathrm{i}}_{\mathrm{rx}}(f) &= \frac{1}{\eta}\left|\vec{\mathscr{E}}^{\mathrm{s}}(R'=R,\theta'=\theta,\varphi'=\varphi;f)\bullet\vec{a}_{\theta'}\right|^2 \\ &= \frac{\sigma_{\mathrm{RCS}}(f)}{(4\pi)^2R^4}\,|F(f,\theta,\varphi)|^2\,\frac{|V^{+}(f)|^2}{Z_0}, \quad \textit{(single scatterer)}\end{aligned} \tag{2.131}$$

[31] Note that generally there would be two polarized elements in (2.129), the co-polarized element and the cross-polarized element. However, because we are assuming a receive antenna with the same polarization at the transmit antenna, only one polarization needs to be defined.

[32] A quasi-monostatic system has dedicated collocated transmit and receive antennas that can function simultaneously.

[33] The "single scatterer" specification is present to remind the reader that this equality is conditioned on the assumption of a single isolated scatterer and is not true in general.

where

$$\sigma_{\mathrm{RCS}}(f) = |\Upsilon(f, \theta' = \theta, \varphi' = \varphi)|^2 \quad [\mathrm{m}^2] \tag{2.132}$$

is the frequency-dependent backscattered *radar cross section* (RCS) in square-meters. Using (2.108) and (2.128), the (2.131) can be rewritten as

$$\bar{\mathcal{P}}^{\mathrm{i}}_{\mathrm{rx}}(f) = \frac{\sigma_{\mathrm{RCS}}(f)}{(4\pi)^2 R^4}\, \mathcal{G}(f, \theta, \varphi)\, \bar{\mathcal{P}}_{\mathrm{tx}}(f). \quad [\mathrm{W/m^2/Hz}] \quad \textit{(single scatterer)} \tag{2.133}$$

The received power per unit frequency is found through a multiplication of the incident power density by the effective area of the receive antenna denoted $\mathcal{A}_{\mathrm{e}}(f, \theta, \varphi)$ in square-meters. Assuming the same antenna is used on receive, the effective area is defined as

$$\begin{aligned} \mathcal{A}_{\mathrm{e}}(f, \theta, \varphi) &= \frac{c^2}{4\pi f^2} \mathcal{G}_{\mathrm{e}}(f, \theta, \varphi) \\ &= \frac{c^2}{4\pi f^2} \mathcal{G}(f, \theta, \varphi)\big(1 - |\Gamma(f)|^2\big), \quad [\mathrm{m}^2] \end{aligned} \tag{2.134}$$

which encapsulates the reflected power at the antenna terminals (same as on transmit) [73]. Thus the power captured (per unit frequency) by the antenna can be expressed as

$$\begin{aligned} \bar{\mathcal{P}}^{\mathrm{c}}_{\mathrm{rx}}(f) &= \mathcal{A}_{\mathrm{e}}(f, \theta, \varphi) \bar{\mathcal{P}}^{\mathrm{i}}_{\mathrm{rx}}(f) \\ &= \sigma_{\mathrm{RCS}}(f) \frac{c^2}{f^2 (4\pi)^3 R^4} \left(\mathcal{G}(f, \theta, \varphi)\right)^2 \left(1 - |\Gamma(f)|^2\right) \bar{\mathcal{P}}_{\mathrm{tx}}(f). \end{aligned} \tag{2.135}$$

At the radar receiver, the backscatter of the illuminated scene is captured by the receive antenna, amplified using a low-noise amplifier (LNA), band-pass filtered (BPF), mixed down to the in-phase and quadrature components (down-converted), low-pass filtered (LPF) for sampling via an analog-to-digital converter (ADC). After amplification and receive filtering, the received power per unit frequency captured from a single scatterer at a range of R is expressed as

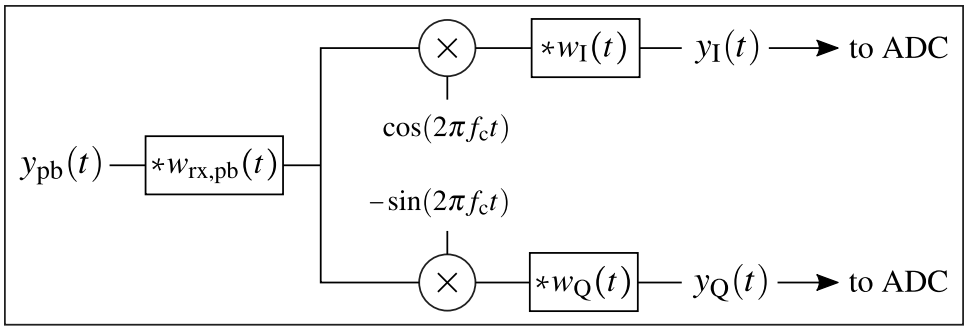

Figure 2.30: Analog down-conversion receiver model.

$$\bar{\mathcal{P}}_{\text{rx}}(f) = \sigma_{\text{RCS}}(f)\frac{c^2}{f^2(4\pi)^3R^4}\left(\mathcal{G}(f,\theta,\varphi)\right)^2\mathcal{G}_{\text{sys}}(f)\bar{\mathcal{P}}^{+}_{\text{tx}}(f), \quad \textit{(single scatterer)} \tag{2.136}$$

where $\mathcal{G}_{\text{sys}}(f)$ represents both transmit and receive power reflections as well any losses/gains in the receiver. Note that (2.136) is reminiscent of the well-known *radar equation* [56] albeit dependent on frequency. The total received energy captured by the monostatic radar system for single pulse scattered at range R with backscatter RCS $\sigma_{\text{RCS}}(f)$ can be found by integrating (2.136) over all frequency, $\mathcal{E}_{\text{rx}} = \left\|\bar{\mathcal{P}}_{\text{rx}}(f)\right\|_2^2$. Note that $\sigma_{\text{RCS}}(f)$ is typically considered frequency independent (i.e. constant over the bandwidth of the transmission), thus $\sigma_{\text{RCS}}(f) = \sigma_{\text{RCS}}$.

2.3.1 Down-conversion to Baseband

Define $y_{\text{pb}}(t)$ as the passband signal captured by the receive antenna normalized by the square-root of characteristic impedance of the line. Therefore $y_{\text{pb}}(t)$ is a normalized wave amplitude with units of square-root watts. Assuming that the LNA stage of reception imparts minimal nonlinear distortion[34] onto receive signal $y_{\text{pb}}(t)$, the distortion in the receiver chain can be represented by three real-valued filters: $w_{\text{rx,pb}}(t)$ that represent filtering prior to mixing, and $w_{\text{I}}(t)$ and $w_{\text{Q}}(t)$ which represent filtering in the in-phase and quadrature chains, respectively. These

[34]The receive LNA operates in the linear region thus does not impart as much nonlinear distortion as the transmit HPA. The largest contributor of nonlinear distortion on receive may come LO leakage in the down-conversion process (shows up as a spike at 0 Hz) though is not considered here.

filters represent both deliberate filtering (i.e. bandpass/lowpass filtering) and as well unintentional filtering (distortion) caused by the uneven frequency responses of the RF components. The in-phase ($y_{\mathrm{I}}(t)$) and quadrature ($y_{\mathrm{Q}}(t)$) signal components of this analog down-conversion receiver model[35] (shown in Figure 2.30) can be defined analytically as

$$y_{\mathrm{I}}(t) = \Big(\big(y_{\mathrm{pb}}(t) * w_{\mathrm{pb,rx}}(t)\big)\cos(2\pi f_{\mathrm{c}} t)\Big) * w_{\mathrm{I}}(t) \tag{2.137}$$

and

$$y_{\mathrm{Q}}(t) = -\Big(\big(y_{\mathrm{pb}}(t) * w_{\mathrm{pb,rx}}(t)\big)\sin(2\pi f_{\mathrm{c}} t)\Big) * w_{\mathrm{Q}}(t). \tag{2.138}$$

These signals are sampled using synchronized analog-to-digital converters (ADCs) and combined digitally into a complex signal within the processor. The low-pass filter bandwidth (contained within $w_{\mathrm{I}}(t)$ and $w_{\mathrm{Q}}(t)$) is assumed to greater than the waveform bandwidth but smaller than the receiver sampling frequency of the ADC to minimize any distortion that might occur during the sampling process (e.g. aliasing). The complex combination of the down-converted signals

$$y(t) = y_{\mathrm{I}}(t) + j y_{\mathrm{Q}}(t) \tag{2.139}$$

represents the continuous, complex-baseband representation of the received signal *before* sampling. A proof of the down-conversion process is provided in Appendix A.2. There are certainly variations on the model of the radar receiver in Figure 2.30 (or completely different systems models for the case of stretch processing [55]) however this description is sufficiently general for analysis purposes and is used throughout this work.

The receiver model can be simplified greatly by using a single complex-valued filter $w_{\mathrm{rx}}(t)$ to take the place of the three real-valued filters: $w_{\mathrm{pb,rx}}(t)$, $w_{\mathrm{I}}(t)$, and $w_{\mathrm{Q}}(t)$. In the frequency domain,

[35] Down-conversion to complex-baseband can also be performed digitally (after sampling) using a single ADC at when the received signal is still at passband frequency or down-converted to a lower center frequency (but still offset of 0 Hz).

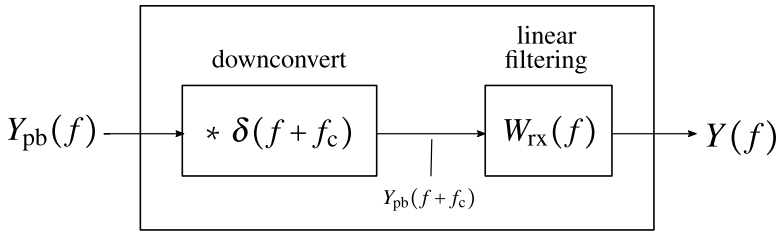

Figure 2.31: Simplified receiver model for analog down-conversion.

this comprehensive receiver distortion/filtering model is expressed in terms of the three filters as[36]

$$W_{\text{rx}}(f) = \tfrac{1}{2} W_{\text{pb,rx}}(f+f_{\text{c}})\big(W_{\text{I}}(f) + W_{\text{Q}}(f)\big). \tag{2.140}$$

Therefore, the down-conversion process can be simplified to a frequency shift and single filtering stage (Figure 2.31). The spectral content of the received complex-baseband signal using this approach is

$$Y(f) = Y_{\text{pb}}(f+f_{\text{c}}) W_{\text{rx}}(f), \tag{2.141}$$

and in the time-domain,

$$y(t) = \left(y_{\text{pb}}(t) e^{-j2\pi f_{\text{c}} t}\right) * w_{\text{rx}}(t). \tag{2.142}$$

A variation of this signal filter model is used in Chapter 5 to model the distortion of an RF chain for use in a waveform optimization cost function.

2.3.2 Received Signal Model

For simulation purposes (or any general radar analysis), it is typical to form a model of the received signal in terms of the scattering profile and the emitted signal. In doing so, it is typical practice to make some general assumptions for the emission structure to simplify the modeling. Making the antenna pattern $F(f,\theta,\varphi)$ a constant over frequency (i.e. $F(f,\theta,\varphi) = F(\theta,\varphi)$) turns the emitted

[36] Proof of this equality is provided in Appendix A.3.

field from (2.120) into a multiplication between two separable variables, $F(\theta,\varphi)$ and $V^+(t)$, which greatly simplifies analysis[37]. Another assumption that is made is one discussed in Section 2.2.2 where the forward transmit voltage $V^+(f)$ is approximately proportional to the waveform $S_{\text{pb}}(f)$. Typically these assumptions are associated with *narrowband* signals since the frequency response of RF device over a small bandwidth can be assumed constant.

Using these two assumptions, the received signal $y_{\text{pb}}(t)$ for a scatterer at coordinates (R,θ,φ) can be modeled using time-domain waveform $s_{\text{pb}}(t)$ as

$$y_{\text{pb}}(t) = \begin{cases} x_{\text{pb}}(\tau,\theta,\varphi)s_{\text{pb}}(t-\tau)+z_{\text{pb}}(t) & \text{for } \tau \le t \le \tau+T \\ z_{\text{pb}}(t) & \text{otherwise} \end{cases}, \quad (\textit{single scatterer}) \tag{2.143}$$

where

$$\tau = \frac{2R}{c} \tag{2.144}$$

is the time delay (in seconds) between transmission of the waveform and reception of the scattering from a target at range R, $x_{\text{pb}}(\tau,\theta,\varphi)$ is the positive, real-valued, amplitude of the scatterer which encapsulates all gains/losses of the target scattering into one variable (e.g. antenna pattern, spherical spreading losses)[38], and $z_{\text{pb}}(t)$ is the additive white Gaussian noise (AWGN) (or thermal noise) signal generated at the passband frequencies and is assumed to be a wide-sense stationary (WSS), zero mean, white Gaussian random process[39] [74]. Like $y_{\text{pb}}(t)$, the units of $x_{\text{pb}}(\tau,\theta,\varphi)$ and $z_{\text{pb}}(t)$ are assumed to be normalized wave amplitudes in square-root watts. Therefore the averaging the squared-magnitude of $x_{\text{pb}}(\tau,\theta,\varphi)s_{\text{pb}}(t-\tau)$ over $\tau \le t \le \tau+T$ represents the average

[37] With this assumption, the antenna impedance $Z(f)$ would also be considered a constant over frequency f, thus simplifying the analysis in Section 2.2.1.

[38] The scattering response of an object viewed over a large bandwidth will be dependent on frequency. However, in this work, the model of $x_{\text{pb}}(\tau,\theta,\varphi)$ is assumed to have scattering of constant amplitude over the bandwidth of $S_{\text{pb}}(f)$. Perhaps the most famous illustration of frequency-dependent scattering is the Rayleigh, resonance, and optical scattering regions of a metallic sphere [56].

[39] In reality, thermal noise is injected continuously and not just at the beginning of receive chain. However, for analysis purposes it is convenient to define the noise at this point and carry it throughout the down-conversion process.

received power $\mathcal{P}_{\text{rx}}$ for this scatterer,

$$\begin{aligned}
\mathcal{P}_{\text{rx}} &= \frac{1}{T}\int_{\tau}^{\tau+T} |x_{\text{pb}}(\tau,\theta,\varphi)s_{\text{pb}}(t-\tau)|^2 dt \quad (\textit{single scatterer}) \\
&= \frac{\big(x_{\text{pb}}(\tau,\theta,\varphi)\big)^2}{T}\int_{\tau}^{\tau+T} |s_{\text{pb}}(t-\tau)|^2 dt \\
&= \frac{\big(x_{\text{pb}}(\tau,\theta,\varphi)\big)^2}{T}\int_{0}^{T} |s_{\text{pb}}(t)|^2 dt \\
&= \big(x_{\text{pb}}(\tau,\theta,\varphi)\big)^2 \mathcal{P}_{\text{s}}^{\text{a}},
\end{aligned} \tag{2.145}$$

where $\mathcal{P}_{\text{s}}^{\text{a}}$ is the analytical power (unitless) from (2.9), an arbitrary quantity which is dependent on our choice of envelope $u(t)$. Assuming $u(t)$ is normalized such that $\mathcal{P}_{\text{s}}^{\text{a}} = 1$, $x_{\text{pb}}(\tau,\theta,\varphi)$ can be expressed in terms of the receive power $\mathcal{P}_{\text{rx}}$ as

$$x_{\text{pb}}(\tau,\theta,\varphi) = \sqrt{\mathcal{P}_{\text{rx}}}. \quad [\text{W}^{\frac{1}{2}}] \quad (\textit{single scatterer}) \tag{2.146}$$

The passband signal captured by the receiver for a *continuous* scattering profile (not just one scatterer) is represented as the convolution over all delays τ and and integration over spatial angles φ and ϑ as[40]

$$y_{\text{pb}}(t) = \int_{0}^{2\pi}\int_{-\pi/2}^{\pi/2}\int_{0}^{\infty} x_{\text{pb}}(\tau,\theta,\varphi)s_{\text{pb}}(t-\tau)d\tau d\theta d\varphi + z_{\text{pb}}(t). \tag{2.147}$$

This model assumes a single antenna configuration thus the scattering profile $x_{\text{pb}}(\tau,\theta,\varphi)$ is not separable in θ and φ during the estimation process, therefore it can be represented as a one-dimensional scattering profile dependent on delay τ as

$$x_{\text{pb}}(\tau) = \int_{0}^{2\pi}\int_{-\pi/2}^{\pi/2} x_{\text{pb}}(\tau,\theta,\varphi)d\theta d\varphi. \tag{2.148}$$

[40]This receive signal model assumes zero fast-time Doppler distortion as discussed in Section 2.1.5.

Thus, (2.147) can be simplified to the form

$$y_{\mathrm{pb}}(t) = \int_0^{\infty} x_{\mathrm{pb}}(\tau) s_{\mathrm{pb}}(t-\tau) d\tau + z_{\mathrm{pb}}(t). \tag{2.149}$$

Assuming the receive filter $w_{\mathrm{rx}}(t)$ imparts minimal distortion to the waveform $s_{\mathrm{pb}}(t)$, the corresponding complex-baseband representation of (2.149) after down-conversion is

$$y(t) = \int_0^{\infty} x(\tau) s(t-\tau) d\tau + z(t) \tag{2.150}$$

where

$$x(\tau) = x_{\mathrm{pb}}(\tau) e^{-j2\pi f_{\mathrm{c}} \tau} \tag{2.151}$$

is the frequency-shifted, complex-valued impulse response of the illuminated scene and

$$z(t) = \left(z_{\mathrm{pb}}(t) e^{-j2\pi f_{\mathrm{c}} t} \right) * w_{\mathrm{rx}}(t) \tag{2.152}$$

is the down-converted, low-pass filtered, complex-baseband noise signal assumed to be wide-sense stationary (WSS), complex-Gaussian random process [74] with zero mean and noise power defined as

$$\sigma_{\mathrm{z}}^2 = \lim_{T' \to \infty} \frac{1}{2T'} \int_{-T'}^{T'} |z(t)|^2 dt. \tag{2.153}$$

Therefore, the initial SNR for receive power $\mathcal{P}_{\mathrm{rx}}$ of the single scatterer at delay τ is

$$\mathrm{SNR}_{\mathrm{init}} = \frac{\mathcal{P}_{\mathrm{rx}}}{\sigma_{\mathrm{z}}^2}. \tag{2.154}$$

Using (2.145) and (2.151), (2.154) can be rewritten as

$$\mathrm{SNR}_{\mathrm{init}} = \frac{|x(\tau)|^2}{\sigma_z^2}. \tag{2.155}$$

2.3.3 The Doppler Effect

Consider a single scatterer traveling at a radial velocity of v meters per second (where $v > 0$ represents a scatter moving towards the radar). A monostatic radar illuminates the scatterer with a pulse of duration T. If the scatterer is moving towards the radar $(v > 0)$ then the reflected pulse will have a slightly shorter pulse duration $(T_{\mathrm{ref}} < T)$ (for T_{ref} the duration of the reflected pulse) due to the motion of the scatterer during the reflection. Conversely, if the scatterer is moving away from the radar $(v < 0)$ then the reflected pulse will have a slightly longer pulse duration $(T_{\mathrm{ref}} > T)$. This effect is referred to as *time dilation* [75] which is responsible for the Doppler effect and, in extreme cases, can significantly alter the modulation of the pulse.

Figure 2.32 illustrates time dilation for the case when the scatterer is moving towards the radar. The pulse initially has pulse duration T which corresponds to a range extent of cT. The leading edge of the pulse first arrive at the scatterer at time $t = 0$. At time $t = \tau'$, the trailing edge of the pulse reflects off the scatterer, thus ending the scattering interaction. During this τ' second duration the scatterer travels $v\tau'$ meters while both the leading and traveling edges of the pulse travel $c\tau'$ meters. From observation, the range extent of the pulse cT is equal to the summation of $v\tau'$ and $c\tau'$. Likewise, the range extent of the reflected pulse cT_{ref} is equal to the difference between $c\tau'$ and $v\tau'$. Thus, the reflected pulse duration T_{ref} and duration τ' can be calculated from the equations

$$cT = (c + v)\tau' \tag{2.156}$$

and

$$cT_{\mathrm{ref}} = (c - v)\tau'. \tag{2.157}$$

Thus the duration τ' can be expressed as

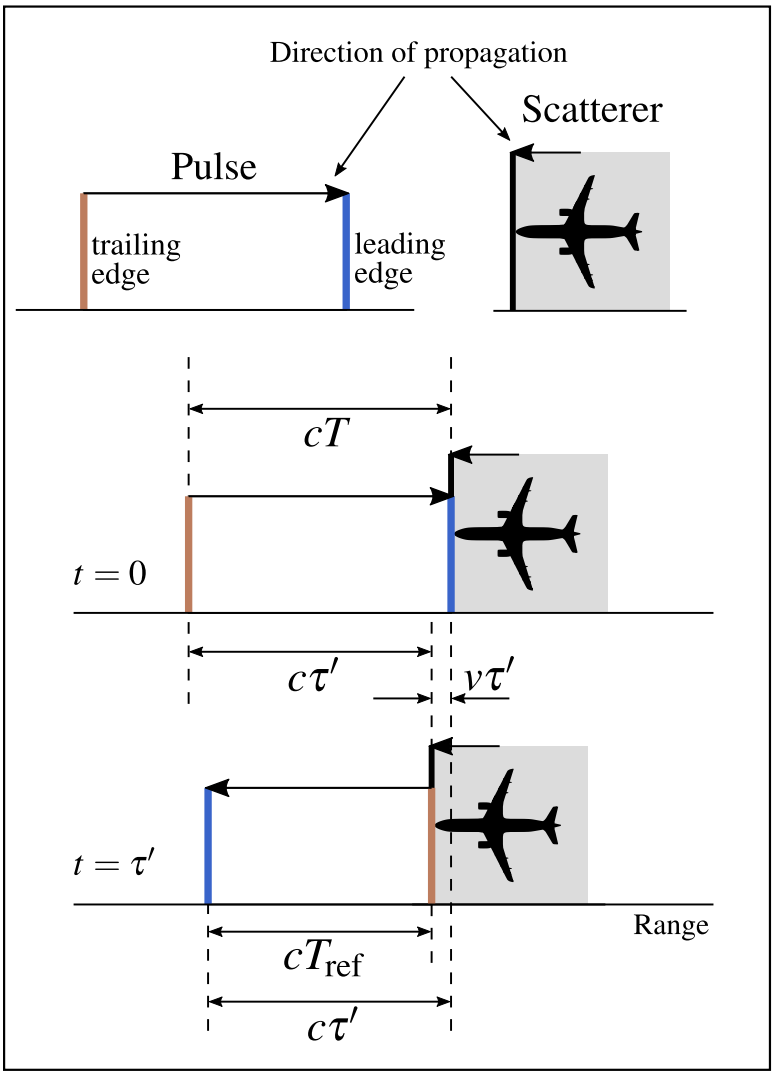

Figure 2.32: Illustration of the time dilation for pulse of duration T reflected off a scatterer traveling v meters per second.

$$\tau' = \frac{cT}{c+v} = \frac{cT_{\text{ref}}}{c-v}. \tag{2.158}$$

The new pulse duration T_{ref} in terms of the original pulse length T is thus

$$T_{\text{ref}} = \frac{c-v}{c+v}T. \tag{2.159}$$

The expression in (2.159) is valid for both positive and negative velocities.

Assuming the passband waveform $s_{\text{pb}}(t)$ is the reflected signal, the time dilation term $\left(\frac{c-v}{c+v}\right)$ is used to model the reflected signal as $s_{\text{pb}}\left(\left(\frac{c+v}{c-v}\right)t\right)$. Thus, if $v > 0$ (traveling towards the radar) the pulse is compressed $(T_{\text{ref}} < T)$ and if $v < 0$ (traveling away from the radar) the pulse is stretched $(T_{\text{ref}} > T)$. The reflected waveform representation $s_{\text{pb}}\left(\left(\frac{c+v}{c-v}\right)t\right)$ can be approximated as the Doppler-shifted waveform $s_{\text{pb}}(t, f_{\text{D}})$ from (2.71) using simplifying relationships that, for most cases in radar, impart negligible distortion to the signal model.

The Fourier transform pair of $s_{\text{pb}}\left(\left(\frac{c+v}{c-v}\right)t\right)$ is represented as

$$s_{\text{pb}}\left(\left(\tfrac{c+v}{c-v}\right)t\right) \overset{\mathcal{F}}{\longleftrightarrow} \left(\tfrac{c-v}{c+v}\right)\cdot S_{\text{pb}}\left(\left(\tfrac{c-v}{c+v}\right)f\right) \tag{2.160}$$

where $S_{\text{pb}}(f)$ is the passband frequency content from (2.10). Because the speed of light c will always be much greater than the scatterer velocities that are observed in radar, the time dilation term $\left(\frac{c-v}{c+v}\right)$ can be approximated using the first two terms of the Taylor series,

$$\frac{c-v}{c+v} \approx 1 - \frac{2v}{c} \qquad \text{if } c >> v. \tag{2.161}$$

Thus, the frequency content of the reflected signal is approximated as

$$\begin{aligned}\left(\tfrac{c-v}{c+v}\right)\cdot S_{\text{pb}}\left(\left(\tfrac{c-v}{c+v}\right)f\right) &\approx \left(1-\tfrac{2v}{c}\right)\cdot S_{\text{pb}}\left(\left(1-\tfrac{2v}{c}\right)f\right) \\ &\approx S_{\text{pb}}\left(f-\tfrac{2v}{c}f\right),\end{aligned} \tag{2.162}$$

where the contribution of the scalar term $\left(1-\frac{2v}{c}\right)$ is negligible. Using (2.13), $S_{\text{pb}}\left(f-\frac{2v}{c}f\right)$ can be

expressed in terms of the baseband spectral content $S(f)$ as

$$S_{\text{pb}}\left(f-\tfrac{2v}{c}f\right)=\frac{1}{\sqrt{2}}\Big(S\left(f-f_{\text{c}}-\tfrac{2v}{c}f\right)+S\left(f+f_{\text{c}}-\tfrac{2v}{c}f\right)\Big). \tag{2.163}$$

Assuming the waveform is narrowband (by some measure of the bandwidths discussed in Section 2.1.3), the frequency-shifted baseband spectrums can be approximated as

$$S\left(f-f_{\text{c}}-\tfrac{2v}{c}f\right)\approx S\left(f-f_{\text{c}}-\tfrac{2v}{c}f_{\text{c}}\right) \tag{2.164}$$

and

$$S\left(f+f_{\text{c}}+\tfrac{2v}{c}f\right)\approx S\left(f+f_{\text{c}}+\tfrac{2v}{c}f_{\text{c}}\right), \tag{2.165}$$

resulting in the approximate relationship,

$$S_{\text{pb}}\left(f-\tfrac{2v}{c}f\right)\approx\frac{1}{\sqrt{2}}\left(S\Big(f-\big(f_{\text{c}}+\tfrac{2v}{c}f_{\text{c}}\big)\Big)+S\Big(f+\big(f_{\text{c}}+\tfrac{2v}{c}f_{\text{c}}\big)\Big)\right). \tag{2.166}$$

Taking the inverse Fourier transform of the expression in (2.166) yields the Fourier transform pair

$$\sqrt{2}u(t)\cos\Big(2\pi\cdot\big(f_{\text{c}}+\tfrac{2v}{c}f_{\text{c}}\big)t+\psi(t)\Big)\overset{\mathcal{F}}{\longleftrightarrow}\frac{1}{\sqrt{2}}\left(S\Big(f-\big(f_{\text{c}}+\tfrac{2v}{c}f_{\text{c}}\big)\Big)+S\Big(f+\big(f_{\text{c}}+\tfrac{2v}{c}f_{\text{c}}\big)\Big)\right), \tag{2.167}$$

where $\frac{2v}{c}f_{\text{c}}$ is known as the Doppler frequency f_{D} (as defined in (2.70)). Note that the reflected signal has the form of the incident signal with a shifted center frequency, $f_{\text{c}}+f_{\text{D}}$. Thus the reflected signal $s_{\text{pb}}\Big(\big(\frac{c+v}{c-v}\big)t\Big)$ can be well-approximated as the Doppler-shifted waveform $s_{\text{pb}}(t,f_{\text{D}})$ from (2.71),

$$s_{\text{pb}}\Big(\big(\tfrac{c+v}{c-v}\big)t\Big)\approx s_{\text{pb}}(t,f_{\text{D}})=\sqrt{2}u(t)\cos\big(\psi_{\text{pb}}(t)+\psi_{\text{D}}(t)\big). \tag{2.168}$$

2.4 Radar Digital Signal Processing

The radar digital signal processor represents the entirety of the digital realm of the data handling (e.g. from the ADC to the outputted synthetic aperture radar (SAR) image). There are many processing methods that combine this data different ways: SAR, space-time adaptive processing, pulse-Doppler processing, monopulse radar, multistatic configurations, and so on [55, 56, 76, 77]. Most of these methods can be boiled down into a single core component: the matched filter response of a signal pulse. Because this work describes the performance of a waveform/emission during a single pulse, the discussion is limited to this scope. Though the results throughout this work form that core component of many radar processing methods (i.e. the matched filter response) thus can be extrapolated accordingly. Here, the theory behind sampling and the optimality of the matched filter (under certain conditions) is presented.

2.4.1 Digitization

On receive, the signals $y_{\mathrm{I}}(t)$ and $y_{\mathrm{Q}}(t)$ (from (2.137) and (2.138)) are sampled using two ADCs at sampling rate $f_{\mathrm{s}} = 1/T_{\mathrm{s}}$ (for T_{s} the sampling period). The two ADCs sampling two real-valued signals can be equivalently modeled as one ADC sampling the complex signal $y(t)$. The Nyquist sampling theorem states that to sufficiently capture the information of band-limited complex-baseband signal, one must sample at a rate greater than or equal to the bandwidth, $f_{\mathrm{s}} \geq B$, where each sample is complex-valued. However, because all real-world signals theoretically have infinite bandwidth due to a finite duration (e.g. pulse duration), the sampling frequency must be defined relative to a bandwidth chosen from various definitions discussed in Section 2.1.3. Here, the sampling rate is defined relative to the 3 dB bandwidth $B_{3\mathrm{dB}}$ of waveform $s(t)$ as

$$f_{\mathrm{s}} = \kappa B_{3\mathrm{dB}} \tag{2.169}$$

where $\kappa \geq 1$ is the 3 dB receiver over-sampling factor. For FM waveforms, κ is typically set high enough to maintain sufficient fidelity of the spectral roll-off of the waveform [3, 38, 44].

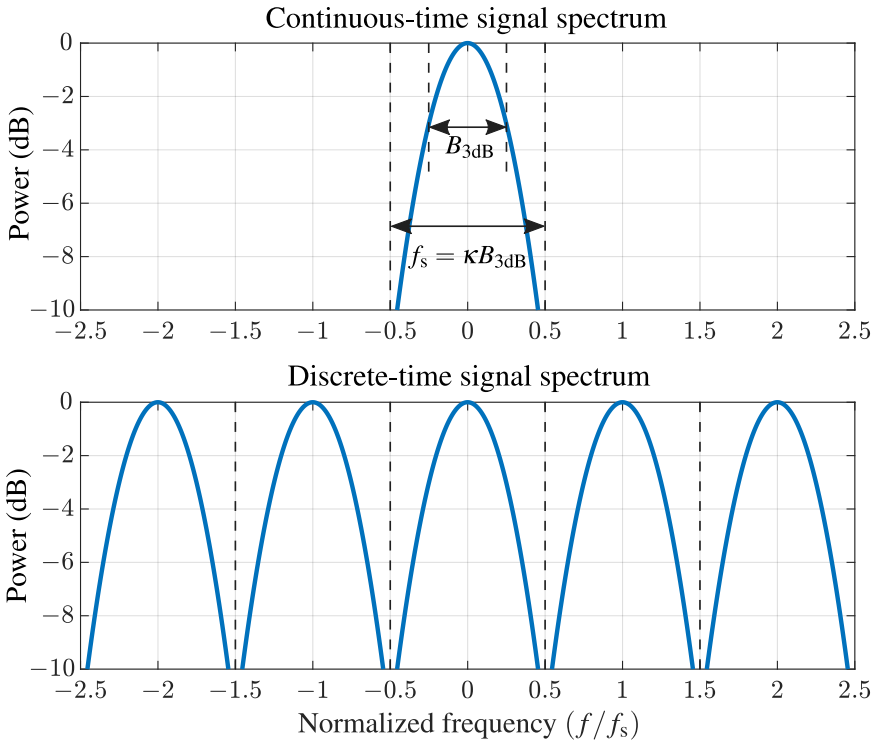

Figure 2.33: Comparison between a continuous-time signal spectrum and the corresponding discrete-time signal spectrum after sampling.

The sampling of signal $y(t)$ can be represented in continuous-time by an infinite impulse-train product, $y(t)\cdot\sum_{\ell=-\infty}^{\infty}\delta(t-\ell T_s)$. The Fourier transform of this sampled signal is $Y(f)*\sum_{\ell=-\infty}^{\infty}\delta(f-\ell f_s)$ which creates the Fourier transform pair

$$y(t)\cdot\sum_{\ell=-\infty}^{\infty}\delta(t-\ell T_s)\overset{\mathcal{F}}{\longleftrightarrow}Y(f)*\sum_{\ell=-\infty}^{\infty}\delta(f-\ell f_s). \tag{2.170}$$

Figure 2.33 compares an example spectrum of the continuous-time signal $y(t)$ and the spectrum of the sampled signal $y(t)\cdot\sum_{\ell=-\infty}^{\infty}\delta(t-\ell T_s)$. The spectrum of $y(t)$ is repeated every multiple of f_s in the frequency domain from the convolution with the infinite summation of impulses. If the spectrum of $y(t)$ extends beyond the sampling frequency, the spectral content from adjacent Nyquist zones wrap into each other causing interference known as *aliasing*. A common practice to prevent aliasing is via the LPF in the down-conversion model from Figure 2.30. This LPF (also referred to as an *anti-aliasing filter*) filters out a majority of the energy outside the frequencies $\pm f_s/2$ resulting in negligible aliased energy.

The ADC has a finite number of bits b_{rx} to represent the real and imaginary parts of a complex sample. The sampled voltage rounds to the nearest quantized voltage represented in the $2^{b_{\text{rx}}}$ total voltage states. This rounding produces a small error in the captured signal referred to as *quantization noise* which is a common figure of merit for ADCs. If the quantization noise is below the noise floor (ideally 10 times smaller [78]), then it only has a negligible effect on the captured signal. To do this the least significant bit (LSB) must be set to a voltage level to sufficiently capture the system noise.

The dynamic range (in power) of an ADC is dictated by the square of the number of the voltage states, $(2^{b_{\text{rx}}})^2 = 2^{2b_{\text{rx}}}$, which in decibels is expressed as

$$\begin{aligned} 10\log_{10}\left(2^{2b_{\text{rx}}}\right) &= 2b_{\text{rx}} \cdot 10\log_{10}(2) \\ &= b_{\text{rx}} \cdot 20\log_{10}(2) \\ &\approx 6.02 b_{\text{rx}}. \end{aligned} \tag{2.171}$$

Therefore, for each additional bit the dynamic range of the ADC increases by ~6 dB. The dynamic range can be set to measure a certain range of voltages. The minimum measurable voltage should be set such that the quantization noise is beneath the system thermal noise, and the maximum measurable voltage should be set to capture the maximum expected voltage on receive without saturating. If an ADC saturates, the data for the duration of saturation is severely distorted and may be unusable.

The nonlinear behavior of quantization of the ADC is considered minimal, and thus is not addressed throughout a majority of this work. In Chapter 5, the quantization of an ADC is reexamined when the sensitivity of a waveform design calls for a higher fidelity RF model.

2.4.2 Matched Filtering

After sampling of the receive signal $y(t)$ from (2.150) at rate f_{s}, the sampled sequence is digitally filtered to increase the SNR. It is advantageous to maximize this SNR to improve both estimation and detection performance [56]. The correlation filter that maximizes SNR at the output of the

filter is called the *matched filter* and is derived from sampled versions of the noise signal $z(t)$ and baseband waveform $s(t)$.

Sampling the waveform $s(t)$ at sampling rate f_s forms the $N \times 1$ vector

$$\mathbf{s} = \begin{bmatrix} s[0] & s[1] & \cdots & s[N-1] \end{bmatrix}^T \tag{2.172}$$

where

$$N = f_s T = \kappa B_{3\text{dB}} T = \kappa B T \tag{2.173}$$

is the discretized length of the waveform, $(\bullet)^T$ is vector transpose, and $s[n] = s(nT_s + \xi)$ where $\xi \in [0, T_s]$ is a subsample time-shift of the waveform. The value of ξ dictates how the waveform $s(t)$ is discretized for the matched filter and is chosen somewhat arbitrarily in practice. Though ξ does have an effect on the matched filter response when the captured signal is *straddled* compared to $\mathbf{s}$ (Section 2.4.3). In Section 5.3 the subsample time-shift ξ is incorporated in a waveform optimization problem to find the optimal value of ξ for a particular waveform.

Another method of generating the matched filter is via a loopback capture where the waveform is sent through the transmit and receive chains and captured by the ADC. This sampled copy of the waveform is used to form matched filter which has the added benefit of capturing distortions caused by the RF chains. In this case, the value of ξ is dictated by the propagation delay between the waveform generator and the ADC. If the analytical waveform $s(t)$ is optimized based on some criteria, this distortion should be accounted for in the optimization process. If the distortion model is not available or too complex to generate, the analytical model of $s(t)$ must be chosen such that the distortion of the RF chains is of limited impact to the captured signal structure (as would be the case for spectrally-contained, constant amplitude waveforms).

Define the ℓth received sample as $y[\ell]$ for $\ell \in \{0, 1, 2, \ldots\}$ where $y[\ell] = y(\ell T_s)$ then the N samples corresponding scattering at delay $\tau = \ell T_s$ are formed into the $N \times 1$ receiver vector,

$$\mathbf{y} = \begin{bmatrix} y[0] & y[1] & \cdots & y[N-1] \end{bmatrix}^T \tag{2.174}$$

Within (2.174) the noise signal $z(t)$ is also sampled and can be defined separately as the $N \times 1$ vector

$$\mathbf{z} = \begin{bmatrix} z[0] & z[1] & \cdots & z[N-1] \end{bmatrix}^T, \tag{2.175}$$

where $z[\ell] = z(\ell T_s)$. The signal $z(t)$ is zero mean therefore

$$E\{\mathbf{z}[\ell]\} = \mathbf{0}_{N\times 1} \tag{2.176}$$

where $E\{\bullet\}$ is the expected value and $\mathbf{0}_{N\times 1}$ is a length-N vector of zeros. The positive definite, $N \times N$ noise covariance of $\mathbf{z}[\ell]$ is defined as

$$E\left\{\mathbf{z}[\ell]\mathbf{z}^H[\ell]\right\} = \mathbf{R}_z \tag{2.177}$$

where the diagonal elements are equal to the noise power from (2.153),

$$\sigma_z^2 = E\left\{|z[\ell]|^2\right\} = E\left\{|z[\ell+1]|^2\right\} = \cdots = E\left\{|z[\ell+N-1]|^2\right\}. \tag{2.178}$$

Define $\mathbf{w}$ as the $N \times 1$ vector used to estimate the complex amplitude of the scattering at sample delay ℓ via the vector inner product,

$$\hat{x}[\ell] = \mathbf{w}^H\mathbf{y}[\ell] = \sum_{n=0}^{N-1} w^*[n]y[\ell+n] \tag{2.179}$$

where $[\bullet]^H = ([\bullet]^T)^*$ is the complex-conjugate (or Hermitian) transpose. We want to form $\mathbf{w}$ to maximize the SNR of $|\mathbf{w}^H\mathbf{y}[\ell]|^2$ to improve both the estimate and detection performance of the scattering at delay ℓ.

For example, assume the receive vector $\mathbf{y}[\ell]$ is comprised of a single scatter at sample delay ℓ

in the presence of noise as

$$\mathbf{y}[\ell] = x[\ell]\mathbf{s} + \mathbf{z}[\ell] \quad (\textit{single scatterer}) \tag{2.180}$$

where $x[\ell] = x(\ell T_s)$. Applying the filter $\mathbf{w}$ to (2.180) is represented as

$$\mathbf{w}^H\mathbf{y}[\ell] = x[\ell]\mathbf{w}^H\mathbf{s} + \mathbf{w}^H\mathbf{z}[\ell]. \quad (\textit{single scatterer}) \tag{2.181}$$

The signal and noise power components of $|\mathbf{w}^H\mathbf{y}[\ell]|^2$ can be found by taking the expected value as

$$\begin{aligned} E\left\{|\mathbf{w}^H\mathbf{y}[\ell]|^2\right\} &= E\left\{|x[\ell]\mathbf{w}^H\mathbf{s} + \mathbf{w}^H\mathbf{z}[\ell]|^2\right\} \quad (\textit{single scatterer}) \\ &= |x[\ell]|^2\mathbf{w}^H\mathbf{s}\mathbf{s}^H\mathbf{w} + \mathbf{w}^H\left(E\left\{\mathbf{z}[\ell]\mathbf{z}^H[\ell]\right\}\right)\mathbf{w} + 2\Re\left\{x^*[\ell]\mathbf{s}^H\mathbf{w}\mathbf{w}^H\left(E\left\{\mathbf{z}[\ell]\right\}\right)\right\} \\ &= |x[\ell]|^2|\mathbf{w}^H\mathbf{s}|^2 + \mathbf{w}^H\mathbf{R}_z\mathbf{w}. \end{aligned} \tag{2.182}$$

Therefore the signal-to-noise ratio after filtering can be expressed as

$$\text{SNR} = |x[\ell]|^2\frac{|\mathbf{w}^H\mathbf{s}|^2}{\mathbf{w}^H\mathbf{R}_z\mathbf{w}}. \tag{2.183}$$

Because $\mathbf{R}_z$ is positive definite, a Cholesky decomposition can be applied as [79]

$$\mathbf{R}_z = \mathbf{A}_z\mathbf{A}_z^H, \tag{2.184}$$

where $\mathbf{A}_z$ is also an $N \times N$, positive definite matrix. Therefore the SNR can be rewritten as

$$\text{SNR} = |x[\ell]|^2\frac{|\mathbf{w}^H\mathbf{s}|^2}{\mathbf{w}^H\mathbf{A}_z\mathbf{A}_z^H\mathbf{w}}. \tag{2.185}$$

The Cauchy-Schwartz inequality for two $N \times 1$ vectors $\mathbf{p}$ and $\mathbf{q}$ is [46]

$$|\mathbf{p}^H\mathbf{q}|^2 \le \|\mathbf{p}\|_2^2\|\mathbf{q}\|_2^2. \tag{2.186}$$

If we define $\mathbf{p} = \mathbf{A}_z^H \mathbf{w}$ and $\mathbf{q} = \mathbf{A}_z^{-1} \mathbf{s}$, the inequality becomes

$$|\mathbf{w}^H \mathbf{s}|^2 \leq (\mathbf{w}^H \mathbf{R}_z \mathbf{w})(\mathbf{s}^H \mathbf{R}_z^{-1} \mathbf{s}). \tag{2.187}$$

Rearranging the inequality, the form of the SNR normalized by $|x[\ell]|^2$ is evident,

$$\frac{\text{SNR}}{|x[\ell]|^2} = \frac{|\mathbf{w}^H \mathbf{s}|^2}{\mathbf{w}^H \mathbf{R}_z \mathbf{w}} \leq \mathbf{s}^H \mathbf{R}_z^{-1} \mathbf{s}. \tag{2.188}$$

Thus the SNR is maximized when

$$\frac{|\mathbf{w}_{\text{MF}}^H \mathbf{s}|^2}{\mathbf{w}_{\text{MF}}^H \mathbf{R}_z \mathbf{w}_{\text{MF}}} = \mathbf{s}^H \mathbf{R}_z^{-1} \mathbf{s}. \tag{2.189}$$

The Cauchy-Schwartz inequality is equal only when $\mathbf{p} = \gamma \mathbf{q}$ where γ is any non-zero scalar. Therefore (2.189) is maximized when $\mathbf{A}_z^H \mathbf{w}_{\text{MF}} = \gamma \mathbf{A}_z^{-1} \mathbf{s}$. Solving for $\mathbf{w}_{\text{MF}}$ yields

$$\begin{aligned} \mathbf{w}_{\text{MF}} &= \gamma \left(\mathbf{A}_z^H \right)^{-1} \mathbf{A}_z^{-1} \mathbf{s} \\ &= \gamma \left(\mathbf{A}_z \mathbf{A}_z^H \right)^{-1} \mathbf{s} \\ &= \gamma \mathbf{R}_z^{-1} \mathbf{s}. \end{aligned} \tag{2.190}$$

The scalar γ is chosen such that $\mathbf{w}_{\text{MF}}^H \mathbf{y}[\ell]$ estimates the complex scattering amplitude $x[\ell]$ without scaling which is the same as constraining $\mathbf{w}_{\text{MF}}^H \mathbf{s} = 1$. Plugging in the relationship from (2.190) to this constraint yields

$$\gamma = \frac{1}{\mathbf{s} \mathbf{R}_z^{-1} \mathbf{s}}. \tag{2.191}$$

Thus, inserting (2.191) into (2.190) produces the scaled matched filter

$$\mathbf{w}_{\text{MF}} = \frac{\mathbf{R}_z^{-1} \mathbf{s}}{\mathbf{s}^H \mathbf{R}_z^{-1} \mathbf{s}}. \tag{2.192}$$

which is the generalized matched filter for any noise covariance $\mathbf{R}_z$ resulting in the matched filter estimate of $x[\ell]$ as

$$\begin{aligned}\hat{x}_{\mathrm{MF}}[\ell] &= \mathbf{w}_{\mathrm{MF}}^{H}\mathbf{y}[\ell] \\ &= \frac{\mathbf{s}^{H}\mathbf{R}_{\mathrm{z}}^{-1}\mathbf{y}[\ell]}{\mathbf{s}^{H}\mathbf{R}_{\mathrm{z}}^{-1}\mathbf{s}}.\end{aligned} \tag{2.193}$$

Therefore, The maximum SNR after matched filtering from (2.183) using (2.192) is

$$\begin{aligned}\mathrm{SNR}_{\mathrm{MF}} &= |x[\ell]|^{2}\frac{|\mathbf{w}_{\mathrm{MF}}^{H}\mathbf{s}|^{2}}{\mathbf{w}_{\mathrm{MF}}^{H}\mathbf{R}_{\mathrm{z}}\mathbf{w}_{\mathrm{MF}}} \\ &= |x[\ell]|^{2}\mathbf{s}\mathbf{R}_{\mathrm{z}}^{-1}\mathbf{s}.\end{aligned} \tag{2.194}$$

Assume that the bandwidth of the LPF in down-conversion stage from Figure 2.30 is equal to $f_{\mathrm{s}}/2$, therefore the sampled signal $\mathbf{z}[\ell]$ can be treated as additive white Gaussian noise (AWGN) where each sample is independent and identically distributed (IID) [74]. The assumption of statistical independence between the noise samples allows for the calculation of the off-diagonal entries of $\mathbf{R}_{\mathrm{z}}$ as

$$E\left\{z[\ell+n]z^{*}[\ell+m]\right\} = E\left\{z[\ell+n]\right\}\cdot E\left\{z^{*}[\ell+m]\right\} = 0 \tag{2.195}$$

for $n \neq m$. Thus, the IID-AWGN covariance reduces to

$$\mathbf{R}_{\mathrm{z}} = \sigma_{\mathrm{z}}^{2}\mathbf{I}_{N}, \tag{2.196}$$

where $\mathbf{I}_{N}$ is the $N \times N$ identity matrix defined as an all zeros matrix with ones on the diagonal,

$$\mathbf{I}_{N} = \begin{bmatrix} 1 & 0 & \cdots & 0 & 0 \\ 0 & 1 & & 0 & 0 \\ \vdots & & \ddots & & \vdots \\ 0 & 0 & & 1 & 0 \\ 0 & 0 & \cdots & 0 & 1 \end{bmatrix}. \tag{2.197}$$

Thus, for the case of IID white noise, the matched filter from (2.192) reduces to

$$\mathbf{R}_z = \sigma_z^2 \mathbf{I}_N \implies \mathbf{w}_{\text{MF}} = \frac{1}{\|\mathbf{s}\|_2^2}\mathbf{s}. \tag{2.198}$$

where

$$\|\mathbf{s}\|_2^2 = \sum_{n=0}^{N-1} |s[n]|^2 \tag{2.199}$$

is the squared l^2-norm of discrete vector $\mathbf{s}$ which has the approximate relationship with (2.6) as

$$\|\mathbf{s}\|_2^2 \approx \frac{1}{T_s}\|s(t)\|_2^2, \tag{2.200}$$

and with (2.9) as

$$\frac{1}{N}\|\mathbf{s}\|_2^2 \approx \frac{1}{T}\|s(t)\|_2^2. \tag{2.201}$$

In this work $\|\mathbf{s}\|_2^2$ and $\frac{1}{N}\|\mathbf{s}\|_2^2$ are referred to as the *vector energy* and *vector average power*, respectively. Unless specified otherwise, the form of the matched filter in (2.198) is used and IID white noise is implicitly assumed.

The SNR after matched filtering from (2.194) using the reduced form of the matched filter from (2.198) is

$$\text{SNR}_{\text{MF}} = \frac{|x[\ell]|^2}{\sigma_z^2}\|\mathbf{s}\|_2^2. \tag{2.202}$$

Note that the maximum SNR depends only on the scattering amplitude $x[\ell]$ and vector energy $\|\mathbf{s}\|_2^2$ of the discretized waveform, and not the specific modulation of $\mathbf{s}$ [80]. Using the approximate relationship from (2.201), (2.202) can be written in terms of (2.155) as

$$\begin{aligned}\text{SNR}_{\text{MF}} &= N\frac{|x[\ell]|^2}{\sigma_{\text{z}}^2}\frac{1}{N}\left\|\mathbf{s}\right\|_2^2 \\ &\approx N\frac{|x[\ell]|^2\mathcal{P}_{\text{s}}^{\text{a}}}{\sigma_{\text{z}}^2} \\ &\approx N\times\text{SNR}_{\text{init}}.\end{aligned} \tag{2.203}$$

Thus the SNR increase after matched filtering is equal to the number samples in the discretized waveform N. Note that the SNR relationship in (2.203) is only the case when the noise samples in $\mathbf{z}[\ell]$ are independent (a requirement for the form of SNR in (2.202)).

Though the matched filter is optimal in an SNR sense, the derivation does not account for interference from scatterers offset in range. The sidelobes of the correlation response (discussed in Section 2.1.4)) extend in range in both directions a range extent equal to $cT/2$. These sidelobes coherently add with the correlation mainlobe of the estimated scatterer, an interference not accounted for in matched filter derivation. Thus the match filter may not be optimal in a signal-to-interference plus noise (SINR) sense. Therefore, it is desirable to minimize these sidelobes to prevent this type of distortion. One method that is widely used to minimize the sidelobes of the correlation response is via application of a spectral window on the receive data, though this method results in a loss is SNR of the estimated scattering response [5]. Mismatch filtering approaches are also common to the reduction of correlation sidelobes and have been found to achieve good results for FM waveforms with low loss [81, 82] though perform best when a waveform already has a low sidelobe autocorrelation response. The ideal method to minimize SINR (via sidelobes of offset scatterers in range) is to use an optimized FM waveform with low sidelobes and compress the response using a matched filter on receive to limit SNR degradation.

2.4.3 Digital Correlation and Waveform Straddling

Along with the delay-Doppler ambiguity function $\chi_{\text{D}}(\tau, f_{\text{D}})$ and continuous autocorrelation $\chi_{\text{a}}(\tau)$ from Section 2.1.5, the digital autocorrelation function for the receiver sampling rate f_{s} is also used to evaluate the quality of a radar waveform. The digital autocorrelation $r[\ell]$ for sample delay ℓ is

defined as

$$\begin{aligned} r[\ell] &= \frac{1}{\|\mathbf{s}\|_2^2} \sum_{n=0}^{N-1} s^*[n-\ell]\, s[n] \\ &= \frac{1}{\|\mathbf{s}\|_2^2} \sum_{n=0}^{N-1} s^*\big((n-\ell)T_\mathrm{s} + \xi\big) s(nT_\mathrm{s} + \xi) \end{aligned} \tag{2.204}$$

which introduces the sampled nature of the radar digital signal processor into the evaluation of the waveform. Recall that ξ is a subsample shift of the utilized when discretizing the continuous waveform $s(t)$ for the matched filter (Section 2.4.2). If amplitude envelope $u(t)$ from (5.1) is a rectangular window, a lower bound on the digital autocorrelation peak sidelobe level (PSL) can be defined as

$$\mathrm{PSL}_{\text{RECT-bound}}\ (\mathrm{dB}) = 20\log_{10}\left(\frac{1}{N}\right) = -20\log_{10}(N) \tag{2.205}$$

which corresponds to the ratios of amplitudes of $r[\ell]$ at $\ell = \pm(N-1)$ and $\ell = 0$.

The fact that the digital autocorrelation is a function of discretized continuous functions has consequences that are otherwise unseen when observing the continuous autocorrelation. Assume the received signal that is incident on the receiver ADC is the continuous waveform $s(t)$ in the absence of noise. The ADC samples every T_s seconds however how the points at which the samples land within the waveform are random, thus the sampled sequence does not necessarily match that of the matched filter. This loss caused by the mismatch between the received signal and the matched filter is known as *straddling loss* and is worst when the received signal is sampled exactly halfway between the points of the matched filter [56]. The net effect is an apparent loss in scattering SNR though the severity of the straddling can be lessened through interpolation techniques or by increasing the sampling rate [56]. Define $r[\ell;\varrho]$ as the matched filter straddled response when the receive signal is offset by subsample shift $\varrho \in \left[-\frac{T_\mathrm{s}}{2}, \frac{T_\mathrm{s}}{2}\right]$ relative to the matched filter samples expressed as

$$r[\ell;\varrho] = \frac{1}{\|\mathbf{s}\|_2^2} \sum_{n=0}^{N-1} s^*\big((n-\ell)T_\mathrm{s} + \xi\big) s(nT_\mathrm{s} + \xi + \varrho). \tag{2.206}$$

Thus the digital cross-correlation function $r[\ell;\varrho]$ becomes the digital autocorrelation function $r[\ell]$ when $\varrho = 0$. Note that the subsample shift ξ is associated with the discretization of the waveform for matched filtering, and the subsample shift ϱ represents the shift of the receive signal relative to the digital matched filter.

2.5 Summary

This chapter provides a extensive background to modeling and analysis of radar waveforms and how its modulation is carried throughout multiple stages: the transmission, the scattering, the receptions, and finally the sampling and subsequent processing. In high power radar applications, it is advantageous to to constrained the waveform structure to be both constant amplitude and spectrally contained to limit the distortion caused by the HPA used on transmit (the largest source of distortion in a radar system).

Chapter 3

Spatially-Diverse Transmission Analysis

In Chapter 2, a background was provided that the mathematical foundation for analysis of a single waveform radar transmission. Here, the analysis is extended to multiple independent, collocated radar transmitter/receivers that have the capability to emit different waveforms, thus granting the ability to produce a spatially-diverse emission; otherwise known as a *fully digital array radar* (DAR) [20]. The term 'spatially-diverse' is a term that is not widely used, but is used here as 'catch-all' for any radar transmission mode that has a spatially-dependent modulation structure, which could include simultaneous multifunction beams or a MIMO mode. The distinction is made here to distinguish between a spatially-diverse emission that provides an enhance spatial resolution capability (MIMO), and a spatially-diverse emission that is comprised of multiple (spatially-separated) beams executing different functions but not necessarily achieving a resolution improvement (simultaneous multifunction). A spatially-diverse emission could dedicate a wide sector of space for a MIMO function while still simultaneously operating a focused (though low total energy) beam performing an separate function.

Here, the angle-dependent far-field emission is defined as well as multiple assumptions that can be made (namley the large-array and narrowband assumptions) that can significantly simply emission modeling. The *angle-delay ambiguity function* is defined which illustrates the achieved spatial resolution enhancement when operating the radar in a MIMO mode by defining the function as the product of two functions: the beam factor and the diversity factor. The beam factor corresponds to the nominal array resolution given a certain geometry, and the diversity factor illustrates the improvement in resolution that can be achieved through the decorrelation of the signal structure in space. An example is presented that compares a DAR operating in the MIMO

mode to that of a traditional phased array radar. As expected, the MIMO mode achieves a better single pulse spatial resolution compared to the phased-array through with a commensurate loss in focused energy. However, flexibility in time-energy-management of the DAR can compensate for the loss in focused energy with longer dwells due to a larger single pulse coverage and relaxed radar function scheduling [20].

In addition to the single waveform analysis in Chapter 2, the mutual coupling present in uniform linear array (ULA) is considered in this chapter. The mutual coupling is defined from both a circuit and scattering perspective. The analytical models for half-wavelength dipole self and mutual impedances (derived using the induced emf method [73]) are utilized to analyze the mutual coupling behavior of two uniform linear arrays matched for broadside transmission: an array with half-wavelength spacing and an array with quarter-wavelength spacing. As the array is scanned, the active impedance behavior of the array changes which can alter the match of the array. In an extreme case, for ULAs with less than half-wavelength spacing, the radar can excite the array such that a majority of the energy lies within what is called in *invisible space* which is associated with low radiation resistances and high reactance. In is shown that for the quarter-wavelength array, there exist array excitations that can reflect/couple 99.99% of the energy back into the array which for high power radar applications can result in RF component damage. Three examples of a spatially-diverse emissions are simulated for both the analyzed arrays to show that the general criteria for array performance in the analysis of scanning arrays can also be applied to spatially-diverse emissions.

3.1 Processing and Evaluation of Spatially-Diverse Emissions

The free-space propagation of electromagnetic waves is a classic example of a linear system which has the property that the state of the system can be defined as a superposition of the system effects caused by its individual components. The state of the electromagnetic spectrum is thus a coherent combination of the individual signals present in the environment at any given coordinate and time. Using this principle, the emission generated by an radar with an array of antenna elements with

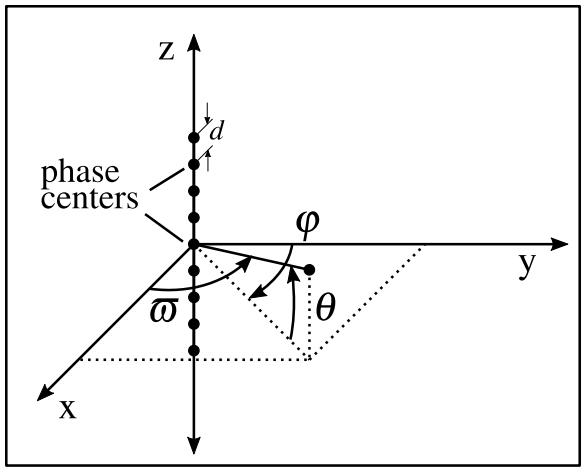

Figure 3.1: Spatial geometry of free-space propagation for uniformly spaced linear array with inter-element spacing d.

independent waveform generation can be predicted. The property of superposition can be applied to any antenna array geometry though only the *uniform linear array* (ULA) is considered.

3.1.1 Array Beamforming

The geometry of a uniform linear array is shown in Figure 3.1. It is assumed that the array is arranged of M identical antenna elements with uniform spacing d laid on the z-axis and placed such that the origin pertains to the center of an array. Assume that the dominant polarization of each element is linearly polarized in the ϖ dimension (e.g. an array of parallel dipoles), and that the maximum of the antenna pattern is pointed in the direction $(\theta = 0^\circ, \varphi = 0^\circ)$. The angle ϖ is defined as the angle off the x-axis and is solely defined to describe the polarization of the antennas and is related to θ and φ as[1]

$$\cos\varpi = \sin\varphi\cos\theta. \tag{3.1}$$

The elements are arranged on the z-axis so there is a symmetry about the coordinate φ. Note that this arrangement does not imply that the array is "vertical" as no absolute coordinates (e.g. zenith

[1]Note that the polarization definition is only true for the plane waves in the far-field of the antennas since all of the elements are not placed at the origin of the coordinate axis.

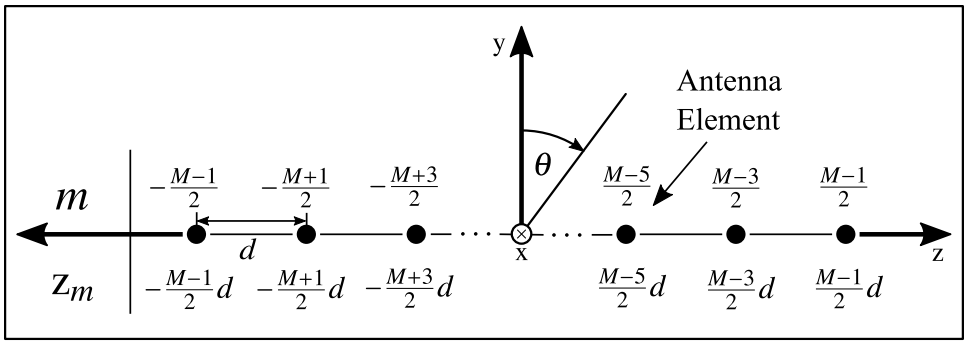

Figure 3.2: Uniform linear array (ULA) geometry.

or nadir) are defined for this system. Figure 3.2 shows the $\varphi = 0°$ cut of the array geometry where each element is indexed from $m = -\frac{M-1}{2}$ and $m = \frac{M-1}{2}$, thus the collection of indices is represented by the set

$$m \in \left\{-\tfrac{M-1}{2}, -\tfrac{M+1}{2}, \ldots, \tfrac{M-3}{2}, \tfrac{M-1}{2}\right\}. \tag{3.2}$$

The elements are evenly spaced by by inter-element spacing d, thus the corresponding z-coordinate for element m is

$$z_m = md. \tag{3.3}$$

The far-field electrical field for these antennas can be defined using the forward voltages for each antenna (denoted $V_m^+(f)$) and *active element patterns* (denoted $F_m(f,\theta,\varphi)$) as [83, 84]

$$\vec{\mathscr{E}}(\theta,\varphi,R;f) = \sqrt{\frac{\eta}{Z_0}}\frac{e^{-j\frac{2\pi f}{c}R}}{R\sqrt{4\pi}}\sum_m F_m(f,\theta,\varphi)V_m^+(f)\,\vec{a}_{\varpi}. \tag{3.4}$$

The active element pattern is measured for each element while the others elements are terminated to the line impedance, thus the active element pattern incorporates mutual coupling effects, impedance mismatches, and delay of propagation differences between elements [84] (more on these topics in Section 3.2.2). Assuming that each generated waveform is undistorted by the transmit chain, we can replace the forward voltages on each of the element in (3.4) with a scaled copy of the ideal waveform $S_{\text{pb},m}(f)$ (via 2.117) as

$$\vec{\mathscr{E}}(\theta,\varphi,R;f) = w_1\sqrt{\frac{\eta}{Z_0}}\frac{e^{-j\frac{2\pi f}{c}R}}{R\sqrt{4\pi}}\sum_m F_m(f,\theta,\varphi)S_{\mathrm{pb},m}(f)\,\vec{a}_{\varpi}, \tag{3.5}$$

and in the time-domain,

$$\vec{\mathscr{E}}(\theta,\varphi,R;t) = w_1\sqrt{\frac{\eta}{Z_0}}\frac{1}{R\sqrt{4\pi}}\sum_m F_m(t,\theta,\varphi) * s_{\mathrm{pb},m}\left(t-\tfrac{R}{c}\right)\vec{a}_{\varpi}. \tag{3.6}$$

Thus summation term describes the coherent summation of the far-field plane wavefronts of each antenna at range R. By removing the dependence on range we can define

$$\tilde{g}_{\mathrm{pb}}(t,\theta,\varphi) = \frac{1}{M}\sum_m F_m(t,\theta,\varphi) * s_{\mathrm{pb},m}(t) \tag{3.7}$$

as the far-field, time-varying beampattern of the ULA (at passband) for the assumption of zero transmitter distortion (it is customary to normalize the summation by the number of elements M). In the frequency domain, (3.7) is expressed as

$$\tilde{G}_{\mathrm{pb}}(f,\theta,\varphi) = \frac{1}{M}\sum_m F_m(f,\theta,\varphi)S_{\mathrm{pb},m}(f). \tag{3.8}$$

The passband representations of the far-field signals in (3.7) and (3.10) can likewise be represented as the complex-baseband signals

$$\tilde{g}(t,\theta,\varphi) = \frac{1}{M}\sum_m \left(F_m(t,\theta,\varphi)e^{-j2\pi f_c t}\right) * s_m(t) \tag{3.9}$$

and

$$\tilde{G}(f,\theta,\varphi) = \frac{1}{M}\sum_m F_m(f+f_{\mathrm{c}},\theta,\varphi)S_m(f), \tag{3.10}$$

respectively. Using the form of $S_{\mathrm{pb}}(f)$ from (2.13), the passband spectral content of the far-field, time-varying beampattern can be rewritten in terms of the baseband waveform spectral content $S_m(f)$ as

$$\tilde{G}_{\mathrm{pb}}(f,\theta,\varphi) = \frac{1}{M\sqrt{2}} \sum_m F_m(f,\theta,\varphi)\left(S_m(f-f_{\mathrm{c}}) + S_m^*(f+f_{\mathrm{c}})\right). \tag{3.11}$$

3.1.1.1 Large Array Assumption

For an infinite ULA, each element theoretically "sees" the same environment, therefore the active element pattern is identical for each antenna [84]. This limiting case leads to the *large array* approximation where the active element pattern is measured for a single antenna element (typically the center antenna) and is used as an approximation for the element patterns for the entirety of the array. For a finite array, the patterns for the edge elements deviate from the infinite array active element pattern, though if the array is large enough these "edge effects" are overpowered by the quantity of elements that do not have edge effects [41, 84]. Therefore, this process ignores edge antenna effects thus greatly simplifying the analysis of large arrays as is it cumbersome to measure the active pattern for all elements [41, 83, 84]. The typical criterion used to assume negligible array edge effects is an array of total length greater than 5λ [85] (10 elements for half-wavelength spacing)[2]

Define $F_{\mathrm{a}}(f,\theta,\varphi)$ as the approximate active antenna pattern used for all elements. The delay of propagation between the antenna elements that was implicit in the individual active element patterns $F_m(f,\theta,\varphi)$ must now be compensated for with the large array approximation. Assuming the approximate common active element is measured from the origin of the coordinate system, the time delay difference between the common pattern and the mth element for an emission toward (θ,φ) is

$$\begin{aligned} \Delta t_m(\theta) &= \frac{\mathrm{z}_m}{c} \sin\theta \\ &= m\Delta t(\theta), \end{aligned} \tag{3.12}$$

where

[2]This rule is dependent on frequency, thus for wideband transmission the array needs to be a length of 5λ according to the lowest operating frequency (largest wavelength) [85].

$$\Delta t(\theta) = \frac{d}{c}\sin\theta \tag{3.13}$$

is the successive time delay between elements in the ULA. Note that this delay is independent of angle φ. For the large array approximation, the electric field from (3.5) can be expressed as

$$\vec{\mathscr{E}}(\theta,\varphi,R;f) = w_1\sqrt{\frac{\eta}{Z_0}}\frac{e^{-j\frac{2\pi f}{c}R}}{R\sqrt{4\pi}}F_{\mathrm{a}}(f,\theta,\varphi)\sum_m S_{\mathrm{pb},m}(f)e^{j2\pi f m\Delta t(\theta)}\,\vec{a}_{\varpi} \quad \textit{(Large array)} \tag{3.14}$$

and in the time-domain,

$$\vec{\mathscr{E}}(\theta,\varphi,R;t) = w_1\sqrt{\frac{\eta}{Z_0}}\frac{1}{R\sqrt{4\pi}}F_{\mathrm{a}}(t,\theta,\varphi) * \sum_m s_{\mathrm{pb},m}\left(t-\tfrac{R}{c}+m\Delta t(\theta)\right)\,\vec{a}_{\varpi}, \quad \textit{(Large array)} \tag{3.15}$$

where $F_{\mathrm{a}}(t,\theta,\varphi) = \mathcal{F}^{-1}\left\{F_{\mathrm{a}}(f,\theta,\varphi)\right\}$. The term $\sum_m s_m\left(t-\frac{R}{c}+m\Delta t(\theta)\right)$ is called the delay-and-sum beamformer which represents the contribution of the array structure to the electric field ($F_{\mathrm{a}}(t,\theta,\varphi)$ represents the element contribution). This decoupling of array and element components is called *pattern multiplication* [41, 73, 84] as the summation is multiplied by the active antenna pattern (in the frequency domain (3.14))[3]. These separation of factors allows for an independent analysis of the antenna array term (called the *array factor*) which is typically defined only from a narrowband perspective [41,73,84]. The generality of the summation term allows for calculation of the antenna contribution for both wideband and narrowband emissions. However, for both wideband and/or MIMO emissions the array factor is dynamic over time, thus define

$$g_{\mathrm{pb}}(t,\theta) = \frac{1}{M}\sum_m s_{\mathrm{pb},m}\left(t+m\Delta t(\theta)\right) \tag{3.16}$$

as the *time-varying array factor* at passband. Note that because of the geometry of the array, this expression is independent of angle φ. The frequency content of (3.16) is denoted as $G_{\mathrm{pb}}(f,\theta)$ and

[3]Note that the form of (3.4) is, in general, not separable thus does not have this decoupling property.

is the summation term of (3.14),

$$G_{\mathrm{pb}}(f,\theta) = \frac{1}{M}\sum_{m} S_{\mathrm{pb},m}(f) e^{j2\pi f m\Delta t(\theta)}. \tag{3.17}$$

Using (2.13), (3.17) can be rewritten in terms of the complex-baseband waveforms $S_m(f)\,\forall m$ (where $\forall m$ represents 'for all m') as

$$G_{\mathrm{pb}}(f,\theta) = \frac{1}{M\sqrt{2}}\sum_{m}\left(S_m(f-f_{\mathrm{c}}) + S_m^*(f+f_{\mathrm{c}})\right)e^{j2\pi f m\Delta t(\theta)}. \tag{3.18}$$

The expression in (3.16) can likewise be expressed via the complex-baseband representations in the time-domain $g(t,\theta)$ and frequency domain $G(f,\theta)$,

$$\begin{aligned} g(t,\theta) &= \frac{1}{M}\sum_{m} s_m\left(t + m\Delta t(\theta)\right)e^{j2\pi f_{\mathrm{c}} m\Delta t(\theta)} \\ &= \frac{1}{M}\sum_{m} s_m\left(t + m\Delta t(\theta)\right)e^{jm\frac{2\pi}{\lambda_{\mathrm{c}}}d\sin\theta} \end{aligned} \tag{3.19}$$

and

$$G(f,\theta) = \frac{1}{M}\sum_{m} S_m(f) e^{j2\pi\cdot(f+f_{\mathrm{c}})m\Delta t(\theta)}, \tag{3.20}$$

where $s_m(t)$ and $S_m(f)$ are the time-domain and frequency-domain complex-baseband representations of the waveform emitted by the mth element, respectively. Proof of the relationship between $g_{\mathrm{pb}}(t,\theta)$ and $g(t,\theta)$ is provided in Appendix A.4.

The distribution of emitted power with respect to spatial angle θ can be found by averaging the energy of these signals over time as

$$A(\theta) = \frac{1}{T}\int_{0}^{T}|g(t,\theta)|^2 dt = \frac{1}{T}\int_{-\infty}^{\infty}|G(f,\theta)|^2 df = \frac{1}{T}\int_{0}^{T}|g_{\mathrm{pb}}(t,\theta)|^2 dt = \frac{1}{T}\int_{-\infty}^{\infty}|G_{\mathrm{pb}}(f,\theta)|^2 df. \tag{3.21}$$

where $A(\theta)$ is the aggregate beam pattern of time-varying array factor. The equalities in (3.21)

come from the Parseval's identity [45] and the up-conversion process from (2.1) which maintains constant energy between $s(t)$ and $s_{\mathrm{pb}}(t)$.

To maximize the the aggregate beampattern $A(\theta)$ towards a desired spatial direction θ_{C}, the time-varying array factor $g_{\mathrm{pb}}(t,\theta)$ must also maximize the energy in this direction for the entirety of the pulsewidth. From (3.16), it is clear that the summation of the waveforms must be such that they coherently align in the direction θ_{C}. Therefore, all antenna elements must emit the same waveform $s_{\mathrm{pb}}(t)$ delayed by $-m\Delta t(\theta_{\mathrm{C}})$ to compensate for propagation delays. This beamforming is what we will call *standard beamforming* as it is the current standard practice for transmit beamforming. Thus, the mth passband waveform emitted from the array for the case of standard beamforming towards angle θ_{C} is

$$s_{\mathrm{pb},m}(t;\theta_{\mathrm{C}}) = s_{\mathrm{pb}}\big(t - m\Delta t(\theta_{\mathrm{C}})\big). \quad \textit{(standard beamforming)} \tag{3.22}$$

The equivalent complex-baseband representation is

$$s_m(t;\theta_{\mathrm{C}}) = s\big(t - m\Delta t(\theta_{\mathrm{C}})\big)e^{-jm\frac{2\pi}{\lambda_c}d\sin\theta_{\mathrm{C}}}. \quad \textit{(standard beamforming)} \tag{3.23}$$

Note that the each of the array factor formulations in (3.16) – (3.20) has a corresponding far-field time-varying antenna pattern through proper application of the approximate active antenna pattern $F_{\mathrm{a}}(t,\theta,\varphi)$. Thus the far-field time-varying beampattern from (3.7) when applying the large array assumption is represented as

$$\begin{aligned} \tilde{g}_{\mathrm{pb}}(t,\theta,\varphi) &= F_{\mathrm{a}}(t,\theta,\varphi) * g_{\mathrm{pb}}(t,\theta) \qquad \textit{(Large array)} \\ &= \frac{1}{M}F_{\mathrm{a}}(t,\theta,\varphi) * \sum_m s_{\mathrm{pb},m}\left(t + m\Delta t(\theta)\right). \end{aligned} \tag{3.24}$$

The frequency content of the far-field time-varying beampattern $\tilde{g}_{\mathrm{pb}}(t,\theta,\varphi)$ can be expressed using either (3.17) or (3.18) as

$$\begin{aligned}\tilde{G}_{\mathrm{pb}}(f,\theta,\varphi) &= F_{\mathrm{a}}(f,\theta,\varphi)G_{\mathrm{pb}}(f,\theta) \qquad \textit{(Large array)} \\ &= \frac{1}{M}F_{\mathrm{a}}(f,\theta,\varphi)\sum_{m}S_{\mathrm{pb},m}(f)e^{j2\pi fm\Delta t(\theta)} \\ &= \frac{1}{M\sqrt{2}}F_{\mathrm{a}}(f,\theta,\varphi)\sum_{m}\left(S_m(f-f_{\mathrm{c}})+S_m^*(f+f_{\mathrm{c}})\right)e^{j2\pi fm\Delta t(\theta)}.\end{aligned} \tag{3.25}$$

At complex-baseband these signals can be represented as

$$\begin{aligned}\tilde{g}(t,\theta,\varphi) &= \left(F_{\mathrm{a}}(t,\theta,\varphi)e^{-j2\pi f_{\mathrm{c}}t}\right) * g(t,\theta) \qquad \textit{(Large array)} \\ &= \frac{1}{M}\left(F_{\mathrm{a}}(t,\theta,\varphi)e^{-j2\pi f_{\mathrm{c}}t}\right) * \sum_{m}s_m\left(t+m\Delta t(\theta)\right).\end{aligned} \tag{3.26}$$

and

$$\begin{aligned}\tilde{G}(f,\theta,\varphi) &= F_{\mathrm{a}}(f+f_{\mathrm{c}},\theta,\varphi)G(f,\theta) \qquad \textit{(Large array)} \\ &= \frac{1}{M}F_{\mathrm{a}}(f+f_{\mathrm{c}},\theta,\varphi)\sum_{m}S_m(f)e^{j2\pi fm\Delta t(\theta)},\end{aligned} \tag{3.27}$$

respectively.

3.1.1.2 Receive Beamforming

For a plane waveform impinging onto an ULA, the received signals are delayed with respect to each other depending on the angle of arrival. Assuming that each element has an independent receive chain and ADC, the data for each element can be stored and combined after sampling as opposed to analog phase shifting that combines the responses prior to sampling. Before combining the data captured by each of the elements, the delays between the received signals must be compensated for by time-shifting the individual signals according to a desired receive spatial angle (denoted as ϑ – the receive counterpart to angle θ)[4]. The delay-and-sum beamforming concept can be applied to maximize the energy incident from receive angle ϑ. Defining $y_{\mathrm{pb},m}(t)$ as the passband signal captured by the mth antenna element in a receive array configuration, the combined signal for a receive angle of ϑ is defined as

[4]For the defined geometry, the uniform linear array can only spatially separate sources in the θ dimension. If a two or three dimensional array geometry is employed the array would also be able to separate sources in the φ dimension.

$$y_{\mathrm{pb}}(t,\vartheta) = \frac{1}{M}\sum_{m} y_{\mathrm{pb},m}\big(t - m\Delta t(\vartheta)\big), \tag{3.28}$$

with corresponding baseband representation expressed as

$$y(t,\vartheta) = \frac{1}{M}\sum_{m} y_m\big(t - m\Delta t(\vartheta)\big)e^{-jm\frac{2\pi}{\lambda_c}d\sin\vartheta}, \tag{3.29}$$

where $y_m(t)$ is the baseband representation of $y_{\mathrm{pb},m}(t)$ and $y_{\mathrm{pb}}(t,\vartheta)$ and $y(t,\vartheta)$ are the respective passband and baseband representations of the received signal beamformed toward receive angle ϑ. The factor $\frac{1}{M}$ normalizes the beamformed signal to the original amplitude of the signal received by each element. Note that the signals $y_{\mathrm{pb}}(t,\vartheta)$ and $y(t,\vartheta)$ are not indicative of the processing that occurs within a digital signal processor, though are helpful expressions for use in array analysis. For example, the digital signals combined to beamform toward ϑ on receive could be modeled as a complex-valued sampling of the signal $y(t,\vartheta)$. Note that array tapering is also common practice in transmit and receive beamforming [56] though is not considered here as it might convolute analysis of the emission design methods presented in this work, however this does not necessarily preclude implementation of tapering.

If a spatially-diverse emission is used, it is sometimes desirable to match filter each received signal $y_m(t)\,\forall m$ by each emitted waveform $s_m(t)\,\forall m$ for a total of M^2 responses (if the same array is used for both transmit and receive) [39, 40]. This process of separating channel paths is beneficial if the desire is to taper the *MIMO virtual array* (discussed in Section 3.1.3.2) which can further improve spatial resolution although at the cost of decreased SNR [86]. Here, it is assumed that zero virtual array tapering is being applied thus the received signals can be beamformed using (3.29) prior to range compression.

3.1.1.3 The Narrowband Assumption

For a signal impinging on or emitted from an array, the methods used to define whether a signal is narrowband depends not only on the spectral content of the signal but also on the geometry of the

array. As a result, there are two distinct narrowband definitions: one that we shall call the *spectral* narrowband definition and the other the *array* narrowband definition. The spectral narrowband definition is based purely on the bandwidth of the signal as compared to the center frequency. This definition uses the fractional bandwidth %BW defined in Section 2.1.3. The array narrowband definition is based on the array geometry and the bandwidth of the signal as [87][5]

$$B_{98\%} \cdot \Delta t_{\max} << 1 \tag{3.30}$$

where $\Delta t_{\max}$ is the maximum delay between any two antennas in the array. For the case of a ULA $\Delta t_{\max}$ is the propagation delay between the end elements of the array. The propagation *distance* is $(M-1)d$ thus the maximum delay is

$$\Delta t_{\max} = (M-1)\frac{d}{c}. \tag{3.31}$$

If the array narrowband assumption condition holds then the complex-baseband representations can be simplified. The array factors $g(t,\theta)$ and $G(f,\theta)$ from (3.19) and (3.20) can be expressed as the narrowband models

$$\begin{aligned} g(t,\theta) &= \frac{1}{M}\sum_m s_m(t) e^{jm\frac{2\pi}{\lambda_c} d\sin\theta} \qquad \textit{(Narrowband)} \\ &= \frac{1}{M}\sum_m s_m(t) e^{jm\phi(f_c,\theta)} \end{aligned} \tag{3.32}$$

and

$$G(f,\theta) = \frac{1}{M}\sum_m S_m(f) e^{jm\phi(f_c,\theta)}. \qquad \textit{(Narrowband)} \tag{3.33}$$

where

[5] In [87], this narrowband criterion is defined using a band-limited bandwidth which has been modified to the 98% bandwidth definition for this work. The 2% of energy not considered with this definition is assumed insufficient to alter the array narrowband properties.

$$\phi(f_c, \theta) = \frac{2\pi}{\lambda_c} d \sin\theta, \tag{3.34}$$

is referred to as the *electrical angle* which defines the successive phase difference between antenna elements.

Another property of a narrowband transmission is that the active antenna pattern $F_m(f, \theta, \varphi)$ (and likewise the approximate pattern $F_a(f, \theta, \varphi)$) can assumed to be constant over the operating band, $F_m(f, \theta, \varphi) = F_m(\theta, \varphi)$ and $F_m(t, \theta, \varphi) = \delta(t) F_m(\theta, \varphi)$. Thus using the approximate narrowband active element pattern $F_a(\theta, \varphi)$, the complex-baseband far-field time-varying beampattern for narrowband transmission from a large array can be defined from the expressions

$$\begin{aligned} \tilde{g}(t, \theta, \varphi) &= F_a(\theta, \varphi) g(t, \theta) \qquad \textit{(Narrowband and large array)} \\ &= \frac{1}{M} F_a(\theta, \varphi) \sum_m s_m(t) e^{jm\phi(f_c, \theta)}. \end{aligned} \tag{3.35}$$

and

$$\begin{aligned} \tilde{G}(f, \theta, \varphi) &= F_a(\theta, \varphi) G(f, \theta) \qquad \textit{(Narrowband and large array)} \\ &= \frac{1}{M} F_a(\theta, \varphi) \sum_m S_m(f) e^{jm\phi(f_c, \theta)}. \end{aligned} \tag{3.36}$$

If the large-array assumption cannot be invoked, these expressions generalize to

$$\tilde{g}(t, \theta, \varphi) = \frac{1}{M} \sum_m F_m(\theta, \varphi) s_m(t) \qquad \textit{(Narrowband only)} \tag{3.37}$$

and

$$\tilde{G}(f, \theta, \varphi) = \frac{1}{M} \sum_m F_m(\theta, \varphi) S_m(f). \qquad \textit{(Narrowband only)} \tag{3.38}$$

Likewise, the definition of the complex-baseband standard beamformer from (3.23) after invoking the narrowband assumption is

$$\begin{aligned} s_m(t;\theta_{\mathrm{C}}) &= s(t)e^{-jm\frac{2\pi}{\lambda_c}d\sin\theta_{\mathrm{C}}} \quad \textit{(Narrowband standard beamforming)} \\ &= s(t)e^{-j\phi(f_{\mathrm{c}},\theta_{\mathrm{C}})}. \end{aligned} \tag{3.39}$$

And the receive beamformer from (3.29) given the narrowband assumption can be represented as

$$y(t,\vartheta) = \frac{1}{M}\sum_m y_m(t)e^{-jm\phi(f_{\mathrm{c}},\vartheta)}. \qquad \textit{(Narrowband)} \tag{3.40}$$

Note that it is possible that the spectral and array narrowband assumptions hold while the antenna pattern remains frequency dependent over the in-band frequencies. However, for simplicity, this work assumes that the if the narrowband definitions hold, the responses of the RF components (including the antenna) are considered constant over the band of the emission.

Often it is useful to define $\sin\theta$ as its own variable commonly referred to as *u-space* [87] defined as

$$\bar{\mathrm{u}}(\theta) = \sin\theta. \tag{3.41}$$

Thus the electrical angle $\phi(f_{\mathrm{c}},\theta)$ can also be written in terms of $\bar{\mathrm{u}}(\theta)$ as

$$\phi(f_{\mathrm{c}},\theta) = \frac{2\pi}{\lambda_{\mathrm{c}}}d\ \bar{\mathrm{u}}(\theta). \tag{3.42}$$

3.1.2 Angle-Dependent Receive Processing and Angle-Delay Ambiguity Function

Here, a receive signal model is defined using the same method as described in Section 2.3.2. From this model we can define an *angle-dependent matched filtering* process which allows for the processing of spatially-diverse emissions. The definition of the angle-dependent matched filter is different from that seen in the MIMO literature [21] where the beamforming is applied after matched filtering. Ordering the processing in this way prevents application of a virtual array taper

although is useful in deriving a simple relationship between receive beamforming and spatial-diversity that illustrates the spatial resolution improvement of collocated MIMO transmissions (Section 3.1.3.2). A proof between the equivalence of the angle-dependent matched filtering method presented here and the traditional MIMO processing method of filtering each received signal by each waveform is provided in Appendix A.5.

The angle-dependent matched filter model is used to develop the *angle-delay ambiguity function* which gives the theoretical performance of a specific spatially-diverse emission as a function of scatterer angle θ, receive beamforming angle ϑ, and delay τ. Note that fast-time Doppler could also be incorporated though is left out for clarity of presentation (see Section 2.1.5 for more info). See [88] for more information on generalized MIMO ambiguity functions.

Assuming a narrowband transmission and monostatic fully digital transmit and receive configuration, the aggregate reflected signal incident upon the mth antenna element can be expressed at complex-baseband as

$$y_m(t) = \int_0^{2\pi} \int_{-\pi/2}^{\pi/2} \int_{-\infty}^{\infty} x(\tau,\theta,\varphi) g(t-\tau,\theta) e^{jm\phi(f_c,\theta)} d\tau d\theta d\varphi + z_m(t) \tag{3.43}$$

where $z_m(t)$ is the noise signal present on the receive chain of the mth element and $x(\tau,\theta,\varphi)$ is the complex-valued scattering as a function of time (delay) and angles θ and φ encapsulating all gains/losses of the target scattering into one variable (e.g. antenna pattern, spherical spreading losses). The term $e^{jm\phi(\theta)}$ takes into account the narrowband propagation delay between the receive antenna elements. Note that because the time-varying array factor is independent of φ, the three-dimensional scattering can be represented in two-dimensions by integrating over φ as

$$x(\tau,\theta) = \int_0^{2\pi} x(\tau,\theta,\varphi) d\varphi. \tag{3.44}$$

Thus, the received signal from (3.43) can be expressed with only two integrations as

$$y_m(t) = \int_{-\pi/2}^{\pi/2} \left(\int_{-\infty}^{\infty} x(\tau,\theta) g(t-\tau,\theta) d\tau \right) e^{jm\phi(f_c,\theta)} d\theta + z_m(t). \tag{3.45}$$

The expression in (3.45) can be combined with (3.40) to form the expression for the receive beamformed signal,

$$y(t,\vartheta) = \frac{1}{M} \sum_m \int_{-\pi/2}^{\pi/2} \left(\int_{-\infty}^{\infty} x(\tau,\theta) g(t-\tau,\theta) d\tau \right) e^{jm(\phi(f_c,\theta)-\phi(f_c,\vartheta))} d\theta + z(t,\vartheta), \tag{3.46}$$

where

$$z(t,\vartheta) = \frac{1}{M} \sum_m z_m(t) e^{-jm\phi(\vartheta)} \tag{3.47}$$

is the noise signal resulting from beamforming in the direction ϑ.

Assuming stationary, white Gaussian noise, the angle-dependent matched filter for scattering received from the direction ϑ is the signal emitted in that direction,

$$w_{\mathrm{MF}}(t,\vartheta) = \gamma(\vartheta) g(t,\vartheta), \tag{3.48}$$

where $\gamma(\vartheta)$ is an angle-dependent, non-zero scalar. Thus the estimate of the scattering at delay τ and receive angle ϑ is

$$\begin{aligned} \hat{x}_{\mathrm{MF}}(\tau,\vartheta) &= \int_{-\infty}^{\infty} w_{\mathrm{MF}}^*(t-\tau,\vartheta) y(t,\vartheta) dt \\ &= \gamma(\vartheta) \int_{-\infty}^{\infty} g^*(t-\tau,\vartheta) y(t,\vartheta) dt. \end{aligned} \tag{3.49}$$

Typically, the scalar $\gamma(\vartheta)$ would be equal the inverse of the energy contained in the signal $g(t,\vartheta)$ $\left(\text{i.e. } \gamma(\vartheta) = \left\| g(t,\vartheta) \right\|_2^{-2}\right)$ so that the estimate $\hat{x}(\tau,\vartheta)$ is not scaled relative to $x(\tau,\vartheta)$. However, if the emission is spatially-variant, the transmitted spatial distribution of power may be

spread unevenly in space. Thus, if the filter normalization is applied as $\gamma(\vartheta) = \left\|g(t,\vartheta)\right\|_2^{-2}$ then the average power of the beamformed noise $z(t,\vartheta)$ would be dependent on beamforming angle, ϑ. Therefore, for spatially-diverse signals is it advantageous to normalize $w_{\mathrm{MF}}(t,\vartheta)$ such that the noise remains constant over ϑ. This *unit-gain* formulation would be

$$w_{\mathrm{MF}}(t,\vartheta) = \gamma \frac{g(t,\vartheta)}{\left\|g(t,\vartheta)\right\|_2}, \tag{3.50}$$

where γ is now a scalar that normalizes the entirely of the output for all ϑ. Using the form of the matched filter in (3.50) prevents fluctuation of the noise power with receive angle ϑ though the matched filter estimator in (3.49) is now biased. However, the scalar γ can be chosen so that there is no bias for the case of standard beamforming when $\varphi = \theta_{\mathrm{C}}$. Thus the updated angle-dependent matched filter is

$$w_{\mathrm{MF}}(t,\vartheta) = \left(M \sum_m \left\|s_m(t)\right\|_2^2\right)^{-\frac{1}{2}} \frac{g(t,\vartheta)}{\left\|g(t,\vartheta)\right\|_2}. \tag{3.51}$$

The matched filter estimate of a scatterer at delay τ and receive angle ϑ from (3.49) can be expressed as

$$\begin{aligned} \hat{x}_{\mathrm{MF}}(\tau,\vartheta) &= \int_{-\infty}^{\infty} w_{\mathrm{MF}}^*(t-\tau,\vartheta) y(t,\vartheta) dt \\ &= \left(\tfrac{1}{M}\left\|g(t,\vartheta)\right\|_2^2 \sum_m \left\|s_m(t)\right\|_2^2\right)^{-\frac{1}{2}} \int_{-\infty}^{\infty} g^*(t-\tau,\vartheta) y(t,\vartheta) dt. \end{aligned} \tag{3.52}$$

The angle-delay ambiguity function can be found by placing a unit amplitude scatterer at a delay of $\tau = 0$ and angle of $\theta = \theta_{\mathrm{T}}$ in the absence of the noise signals $z_m(t) \forall m$ (recall that this ULA configuration cannot estimate the φ dimension of a scatterer thus is defined independent of this variable). For this scenario, the "received" signal beamformed toward ϑ is

$$y(t,\vartheta) = \frac{1}{M} g(t,\theta_{\mathrm{T}}) \sum_m e^{jm(\phi(f_{\mathrm{c}},\theta_{\mathrm{T}}) - \phi(f_{\mathrm{c}},\vartheta))}. \tag{3.53}$$

Matched filtering this signal using (3.49) and (3.51) yields the estimate of this theoretical scatterer as

$$\hat{x}(\tau,\vartheta) = \left(M\left\|g(t,\vartheta)\right\|_2^2 \sum_m \left\|s_m(t)\right\|_2^2\right)^{-\frac{1}{2}} \int_{-\infty}^{\infty} g^*(t-\tau,\vartheta)g(t,\theta_{\mathrm{T}})dt \sum_m e^{jm(\phi(f_{\mathrm{c}},\theta_{\mathrm{T}})-\phi(f_{\mathrm{c}},\vartheta))}. \quad (3.54)$$

Generalizing this expression for any target angle (i.e. transmission direction) θ and expanding $\phi(f_{\mathrm{c}},\theta)$ into the form from (3.34) yields the angle-delay ambiguity function as

$$\chi_{\mathrm{s}}(\tau,\theta,\vartheta) = \left(M\left\|g(t,\vartheta)\right\|_2^2 \sum_m \left\|s_m(t)\right\|_2^2\right)^{-\frac{1}{2}} \int_{-\infty}^{\infty} g^*(t-\tau,\vartheta)g(t,\theta)dt \sum_m e^{jm\frac{2\pi}{\lambda_{\mathrm{c}}}d(\sin\theta-\sin\vartheta)}, \quad (3.55)$$

which gives the expected estimator response over delay τ for a single scatterer at angle θ received in a beam directed toward ϑ. The ambiguity function is normalized such that it is unity for standard beamforming (directed toward angle θ_{C}) at the point $\chi_{\mathrm{s}}(\tau = 0, \theta = \theta_{\mathrm{C}}, \vartheta = \theta_{\mathrm{C}})$. Note that this representation is only true when invoking the narrowband assumption. In Section 4.2, the angle-delay ambiguity function is revisited from a wideband perspective.

3.1.3 Beampattern and Spatial Resolution

Figure 3.3 displays the beampattern (ignoring element patterns) pointed towards *broadside* $(\theta = 0^\circ)$ for a ULA of $M = 30$ elements spaced $d = \frac{\lambda_{\mathrm{c}}}{2}$ in three different spaces: θ-space, ϕ-space, and ū-space. The relationships between these three variables are given in (3.34) – (3.42). This beampattern could either be the receive beamformer (when $\vartheta = 0^\circ$) or the transmit beamformer for the case of standard beamforming (when $\theta_{\mathrm{C}} = 0^\circ$)[6]. For the receive beamformer, the beampattern illustrates the "filter" response of the beamformer in the spatial dimension, thus other sources of energy coming from directions corresponding to the sidelobes will "leak" into the beamformed

[6]Again the beampatterns can be altered via array tapering [56] though is not considered here.

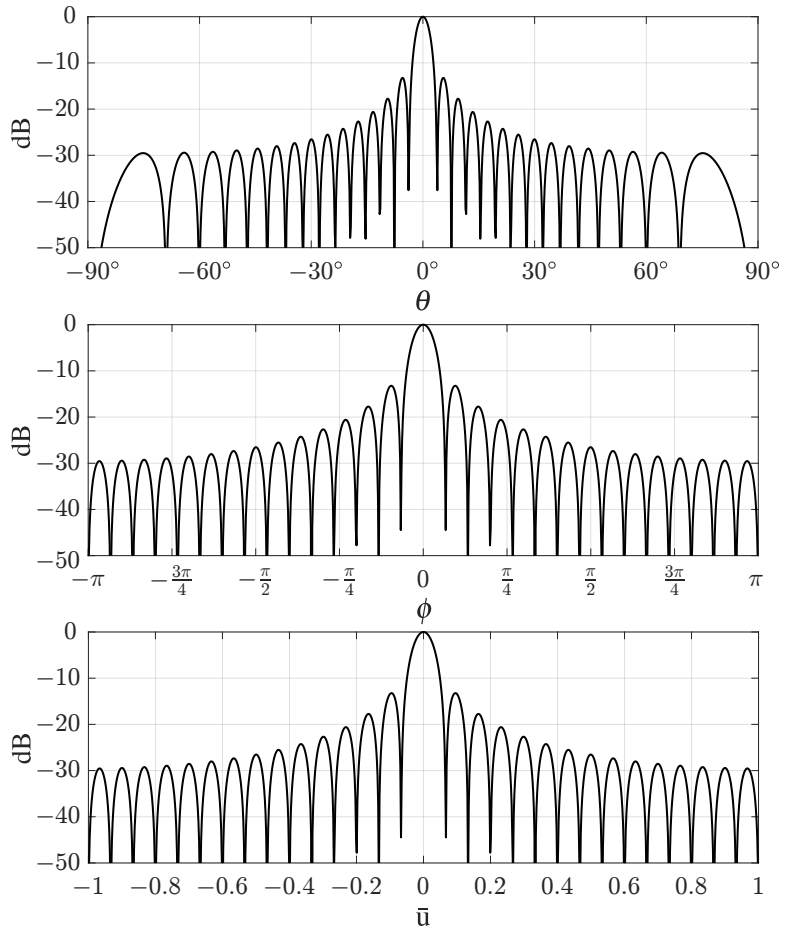

Figure 3.3: Normalized beampattern (in dB) in different spaces for an $M = 30$ element ULA with $d = \frac{\lambda_c}{2}$.

signal response $y(t, \vartheta)$ causing interference in the estimation. How much the signals leak is dependent on the source power and sidelobe level of the interferer direction of arrival. On transmit, the beampatterns in Figure 3.3 are equivalent to the peak-normalized aggregate beampattern $A(\theta)$ (in three different spaces) when employing standard beamforming with maximum steered towards $\theta_C = 0°$. For spatially-diverse emissions, the spatial allocation of energy in $A(\theta)$ may appear drastically different than the stadard beamforming case depending on how the set of M waveforms are designed.

3.1.3.1 Receive-only Spatial Resolution

For a moment consider a ULA operating in a receive-only mode estimating direction-of-arrival of RF energy sources. Here, only consider the traditional "matched filter" type beamformer that has been discussed up until now. The spatial resolution of a source estimate that can be achieved (on receive) using a ULA is dictated by the array beampattern shown in Figure 3.3. There are two main methods of defining the spatial resolution of the beampattern: the peak-to-null and 3 dB mainbeam (or mainlobe) widths.

The trigonometric relationship of the geometry of the linear array to the spatial dimension θ results in a sidelobe-width broadening toward *endfire* $(\theta = \pm 90°)$ for the θ-space beampattern. This stretching of the beampattern likewise occurs in the mainbeam when steered towards endfire. Thus the θ-space dimension would not be suitable to measure the spatial resolution of the array is it would be dependent on the look angle of the beampattern.

The ϕ-space coordinate system does not have the sidelobe warping issue of the θ-space, thus the resolution of the beampattern is invariant of the beampattern look angle. The resolutions in ϕ-space are [87]

$$[\Delta\phi]_{\text{p-n}} = \frac{2\pi}{M} \tag{3.56}$$

for the peak-to-null mainlobe width, and

$$[\Delta\phi]_{3\text{dB}} = 0.891\frac{2\pi}{M} \tag{3.57}$$

for the 3 dB mainlobe width. These resolutions are equivalent to the frequency resolution of a discrete-time Fourier transform (DTFT) where the number of elements M would be the "time samples" of the DTFT. While the resolutions are quite simple and easy to calculate, they do not provide much perspective on the achievable resolution in physical space given the parameters of a ULA.

The resolution in the $\bar{u}$-space coordinate system is likewise invariant of the look angle and is tied to the physical spatial angle θ through a trigonometric relationship (recall that $\bar{u} = \sin\theta$), thus is best candidate for measuring the spatial resolution of an array. The resolutions of the array in $\bar{u}$-space is defined via the operating wavelength λ_c, the inter-element spacing d, and the number of elements M as [87]

$$[\Delta\bar{u}(f_c)]_{\text{p-n}} = \frac{\lambda_c}{Md} \tag{3.58}$$

for the peak-to-null mainlobe width, and

$$[\Delta\bar{u}(f_c)]_{3\text{dB}} = 0.891\frac{\lambda_c}{Md} \tag{3.59}$$

for the 3 dB mainlobe width. Note that the resolutions defined here are the finest achievable using this method of beamforming for a given array structure. Any attempt to apply tapers to the receive beamforming to lower sidelobes will result in a spoiling (broadening) of the mainbeam and a loss in estimated SNR [56].

3.1.3.2 Target Spatial Resolution in a MIMO Transmission Mode

The theorized improvement in spatial resolution when implementing a collocated MIMO radar transmission mode is typically derived using the *virtual array* concept which makes the assumption of orthogonality between the signals [39, 40]. However, as discussed in [39] each dimension

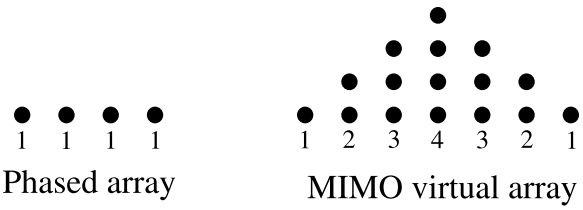

Figure 3.4: Effective receive array geometry for phased array and MIMO virtual array (convolution of physical array) for $M = 4$ element ULA $(d = \frac{\lambda_c}{2})$.

of orthogonality (time division, frequency division, and code division) have their individual drawbacks. Though for the purposes of derivation, the waveforms emitted by each element are considered orthogonal, then any deviation from this assumption is attributed to interference or error in the scattering estimation.

If the waveforms are orthogonal then the individual contributions of each waveform can be separated on receive. Thus by match filtering each received signal $y_m(t) \forall m$ by each waveform $s_m(t) \forall m$, M^2 decoupled responses are achieved (assuming M elements for both transmit and receive). The decoupled responses form the *MIMO virtual array* which can then be steered in a desired direction. For a ULA, the M^2 responses form $2M - 1$ unique phase centers where $M^2 - 2$ are over-represented. The responses form a triangular array weighting, as shown in Figure 3.4 for an $M = 4$ element ULA, which amounts to a convolution of the physical array.

For the assumption of orthogonal waveforms, the transmit aggregate beampattern $A(\theta)$ (from (3.21) of the time-varying array factor $g(t, \theta)$ is isotropic. Figure 3.5 compares the aggregate beampatterns for standard beamforming and for a MIMO transmit mode (orthogonal waveforms) for the $M = 4$ element ULA. Note how the MIMO emission does not coherently beamform in the direction $\sin\theta = 0$ which results in a decreased estimation SNR for the MIMO transmission (in this direction) [18]. On receive, the over-representation of the phase center locations amounts to a triangular array taper in the receive virtual array. Figure 3.6 shows the resulting beampatterns for the phased array and MIMO virtual arrays as shown in Figure 3.4. The MIMO virtual array beampattern has an improvement of $1/\sqrt{2}$ in 3 dB spatial resolution over the traditional phased array [86]. Note that the triangular array weighting could be flattened via a virtual array taper (thus improving the spatial resolution further) though would result in a loss in SNR [86]. Because a

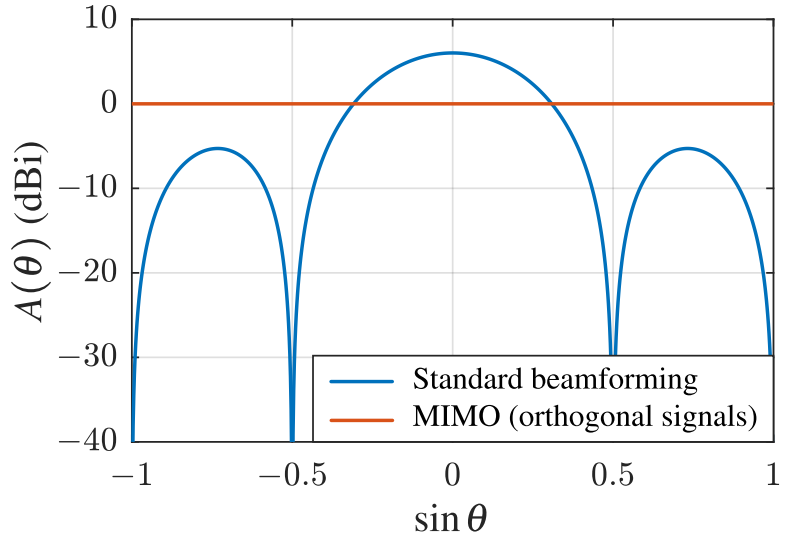

Figure 3.5: Aggregate beampattern $A(\theta)$ relative to isotropic antenna power (dBi) for $M = 4$ element ULA ($d = \frac{\lambda_c}{2}$) vs. transmit angle $\sin\theta$ for standard beamforming (blue) and MIMO transmission (with orthogonal signals) (red).

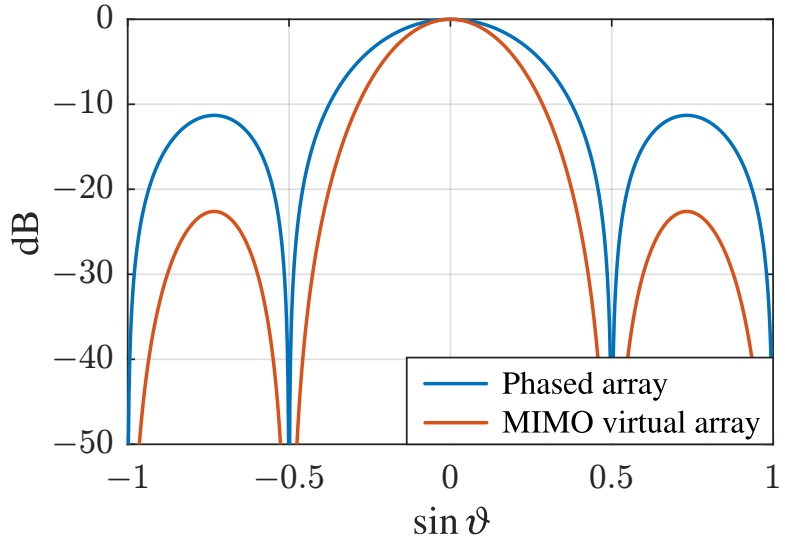

Figure 3.6: Receive beampatterns (in dB) for $M = 4$ element ULA ($d = \frac{\lambda_c}{2}$) vs. receive beamforming angle $\sin\theta$ for phased array (blue) and MIMO virtual array (red) for scatterer at $\theta = 0°$

spatially-diverse emission already induces an SNR loss on transmit, this virtual array tapering is not considered here. For this four element example, the first sidelobe (which represents the largest spatial ambiguity) is at -11.3 dB for the phased array and -22.6 dB for the MIMO virtual array. Thus the orthogonal MIMO array produces a "doubling" (in dB) effect of the expected spatial ambiguity sidelobe level for a uniform array taper.

The insight that the virtual array provides is useful for determining the theoretical spatial resolution given a transmit and receive array in a MIMO mode. However when considering the implementation of the physical waveforms, the performance of the array may vary. Specifically, the issues that arise when implementing truly orthogonal waveforms [39]. Here, it is assumed that the waveforms that are transmitted simultaneously and occupy the same bandwidth, thus are separable only via the waveform modulation sometimes referred to as "coding diversity". It can be shown that the if two signals signals occupy the same bandwidth, the cross-correlation is limited by the energy contained in the product of the two waveform spectrums. Thus, for waveforms with finite time-bandwidth products orthogonality via coding diversity is not possible over all delays in the waveform cross-correlation. Another issue of the orthogonal waveform assumption is that the energy is spread evenly over all space when it is possible that the some directive properties are desired in the emission [21, 89–92]. It is unclear how the virtual array concept applies to non-isotropic (non-orthogonal) transmissions thus requires a more specific analysis. The angle-delay ambiguity diagram $\chi_{\mathrm{s}}(\tau,\theta,\vartheta)$ (from (3.55)) can be used to directly observe the spatial resolution for a theoretical target location.

The expected spatial resolution of scatterer whose complex amplitude is estimated via the matched filtered method presented in Section 3.1.2 is predicted via the angle-delay ambiguity function $\chi_{\mathrm{s}}(\tau,\theta,\vartheta)$ from (3.55). Note that terms in (3.55) $\int_{-\infty}^{\infty} g^*(t-\tau,\vartheta)g(t,\theta)dt$ and $\sum_m e^{jm\frac{2\pi}{\lambda_c}d(\sin\theta-\sin\vartheta)}$ are separable thus can be independently analyzed. The cross-correlation term $\int_{-\infty}^{\infty} g^*(t-\tau,\vartheta)g(t,\theta)dt$ purely represents the spatial diversity of $g(t,\theta)$, while the term $\sum_m e^{jm\frac{2\pi}{\lambda_c}d(\sin\theta-\sin\vartheta)}$ is the separability contributed by receive beamforming. Thus, define

$$\bar{\chi}_{\mathrm{s,b}}(\theta,\vartheta) = \frac{1}{M}\sum_{m} e^{jm\frac{2\pi}{\lambda_{\mathrm{c}}}d(\sin\theta-\sin\vartheta)} \tag{3.60}$$

as the *beam factor* of the angle-delay ambiguity diagram which is entirely based on the receive array geometry (and any tapers that would be applied), and

$$\bar{\chi}_{\mathrm{s,d}}(\tau,\theta,\vartheta) = \left(\tfrac{1}{M}\left\|g(t,\theta)\right\|_2^2 \sum_{m}\left\|s_m(t)\right\|_2^2\right)^{-\frac{1}{2}} \int_{-\infty}^{\infty} g^*(t-\tau,\vartheta)g(t,\theta)dt \tag{3.61}$$

as the *diversity factor* of the angle-delay ambiguity diagram which defines the separability of the emission solely due to the spatially-diverse structure. The full angle-delay ambiguity diagram is found by taking the product of these two functions, $\chi_{\mathrm{s}}(\tau,\theta,\vartheta) = \bar{\chi}_{\mathrm{s,d}}(\tau,\theta,\vartheta)\bar{\chi}_{\mathrm{s,a}}(\theta,\vartheta)$.

As an example, consider an $M = 30$ element ULA with $d = \frac{\lambda_{\mathrm{c}}}{2}$ implementing standard transmit beamforming steered toward $\theta = 0°$ via (3.39). The spatial resolution of the emission is observed at the $\tau = 0$ cut of the angle-delay ambiguity diagram. For the case of standard beamforming the modulation of the waveforms $s_m(t)\forall m$ do not effect the spatial resolution results, however the waveforms are chosen to be LFM with analytical time-bandwidth product $B_{\mathrm{a}}T = 100$.

Figure 3.7 shows the square-magnitudes (in dB) of (a) the beam factor, (b) the zero-delay cut of the diversity factor, and (c) the zero-delay cut of the angle-delay ambiguity diagram (product of (a) and (b)) versus the scatterer direction $\sin\theta$ and receive direction $\sin\vartheta$ for the standard beamforming transmission. The beam factor in Figure 3.7(a) shows a diagonal lobe sweeping left to right representing the receive beamformer sweeping over all ϑ. The horizontal (constant θ) cuts through the beam factor illustrate the expected receive beamformed response for a particular scatterer direction $\sin\theta$. The diversity factor in Figure 3.7(b) for standard beamforming has a constant lobe centered at the transmission direction $\sin\theta = 0$ and is independent of receive angle ϑ thus indicating that $g(t,\theta)$ is not a spatially-diverse time-varying array factor. The product of the two factors yields $\chi_{\mathrm{s}}(\tau,\theta,\vartheta)$ in Figure 3.7(c). The resolution of the of $\chi_{\mathrm{s}}(\tau,\theta,\vartheta)$ remains the same as the beam factor $\bar{\chi}_{\mathrm{s,b}}(\theta,\vartheta)$ due to the lack of spatial diversity in $g(t,\theta)$.

Now consider a spatially-diverse time-varying antenna factor $g(t,\theta)$ using the same array

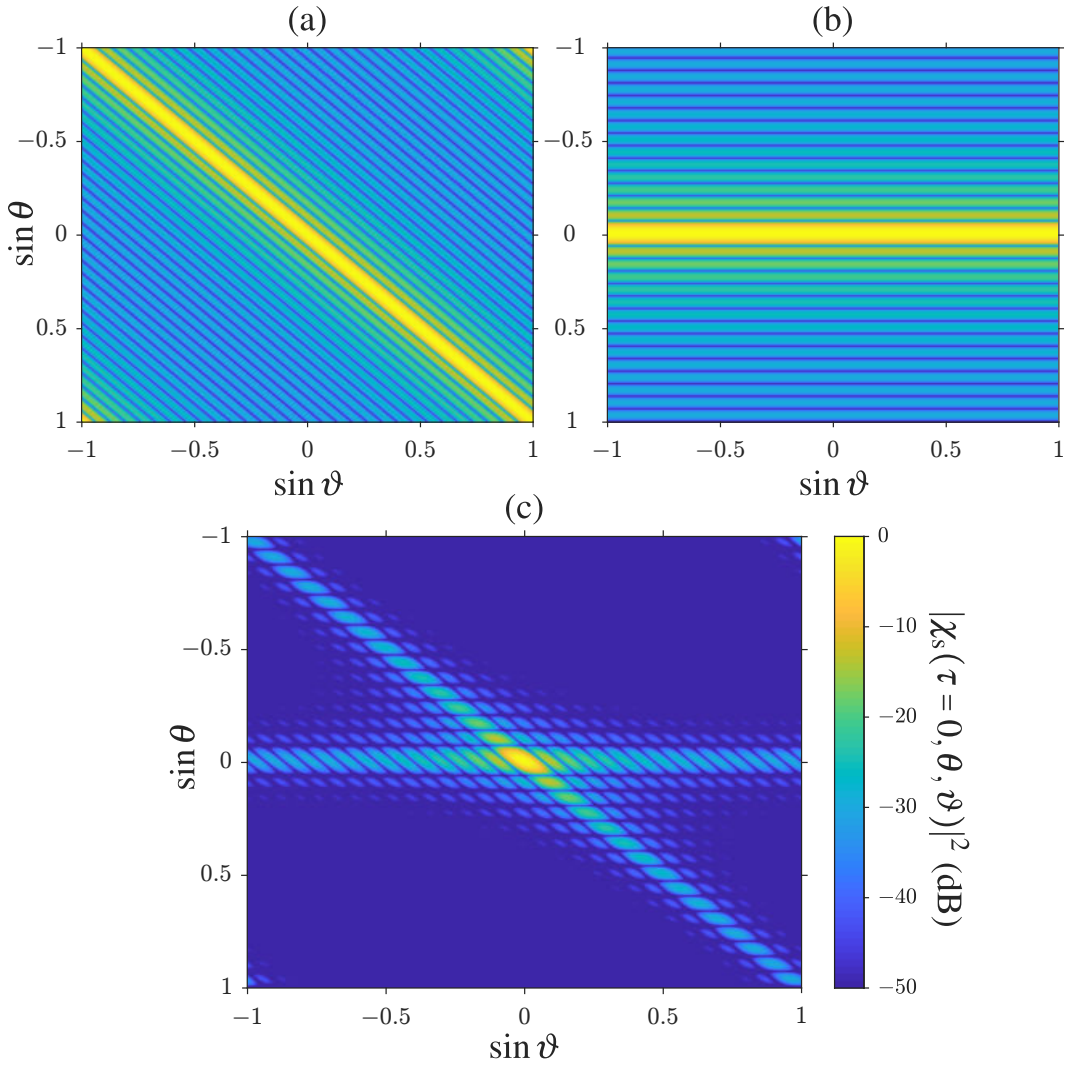

Figure 3.7: (a) Beam factor $|\bar{\chi}_{s,b}(\theta, \vartheta)|^2$ (in dB), (b) zero-delay cut of diversity factor $|\bar{\chi}_{s,d}(\tau = 0, \theta, \vartheta)|^2$ (in dB) , and (c) zero-delay cut of angle-delay ambiguity diagram $|\chi_s(\tau = 0, \theta, \varphi)|^2$ (in dB) (product of (a) and (b)) vs. $\sin\theta$ and $\sin\vartheta$ for $M = 30$ element ULA ($d = \frac{\lambda_c}{2}$) and standard beamforming steered toward $\theta_C = 0°$.

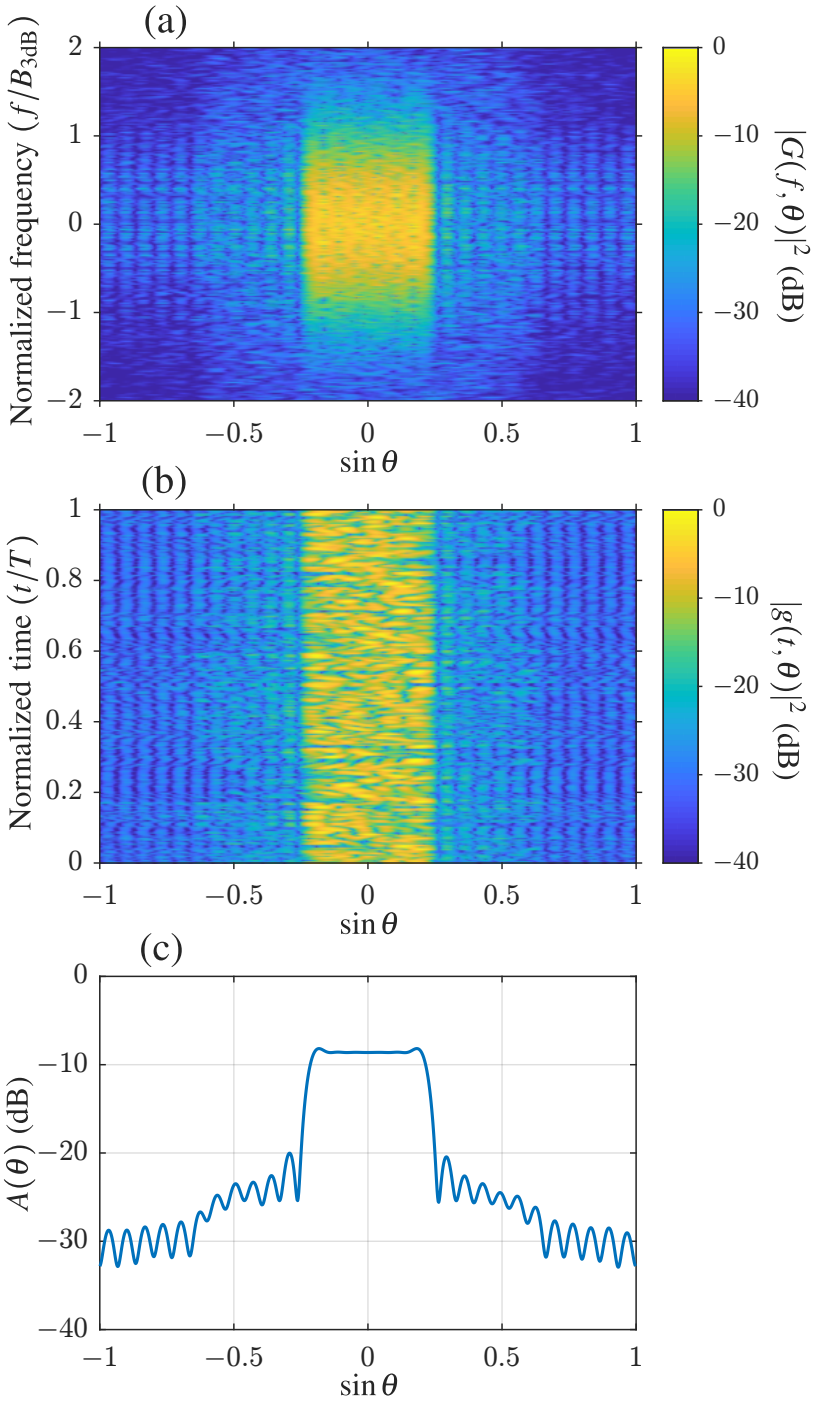

Figure 3.8: (a) $|G(f,\theta)|^2$ (in dB) vs. $\sin\theta$ and normalized frequency $(f/B_{3\text{dB}})$, (b) $|g(t,\theta)|^2$ (in dB) vs. $\sin\theta$ and normalized time (t/T), and (c) beampattern $A(\theta)$ (in dB) vs. $\sin\theta$ for spatially-diverse emission with $M = 30$ elements $(d = \frac{\lambda_c}{2})$ and $BT = 100$.

parameters as the case above. Figures 3.8(a,b) show the squared-magnitude of the spectral content $|G(f,\theta)|^2$ and time-varying antenna factor $|g(t,\theta)|^2$ for a spatially-diverse transmission mode. The waveforms $s_m(t)\forall m$ were optimized using the method presented in Section 4.2 for a narrowband scenario[7]. The time-varying antenna factor $g(t,\theta)$ was optimized to place an even amount of energy between $\sin\theta = -0.2$ and $\sin\theta = 0.2$ for a Gaussian shaped spectral content while constraining the set of M waveforms to be constant amplitude. The structure of $|g(t,\theta)|^2$ in Figure 3.8(b) confirms that this is a spatially-diverse array factor. Figure 3.8(c) shows the aggregate beampattern $A(\theta)$ which displays spatial power distribution of $g(t,\theta)$ which was chosen to be flat between $\sin\theta = -0.2$ and $\sin\theta = 0.2$. The aggregate beampattern is normalized such that 0 dB represents the array factor maximum (only acheived with standard beamforming), thus (for a single pulse) this transmission would result in a loss of approximately 8 dB relative to standard beamforming.

Figure 3.9 shows the square-magnitudes (in dB) of (a) the beam factor, (b) the zero-delay cut of the diversity factor, and (c) the zero-delay cut of the angle-delay ambiguity diagram (product of (a) and (b)) versus the scatterer direction $\sin\theta$ and receive direction $\sin\vartheta$ for the spatially-diverse emission depicted in Figure 3.8. Note that because the beam factor is independent of $g(t,\theta)$, the response in Figure 3.9(a) is identical to that of the standard beamforming case in Figure 3.7(a). The spatial diversity in $g(t,\theta)$ translates into the diagonal response in the diversity factor in Figure 3.9(b). Recall that the diversity factor for standard beamforming was invariant over the receive beamforming angle $\sin\vartheta$, therefore the only contributor to the spatial resolution of the estimator was the beam factor. However because the signal structure of $g(t,\theta)$ varies with transmission angle θ, the diversity factor $\bar{\chi}_{\mathrm{s,d}}(\tau,\theta,\vartheta)$ further improves the target spatial resolution over a range of angles. The $\tau = 0$ cut of the angle-delay ambiguity function for the spatially-diverse transmission (shown in Figure 3.9(c)) is elongated on the diagonal and lowered in magnitude relative to the loss due to the spreading of energy in space. In fact, the diagonal of Figure 3.9(c) corresponds to the normalized aggregate beampattern $A(\theta)$ in Figure 3.8(c).

[7]Section 4.2 introduces a method of generating wideband spatially-diverse emissions though is generalizable to narrowband as well.

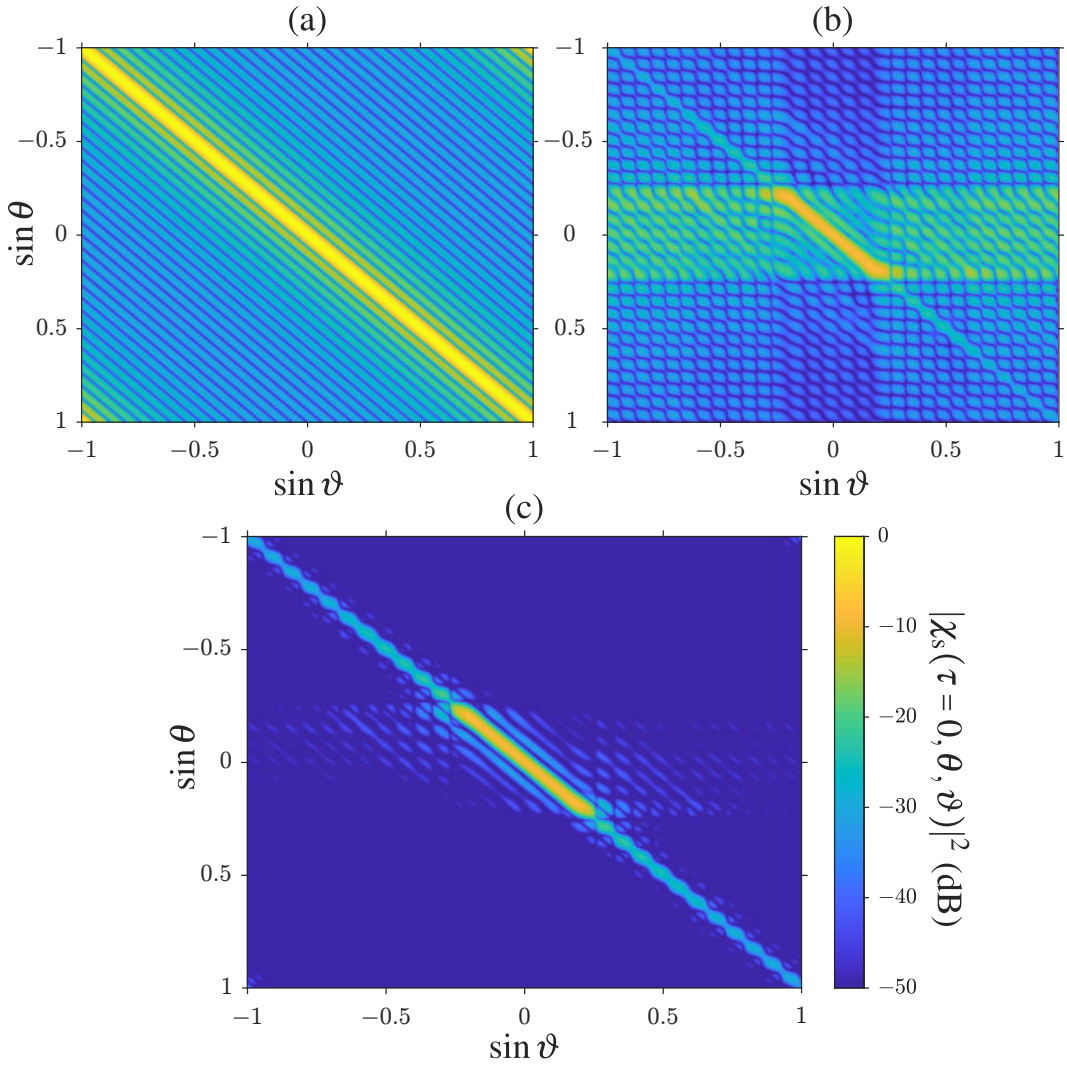

Figure 3.9: (a) Beam factor $|\bar{\chi}_{s,b}(\theta, \vartheta)|^2$ (in dB), (b) zero-delay cut of diversity factor $|\bar{\chi}_{s,d}(\tau = 0, \theta, \vartheta)|^2$ (in dB) , and (c) zero-delay cut of angle-delay ambiguity diagram $|\chi_s(\tau = 0, \theta, \varphi)|^2$ (in dB) (product of (a) and (b)) vs. $\sin\theta$ and $\sin\vartheta$ for $M = 30$ element ULA ($d = \frac{\lambda_c}{2}$) and the spatially-diverse emission portrayed in Figure 3.8.

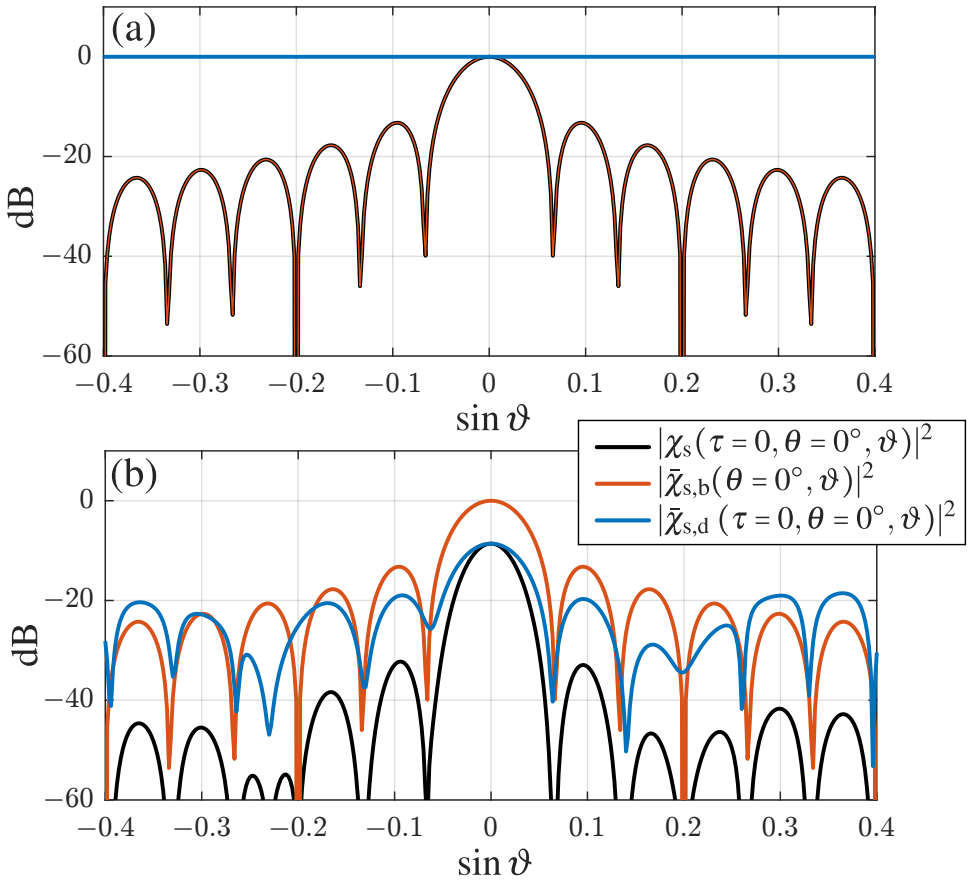

Figure 3.10: Comparison of estimation resolution $\chi_s(\tau, \theta, \vartheta)$ (black), $\bar{\chi}_{s,b}(\theta, \vartheta)$ (red), and $\bar{\chi}_{s,d}(\tau, \theta, \vartheta)$ (blue) at $\tau = 0$ and $\theta = 0°$ with a $M = 30$ element ULA $(d = \frac{\lambda_c}{2})$ for (a) standard beamforming steered toward $(\theta_C = 0°)$ and (b) the spatially-diverse emission portrayed in Figure 3.8.

The $\tau = 0$ and constant $\sin\theta$ cut of the ambiguity diagram provides the spatial filter response of the estimator for a particular scatterer location (transmit direction) θ. Through observation of Figures 3.9(a,b), the product of the two responses narrows the spatial resolution of an estimated scatterer (as compared to standard beamforming). To illustrate this beam narrowing, Figure 3.10 compares the $\tau = 0$ and $\theta = 0°$ cuts of the angle-delay ambiguity function as well as both the beam and diversity factors of the emission. Recall that the $\tau = 0$ and $\theta = 0°$ cut of $\chi_s(\tau, \theta, \vartheta)$ represents expected spatial responses for a single theoretical scatterer of unit amplitude at delay $\tau = 0$ and angle $\theta = 0°$. For the standard beamforming case in Figure 3.10(a), the responses of the beam factor (red) and angle-delay ambiguity function (black) are identical due to the flat response of the diversity factor (blue). Though the spatial response for the standard beamforming case is maximized (0 dB) at $\vartheta = 0°$ because the cut is taken at $\theta = \theta_C = 0°$. For the spatially-diverse emission in Figure 3.10(b), the beam factor (red) is the same as for standard beamforming and the diversity factor response has a mainlobe surrounded by a high sidelobe response. The product of the curvatures of the diversity and beam factors produces a narrowed 3 dB spatial resolution of 0.04217 (in $\sin\theta$ or ū-space) compared to the standard beamforming case of 0.0594 calculated using (3.59). The theorized spatial resolution improvement from the virtual array is the standard beamforming resolution divided by $\sqrt{2}$ which results in a resolution of $0.0594/\sqrt{2} = 0.04200$. Therefore the spatially-diverse array factor and the theorized MIMO spatial resolution have difference in spatial resolution of 0.00017 (in ū-space).

Recall that the resolution derived from the MIMO virtual array assumes orthogonal waveforms which implies an isotropic aggregate beampattern. Figure 3.8 shows that even for a directive (non-isotropic) emission, the theoretical MIMO virtual array spatial resolution can be met. However, the beam peak for the spatially diverse scenario exhibits a loss of approximately 8 dB compared to standard beamforming (the same loss seen in the aggregate beam pattern in Figure 3.8(c)). For a single pulse, the spatially diverse emission achieves a finer 3 dB spatial resolution and wider spatial coverage where standard beamforming achieves the maximum focused beam amplitude. Depending on the current priorities of the radar, the DAR may switch between standard

beamforming and a spatially-diverse transmission mode on a pulse by pulse basis.

3.2 Mutual Coupling in Uniform Linear Arrays

For any transmission involving multiple antenna elements the physical electromagnetic interaction between these elements needs to be considered. This *mutual coupling* interaction can be described using a frequency-dependent mutual impedance between each pair of antennas ($Z_{mk}(f)$ for $m \neq k$) just as every antenna has a frequency-dependent self-impedance ($Z_{mm}(f)$). The impedance relationship describes the coupling of energy between antennas in the array which directly alters the phase and amplitude of the terminal currents and voltages on each element. It is assumed that the coupling only scales these terminal voltage/current values and does not affect the shape of the current distribution on the element (thus the antenna pattern remains constant) [83]. However, the excitation of a single element also excites the other $M-1$ elements in the array, thus the net total antenna pattern of a single element deviates from the isolated antenna pattern. This new pattern response is called the *active antenna pattern* [83,84] which was defined as $F_m(f,\theta,\varphi)$ in (3.4). The active element pattern inherently encapsulates all the individual coupling relationships between the elements that effect the far-field pattern though does not explicitly indicate how much energy is returned to the array transmitters through reflection/coupling of energy back into the array.

There are two methods of analysis when considering coupled energy into an array: a circuit model point of view (i.e. currents, voltages, and impedances), and a scattering point of view (i.e. forward/backward traveling waves and the scattering matrix). Here, both methods are considered as each could provide different insights into the behavior of the antenna coupling. The circuit point of view is based around the effective impedance at the terminals of the antenna elements when placed in the array which deviates from that of an isolated element. In fact, the effective impedance is dependent on the phase and amplitude of the array excitation thus is denoted the *active element impedance* (sometimes called *driving impedance*) [73,93]. The match of the antenna is determined by this active element impedance thus could result in significant reflected/coupled energy with the radar given certain excitations [41]. The scattering matrix point of view models the array as a

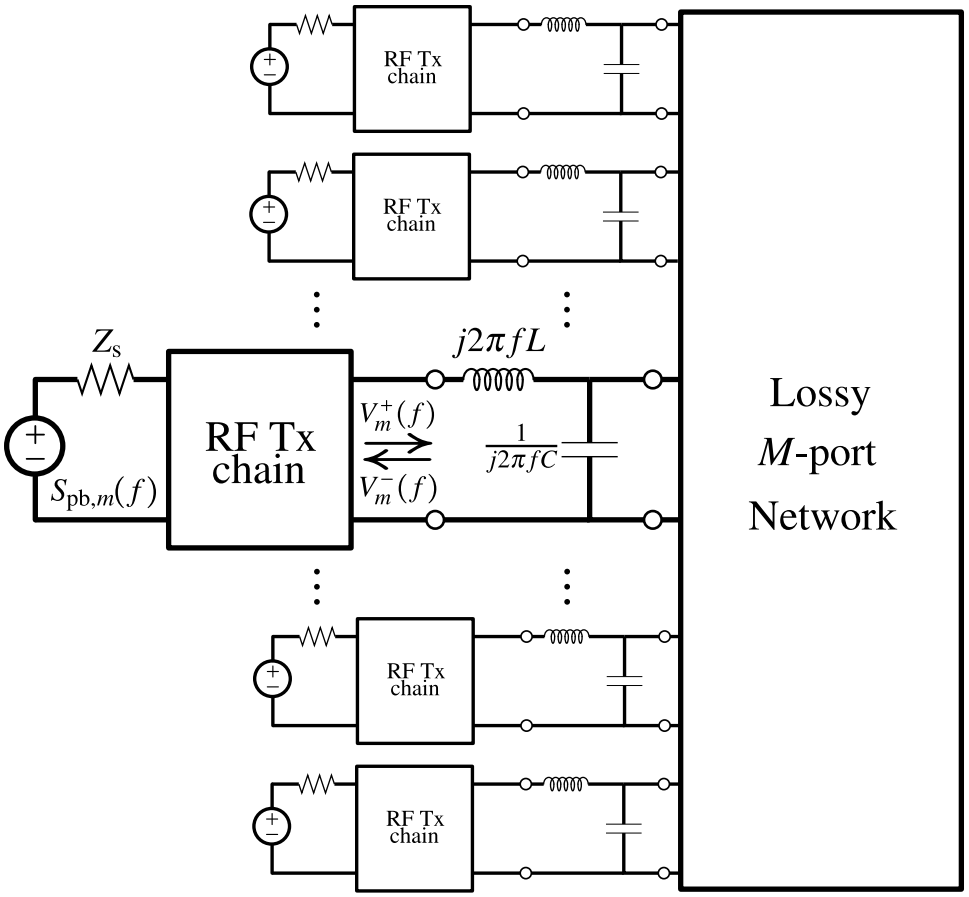

Figure 3.11: Antenna array modeled as a lossy M-port network with simple matching L-network.

lossy M-port network where the power dissipation represents radiated energy (and ohmic losses if a lossy antenna is considered). This network illustrates a more direct coupling behavior where the backward traveling waves for all elements are determined directly from the forward wavefronts excited by each element and the scattering matrix.

Figure 3.11 illustrates the M-port network model of an antenna array including an independent transmission chain model and a simple matching L-network for each antenna where L and C are the inductance and capacitance of the matching network, respectively. For spatially-diverse transmission, the array must be matched over the spatial sector that we wish to emit (which may be quite large) so as to not inadvertently couple energy back into the array. These desired properties for a spatially-diverse transmission align with that of a traditional scanning phased-array which also must be matched over a sector in space. The matching network is assumed to be

designed based on a broadside transmission (excluding array tapering) which is typical practice for a scanning array [73,84]. The L-network is a simplistic model for impedance matching though it is satisfactory for analysis purposes. There exist more complex methods for *wide-angle impedance matching* (WAIM) that utilize dielectric sheets to match the array over wide-angles [94–96].

If the spacing between the elements is less than $\lambda/2$, the array could radiate a portion of its energy into the *invisible space* of the array. The term "radiate" is really a misnomer in this context as the majority of the power is actually not radiated due to the element active impedances becoming primarily reactive within this region. The result is storage of energy locally in the near field of the array, in the matching networks of each element, or in any of the transmit chains of the antenna array. This "reactive" region resides beyond the endfire direction for linear arrays and does not correspond to a physical angular direction[8]. If the array is not designed to place energy into this region (which is the case for scanning phased-arrays) the array will not be matched thus the energy is reflected/coupled back into the array and dissipated within the transmit chain which could damage the transmitter [42]. Likewise, the angle-dependent element impedance variation can also result in what is known as *blind angles* where the mismatch between the transmitter and antenna is such that little to no power is transmitted in a particular transmit angles [41]. These directions have been linked to angles at which a grating lobe appears in visible space [41, 97] thus exist for arrays that have spacing $d \geq \frac{\lambda}{2}$.

3.2.1 Active Element Impedance and the Scattering Matrix

The mutual impedance between elements in the array describes the relationship between the antenna terminals and currents as

$$V_m(f) = \sum_k Z_{mk}(f) I_k(f) \tag{3.62}$$

where $Z_{mk}(f)$ is the mutual-impedance between the mth and kth antenna elements and $Z_{mm}(f)$ is

[8]The invisible space is leveraged in the design of super-directive array patterns, which are known to store large amounts of energy [41, 84, 95].

the self-impedance of the mth element for $m,k \in \left\{-\frac{M-1}{2},\ldots,\frac{M-1}{2}\right\}$. These impedance elements are collected into an $M \times M$ matrix form known as the impedance matrix where the (m,k)th element is $[\boldsymbol{Z}(f)]_{mk} = Z_{mk}(f)$.

Because the mutual impedances are derived from the terminal voltage and current of the antenna, they do not inherently capture the effect of the matching network. If the L-network from in Figure 3.11 is assumed to be the same for each element (to maintain array symmetry) [98], the impedance matrix measured from the beginning of the matching network (denoted $\boldsymbol{Z}'(f)$) expressed in terms of $\boldsymbol{Z}(f)$ is

$$\boldsymbol{Z}'(f) = \left(\boldsymbol{Z}^{-1}(f) + j2\pi fC\mathbf{I}_M\right)^{-1} + j2\pi fL\mathbf{I}_M. \quad \textit{(L-network transformation)} \tag{3.63}$$

Assuming that the generator impedance Z_s is real and equal to the characteristic impedance of the transmission line Z_0, the model from Figure 3.11 can be simplified to an M-port network and equivalent sources that include the effects of the matching networks and transmit chains, respectively, shown in Figure 3.12.

The scattering matrix for this updated M-port network is found via the new impedance matrix $\boldsymbol{Z}'(f)$ as [99]

$$\boldsymbol{S}(f) = \left(\boldsymbol{Z}'(f) + Z_0\mathbf{I}_M\right)^{-1}\left(\boldsymbol{Z}'(f) - Z_0\mathbf{I}_M\right). \tag{3.64}$$

The backward traveling wave at the mth element, $V_m^-(f)$ is expressed as a summation of the coupled energy from the forward voltages from all antenna elements,

$$V_m^-(f) = \sum_k \mathcal{S}_{mk}(f)V_k^+(f) \tag{3.65}$$

where $\mathcal{S}_{mk}(f) = [\boldsymbol{S}(f)]_{mk}$. The voltages and currents at the terminals of the matching networks are found via a combination of the forward and backward traveling waves as

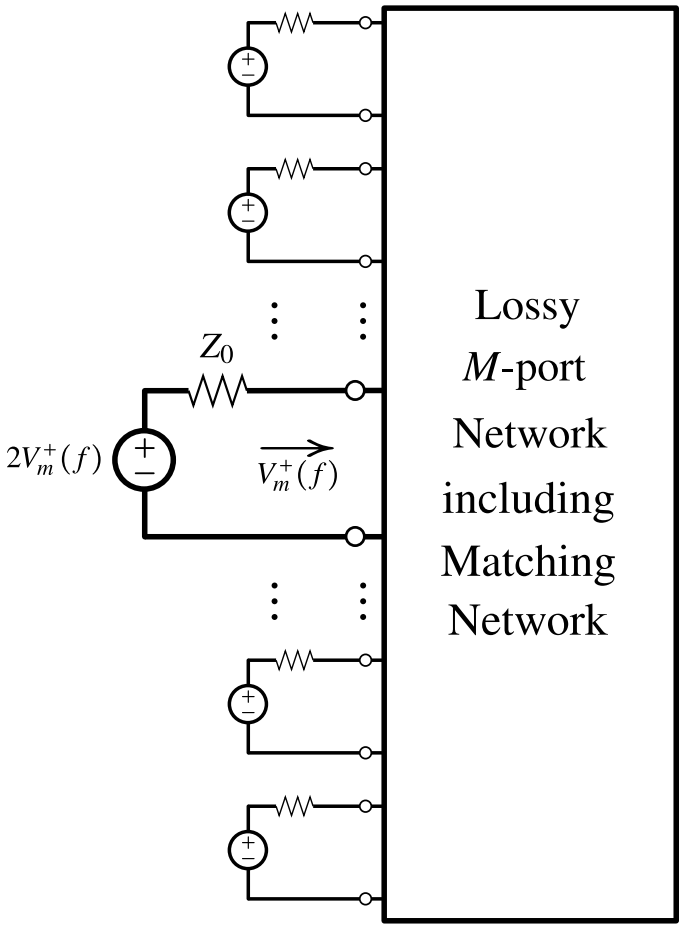

Figure 3.12: Simplified M-port network including antenna matching networks.

$$\begin{aligned} V'_m(f) &= V^+_m(f) + V^-_m(f) \\ &= V^+_m(f) + \sum_k \mathcal{S}_{mk}(f) V^+_k(f) \end{aligned} \tag{3.66}$$

and

$$\begin{aligned} I'_m(f) &= \frac{V^+_m(f) - V^-_m(f)}{Z_0} \\ &= \frac{V^+_m(f)}{Z_0} - \frac{1}{Z_0} \sum_k \mathcal{S}_{mk}(f) V^+_k(f), \end{aligned} \tag{3.67}$$

respectively. Thus, define the *active element impedance*[9]. for element m (as a function of function f) as the ratio of these two quantities,

$$Z^{\mathrm{a}}_m(f) = \frac{V'_m(f)}{I'_m(f)}. \tag{3.68}$$

Note that the matching network terminal voltages and currents are also related through the transformed impedance matrix $\boldsymbol{Z}'(f)$ as

$$V'_m(f) = \sum_k Z'_{mk}(f) I'_k(f). \tag{3.69}$$

Therefore, the active element impedance from (3.68) can be written in terms of the currents at the matching network terminals,

$$Z^{\mathrm{a}}_m(f) = \sum_k Z'_{mk}(f) \frac{I'_k(f)}{I'_m(f)}. \tag{3.70}$$

The *active reflection coefficient* at the matching network terminals of the mth antenna element (as a function of frequency f) describes the ratio of power returned to the generator to the power incident on the matching network. This quantity can be defined using both the circuit and wave models as [84, 95]

[9]Term *scan element impedance* is also used to describe the excitation-dependent terminal impedance [41] though implies that only scanning excitations are applied to the array thus does not qualify here.

$$\begin{aligned}\Gamma_m^{\mathrm{a}}(f) &= \frac{Z_m^{\mathrm{a}}(f) - Z_0}{Z_m^{\mathrm{a}}(f) + Z_0} \\ &= \frac{V_m'(f) - Z_0 I_m'(f)}{V_m'(f) + Z_0 I_m'(f)}\end{aligned} \tag{3.71}$$

and

$$\begin{aligned}\Gamma_m^{\mathrm{a}}(f) &= \frac{V_m^-(f)}{V_m^+(f)} \\ &= \sum_k \mathcal{S}_{mk}(f) \frac{V_k^+(f)}{V_m^+(f)},\end{aligned} \tag{3.72}$$

respectively. Note that because this formulation of reflection coefficient includes energy from coupled sources (instead of just $V_m^+(f)$), the magnitude of the "reflection" coefficient can be greater than unity. The definition of the reflection coefficient from (2.80) was based on system parameters only (antenna impedance and characteristic impedance), however the formulation in (3.71) is dependent on the array excitation (due to the coherent combination of coupled waves) thus is termed the *active reflection coefficient* for element *m*. The *total active reflection coefficient* describes the square-root ratio of the total reflected/coupled power to the total incident power as a function of frequency defined as

$$\Gamma^{\mathrm{a}}(f) = \left(\frac{\sum_m |V_m^-(f)|^2}{\sum_m |V_m^+(f)|^2} \right)^{\frac{1}{2}}. \tag{3.73}$$

The frequency-dependent form of the reflection coefficients from (3.72) and (3.73) are convenient for visualizing the reflected/coupled energy as a function of frequency and for time-harmonic analysis. However the ratio of the integrated reflected/coupled energy to incident energy for each element is a more practical quantity when considering energy dissipation within each transmit chain for a finite duration emission. Thus define net energy flow crossing the *m*th antenna element for a single pulse as

$$\begin{aligned}\mathcal{E}_{\mathrm{tx},m} &= \mathcal{E}^{+}_{\mathrm{tx},m} - \mathcal{E}^{-}_{\mathrm{tx},m} \\ &= \frac{\|V^{+}_{m}(f)\|_2^2 - \|V^{-}_{m}(f)\|_2^2}{Z_0},\end{aligned} \tag{3.74}$$

where

$$\mathcal{E}^{+}_{\mathrm{tx},m} = \frac{\left\|V^{+}_{m}(f)\right\|_2^2}{Z_0} \tag{3.75}$$

and

$$\mathcal{E}^{-}_{\mathrm{tx},m} = \frac{\left\|V^{-}_{m}(f)\right\|_2^2}{Z_0} \tag{3.76}$$

are the incident and reflected/coupled energies corresponding to the mth element, respectively. Express the square-root ratio of the reflected/coupled energy to the incident energy on the mth element as

$$\begin{aligned}\Gamma^{\mathrm{a}}_{m} &= \left(\frac{\mathcal{E}^{-}_{\mathrm{tx},m}}{\mathcal{E}^{+}_{\mathrm{tx},m}}\right)^{\frac{1}{2}} \\ &= \frac{\|V^{-}_{m}(f)\|_2}{\|V^{+}_{m}(f)\|_2},\end{aligned} \tag{3.77}$$

and the square-root fraction of *total* incident energy coupled back into the array as

$$\begin{aligned}\Gamma^{\mathrm{a}} &= \left(\frac{\sum\limits_{m}\mathcal{E}^{-}_{m}}{\sum\limits_{m}\mathcal{E}^{+}_{m}}\right)^{\frac{1}{2}} \\ &= \left(\frac{\sum\limits_{m}\|V^{-}_{m}(f)\|_2^2}{\sum\limits_{m}\|V^{+}_{m}(f)\|_2^2}\right)^{\frac{1}{2}}.\end{aligned} \tag{3.78}$$

Define (3.77) as the *integrated reflection coefficient* for the mth element and (3.78) as the *total integrated reflection coefficient*. The time domain equivalents for the derivations in this section are provided in Appendix A.6.

3.2.2 Coupled Energy and the Invisible Space

The periodic nature of the array is illustrated via the grating lobe series [93, 100] which for an infinite ULA is represented as an infinite series of impulse functions in ū-space. Figure 3.13 shows the grating lobe series for an infinite array steered toward $\theta_C = 0°$ for $d = \frac{\lambda_c}{2}$, $d = \frac{\lambda_c}{4}$, and $d = \lambda_c$. As the array is scanned these grating lobes leave and enter the *visible space* (sometimes called the *real space*) which corresponds to $|\sin\theta| \leq 1$. The space $|\sin\theta| > 1$ corresponds to the *invisible space* (sometimes called *imaginary space*) which contains the remainder of the infinite grating lobe series [93].

For the case of $d = \frac{\lambda_c}{4}$ from Figure 3.13(b), the grating lobe series can be steered such that the spacing between grating lobes straddles the visible-space. At this point no energy can radiate and only evanescent waves are possible [98]. This property is true for any infinite array with $d < \frac{\lambda_c}{2}$. From a active impedance point of view, the radiation resistance of the elements when steering into the invisible space reduces to zero thus the impedance is completely reactive and contributes only to reactive power [93, 98]. For the case of $d = \lambda_c$ from Figure 3.13(c), multiple beams can be present in visible space at the same time (e.g. when $\sin\theta_C = 0.5$). The behavior of the array when a grating lobe enters the visible space depends on the antenna pattern in those directions. If a null is present at $\sin\theta = \pm 1$, then the entrance of the grating lobe has little effect on active impedance of the infinite array. However if the antenna has a non-zero antenna pattern toward endfire, a discontinuity occurs turning the active impedance resistive to reactive as the grating lobe enters the visible space [93] resulting total reflection and a *blind angle* in the array beampattern [41][10].

As the infinite array is scanned, the active impedance of each element varies with look direction θ_C. This scan impedance variation is dependent on the element type as well as the spacing between the elements. If the array is matched at boresight (typical for a general scanning array) the impedance variation limits the usable sector in space where the reflected/coupled energy is at an acceptable level. For an infinite parallel dipole ULA with spacing $d \leq \frac{\lambda_c}{2}$, it can be shown that the

[10] These qualitative behaviors of an infinite array (along with scan impedance variation) can be visualized via the grating lobe series and the *impedance crater* for a particular antenna element [100].

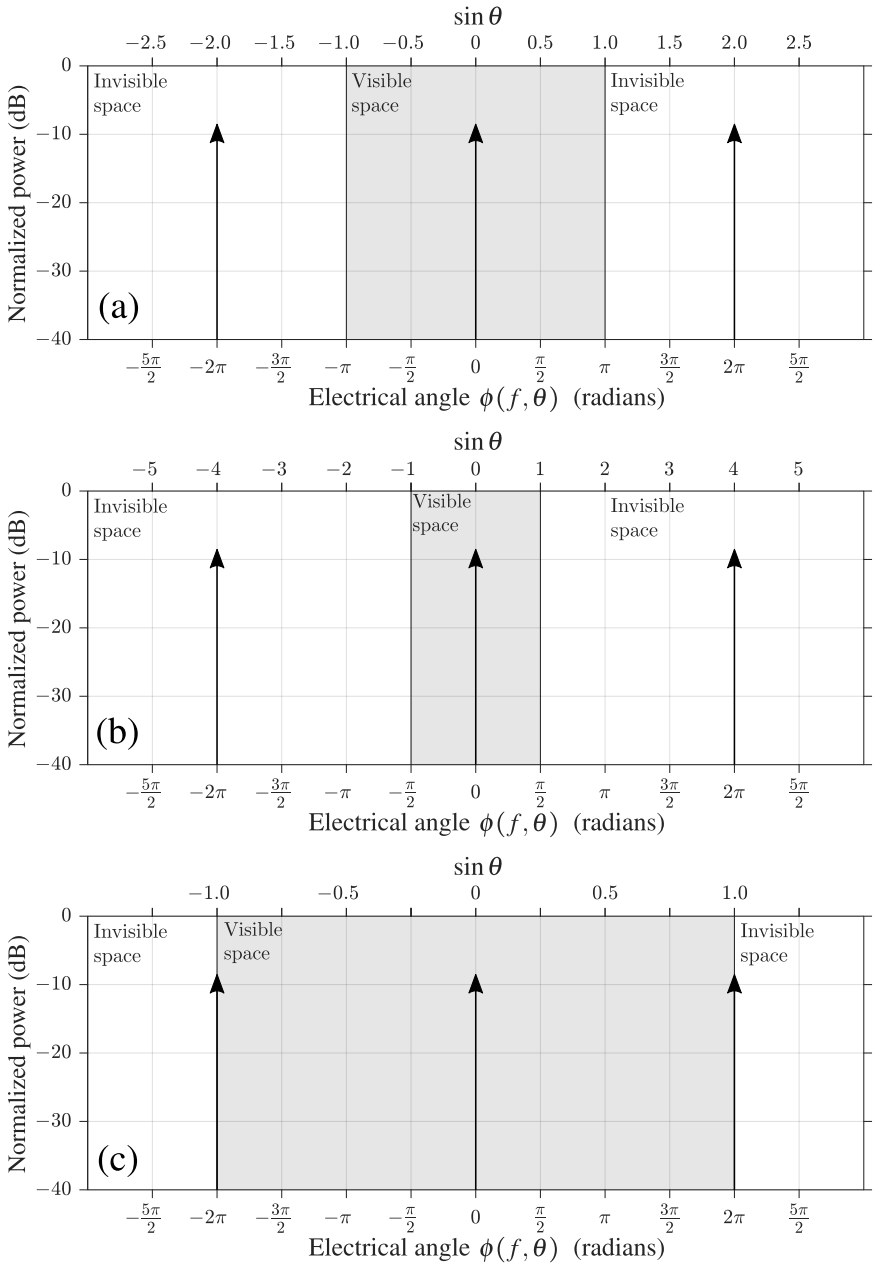

Figure 3.13: Visible and invisible regions for an infinite ULA steered toward $\theta_C = 0°$ for (a) $d = \frac{\lambda_c}{2}$, (b) $d = \frac{\lambda_c}{4}$, and (c) $d = \lambda_c$.

resistive portion of the active impedance diverges to infinity (reduces to 0 Ω for a collinear dipole array) as the beam is scanned resulting in total reflection at $\theta = \pm 90°$ [73, 93, 100, 101].

Figure 3.14 shows the grating lobe series for a finite $M = 30$ element ULA steered toward $\theta_C = 0°$ for (a) $d = \frac{\lambda_c}{2}$, (b) $d = \frac{\lambda_c}{4}$, and (c) $d = \lambda_c$. Instead of the series taking the form of impulses like the infinite array case, the finite nature of the array creates lobing across space that is dependent on the size of the array. For finite arrays, the impedance discontinuities that occur in infinite arrays translate into steep impedance variations. The end elements of the array experience a different surrounding than the center elements, thus the variation in impedance is also different. It is desirable to use the same matching network for each element thus the variation in scan impedance over the desired region in space must be minimized [98]. Dielectric sheets and reduced element spacing have been shown to limit this impedance variation where the reactive portion of active impedance is balanced using a ground plane. This array building method called *wide-angle impedance matching* (WAIM) allows for the array to match at extreme scan angles (and bandwidths) [95, 96, 102].

For the $d < \frac{\lambda_c}{2}$ finite array, instead of the radiation resistance reducing to zero when the mainlobe of the array is steered into the invisible space, there still exists a small radiation resistance for each element that corresponds to the sidelobes that still exist in the real space. However, the reactive portion of the active impedance dominates the resistive portion thus making matching in this scenario difficult. This type of excitation creates a superdirective beam which are notoriously difficult to match without experiencing large ohmic losses in the antenna, matching network, or transmit chain due to large circulating currents exchanging energy between the reactive components and the near field of the array [41][11]. Define the region between $1 < |\sin\theta| < \frac{\lambda_c}{2d}$ as the *reactive region* as the portion of energy placed into this region contributes to the overall reactive power of the array excitation [42].

In the following sections, two finite uniform linear arrays are investigated using time-harmonic

[11] Because these superdirective excitations are difficult to match and scanning beam pattern are typically matched at broadside. It may be possible to match an array at broadside *and* for superdirective excitations though no evidence of any theoretical development could be found.

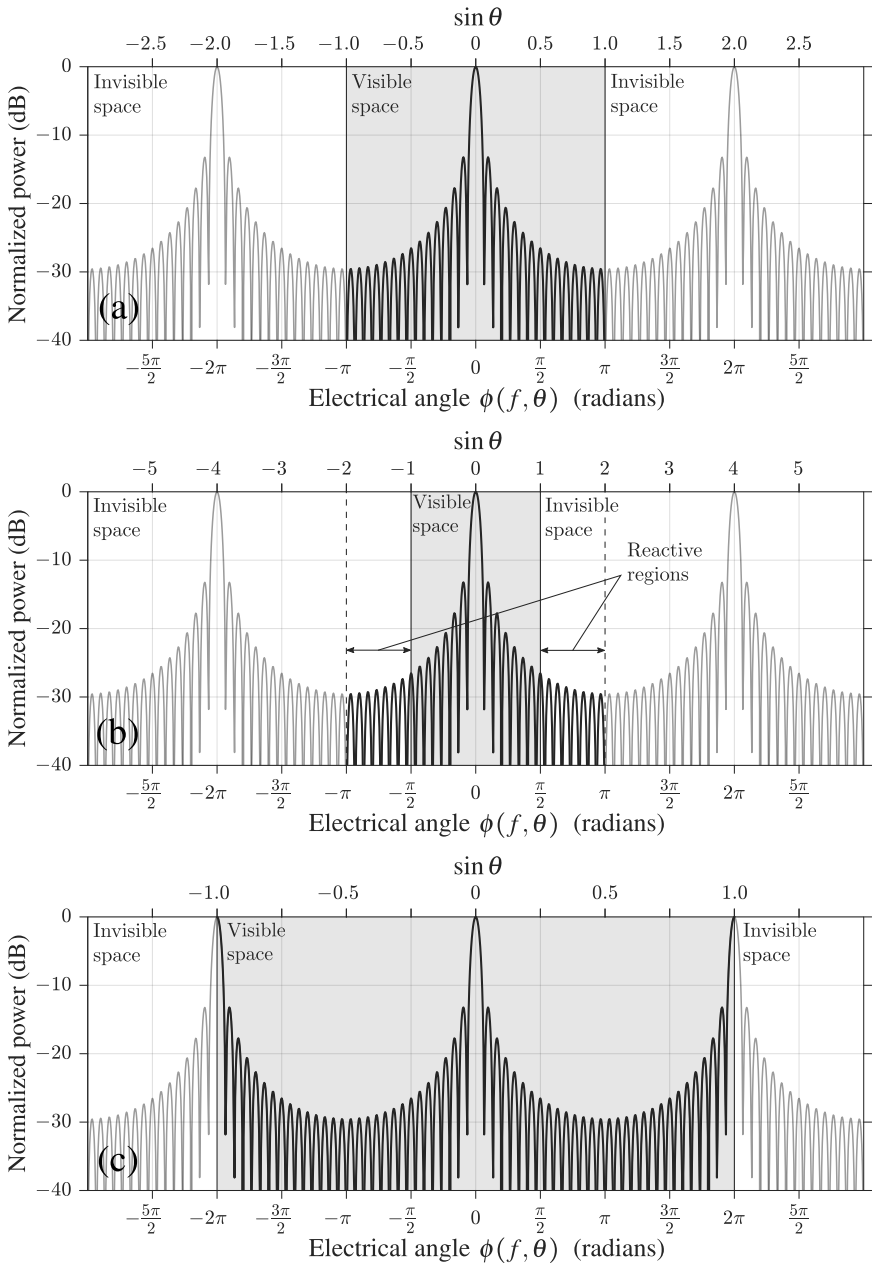

Figure 3.14: Visible and invisible regions for an $M = 30$ element ULA steered toward $\theta_C = 0°$ for (a) $d = \frac{\lambda_c}{2}$, (b) $d = \frac{\lambda_c}{4}$, and (c) $d = \lambda_c$.

analysis: an array with half-wavelength spacing (Section 3.2.2.1), and an array with quarter-wavelength spacing (Section 3.2.2.2). The time-harmonic analysis and dipole dimensions are evaluated according to frequency $f = f_c$. Define the time-harmonic voltages, active impedance, mutual impedance and scattering matrix for frequency $f = f_c$ as $V_m^+(f_c)$, $Z_m^a(f_c)$, $Z_{mk}(f_c)$ and $\boldsymbol{S}(f_c)$, respectively. The time-harmonic active reflection coefficient from (3.72) and total active reflection coefficient from (3.73) are $\Gamma_m^a(f_c)$ and $\Gamma^a(f_c)$, respectively. The arrays are comprised of $M = 30$ identical parallel half-wavelength dipoles with diameter $0.001\lambda_c$. The self and mutual impedances are found via the induced emf method [73] as it has a analytical approximation of the mutual impedances between elements. The mutual impedance between two dipoles given these parameters is shown in Figure 3.15 versus distance in wavelengths. The arrays are matched using the simple L-networks [84] shown in Figure 3.11 and calculated based on the initial active impedance based on a boresight standard beamforming excitation[12]. Because the active impedances are different for each element, the calculated matching network parameters are averaged over all elements to maintain identical matching networks. Assume that the shape current distributions on each wire of the dipole are balanced and not altered with mutual coupling.

3.2.2.1 Time-harmonic Analysis of ULA of Parallel Half-wavelength Dipoles with Half-wavelength Spacing

Figure 3.16 shows the magnitude (in dB) of the mutual and self impedances for the ULA comprised of $M = 30$ half-wavelength dipoles at half-wavelength spacing. These magnitudes correspond to the black curve in Figure 3.15 relating to the magnitude of the mutual impedance with distance. These impedances are measured at the terminals of the antennas prior to application of the matching networks. The magnitude of the impedance decays approximately proportional to the inverse of the distance between the elements [73], thus showing that the elements have less interaction the further they are spread apart.

The L-network values for each element were determined via a broadside steering excitation

[12]Note that the L-network is used for simplicity of analysis.

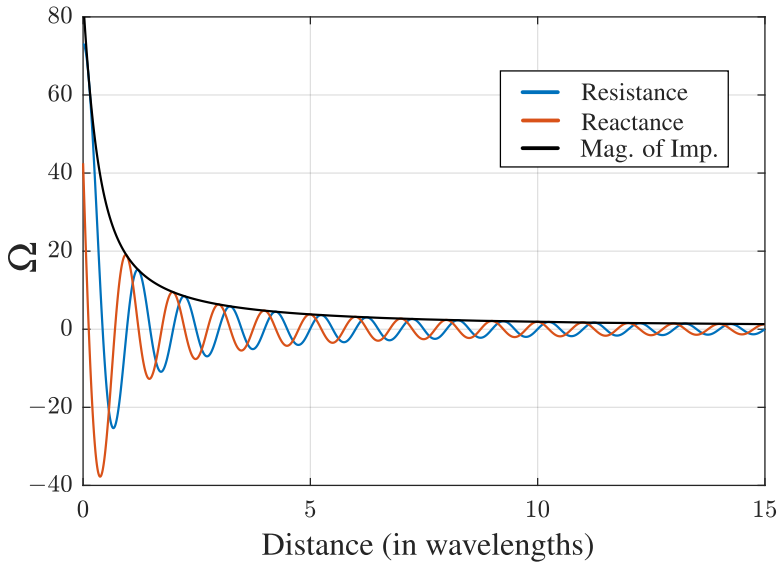

Figure 3.15: Resistance, reactance, and magnitude of time-harmonic mutual impedance $Z_{mk}(f_c)$ between two parallel, half-wavelength dipoles of diameter $0.001\lambda_c$ vs. distance (in wavelengths) calculated via the induced emf method [73].

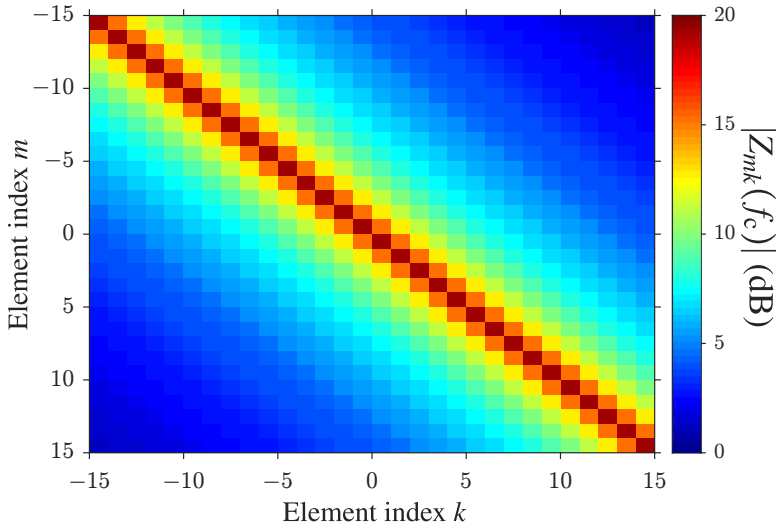

Figure 3.16: Magnitude of mutual and self impedances (before matching) $|Z_{mk}(f_c)|$ (in dB) for $M = 30$ element ULA of half-wavelength dipoles and half-wavelength spacing calculated using induced emf method [73].

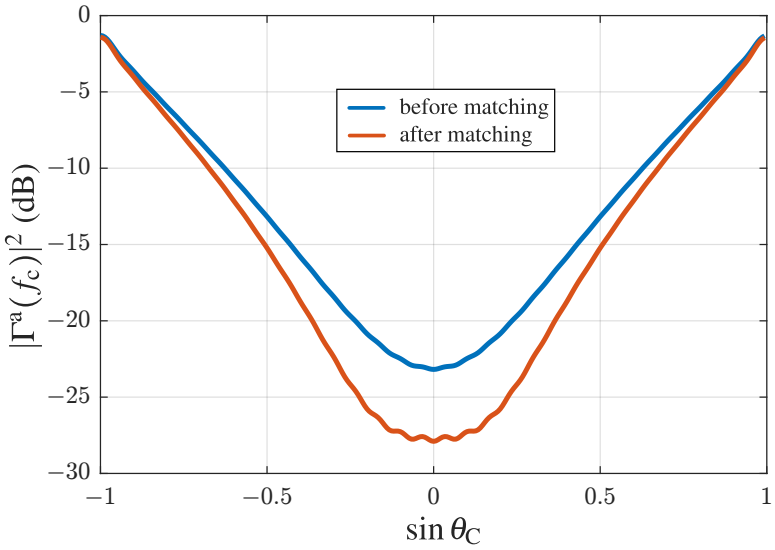

Figure 3.17: Total active reflection coefficient $|\Gamma^{\mathrm{a}}(f_{\mathrm{c}})|^2$ (in dB) from (3.73) vs. standard beamforming steering direction $\sin\theta_{\mathrm{C}}$ for $M = 30$ element ULA with half-wavelength spacing before matching network (blue) and after matching network (red).

prior to the addition of a matching network. The averaged values for the network parameters are $j2\pi f_{\mathrm{c}}C = j0.00646\ \Omega^{-1}$ for the parallel capacitive susceptance and $j2\pi f_{\mathrm{c}}L = j13.94\ \Omega$ for the series inductive reactance. Figure 3.17 shows the total active power reflection coefficient $|\Gamma^{\mathrm{a}}(f_{\mathrm{c}})|^2$ from (3.73) for standard beamforming excitations steering from $\sin\theta_{\mathrm{C}} = -1$ to $\sin\theta_{\mathrm{C}} = +1$ before and after L-network matching. The active power reflection coefficients $|\Gamma^{\mathrm{a}}_m(f_{\mathrm{c}})|^2 \forall m$ from (3.72) are shown in Figure 3.18 versus $\sin\theta_{\mathrm{C}}$. Note that the inner elements have similar integrated reflection coefficients while the outer elements experience much different responses due to the edge effects of the array.

The standard criterion for antenna operation is any reflection below 10 dB is considered satisfactory. Thus the usable sectors in space for the unmatched and matched arrays are $\sin\theta = \pm 0.6267$ $(\theta = \pm 38.8°)$ and $\sin\theta = \pm 0.6733$ $(\theta = \pm 42.3°)$. These scan angles are not very wide though could be increased through use of a more sophisticated matching network. Note that the total active reflection coefficient at the endfire scanning angles $(\theta = \pm 90°)$ is $|\Gamma^{\mathrm{a}}(f_{\mathrm{c}})|^2$ (dB) $= -1.425$ dB. Therefore 72.03% of the total incident power is being reflected/coupled back into the array at these angles. This amount of reflected power (as well as the increasing reflection coefficient toward endfire) can be attributed to the emergence of a grating lobe as the mainlobe is

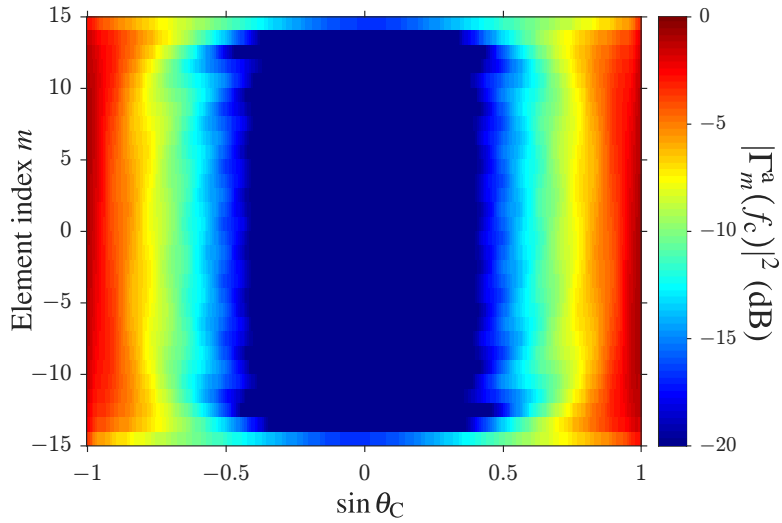

Figure 3.18: Active power reflection coefficient $|\Gamma_m^a(f_c)|^2$ (in dB) from (3.72) vs. element index m and standard beamforming steering direction $\sin\theta_C$ for $M = 30$ element ULA with half-wavelength spacing after matching.

steered out of visible space. The antenna pattern of a dipole in the endfire (array) direction does not contain a null thus the active impedance in this region changes dramatically from that of the broadside excitation [93].

The change in active impedance versus scan angle θ_C can be seen in Figure 3.20 for resistance (above) and reactance (below) after matching. Note that this response is particular to the L-network with a parallel capacitance and series inductance and would be different for a parallel inductance and series capacitance. While the resistance and reactance images would be different for the alternate L-network configuration, the resulting reflection/coupled power response would be similar to that of Figures 3.17 and 3.18. Towards endfire, the active impedance for most elements increases in resistance and becomes highly capacitive which degrades the match of the array at these angles. The active impedances for the center elements are relatively similar however the edge elements experience much a different scan impedance variation. These edge effects can be minimized by including dummy elements terminated to the line impedance, thus effectively increasing the array size from the viewpoint of the edge elements and reducing the impedance variation. Note that the matching network would need to be redetermined if dummy elements are introduced.

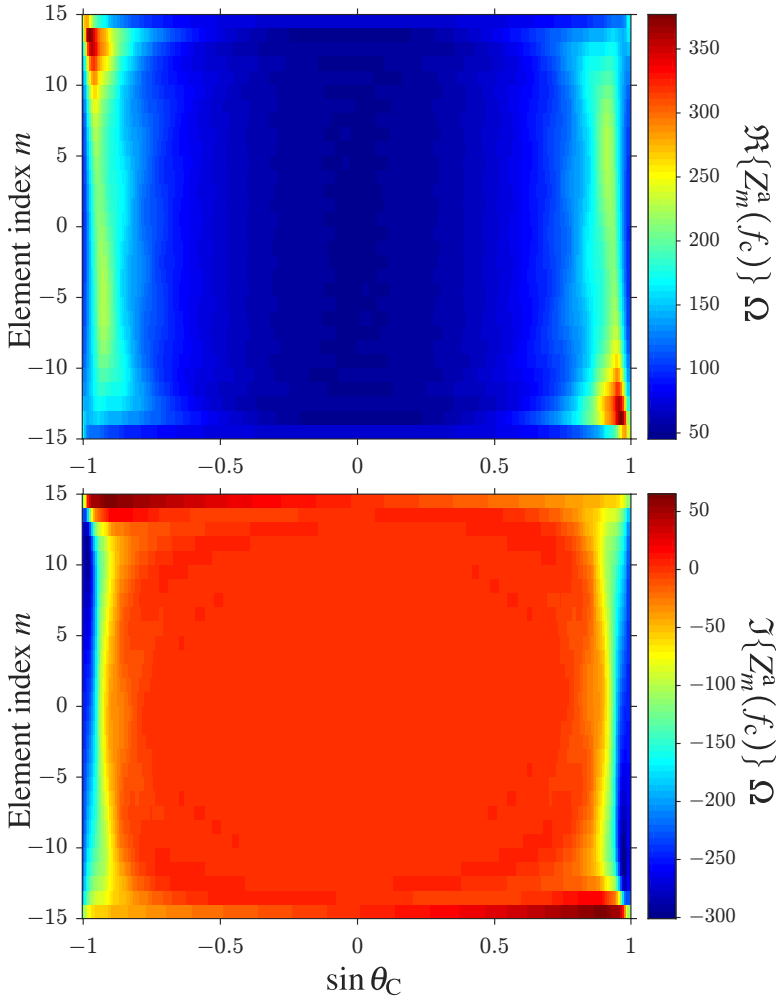

Figure 3.19: Time-harmonic active resistance $\Re\{Z_m^{\mathrm{a}}(f_{\mathrm{c}})\}$ (above) and active reactance $\Im\{Z_m^{\mathrm{a}}(f_{\mathrm{c}})\}$ (below) from (3.70) vs. element index m and standard beamforming steering direction θ_{C} for $M = 30$ element ULA with half-wavelength spacing after matching.

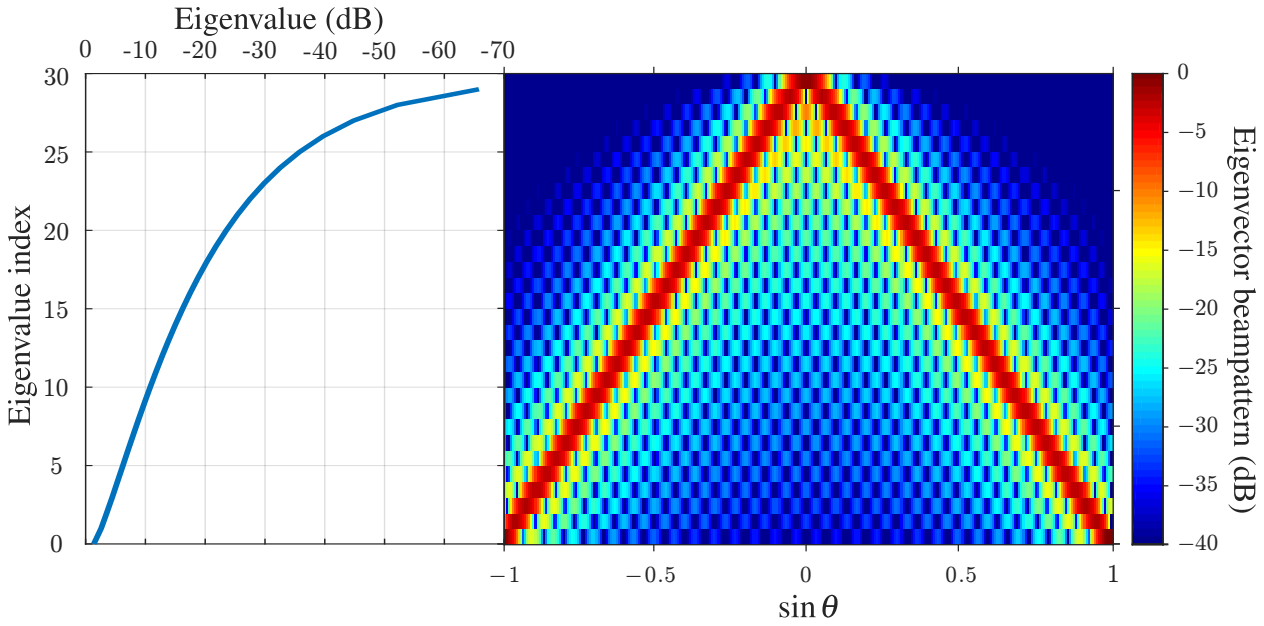

Figure 3.20: Squared-magnitude of eigenvalues (in dB) and corresponding eigenvector beampatterns (in dB) vs. $\sin\theta$ for the decomposed scattering matrix $\boldsymbol{S}(f_c)$ of an $M = 30$ element ULA with half-wavelength spacing at the terminals of the matching network.

Perhaps the easiest method to analyze how power is reflected/coupled back into the array is via an eigendecomposition of the time-harmonic scattering matrix $\boldsymbol{S}(f_c)$. Recall from (3.65) that the backward traveling waves for each transmit chain are determined by the scattering matrix and the forward traveling voltages. The eigendecomposition of $\boldsymbol{S}(f_c)$ provides both eigenvectors and eigenvalues of the scattering matrix. The eigenvectors provide an orthogonal basis of array excitations that have a coupling behavior determined by the corresponding eigenvalue. Figure 3.20 shows the eigenvalues (left) and the beampatterns of the corresponding eigenvectors (right) for the half-wavelength spaced ULA. The representation of both the eigenvalues and eigenvector beampatterns are in square-magnitudes thus represent powers. It should be noted that the eigenvalues of the scattering matrix are complex valued which represents propagation delays between the elements. The beampatterns correspond to the array factor of the corresponding eigenvector excitation.

The beampattern corresponding to the lowest eigenvalue (top row) represents the array excitation that results in the least amount of coupled power (for unit incident power). In fact, for

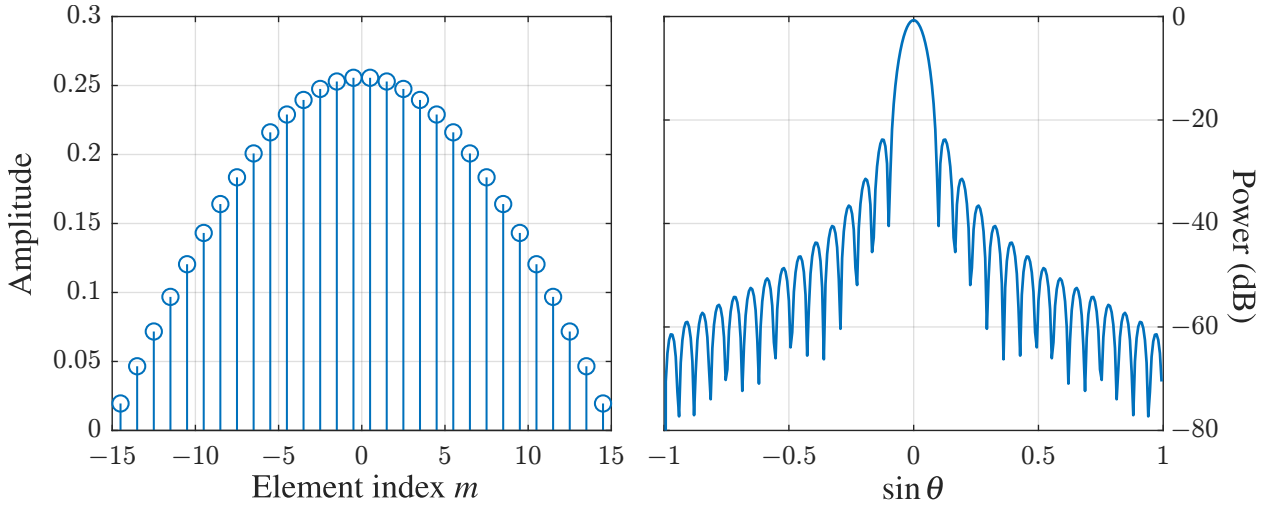

Figure 3.21: Eigen-excitation (left) and beampattern (right) corresponding to lowest eigenvalue in the scattering matrix for a ULA comprised of $M = 30$ parallel half-wavelength dipoles space $d = \frac{\lambda_c}{2}$ apart.

these "eigen-excitations", the squared-magnitude of the eigenvalue corresponds to the total active power reflection coefficient $|\Gamma^a(f_c)|^2$. Thus the beampattern with the lowest eigenvalue produces a total power reflection coefficient of $|\Gamma^a(f_c)|^2$ (dB) ≈ -66 dB and is pointed directly at boresight. The amplitude of this excitation and corresponding beampattern are shown in Figure 3.21. The fact that a beampattern at boresight produces the lowest coupled power makes intuitive sense as the array was matched at boresight however the excitation has a taper across the elements thus is not constant amplitude. This tapering produces a broadening of the beam, but more importantly a lowering of the sidelobe level. For a uniform amplitude boresight array excitation with $M = 30$ elements, the sidelobe level drops to approximately -30 dB near endfire relative to peak power whereas the beampattern in Figure 3.21 is approximately -60 dB. This result is qualitative, though there is no doubt that the sidelobe level at the edges (where the reflected/coupled power is highest) is a contributing factor as to why the beam pattern in Figure 3.21 couples less power than a uniform amplitude boresight excitation.

As the eigenvalue index decreases, two symmetric lobes start to form in the eigenvector beampatterns. As the total reflected powers (i.e. the eigenvalues) increase, so does the separation between the two lobes until the lobes reach endfire. Thus the excitation that produces to *highest*

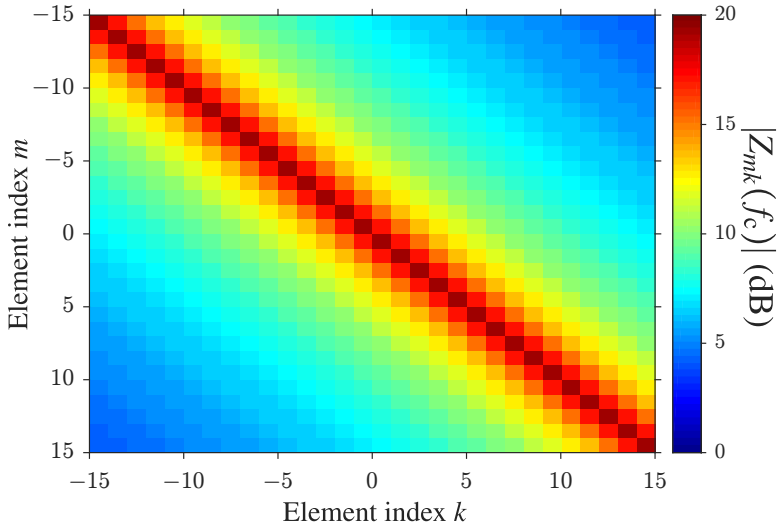

Figure 3.22: Magnitude of time-harmonic mutual and self impedances (before matching) $|Z_{mk}(f_c)|$ (in dB) for $M = 30$ element ULA of half-wavelength dipoles and quarter-wavelength spacing calculated using induced emf method [73].

reflected/coupled power for this $M = 30$ element, half-wavelength spacing ULA is the endfire beampattern shown in the last row of Figure 3.20 which corresponds to a total active power reflection coefficient of $\Gamma^{\mathrm{a}}(f_c)$ (dB) $= -1.368$ dB. Therefore 72.98% of the incident power is reflected/coupled back into the array for this eigen-excitation.

3.2.2.2 Time-harmonic Analysis of ULA of Parallel Half-wavelength Dipoles with Quarter-wavelength Spacing

Consider the same array $M = 30$ element uniform linear comprised of parallel half-wavelength dipoles however the spacing between them has been reduced to $d = \frac{\lambda_c}{4}$. Arrays of spacing $d < \frac{\lambda}{2}$ are called *over-sampled* arrays as the critically spatial sampled array has inter-element spacing $d = \frac{\lambda}{2}$. This spacing produces the reactive regions shown in Figure 3.14(b) where it is possible to create excitations that place a majority of energy within this region. The closer spacing between the elements increases the mutual impedances between the elements as shown in Figure 3.22 which is directly tied to the "sampling" of the impedance curve in Figure 3.15 at points closer to the origin. Thus, the surrounding elements have a greater influence on the terminal voltages and currents (as compared to the $d = \frac{\lambda_c}{2}$ array).

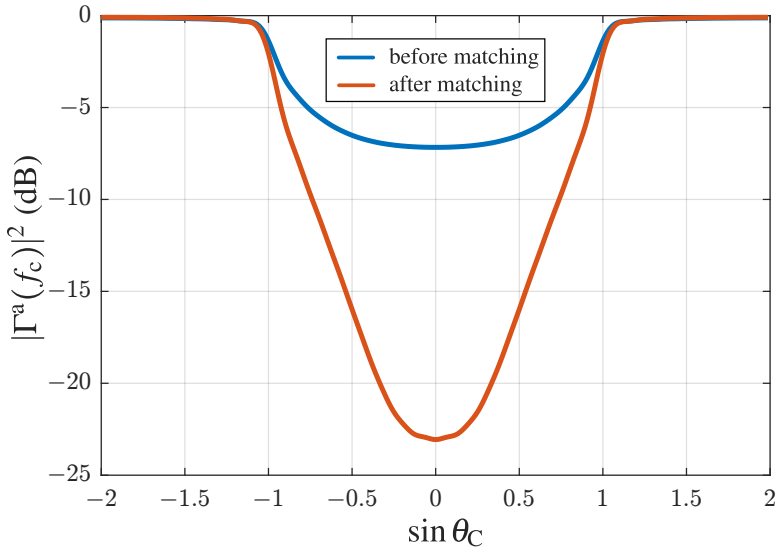

Figure 3.23: Total active power reflection coefficient $|\Gamma^{\mathrm{a}}(f_{\mathrm{c}})|^2$ (in dB) from (3.73) vs. standard beamforming steering direction $\sin\theta_{\mathrm{C}}$ for $M = 30$ element ULA with quarter-wavelength spacing before matching network (blue) and after matching network (red).

The L-network values were calculated based on a boresight excitation absent of a matching network. The calculated values were averaged to enforce identical matching networks across the array. The average parallel capacitive susceptance is $j2\pi f_{\mathrm{c}}C = j0.00660\ \Omega^{-1}$, and the averaged series inductive reactance is $j2\pi f_{\mathrm{c}}L = j60.60\ \Omega$. Figure 3.24 shows the total active power reflection $|\Gamma^{\mathrm{a}}(f_{\mathrm{c}})|^2$ from (3.73) before and after boresight matching versus standard beamforming scan angle θ_{C} for $-2 \le \sin\theta_{\mathrm{C}} \le 2$. Before the matching network is applied, the total reflection coefficient does not dip below the -10 dB threshold to satisfy operation. After matching using the L-network, the acceptable scan range for this array is between $\sin\theta_{\mathrm{C}} = \pm 0.735$ or $\theta_{\mathrm{C}} = \pm 47.31°$, a modest increase in scan range compared to the half-wavelength space ULA. Again, this limited scan range is most like constrained by the simplistic matching network however is sufficient for analysis purposes. Note how the total active power reflection coefficient is near unity for scan angles where $|\sin\theta_{\mathrm{C}}| > 1$ where the mainbeam of the beampattern is within the invisible space. As will be shown, this characteristic is a result of the active impedance of the array become primarily reactive (hence the name, *reactive region*) with very low radiation resistance.

Figure 3.24 shows the active power reflection $|\Gamma^{\mathrm{a}}_m(f_{\mathrm{c}})|^2 \forall m$ from (3.72) versus standard beamforming scan angle θ_{C} after matching for $-2 \le \sin\theta_{\mathrm{C}} \le 2$. The blackened areas of the image

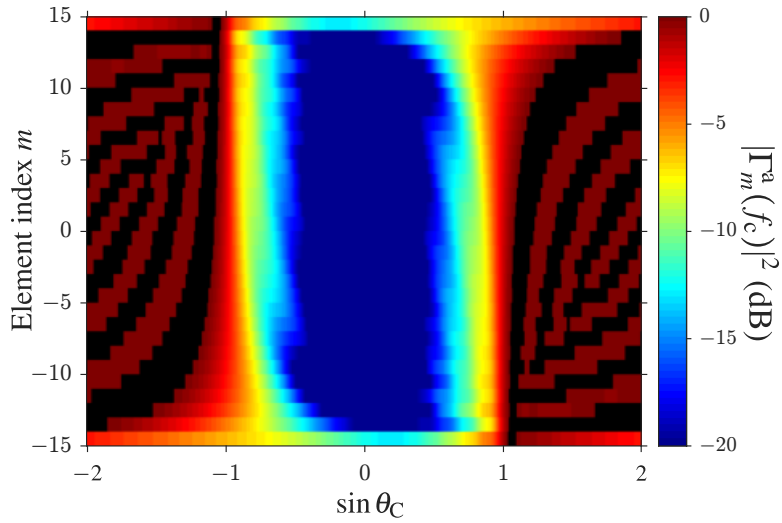

Figure 3.24: Active power reflection coefficient $|\Gamma^{\mathrm{a}}_m(f_{\mathrm{c}})|^2$ (in dB) from (3.72) vs. element index m and standard beamforming steering direction $\sin\theta_{\mathrm{C}}$ for $M = 30$ element ULA with quarter-wavelength spacing. Blackened areas indicate $|\Gamma^{\mathrm{a}}_m(f_{\mathrm{c}})|^2 > 1$.

correspond to the active power reflections greater than unity for the corresponding element. In these regions, more power is reflected/coupled back into the transmit chain than was initially incident on the antenna. For this array configuration there exist two distinct operating regions: the center blue region which corresponds to a satisfactory array operating region, and the red/black region which corresponds to high amounts of reflected/coupled energy back into the array which would dissipate within the transmitter causing heating and possibly damage [42]. Therefore, care must be taken when designing spatially-diverse emissions so as to not transmit within these regions for this array configuration.

Figure 3.25 shows the active resistance $\Re\{Z^{\mathrm{a}}_m(f_{\mathrm{c}})\}$ (blue) and active reactance $\Im\{Z^{\mathrm{a}}_m(f_{\mathrm{c}})\}$ (red) for (one of) the center elements versus the standard beamforming steering direction $\sin\theta_{\mathrm{C}}$ for $-2 \leq \sin\theta_{\mathrm{C}} \leq 2$ after matching[13]. The active resistance reduces to negligible amounts within the reactive region allowing for no (or very little) dissipation (radiation) of the antenna in this region[14]. For this matching network the reactive region is dominated by an inductive reactance. The combination of the low resistance and high reactance results in a poor match of the array for

[13]Note that this response is particular to the L-network with a parallel capacitance and series inductance. However, the important qualitative aspects of the response do not change when considering a different L-network configuration.

[14]The negative resistances within the reactive region correspond angles where active power reflection coefficient is greater than unity.

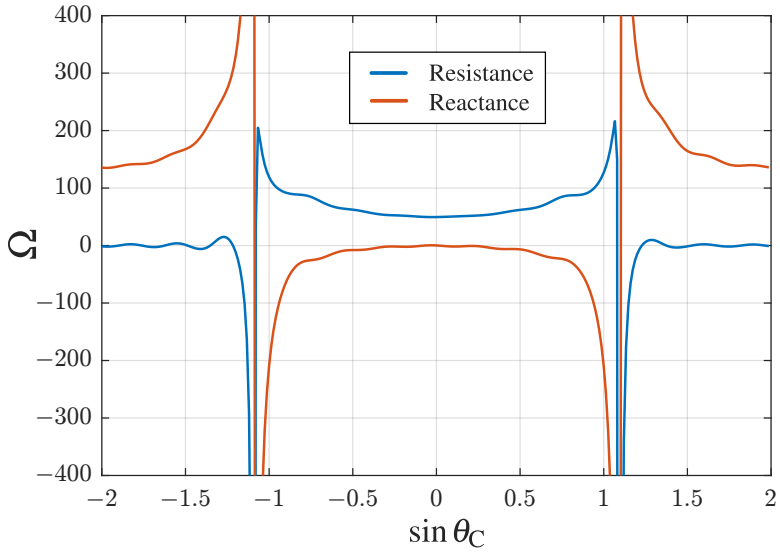

Figure 3.25: Time-harmonic active resistance $\Re\{Z_m^{\mathrm{a}}(f_{\mathrm{c}})\}$ (blue) and active reactance $\Im\{Z_m^{\mathrm{a}}(f_{\mathrm{c}})\}$ (red) from (3.70) vs. standard beamforming steering direction $\sin\theta_{\mathrm{C}}$ for middle element of $M = 30$ element ULA with quarter-wavelength spacing after matching with L-network comprised of parallel capacitive susceptance and series inductive reactance.

these excitations resulting in an almost total reflection of the incident energy on the array.

The squared-magnitude of the eigenvalues and eigenvector beampatterns of the scattering matrix $\boldsymbol{S}(f_{\mathrm{c}})$ for this $M = 30$ element, quarter-wavelength spaced ULA are shown in Figure 3.26. Recall that the eigenvectors of the scattering matrix correspond to "eigen-excitations" that produce an total active power reflection coefficient equal to the corresponding square-magnitude of the eigenvalue. The excitation that produces the lowest amount of reflected/coupled power for this particular array and matching network corresponds to a beam in the first row of Figure 3.26 which has a similar tapered response and beam shape as that of Figure 3.21 (instead ranging from $-2 \leq \sin\theta_{\mathrm{C}} \leq 2$). This excitation produces a low total active power reflection of approximately -46 dB.

Much like Figure 3.20, as the eigenvalue index decreases the beampatterns split into a two lobes which separate until they reach the edges of the feasible excitations. Note that this limit is not endfire (like for the case of half-wavelength spacing), but an excitation that places the mainlobe(s) of the beampattern deep within the reactive region. The beampattern of the array excitation that produces the most reflected/coupled power (for unit incident power) is seen in the final row of

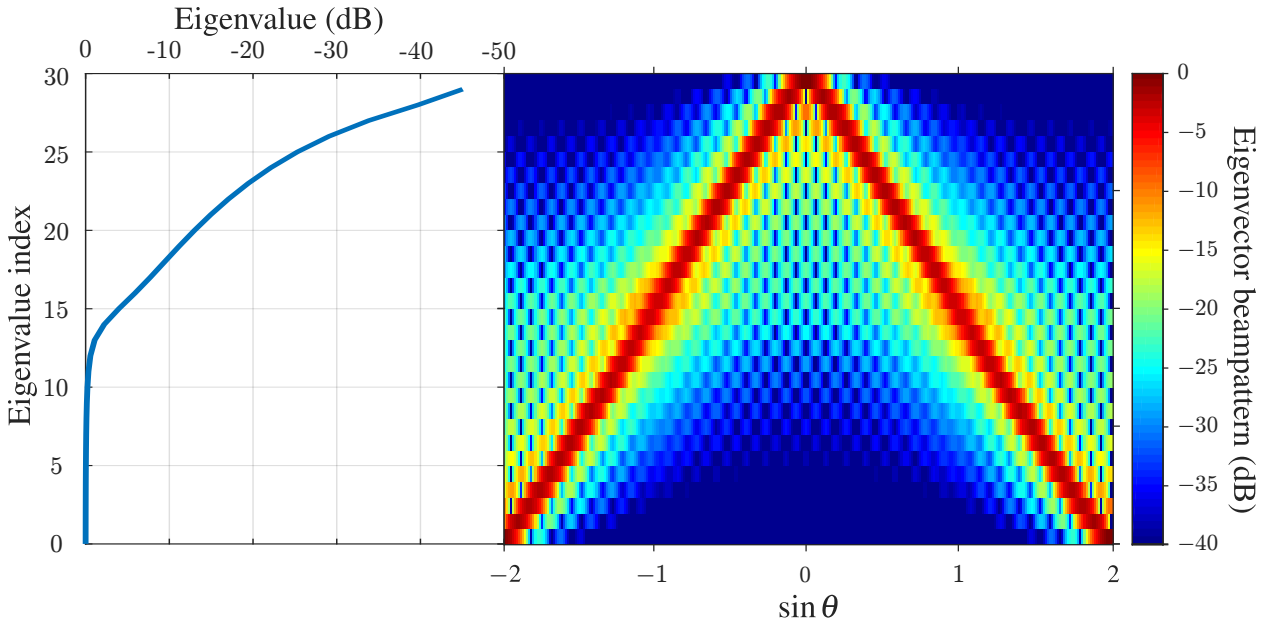

Figure 3.26: Squared-magnitude of eigenvalues (in dB) and corresponding eigenvector beampatterns (in dB) vs. $\sin\theta$ for the decomposed scattering matrix $\boldsymbol{S}(f_c)$ of an $M = 30$ element ULA with quarter-wavelength spacing at the terminals of the matching network.

Figure 3.26. This excitation reflects/couples 99.99% of the total incident power implying that there would be essentially zero radiation. In fact, eigenvalue indices 0 thru 9 have greater than 95% reflected coupled energy, and only eigenvalue indices 18 and greater correspond to excitations that meet the −10 dB threshold for satisfactory performance.

3.2.2.3 Geometric Quality Factor and Fractional Reactive Power

For superdirective arrays (and antennas), the invisible spaced was leveraged to form array/antenna patterns that theoretically have a higher directivity than a standard array/antenna of the same size [41, 73, 84]. To form these superdirective beams, a portion of the incident energy is purposely placed in the invisible space resulting in a low radiation resistance and high reactance impedance at which to match the antenna/array [41]. Because of the high reactance, the matching network applied to the antenna/array result in large circulating currents exchanged between the near field and matching network of the antennas [41]. The large amount of energy exchanged between that matching network and near field of the array "magnifies" any ohmic losses in the antenna

or matching network [41], thus the realized gain of the antenna might not be any better than the standard implementation. Although the study of these arrays brought with it metrics to define how superdirective (i.e. how much energy is within the invisible space) in a given array excitation.

Define the quality ($\mathcal{Q}$) factor of the array as the ratio of reactive power to radiated power [103]. The $\mathcal{Q}$-factor (of an array, antenna, or circuit) has been proven to limit the usable bandwidth as the ratio increases [84]. The $\mathcal{Q}$-factor for superdirective arrays is high due to the large storage of energy therefore must be narrowband the maintain a match for the array. For spatially-diverse transmission where broad spatial beams and wide bandwidths may be desired, the $\mathcal{Q}$-factor of the array (over the entirety of the emission) must be as small as possible.

It is useful to define the $\mathcal{Q}$-factor in terms of isotropic antennas to assess the propensity of the array factor to emit into the invisible region. This factor, derived in [104], was termed the *geometric quality factor* $\mathcal{Q}_{\mathrm{g}}$, where the overall quality of the array $\mathcal{Q}$ is approximated be the product of the geometric quality factor and the quality factor of an individual element $\mathcal{Q}_{\mathrm{e}}$, as $\mathcal{Q} = \mathcal{Q}_{\mathrm{g}}\mathcal{Q}_{\mathrm{e}}$. For a ULA with inter-element spacing d and the array geometric quality factor for the time-harmonic excitations $V_m^+(f_{\mathrm{c}})$ is defined as [103–105]

$$\mathcal{Q}_{\mathrm{g}} = \frac{\sum\limits_{m} |V_m^+(f_{\mathrm{c}})|^2}{\sum\limits_{m}\sum\limits_{k} V_m^+(f_{\mathrm{c}}) V_k^+(f_{\mathrm{c}})^* \operatorname{sinc}\left((m-k)\frac{2\pi}{\lambda_{\mathrm{c}}}d\right)}, \tag{3.79}$$

where $\operatorname{sinc}(\bullet)$ is defined in (2.31). The $\mathcal{Q}_{\mathrm{g}}$-function allows for analysis of the quality variation specifically due to the geometry of the array absent of any individual antenna patterns.

Figure 3.27 displays the geometric quality factor $\mathcal{Q}_{\mathrm{g}}$ for a ULA with spacing $d = \frac{\lambda_{\mathrm{c}}}{4}$ for standard beamforming excitations scanning over $\sin\theta_{\mathrm{C}} = \pm 2$. The Q_{g}-factor stays at approximately 0.25 over a majority of the visible space scan angles. Outside of this region, the Q_{g}-factor starts to rise dramatically at scan angles $|\sin\theta_{\mathrm{C}}| > 0.9$, indicating that for this array and these scans angles, the array $\mathcal{Q}$-factor will be large. Note that this conclusion was made irrespective to the element that is used within the array.

A brute force method of approximating the impact of emitting into the invisible space is simply

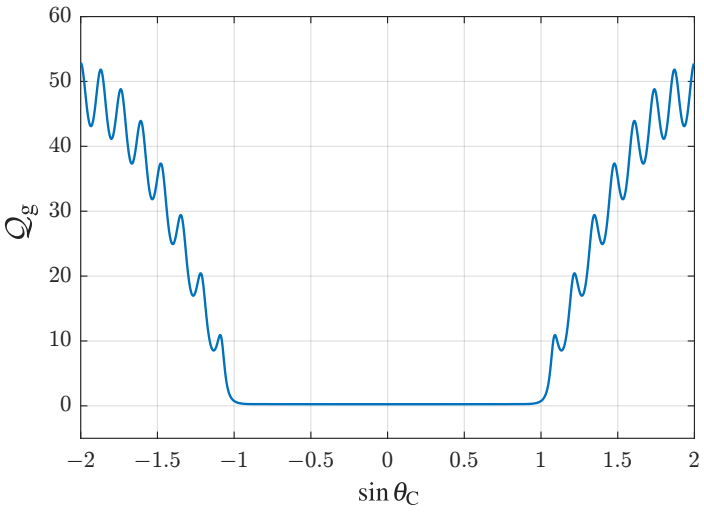

Figure 3.27: $\mathcal{Q}_g$-factor versus standard beamforming scan angle $\sin\theta_C$ for a ULA with inter-element spacing $d = \frac{\lambda_c}{4}$.

to integrate the array factor power over the reactive region and normalize it by the total array factor power. Because the invisible space is dominated by reactive impedance, we call this ratio the *fractional reactive power* (FRP). Define $G(f_c, \bar{u}) = \frac{1}{M}\sum_m V^+(f_c)e^{j\frac{2\pi}{\lambda_c}d\bar{u}}$ as the time-harmonic array factor for a ULA in $\bar{u}$-space. Thus, for an inter-element spacing of $d < \frac{\lambda_c}{2}$ the FRP is defined as[15]

$$\text{FRP} = \frac{\displaystyle\int_{-\frac{\lambda_c}{2d}}^{-1} |G(f_c,\bar{u})|^2 d\bar{u} + \int_{1}^{\frac{\lambda_c}{2d}} |G(f_c,\bar{u})|^2 d\bar{u}}{\displaystyle\int_{-\frac{\lambda_c}{2d}}^{\frac{\lambda_c}{2d}} |G(f_c,\bar{u})|^2 d\bar{u}}. \quad \textit{(time-harmonic)} \tag{3.80}$$

where $\bar{u} = \pm 1$ represents the edges of the visible space and $\bar{u} = \pm\frac{\lambda_c}{2d}$ represents the bounds on the feasible excitations. Note that because the array is discrete the array factor is periodic in the invisible space (i.e. the grating lobe series). Calculations similar to (3.80) have been defined for continuous aperture antennas where limits of the integrals in $\bar{u}$-space extend out to infinity (see [84]

[15]The FRP in (3.80) is specified as a time-harmonic expression as later in Section 4.2 the FRP is redefined for wideband transmission.

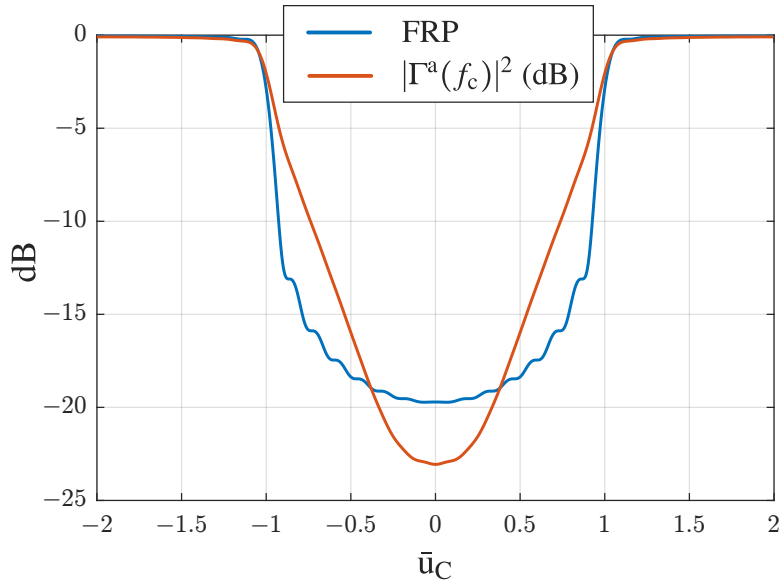

Figure 3.28: Fractional reactive power (FRP) from (3.80) and total active power reflection coefficient $|\Gamma^{a}(f_c)|^2$ (after matching) versus standard beamforming scan angle $\bar{u}_C = \sin\theta_C$. The power reflection coefficient $|\Gamma^{a}(f_c)|^2$ was calculated via the array specifications in Section 3.2.2.2, and the FRP was calculated only on the array factor of the standard beamformer.

for an approximation of antenna $\mathcal{Q}$ for a superdirective line source). These two antenna scenarios (discrete array and continuous aperture) mimic that of Fourier transform (continuous aperture to continuous beampattern) and the discrete "time" Fourier transform (discrete array to continuous beampattern). The calculation of energy in the spectrum/beampattern for these two transformations is from $-\infty$ to ∞ for the Fourier transform and $-\pi$ to π for the DTFT. Thus the total energy of the ULA beampattern is integrated from electrical angles $\phi = -\pi$ to $\phi = +\pi$, where the limits $\bar{u} = \pm\frac{\lambda_c}{2d}$ correspond to the electrical angles $\phi = \pm\pi$.

If the assumption is made that all energy within the real space is transmitted and all energy within the invisible space is reflected back into the transmitter, then the FRP should approximate the total power reflection coefficient for a given excitation. Note that this does not incorporate matching networks or active impedances into the approximation. However, if it is assumed that the array has a good match at boresight and over a wide range of angles, the shapes of the FRP and reflection coefficient are similar. Figure 3.28 shows the FRP and total active power reflection coefficient $|\Gamma^{a}(f_c)|^2$ (after matching) versus standard beamforming scan angle $\bar{u}_C = \sin\theta_C$ for the

$M = 30$ element half-wavelength parallel dipole ULA with spacing $d = \frac{\lambda_c}{4}$. Note that while the shape of the traces deviate in the visible space, they match to a high degree once the beam is steered in the invisible space. Thus the FRP provides a useful metric in evaluating array factors (time-varying or not) when the array spacing is $d < \frac{\lambda_c}{2}$ when the frequency-dependent scattering matrix is unknown.

The geometric quality factor and fractional reactive power represent metrics that can be applied to generic arrays with element spacing $d < \frac{\lambda_c}{2}$. These metrics (along with constant amplitude and spectrally containment) represent *system considerate* waveform/emission design metrics that can be used when specific array information is not present. If the scattering matrix $\boldsymbol{S}(f)$ for a specific array is known, $\mathcal{Q}_g$ and FRP are not needed as metrics because the amount of reflected/coupled energy can be directly calculated given an array excitation from the scattering model. In this scenario, the design would be *system specific* as the unique properties of the array would be known during the waveform/emission design process.

3.2.3 Mutual Coupling for Spatially-Diverse Transmission

The array excitations analyzed in Section 3.2.2 were limited to standard beamformed, time-harmonic signals. Applying other excitations (e.g. phase-only tapers, multi-lobe beampatterns) will have an effect on the array that has not yet been characterized. Furthermore, for spatially-diverse transmissions, the waveforms emitted by each element are different thus the excitation across the array is a time-varying response which produces a non-zero bandwidth for the emission. Thus the time-harmonic results versus scan angle in Section 3.2.2 may not be directly applicable to spatially-diverse transmissions, however they do provide valid analytic approaches and a qualitative basis of understanding of how mutual coupling might affect a spatially-diverse transmission.

The scattering matrix of the array is valid for any excitation, thus remains a strong analysis tool for evaluating the reflected/coupled energy on an array. If the array and/or transmission is not considered narrowband then the scattering matrix must become frequency dependent like the analysis in Section 3.2.1. By performing a eigendecomposition of the scattering matrix, a natural

excitation basis is created in the form of eigenvectors. This basis can be used in the optimization of array factors to execute a certain function but are constrained to limit the amount of coupled energy (see [106] for an circular array example). Likewise, this functionality can be extended to the design of time-varying array factors for spatially-diverse applications where the limits in the usable spatial transmission region can be tested.

If provided with a set of waveforms that produce a spatially diverse transmission, the scattering matrix may be used to predict the reflected/coupled power of the array. If the coupled energy is deemed too high, the eigenvectors (excitation basis) of the scattering matrix can be used to remove high coupling components from the set of waveforms via an orthogonal projection. Similarly in [42, 43] the waveforms of a MIMO emission of an oversampled over-the-horizon radar are transformed into a beamspace approach where the energy in the invisible region is reduced via reconstruction of the emission via Slepian beams. In [107], it was shown that the active VSWR of a spatially-diverse emission can be reduced via application of an inverted coupling matrix to the waveforms[16]. All of these mutual coupling reduction methods have the detriment of altering the envelopes of the spatially-diverse waveforms that are to be emitted. If a constant amplitude waveform implementation is required due to saturated amplifiers (Section 2.2.2) none of these methods would be a viable choice.

To circumvent the issue of waveform distortion when applying the coupling reduction transformation methods, the spatially-diverse waveforms can be designed/optimized with potential implementation issues in mind. However, this practice requires at least some knowledge of the array that is excited by the waveforms. Ideally, the design method would be *system specific* where the active element patterns $F_m(f, \theta, \vartheta) \forall m$ and scattering matrix $\boldsymbol{S}(f)$ are accurately known for all in-band frequencies. This knowledge would allow for the design of physical waveforms while accurately predicting both the far-field solution and the amount of reflected/coupled energy during transmission. If only the active element patterns are known, it was shown in [108] that both the

[16]The ULA was spaced at half-wavelength and the waveform were implemented via Gold codes (binary sequences) for a $d = \frac{\lambda_c}{2}$. Therefore, adjacent elements would either have 0° or 180° relative instantaneous phase producing large coupling between elements.

scattering matrix and active input impedance can be obtained from the active element pattern data.

If neither the active element pattern or scattering matrix are known a *system considerate* design approach can be utilized where the geometry of the array, frequency of operation, and general antenna pattern can be presumed. For example, say a time-varying antenna factor is being designed for a spatially-diverse emission for a ULA with half-wavelength spacing. Are the antennas assumed to be directive or omnidirectional in the scan plane of the array? If the assumption is directive, over what spatial region are the antennas directive? We would not want to design a time-varying antenna factor that places energy over a broad region in space if the antenna pattern is directive in the scan plane. If the array is over-sampled (over at least some portion of the bandwidth) the invisible space must be avoided to prevent reflections due to low radiation resistance. And if the array is spaced at half-wavelength, the endfire direction should generally be avoided as the impedance variation in those directions would also cause reflections.

To attain the best results for the waveform/emission design, the scattering matrix and active antenna patterns are necessary. However, simulated analysis of a spatially-diverse emission can be insightful as to what its behavior/performance could be under certain scenarios. The general assumptions described in the previous paragraph allow us to place reasonable constraints on the emission design/optimization problem without having knowledge of a specific array data.

To illustrate why these general array constraints are helpful in emission design, consider the design of a single pulse, spatially-diverse emission with time-bandwidth $BT = 100$ for a $M = 30$ element ULA without consideration of element patterns, scattering matrix, or element spacing[17]. Three different sets of $M = 30$ waveforms are designed[18] to be constant amplitude with equal energy, constrained to a Gaussian spectral shape, and designed to place energy over three different spatial extents: case 1) an omnidirectional pattern, where energy is place over all ϕ-space; case 2) a quasi-omnidirectional pattern, where energy is placed in electrical angles $\phi \in [-0.9\pi,\ 0.9\pi]$; and case 3) a spatially-constrained beampattern, where energy is placed in $\phi \in [-0.45\pi,\ 0.45\pi]$.

[17]Because the emission is designed absent of any antenna spacing, the dimension of design is in electrical angle ϕ-space from (3.34) instead of $\bar{u}$-space.

[18]The waveform sets are optimized using the narrowband version of the optimization procedure discussed in Section 4.2.

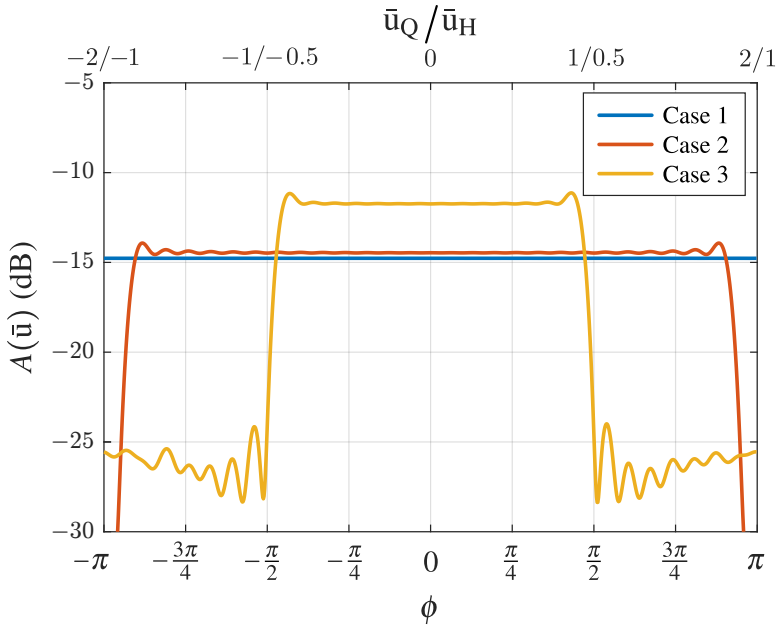

Figure 3.29: Aggregate beampatterns $A(\bar{u})$ in $\bar{u}$-space versus $\bar{u}_H$ and $\bar{u}_Q$ spaces for case 1 (blue), case 2 (red), and case 3 (yellow) transmissions.

Assuming the transmission is narrowband (no frequency-dependence), these optimized sets of waveforms can then be applied to the simulated half-wavelength dipole ULA models discussed in Sections 3.2.2.1 ($d = \frac{\lambda_c}{2}$) and 3.2.2.2 ($d = \frac{\lambda_c}{4}$). The edges of the ϕ-space (before phase wrapping) $\phi = \pm\pi$ correspond to $\bar{u}_H = \pm 1$ for the half-wavelength spaced array and $\bar{u}_Q = \pm 2$ for the quarter-wavelength spaced array in $\bar{u}$-space.

Figure 3.29 shows the aggregate beampatterns in $\bar{u}$-space ($A(\bar{u})$) for the three different design cases. Note that the bottom horizontal axis is electrical angle ϕ where the top horizontal axis contains both the $\bar{u}_H$ and $\bar{u}_Q$ axes. The aggregate beampatterns were normalized such that 0 dB represents the maximum output of the array. Thus the case 1 beampattern, at a constant of $-10\log_{10} M = -10\log_{10} 30 = -14.77$ dB, represents an isotropic power level. The beam patterns of cases 2 and 3 increase in power level (only slightly for case 2) due to the focusing of energy away from endfire. Figure 3.30 shows the complex-baseband power spectra $|G(f,\bar{u})|^2$ (in $\bar{u}$-space)[19] of the time-varying array factor for case 1 (left), case 2 (middle), and case 3 (right). Recall that each waveform is constrained to be constant modulus and to produce an emission with a spectrum

[19]The variable $G(f,\bar{u})$ is the same form as $G(f,\theta)$ from (3.20) and (3.33) with $\sin\theta$ replace with $\bar{u}$.

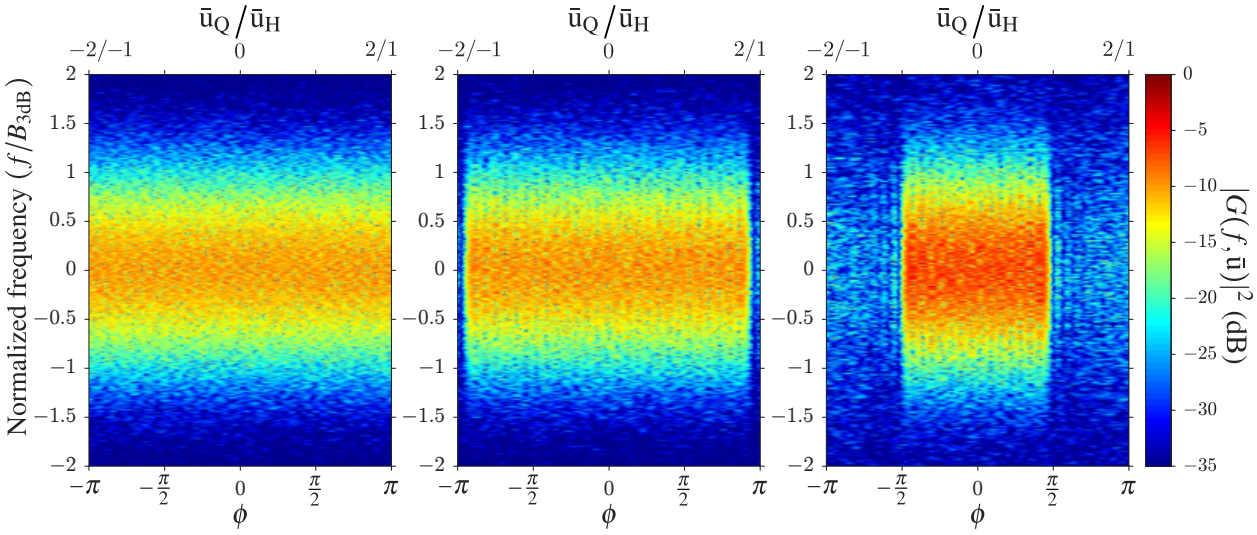

Figure 3.30: Power spectra $|G(f,\bar{u})|^2$ (in dB) of the time-varying array factor for case 1 (left), case 2 (middle), and case 3 (right) transmissions.

constrained to a Gaussian shape (which can be seen in all three cases in Figure 3.30). For the array with spacing $d = \frac{\lambda_c}{2}$, case 1 places energy over all space $\bar{u}_H = \pm 1$, case 2 places energy between $\bar{u}_H = \pm 0.9$, and case 3 places energy between $\bar{u}_H = \pm 0.45$. For the array with spacing $d = \frac{\lambda_c}{4}$, cases 1 and 2 place significant energy within the invisible space $(\bar{u}_Q > 1)$, while case 3 places a majority of the energy between $\bar{u}_Q = \pm 0.9$ (some sidelobe energy remains in invisible space).

The scattering matrices from Sections 3.2.2.1 and 3.2.2.2 are applied to the waveforms to simulate the predicted amount reflected/coupled energy for the three optimized emissions when applied to two differently spaced dipole ULAs. The waveform constraints of constant amplitude and spectral containment allow us to assume the signals $V_m^+(f)\forall m$ incident on the terminals of the matching network are proportional to the optimized waveforms $S_m(f)\forall m$. Thus the backward traveling waves $V_m^-(f)\forall m$ are calculated via (3.65) which allows for the calculation of the integrated reflection coefficient $\Gamma_m^a \forall m$ via (3.77).

Figure 3.31 shows the integrated power reflection coefficient $|\Gamma_m^a|^2 \forall m$ for the $d = \frac{\lambda_c}{2}$ (blue) and $d = \frac{\lambda_c}{4}$ (red) arrays and case 1 (left), case 2 (middle) and case 3 (right). For the $d = \frac{\lambda_c}{2}$ array, the omnidirectional beampattern results in a integrated power reflection coefficient > 0.1 for all elements in the array, thus does not meet the standards for a satisfactory emission. By moving

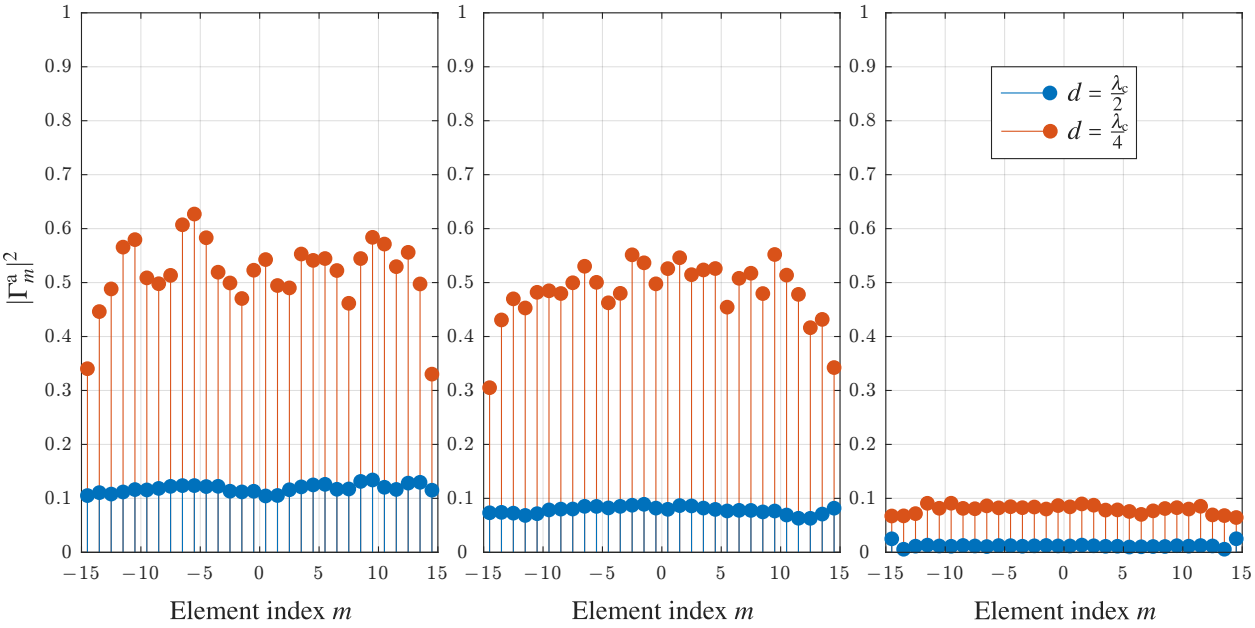

Figure 3.31: Integrated power reflection coefficient $|\Gamma_m^a|^2 \forall m$ from (3.77) for case 1 (left), case 2 (middle), and case 3 (right) transmissions.

energy away from endfire as in case 2 (middle), all elements are now beneath the acceptable threshold for operation. This change in reflection coefficient indicates that the energy in the time-varying antenna factor near endfire in case 1 was reflected when implemented on the $d = \frac{\lambda_c}{2}$ array. By making a slight modification in the emission constraints, we can achieve a near-omnidirectional beampattern with satisfactory reflection performance. The case 3 reflected energy for the $d = \frac{\lambda_c}{2}$ array is reduced more than in case 2 as the energy is focused between $\bar{u}_H = \pm 0.45$ which in nearer to the boresight match of the array.

For the $d = \frac{\lambda_c}{4}$ ULA (shown in red in Figure 3.31), cases 1 and 2 both result in a large amount of reflected energy that could damage the transmit chains of the elements if operated at high enough power. At the very least, the emission is inefficient as half of the pulse energy is dissipated in the resistive elements of the transmit chain and not radiated. By spatially containing the energy as in case 3 (which corresponds to energy placement between $\bar{u}_Q = \pm 0.9$), the active integrated power reflection coefficients for each element is beneath $|\Gamma_m^a|^2 = 0.1$ threshold for satisfactory performance. The energy of the $d = \frac{\lambda_c}{4}$ time-varying array factor is largely placed away from endfire and the reactive region to limit the amount of reflected/coupled power.

Table 3.1: Total integrated power reflection coefficient from (3.78) and FRP from (3.80)

	$d = \frac{\lambda_c}{2}$	$d = \frac{\lambda_c}{4}$	
	$\lvert\Gamma^a\rvert^2$	$\lvert\Gamma^a\rvert^2$	FRP
Case 1	0.1182	0.5177	0.5010
Case 2	0.0780	0.4831	0.4643
Case 3	0.0122	0.0797	0.0359

Table 3.1 shows the total integrated power reflection coefficient $|\Gamma^a|^2$ (calculated using (3.78)) for each array configuration and each transmission case, and the fractional reactive power (FRP) from (3.81) for the $d = \frac{\lambda_c}{4}$ array for comparison. Recall that the form of the FRP from (3.80) is only valid for a time-harmonic emission (a static array factor), thus cannot evaluate the FRP for a spatially-diverse emission. The FRP can generalized by integrating the complex-baseband, time-varying array factor over time (or frequency) as

$$\begin{aligned}\text{FRP} &= \frac{\displaystyle\int_0^T \left(\int_{-\frac{\lambda_c}{2d}}^{-1} |g(t,\bar{u})|^2 d\bar{u} + \int_1^{\frac{\lambda_c}{2d}} |g(t,\bar{u})|^2 d\bar{u} \right) dt}{\displaystyle\int_0^T \int_{-\frac{\lambda_c}{2d}}^{\frac{\lambda_c}{2d}} |g(t,\bar{u})|^2 d\bar{u} dt} \quad \textit{(spatially-diverse and narrowband)} \\ &= \frac{\displaystyle\int_{-\infty}^{\infty} \left(\int_{-\frac{c}{2f_c d}}^{-1} |G(f,\bar{u})|^2 d\bar{u} + \int_1^{\frac{c}{2f_c d}} |G(f,\bar{u})|^2 d\bar{u} \right) df}{\displaystyle\int_{-\infty}^{\infty} \int_{-\frac{c}{2f_c d}}^{\frac{c}{2f_c d}} |G(f,\bar{u})|^2 d\bar{u} df}.\end{aligned} \tag{3.81}$$

Note that because the waveforms contained in each waveform set have equal energy, the total integrated power reflection coefficient $|\Gamma^a|^2$ corresponds to the mean of the integrated power reflection coefficients from Figure 3.31 and thus retain similar behaviors to that discussed above. Recall that the FRP for the dipole array with spacing $d = \frac{\lambda_c}{4}$ gave a rough approximation of

the expected reflected power for the standard beamforming excitations (see Figure 3.28). This approximation also holds for cases 1 and 2 (within 2%) when the time-varying array factor has half the waveform energy in the invisible space. The approximation is less accurate when the reflection coefficient is small (case 3) likely due to the deviation between the FRP and $|\Gamma^{\mathrm{a}}|^2$ responses for excitations in the visible space shown in Figure 3.28. However, the correlation between the FRP and the total integrated power reflection coefficient $|\Gamma^{\mathrm{a}}|^2$ shows the FRP is valid metric for *system considerate* emission design methods where the specific array parameters are unknown.

3.3 Summary

In this chapter an analytical model of the far-field transmission was defined along with simplifying assumptions that are practical in certain radar transmission modes. The large array assumption allows for an approximate active element pattern to be used which decouples the array and element contributions. For a spatially-diverse emission mode, the array contribution takes the form of the time-varying antenna factor $g(t, \theta)$ which can be constructed and analyzed independent to the elemental pattern. The narrowband assumption allows the angle-delay ambiguity function $\chi_{\mathrm{s}}(\tau, \theta, \vartheta)$ to be separated into two individual components: the beam factor, which represents the nominal array resolution; and the diversity factor, which qualitative represents the spatial resolution enhancement achieved when operating in a MIMO transmission mode. The relationship between the invisible space/reactive region and reflected energy was made for dipole arrays with element spacing less than half-wavelength that are matched for broadside transmission. The invisible space is also discussed in the following chapter for a wideband spatially-diverse emission mode where the element spacing (in terms of wavelength) is frequency-dependent. Therefore the size of the reactive region changes depending on the operating frequency, antenna spacing (in meters), and bandwidth of the transmission.

Chapter 4

Waveform Design for Physical Spatially-Diverse Transmission

The practical insights to waveform and emission analysis provided by Chapters 2 and 3 provide a foundation for the design of spatially-diverse emissions with realistic restrictions/considerations. The waveforms that are optimized and designed throughout this chapter are all chosen to be constant amplitude and spectrally contained to limit both linear and nonlinear transmitter distortions to better model the modulation structure of the far-field emission, and to maximize efficiency of the overall emission (see Section 2.2.2). Furthermore, a spatially-diverse emission implies a DAR implementation thus the mutual coupling between elements must also be considered. In Chapter 3 it was shown that certain array excitations can produce more reflected/coupled energy than others. Assuming that the array is matched to broadside, energy directed towards endfire (via the array excitation), for arrays of element spacing half-wavelength or less, is reflected/coupled back into the array. Thus, the spatially-diverse emissions are constrained/designed to avoid emitting significant energy towards these directions. In this chapter, three different spatially-diverse transmission design modalities are presented with various levels of complexity and application[1].

In Section 4.1 a form of MIMO transmission is presented that is inspired by the fixational movements of the human eye [92, 109]. The emission maintains a coherent beam throughout its transmission and modulates the beam look direction throughout the pulse duration. This *spatially-modulated emission* was recently demonstrated to provide an improvement in spatial resolution similar to that theorized by the MIMO virtual array but with highly correlated waveforms. By maintaining a focused beam in this MIMO mode, spatial modulation could be applied to tracking

[1]Note that these sections all invoke the narrowband and large-array assumption differently based on possible applications. However, all emissions designs can be generalized to any combination of assumptions if desired.

situations where a higher energy-on-target is needed but a MIMO capability is still desirable.

A design approach is presented in Section 4.2 that jointly optimizes the beampattern and spectral content of a wideband spatially-diverse radar emission within the context of physically realizable frequency-modulated (FM) waveforms emitted from a uniform linear array [90,91]. The design approach is a specific form of alternating projections that shapes the emission spectrum as a function of spatial angle while intrinsically addressing the problem of the reactive region that arises for the wideband emission. This scheme also permits incorporation of joint space-frequency nulling to facilitate spectrum cohabitation with other nearby RF users. The design process is performed in a discretized manner that is "over-sampled" relative to waveform 3-dB bandwidth to capture a sufficient portion of the spectral roll-off to realize the physical waveform, which is subsequently implemented via the polyphase-coded FM (PCFM) structure. This flexible emission structure matches well with the flexibility of the DAR to form emissions that can perform multiple simultaneous radar functions.

Section 4.3 explores a spatial diversity technique where predetermined radar and communications signals having the same time and spectral support are simultaneously transmitted in different spatial directions via a digital array [24]. To increase the power efficiency of the emission, an iterative process denoted far-field radiated emission design (FFRED) is introduced that establishes a constant amplitude waveform constraint. The power efficiency of the emission under different scenarios is characterized through a percent orthogonal power and energy on target metric. Finally, the spatially-dependent bit error rate performance of the communications is analyzed under different scenarios. In [25], experimental results of this multifunction spatially-diverse mode were presented using the AFRL BEEMER system [110] and are also presented here.

4.1 Fast-time Spatial Modulated Radar

The physical waveform implementation of the PCFM waveform discussed in Section 2.1.2.4

A portion of the text in Section 4.1 is taken from "Adaptive Receive Processing of Spatially Modulated Physical Radar Emissions" by McCormick et al. printed in *IEEE Journal of Selected Topics in Signal Processing* in December 2015.

can extend to likewise parameterize a form of intra-pulse spatial modulation during the pulse by controlling the relative phases across the antenna array during the pulse transmission [38, 44]. Much like the frequency-diverse array (FDA) concept [15, 111–114], spatial modulation maintains a coherent beam throughout the transmission, however because the implementation of the emission is at the waveform level (as opposed to the carrier frequency as with FDA) the instantaneous beam location is not limited to constant scanning over all space thus avoiding the endfire regions of the array which were shown to reflected energy in Section 3.2.2. The spatial modulation emission architecture allows the waveform designer to uninhibitedly control the beam direction permitting precise command the spatial power distribution thus may have applications in tracking where the beamloss from omnidirectional spatially-diverse transmission would not be acceptable.

The spatially modulated emission structure was inspired by the biological process of the human eye (and of other animals possessing fovea) known as fixational eye movement in which the eye performs slow movements known as drift and rapid movements known as microsaccades [115, 116]. The current scientific consensus is that such movements enhance contrast and aid in resolving spatial ambiguities. There is even evidence [117] that these eye movements adapt according to environmental conditions (e.g. amount of lighting) and the active attention of the observer, thus suggesting a connection to cognitive sensing [29] within the visual cortex for this waveform-diverse emission paradigm [1, 2, 4].

It is observed that the "goodness" of a particular spatially modulated emission is dependent on the underlying waveform and the specific nature of the spatial modulation [92]. For example, use of a linear frequency modulated (LFM) chirp combined with relatively linear intra-pulse spatial steering provides what amounts to a tapering effect in the range domain that realizes significant range sidelobe suppression (with the associated range resolution degradation as well). Here it is demonstrated that, using only standard (non-adaptive) pulse compression and beamforming, spatial resolution and target discrimination can be enhanced by as much as 30%, albeit with a commensurate trade-off in range resolution and focused energy in the directions of transmission [92, 109].

4.1.1 Assumptions and Restrictions

It is assumed that the waveforms designed in Section 4.1 are implemented in a high power transmitter design thus necessitate the use of a high power amplifier operating in saturation. To limit distortions imparted to the signals traveling through a transmit chain with saturated amplifiers, each waveform is restricted to FM with constant amplitude envelope $u(t)$ (Section 2.2.2), thus the forward voltage at each element $V^+(t)$ is assumed to be a scaled version of the ideal waveform $s_{\text{pb}}(t)$. The assumption is made that the spectral content of the emission and array geometry are considered narrowband, therefore the active antenna patterns are assumed to be frequency-independent (Section 3.1.1.3). Also, the spatially modulated transmissions are designed for an $M = 30$ element uniform linear array with $d = \frac{\lambda_c}{2}$ inter-element spacing thus the *large array* approximation is invoked (Section 3.1.1.1). Each transmit chain is assumed to have independent waveform generation and identical transmit hardware, antennas, and matching networks. Assuming the array is at matched broadside, the impedance variation across space can be assumed low if the time-varying antenna factor focuses the energy near broadside (Section 3.2).

Recall from (3.35) that the complex-baseband, far-field time-varying beampattern $\tilde{g}(t, \theta, \varphi)$ when invoking both the narrowband and large array assumptions is the product between the approximate narrowband active antenna pattern $F_{\text{a}}(\theta, \varphi)$ and the time-varying antenna factor $g(t, \theta)$. Because $F_{\text{a}}(\theta, \varphi)$ only scales our emission in space, we consider just the time-varying antenna factor for Section 4.1.

4.1.2 Spatially Modulated Emission Structure

The time-varying array factor for spatial modulation maintains a coherent beam throughout the duration of the pulse duration T, thus the array pattern is a focused beam for any instant in time. The focused beam allows for precise control of the emitted energy in space without the need for iterative optimization methods. The energy of the beam can intuitively be allocated by simply scanning the beam over a desired region in space. This implementation is inherently spatially diverse thus benefits from an improved spatial resolution as discussed in Section 3.1.3.2.

Structure of the spatially modulated transmission is represented by two decoupled terms: the waveform $s(t)$ and the steering function $\phi_{\mathrm{s}}(t;\theta_{\mathrm{C}})$ which defines how the transmit beam is controlled with respect to the center look direction θ_{C}. Thus, the continuous waveform generated by the mth array channel is defined as a time-varying implementation of narrowband standard beamforming from (3.39) as

$$\begin{aligned} s_m(t) &= s(t)e^{-jm\phi_{\mathrm{s}}(t;\theta_{\mathrm{C}})} \\ &= \exp\Big(-j\cdot\big(\psi(t)-m\phi_{\mathrm{s}}(t;\theta_{\mathrm{C}})\big)\Big), \end{aligned} \tag{4.1}$$

where $u(t)$ is assumed to be constant over the pulse duration. Here, the waveform phase function $\psi(t)$ is realized via the PCFM waveform structure (Section 2.1.2.4) to achieve a continuous-phase. Recall that the phase function of the PCFM waveform was parameterized by a discrete sequence $\mathbf{x}_{\mathrm{w}} = [\alpha_0,\ldots,\alpha_{N_{\mathrm{p}}-1}]^T$. Likewise, define $\mathbf{x}_{\mathrm{s}} = [\varepsilon_0,\ldots,\varepsilon_{N_{\mathrm{p}}-1}]^T$ as the length N_{p} discrete sequence that parameterizes the spatial modulation phase $\phi_{\mathrm{s}}(t;\theta_{\mathrm{C}})$. This sequence is constructed via a set of $N_{\mathrm{p}}+1$ spatial angle offsets Δ_0, Δ_1, $\cdots$, $\Delta_{N_{\mathrm{p}}}$ relative to center direction θ_{C}. Thus, the nth spatial modulation parameter ε_n is defined as the different between the equivalent electrical angles of the spatial offset sequence,

$$\varepsilon_n = \frac{2\pi}{\lambda_{\mathrm{c}}}d\cdot\big(\sin(\theta_{\mathrm{C}}+\Delta_{n+1})-\sin(\theta_{\mathrm{C}}+\Delta_n)\big) \tag{4.2}$$

for $n\in\{0,\ldots,N_{\mathrm{p}}-1\}$, noting that each Δ_n can be positive or negative. It shall be assumed that the values of Δ_n are sufficiently small to avoid steering the beam near endfire. The spatial phase modulation can then be represented as a time-varying electrical angle (from (3.34)) via the PCFM formulation as

$$\phi_{\mathrm{s}}(t;\mathbf{x}_{\mathrm{s}},\theta_{\mathrm{C}}) = \sum_{n=1}^{N_{\mathrm{p}}}\varepsilon_n h_n(t) + \frac{2\pi}{\lambda_{\mathrm{c}}}d\sin(\theta_{\mathrm{C}}+\Delta_0), \tag{4.3}$$

for $t\in[0,T]$, where $h_n(t)$ is the PCFM phase function from (2.47) and $\frac{2\pi}{\lambda_{\mathrm{c}}}d\sin(\theta_{\mathrm{C}}+\Delta_0)$ is the initial phase offset to steer toward $\theta_{\mathrm{C}}+\Delta_0$. The sequence of spatial phase changes from (4.2) are collected

in the $N_\mathrm{p} \times 1$ spatial modulation code vector $\mathbf{x}_\mathrm{s} = [\varepsilon_1, \varepsilon_2, \ldots, \varepsilon_{N_\mathrm{p}}]^T$ that defines the fast-time spatial modulation.

Combining the spatial modulation signal $\phi_\mathrm{s}(t; \mathbf{x}_\mathrm{s}, \theta_\mathrm{C})$ with the waveform PCFM implemented waveform phase function $\psi(t; \mathbf{x}_\mathrm{w})$, the waveform generated by the mth antenna element is expressed as

$$\begin{aligned} s_m(t; \mathbf{x}_\mathrm{w}, \mathbf{x}_\mathrm{s}, \theta_\mathrm{C}) &= \exp\Big(j \cdot \big(\psi(t; \mathbf{x}_\mathrm{w}) - m\phi_\mathrm{s}(t; \mathbf{x}_\mathrm{s}, \theta_\mathrm{C}) \big) \Big) \\ &= \exp\left(j \cdot \left(\sum_{n=1}^{N_\mathrm{p}} (\alpha_n - m\varepsilon_n) h_n(t) + \psi_{0,m} \right) \right) \end{aligned} \tag{4.4}$$

where

$$\psi_{0,m} = \psi_0 - m\frac{2\pi}{\lambda_\mathrm{c}} d \sin(\theta_\mathrm{C} + \Delta_0) \tag{4.5}$$

is the initial phase of the mth waveform. In the case of no spatial modulation, the set of spatial offsets are $\Delta_0 = \Delta_1 = \cdots = \Delta_{N_\mathrm{p}} = 0$, such that the resulting N_p phase changes are likewise $\varepsilon_0 = \varepsilon_1 = \cdots = \varepsilon_{N_\mathrm{p}-1} = 0$. As a result, (4.3) simplifies to $\phi_\mathrm{s}(\theta_\mathrm{C}) = \frac{2\pi}{\lambda_\mathrm{c}} d \sin\theta_\mathrm{C}$, which is simply the electrical angle from (3.34) needed to steer a stationary beam in the direction of spatial angle θ_C, thus realizing standard beamforming.

Recall from Section 2.1.2.4 that the code values α_n are equivalent to the instantaneous frequencies given the form of the PCFM basis function from (2.47). Thus by observing (4.4), the code values of the spatially modulated waveforms are controlled by both the base waveform $s(t; \mathbf{x}_\mathrm{w})$ and the spatial modulation $\phi_\mathrm{s}(t; \mathbf{x}_\mathrm{s}, \theta_\mathrm{C})$, where the nth code value of the mth waveform is $\alpha_n - m\varepsilon_n$. Therefore, it is to be expected that the inclusion of the spatially-modulated structure will alter the spectral response of each waveform $s_m(t)$. Because the spatial modulation code ε_n is multiplied by $m \in \{-\frac{M-1}{2}, \ldots, \frac{M-1}{2}\}$, the spectral deviation is exaggerated at the ends of the array. However, it is shown that the waveform code vector $\mathbf{x}_\mathrm{w}$ and the spatial modulation code vector $\mathbf{x}_\mathrm{s}$ can be designed together to limit the spectral responses from shifting out of the bandwidth of the base radar waveform $s(t)$.

4.1.3 Spatially Modulated Emission Evaluation

To evaluate the physical emission structure described in Section 4.1.2, a length $N_p = 200$ waveform parameter vector $\mathbf{x}_w$ is considered to produce a PCFM approximation[2] to an up-chirped, linear frequency modulated waveform (LFM) of analytical time-bandwidth of $B_a T = 200$. The array is comprised of $M = 30$ antenna elements arranged in a ULA configuration with element spacing $d = \frac{\lambda_c}{2}$.

Four different spatial modulation vectors $\mathbf{x}_s$ are generated to form four different time-varying array factors all centered about $\theta_C = 0°$. Case 1 is implemented as standard beamforming to serve as a baseline case for comparison. Case 2 is a linearly steered spatially modulated transmission beginning at $\sin\theta = -0.0667$ and ending at $\sin\theta = 0.0667$. The angles $\sin\theta = \pm 0.0667$ correspond to the first null locations of the $M = 30$ beampattern when pointed towards $\theta_C = 0°$. The case 3 transmission scans linearly beginning and ending at the second null locations, $\sin\theta = \pm 0.1333$. The final case 4 time-varying array factor implements a half-cycle sinusoidal scan beginning and ending at the first null locations.

Figure 4.1 shows the squared-magnitude of the time-varying array factor $|g(t,\theta)|^2$ (in dB) for all four spatial modulation cases as a function of normalized time t/T and spatial angle $\sin\theta$. The identifying characteristic of the spatial modulation mode is apparent as the beams in all four cases remain coherent throughout the pulse duration. Observing the spatial beampattern of each case at a cut of any instant in time would have the equivalent form of an $M = 30$ element beampattern with rectangular weighting (steered toward a look direction).

Averaging the energy of the time-varying array factor over the pulse duration T produces the aggregate beampattern from (3.21) shown in Figure 4.2 for all four cases. The beampatterns are normalized such that the maximum possible value $A(\theta)$ can assume is 0 dB. This maximum is achieved by the standard beamforming case (blue) at $A(\theta_C)\,(\text{dB}) = 0\,\text{dB}$ due to the "staring" property of standard beamforming that achieves maximum energy toward θ_C. For cases 2 – 4, the

[2]The rectangular filter $w_p(t)$ in the PCFM implementation amounts to a piecewise linear phase function $\psi(t;\mathbf{x}_w)$ thus cannot fully express the up-chirped LFM phase function from (2.35). However, the piecewise linear approximation produces minimal distortion as compared to the ideal waveform from (2.36).

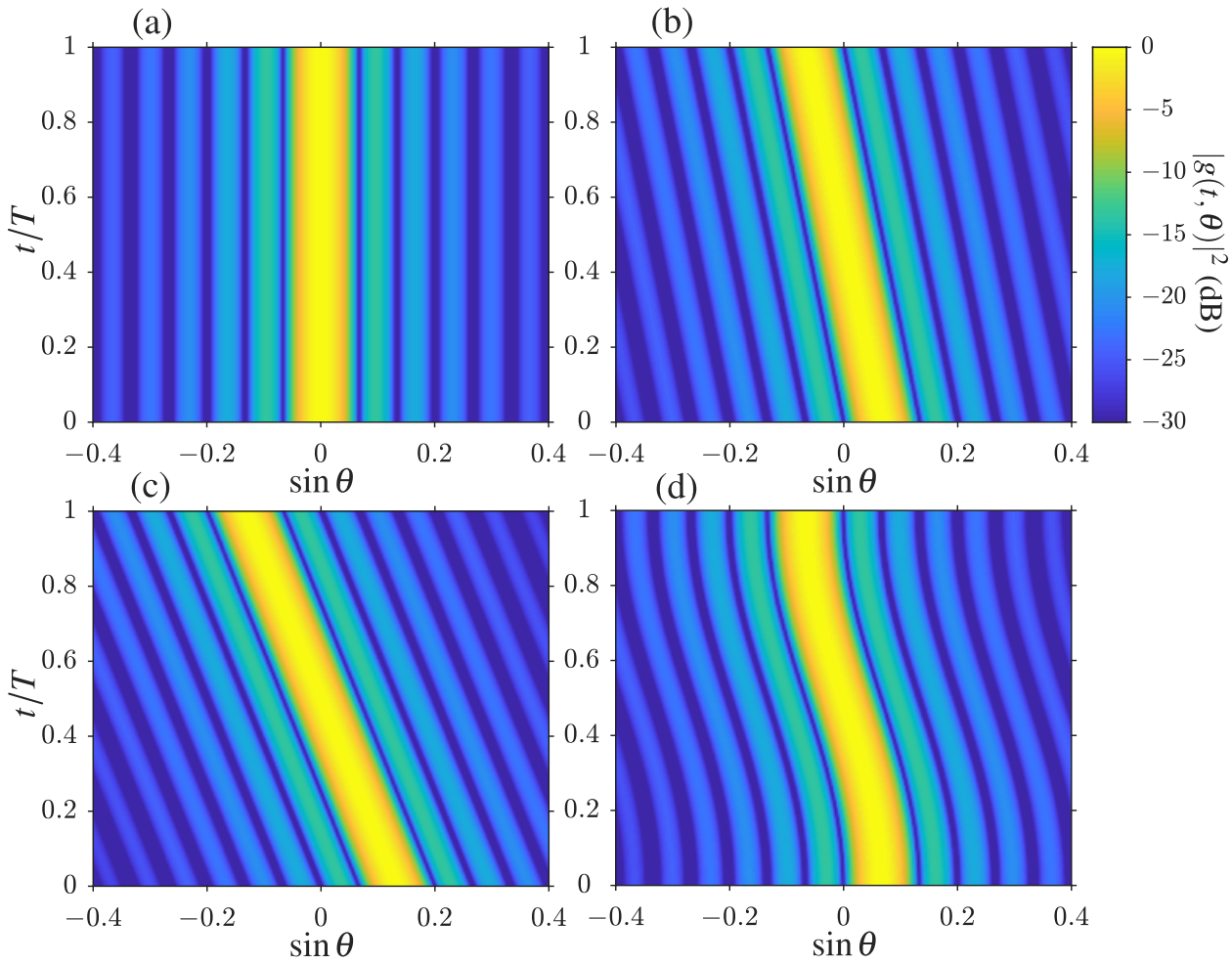

Figure 4.1: Time-varying antenna factor $|g(t,\theta)|^2$ (in dB) for (a) standard beamforming (case 1), (b) null-to-null linear spatial modulation (case 2), (c) second null-to-second null linear spatial modulation (case 3), and (d) null-to-null half-cycle sinusoidal spatial modulation (case 4).

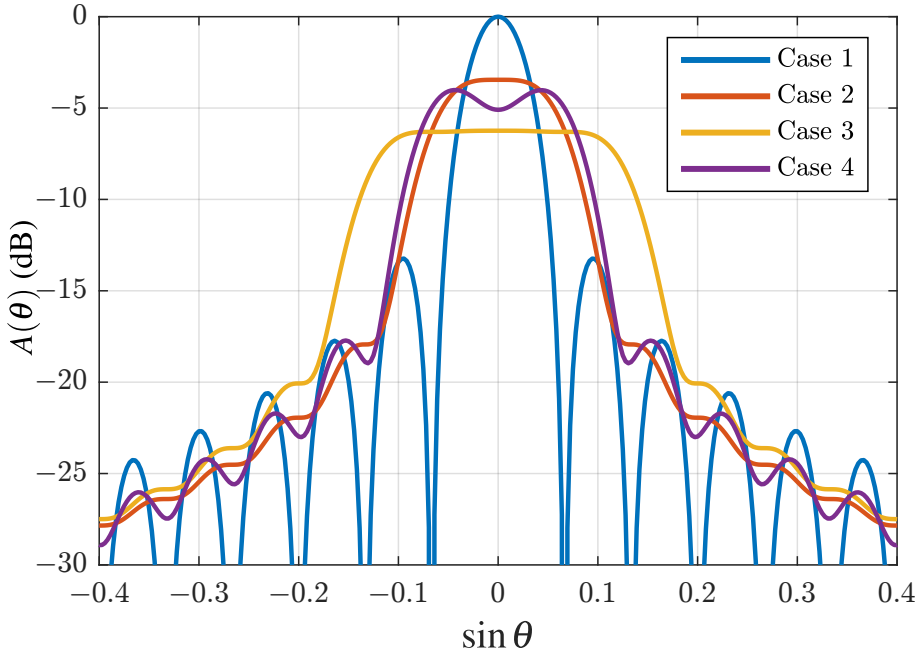

Figure 4.2: Aggregate beampattern $A(\theta)$ (in dB) from (3.21) for (a) standard beamforming (case 1), (b) null-to-null linear spatial modulation (case 2), (c) second null-to-second null linear spatial modulation (case 3), and (d) null-to-null half-cycle sinusoidal spatial modulation (case 4).

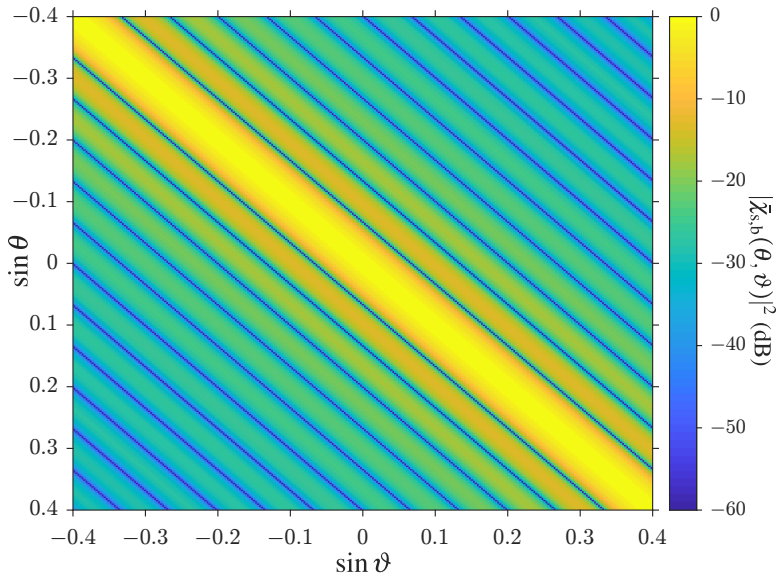

Figure 4.3: Beam factor $|\bar{\chi}_{s,b}(\theta,\vartheta)|^2$ from (3.60) (in dB) for $M = 30$ element ULA with $d = \frac{\lambda}{2}$ spacing.

energy in spread in space thus reducing the aggregate beampattern below 0 dB. The first null to first null linear steering emission (case 2) has the least loss at the center look direction for the remaining three cases with $A(\theta_C)$ (dB) = −3.45 dB. Case 4 resulted in a loss of $A(\theta_C)$ (dB) = −5.09 dB, however aggregate beam pattern increases in transmitted power on either side of θ_C due to the sinusoidal spatial modulation structure. Finally, case 3 had the most significant loss at $A(\theta_C)$ (dB) = −6.25 dB however has the most spatial coverage due to the second null to second null spatially modulated sweep.

Figure 4.3 displays the *beam factor* $|\bar{\chi}_{s,b}(\theta,\vartheta)|^2$ (in dB) from (3.60) versus spatial angle $\sin\theta$ and receiver beamformed angle $\sin\vartheta$ for the $M = 30$ element ULA. Recall from Section 3.1.3.2 that the beam factor is completely independent of the emission thus remains constant over all four transmission cases. Figure 4.4 shows the $\tau = 0$ cut of the *diversity factor* $|\bar{\chi}_{s,d}(\tau,\theta,\vartheta)|^2$ from (3.61) for all four spatially-modulated time-varying array factors. Note that the standard beamforming case in Figure 4.4(a) does not contribute to the spatial resolution for this spatially-dependent matched filter estimator (see Section 3.1.3.2 for more details). Cases 2 thru 4 in Figures 4.4(b,c,d) do provide spatial diversity thus will contribute to improving the spatial resolution for the illuminated region.

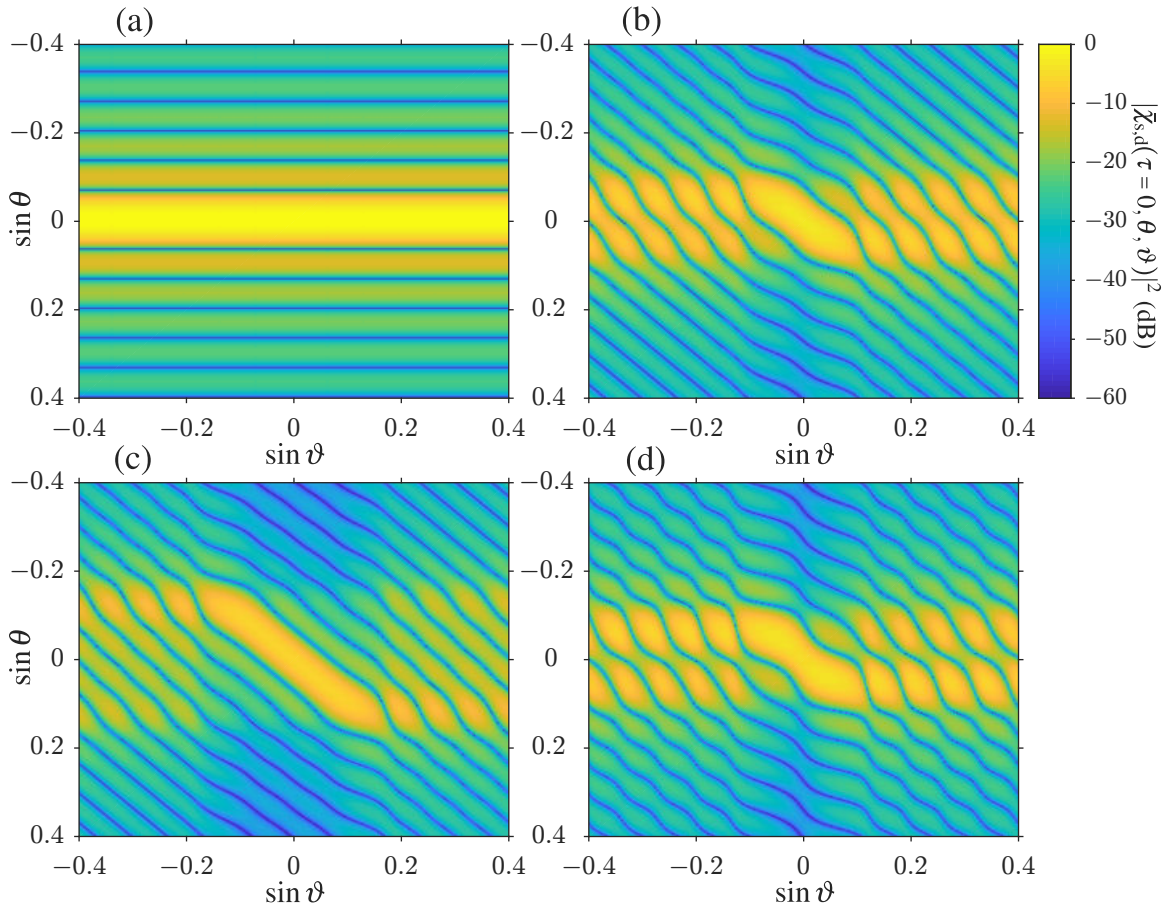

Figure 4.4: Zero delay $\tau = 0$ cut of the diversity factor $|\bar{\chi}_{s,d}(\tau = 0, \theta, \vartheta)|^2$ (in dB) from (3.61) for (a) standard beamforming (case 1), (b) null-to-null linear spatial modulation (case 2), (c) second null-to-second null linear spatial modulation (case 3), and (d) null-to-null half-cycle sinusoidal spatial modulation (case 4).

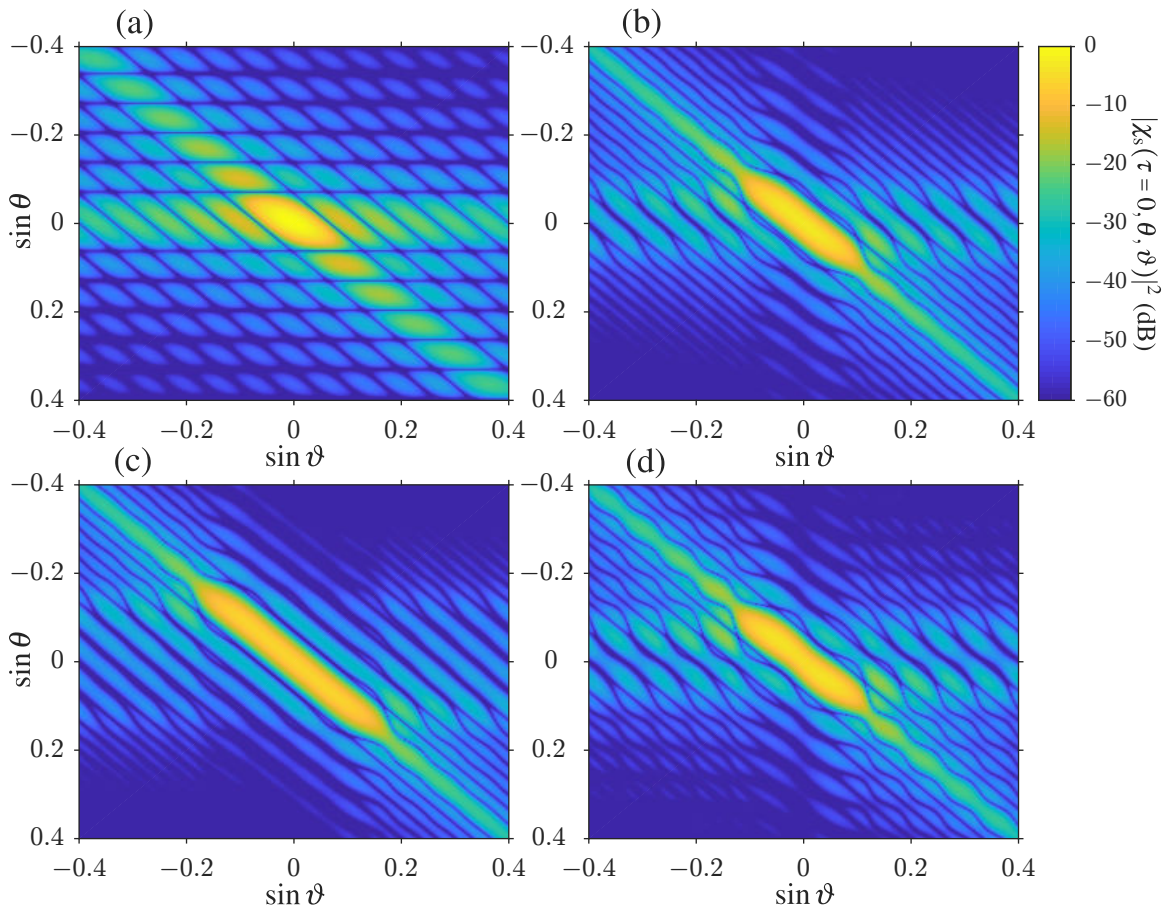

Figure 4.5: Zero delay $\tau = 0$ cut of the angle-delay ambiguity function $|\chi_s(\tau = 0, \theta, \vartheta)|^2$ (in dB) from (3.55) for (a) standard beamforming (case 1), (b) null-to-null linear spatial modulation (case 2), (c) second null-to-second null linear spatial modulation (case 3), and (d) null-to-null half-cycle sinusoidal spatial modulation (case 4).

The product of the beam factor $\bar{\chi}_{s,b}(\theta, \vartheta)$ and the diversity factor $\bar{\chi}_{s,d}(\tau, \theta, \vartheta)$ produces the angle-delay ambiguity function $\chi_s(\tau, \theta, \vartheta)$ from (3.55) which gives the theoretical spatially-dependent matched filter response for a unit amplitude scatterer in the absence of noise at location $(\tau = 0, \theta)$ when receive beamforming toward ϑ. Figure 4.5 displays the $\tau = 0$ cut of the angle-delay ambiguity function $|\chi_s(\tau, \theta, \vartheta)|^2$ which displays the cross-correlation of the spatially-diverse transmission while incorporating receive beamforming. The extent of the center lobe is elongated with relation to the the allocation of energy in space. In fact, the values on this diagonal $|\chi_s(\tau = 0, \theta, \vartheta = \theta)|^2$ are equivalent to the aggregate beapatten for the case when $A(\theta)$ is normalized such that 0 dB is the maximum for standard beamforming.

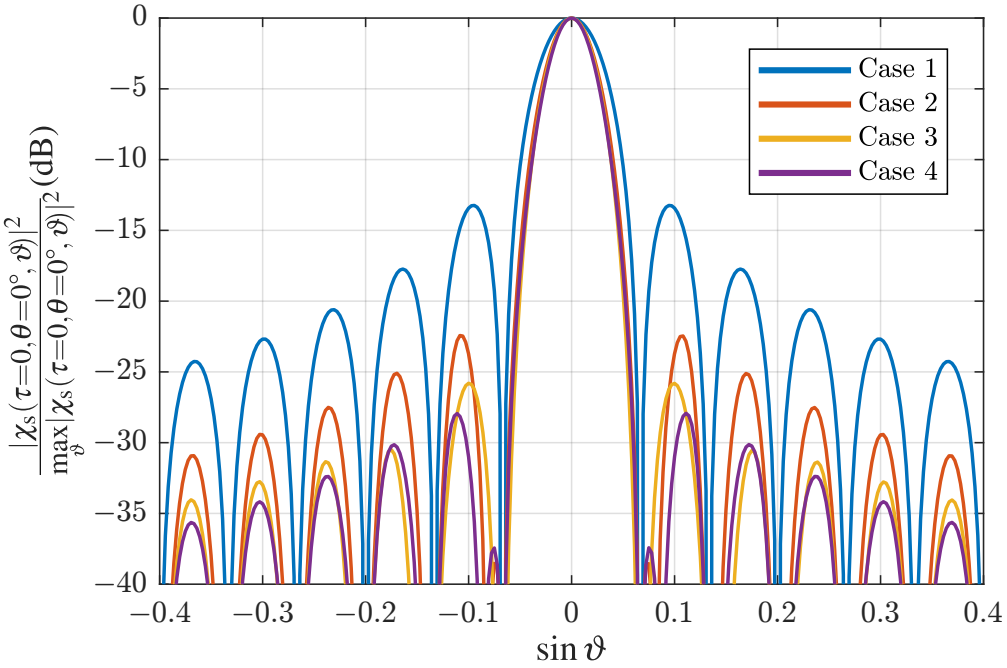

Figure 4.6: Peak-normalized $\tau = 0$ and $\theta = 0°$ cut of the angle-delay ambiguity function $|\chi_s(\tau = 0, \theta = 0°, \vartheta)|^2$ (in dB) from (3.55) for (a) standard beamforming (case 1), (b) null-to-null linear spatial modulation (case 2), (c) second null-to-second null linear spatial modulation (case 3), and (d) null-to-null half-cycle sinusoidal spatial modulation (case 4).

Figure 4.6 shows the peak-normalized, $\tau = 0$ and $\theta = \theta_C = 0°$ cut of $|\chi_s(\tau, \theta, \vartheta)|^2$ versus receive beam angle $\sin\vartheta$. The sidelobe response of this beampattern illustrates how scatterering from a target at $\theta = \theta_C = 0°$ responds when received beamformed and matched filtered over all $\sin\vartheta$. The sidelobe response may mask lower power scattering coming from directions off θ_c thus it is advantageous to reduce the sidelobe energy when possible. The first sidelobe of the standard beamforming scenario (case 1) is −13.2 dB down from the peak response which is the typical sidelobe response when using a rectangular receive window. All of the spatial modulation cases reduce the sidelobe response relative to the baseline standard beamforming case: case 2 reduces the first sidelobe to a level of −22.4 dB (an improvement of 9.1 dB), case 3 reduces the first sidelobe to −25.9 dB (an improvement of 12.7 dB), and case 4 had the most improvement at 14.7 dB with a sidelobe level of −27.9 dB.

The spatial modulation scenarios (cases 2 – 4) also result in a spatial resolution enhancement of the theoretical scatterer as compared to the standard beamforming case as theorized in the

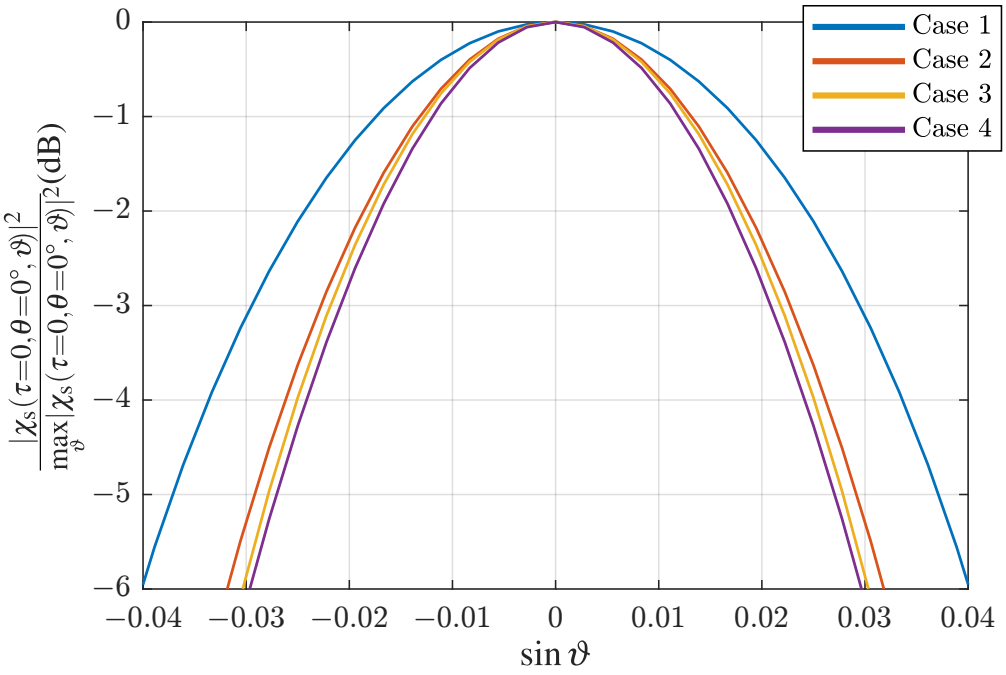

Figure 4.7: Peak-normalized $\tau = 0$ and $\theta = 0°$ cut of the angle-delay ambiguity function $|\chi_s(\tau = 0, \theta = 0°, \vartheta)|^2$ (in dB) from (3.55) (zoomed-in) for (a) standard beamforming (case 1), (b) null-to-null linear spatial modulation (case 2), (c) second null-to-second null linear spatial modulation (case 3), and (d) null-to-null half-cycle sinusoidal spatial modulation (case 4).

diversity factor (Figure 4.4). Figure 4.7 shows a zoomed-in look at the peak-normalized, $\tau = 0$ and $\theta = \theta_C = 0°$ cut of $|\chi_s(\tau, \theta, \vartheta)|^2$ versus receive beam angle $\sin\vartheta$ as was shown in Figure 4.6. For $M = 30$ element with $d = \frac{\lambda_c}{2}$, the 3 dB resolution beamwidth for the standard beamforming case is calculated using (3.59) as $\Delta\bar{u}_{3dB} = 0.0594$ in $\bar{u} = \sin\theta$ space [87]. The 3 dB resolution beamwidth for case 2 has a $\bar{u}$-space resolution of $\Delta\bar{u}_{3dB} = 0.0454$ which corresponds to a $1 - 0.0454/0.0594 = 23.6\%$ spatial resolution improvement. The 3 dB beamwidth for case 3 has a resolution of $\Delta\bar{u}_{3dB} = 0.0436$ (26.6% resolution improvement). Finally, case 4 provides the best performing spatial resolution with a 29.6% spatial resolution enhancement corresponding to a half power beamwidth of $\Delta\bar{u} = 0.0418$. For comparison, the theoretical spatial resolution improvement calculate using the MIMO virtual array concept is $\Delta\bar{u} = 0.0420$ from Section 3.1.3.2, thus the half-cycle sinusoid actually improves upon the spatial resolution for the orthogonal waveform virtual array derivation while maintaining a directive aggregate beampattern.

Figure 4.8 shows the $\theta = 0°$ cut of the angle-delay ambiguity diagram $|\chi_s(\tau, \theta = 0°, \vartheta)|^2$ for

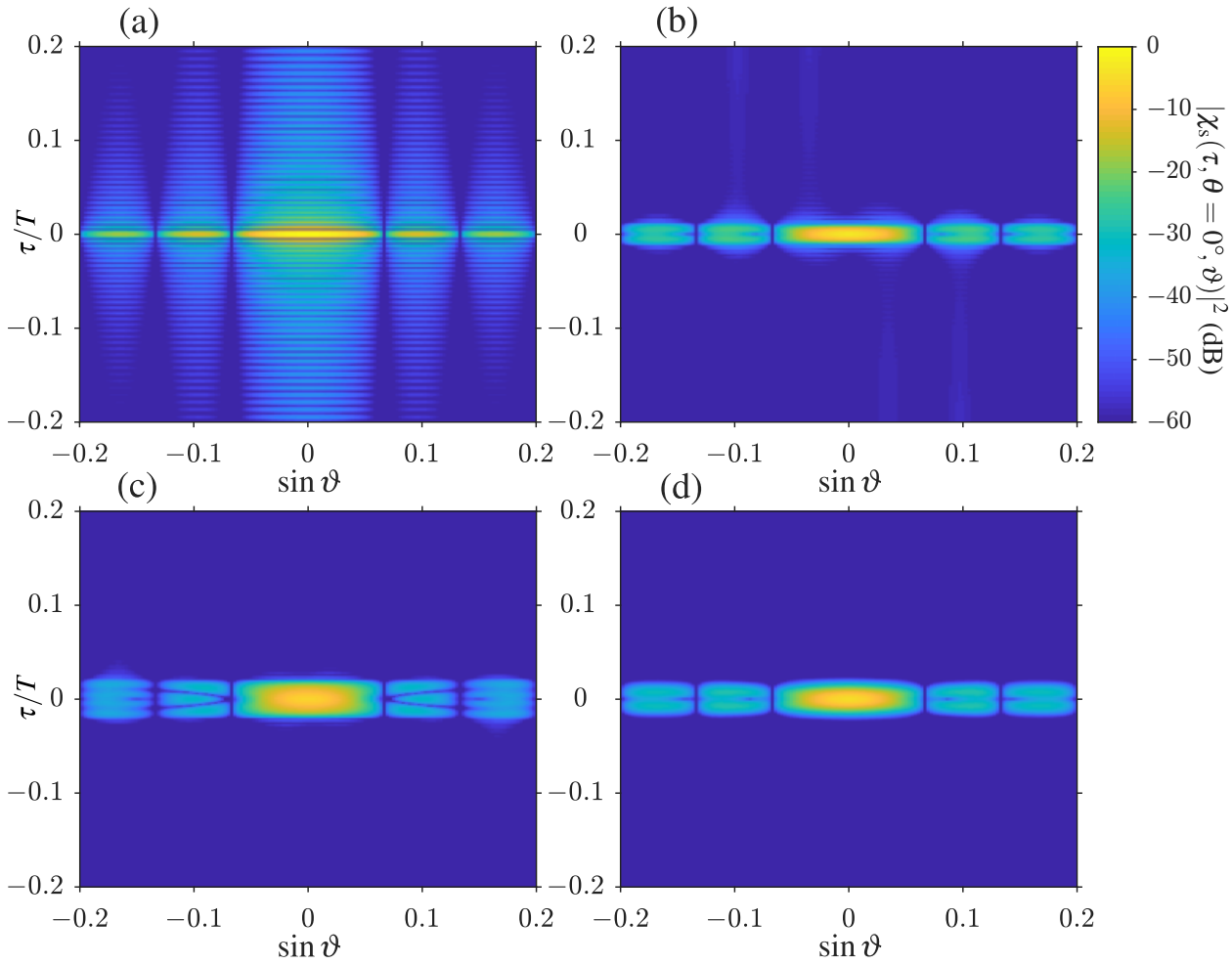

Figure 4.8: $\theta = 0°$ cut of the angle-delay ambiguity function $|\chi_s(\tau, \theta = 0°, \vartheta)|^2$ (in dB) from (3.55) for (a) standard beamforming (case 1), (b) null-to-null linear spatial modulation (case 2), (c) second null-to-second null linear spatial modulation (case 3), and (d) null-to-null half-cycle sinusoidal spatial modulation (case 4).

all four transmission cases which shows the theoretical range-angle response of a scatterer located at $(\tau = 0, \theta = 0°)$. Figure 4.7 displays the typical range sidelobe response of an LFM (see Figure 2.15). Interestingly, the time-varying array factor for cases 2 – 4 result in a much lower sidelobe response. The reduction of the sidelobes can be attributed to an effective time envelope tapering, not applied at the waveform level, but caused from steering the beam in space thus resulting in a corresponding range resolution degradation and SNR loss. Figure 4.9 show the $\vartheta = 0°$ and $\theta = 0°$ cut of the angle-delay ambiguity function ($\vartheta = 0°$ cut of Figure 4.8) which shows the range response of a theoretical scatterer located at $(\tau = 0, \theta = 0°)$. The SNR loss (peak loss) for each case is exactly equal to that of the aggregate beampatterns shown in Figure 4.2 in the direction $\sin\theta = 0$ which coincides with spatial diversity beam loss from spreading energy in space. Note that this sidelobe reduction is a particular attribute of using an LFM as the base radar waveform $s(t)$ due to its time-frequency relationship. Though that is not to say that this could not be accomplished with a different base waveform and corresponding spatial modulation.

Figure 4.10 shows the power spectrum of the base LFM radar waveform $|S(f)|^2$ versus normalized frequency f/B_a. Figures 4.11 and 4.12 show the spectral responses of the waveforms associated with each edge element as well as a center element[3] for the first null-to-first null and second null-to-second null spatially modulated scenarios (cases 2 and 3), respectively. Note how spectral content of the edge waveforms deviate from that of the base radar waveform (Figure 4.10) due to the inclusion of the spatial modulation term $m\varepsilon_n$ in the PCFM formulation from (4.4). The center element stays relatively similar to the base radar spectral shape (if there were an odd number of elements it would be exactly the base radar shape). Not surprisingly, the case 3 beam steering scenario produces a larger deviation in the spectral content as the beam is steering over a larger spatial swath during the pulse thus is traveling "faster" than in case 2. This "faster" beam amounts to a "faster" phase change (i.e. frequency) thus results in a larger frequency deviation.

Figure 4.13 shows the spectra of the edge and center elements for the half-cycle sinusoidal beam steering scenario (case 4). All three spectrums remain within the bandwidth of the base radar

[3]Note that there is no center element as the array contains an even number of antennas. Instead, *one of* the center elements is shown as there is little difference between the two center elements.

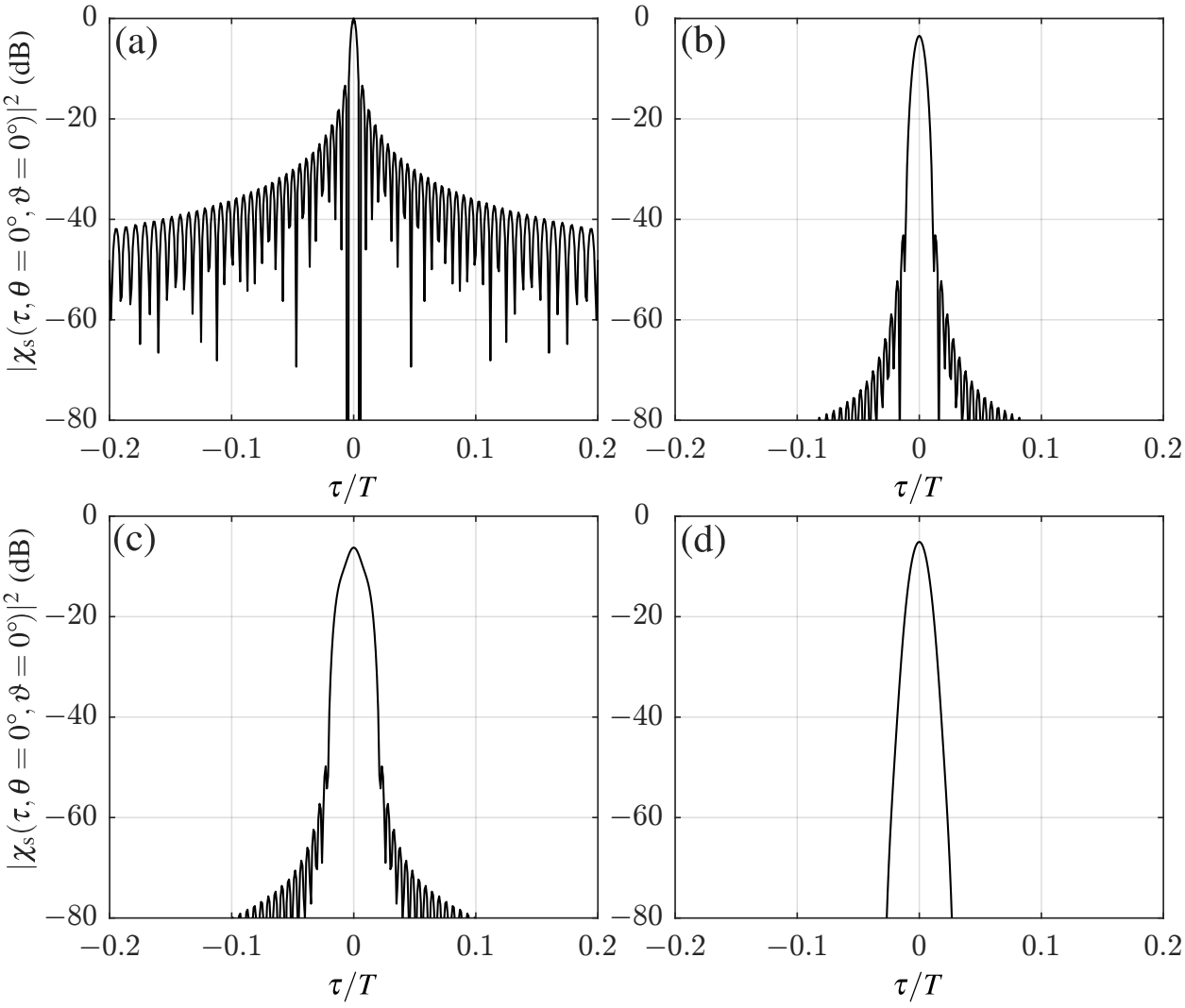

Figure 4.9: $\theta = 0°$ and $\vartheta = 0°$ cut of the angle-delay ambiguity function $|\chi_s(\tau, \theta = 0°, \vartheta = 0°)|^2$ (in dB) from (3.55) for (a) standard beamforming (case 1), (b) null-to-null linear spatial modulation (case 2), (c) second null-to-second null linear spatial modulation (case 3), and (d) null-to-null half-cycle sinusoidal spatial modulation (case 4).

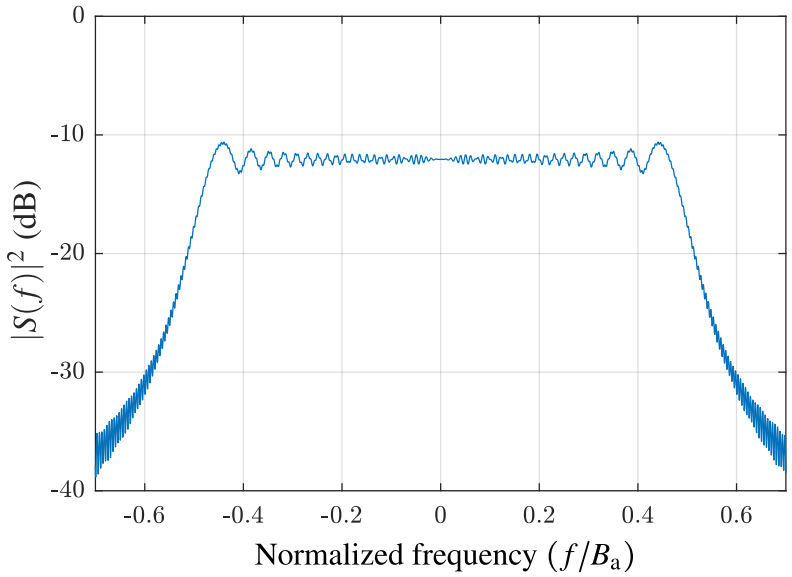

Figure 4.10: Power spectrum of base radar waveform $|S(f)|^2$ versus normalized frequency (f/B).

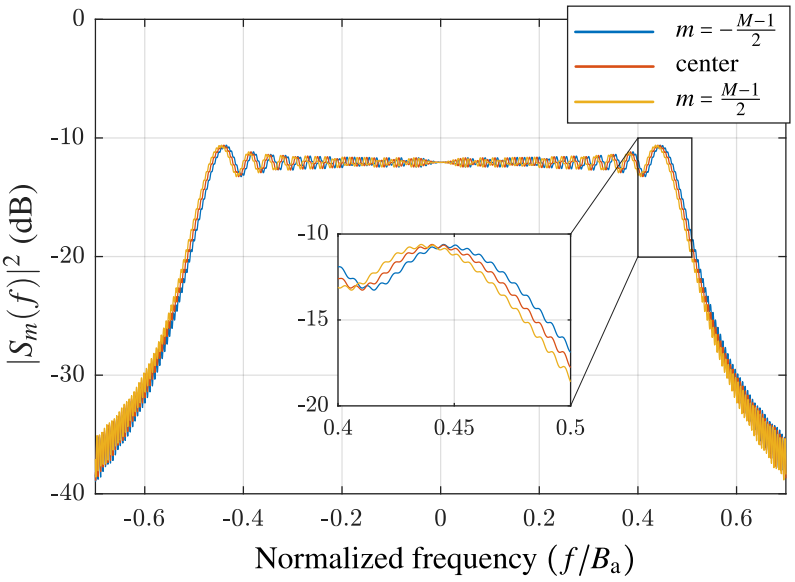

Figure 4.11: Power spectra $|S_m(f)|^2$ for both edge elements and a center element for Case 2 versus normalized frequency (f/B_a).

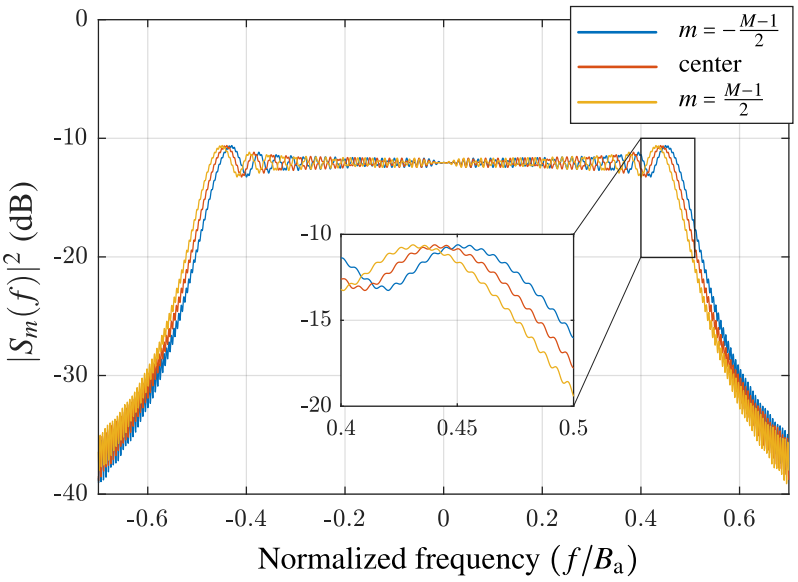

Figure 4.12: Power spectra $|S_m(f)|^2$ for both edge elements and a center element for Case 3 versus normalized frequency (f/B_a).

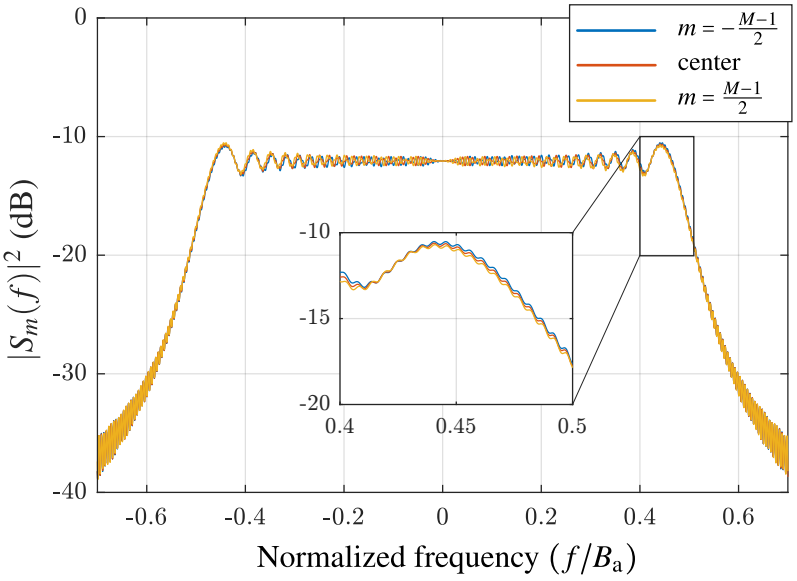

Figure 4.13: Power spectra $|S_m(f)|^2$ for both edge elements and a center element for Case 4 versus normalized frequency (f/B_a).

spectral response. Therefore, it can be inferred that the entirety of waveform spectral responses are also contained with the base radar spectral response. This contained response is a result of the combination of the waveform code vector $\mathbf{x}_{\mathrm{w}}$ and the spatial modulation code vector $\mathbf{x}_{\mathrm{s}}$. The waveform code vector in this case is the PCFM-approximated up-chirped LFM thus the edges of the spectral response (high and low frequencies) occur at the beginning and ends of the pulse. Observing the time-varying array factor for this case in Figure 4.1(d), there is little beamsteering at the beginning and ends of the pulse thus the spatial modulation code ε_n at these points is small and does not contribute much to the overall instantaneous frequency of the waveforms. The spatial modulation steers the fastest in the middle of the pulse where the frequency content of the LFM is near the center frequency, thus any frequency deviation that occurs does not extend outside the bandwidth of the base radar waveform spectral response.

4.1.4 Summary

In Section 4.1, a practical MIMO emission framework is presented denoted spatial modulation that steers a coherent beam over a region in space. The PCFM framework is expanded to for implementation of a spatial coded structure that allows for precise control over the beam location and thus the spatial distribution of energy in space. The angle-delay ambiguity function for four transmit scenarios was analyzed. The three spatially-diverse transmission scenerios were shown to improve the spatial resolution with respect to the standard beamforming control scenario. The two linear spatially-modulated emissions were close to achieving the theoretical virtual array resolution (for $\theta = 0°$) while the half-cycle sinusoid actually achieves a resolution below that of the virtual array.

4.2 Wideband Spatially-Diverse Frequency Modulated Emission Design with Space-Frequency Nulling

Within the broader context of waveform diversity [1–4], the design of spatially-diverse radar emissions is typically approached from a narrowband perspective where the steering vectors of the array are assumed to be constant throughout the bandwidth of the emission (the narrowband assumption) [17, 118, 119]. The optimal power allocation in space for traditional wideband emissions has also been investigated [120, 121]. Likewise in [89], the wideband MIMO beampattern was optimized using the relationship between the beampattern and the cross-spectral density matrix. In [122] the waveform matrix was obtained by first determining the optimal waveform spectra (in a least-squares sense) that matches a desired space-frequency beampattern and then optimizing the waveform matrix in the time-domain given a PAPR constraint.

Here an iterative wideband spatially-diverse waveform design scheme is presented where the spectrum in certain transmission angles, denoted as "beamlets", are shaped according to a predefined spectral window that includes a sufficient portion of the spectral roll-off region [90,91]. In so doing, physical waveforms can be realized in a discretized fashion that a) are constant amplitude and spectrally well-contained so as to be robust to the distortion induced by the transmitter power amplifier (Section 2.2.2), b) minimize the reactive power otherwise generated by omnidirectional wideband MIMO emissions (Section 4.2.3), and c) can be readily implemented with high fidelity via the polyphase-coded FM (PCFM) framework (Section 2.1.2.4) [38].

Space-frequency nulling is incorporated into the emission design to facilitate coexistence with other spectrum users in the vicinity of the radar. The space-frequency beampattern matching problem using the alternating projections algorithm [123–128]) cannot produce nulls of sufficient depth, thus an additional stage is needed to enforce null constraints. To do so, the reiterative uniform weight optimization (RUWO) method [129] is included within the larger emission design

A portion of the text and figures in Section 4.2 are taken from "Wideband MIMO Frequency-Modulated Emission Design With Space-Frequency Nulling" by McCormick et al. printed in *IEEE Journal of Selected Topics in Signal Processing* in March 2017. ©2011 IEEE

scheme. Analysis of the overall design process is presented to evaluate emission correlation, calculation of the *fractional reactive power* (FRP), and convergence behavior.

The proposed design scheme leverages the body of work on phase retrieval algorithms (e.g. [123–128]) which typically applied to cost functions that do not have closed form solutions but can be solved via an iterative transform method generally referred to as alternating projections. Such methods have been shown to be effective to synthesize polyphase codes via shaping of the power spectral density (PSD) [128]. Similar methods have likewise been recently shown to facilitate the optimization of frequency modulated (FM) waveforms [60, 130]. Typically, signal synthesis algorithms of this type possess sets of constraints in two domains referred to as the *object* and *image* domains. A solution is found by alternating between the two domains, enforcing the constraints during each stage. For this joint space/frequency formulation, the object domain is element-time, with a constant amplitude constraint on the waveform generated by each of the M array elements. The image domain is space-frequency, with the time-varying array factor constrained to particular spatial directions (the "beamlets") with predefined spectral windows.

The construction of wideband, wide scan angle arrays leverages low scan impedance variation and wide achievable bandwidths from closely spaced antennas and wide angle impedance matching (WAIM) via dielectric sheets [94, 96, 131–133]. Standard design guidelines require an element spacing that excludes the appearance of grating lobes for all operating frequencies over extreme scan angles to prevent rapid impedance variation that might occur [98]. In fact, in [134] it is shown that array blindness may occur at angles nearer to broadside than an angle at which a grating lobe occurs, thus the element spacing must be a few percent *less* than half-wavelength over all operating frequencies to limit this effect [133].

The element spacing must be close to half-wavelength according to the highest operating frequency (smallest wavelength), therefore the spacing according to the *lowest* frequency in the wideband transmission is highly oversampled. For example, assume an array is spaced half-wavelength according to the largest frequency. For an array operating over an octave bandwidth (highest frequency is twice the lowest frequency), the array is spaced at a quarter-wavelength with

respect to the lowest frequency. In Section 3.2.2, it was shown that spacing an array less than half-wavelength makes the array susceptible to placing energy within the invisible space which can be reflected at the terminals of the element matching networks back into the transmit array when the array is matched for broadside transmission [18, 42, 43, 135]. Thus for wideband transmission, the frequency dependence of the emission must be consider to avoid placing energy in this region to maximize efficiency of the array. The *fractional reactive power* (FRP) metric (defined in (3.80)) is redefined for wideband transmission and used to measure the percentage of energy imparted to this region. It is shown that the proposed emission design effectively mitigates the energy contained in this region ensuring the spatial angles of the beamlets reside within the visible space.

To demonstrate the utility of this approach three wideband emission scenarios are considered: 1) three spatially separated narrow beams (e.g. to track multiple targets in different spatial directions simultaneously), 2) a near omnidirectional wide beam comprised of many closely-spaced beamlets (e.g. for SAR applications [19]), and 3) a moderately wide beam concurrent with a narrow secondary beam in a different spatial direction (e.g. for multi-mode operation [136]). Each case includes one to two space-frequency nulls that encompass large regions in space-frequency. For each scenario, the frequency content of the designed emission and spatial beampattern are presented along with convergence plots, correlation analysis, and determination of the FRP.

4.2.1 Assumptions and Restrictions

Again is it assumed that the waveforms that are designed in Section 4.2 are implemented in a high power transmitting mode thus require the use of a high power amplifier operating in saturation. In Section 2.2.2 it was shown that spectrally contained, constant amplitude (constant $u(t)$) waveforms can be modeled as being undistorted by the transmitted chain, thus it is assumed that the forward voltage $V_m^+(f)\forall m$ is approximately a scaled version of the ideal passband waveforms $S_{\text{pb},m}(f)\forall m$.

When considering the frequency-dependent element spacing of a wideband transmission, the 98% bandwidth definition $B_{98\%}$ from (2.53) is attractive as it limits the amount of energy in the roll-off region to a small percentage of the total. The array spacing is placed to be $\frac{\lambda}{2}$ based on

the highest frequency content of the bandwidth, thus the energy beyond this "highest frequency" is 1% of the total and is considered negligible. At these high of frequencies, the array appears undersampled thus is associated with grating lobes which can produce blind angles [41], thus it is standard practice to avoid designing arrays where a portion of the band appears undersampled in space [133]. Likewise, the energy content below the lowest frequency is 1% of the total thus is also considered negligible. Therefore the frequency range containing the significant portion energy (i.e. the bandwidth) is clearly defined for analyzing the energy in invisible space.

The array is assumed to be comprised of $M = 30$ elements that are spaced at half-wavelength according to the highest frequency in the emission bandwidth which is assumed to have a fractional bandwidth of $[\%\mathrm{BW}]_{98\%} = 0.4$ from (2.57). Thus at the lowest frequency in the 98% bandwidth, the array appears to be at 0.32 wavelengths which exposes the array to placing energy within the invisible space (or reactive region). The lowest frequency (largest wavelength) in the band results in the "smallest" array length (in wavelengths) of $30(0.32\lambda) = 9.6\lambda$. Recall that the array must be greater than 5λ to invoke the large array assumption [85] which can separate the far-field time-varying beampattern $\tilde{g}_{\mathrm{pb}}(t,\theta,\varphi)$ into two components: the approximate active element pattern $F_{\mathrm{a}}(t,\theta,\varphi)$, and the time-varying array factor $g_{\mathrm{pb}}(t,\theta)$. Thus, to analyze the wideband array the true-delay emission models with the large-array assumption from (3.24) – (3.27) are implemented, which achieves an accurate assessment of the far-field emission.

In Section 4.2, no measured antenna patterns or frequency-dependent scattering matrices are applied during the analysis of the wideband array. Thus only practical constraints are applied in this *system considerate* design method. In Section 3.2.2, it was shown that the *fractional reative power* (FRP) closely matches that of the total integrated power reflection coefficient $|\Gamma^{\mathrm{a}}|^2$ from (3.78) when the spatially oversampled dipole array was matched to broadside. Thus, it is assumed that the array analyzed in Section 4.2 is matched over the entire visible space and the energy in the invisible space is completely reflected. As a precaution, the entirety of the array mainlobe (for all in-band frequencies) is constrained to be within the visible domain to limit energy placed within the invisible space. During analysis of the emission, the array pattern is assumed to be

isotropic over the band of the emission which may not be practical when applying a design using the proposed method to a physical array. It is assumed that the frequency-dependent approximate active element pattern $F(f,\theta,\varphi)$ and scattering matrix $S(f)$ are available during the design of the emission, thus the mathematical formulation is derived using these variables.

4.2.2 Wideband Array Analysis

Recall from (3.25) the form of the passband spectral content of the far-field time-varying beampattern $\tilde{G}_{\text{pb}}(f,\theta,\varphi)$ in terms of the spectral content of the time-varying beampattern $G_{\text{pb}}(f,\theta)$ is

$$\tilde{G}_{\text{pb}}(f,\theta,\varphi) = F_{\text{a}}(f,\theta,\varphi)G_{\text{pb}}(f,\theta). \tag{4.6}$$

For positive frequencies $(f > 0)$, the spectral content of the time-varying array factor $G_{\text{pb}}(f,\theta)$ from (3.18) can approximated as

$$G_{\text{pb}}(f,\theta) \approx \frac{1}{M\sqrt{2}} \sum_m S_m(f - f_{\text{c}}) e^{jm\phi(f,\theta)}, \tag{4.7}$$

where

$$\phi(f,\theta) = \frac{2\pi f}{c} d \sin\theta \tag{4.8}$$

is the frequency-dependent electrical angle (compare to the narrowband electrical angle from (3.34)). The positive frequency approximation from (4.7) holds as long as $|S_m(f)|^2 \approx 0$ for $f < -f_{\text{c}}$ for all m.

Define the element spacing d as half of wavelength λ_{E} corresponding to some frequency f_{E},

$$d = \frac{\lambda_{\text{E}}}{2} = \frac{c}{2f_{\text{E}}}. \tag{4.9}$$

Thus, the frequency-dependent electrical angle from (4.8) can be defined as

$$\phi(f,\theta) = \pi \frac{f}{f_{\mathrm{E}}} \sin\theta. \tag{4.10}$$

This form of the electrical is convenient for analyzing wideband arrays as it does not depend on an absolute element spacing d.

Using the 98% fractional bandwidth $[\%\mathrm{BW}]_{98\%}$ from (2.57) and element spacing d from (4.9), the form of the array narrowband assumption from (3.30) can be expressed as

$$1 >> B_{98\%}\Delta t_{\max} = [\%\mathrm{BW}]_{98\%} \frac{M-1}{2f_{\mathrm{E}}/f_{\mathrm{c}}}. \tag{4.11}$$

To indicate the extent of the wideband nature of the emission, the expression in (4.11) is defined as the metric

$$\Pi = [\%\mathrm{BW}]_{98\%} \frac{M-1}{2f_{\mathrm{E}}/f_{\mathrm{c}}}, \tag{4.12}$$

which we will refer to as the *wideband factor*. Thus, the number of array elements M, the frequency ratio $f_{\mathrm{E}}/f_{\mathrm{c}}$ and the fractional bandwidth $[\%\mathrm{BW}]_{98\%}$ are the three relative parameters that fully characterize a wideband ULA[4].

Now consider an $N \times M$ discretized complex-baseband waveform matrix $\mathbf{S}$ in which the columns correspond to discretized waveforms emitted by each of the M antenna elements for N the length of the discretized waveforms in the time-domain. Thus, the mth column of $\mathbf{S}$ is the $N \times 1$ discretized waveform vector $\mathbf{s}_m = \left[s_m[0],\ldots,s_m[N-1]\right]^T$ and $s_m[n]$ is the nth sample of the waveform corresponding to the mth antenna element for $n \in \{0,1,\ldots,N-1\}$ and $m \in \{-\frac{M-1}{2},\ldots,\frac{M-1}{2}\}$. The matrix can be vectorized into an $MN \times 1$ vector

$$\mathbf{s}_{\mathrm{v}} = \mathrm{vec}\{\mathbf{S}\}, \tag{4.13}$$

where $\mathrm{vec}\{\bullet\}$ is the vectorize operation that stacks the columns of a matrix (leftmost vector on top

[4]The 98% bandwidth is only one example of a bandwidth definition that could be used here.

and rightmost on bottom). To adequately represent these continuous waveforms in discrete form, it is necessary to "over-sample" (in time) with respect to some bandwidth measure so as to capture an adequate portion of the spectral roll-off (which is theoretically infinite due to the pulsed nature of the signal). The sampling rate using $B_{98\%}$ is defined as

$$f_{\mathrm{s}} = \bar{\kappa} B_{98\%}, \tag{4.14}$$

where $\bar{\kappa}$ is the over-sampling factor with respect to the 98% bandwidth chosen such that it captures an adequate portion of the spectral roll-off. The vector length N in this case can be defined using (4.14) as

$$N = f_{\mathrm{s}} T = \bar{\kappa} B_{98\%} T. \tag{4.15}$$

Define the $MN \times 1$ space-frequency steering vector as

$$\mathbf{t}(f,\theta) = \mathbf{v}(f,\theta) \otimes \mathbf{a}(f), \tag{4.16}$$

where $\otimes$ is the Kronecker product,

$$\mathbf{v}(f,\theta) = \begin{bmatrix} 1 & \exp(-j\phi(f,\theta)) & \cdots & \exp(-j\cdot(M-1)\phi(f,\theta)) \end{bmatrix}^T \tag{4.17}$$

is the $M \times 1$ frequency-dependent steering vector, and

$$\mathbf{a}(f) = \begin{bmatrix} 1 & \exp\left(j2\pi\frac{f-f_{\mathrm{c}}}{f_{\mathrm{s}}}\right) & \cdots & \exp\left(j2\pi\cdot(N-1)\frac{f-f_{\mathrm{c}}}{f_{\mathrm{s}}}\right) \end{bmatrix}^T \tag{4.18}$$

is the $N \times 1$ discrete-time Fourier transform (DTFT) vector as a function of frequency f. Because the waveforms are over-sampled relative to the bandwidth $B_{98\%}$, the passband emission $G_{\mathrm{pb}}(f,\theta)$ from (4.7) (for $f > 0$) can be well approximated as the inner-product

$$G_{\mathrm{pb}}(f,\theta) \approx \frac{1}{M\sqrt{2}} [\mathbf{t}(f,\theta)]^H \mathbf{s}_{\mathrm{V}}. \tag{4.19}$$

Discretizing the frequency spectrum into Q_{F} equally spaced points, define the discrete passband frequencies as

$$f_q = \frac{-f_{\mathrm{s}}}{2} + \frac{q}{Q_{\mathrm{F}}} f_{\mathrm{s}} + f_{\mathrm{c}} \tag{4.20}$$

for $q \in \{0, 1, \ldots, Q_{\mathrm{F}} - 1\}$. Thus, the DTFT vector (4.18) can be represented as the $N \times 1$ DFT vector associated at discretized passband frequency f_q as

$$\mathbf{a}(f_q) = \begin{bmatrix} 1 & \exp\left(j2\pi\left(-\frac{1}{2} + \frac{q}{Q_{\mathrm{F}}}\right)\right) & \cdots & \exp\left(j2\pi(N-1)\left(-\frac{1}{2} + \frac{q}{Q_{\mathrm{F}}}\right)\right) \end{bmatrix}^T. \tag{4.21}$$

Define

$$\begin{aligned} \mathbf{g}_{\mathrm{F}}(\theta) &= \begin{bmatrix} G_{\mathrm{pb}}(f_0, \theta) & G_{\mathrm{pb}}(f_1, \theta) & \cdots & G_{\mathrm{pb}}(f_{Q_{\mathrm{F}}-1}, \theta) \end{bmatrix}^T \\ &\approx \frac{1}{M\sqrt{2}} \mathbf{T}^H(\theta) \mathbf{s}_{\mathrm{v}} \end{aligned} \tag{4.22}$$

as the $Q_{\mathrm{F}} \times 1$ vector containing the passband spectral points $\{f_0, f_1, \ldots, f_{Q_{\mathrm{F}}-1}\}$ of $G_{\mathrm{pb}}(f, \theta)$, where

$$\mathbf{T}(\theta) = \begin{bmatrix} \mathbf{t}(f_0, \theta) & \cdots & \mathbf{t}(f_{Q_{\mathrm{F}}-1}, \theta) \end{bmatrix} \tag{4.23}$$

is the $MN \times Q_{\mathrm{F}}$ transformation matrix that steers towards spatial angle θ and performs a discrete Fourier transform. Thus, the discretized frequency content of the far-field time-varying beampattern can likewise be represented as the $Q_{\mathrm{F}} \times 1$ vector

$$\begin{aligned} \tilde{\mathbf{g}}_{\mathrm{F}}(\theta, \varphi) &= \begin{bmatrix} \tilde{G}_{\mathrm{pb}}(f_0, \theta, \varphi) & \tilde{G}_{\mathrm{pb}}(f_1, \theta, \varphi) & \cdots & \tilde{G}_{\mathrm{pb}}(f_{Q_{\mathrm{F}}-1}, \theta, \varphi) \end{bmatrix}^T \\ &= \mathbf{f}(\theta, \varphi) \odot \mathbf{g}_{\mathrm{F}}(\theta), \end{aligned} \tag{4.24}$$

where $\odot$ is the Hadamard product, and

$$\mathbf{f}(\theta, \varphi) = \begin{bmatrix} F_{\mathrm{a}}(f_0, \theta, \varphi) & F_{\mathrm{a}}(f_1, \theta, \varphi) & \cdots & F_{\mathrm{a}}(f_{Q_{\mathrm{F}}-1}, \theta, \varphi) \end{bmatrix}^T \tag{4.25}$$

is the $Q_{\mathrm{F}} \times 1$ vector of the approximate active antenna pattern $F_{\mathrm{a}}(f, \theta, \varphi)$ sampled in frequency.

In [90], it was stated that the number of frequency points Q_{F} needs to be "over-represented" with respect to N to account for true-time delays to occur in wideband processing as well as to reduce the aliasing of the Gibbs phenomenon that produces time sidelobes that occur during non-integer sample shifts in the discrete domain [137]. These two considerations are valid, however the most strict limitation is in the accuracy of the spectral matching for improved correlation performance. Over-specifying the spectrum (i.e. $Q_{\mathrm{F}} > N$) amounts to zero padding in the time domain thus accounting for the pulsed nature of the spatially-diverse emission. A number of frequency points $Q_{\mathrm{F}} \geq 2N-1$ sufficiently zero pads the signals to prevent any unintentional aliasing from occuring during the discrete correlation analysis of the optimized transmission model. The restriction of $Q_{\mathrm{F}} \geq 2N-1$ inherently accounts for both the true-time delay and reduces the Gibbs sidelobe aliasing to a negligible amount.

4.2.3 Coupled Energy and The Invisible Space for Wideband Arrays

In Section 3.2.2, the link between the reactive region and reflected/coupled energy was made for a narrowband ULA (matched to boresight) with $d < \frac{\lambda_{\mathrm{c}}}{2}$. For a wideband scenario, the electrical spacing (in wavelengths) between antenna elements cannot be assumed to be constant over the bandwidth of the emission. Figure 4.14 shows how the ratio of invisible space to visible space changes as the normalized frequency f/f_{E} is varied. The frequency f in Figure 4.14 is varied from 0 to $2f_{\mathrm{E}}$ on the vertical axis. The diagonal traces correspond to particular values of $\sin\theta$. The vertical dashed lines signify the points at which the electrical angle is $\phi = \pm\pi$. The frequency $f = f_{\mathrm{E}}$ is the point at which the vertical dashed lines intersects the diagonal solid black lines (corresponding to $\sin\theta = \pm 1$). The area bounded in red is the reactive region as described in Section 3.2.2 for frequencies less than f_{E}. The reactive region can become a problem for wideband, wide beam emissions where energy could unknowingly be placed within the reactive region.

The fractional reactive power metric from (3.80) in Section 3.2.2 was shown to approximate the total reflected energy for the narrowband array (when matched to boresight) and was calculated using only the time-varying array factor. Here, the FRP is redefined for wideband transmission as

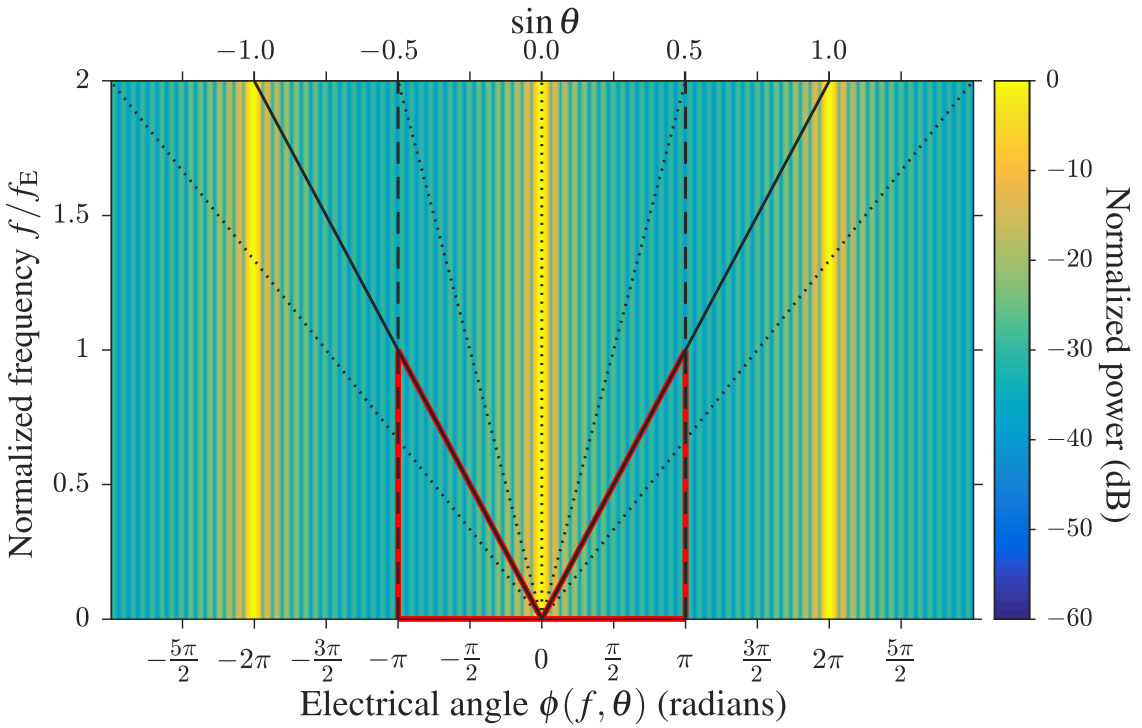

Figure 4.14: Visible and invisible regions for an $M = 30$ element narrowband array with variable f/f_E. The reactive region is bounded inside the red triangles. ©2017 IEEE

$$\text{FRP} = \frac{\displaystyle\int_0^{f_E}\left(\int_{-\frac{f_E}{f}}^{-1}|G_{pb}(f,\bar{u})|^2 d\bar{u} + \int_{1}^{\frac{f_E}{f}}|G_{pb}(f,\bar{u})|^2 d\bar{u}\right) df}{\displaystyle\int_0^{\infty}\int_{-\frac{f_E}{f}}^{\frac{f_E}{f}}|G_{pb}(f,\bar{u})|^2 d\bar{u} df}, \tag{4.26}$$

where $\bar{u} = \pm\frac{f_E}{f}$ corresponds to the bounds of electrical angle $\phi = \pm\pi$ (before phase wrapping) for $f < f_E$.

To examine how a spatially-diverse set of waveforms might affect a widband ULA, consider an array comprised of $M = 30$ equispaced elements designed for a wideband emission with fractional bandwidth $[\%\text{BW}]_{98\%} = 40\%$ and half-wavelength inter-element spacing set according to frequency $f_E = 1.2 f_c$ (the highest frequency within the bandwidth) to prevent grating lobes from appearing in-band [87, 98]. A set of $M = 30$ FM waveforms (with Gaussian spectral shapes)

are applied to this array over the entirety of the band. The waveforms are designed to produce a spatially-diverse emission with an omnidirectional beampattern without consideration of the reactive region. The omnidirectional beampattern implies that the waveforms are orthogonal (in terms of zero-delay inner product) [17, 89] which is a common assumption in MIMO applications [21].

Figure 4.15 shows the passband frequency content of the time-varying array factor $|G_{\text{pb}}(f,\theta)|^2$ (in dB) of the described emission versus electrical angle $\phi(f,\theta)$ and normalized frequency f/f_{c}. Note the intersection points of $\sin\theta = \pm 1$ and $\phi = \pm\pi$ occurs at frequency $f_{\text{E}} = 1.2f_{\text{c}}$. The reactive region is again bounded by the red triangles. Using (4.26), the FRP for this scenario is 0.174 which, if assumed to be approximately equal to the total integrated power reflection coefficient, exceeds the $|\Gamma^{\text{a}}|^2 = 0.1$ level for satisfactory transmission. This scenario shows the need to consider the invisible space for wideband emission design when a portion of the bandwidth has an electrical antenna spacing less than a half-wavelength.

The energy placed into the reactive region by the time-varying array factor can be minimized by either 1) increasing the spacing between antenna elements such that no portion of the bandwidth has an electrical spacing below half-wavelength or 2) constraining the emitted energy to the visible space either by design or traditional beamforming. The first method, while valid, does not prevent grating lobes from appearing [98, 138]. Thus we shall consider how to design of the emission spectral content in the visible space as a means to minimize the power in the reactive region.

4.2.4 Spatially-Diverse, Wideband Waveform Optimization Goals

Here, we define the "big picture" goals for both the spatially-diverse transmission and the design of waveforms that produce the emission. The goals, listed briefly, include: constant amplitude and spectrally contained waveforms, desired space-frequency beampattern (including minimal energy put into the reactive region), and a space-frequency nulling capability. These attributes, while are desirable from a radar transmission point of view, are not cooperative from an emission design standpoint. For instance, better spectral containment can be achieved by relaxing the constant

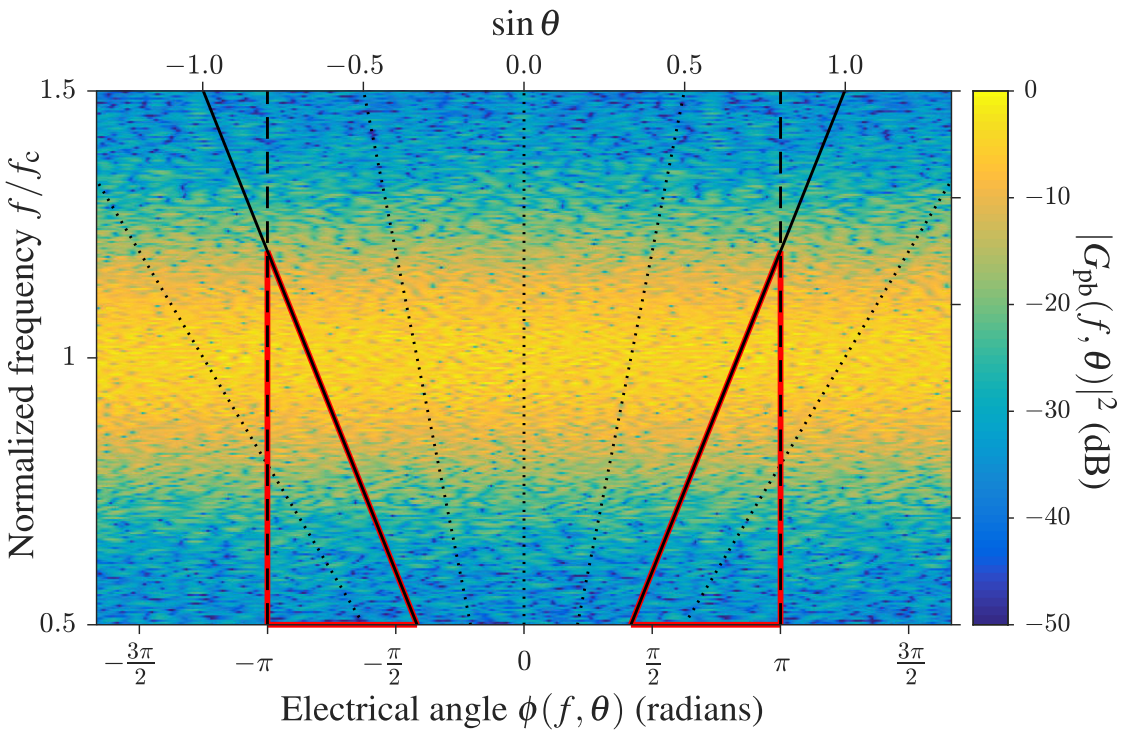

Figure 4.15: Spectrum of the time-varying array factor $|G_{\text{pb}}(f,\theta)|^2$ (in dB) of wideband ($[\%\text{BW}]_{98\%} = 40\%$ bandwidth) omnidirectional MIMO emission vs. electrical angle $\phi(f,\theta)$ for an $M = 30$ element ULA with $f_{\text{E}} = 1.2f_{\text{c}}$. The reactive region is bounded inside the red triangles with FRP = 0.174 from (4.26). ©2017 IEEE

amplitude waveform constraint.

4.2.4.1 Constant Amplitude and Spectrally Contained Waveforms

Just as in Section 4.1, the waveforms that produce the spatially-modulated emission are constrained such that they are constant amplitude (thus can be sent through a saturated amplifier with minimal distortion) and spectrally contained (to minimize envelope distortion due to bandlimiting within the transmitter) (see Section 2.2.2 for more information). The waveform design problem for the wideband, wide-beam transmission is investigated using the over-sampled discretized model of the waveform set as shown in (4.13). Thus the constant modulus constraint is enforced by requiring the amplitude of each sample in (4.13) to be equal, (i.e. $|s_m[n]|$ = 'constant' $\forall m,n$). Also, by constraining the discretized waveforms to be spectrally contained, the conversion back into continuous-time can be implemented with little distortion. In Section 4.2.6, it is shown how the discretized waveform vectors can be implemented in continuous-time using the PCFM waveform model discussed in Section 2.1.2.4. Here, the spectrum of the waveforms are contained by designing the far-field transmission to have a desired space-frequency power distribution (Section 4.2.4.2) by leveraging the fact that the spectral content of the designed waveforms is inherently contained by containing the spectral content of the emission.

4.2.4.2 Space-Frequency Power Distribution

To form the desired allocation of energy in space-frequency, the spectral energy spectrum is shaped in certain pre-defined angles denoted as "beamlets", where each beamlet has a specific spectral window (e.g. Gaussian) with predefined 98% bandwidth. The spectral containment of the waveforms is controlled directly by the choice in spectral window. The distribution of energy in space is structured simply by placing the beamlets in directions where energy is scheduled to be allocated and scaling the beamlet to control the relative power level.

Denote $\Theta = \{\theta_0,\ldots,\theta_{P_B-1}\}$ as the set containing the P_B beamlets representing the desired transmission spatial angles to be included in the emission design. Using (4.20), the frequency-

dependent electrical angles from (4.10) can be expressed as

$$\phi(f_q, \theta_p) = \pi \frac{\left(f_s \cdot \left(-\frac{1}{2} + \frac{q}{Q_F}\right) + f_c\right)}{f_E} \sin\theta_p, \tag{4.27}$$

for $q \in \{0, 1, \ldots, Q_F - 1\}$ over the set of $p \in \{0, 1, \ldots, P_B - 1\}$ beamlets. Inserting $f_s = \bar{\kappa} B_{98\%}$ into (4.27) and dividing the numerator and demoninator by f_c yields

$$\phi(f_q, \theta_p) = \pi \frac{\left(\bar{\kappa}\,[\%\mathrm{BW}]_{98\%} \cdot \left(-\frac{1}{2} + \frac{q}{Q_F}\right) + 1\right)}{f_E/f_c} \sin\theta_p, \tag{4.28}$$

which can be readily inserted into (4.17) to form the steering vector $\mathbf{v}(f_q, \theta_p)$ and subsequently the space-frequency steering vector $\mathbf{t}(f_q, \theta_p)$ using (4.16) that corresponds to the pth beamlet and qth frequency. The formulation in (4.28) allows for direct implementation of the fractional bandwidth $[\%\mathrm{BW}]_{98\%}$ and the ratio f_E/f_c which sets the intersection points of $\sin\theta = \pm 1$ and $\phi = \pm\pi$ as described in Figures 4.14 and 4.15.

In Section 3.1.1, the assumption was made that the embedded antenna pattern $F_m(f, \theta, \varphi) \forall m$ is maximized toward $\varphi = 0°$. Because the wideband ULA has no degree of beampattern control in the φ-dimension, the far-field spectral content emitted toward $\varphi = 0°$ is shaped according to a desired spectral window for each beamlet. Define the $Q_F \times 1$ (magnitude) spectral window for the pth beamlet as

$$\tilde{\mathbf{u}}(\theta_p) = \left[\tilde{U}(f_0, \theta_p) \;\; \cdots \;\; \tilde{U}(f_{Q_F-1}, \theta_p)\right]^T, \tag{4.29}$$

where $\tilde{U}(f_q, \theta_p)$ is the positive, real-valued desired spectral magnitude for $\tilde{G}_{\mathrm{pb}}(f_q, \theta_p, \varphi = 0°)$ at frequency f_q and angle θ_p. Thus, $\tilde{\mathbf{u}}(\theta_p)$ is the desired spectral magnitude for $\tilde{\mathbf{g}}_F(\theta_p, \varphi = 0°)$, the discretized far-field spectral content from (4.24) corresponding the direction $(\theta_p, \varphi = 0°)$. The vector $\tilde{\mathbf{u}}(\theta_p)$ is scaled such that $\|\tilde{\mathbf{u}}(\theta_p)\|_2^2$ is equal to a desired amount of energy for the corresponding beamlet. Note that the spectral window extends over the frequency interval $f_c \pm f_s/2$, such that the 98% bandwidth is contained in $1/\bar{\kappa}$ of the total spectral window centered at f_c.

Recall from (3.25) that for the large array assumption the relationship between the spectral

content of the time-varying far-field beampattern and the time-varying antenna factor is the application of the approximate active antenna pattern, $\tilde{G}_{\text{pb}}(f,\theta,\varphi) = F_{\text{a}}(f,\theta,\varphi)G_{\text{pb}}(f,\theta)$ (shown in discretized frequency form in (4.24)). Therefore, the $Q_{\text{F}} \times 1$ discretized (in frequency) approximate active antenna pattern at $\varphi = 0^\circ$ from (4.25) can be applied to (4.29) to form the desired spectral magnitude for $\mathbf{g}_{\text{F}}(\theta_p)$ from (4.22) as

$$\begin{aligned}\mathbf{u}(\theta_p) &= \tilde{\mathbf{u}}(\theta_p) \oslash \mathbf{f}(\theta_p, \varphi = 0^\circ) \\ &= \left[U(f_0,\theta_p) \;\; \cdots \;\; U(f_{Q_{\text{F}}-1},\theta_p)\right]^T,\end{aligned} \tag{4.30}$$

where $\oslash$ is the element-wise vector division and

$$U(f_q,\theta_p) = \frac{\tilde{U}(f_q,\theta_p)}{F(f_q,\theta_p,\varphi = 0^\circ)} \tag{4.31}$$

is the desired spectral magnitude for $G_{\text{pb}}(f_q,\theta_p)$. The shaping the magnitude of $\mathbf{g}_{\text{F}}(\theta_p)$ according to the desired response in (4.30) amounts to a predistortion of desired spectral response such that the desired far-field spectral content $\tilde{G}(f_q,\theta_p,\varphi = 0^\circ)$ approximates the desired spectral window $\tilde{U}(f_q,\theta_p)$ after application of the approximate active antenna pattern.

Note that it is assumed that the choice of beamlet direction θ_p and frequency f_q is contained to a region in space-frequency where the array is designed for operation. Thus, for all beamlets θ_p for $p \in \{0,1,\ldots,P_{\text{B}}-1\}$ and frequencies f_q for $q \in \{0,1,\ldots,Q_{\text{F}}-1\}$, the approximate active antenna pattern $F_{\text{a}}(f_q,\theta_p,\varphi = 0^\circ)$ does not contain any nulls or low transmission/high reflection points in the beampattern which would cause $U(f_q,\theta_p)$ to be exceedingly large from the predistortion in (4.31). This assumption implicitly addresses the invisible space of the wideband array as well. To limit the energy contained within the invisible space, we limit the available beamlet directions in $\boldsymbol{\Theta}$ such that the entire mainlobe of each beamlet is within the visible space according to the lowest frequency (widest spatial beamwidth) as

$$|\sin\theta_p| \leq 1 - \frac{2f_{\text{E}}/f_{\text{c}}}{M \cdot \left(1 - \frac{[\%\text{BW}]_{98\%}}{2}\right)}. \tag{4.32}$$

for $p \in \{0, 1, \ldots, P_{\mathrm{B}} - 1\}$. This constraint is established in Appendix A.7.

The beampattern matching problem for the desired spectral responses $\mathbf{u}(\theta_p)$ for all P_{B} beamlets can be formulated as

$$\underset{\mathbf{s}_{\mathrm{v}}}{\text{minimize}} \quad \sum_{p=0}^{P_{\mathrm{B}}-1} \left\| \left| \frac{1}{M\sqrt{2}} \mathbf{T}^H(\theta_p) \mathbf{s}_{\mathrm{v}} \right| - \mathbf{u}(\theta_p) \right\|_2^2. \tag{4.33}$$

Note that (4.33) is based only on the form of the time-varying array factor from (4.22) and its desired spectral content $\mathbf{u}(\theta_p)$. The desired spectral content $\tilde{\mathbf{u}}(\theta_p)$ for the true emission $\tilde{\mathbf{g}}_{\mathrm{F}}(\theta_p)$ is implied in the predistorted $\mathbf{u}(\theta_p)$.

4.2.4.3 Nulled Regions in Space-Frequency

A nulled region is space-frequency can be formed by defining L_{n} space-frequency points to be nulled (f_ℓ, θ_ℓ) for $\ell \in \{0, 1, \ldots, L_{\mathrm{n}} - 1\}$. Denote $\mathcal{R}_{\mathrm{n}} = \{(f_0, \theta_0), \ldots, (f_{L_{\mathrm{n}}-1}, \theta_{L_{\mathrm{n}}-1})\}$ as the set containing the ordered pairs of spatial angles and corresponding frequencies to be nulled. These points can be condensed into a region to achieve a broad null or can be placed individually. Collecting the corresponding space-frequency steering vectors into the $MN \times L_{\mathrm{n}}$ nulling matrix yields

$$\mathbf{D} = \begin{bmatrix} \mathbf{t}(f_0, \theta_0) & \mathbf{t}(f_1, \theta_1) & \cdots & \mathbf{t}(f_{L_{\mathrm{n}}-1}, \theta_{L_{\mathrm{n}}-1}) \end{bmatrix}. \tag{4.34}$$

Thus the nulling problem can be represented as

$$\underset{\mathbf{s}_{\mathrm{V}}}{\text{minimize}} \quad \|\mathbf{D}^H \mathbf{s}_{\mathrm{v}}\|_2^2. \tag{4.35}$$

If the space-frequency null locations defined by the set $\mathcal{R}_{\mathrm{n}}$ coincide with a value in $U(f_q, \theta_p)$, for $p \in \{0, 1, \ldots, P_{\mathrm{B}} - 1\}$ and $q \in \{0, 1, \ldots, Q_{\mathrm{F}} - 1\}$, then the spectral window points $U(f_q, \theta_p)$ in $\mathcal{R}_{\mathrm{n}}$ must be set to zero to prevent competing goals in problems (4.33) and (4.35). Note that zeroing values within a spectral window necessitates additional scaling to compensate for the energy that is removed.

4.2.5 Wideband Spatially-Diverse Emission Design with Space-Frequency Nulling

The goals discussed Section 4.2.4 show that the wideband emission design problem is convoluted when considering the aggregate of desired emission properties. Here, a heuristic iterative design method is discussed that qualitatively accomplishes all the design goals. The method cannot be directly linked to optimization theory though is shown to converge onto a satisfactory solution. In the future, this design problem will be reexamined using strict optimization theory in an attempt to improve on the presented results. The proposed design method was first presented in [91] and extended in [90] to also include space-frequency nulling to address spectral coexistence issues [6, 8]. In general, this manner of optimization is inspired by the class of alternating projection approaches, such as [123–128].

The $Q_{\mathrm{F}} \times 1$ frequency vector of the pth beamlet at the ith iteration of the design can be found via (4.22) as

$$\mathbf{g}_{\mathrm{F},i}(\theta_p) = \frac{1}{M\sqrt{2}} \mathbf{T}^H(\theta_p) \mathbf{s}_{\mathrm{v},i}. \tag{4.36}$$

In (4.33), it is assumed that the relative scaling between $\mathbf{u}(\theta_p)$ and $\mathbf{g}_{\mathrm{F}}(\theta_p)$ is such that they can be directly compared. However, it has been found that this relationship tends to not occur due to the constant amplitude constraint. Thus, a normalized emission design cost function can be defined as

$$\mathcal{J}_{\mathrm{B}}(\mathbf{s}_{\mathrm{v},i}) = \sum_{p=0}^{P_{\mathrm{B}}-1} \left\| \frac{\left|\mathbf{g}_{\mathrm{F},i}(\theta_p)\right|}{\sqrt{\gamma_{\mathrm{g},i}}} - \frac{\mathbf{u}(\theta_p)}{\sqrt{\gamma_{\mathrm{u}}}} \right\|_2^2, \tag{4.37}$$

where

$$\gamma_{\mathrm{g},i} = \sum_{p=0}^{P_{\mathrm{B}}-1} \left\| \mathbf{g}_{\mathrm{F},i}(\theta_p) \right\|_2^2 \tag{4.38}$$

and

$$\gamma_{\mathrm{u}} = \sum_{p=0}^{P_{\mathrm{B}}-1} \left\| \mathbf{u}(\theta_p) \right\|_2^2 \tag{4.39}$$

are the summations of the vector energies contained in the beamlets of the current iteration i and the predefined spectral windows, respectively. The formulation in (4.37) compares the relative difference rather than the absolute difference to prevent artificially increasing cost due to scaling. Note that the cost function in (4.37) serves as only an observation of the performance of the heuristic approach.

At this point, the desired spectral magnitude $\mathbf{u}(\theta_p)$ from (4.30) is forced by only retaining the phase of $\mathbf{g}_{\mathrm{F},i}(\theta_p)$ and applying it to $\mathbf{u}(\theta_p)$ as

$$\mathbf{b}_i(\theta_p) = \mathbf{u}(\theta_p) \odot \exp\left(j \angle \mathbf{g}_{\mathrm{F},i}(\theta_p)\right), \tag{4.40}$$

where $\odot$ is the Hadamard product and $\angle$ extracts the phase angle of the argument (for each element in the vector). The standard beamforming set of finite duration waveforms (in vectorized form) that approximates the desired emission $\mathbf{b}_i(\theta_p)$ (4.40) for a single beamlet θ_p is represented as

$$\tilde{\mathbf{s}}_{\mathrm{v},i}(\theta_p) = \mathbf{T}(\theta_p)\mathbf{b}_i(\theta_p). \tag{4.41}$$

Therefore there are P_{B} different standard beamforming sets of waveforms $\tilde{\mathbf{s}}_{\mathrm{v},i}(\theta_p) \forall p$ that approximate the desired transmissions $\mathbf{b}_i(\theta_p) \forall p$. The total unconstrained (in amplitude) vectorized waveform set at the ith iteration can then be constructed via a weighted summation of the different beamlet contributions as

$$\tilde{\mathbf{s}}_{\mathrm{v},i} = \sum_{p=0}^{P_{\mathrm{B}}-1} \varsigma_i(\theta_p)\tilde{\mathbf{s}}_{\mathrm{v},i}(\theta_p). \tag{4.42}$$

where $\varsigma_i(\theta_p)$ is the adaptive weighting corresponding to the pth beamlet θ_p. The weighting is needed as the P_{B} beamlets will likely be correlated to some extent. Therefore the relative scaling of the standard beamforming contributions $\mathbf{s}_{\mathrm{v},i}(\theta_p)$ must be adapted to prevent the design process

from overemphasizing (or underemphasizing) the energy in a certain direction, thus ensuring that the desired beampattern is formed. The weighting is adaptive and is updated each iteration depending on the resulting energy levels in the desired transmission directions contained in Θ. Using (4.36), the adaptive weighting for the pth beamlet is updated as

$$\varsigma_i(\theta_p) = \varsigma_{i-1}(\theta_p)\sqrt{\frac{\left\|\mathbf{u}(\theta_p)\right\|_2^2 \Big/ \gamma_{\mathrm{u}}}{\left\|\mathbf{g}_{\mathrm{F},i}(\theta_p)\right\|_2^2 \Big/ \gamma_{\mathrm{g},i}}}. \tag{4.43}$$

For example, if the energy in the direction $\|\mathbf{g}_{\mathrm{F},i}(\theta_p)\|_2^2$ is under the desired amount $\|\mathbf{u}(\theta_p)\|_2^2$, the adaptive weight $\varsigma_i(\theta_p)$ is increased thus increasing the relative contribution of $\tilde{\mathbf{s}}_{\mathrm{v},i}(\theta_p)$ in (4.42). This process eventually yields a weighting $\varsigma(\theta_p)$ that produces the desired spatial beam energy specified in $\mathbf{u}(\theta_p)$. As the iterative design progresses the term inside the $\sqrt{\bullet}$ either converges unity or the beamlet is removed altogether $(\varsigma_i(\theta_p) = 0)$. A removal of a beamlet only occurs when designing for a wide beampattern where not all the points $\theta_p \forall p$ are needed to form the desired spatial beampattern. At the beginning of the design process the adaptive scaling is initialized to unity for all beamlets.

If no space-frequency nulling is required, the constant amplitude condition is forced as

$$\mathbf{s}_{\mathrm{v},i+1} = \exp\left(j \angle \tilde{\mathbf{s}}_{\mathrm{v},i}\right), \tag{4.44}$$

and the iteration index i it increased by 1. The expression (4.44) is then in turn used in the calculation of (4.36) and the process is repeated until convergence.

If nulling is required, (4.42) is inputted into the Reiterative Uniform-Weight Optimization (RUWO) algorithm which iteratively enforces nulls specified in interference matrix $\mathbf{R}_{\mathrm{n}}$ while maintaining constant amplitude vectors [129]. The deterministic form of the $MN \times MN$ wideband space-frequency interference matrix can be defined using $\mathbf{D}$ from (4.34) as

$$\mathbf{R}_{\mathrm{n}} = \frac{1}{L_{\mathrm{N}}}\mathbf{D}\mathbf{D}^H + \eta \mathbf{I}_{MN} \tag{4.45}$$

where η is a loading factor and $\mathbf{I}_{MN}$ is the $MN \times MN$ identity matrix. The loading factor η supplements the rank of the interference matrix so that it can be inverted. If the loading factor is too large, the depth of the null will decrease due to the loading factor masking essential eigenvalues. The RUWO algorithm is also an iterative process, thus the entirety of the design process (when nulling) has two nested loops: the outer loop, which allocates the transmitted energy in space-frequency; and the inner loop (RUWO), which enforces the space-frequency nulls.

Denote the current RUWO iteration as k and the total number of iterations K. The RUWO loop is initialized using the current estimate of the unconstrained waveforms as $\mathbf{r}_{0,i} = \exp\left(j \angle \tilde{\mathbf{s}}_{\mathrm{V},i}\right)$. The update of the nulled, vectorized waveform set is defined as [129]

$$\mathbf{r}_{k+1,i} = \exp\left(j \angle \left(\mathbf{R}_{\mathrm{n}}^{-1} \mathbf{r}_{k,i}\right)\right) \tag{4.46}$$

where $\mathbf{R}_{\mathrm{n}}^{-1}$ is the inverse of the interference covariance matrix from (4.45). The RUWO algorithm is not guaranteed to converge onto a solution that has nulls of a desired depth, though it has been proven that the cost function in null depth reduces at each iteration k establishing that it does not diverge [129, 139, 140]. The convergence speed of RUWO is dependent on the eigenspread of interference covariance matrix $\mathbf{R}_{\mathrm{n}}$, but typically converges to a stable solution within $K = 50$ iterations [129].

The vectorized waveform set is then updated as

$$\mathbf{s}_{\mathrm{v},i+1} = \begin{cases} \mathbf{r}_{K,i}, & \text{when nulling} \\ \exp\left(j \angle \tilde{\mathbf{s}}_{\mathrm{v},i}\right), & \text{otherwise} \end{cases}. \tag{4.47}$$

The process is repeated a predefined[5] number of times, Φ. Table 4.1 provides a summary of the optimization steps. If nulling is being applied, the per iteration computational cost is dominated by the RUWO loop and is $\mathcal{O}(K(MN)^2)$ in complexity. If no nulling is applied $(K = 0)$, then the cost is $\mathcal{O}(MNPQ)$ in complexity.

[5]Note a convergence criteria could be included though is not considered here.

Table 4.1: Wideband Spatially-Diverse Emission Design with Space-Frequency Nulling

1.	Establish the number of antenna elements M and discretized waveform length N for over-sampling factor $\bar{\kappa}$ and 98% time-bandwidth product $B_{98\%}T$.
2.	Select quantity P_{B} and specific directions Θ of the beamlets, the number of frequency bins Q_{F}, fractional bandwidth $[\%\mathrm{BW}]_{98\%}$, and the ratio $f_{\mathrm{E}}/f_{\mathrm{c}}$ that dictates element spacing.
3.	(optional) Determine the L_{n} space-frequency points $\mathcal{R}_{\mathrm{n}}$ to be nulled (if any). Form the $MN \times MN$ interference matrix $\mathbf{R}_{\mathrm{n}}$ using (4.45) and calculate the inverse. Select the number of RUWO iterations K.
4.	Form the desired spectral magnitude $\mathbf{u}(\theta_p)$ for each of the P_{B} beamlets via (4.30) and calculate γ_{u} via (4.39). Zero values in $\mathbf{u}(\theta_p)$ they contradict with a nulled region.
5.	Set the number of optimization iterations to perform, Φ. Initialize vectorized waveform set $\mathbf{s}_{\mathrm{v},0}$, loop index to $i = 0$, and the adaptive weights $\varsigma_{-1}(\theta_p)$ to unity.
6.	Calculate $\mathbf{g}_{\mathrm{F},i}(\theta_p)$ for $p \in \{0, \ldots, P_{\mathrm{B}} - 1\}$ via (4.36).
7.	Force desired spectral magnitude $\mathbf{u}(\theta_p)$ to find $\mathbf{b}_i(\theta_p)$ for $p \in \{0, \ldots, P_{\mathrm{B}} - 1\}$ via (4.40).
8.	Calculate $\gamma_{\mathrm{g},i}$ via (4.38) and update adaptive weighting $\varsigma_i(\theta_p)$ via (4.43).
9.	Form the unconstrained vectorized waveform set $\tilde{\mathbf{s}}_{\mathrm{v},i}$ via (4.42).
10.	If no nulling is being applied, set $\mathbf{s}_{\mathrm{v},i+1} = \exp\left(j \angle \tilde{\mathbf{s}}_{\mathrm{v},i}\right)$ and go to step 12.
11.	Initiate RUWO nulling loop. Set loop index to $k = 0$.
a.	Form initial vectorized solution $\mathbf{r}_{0,i} = \exp\left(j \angle \tilde{\mathbf{s}}_{\mathrm{V},i}\right)$.
b.	Update vectorized solution $\mathbf{r}_{k+1,i}$ using (4.46).
c.	Increment $k = k + 1$. Stop if $k = K$. Otherwise, go to step 11b.
d.	Set $\mathbf{s}_{\mathrm{v},i+1} = \mathbf{r}_{K,i}$.
12.	Increment $i = i + 1$. If $i = \Phi$, go to step 12. Otherwise, go to step 6.
13.	Implement discretized waveform set $\mathbf{s}_{\mathrm{v},\Phi}$ as physically realizable FM waveforms as shown in Sect. 4.2.6.

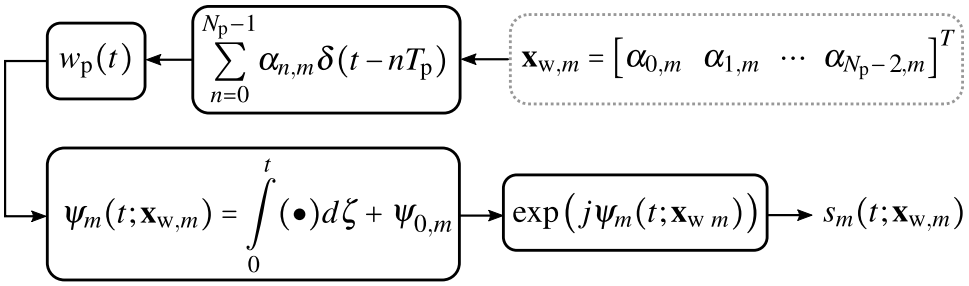

Figure 4.16: Implementation of mth polyphase-coded frequency-modulated (PCFM) waveform

4.2.6 Implementation

The constant modulus, discrete-time, baseband representation of the vectorized set of waveforms in $\mathbf{s}_{\mathrm{v},\Phi}$ can be translated into M continuous-time waveforms using the polyphase-coded FM (PCFM) implementation [38] discussed in Section 2.1.2.4. Recall that the vectorized form $\mathbf{s}_{\mathrm{v}}$ is related to the discretized waveform matrix $\mathbf{S}$ via (4.13) where the mth column is the discretized waveform $\mathbf{s}_m = \left[s_m[0] \;\; s_m[1] \;\; \cdots \;\; s_m[N-1]\right]^T$ corresponding to the mth antenna element.

Given the length-N phase sequence of the mth discretized waveform $\psi_{0,m}, \psi_{1,m}, \ldots \psi_{N-1,m}$, for $\psi_{n,m} = \angle s_m[n]$, a train of $N-1$ impulses with time separation $T_{\mathrm{p}} = 1/f_{\mathrm{s}}$ are formed. The nth impulse is weighted by $\alpha_{n,m}$, which is equal to the modulo phase change between the nth and $(n+1)$th phase value as determined by

$$\alpha_{n,m} = \begin{cases} \psi_{n+1,m} - \psi_{n,m} & \text{if } |\psi_{n+1,m} - \psi_{n,m}| \le \pi \\ (\psi_{n+1,m} - \psi_{n,m}) - 2\pi \mathrm{sgn}(\psi_{n+1,m} - \psi_{n,m}) & \text{if } |\psi_{n+1,m} - \psi_{n,m}| > \pi \end{cases}, \tag{4.48}$$

where $\mathrm{sgn}(\bullet)$ is the sign operation that wrap the values of $\alpha_{n,m}$ to $(-\pi, \pi]$. The values of (4.48) can then be collected into the code vector $\mathbf{x}_{\mathrm{w},m} = [\alpha_{0,m} \;\; \alpha_{1,m} \cdots \alpha_{N-2,m}]^T$ that parameterizes the mth complex-baseband waveform. Thus, the PCFM phase function from (2.46) for the mth waveform is thus

$$\psi_m(t;\mathbf{x}_{\mathrm{w},m}) = \sum_{n=0}^{N-2} \alpha_{n,m} h_n(t) + \psi_{0,m}, \tag{4.49}$$

and the PCFM implementation (for amplitude envelope $u(t) = 1$) is

$$s_m(t;\mathbf{x}_{\mathrm{w},m}) = \exp\left(j\psi_m(t;\mathbf{x}_{\mathrm{w},m})\right). \tag{4.50}$$

The continuous-time waveforms are related to the discrete waveforms as $s_m(nT_\mathrm{p};\mathbf{x}_{\mathrm{w},m}) = s_m[n]$ for $n \in \{0,1,\ldots,N-1\}$.

Note that the inherent filtering (by shaping filter $w_\mathrm{p}(t)$) involved in the PCFM implementation may slightly alter the spectrum in lower power areas of the frequency response. Thus the nulls that have been enforced in the optimization may "fill in" to some degree. The loss in null sensitivity can be mitigated by applying the design process at a higher sampling rate [141].

4.2.7 Emission Optimization Analysis

For the results in Section 4.2.7 it is assumed that $F_\mathrm{a}(f,\theta,\varphi = 0^\circ) = 1$ over the band and within the visible space thus $\tilde{\mathbf{u}}(\theta_p) = \mathbf{u}(\theta_p)\ \forall p$ (from (4.30)). Note that this is not true in general though provides a means to show illustrative examples of the wideband waveform design process without specific wideband array knowledge. Thus, here it is assumed that the array is matched over the visible space and completely mismatched in the reactive region. In practice, the vectors $\mathbf{u}(\theta_p)\forall p$ would be predistorted using the approximate active antenna pattern as discussed in Section 4.2.4.2 and the user would want to avoid array excitations that would reflect/couple energy (which can be analyzed via the frequency-dependent scattering matrix $\boldsymbol{S}(f)$).

Consider the design of a wideband emission having 98% time-bandwidth product $B_{98\%}T = 50$ and fractional bandwidth $[\%\mathrm{BW}]_{98\%} = 40\%$ for a uniform linear array comprised of $M = 30$ antenna elements. The antenna element spacing is set according to the highest frequency in bandwidth $B_{98\%}$ to reduce the effect of grating lobes [87]. The normalized frequency associated with this spacing is

$$\begin{aligned}\frac{f_{\mathrm{E}}}{f_{\mathrm{c}}} &= \frac{f_{\mathrm{c}} + B_{98\%}}{f_{\mathrm{c}}} \\ &= 1 + \frac{[\%\mathrm{BW}]_{98\%}}{2} \\ &= 1.2,\end{aligned} \tag{4.51}$$

which sets the wideband factor Π from (4.12) at

$$\begin{aligned}\Pi &= [\%\mathrm{BW}]_{98\%} \frac{M-1}{2f_{\mathrm{E}}/f_{\mathrm{c}}} \\ &= 0.4 \cdot \frac{30-1}{2 \cdot 1.2} \\ &\approx 4.83.\end{aligned} \tag{4.52}$$

Recall that wideband factor must be $\Pi << 1$ to be considered narrowband therefore the described emission is considerably wideband. The sampling frequency is set to $\bar{\kappa} = 5$ times the time-bandwidth product of $B_{98\%}T = 50$ to closely approximate a continuous-time waveform (therefore $N = 5(50) = 250$)). For the given array, the set of beamlets must be contained within the spatial region established by (4.32) as

$$|\sin\theta_p| \leq 1 - \frac{2f_{\mathrm{E}}/f_{\mathrm{c}}}{M\left(1 - \frac{\%\mathrm{BW}}{2}\right)} = 0.9 \tag{4.53}$$

for $p \in \{0, 1, \ldots, P-1\}$ to avoid placing appreciable energy in the reactive region. The number of frequency bins is set to be twice the discrete length of the waveforms, $Q_{\mathrm{F}} = 2N = 500$.

Using these parameters as a baseline, three different scenarios are simulated and analyzed to highlight the customizable design capabilities that are possible. The first case is a wide beam scenario that could be used for a ubiquitous MIMO mode like that discussed in [20, 28] where the entirety of the spatial region is illuminated and multiple functions are performed on receive in a ubiquitous radar mode [142]. For the second case, three focused beams are optimized for a high directive array mode which may correspond to simultaneous multifunction mission (e.g. multiple target tracking). The third case is a combination of the two where a wide beam and a directive focused beam are optimized for simultaneous transmission. This scenario could

correspond to a simultaneous search and track mode. These scenarios are only three examples of the space-frequency beampatterns that could be achieved. The customizable ability of this design area permits simultaneous multi-function array operation alleviating timing constraints that are present in traditional multifunction arrays [142]. Below is a detailed description of the three cases considered:

Case 1: Wide beam scenario A wide (nearly omnidirectional) beam is generated over the angular interval $\sin\Theta \in [-0.9,\ 0.9]$, which is realized using $P_{\mathrm{B}} = 60$ evenly spaced beamlets over the region. Power is distributed equally over this wide beam. Two nulled regions are collected into the nulled set $\mathcal{R}_{\mathrm{n}}$. The first nulled region is defined as intersection of the interval in frequency $f/f_{\mathrm{c}} \in [0.8, 0.9]$ and the interval in space $\sin\theta \in [-0.5, -0.42]$. The second nulled region is defined as intersection of the interval in frequency $f/f_{\mathrm{c}} \in [1.2, 1.4]$ and the interval in space $\sin\theta \in [0.10, 0.25]$. The nulled regions are approximated by multiple finely placed points within the region.

Case 2: Three-beam scenario A total of $P_{\mathrm{B}} = 3$ beamlets are chosen to point in the directions $\sin\Theta = \{-0.71, 0, 0.17\}$. The $\sin\theta = 0$ beam is set to have 3 dB higher power than the other two beams. The nulled set $\mathcal{R}_{\mathrm{n}}$ is defined via intersection of the interval in frequency $f/f_{\mathrm{c}} \in [1.2, 1.4]$ and the interval in space $\sin\theta \in [0.10, 0.25]$.

Case 3: Wide beam + secondary beam scenario A moderately wide beam and a narrow secondary beam are jointly optimized over $\sin\Theta \in \{[-0.5,\ 0.5], 0.75\}$. The wide beam is generated using 30 evenly spaced beamlets over the interval, thus making for a total of $P_{\mathrm{B}} = 31$ beamlets. The secondary beam points in the direction $\sin\theta = 0.75$ and is set to be 2 dB higher than the peak power of the wide beam. The wide beam is specified to have a Gaussian-tapered spatial power distribution. The nulled regions are defined the same as in Case 1.

Optimization settings All the beamlets are nominally (excluding nulls) designed to have a Gaussian spectral shape in frequency for three reasons: 1) to establish the bandwidth of the emission, 2) to incorporate the spectral roll-off and thus well approximate a continuous-time emission, and 3) to leverage the desirable autocorrelation properties associated with a Gaussian power spectral density [57]. Note that the 98% bandwidth definition becomes ambiguous when considering nulled spectra. Thus, assuming that nulling is applied to a base spectral shape, we shall define the bandwidth of the nulled spectrum according to $B_{98\%}$ of this base spectral shape prior to nulling.

Each case uses $\Phi = 100$ design iterations along with $K = 20$ RUWO iterations. These values were selected because it was observed that sufficient convergence was obtained, though more sophisticated stopping criteria could alternatively be employed. Convergence plots are presented for the emission design cost function $\mathcal{J}_{\mathrm{B}}(\mathbf{s}_{\mathrm{v},i})$ from (4.37). The waveform matrix $\mathbf{S}$ for each of the 3 cases is independently initialized with white, complex-Gaussian distributed data having unit variance and zero mean so as to start with relatively low cross-correlation between the waveforms.

4.2.7.1 Wideband Radar Emission Analysis

Using the approximate form of $G_{\mathrm{pb}}(f,\theta)$ from (4.7), the time-varying array factor is assessed by considering the aggregate beampattern $A(\theta) = \frac{1}{T}\|G_{\mathrm{pb}}(f,\theta)\|_2^2$ from (3.21), the angle-delay ambiguity function $\chi_{\mathrm{s}}(\tau,\theta,\vartheta)$, and the fractional reactive power (FRP) defined in (4.26). The angle-delay ambiguity function as defined in (3.55) implicitly adopts the narrowband assumption. Generalizing (3.55) to a wideband ULA as a function of delay τ, spatial angle θ, and receive beamformed spatial angle ϑ, yields

$$\chi_{\mathrm{s}}(\tau,\theta,\vartheta) = \left(M\left\|G_{\mathrm{pb}}(f,\vartheta)\right\|_2^2 \sum_m \left\|s_m(t)\right\|_2^2\right)^{-\frac{1}{2}} \int_0^{\infty} G_{\mathrm{pb}}^{*}(f,\vartheta) G_{\mathrm{pb}}(f,\theta) e^{j2\pi f\tau} \left[\sum_m e^{jm\pi \frac{f}{f_{\mathrm{E}}}(\sin\theta - \sin\vartheta)}\right] df. \tag{4.54}$$

Note that because the beamforming is frequency dependent (true-time delay), the form of the

angle-delay ambiguity function cannot be separated into a beam factor $\bar{\chi}_{\mathrm{b}}(\theta,\vartheta)$ and diversity factor $\bar{\chi}_{\mathrm{s,d}}(\tau,\theta,\vartheta)$ like was done for the narrowband model in Section 3.1.3.2. Define the $\vartheta=\theta$ cut of the ambiguity diagram as the *spatial autocorrelation* $\chi_{\mathrm{a}}(\tau,\theta)$ expressed as

$$\begin{aligned}\chi_{\mathrm{a}}(\tau,\theta) &= \chi_{\mathrm{s}}(\tau,\theta,\vartheta=\theta)\\ &= \left(M\left\|G_{\mathrm{pb}}(f,\theta)\right\|_2^2\sum_m\left\|s_m(t)\right\|_2^2\right)^{-\frac{1}{2}}\int_0^\infty |G_{\mathrm{pb}}(f,\theta)|^2 e^{j2\pi f\tau}df.\end{aligned} \tag{4.55}$$

4.2.7.2 Case 1: Wide Beam Scenario Results

Figure 4.17 shows the spectrum $|G_{\mathrm{pb}}(f,\theta)|^2$ (in dB) for Case 1 where a near-omnidirectional wide beam has been designed to exist between $\sin\theta=-0.9$ and $\sin\theta=0.9$, where the bound described in (4.53) prevents the mainlobe of each beamlet from residing in the reactive region (bounded in red) for all in-band frequencies. The wide beam is constructed using $P_{\mathrm{B}}=60$ equal-spaced beamlets and shaped to a Gaussian frequency spectrum. By constructing the waveforms via a summation of weighted standard beamforming responses via (4.42), the energy of the aggregate emission is guaranteed to not place substantial energy in directions other than the angles specified in Θ. Thus, the energy in invisible space is limited to sidelobe energy which corresponds to an FRP = 0.0135 which is a substantial reduction from the FRP = 0.174 for the previous omnidirectional emission presented in Section 4.2.3.

Figure 4.18 shows the same Case 1 spectrum $|G_{\mathrm{pb}}(f,\theta)|^2$ as a function of $\sin\theta$. The deformations of the array beampattern can be seen at low and high frequencies. At low frequencies the beampattern is wider due to the array appearing smaller in wavelengths at these frequencies. Conversely, at higher frequencies the beampattern takes on a narrower beamwidth thus the spectral energy appears finer. The heuristic wideband emission design inherently accounts for the beampattern deformation and places energy evenly over all space.

A detailed view of the two nulled regions in the space-frequency beampattern are shown in Figure 4.19. Recall that the nulled regions are defined as the intersection of the interval in frequency $f/f_{\mathrm{c}}\in[0.8,0.9]$ and the interval in space $\sin\theta\in[-0.5,-0.42]$, and the intersection of the

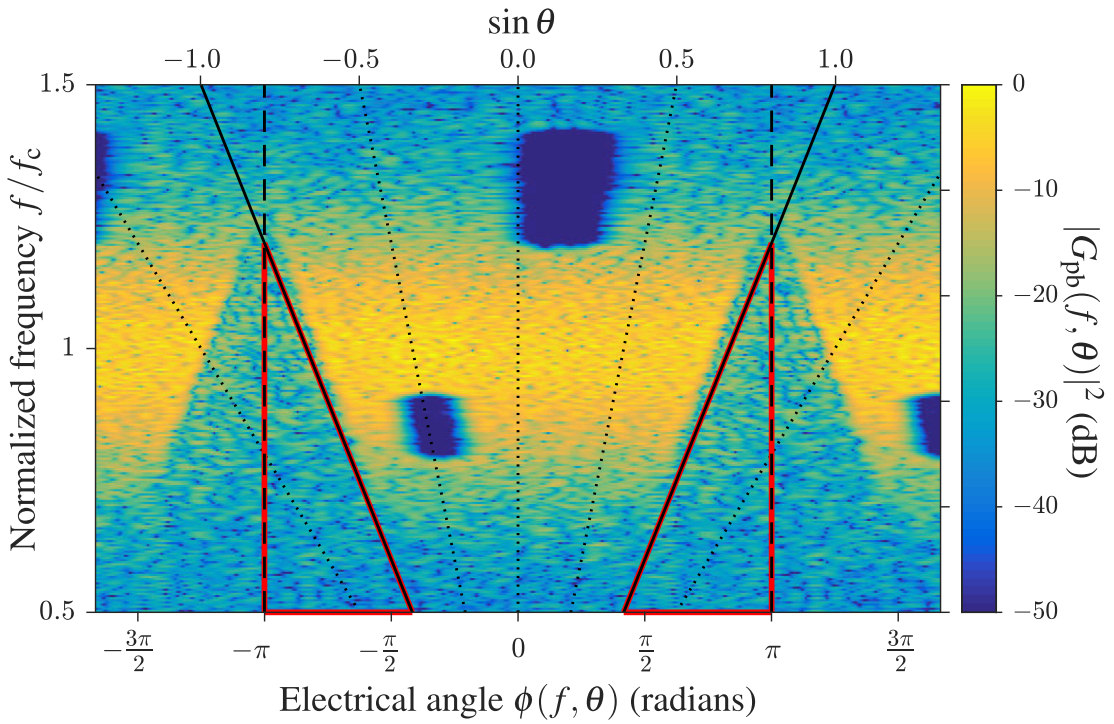

Figure 4.17: Spectrum $|G_{\text{pb}}(f,\theta)|^2$ (in dB) from (4.7) of wideband $\left([\%\text{BW}]_{98\%} = 40\%\text{ bandwidth}\right)$ wide beam MIMO emission versus electrical angle $\phi(f,\theta)$ for an $M = 30$ element ULA with $f_{\text{E}} = f_{\text{c}} + B_{98\%}/2$. The reactive region is bounded inside the red triangles with FRP = 0.0135 from (4.26). ©2017 IEEE

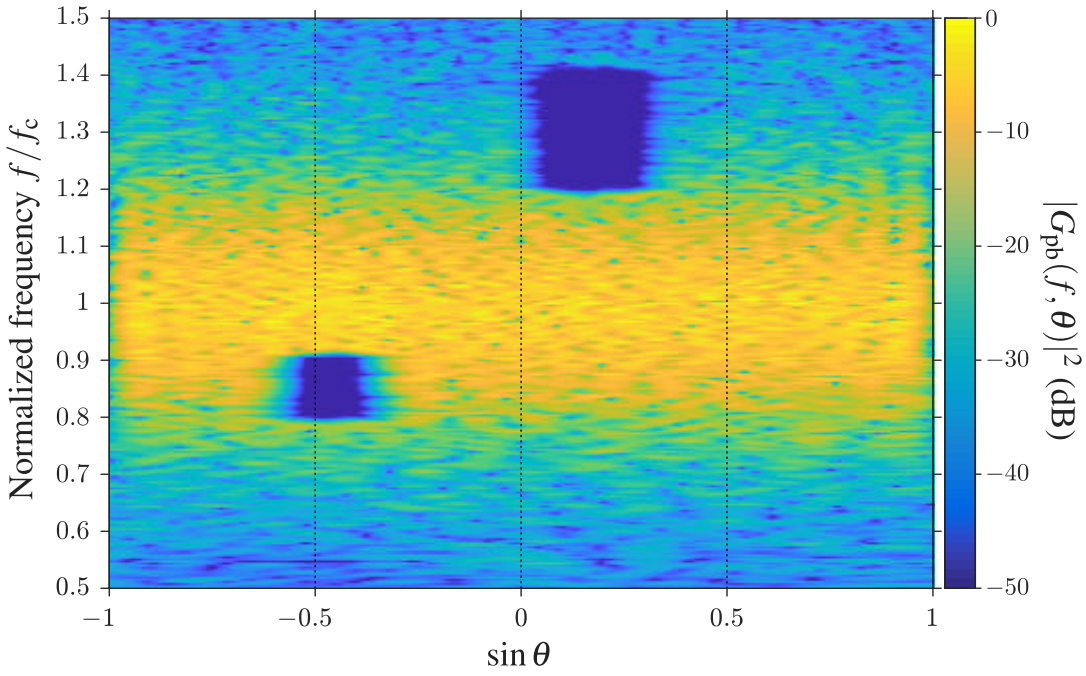

Figure 4.18: Spectrum $|G_{\text{pb}}(f,\theta)|^2$ (in dB) from (4.7) of wideband $\left([\%\text{BW}]_{98\%} = 40\%\text{ bandwidth}\right)$ wide beam MIMO emission versus $\sin\theta$ for an $M = 30$ element ULA with $f_{\text{E}} = f_{\text{c}} + B_{98\%}/2$.

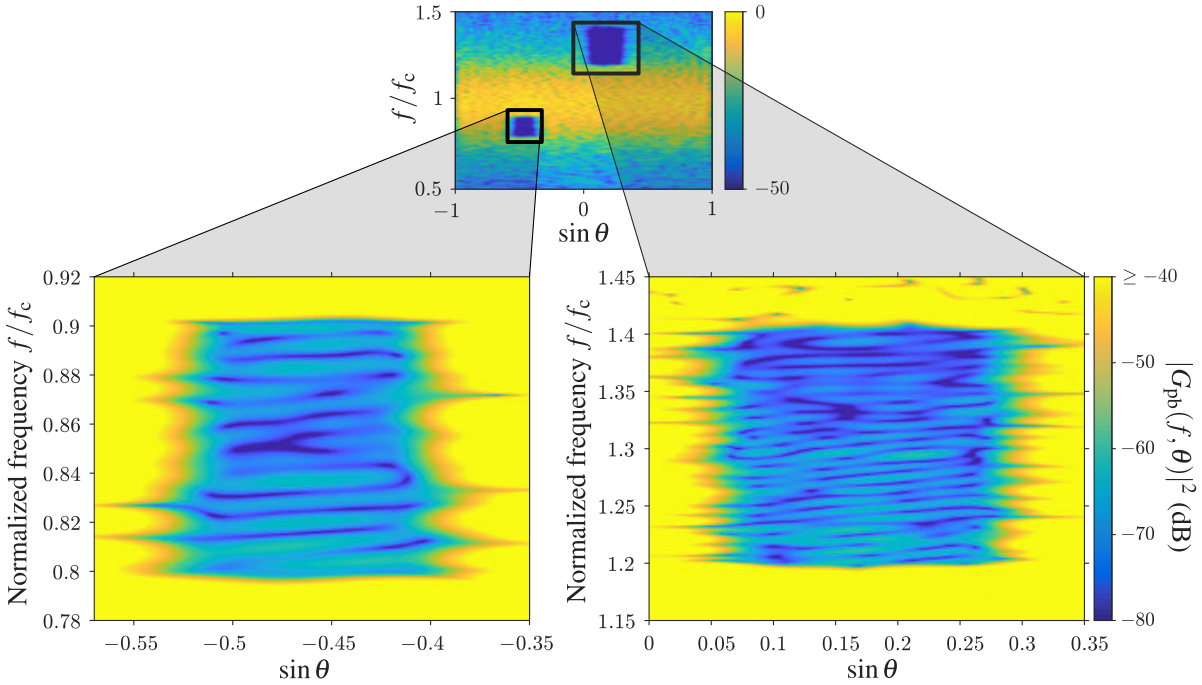

Figure 4.19: Detailed view of nulls for wideband $\left([\%\text{BW}]_{98\%} = 40\%\text{ bandwidth}\right)$ wide beam MIMO emission versus $\sin\theta$ for an $M = 30$ element ULA with $f_E = f_c + B_{98\%}/2$.

interval in frequency $f/f_c \in [1.2, 1.4]$ and the interval in space $\sin\theta \in [0.10, 0.25]$. The null width in frequency is the desired extent, however the spatial extent of both nulls are wider than specified. This effect is due to the construction of the interference matrix $\mathbf{R}_n$ where the eigenspread of the deterministic space-frequency steering vectors resulting in the increased null width. To prevent this increase in null width, an orthogonalization of $\mathbf{R}_n$ can be performed to create a projection matrix the explicitly nulls the desired region [140].

Figure 4.20 shows the aggregate $A(\theta)$ for this emission ($P = 60$ beamlets in blue) and, for comparison, the same emission was generated using $P = 30$ beamlets (shown in red) spaced evenly over the desired spatial region. By over-specifying the beamlets in space, the aggregate beampattern maintains 0.74 dB of variation over the optimized spatial region of $\sin\Theta \in [-0.90, 0.90]$. For $P = 30$ beamlets, the beampattern has over 2 dB of variation over this optimized spatial region. The adaptive weightings $\varsigma(\theta_p) \forall p$ are only altered to maintain the desired spatial energy contained in $\mathbf{u}(\theta_p)$, thus if the spacing between the beamlets in Θ are too wide the spatial power distribution is allowed to deviate between adjacent beamlet angles (as shown in $P = 30$ trace in Figure 4.20). The

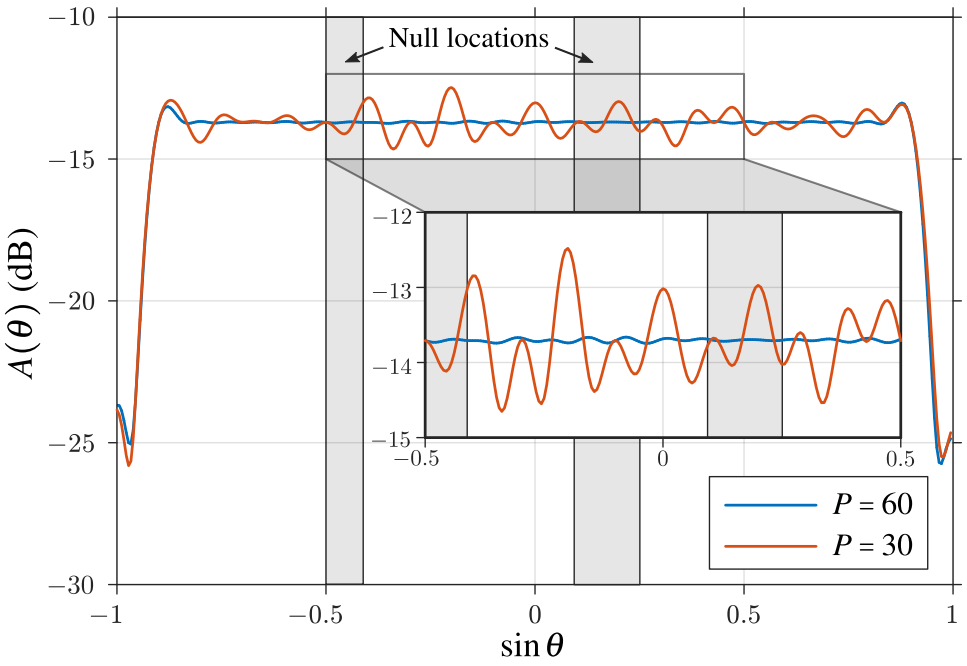

Figure 4.20: Aggregate beampattern $A(\theta)$ (in dB) from (3.21) of wideband $\left([\%\text{BW}]_{98\%} = 40\%\text{ bandwidth}\right)$ wide beam MIMO emission versus $\sin\theta$ for with $P = 60$ beamlets (blue) and $P = 30$ beamlets (red) for an $M = 30$ element ULA with $f_{\text{E}} = f_{\text{c}} + B_{98\%}/2$.

spatial extent of the two nulled regions is shown in gray. The energy compensation after zeroing the desired spectral magnitudes in these directions is effective in maintaining a constant energy level over the nulled regions even though energy is removed.

The spatial autocorrelation $|\chi_{\text{a}}(\tau,\theta)|^2$ from (4.55) for normalized delays $\tau/T \in [-0.5, 0.5]$ is shown in Figure 4.21. Note that the peaks of the autocorrelation are normalized to indicated to losses associated with spreading energy over space (i.e. 0 dB corresponds to a standard beamformed transmission). The mainlobe of the autocorrelation from spatial regions $\sin\theta = -0.6$ to $\sin\theta = -0.3$ is broadened slightly due the null placement between $\sin\theta = -0.5$ and $\sin\theta = -0.42$. This null lies entirely within the bandwidth of the emission thus has a larger effect on the resulting correlation response compared to the second null which lies in the spectral roll-off of the emission.

Figure 4.22 depicts the maximum angular cross-correlation $\max_{\tau}\{|\chi_{\text{s}}(\tau,\theta,\vartheta)|^2\}$ as a function of θ and ϑ. A maximum was taken over τ instead of showing the $\tau = 0$ to depict the largest cross-correlation sidelobe response that could leak into the matched filtered and receive beamformed response. Again, the loss due to spreading energy in space is incorporated in the maximum of

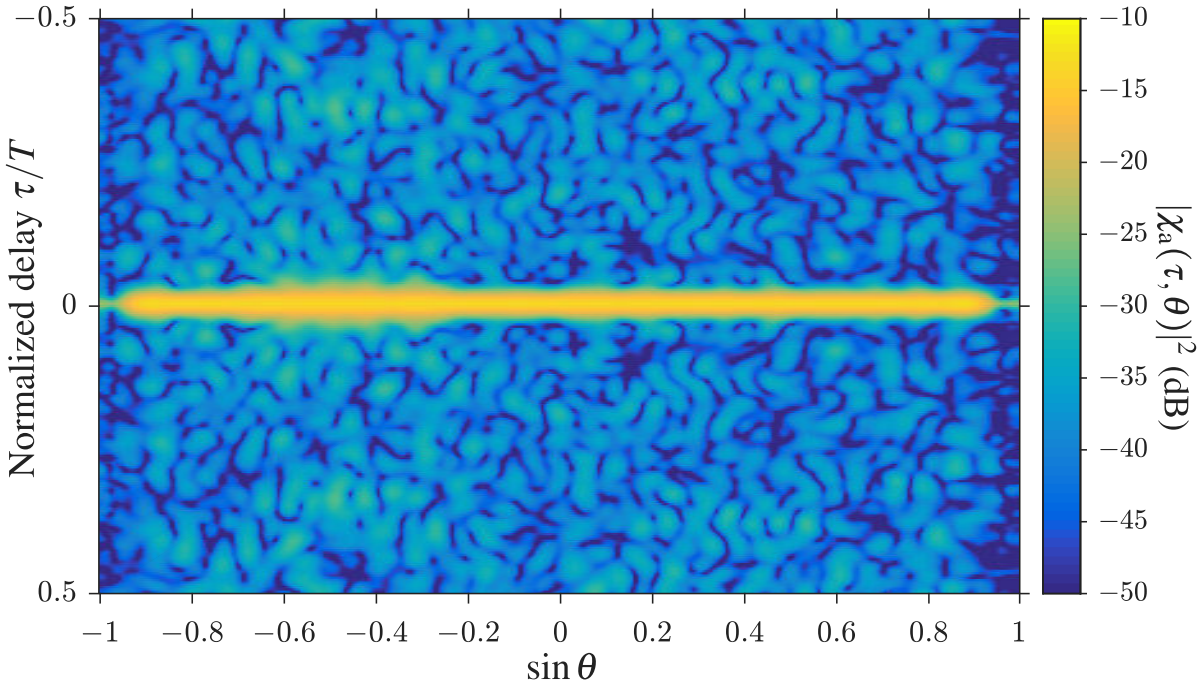

Figure 4.21: Spatial autocorrelation function $|\chi_a(\tau,\theta)|^2$ (in dB) from (4.55) for wideband $\left([\%\text{BW}]_{98\%} = 40\%\text{ bandwidth}\right)$ wide beam MIMO emission versus $\sin\theta$ for normalized delay $\tau/T \in [-0.5\ 0.5]$. ©2017 IEEE

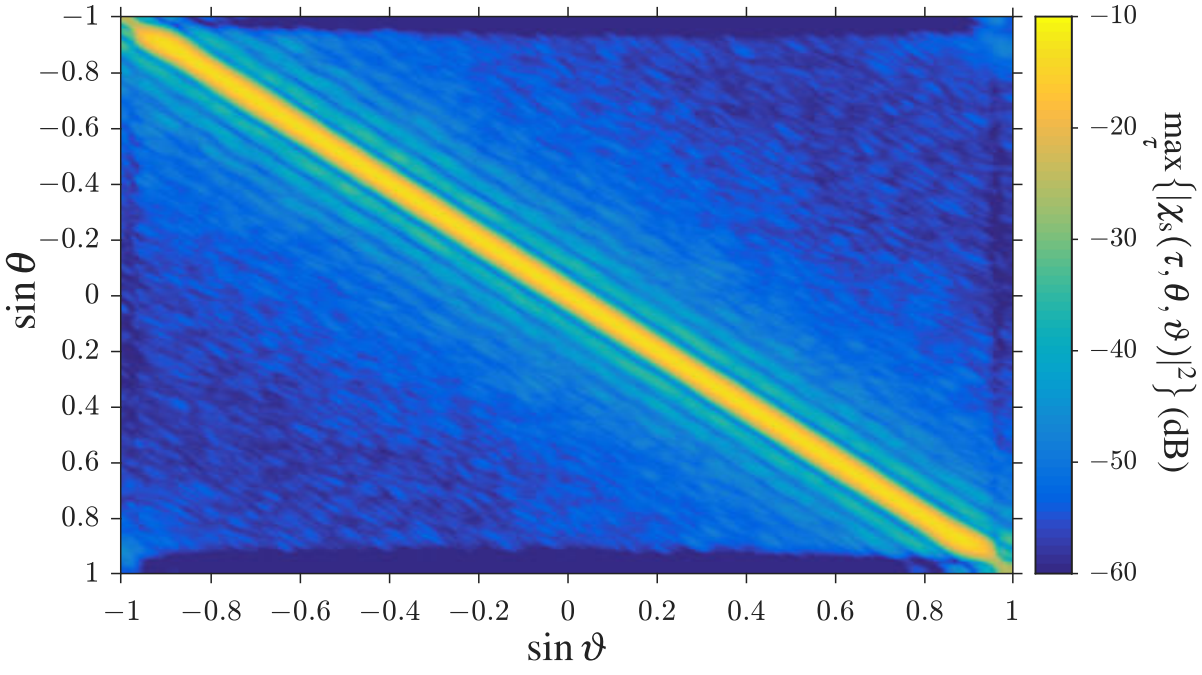

Figure 4.22: Maximum angular cross-correlation $\max_\tau\left\{|\chi_s(\tau,\theta,\vartheta)|^2\right\}$ for wideband ($[\%\text{BW}]_{98\%} =$ 40% bandwidth) wide beam MIMO emission as a function of $\sin\theta$ and $\sin\vartheta$ for an $M = 30$ element ULA with $f_E = f_c + B_{98\%}/2$. ©2017 IEEE

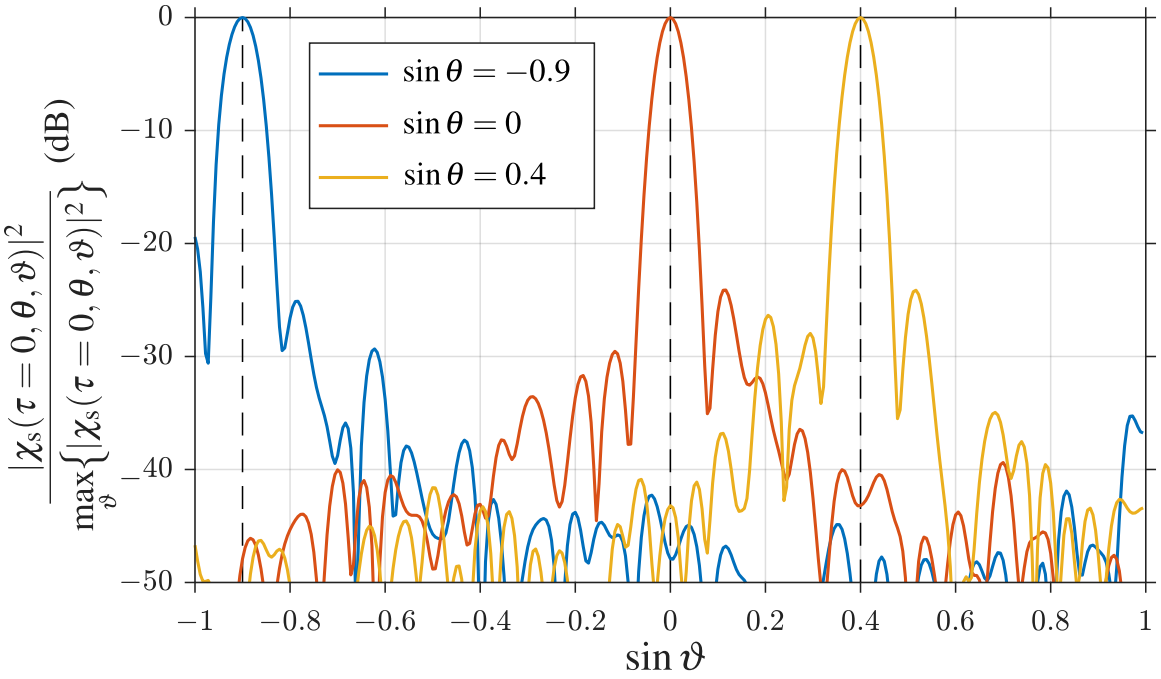

Figure 4.23: Peak-normalized angle-delay ambiguity function at $\tau/T = 0$ for wideband $\left([\%\text{BW}]_{98\%} = 40\%\text{ bandwidth}\right)$ wide beam MIMO emission versus $\sin\vartheta$ for the transmit angles $\sin\theta = -0.9$ (blue), $\sin\theta = 0$ (red), and $\sin\theta = 0.4$ (yellow). ©2017 IEEE

the diagonal. Recall from Section 3.1.3.2 that for the narrowband array the nominal resolution and spatial ambiguities (sidelobes) are dictated by the receive beamformer (beam factor) and are improved upon when spatial diversity is introduced (diversity factor). For an $M = 30$ element ULA, the first sidelobe of the nominal array pattern is approximately 13.2 dB down from the peak response. In Figure 4.22, the first sidelobe is (on average) approximately 25 dB down from the peak, thus illustrating the diversity improvement in spatial ambiguity. Recall from Section 3.1.3.2 that the expected level of the first spatial ambiguity for an orthogonal (in terms of inner product) MIMO emission is "double" (in dB) that of the nominal phased array response for uniform array tapering, thus would be 26.4 dB down from the peak for this case.

Figure 4.23 shows the peak-normalized angle-delay ambiguity function versus $\sin\vartheta$ for the transmit directions $\sin\theta \in \{-0.9, 0, 0.4\}$ at $\tau/T = 0$. These are the expected spatial response for theoretical scatterers in these direction in the absence of noise. The expected spatial resolution improvement for an orthogonal MIMO *narrowband* emission is $1/\sqrt{2}$ for a uniform linear array with uniform array tapering. This resolution improvement is ambiguous for wideband arrays due to

Table 4.2: Improvement/degradation ratio of 3 dB spatial resolution for Case 1 transmission

		$\sin\theta = -0.9$	$\sin\theta = 0$	$\sin\theta = 0.4$
	$[\Delta\bar{u}]_{3dB}$	0.06053	0.05087	0.05116
$f = 0.8f_c$	0.08910	0.6793	0.5709	0.5742
$f = f_c$	0.07128	0.8492	0.7137	0.7177
$f = 1.2f_c$	0.05940	1.019	0.8564	0.8613

the beampattern deformation over the operating band. Table 4.2 shows the 3 dB spatial resolution $[\Delta\bar{u}]_{3dB}$ for these scatterer locations as well as the nominal spatial resolutions for $f = 0.8f_c$, $f = f_c$, and $f = 1.2f_c$. The ratio of the spatial resolutions are also provided where a value < 1 indicates an improvement of spatial resolution while > 1 indicated a resolution degradation. Intuitively, the nominal wideband resolution should near the resolution of the center frequency $f = f_c$ which is the assumption for narrowband transmissions. For all three beams, the spatial resolution improves compared to the nominal resolution at the center frequency with the only comparative resolution degradation occuring in the $\sin\theta = -0.9$ beam at the high in-band frequency $f = 1.2f_c$.

4.2.7.3 Case 2: Three-beam Scenario Results

Figure 4.24 shows the wideband spectrum $|G_{pb}(f,\theta)|^2$ (dB) of Case 2 where $P_B = 3$ discrete beams are optimized in the directions $\sin\theta = -0.71$, $\sin\theta = 0$, and $\sin\theta = 0.17$ (e.g. for simultaneous tracking), each with a Gaussian spectral shape and the $\sin\theta = 0$ beam is designed to have 3 dB higher power than the other two beams to illustrate a higher transmit priority level. The space-frequency null bounded between $f/f_c = 1.2$ and $f/f_c = 1.4$ and between $\sin\theta = 0.1$ and $\sin\theta = 0.25$ can also be observed in this figure. This beam scenario has FRP = 0.0188 though is not at risk of placing significant energy in the reactive region due to the beamlet locations.

Figure 4.25 shows the aggregate beampattern $A(\theta)$ after emission optimization. The peaks of the $\sin\theta = -0.71$ and $\sin\theta = 0.17$ beams exhibit relative powers of −6.25 dB while that of the $\sin\theta = 0$ beam is −3.23 dB which is within 0.02 dB of the 3 dB relative power constraint. The null location (shown in gray) is shown to not effect the power level of the $\sin\theta = 0.17$ beamlet. Simultaneous transmission of multiple directive transmit beams does produce a single

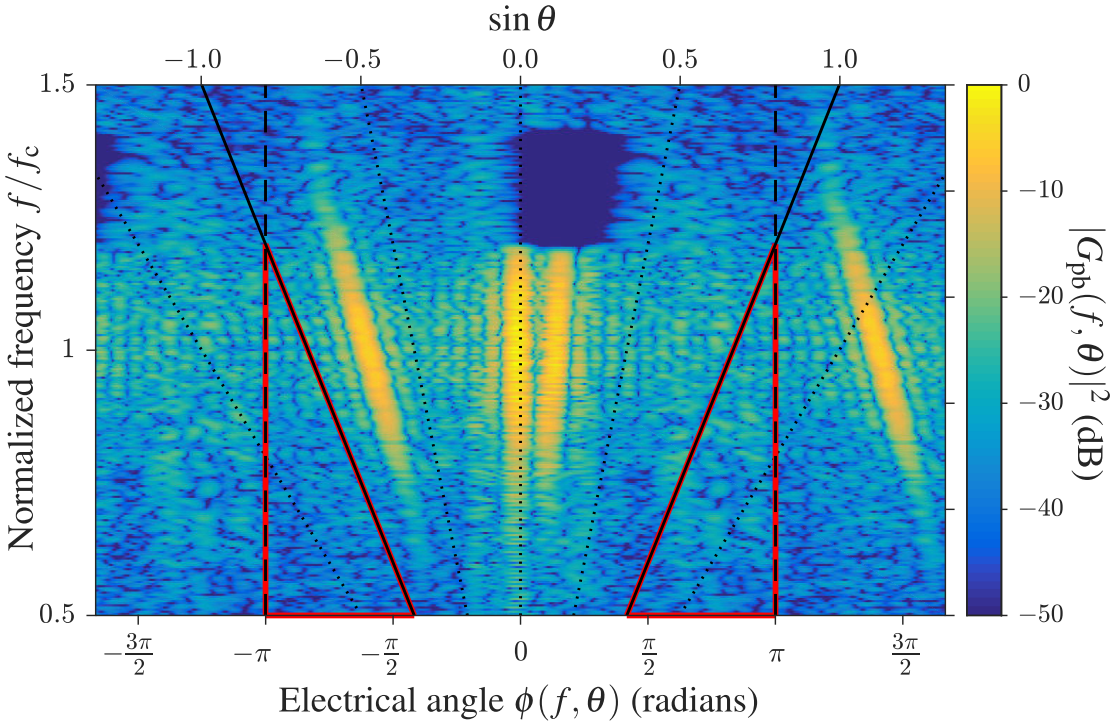

Figure 4.24: Spectrum $|G_{\text{pb}}(f,\theta)|^2$ (in dB) from (4.7) of wideband ($[\%\text{BW}]_{98\%} = 40\%$ bandwidth) multi-beam emission versus electrical angle $\phi(f,\theta)$ for an $M = 30$ element ULA with $f_{\text{E}} = f_{\text{c}} + B_{98\%}/2$. The reactive region is bounded inside the red triangles with FRP = 0.0188 from (4.26). ©2017 IEEE

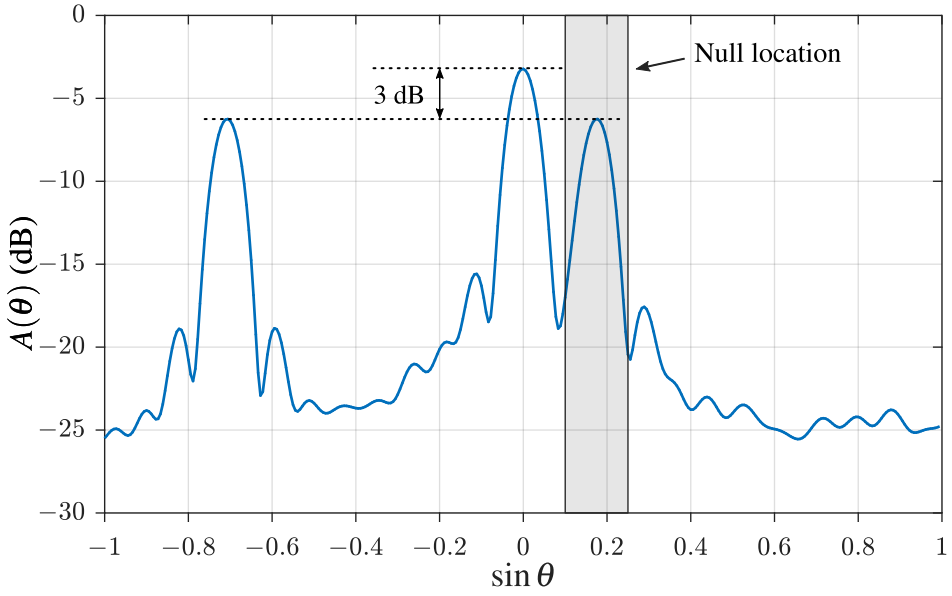

Figure 4.25: Aggregate beampattern $A(\theta)$ (in dB) from (3.21) of wideband ($[\%\text{BW}]_{98\%} = 40\%$ bandwidth) multi-beam emission versus $\sin\theta$ for an $M = 30$ element ULA with $f_{\text{E}} = f_{\text{c}} + B_{98\%}/2$.

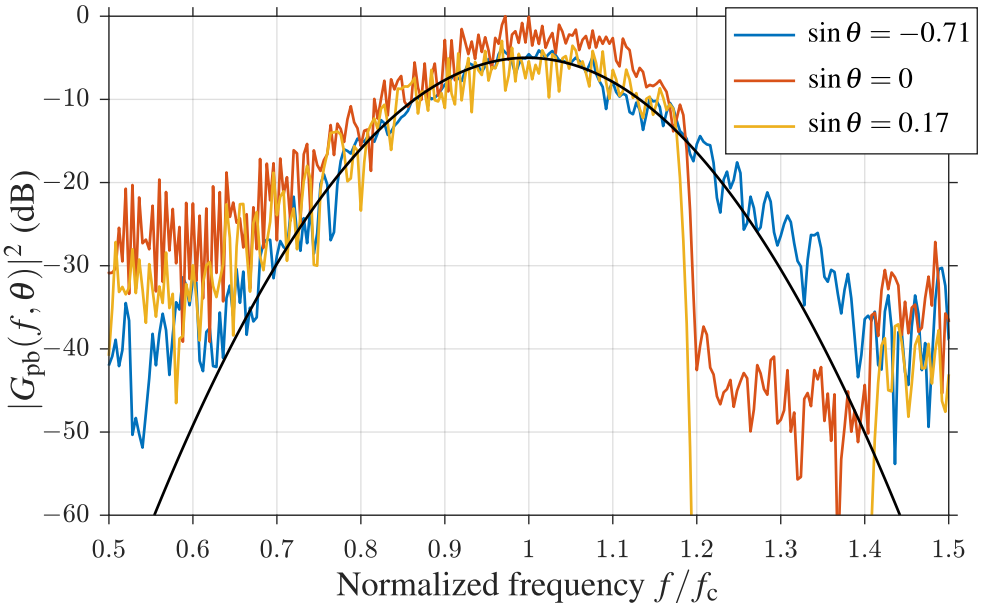

Figure 4.26: Emission spectrum $|G_{\text{pb}}(f,\theta)|^2$ (in dB) from (4.7) for wideband ($[\%\text{BW}]_{98\%} = 40\%$ bandwidth) multi-beam emission versus normalized frequency f/f_{c} of the $P_{\text{B}} = 3$ beams in the directions $\sin\theta = -0.71$ (blue), $\sin\theta = 0$ (red), and $\sin\theta = 0.17$ (yellow) and the spectral window used for design (black). ©2017 IEEE

pulse loss in transmitted energy due to spreading energy in space. Though by transmitting the beams simultaneously, the total energy emitted in these directions would be close to that of a traditional phased array over a dwell period. Furthermore, the simultaneous beampattern in Figure (4.25) has a continuously customizable relative power level between the beam directions which would be difficult for a scenario where the resource time is split between the three locations.

Figure 4.26 shows the resulting power spectrum $|G_{\text{pb}}(f,\theta)|^2$ for the three beam directions $\sin\Theta \in \{-0.71, 0, 0.17\}$ along with the Gaussian spectral window used in the design (shown in black). All three beams approximate the form of the Gaussian template (a true match cannot be achieved due to the constant amplitude constraint and finite pulse duration). The $\sin\theta = 0.17$ beam conflicts with the nulled region thus the Gaussian template for that direction was altered accordingly. The $\sin\theta = 0$ spectrum also has a dip in the nulled region due to the increase in width of the null caused by the RUWO nulling stage (as discussed in Figure 4.19).

Figure 4.27 displays the resulting spatial autocorrelation $|\chi_{\text{a}}(\tau,\theta)|^2$ from (4.55) for the three beam directions. The peak sidelobe levels relative to their respective mainlobes are −26 dB for

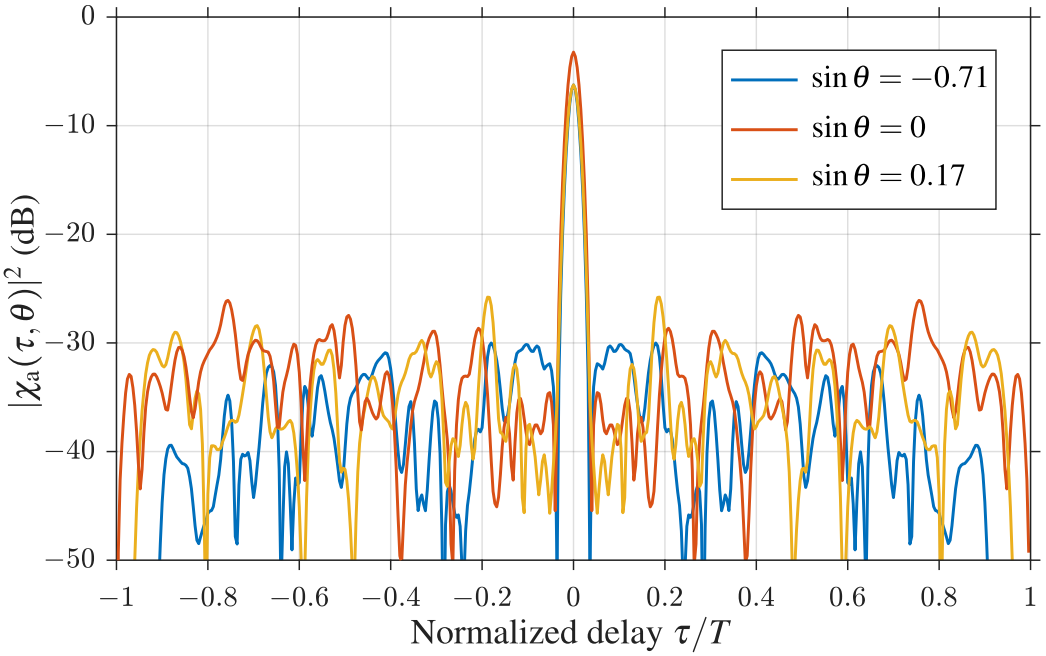

Figure 4.27: Spatial autocorrelation function $|\chi_a(\tau,\theta)|^2$ (in dB) from (4.55) for wideband ($[\%\text{BW}]_{98\%} = 40\%$ bandwidth) multi-beam emission of the $P_B = 3$ beams in the directions $\sin\theta = -0.71$ (blue), $\sin\theta = 0$ (red), and $\sin\theta = 0.17$ (yellow). ©2017 IEEE

$\sin\theta = -0.71$, -22.5 dB for $\sin\theta = 0$, and -19.45 dB for $\sin\theta = 0.17$. The slight sidelobe increase for the $\sin\theta = 0.17$ beam is a result of the null in its spectrum. The resulting high sidelobe level can be reduced by coherently processing multiple pulse agile waveforms [59], or by leveraging adaptive/non-adaptive mismatch filter receive processing [81, 143].

Figure 4.28 depicts the maximum temporal cross-correlation of the angle-delay ambiguity function $\max_{\tau}\{|\chi_s(\tau,\theta,\vartheta)|^2\}$. The responses from the three beamlets are clearly shown on the diagonal of the plot. The peak-normalized, $\tau/T = 0$ cut of the angle-delay ambiguity function versus $\sin\vartheta$ for the transmit angles $\sin\theta = -0.71$, $\sin\theta = 0$, and $\sin\theta = 0.17$ is shown in Figure 4.29. The desired beam locations are indicated by the black, vertical dashed lines. Unlike the Case 1 transmission which operated in a wide beam MIMO mode, the spatial resolution and spatial sidelobe level for Case 2 are not improved. The difference in resultion lies in the correlation levels of the emission *around* that beam. Because the beams are widely-separated, the spatial ambiguity level and spatial resolution remain similar to that of a standard coherent beamformed emission. Table 4.3 shows the 3 dB spatial resolutions of the three theoretical target locations and

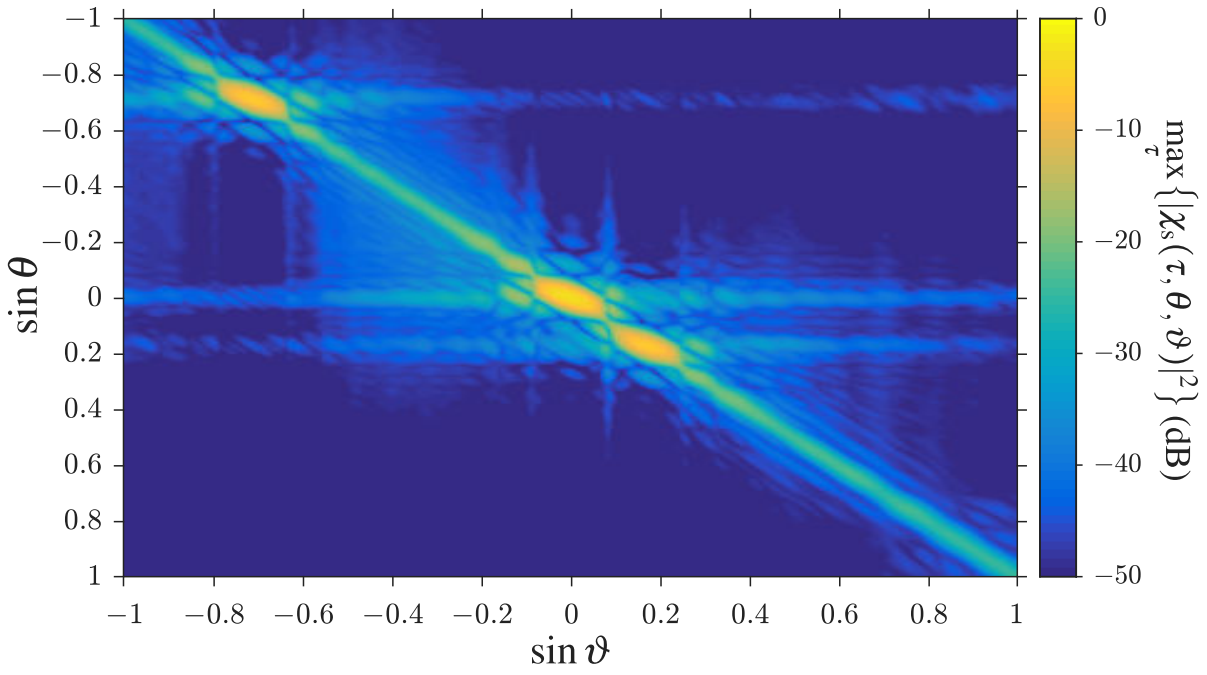

Figure 4.28: Maximum angular cross-correlation $\max_{\tau}\left\{|\chi_{\mathrm{s}}(\tau,\theta,\vartheta)|^2\right\}$ for wideband ($[\%\mathrm{BW}]_{98\%}$ = 40% bandwidth) multi-beam emission as a function of $\sin\theta$ and $\sin\vartheta$ for an $M = 30$ element ULA with $f_{\mathrm{E}} = f_{\mathrm{c}} + B_{98\%}/2$. ©2017 IEEE

Table 4.3: Improvement/degradation ratio of 3 dB spatial resolution for Case 2 transmission

		$\sin\theta = -0.71$	$\sin\theta = 0$	$\sin\theta = 0.17$
	$[\Delta\bar{\mathrm{u}}]_{3\mathrm{dB}}$	0.06961	0.06937	0.06758
$f = 0.8f_{\mathrm{c}}$	0.08910	0.7813	0.7786	0.7585
$f = f_{\mathrm{c}}$	0.07128	0.9766	0.9732	0.9481
$f = 1.2f_{\mathrm{c}}$	0.05940	1.172	1.168	1.138

the nominal response for the low, center, and high frequencies in the bandwidth. As expected, each of the beams are near to the nominal spatial resolution of the center frequency due to the lack in spatial diversity in the vicinity of each beam.

4.2.7.4 Case 3: Wide Beam + Secondary Beam Scenario Results

Finally, Figure 4.30 shows the wideband spectrum $|G_{\mathrm{pb}}(f,\theta)|^2$ (dB) for Case 3 where a moderately wide beam is designed to lie between $\sin\theta = -0.5$ and $\sin\theta = 0.5$ with a Gaussian spatial power

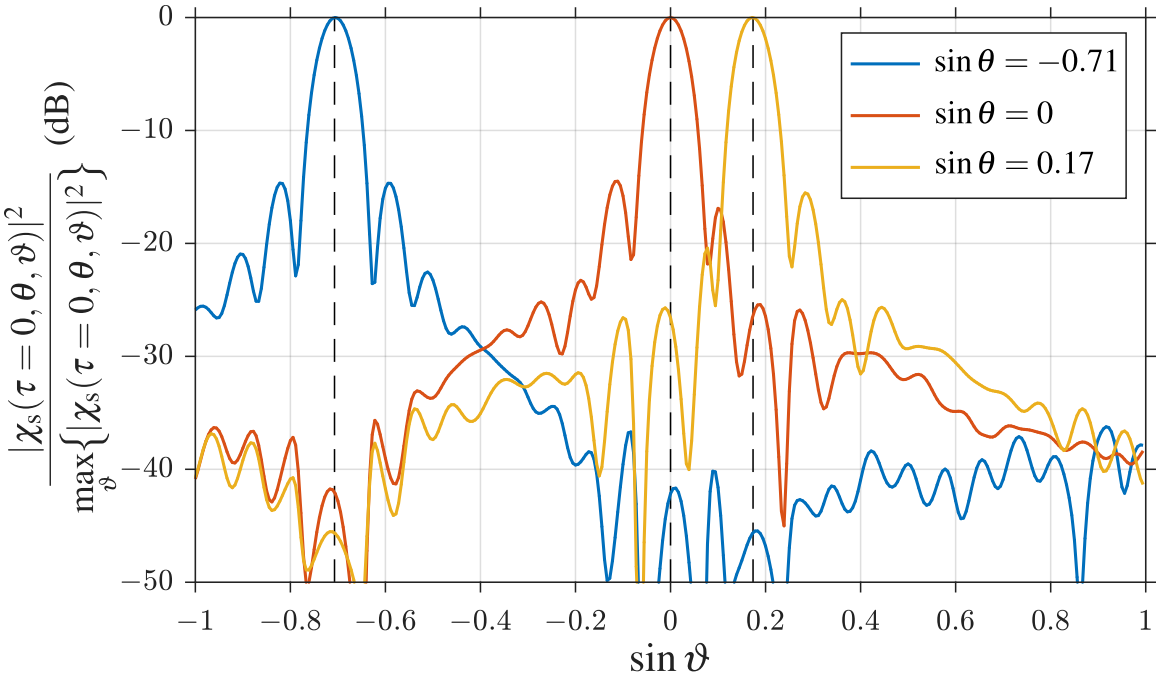

Figure 4.29: Peak-normalized angle-delay ambiguity function at $\tau/T = 0$ for wideband ($[\%\text{BW}]_{98\%}$ = 40% bandwidth) multi-beam emission versus $\sin\vartheta$ for the transmit angles $\sin\theta = -0.71$ (blue), $\sin\theta = 0$ (red), and $\sin\theta = 0.17$ (yellow), corresponding to the $P_B = 3$ beam directions. ©2017 IEEE

distribution[6] (e.g. for SAR or surveillance) as well as a narrow secondary beam at $\sin\theta = 0.75$ that is designed to be 2 dB larger than the peak power of the wide beam (e.g. for tracking). The wide beam was approximated using 30 equally spaced beamlets over the angular region makings a total of $P_B = 31$ beamlets including the secondary beam. All beams are designed to have a Gaussian spectral shape and the same null constraints as in Case 1. The beamlet locations place the energy away from the invisible space thus the FRP = 0.0174.

The aggregate beam pattern is shown in Figure 4.31. The discrete beam at $\sin\theta = 0.75$ is effectively set 2 dB above the wide beam. The wide beam has the desired Gaussian spatial power distribution, and the beamlet compensation is effective in accounting for the energy removed by zeroing the desired spectrums within the nulled region.

The spatial autocorrelation for normalized delays $\tau/T \in [-0.5,\ 0.5]$ can be seen in Figure 4.32. Again, it is observed that the mainlobe of the autocorrelation between $\sin\theta = -0.6$ and $\sin\theta = -0.3$

[6]The Gaussian spatial power distribution is only included to showcase the variability of the possible spatial beampattern designs. Ideally a spatial priority metric would be used to determine the desired energy placement.

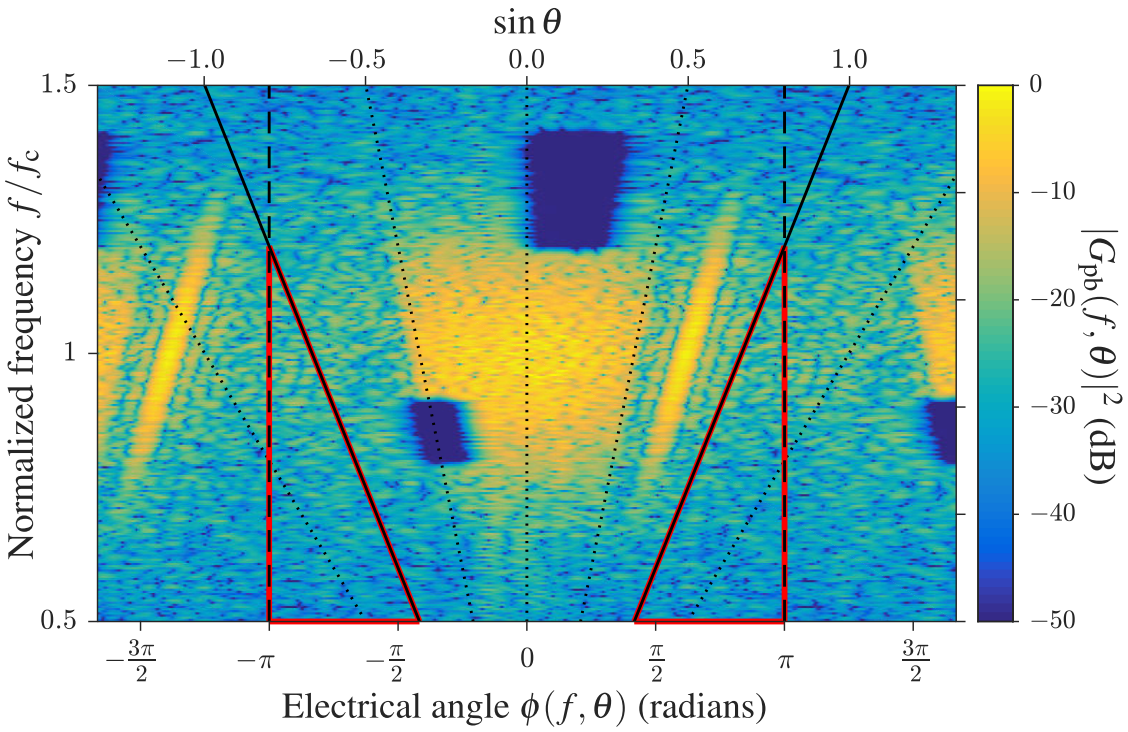

Figure 4.30: Spectrum $|G_{\text{pb}}(f,\theta)|^2$ (in dB) from (4.7) of wideband $\big([\%\text{BW}]_{98\%} = 40\%$ bandwidth$\big)$ wide beam + secondary beam emission versus electrical angle $\phi(f,\theta)$ for an $M = 30$ element ULA with $f_{\text{E}} = f_{\text{c}} + B_{98\%}/2$. The reactive region is bounded inside the red triangles with FRP = 0.0174 from (4.26). ©2017 IEEE

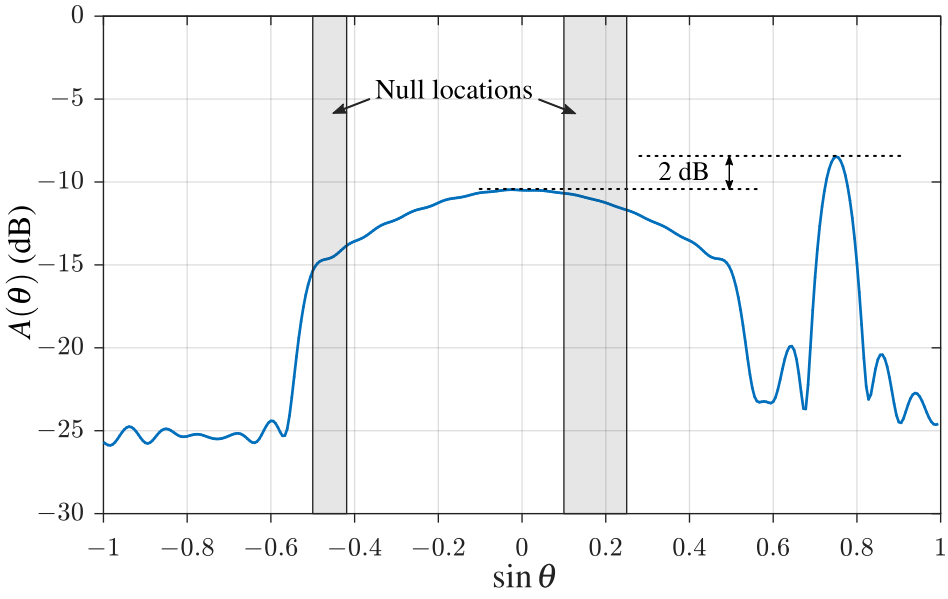

Figure 4.31: Aggregate beampattern $A(\theta)$ (in dB) from (3.21) of wideband $\big([\%\text{BW}]_{98\%} = 40\%$ bandwidth$\big)$ wide beam + secondary beam emission versus $\sin\theta$ for an $M = 30$ element ULA with $f_{\text{E}} = f_{\text{c}} + B_{98\%}/2$.

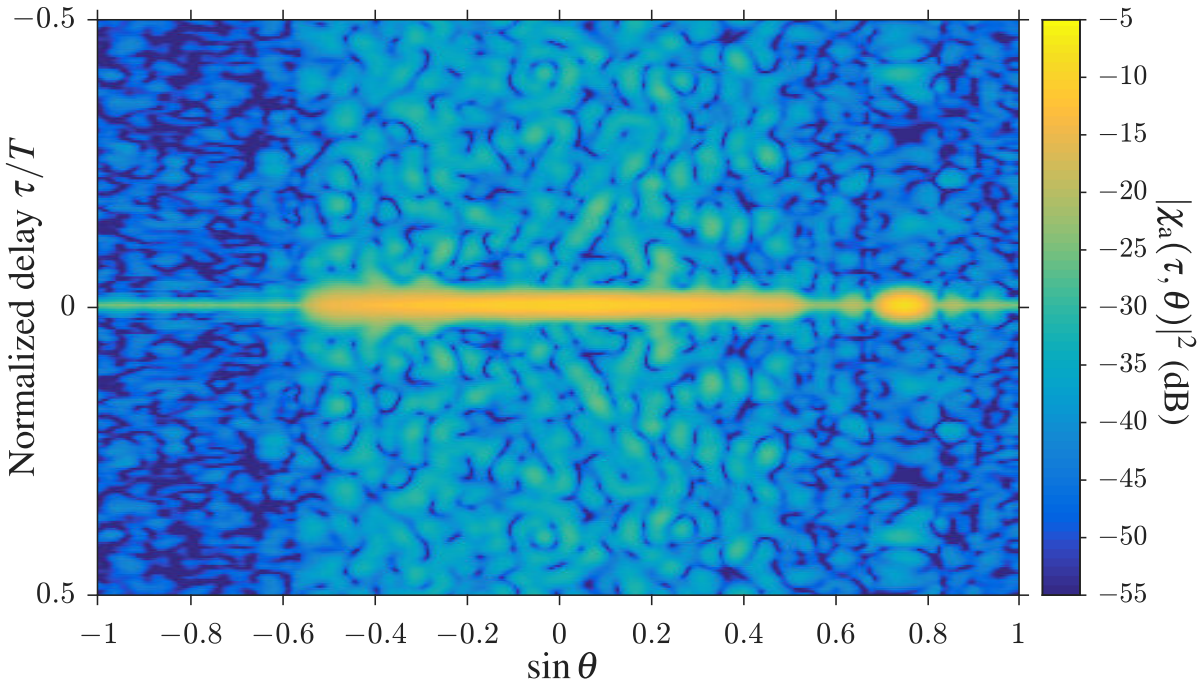

Figure 4.32: Spatial autocorrelation function $|\chi_a(\tau,\theta)|^2$ (in dB) from (4.55) for wideband $\left([\%\text{BW}]_{98\%} = 40\%\text{ bandwidth}\right)$ wide beam + secondary beam emission versus $\sin\theta$ for normalized delay $\tau/T \in [-0.5\ 0.5]$. ©2017 IEEE

is slightly broadened due to the presence of the null in the bandwidth of the emission. The range sidelobes of the narrow secondary beam, on average, are lower than any angle within the wide beam. This difference in sidelobe level arises because the wide beam design involves the conflicting goals of spatial decorrelation and spectral shaping of adjacent beamlets thus cannot achieve the spectral match of the isolated beam.

The maximum angular cross-correlation $\max_\tau\{|\chi_s(\tau,\theta,\vartheta)|^2\}$ is shown in Figure 4.33. The peak cross-correlation response is clearly larger in the vicinity of the narrow secondary beam than it is near the wide beam. Expanding on this result, Figure 4.34 shows the peak-normalized angle-delay ambiguity function at $\tau/T = 0$ versus $\sin\vartheta$ for the transmit angles $\sin\theta = \{0, 0.4, 0.75\}$. Note the difference in ambiguity sidelobe level and shape of the mainlobe for the three directions. The angles $\sin\theta \in \{0, 0.4\}$ reside within the wide beam and thus have an improved spatial resolution and decreased spatial ambiguities compared to the secondary beam in $\sin\theta = 0.75$, whose resolution and sidelobe level are comparable to a standard beamforming ambiguity function. Table 4.4 shows the 3 dB spatial resolutions of the three theoretical target locations and the nominal response for

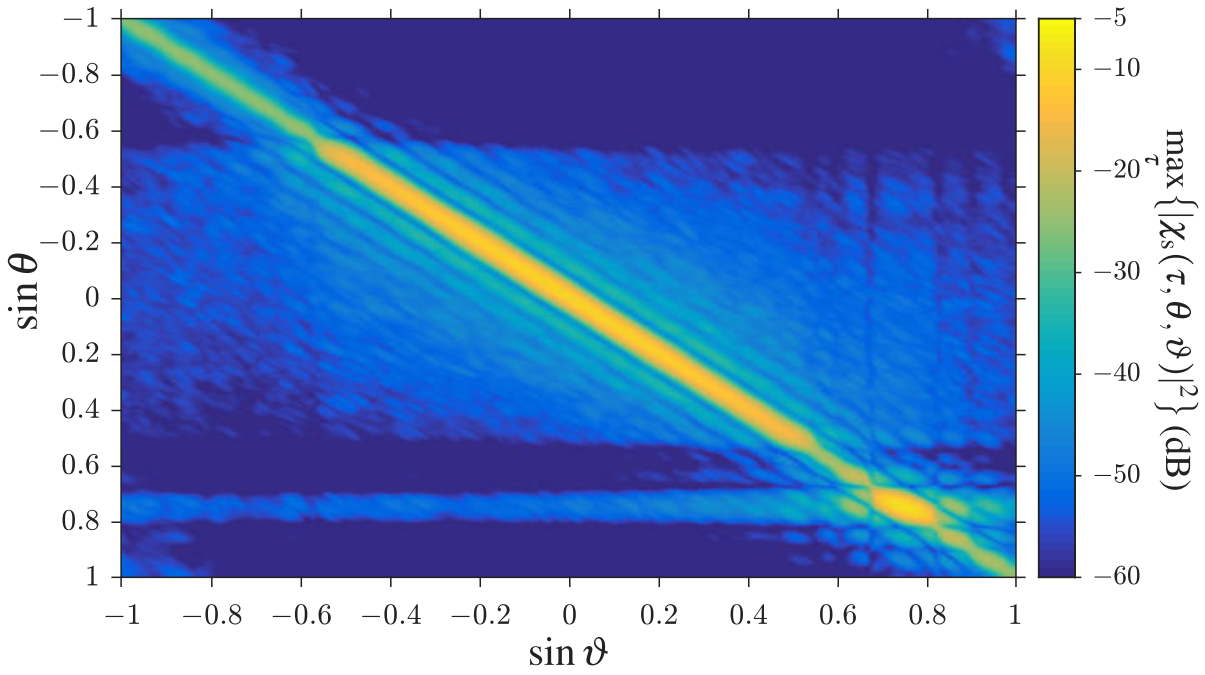

Figure 4.33: Maximum angular cross-correlation $\max_{\tau}\left\{|\chi_{\mathrm{s}}(\tau,\theta,\vartheta)|^2\right\}$ for wideband ($[\%\mathrm{BW}]_{98\%}$ = 40% bandwidth) wide beam + secondary beam emission as a function of $\sin\theta$ and $\sin\vartheta$ for an $M = 30$ element ULA with $f_{\mathrm{E}} = f_{\mathrm{c}} + B_{98\%}/2$. ©2017 IEEE

Table 4.4: Improvement/degradation ratio of 3 dB spatial resolution for Case 3 transmission

		$\sin\theta = 0$	$\sin\theta = 0.4$	$\sin\theta = 0.75$
	$[\Delta\bar{\mathrm{u}}]_{3\mathrm{dB}}$	0.05280	0.05087	0.06913
$f = 0.8f_{\mathrm{c}}$	0.08910	0.5926	0.5701	0.7759
$f = f_{\mathrm{c}}$	0.07128	0.7407	0.7137	0.9698
$f = 1.2f_{\mathrm{c}}$	0.05940	0.8889	0.8564	1.164

the low, center, and high frequencies in the bandwidth. The $\sin\theta = 0$ and $\sin\theta = 0.4$ beam clearly have an improved spatial resolution while the $\sin\theta = 0.75$ beam is near to the nominal response of the center frequency. The use of multiple proximate beamlets in the design of the wide beam results in enhanced spatial decorrelation and therefore an improvement in both spatial resolution and ambiguity sidelobe level.

The emission design cost function $\mathcal{J}_{\mathrm{B}}(\mathbf{s}_{\mathrm{v},i})$ from (4.37) is shown in Figure 4.35 versus iteration index i for Case 1 (blue), Case 2 (red), and Case 3 (yellow). This curve indicates that the algorithm improves upon the desired goal of space-frequency beampattern matching over time and does not diverge during the optimization. All calculations throughout the optimization are

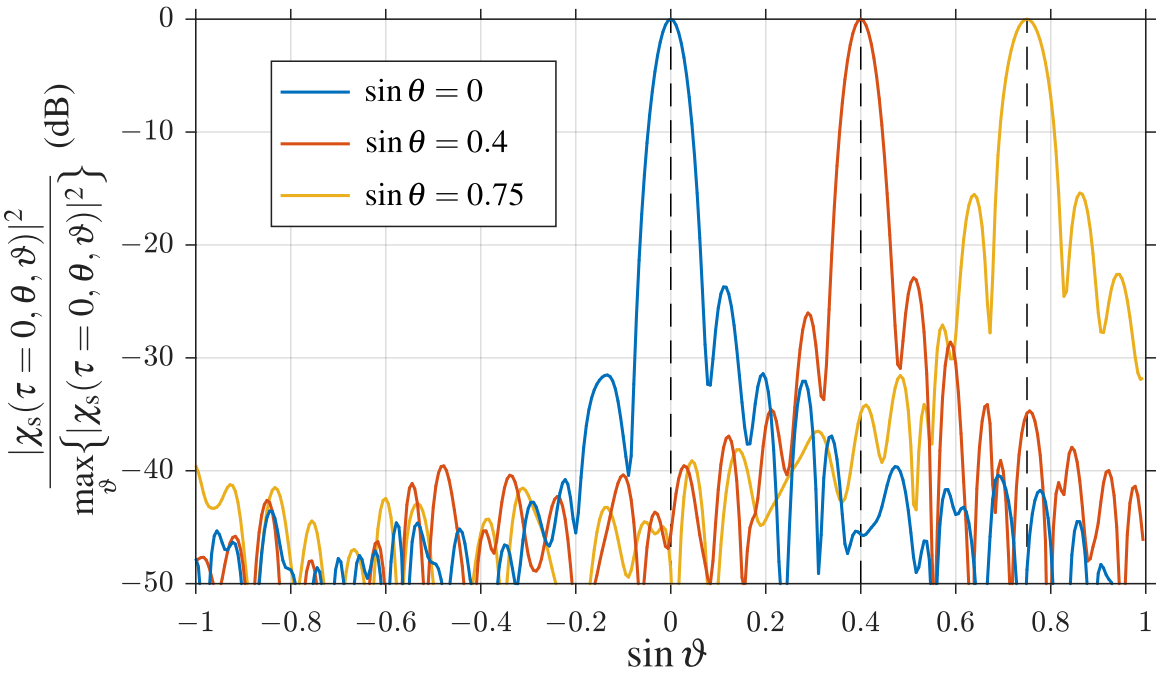

Figure 4.34: Peak-normalized angle-delay ambiguity function at $\tau/T = 0$ for wideband $\left([\%\mathrm{BW}]_{98\%} = 40\%\ \text{bandwidth}\right)$ wide beam + secondary beam emission versus $\sin\vartheta$ for the transmit angles $\sin\theta = 0$ (blue) and $\sin\theta = 0.4$ (red), directions within the wide beam, and $\sin\theta = 0.75$ (yellow), the secondary beam direction. ©2017 IEEE

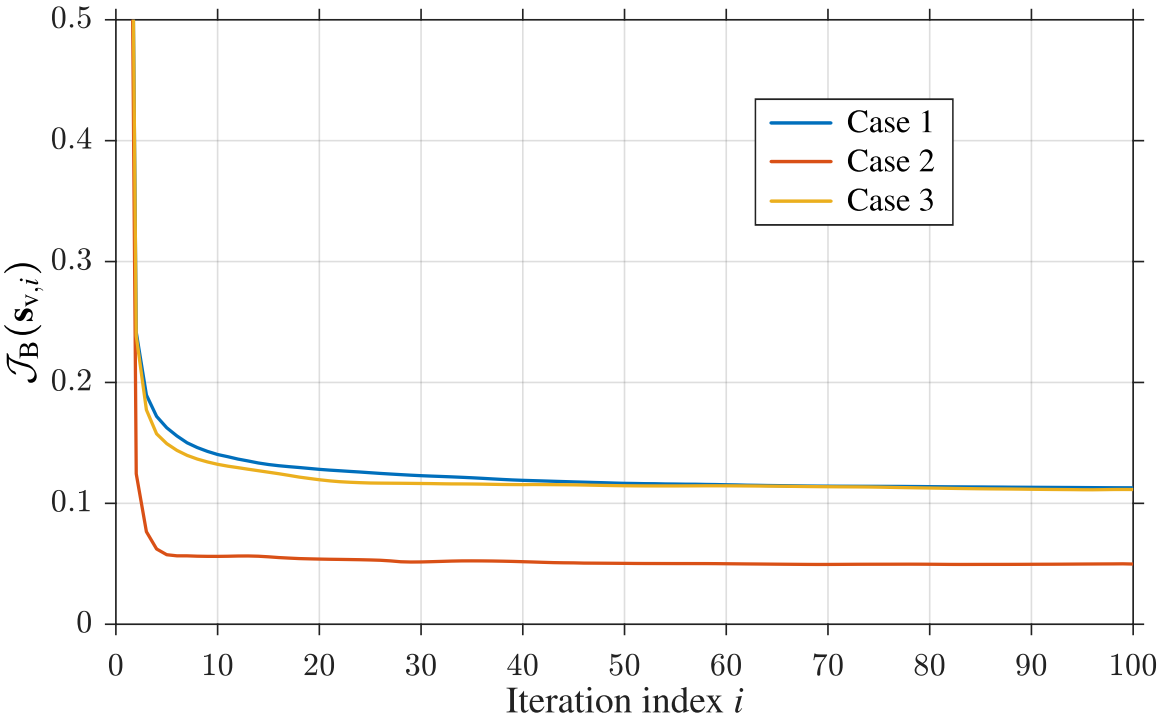

Figure 4.35: Emission design cost function $\mathcal{J}_B(\mathbf{s}_{v,i})$ from (4.37) versus iteration index i ($\Phi = 100$ iterations; $K = 20$ nulling iterations) for Case 1 (blue), Case 2 (red), and Case 3 (yellow).

either summations, phase retrievals, or matrix transformations, thus this heuristic design method is robust to diverging.

4.2.8 Summary

An iterative, wideband spatially-diverse optimization scheme for far-field emission design has been presented that optimizes the spectral content in certain predefined angles denoted as beamlets. Space-frequency nulling is also implemented inside the iterative process via the reiterative uniform-weight optimization (RUWO) method. The design process avoids placing energy in the invisible space by maximizing power emitted into the visible space, thus avoiding reactive power that could potentially damage the radar. The resulting waveforms are constrained to be constant-modulus and can be implemented as continuous-time PCFM waveforms. Three different scenarios have been examined to show the versatility of the design scheme to simultaneously perform multiple different functions. The results demonstrate that for a randomized waveform initialization, the subsequent wide beam emission design provides greater spatial decorrelation, and thus finer spatial resolution and lower spatial ambiguity sidelobes than a narrow beam emission, though the latter can achieve better waveform autocorrelation properties (lower range sidelobes).

4.3 Simultaneous Radar and Communications Emissions from a Common Aperture

The ability to independently control the waveforms emitted from the elements comprising an antenna array enables the design of fast-time emissions that are spatially dependent by virtue of a significant increase in design degrees-of-freedom. This array structure, known as a fully digital array radar (DAR), facilitates the execution of multiple functions concurrently by the same system.

A portion of the text in Section 4.3 is taken from "Simultaneous radar and communications emissions from a common aperture, Part I: Theory" by McCormick et al. printed in *2017 IEEE Radar Conference Proceedings* in May 2017.

An early example of this idea was the advanced multi-function RF concept (AMRFC) [136] that introduced an adaptable sub-arrayed arrangements to achieve multiple functions simultaneously. The capability of the fully digital array expands on this notion by allowing control over the waveforms emitted by every antenna element so as to achieve a desired emission structure through the coherent combination of the transmitted waveforms in the far-field of the antenna array.

Through careful design of these waveforms, the fully digital array can be utilized to simultaneously transmit spatially-separated radar and communication signals that have the same time and spectral support (see Figure 4.36). This type of dual-function emission is a particular form of spatially-diverse beampattern design (e.g. [17,119,122,144,145]). In [24], an iterative waveform optimization method denoted as far-field radiated emission design (FFRED) was introduced that generates pulsed spatially-diverse waveforms, the far-field combination of which realizes simultaneous radar and communications beams, along with the particular constraint that the waveforms are physically realizable and amenable to a high-power amplifier (HPA); i.e. constant amplitude and well contained spectrally (see [38, 59, 90] and Section 2.2.2). In [25], this method was experimentally demonstrated on the Air Force Research Lab's four-channel software-defined radar testbed BEEMER (Baseband-digital at Every Element MIMO Experimental Radar) [110] and are also presented here.

In [24], it was shown that to achieve simultaneous emission of two distinct signals in different spatial directions through the use of constant amplitude spatially-diverse waveforms, one must also consider the totality of signals in the orthogonal complement directions. In other words, a portion of the overall energy must be emitted into the spatial regions that are not the desired radar or communications directions (beyond the amount one would normally associate with sidelobes). An interesting trade-off then emerges between the power efficiency gained by enforcing the constant amplitude constraint (and associated use of efficient power amplifiers) and the efficiency lost due to allocation of power in the orthogonal space. This trade space is explored in this section by examining the percentage of power emitted into the orthogonal space as well as through the definition of a average directed power (ADP) metric that quantifies the power efficiency of a set of

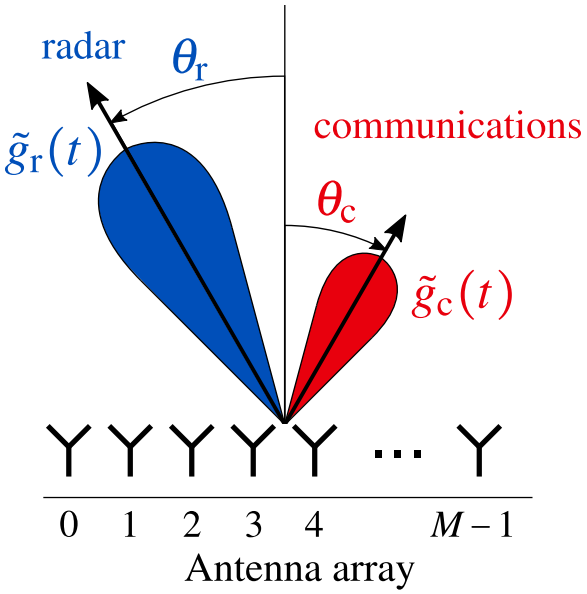

Figure 4.36: Illustration of simultaneous radar and communication signals emitted towards directions θ_r and θ_c, respectively.

waveforms given a simple amplifier model. Furthermore, how this orthogonal complement power manifests itself in the spatial and spectral domains is also examined. As a result of this orthogonal power, it was observed in [24] that a side effect of the design procedure is that the time domain signals in the directions away from the communication direction are naturally uncorrelated with the intended communication signal. This behavior is examined further by forming bit error rate (BER) versus spatial angle plots for various relative radar/communications beam spacings and power levels.

4.3.1 Assumptions and Restrictions

The FFRED approach generates a set of constant-amplitude FM waveforms that, when emitted from a digital array, coherently combine in the far-field to realize the intended radar and communications signals that are separated in space. In this section, both non-constant modulus and constant-modulus waveforms are considered to compare the energy efficiency between the results. A simple amplifier model is defined in Section 4.3 to model the "power back-off" needed with non-constant amplitude waveforms to minimize signal distortion.

The active antenna patterns $F_m(f,\theta,\varphi)$ are considered narrowband (not frequency dependent) thus the antenna patterns are assumed constant over the band of the emission, $F_m(f,\theta,\varphi) = F_m(\theta,\varphi)$. Also, because the signal structures of the radar and communications signals are dependent on the coherent combination of the far-field contributions of each antenna, the derivation of the proposed method does not adopt the large array model thus the approximate active antenna pattern is not used. It is assumed the transmission is in the direction of maximum gain (i.e. $\varphi = 0°$), thus for convenience the active element patterns are redefined as

$$F_m(\theta) = F_m(\theta, \varphi = 0°). \tag{4.56}$$

Also, the element index is redefined from $m \in \{-\frac{M-1}{2}, -\frac{M+1}{2}, \ldots, \frac{M-1}{2}\}$ to $m \in \{0, 1, \ldots, M-1\}$ for cleaner notation.

It is assumed that a pulsed radar emission is the primary function and thus the communications beam is transmitted at a lower power and must exist entirely within the pulse duration and spectral content of the radar emission. The embedding of the communication function into the radar emission represents a loss in transmit power (and therefore loss in received target SNR) for the radar. However, this formulation allows for the data throughput of the communications link to scale with the available bandwidth. It should be noted that this concept can easily revert to a radar-only mission depending on the priority level of the radar transmit power and could be combined with the spatially-diverse emission discussed in Sections 4.1 and 4.2.

4.3.2 Far-Field Radiated Emission Design (FFRED)

Consider an M element uniform linear array (ULA) with inter-element spacing d. Here the narrowband assumption is invoked but not the large array assumption, thus the far-field transmission $\tilde{g}(t,\theta,\varphi)$ is modeled as in (3.37). Assuming the emission is sufficiently narrowband, the far-field baseband radar and communication signals must respectively satisfy the constraints

$$\sum_{m=0}^{M-1} F_m(\theta_\mathrm{r}) s_m(t) = \tilde{g}_\mathrm{r}(t) \tag{4.57}$$

and

$$\sum_{m=0}^{M-1} F_m(\theta_\mathrm{c}) s_m(t) = \tilde{g}_\mathrm{c}(t), \tag{4.58}$$

where $\tilde{g}_\mathrm{r}(t)$ and $\tilde{g}_\mathrm{c}(t)$ are the desired far-field radar and communication signals of pulse duration T to be emitted in directions θ_r and θ_c, respectively. Recall that the active element pattern $F_m(\theta) \forall m$ inherently includes all phasing corresponding to each antenna element. Discretizing $\tilde{g}_\mathrm{r}(t)$, $\tilde{g}_\mathrm{c}(t)$, and $s_m(t)$ into $N \times 1$ vectors, where $N = f_\mathrm{s} T$, (4.57) and (4.58) can be rewritten as

$$\tilde{\mathbf{v}}^H(\theta_\mathrm{r}) \mathbf{S} = \tilde{\mathbf{g}}_\mathrm{r}^T \tag{4.59}$$

and

$$\tilde{\mathbf{v}}^H(\theta_\mathrm{c}) \mathbf{S} = \tilde{\mathbf{g}}_\mathrm{c}^T, \tag{4.60}$$

where $\tilde{\mathbf{g}}_\mathrm{r}$ and $\tilde{\mathbf{g}}_\mathrm{c}$ are the $N \times 1$ vectors of the desired radar and communications signals, $\mathbf{S}$ is an $M \times N$ comprised of the M discretized waveforms where the mth *row* corresponds to the $1 \times N$ discretized waveform $\mathbf{s}_m^T$, and $\tilde{\mathbf{v}}(\theta)$ is the $M \times 1$ spatial steering vector for direction θ which is comprised of the complex-conjugated antenna patterns defined as

$$\tilde{\mathbf{v}}(\theta) = \frac{1}{M} \begin{bmatrix} F_0^*(\theta) & F_1^*(\theta) & \cdots & F_{M-1}^*(\theta) \end{bmatrix}^T. \tag{4.61}$$

The $N \times 1$ vectors $\tilde{\mathbf{g}}_{\mathrm{r}}$, $\tilde{\mathbf{g}}_{\mathrm{c}}$, and $\mathbf{s}_m \forall m$ are each sufficiently "over-sampled" with respect to 3 dB bandwidth (see [38, 59, 90]) to maintain sufficient fidelity for physical realization (if the desired $\tilde{\mathbf{g}}_{\mathrm{r}}$ and $\tilde{\mathbf{g}}_{\mathrm{c}}$ possess good spectral containment then, by extension, so will the waveforms $\mathbf{s}_m$ used to construct them). The discretized constraints of (4.59) and (4.60) can be combined as

$$\mathbf{C}^H \mathbf{S} = \mathbf{G}, \tag{4.62}$$

where the $M \times 2$ matrix

$$\mathbf{C} = \left[\tilde{\mathbf{v}}(\theta_{\mathrm{r}}) \;\; \tilde{\mathbf{v}}(\theta_{\mathrm{c}}) \right] \tag{4.63}$$

contains the spatial steering vectors and the $N \times 2$ matrix

$$\mathbf{G} = \left[\tilde{\mathbf{g}}_{\mathrm{r}} \;\; \tilde{\mathbf{g}}_{\mathrm{c}} \right]^T \tag{4.64}$$

contains the discretized far-field signals.

4.3.2.1 Optimality of Waveforms

The optimal waveform matrix (in a minimum-norm sense) can be found by solving the optimization problem

$$\begin{aligned} &\underset{\mathbf{S}}{\text{minimize}} \quad \|\mathbf{S}\|_F^2 \\ &\text{subject to} \quad \mathbf{C}^H \mathbf{S} = \mathbf{G}, \end{aligned} \tag{4.65}$$

where $\|\bullet\|_F^2$ is the squared-Frobenius norm [146]. This problem is convex and has the closed-form

solution [146]

$$\mathbf{S}_\star = \mathbf{C}\left(\mathbf{C}^H\mathbf{C}\right)^{-1}\mathbf{G}. \tag{4.66}$$

This formulation of the waveform matrix is optimal in the sense that all of the energy in $\mathbf{S}_\star$ is used to achieve the emission constraint in (4.62). However, the waveforms in $\mathbf{S}_\star$ are typically not constant amplitude and thus they preclude the use of an HPA operating in saturation (which is associated with high power efficiency). From this perspective, it is instructive to reconsider the definition of optimal within the context of a physical system.

Instead, optimality can be viewed in terms of power efficiency, which supports the maximization of energy emitted in the directions θ_r and θ_c. To achieve the peak power requirement of many high-power radar applications constant amplitude is a necessity [3]. Therefore, under this new interpretation, the constraints of the optimization problem in (4.65) are modified to produce constant amplitude FM waveforms that are amenable to a HPA in saturation. The modified optimization problem is thus

$$\begin{aligned} \underset{\mathbf{S}}{\text{minimize}} \quad & \|\mathbf{S}\|_F^2 \\ \text{subject to} \quad & \mathbf{C}^H\mathbf{S} = \mathbf{G} \\ & |s_m(n)| = |s_p(q)| \quad \text{for} \quad n,q = 0,\ldots,N-1 \\ & \qquad\qquad\qquad\qquad\quad m,p = 0,\ldots,M-1, \end{aligned} \tag{4.67}$$

where $s_m(n)$ is the nth time sample of the mth waveform. An equivalent formulation of (4.67) is

$$\begin{aligned} \underset{\mathbf{S},\gamma}{\text{minimize}} \quad & \gamma^2 \\ \text{subject to} \quad & \mathbf{C}^H\mathbf{S} = \mathbf{G} \\ & |s_m(n)| = \gamma \quad \text{for} \quad n = 0,\ldots,N-1 \\ & \qquad\qquad\qquad\quad m = 0,\ldots,M-1, \end{aligned} \tag{4.68}$$

where γ is the real, positive-valued amplitude of the elements in waveform matrix $\mathbf{S}$ thus $\|\mathbf{S}\|_F^2 \propto \gamma^2$. Therefore, the optimal waveform matrix (according to optimization problem (4.68)) is one that minimizes amplitude γ while maintaining the constraint $\mathbf{C}^H\mathbf{S} = \mathbf{G}$. Note that the amplitude γ is dependent on the relative amplitudes in $\mathbf{C}$ and $\mathbf{G}$ and thus can be scaled after the optimization process without affecting the desired signal structure. Unlike (4.65), this problem does not have a closed-form solution, so we shall consider an iterative approach.

4.3.2.2 Utilization of the Null Space and the Average Directed Power

To realize a waveform matrix that achieves the constraints in (4.68), the null space of the steering vector matrix $\mathbf{C}$ must be leveraged to design a spatial orthogonal complement matrix $\mathbf{S}_\perp$ (where $\mathbf{S}_\star^H\mathbf{S}_\perp = \mathbf{0}_{N\times N}$) such that the summation

$$\mathbf{S} = \mathbf{S}_\star + \mathbf{S}_\perp \tag{4.69}$$

produces the constant amplitude waveform matrix $\mathbf{S}$. Further, the columns of $\mathbf{S}_\perp$ are orthogonal to $\mathbf{v}(\theta_\mathrm{r})$ and $\mathbf{v}(\theta_\mathrm{c})$, or simply

$$\mathbf{C}^H\mathbf{S}_\perp = \mathbf{0}_{2\times N}, \tag{4.70}$$

thus maintaining the constraint $\mathbf{C}^H\mathbf{S} = \mathbf{C}^H(\mathbf{S}_\star + \mathbf{S}_\perp) = \mathbf{G}$. Due to the orthogonality between $\mathbf{S}_\star$ and $\mathbf{S}_\perp$, the average power in $\mathbf{S}$ is represented as

$$\gamma^2 = \rho_\star + \rho_\perp \tag{4.71}$$

or alternatively as

$$\gamma^2 = \frac{1}{MN}\|\mathbf{S}\|_F^2, \tag{4.72}$$

where

$$\rho_\star = \frac{1}{MN}\|\mathbf{S}_\star\|_F^2 \tag{4.73}$$

and

$$\rho_\perp = \frac{1}{MN}\|\mathbf{S}_\perp\|_F^2 \tag{4.74}$$

are the average powers in $\mathbf{S}_\star$ and $\mathbf{S}_\perp$, respectively. These average powers are found using the identity $\|\mathbf{S}\|_F^2 = \mathrm{Tr}\{\mathbf{S}\mathbf{S}^H\}$, then substituting in (4.69) and simplifying.

The average power of the minimum-norm solution $\rho_\star$ is fixed for a given $\mathbf{C}$ and $\mathbf{G}$; hence by minimizing amplitude γ (via optimization problem (4.68)), we are effectively minimizing the orthogonal power $\rho_\perp$ necessary to achieve the desired emission using constant amplitude waveforms. The inclusion of the orthogonal emission requires some percentage of the average power from (4.71). Therefore, there exists a trade-off between the power efficiency lost by placing

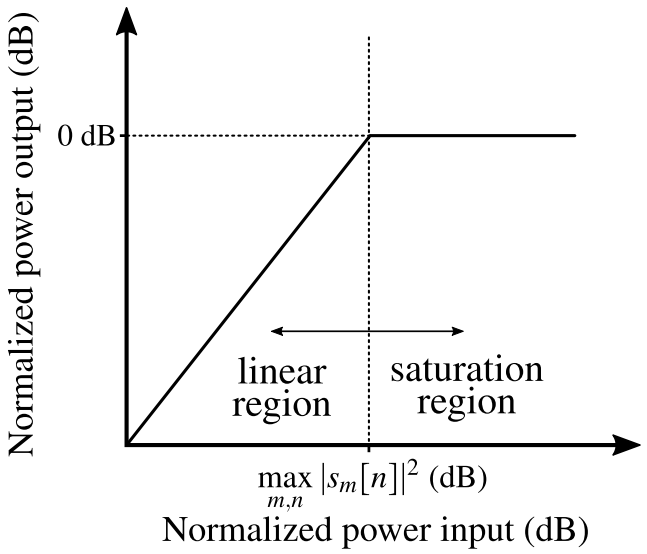

Figure 4.37: Simple amplifier model defining linear and saturation regions.

power into the orthogonal space (via $\mathbf{S}_\perp$) and the efficiency gained by using constant amplitude waveforms that are amenable to an efficient HPA. In Section 4.3.4 we show that, for a range of parameterizations, the power efficiency always increases when forming the set of waveforms in this manner.

To quantify the power efficiency of a given waveform matrix we must first establish an amplifier model to ascertain the transmitter performance given waveforms of different peak-to-average power ratios (PAPRs). A simple amplifier model is shown in Figure 4.37 where the maximum output power is normalized to 0 dB and the power transfer curve has two distinct regions: a linear region and a fully saturated region (in reality a transition region would exist between these but is omitted here). The amplifier model is enforced by scaling the waveform matrix such that the peak amplitude is unity (thus establishing a maximum instantaneous normalized output power of 0 dB). As such, any amplitude values less than the peak represent a loss relative to constant amplitude waveforms. This notion of “power back-off" is commonly used to prevent amplifier distortion when linear operation is required [147].

Using the amplifier model in Figure 4.37, a normalized average directed power (ADP) metric can be defined that calculates the average power contained in waveform matrix $\mathbf{S}$ that contributes

to the desired emission. Using (4.66), the normalized ADP for $\mathbf{S}$ satisfying constraint (4.62) is thus

$$\text{ADP}(\mathbf{S}) = \frac{1}{MN}\left\| \frac{\mathbf{P}_\star \mathbf{S}}{\max\limits_{m,n}\{|s_m(n)|\}} \right\|_F^2 = \frac{\rho_\star}{\max\limits_{m,n}\{|s_m(n)|^2\}}, \tag{4.75}$$

where $\mathbf{P}_\star = \mathbf{C}(\mathbf{C}^H\mathbf{C})^{-1}\mathbf{C}^H$ is a projection matrix that selects only the portion of the waveform matrix that emits in the desired directions specified in $\mathbf{C}$. Because the maximum amplitude of the waveform matrix is normalized to unity, the the possible values of (4.75) are $0 \leq \text{ADP} \leq 1$, with $\text{ADP} = 1$ representing maximum array power efficiency. For a constant amplitude waveform matrix $\mathbf{S}$, the ADP simplifies to $\frac{\rho_\star}{\gamma^2}$. Thus the minimization of amplitude γ (via optimization problem (4.68)) produces a constant modulus waveform matrix $\mathbf{S}$ that maximizes ADP. Equivalently, the ADP for waveform matrix $\mathbf{S}$ can be expressed as $\frac{\rho_\star}{\rho_\star+\rho_\perp}$, illustrating that when the orthogonal power is minimized, the ADP is maximized. Maximum array power efficiency $(\text{ADP} = 1)$ can only occur when $\rho_\perp = 0$, implying that the minimum-norm solution $\mathbf{S}_\star$ is constant amplitude, which can only be achieved when $\mathbf{C}$ contains a single emission direction and $\mathbf{G}$ contains a single constant amplitude waveform.

4.3.3 Realization of Emission Constraints using Error Reduction Algorithm

The optimization problem in (4.68) does not have a closed-form solution and is non-convex due to the inclusion of the constant amplitude constraint. A fast and useful approach to perform optimization involving two distinct constraints is to alternate between projecting onto the sets satisfying each constraint. If these sets are convex, this procedure is known as projection onto convex sets (POCS) [148, 149]. If one or more of the sets is non-convex, the procedure is known as the error reduction algorithm (ERA) [124, 127, 128, 150]. While the procedure remains the same for these two general methods, the difference lies in the convergence claims. The convergence to an intersection point (or minimum distance point) between the sets can be proven for POCS, but cannot be proven for ERA. However, the error in ERA can be shown to be a non-increasing

sequence [124, 127, 128, 150]. Since the constant amplitude constraint in (4.67) represents a non-convex set, the convergence properties of ERA apply here.

4.3.3.1 FFRED Implementation

For a given constant amplitude initialization $\mathbf{S}_0$, this iterative design procedure alternates between two stages until sufficient convergence is achieved. The first stage projects onto some set A that satisfies a constraint using projection operator $P_A(\bullet)$. Subsequently, the second stage projects onto some set B satisfying the other constraint using projection operator $P_B(\bullet)$. For this problem, set A satisfies the constraint $\mathbf{C}^H\mathbf{S} = \mathbf{G}$ from (4.62) and set B satisfies the constant amplitude constraint from (4.68). Here set A is convex and set B is non-convex. This procedure is summarized in Algorithm 4.1.

Algorithm 4.1 Alternating Projections

Initialize: $\mathbf{S}_0$, $i = 0$
repeat
  $\tilde{\mathbf{S}}_i = P_A(\mathbf{S}_i)$
  $\mathbf{S}_{i+1} = P_B(\tilde{\mathbf{S}}_i)$
  $i = i + 1$
until sufficiently converged
return $\mathbf{S}_i$

The projections $P_A(\bullet)$ and $P_B(\bullet)$ can be defined as the minimum change one could impart to $\mathbf{S}_i$ or $\tilde{\mathbf{S}}_i$, respectively, such that the corresponding constraints are met. Thus the projections themselves can be viewed as optimization problems. The first problem is formulated such that the squared distance is minimized between the waveform matrix $\mathbf{S}_i$ obtained in the previous iteration and the projected waveform matrix $\tilde{\mathbf{S}}_i$ while maintaining the form of constraint (4.62). The first stage projection $P_A(\mathbf{S}_i)$ is therefore defined as

$$\begin{aligned} \underset{\tilde{\mathbf{S}}_i}{\text{minimize}} \quad & \left\| \tilde{\mathbf{S}}_i - \mathbf{S}_i \right\|_F^2 \\ \text{subject to} \quad & \mathbf{C}^H \tilde{\mathbf{S}}_i = \mathbf{G}, \end{aligned} \tag{4.76}$$

which has the closed-form solution

$$\tilde{\mathbf{S}}_i = \mathbf{P}_\perp \mathbf{S}_i + \mathbf{S}_\star \tag{4.77}$$

for projection matrix

$$\mathbf{P}_\perp = \mathbf{I}_M - \mathbf{C}\left(\mathbf{C}^H\mathbf{C}\right)^{-1}\mathbf{C}^H. \tag{4.78}$$

The proof that (4.77) is the solution to (4.76) is provided in Appendix A.8.

Likewise, the second stage projection $P_B(\tilde{\mathbf{S}}_i)$ can be expressed as

$$\begin{aligned} \underset{\mathbf{S}_{i+1}}{\text{minimize}} \quad & \left\|\mathbf{S}_{i+1} - \tilde{\mathbf{S}}_i\right\|_F^2 \\ \text{subject to} \quad & \left|s_{m,i+1}(n)\right| = \gamma \quad \text{for} \quad n = 0,\ldots,N-1 \\ & \qquad\qquad\qquad\qquad\quad m = 0,\ldots,M-1, \end{aligned} \tag{4.79}$$

which has the closed-form solution

$$\mathbf{S}_{i+1} = \gamma \exp\left(j \angle \tilde{\mathbf{S}}_i\right). \tag{4.80}$$

The proof that (4.80) is the solution to (4.79) is provided in Appendix A.9. After incorporating the projections from (4.77) and (4.80), the FFRED procedure is stated in Algorithm 4.2 for given spatial steering vectors in **C** and desired far-field signals **G**.

Instead of minimizing amplitude γ (as in problem (4.68)) it is incorporated as a predefined parameter for the FFRED algorithm. We can find a value of γ close to the minimum through a sequence of feasibility problems where, for a given amplitude γ, the intersection between sets A

Algorithm 4.2 Far-field Radiated Emission Design

FAR-FIELD RADIATED EMISSION DESIGN
Initialize: $\mathbf{S}_0$, γ, $i = 0$
repeat
$\tilde{\mathbf{S}}_i = \mathbf{P}_\perp \mathbf{S}_i + \mathbf{S}_\star$
$\mathbf{S}_{i+1} = \gamma \exp\left(j \angle \tilde{\mathbf{S}}_i\right)$
$i = i + 1$
until sufficiently converged
return $\mathbf{S}_i$

and B is tested (i.e. when both constraints are satisfied). If the intersection exists, the amplitude is reduced, if not, the amplitude is increased. This process can be implemented via a simple bisection procedure and iterated until γ is within some tolerance. As previously stated, the convergence properties of ERA do not guarantee that, for a given initialization $\mathbf{S}_0$ and amplitude γ, a solution that intersects the sets A and B will be found. Instead, ERA has the error reduction property

$$\ldots \geq \|\tilde{\mathbf{S}}_i - \mathbf{S}_i\|_F^2 \geq \|\mathbf{S}_{i+1} - \tilde{\mathbf{S}}_i\|_F^2 \geq \|\tilde{\mathbf{S}}_{i+1} - \mathbf{S}_{i+1}\|_F^2 \geq \ldots \tag{4.81}$$

which shows that the squared-distance between the solutions of problems (4.76) and (4.79) form a non-increasing sequence. However, in [24] it was shown that by increasing the amount of orthogonal power $\rho_\perp$ (through increase of amplitude γ) the convergence behavior improves by enhancing the overall solution's ability to satisfy the constraints of (4.68). The feasibility procedure to find amplitude γ as described above is obviously not conducive for real-time application. However, prior knowledge of a feasible γ for a given transmission scenario could be used to bypass this process.

The computational complexity of one iteration of FFRED is $8M^2N + 7MN$ floating point operations or "flops", with $8M^2N$ operations arising from (4.77) and $7MN$ operations for (4.80). However, a majority of these operations are readily parallelizable. The number of iterations required to reach convergence depends on the parameter initializations and the convergence criterion, though it has been found to average on the order of 10s to 100s of iterations. Clearly,

more effort is needed to guarantee convergence (to a high certainty) given a requirement to operate in real-time.

In regards to the initialization $\mathbf{S}_0$, it has been found thus far that randomly coded PCFM waveforms (see [38] and Section 2.1.2.4) produce good, consistent results. However, depending on the particular initialization, it is known that ERA-based algorithms may encounter a "tunnel" or "trap" that can slow convergence or prevent the algorithm from finding a solution (see [124] for more details on ERA). Because the foresight to predict these "traps" and "tunnels" does not exist, it is impossible to guarantee that one will not be encountered for a given initialization. Further investigation is necessary to understand how to intelligently choose the initialization of $\mathbf{S}_0$ so as to best avoid these obstacles. While not elegant, a "brute force" option is simply to employ multiple different initializations and select the best result after each has attained a sufficient degree of convergence.

4.3.4 Simulated Characterization of FFRED Emissions

To evaluate the performance of the FFRED emission we examine how multiple factors behave under different parameter initializations. The factors considered here include the ADP, the spatial beampattern, the emission spectral content, and BER for the communications component. The parameter initializations that dictate these factors are relative radar/communication powers, relative radar/communication beam spacing, and the structure of the communication modulation. The results that follow are not to be considered a comprehensive examination into the performance of these emissions after FFRED optimization. Instead, the results provide insight into the benefits and potential obstacles that can emerge from this waveform optimization technique, with particular attention paid to power efficiency and how the orthogonal power manifests itself in space and frequency.

For the results that follow consider an $M = 16$ element narrowband uniform linear array (ULA) with inter-element spacing $d = \frac{\lambda_c}{2}$. Here it is assumed that all elements are omni-directional in the $\varphi = 0^\circ$ plane. Thus, the beampatterns correspond to the electrical phasing difference between the

elements as

$$F_m(\theta) = e^{jm\phi(f_c,\theta)} \qquad \textit{(narrowband omnidirectional antenna patterns)}. \tag{4.82}$$

Therefore, the far-field emission $\tilde{g}(t,\theta)$ is approximated as time varying array factor $g(t,\theta)$. This assumption is beneficial from an analysis perspective and provides a sense of the general emission behavior given certain parameters. Though in practice, the results presented in Section 4.3.4 may vary depending on the individual active element pattern responses. In Section 4.3.5, the FFRED emission design is experimentally demonstrated thus the active element patterns for a four element patch array are determined prior to optimization.

The radar waveform $\tilde{g}_r(t)$ is designed to be an up-chirped LFM waveform of analytical time-bandwidth $B_a T = 64$. Three different communication modulations are considered for signal $\tilde{g}_c(t)$: quadrature phase-shift keying (QPSK) signal with rectangular (RECT) and square-root-raised-cosine (SRRC) shaping filters [47], and 4-ary CPM with a RECT shaping filter and modulation index $h = 1/2$ [151]. The RECT shaping filter spans one symbol duration while the SRRC filter spans 10 symbols. Both the RECT-filtered QPSK and CPM communication signals contain 128 information bits per pulse within the given time-bandwidth product of the radar emission while the SRRC-filtered communication emission contains 108 bits per pulse (due to the temporal extent of the shaping filter). The discretized versions $\mathbf{g}_r$ and $\mathbf{g}_c$ are both over-sampled in time with respect to the LFM analytical bandwidth B_a such that the final optimized waveform matrix can be readily converted into a set of FM waveforms much like in Section 4.2.6 [38]. The FFRED algorithm is terminated when the result from (4.77) produces a waveform matrix that has a PAPR of 1.01 from (2.116) (thus the subsequent enforcement of constant amplitude produces a negligible deviation from this result).

Figures 4.38 through 4.40 show the ADP via (4.75) of the minimum-norm waveform matrices and FFRED optimized waveform matrices for the RECT-filtered QPSK, SRRC-filtered QSPK, and RECT-filtered CPM communications scenarios, respectively. Taking advantage of the spatial invariance of the array factor of a ULA, only the relative spacing between the beams needs to

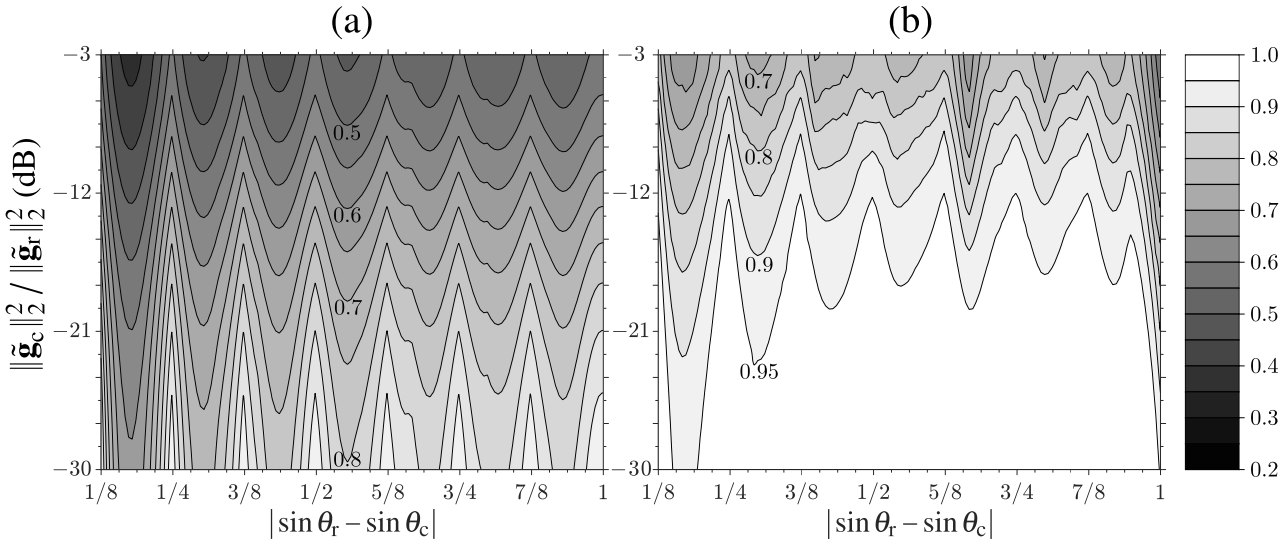

Figure 4.38: ADP via (4.75) of (a) minimum-norm solution $\mathbf{S}_\star$ and (b) FFRED optimized solution $\mathbf{S}$ versus $|\sin\theta_r - \sin\theta_c|$ and $\|\tilde{\mathbf{g}}_c\|^2/\|\tilde{\mathbf{g}}_r\|_2^2$ using RECT-filtered QPSK.

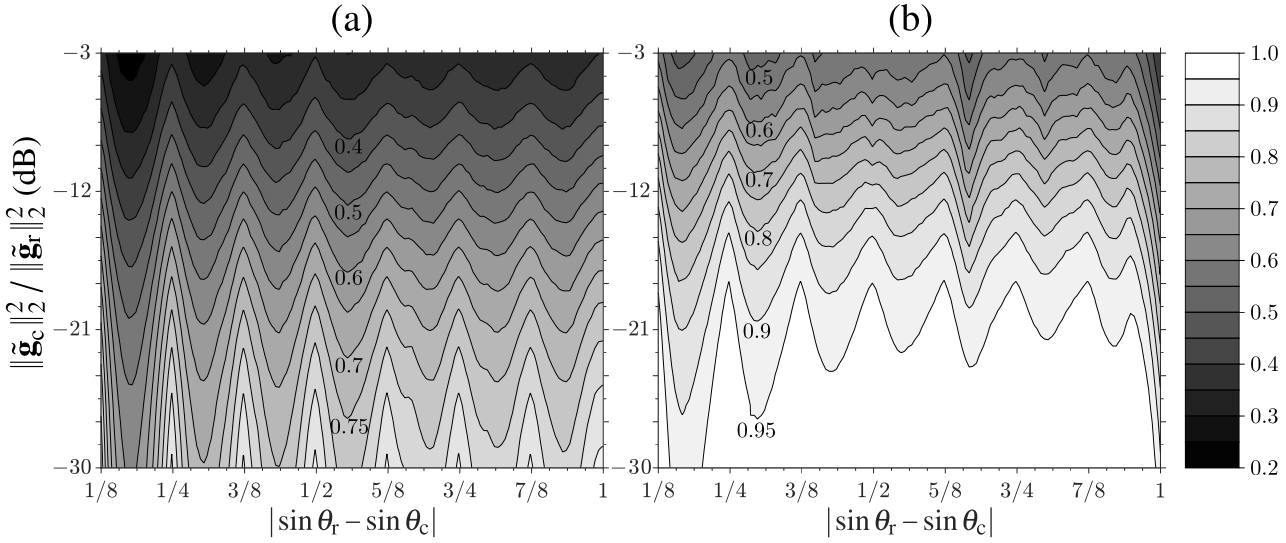

Figure 4.39: ADP via (4.75) of (a) minimum-norm solution $\mathbf{S}_\star$ and (b) FFRED optimized solution $\mathbf{S}$ versus $|\sin\theta_r - \sin\theta_c|$ and $\|\tilde{\mathbf{g}}_c\|^2/\|\tilde{\mathbf{g}}_r\|_2^2$ using SRRC-filtered QPSK.

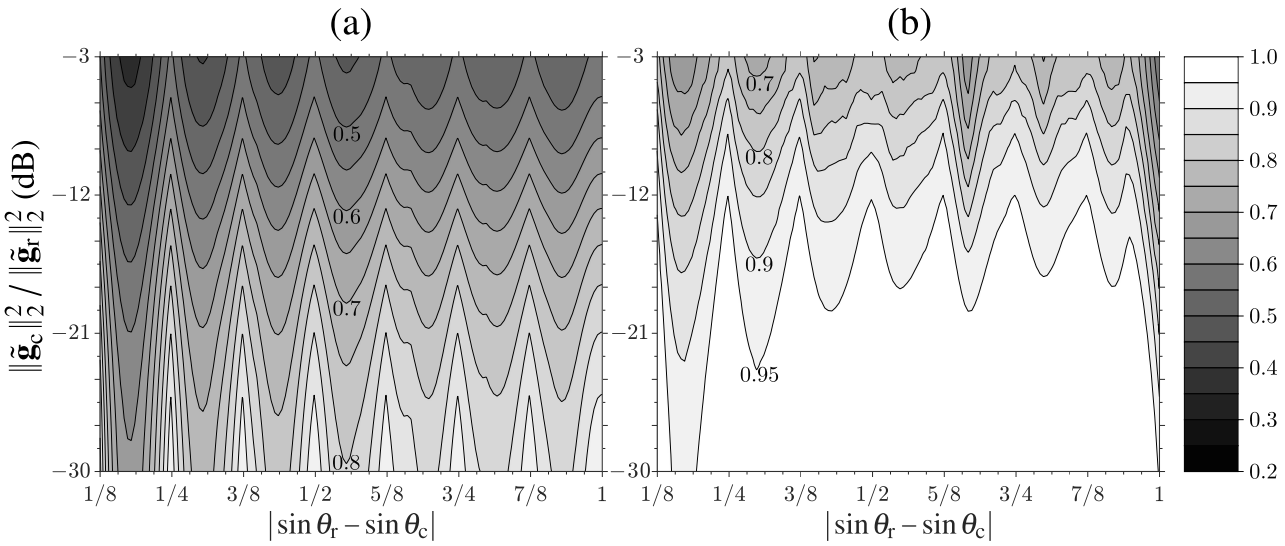

Figure 4.40: ADP via (4.75) of (a) minimum-norm solution $\mathbf{S}_\star$ and (b) FFRED optimized solution $\mathbf{S}$ versus $|\sin\theta_r - \sin\theta_c|$ and $\|\tilde{\mathbf{g}}_c\|^2/\|\tilde{\mathbf{g}}_r\|_2^2$ using RECT-filtered 4-ary CPM with $h = 1/2$.

be considered. The relative spacing between the radar and communication beams was varied from $|\sin\theta_r - \sin\theta_c| = 1/8$ (representing the first null of the 16 element ULA beampattern) to $|\sin\theta_r - \sin\theta_c| = 1$ in $1/160$ increments. The relative power of the communication signal to the radar signal, computed via $\|\tilde{\mathbf{g}}_c\|_2^2/\|\tilde{\mathbf{g}}_r\|_2^2$, was varied from -30 dB to -3 dB in 1 dB increments. Each evaluation was averaged over 50 Monte Carlo trials with independent, randomly generated bit sequences and initialized with a set of $M = 16$ randomly coded PCFM-implemented waveforms.

For all three scenarios in Figures 4.38 through 4.40, the ADP for the FFRED optimized waveforms in $\mathbf{S}$ is strictly greater than the ADP for the minimum-norm solution $\mathbf{S}_\star$ for every parameterization, confirming that the FFRED solution is in fact a more power efficient emission. The difference in ADP between $\mathbf{S}$ and $\mathbf{S}_\star$ for all three cases reaches a maximum of ~35% and occurs at beam spacing $|\sin\theta_r - \sin\theta_c| \approx 3/16$. Note that the ADP for the RECT-filtered QPSK and RECT-filtered CPM scenarios in Figures 4.38 and Figures 4.40 have similar outcomes while a significant decrease in ADP is observed for the SRRC-filtered QPSK case. This result is likely due to the amplitude variation of the communication signal $\mathbf{g}_c$ for the latter scenario. Since both the RECT-filtered QPSK and CPM signals have unity PAPR, their ADP efficiencies are likewise similar. In contrast, the SRRC-filtered QPSK signal has an average PAPR of ~2.2, and thus the

emission requires more power to be placed in the orthogonal complement region to attain a solution satisfying the constraints in (4.68), thereby reducing the overall power efficiency of the emission.

Observe in Figures 4.38 through 4.40 that when the beam separation corresponds to the nulls of the $M = 16$ ULA beampattern as

$$|\sin\theta_{\mathrm{r}} - \sin\theta_{\mathrm{c}}| = \frac{u}{8} \quad \text{for } u = 1, \ldots, 7, \tag{4.83}$$

the ADP increases for both $\mathbf{S}$ and $\mathbf{S}_\star$ (indicated by the lighter regions in the plots). At these angles, the radar and communication beams are orthogonal, and therefore no extra power is needed to achieve the spatial orthogonality, hence an increase in ADP.

Figure 4.41 shows the beam patterns of the converged solutions over the 50 Monte Carlo trials for the beam separation case of $|\sin\theta_{\mathrm{r}} - \sin\theta_{\mathrm{c}}| = 5/8$ in each of the three scenarios. Here the absolute directions are $\sin\theta_{\mathrm{r}} = 0$ and $\sin\theta_{\mathrm{c}} = 5/8$. The beampatterns are normalized such that 0 dB represents the maximum power that the array can emit in any direction. As the relative power $\|\tilde{\mathbf{g}}_{\mathrm{c}}\|^2/\|\tilde{\mathbf{g}}_{\mathrm{r}}\|^2$ increases, the communication beam emerges from the location of the fifth null of the radar beampattern. As before, the average beampatterns of the RECT-filtered QPSK and the CPM scenarios are nearly identical. It should be noted that for these two scenarios an additional spurious beam has emerged in the direction $\sin\theta = -5/8$. While symmetry may seem to imply that this spurious beam and the communication beam possess a similar time-domain structure, there is in fact no clear presence of the transmitted information in this direction (as will be shown in the BER plots). In contrast, the average beampattern of the SRRC-filtered QPSK scenario has a much flatter spatial response in the orthogonal complement directions, albeit with a noticeable peak power loss compared to the other cases. The peak power loss of the radar beam (compared to maximum transmit power) is 0.12 dB at a relative beam power of −30 dB for all three scenarios. However, at a relative beam power of −3 dB, the losses of the RECT-filtered QPSK and CPM cases rise to 5.56 dB and 5.53 dB, respectively, and 8.82 dB for the SRRC-filtered QPSK scenario. Again, this

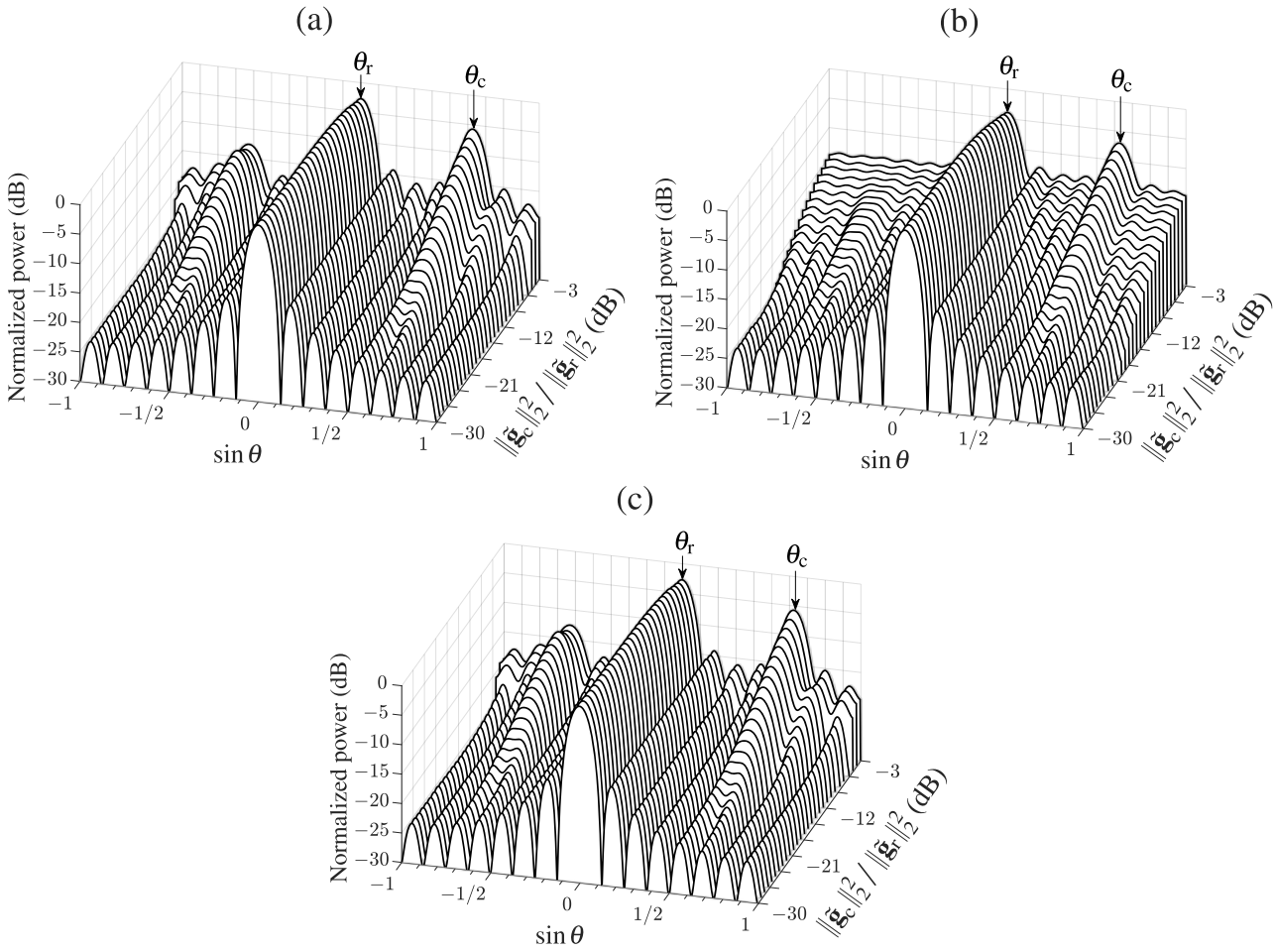

Figure 4.41: Average beam patterns for $\mathbf{S}$ versus $\|\tilde{\mathbf{g}}_c\|^2/\|\tilde{\mathbf{g}}_r\|^2$ using (a) RECT-filtered QPSK, (b) SRRC-filtered QPSK, and (c) RECT-filtered 4-ary CPM for $\sin\theta_r = 0$ and $\sin\theta_c = 5/8$.

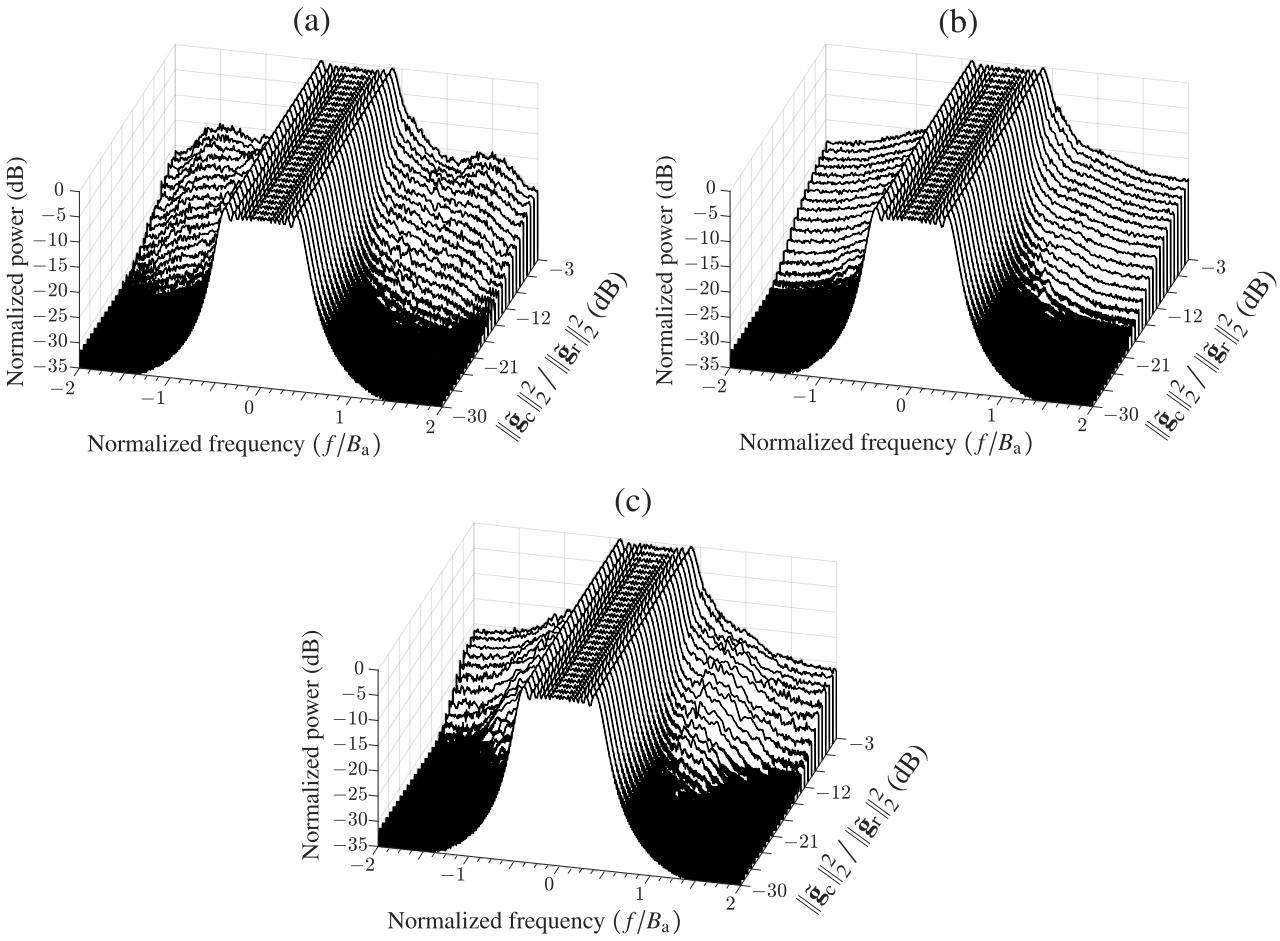

Figure 4.42: Maximum spectral content for $\mathbf{S}$ versus $\|\tilde{\mathbf{g}}_{\mathrm{c}}\|^2/\|\tilde{\mathbf{g}}_{\mathrm{r}}\|^2$ using (a) RECT-filtered QPSK, (b) SRRC-filtered QPSK, and (c) RECT-filtered 4-ary CPM for $\sin\theta_{\mathrm{r}} = 0$ and $\sin\theta_{\mathrm{c}} = 5/8$.

loss in overall power efficiency for the SRRC-filtered QPSK case is a direct result of requiring a larger amount of orthogonal power to satisfy the constraints of (4.68).

Figure 4.42 shows the maximum spectral response over $\sin\theta$ of the converged emissions for all three scenarios when the relative beam separation is $5/8$ with $\sin\theta_{\mathrm{r}} = 0$ and $\sin\theta_{\mathrm{c}} = 5/8$ (same as Figure 4.41 and likewise averaged over the 50 Monte Carlo trials). As there is no spectral containment constraint applied during optimization, the orthogonal emission (dictated by $\mathbf{S}_{\perp}$) is allowed to spread into the spectral roll-off region. For the RECT-filtered QPSK scenario, the sinc structure of the communication spectrum starts to emerge at a relative beam power $\|\tilde{\mathbf{g}}_{\mathrm{c}}\|^2/\|\tilde{\mathbf{g}}_{\mathrm{r}}\|^2$ (dB) $= -3$ dB. Interestingly, the SRRC-filtered QPSK scenario (which is implemented for its spectral containment properties) also suffers from spectral regrowth in the FFRED optimized

solution. The CPM scenario has the least amount of power increase because the communication signal $\tilde{\mathbf{g}}_c$ is both spectrally well-contained and constant modulus [151].

To evaluate the BER performance of the communication link, a maximum likelihood (ML) symbol detector [47] is applied for the QPSK cases and the Viterbi algorithm [152] is applied for CPM [151]. Specifically, these symbol decoders are applied to the associated fast-time emission across all spatial angles. The decoding of a signal that is transmitted in a direction other than the communications direction θ_c is expected to produce increased communication errors due to the fast-time/spatial coupling of the emission. Quantifying the expected BER versus spatial angle under different scenarios provides an effective "coherence beamwidth" of spatial angles around the communication direction θ_c that are amenable for communications. To isolate the effects of the spatial dependence of the emission, no additional noise is added to the simulation. The signals received at a hypothetical receiver as a function of spatial angle were phase rotated before symbol estimation so as to achieve the minimum BER possible for the given constellation.

In [24] it was shown that, increasing the relative amount of orthogonal power by increasing γ above the minimum feasible amplitude (Section 4.3.3.1), the BER is increased in directions other than θ_c. Here, the amplitude γ is not inflated beyond the minimum. Instead, consider three different relative beam powers $\|\tilde{\mathbf{g}}_c\|_2^2/\|\tilde{\mathbf{g}}_r\|_2^2$ (dB) $= \{-20, -13, -6\}$ dB with the radar beam directed toward $\sin\theta_r = 0$ and the communication beam varied from $\sin\theta_c = 1/8$ to $\sin\theta_c = 1$ in $1/80$ increments. Here the BER of the RECT-filtered QPSK and CPM communication scenarios are examined as they have similar ADP responses (and thus similar orthogonal power) for the parameterizations considered. The same emission configuration is used from the above examples (up-chirped LFM for $\tilde{\mathbf{g}}_r$, $BT = 64$, 16 element ULA, etc.), though the number of Monte Carlo trials is increased to 200 to better estimate the BER. Recall that both the RECT-filtered QPSK and the CPM signals could transmit 128 information bits per pulses with this parameterization and therefore the BER at each relative power level and beam separation is based on a total of 25,600 bits.

Figures 4.43 through 4.45 show the BER versus spatial angle $\sin\theta$ and communication direction $\sin\theta_c$ for relative beam powers of -20 dB, -13 dB, and -6 dB, respectively. Each figure

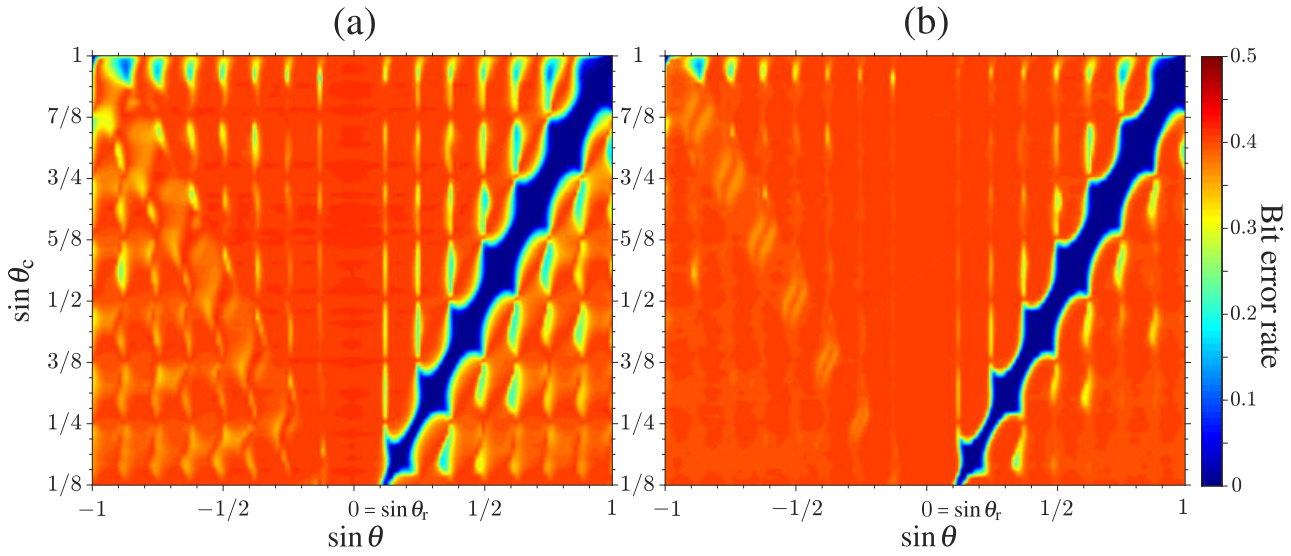

Figure 4.43: Average BER versus $\sin\theta$ and $\sin\theta_c$ for $\|\tilde{\mathbf{g}}_c\|^2/\|\tilde{\mathbf{g}}_r\|^2$ (dB) = −20 dB and $\sin\theta_r = 0$ using (a) RECT-filtered QPSK and (b) RECT-filtered 4-ary CPM.

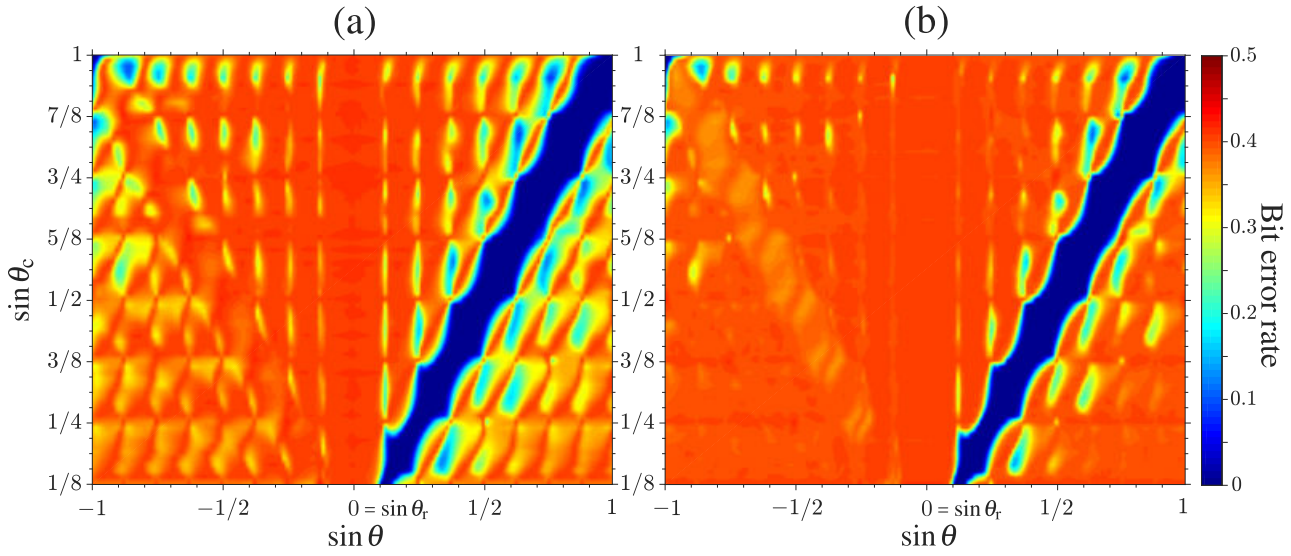

Figure 4.44: Average BER versus $\sin\theta$ and $\sin\theta_c$ for $\|\tilde{\mathbf{g}}_c\|^2/\|\tilde{\mathbf{g}}_r\|^2$ (dB) = −13 dB and $\sin\theta_r = 0$ using (a) RECT-filtered QPSK and (b) RECT-filtered 4-ary CPM.

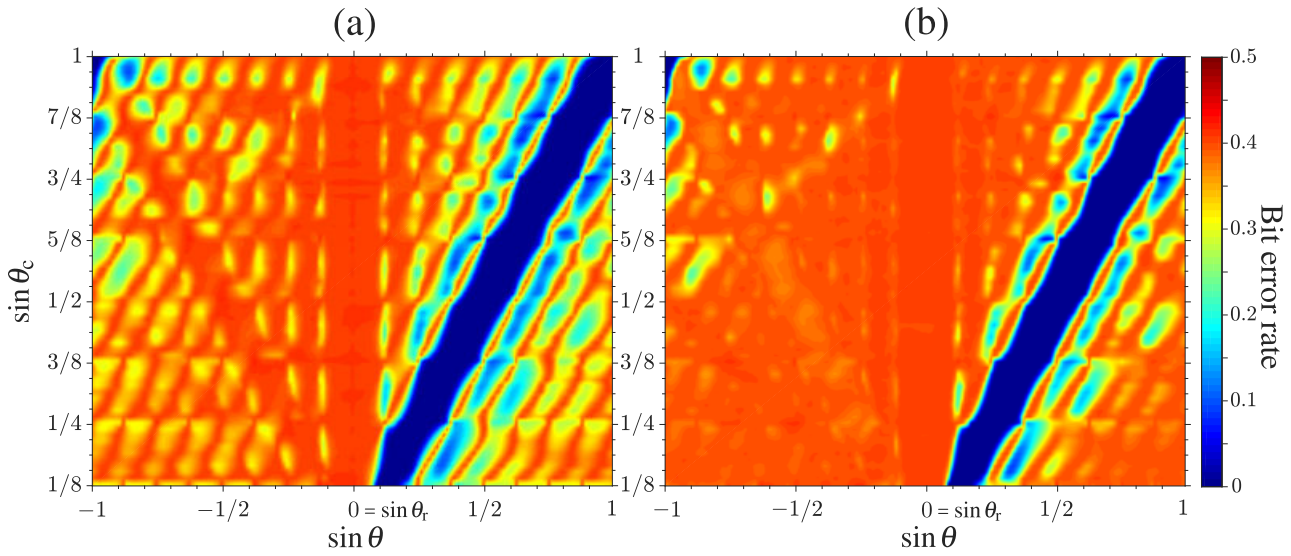

Figure 4.45: Average BER versus $\sin\theta$ and $\sin\theta_c$ for $\|\tilde{\mathbf{g}}_c\|^2/\|\tilde{\mathbf{g}}_r\|^2$ (dB) = −6 dB and $\sin\theta_r = 0$ using (a) RECT-filtered QPSK and (b) RECT-filtered 4-ary CPM.

displays the BER for the RECT-filtered QPSK and the RECT-filtered 4-ary CPM communications scenarios. The communication direction is illustrated by the diagonal blue bar on each image. The width of this bar signifies the "coherence beamwidth" within which communication symbols can be detected successfully. Thus, by inspection, this coherence beamwidth becomes wider as the relative beam power $\|\tilde{\mathbf{g}}_c\|^2/\|\tilde{\mathbf{g}}_r\|^2$ increases, which may or may not be desirable. Recall in Figure 4.41 that an apparent symmetric beam appeared opposite to the communication direction. Here, this beam can be clearly observed as a diagonal red stripe to the left of the radar emission direction. The high BER of this stripe indicates that the beam does not transmit communication information in the symmetric direction.

Another point of interest is the distinction in the BER performance between the RECT-filtered QPSK and CPM communication scenarios. In Figures 4.43 through 4.45, the emission containing CPM signal results in a higher BER in directions other than $\sin\theta_c$ compared to the QPSK-based emission. Thus, the modulation scheme also has an effect on the resulting BER performance in unintended directions.

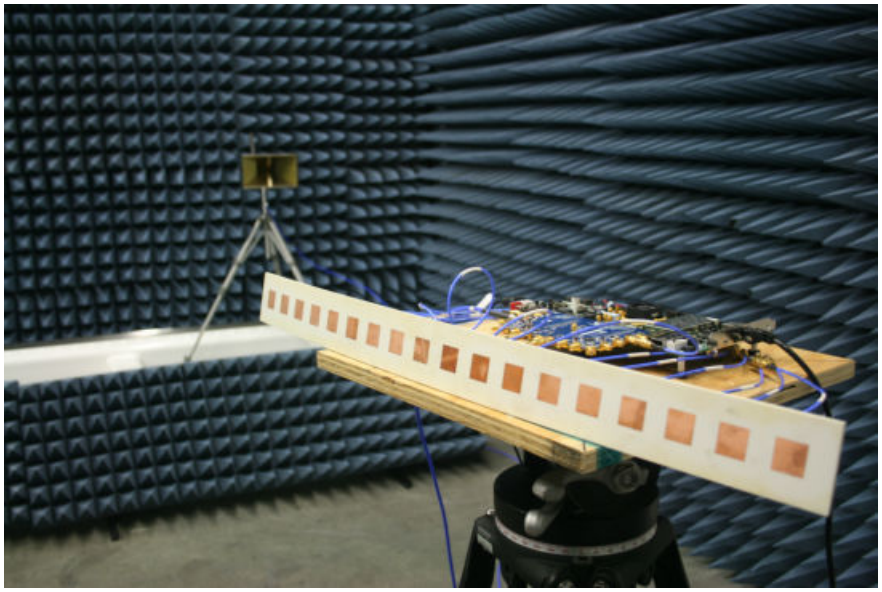

Figure 4.46: Experimental setup: BEEMER and array in foreground, and receive horn antenna in background [25].

4.3.5 Experimental Demonstration

The FFRED-derived multi-function waveforms were experimentally validated through open air testing in an indoor facility at the AFRL Sensors Directorate. The BEEMER software-defined radar (SDR) system [110] served as the RF and digital backend for the experiment. These experiments require hardware that provides independent, element-level waveform generation, a requirement met by the BEEMER SDR.

The aperture consisted of an 18 element linear patch array antenna with half-wavelength inter-element spacing at 3.5 GHz. Four transmit channels were connected to the centermost elements of the array to reduce edge effects on the element patterns. The emission was measured using one receive channel of the BEEMER system captured at 40 MS/s baseband I/Q connected to a quad-ridge horn with 18 dBi of gain. Figure 4.46 shows the transmit array, BEEMER system, and horn antenna inside the chamber used to capture the signals, with the transmit and receive antennas

A portion of the text and figures in Section 4.3.5 are taken from "Simultaneous radar and communications emissions from a common aperture, Part II: Experimentation" by McCormick et al. printed in *2017 IEEE Radar Conference Proceedings* in May 2017. ©2011 IEEE

separated by 3 meters. Boresight calibration was initially performed to calibrate the amplitude and phase offsets across the four transmit channels of the SDR. Frequency-dependent calibration of the SDR was not performed as this would alter the constant amplitude structure of the waveforms.

The radar waveform is an up-chirped LFM with an analytical bandwidth of $B_{\mathrm{a}} = 10$ MHz and pulse duration of $T = 10$ μs for a analytical time-bandwidth product of $B_{\mathrm{a}}T = 100$. The communications beam is set to have 13 dB less power than the radar beam as the communication link is assumed to be secondary to the radar mission and would only have to contend with one-way path losses in practice. For these tests, the communication beam was pointed at $\theta_{\mathrm{c}} = 30°$. Two different radar beam directions were considered at $\theta_{\mathrm{r}} = -15°$ and $\theta_{\mathrm{r}} = 0°$, such that the communication emission corresponds to the first sidelobe and first null of the radar emission, respectively.

The narrowband active element patterns $F_m(\theta)\forall m$ were estimated in the emission directions $\theta_{\mathrm{r}} = \{-15°, 0°\}$ and $\theta_{\mathrm{c}} = 30°$ prior to testing for use in the $M \times 1$ spatial steering vector $\tilde{\mathbf{v}}(\theta)$ used during waveform optimization. A tone at a frequency of $f = 3.501$ GHz was generated on each of the four antenna element channels. The tone was offset from the center frequency by 1 MHz to avoid interference with the leakage of the LO which appears as a DC term in the baseband data. The patch array was oriented such that the horn receive antenna captures the tonal open-air data in the directions $\theta_{\mathrm{r}} \in \{-15°, 0°\}$ and $\theta_{\mathrm{c}} = 30°$. The beampatterns $F_m(\theta)\forall m$ for the radar and communication transmission directions were determined via a fast-Fourier transform (FFT) of the complex-baseband data to observe the phase and amplitude of the $f = 1$ MHz FFT bin for each antenna element.

Again, the communication signals are modulated using a QPSK constellation with either a RECT filter, yielding 200 bits per pulse, or a SRRC filter that yields 180 bits per pulse. The latter provides better spectral containment but introduces a high amount of amplitude modulation that increases the average power in $\mathbf{S}_{\perp}$ needed for convergence. Figure 4.47 shows the baseband spectra of the radar waveform (blue) and the envelopes of the communication signals with RECT (red) and SRRC (yellow) shaping filters.

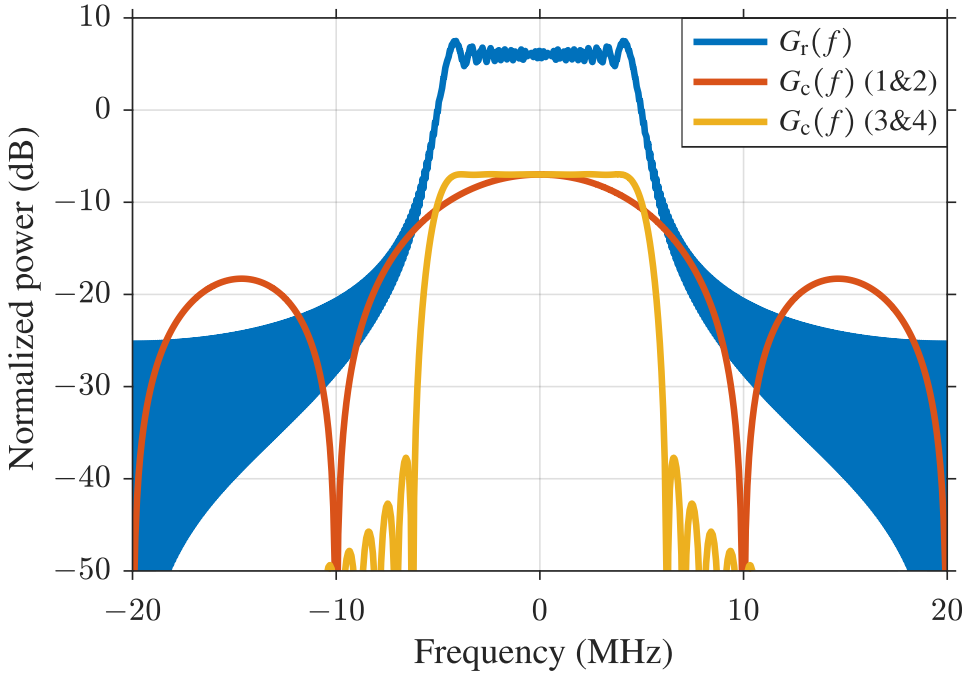

Figure 4.47: Spectral content of radar waveform (blue) and QPSK modulated communications using a RECT filter (red) and SRRC filter (yellow). ©2017 IEEE

Table 4.5: TEST CASE PARAMETERS

	Radar direction θ_r	**Shaping filter**
Case 1	−15°	RECT
Case 2	0°	RECT
Case 3	−15°	SRRC
Case 4	0°	SRRC

Table 4.6: SUMMARY OF FIXED PARAMETERS

Parameter	**Value**
Center frequency	3.5 GHz
Bandwidth	10 MHz
Pulse duration	10 μs
Active antenna elements	4
Antenna element spacing	4.28 cm (half-wavelength)
Receiver sampling rate	40 MS/s
Communication direction θ_c	30°
Relative comm power (dB)	−13 dB
Communications modulation	QPSK (gray-coded)
Radar modulation	Up-chirped LFM
Transmitted pulses	20
Bits transmitted per pulse	200 (RECT)
	180 (SRRC)

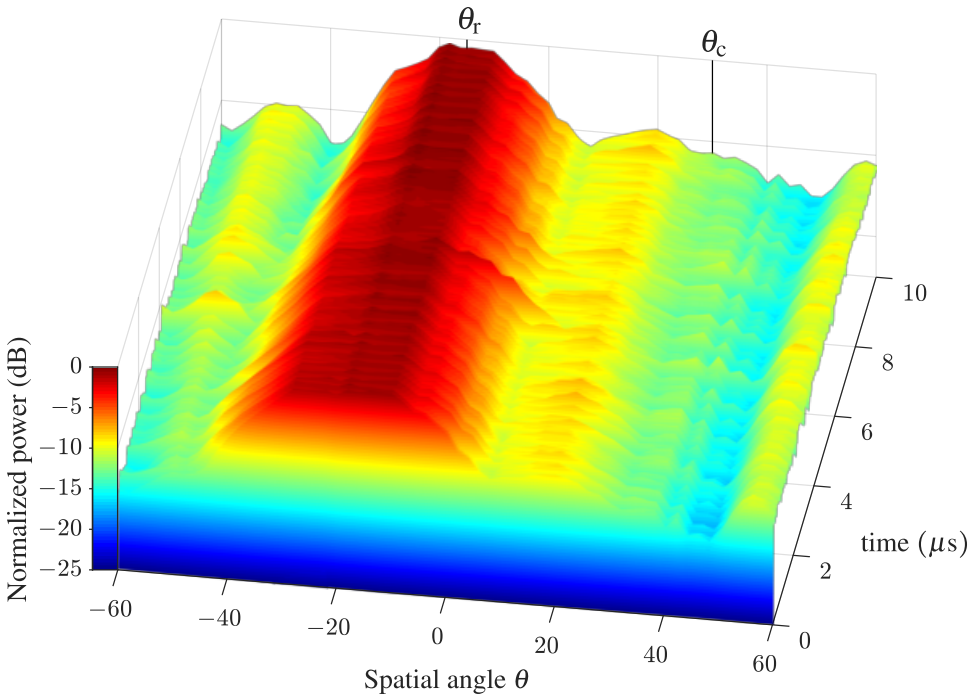

Figure 4.48: Average emitted power versus spatial angle θ and fast-time for case 1 ($\theta_r = -15°$ and RECT shaping filter). ©2017 IEEE

Table 4.5 summarizes the four test cases arising from the combination of two different modes of communication modulation and two different radar emission directions. Twenty pulses were transmitted for each test case resulting in a total of 4000 bits for cases 1 and 2, and 3600 bits for cases 3 and 4. While sample size is clearly not large enough to accurately predict the true bit error rate, it is sufficient to demonstrate the validity of this manner of dual-function radar/communication.

The goals of these tests are to characterize how accurately the far-field signals could be produced in their corresponding desired directions and to assess the impact of the minimum orthogonal power for optimization. A summary of all other parameters is provided in Table 4.6. These parameters and the steering vector estimates were then used inside the optimization procedure to generate the multi-function waveforms according to Algorithm 4.2.

Table 4.7 shows the average ADP from (4.75) for all four transmission cases both before optimization (minimum-norm solution) and after optimization (FFRED optimization solution). The ADP for the minimum norm solution is lowest where the radar beam is pointed toward

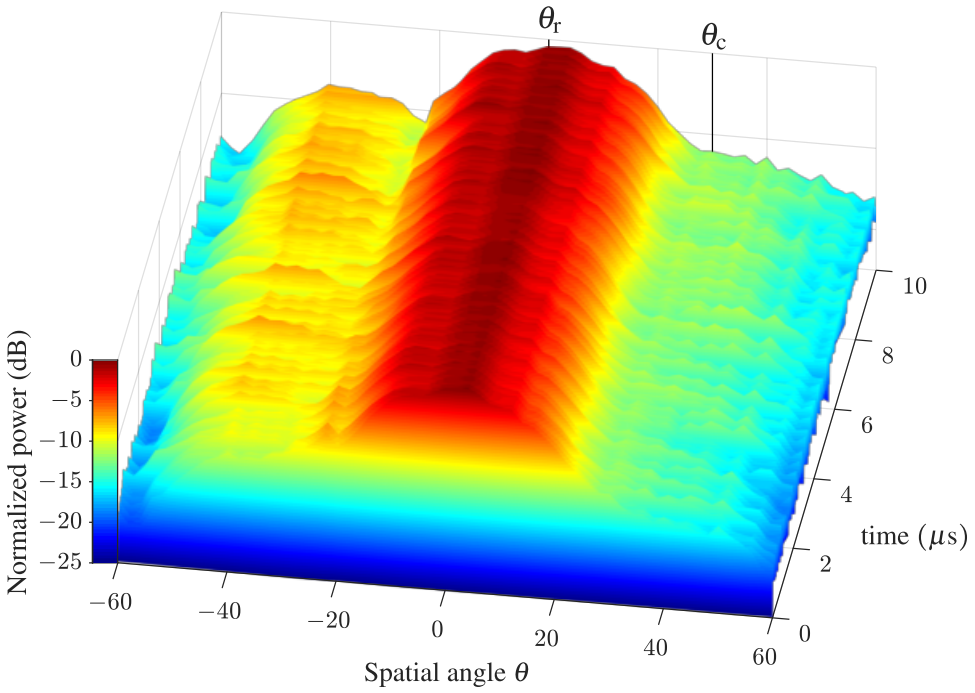

Figure 4.49: Average emitted power versus spatial angle θ and fast-time for case 2 ($\theta_r = 0°$ and RECT shaping filter). ©2017 IEEE

Table 4.7: ADP from (4.75) of Minimum-norm solutions $\mathbf{S}_\star$ and FFRED optimized Solutions $\mathbf{S}$

	Minimum norm $\mathbf{S}_\star$		FFRED Optimized $\mathbf{S}$	
	$\theta_r = -15°$	$\theta_r = 0°$	$\theta_r = -15°$	$\theta_r = 0°$
RECT	0.5119	0.7011	0.8313	0.8381
SRRC	0.4327	0.5820	0.6987	0.6975

$\theta_r = -15°$ and for an SRRC-filtered communications solution; likely a combination of a non-unity PAPR for the SRRC signal and the placement of the communications in the first sidelobe of the radar beam. The FFRED optimized solution increase the ADP with respect to all the corresponding minimum-norm solutions. The amplitude modulation induced by the SRRC shaping filter necessitates an increase in the amount of orthogonal power needed to converge thus lowering the ADP. The different spatial separations between the radar and communication beams had a negligible impact on the ADP for the FFRED optimized solutions.

The four sets of MIMO emissions were captured from $-60°$ to $60°$ at $2°$ increments using the quad-ridge horn antenna. The average emitted power versus angle θ and fast-time are shown in Figures 4.48 and 4.49 for cases 1 and 2, respectively. Note how additional transmit power is

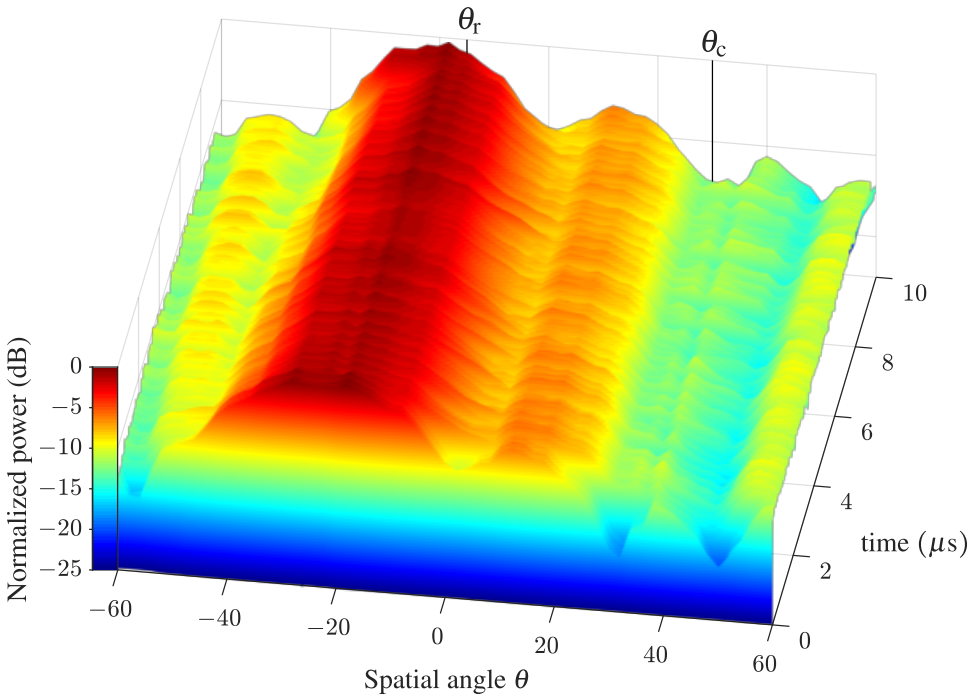

Figure 4.50: Average emitted power versus spatial angle θ and fast-time for case 3 ($\theta_r = -15°$ and SRRC shaping filter). ©2017 IEEE

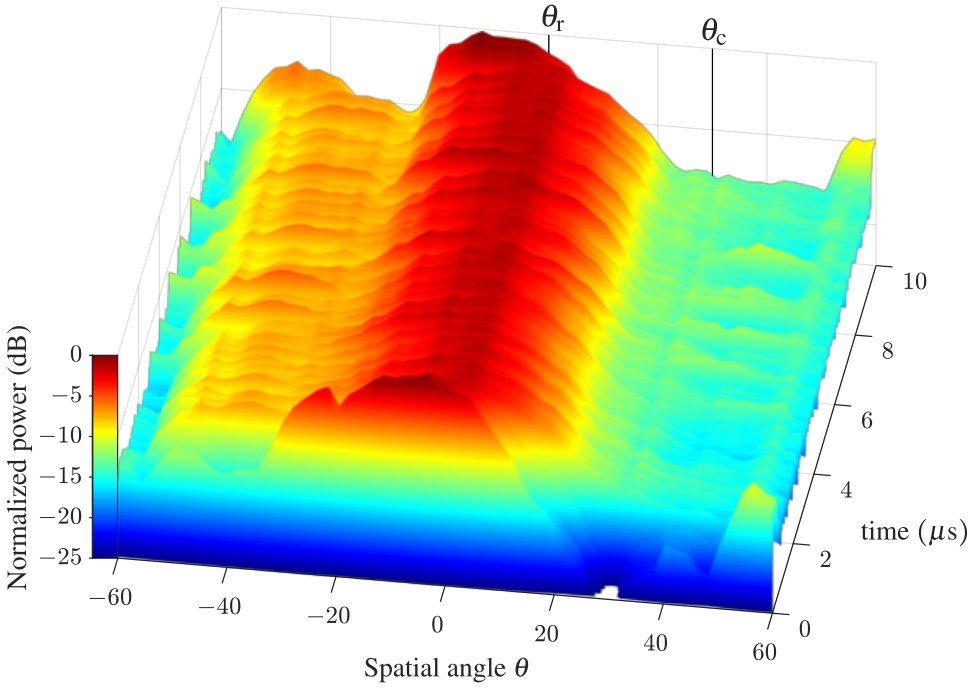

Figure 4.51: Average emitted power versus spatial angle θ and fast-time for case 4 ($\theta_r = 0°$ and SRRC shaping filter). ©2017 IEEE

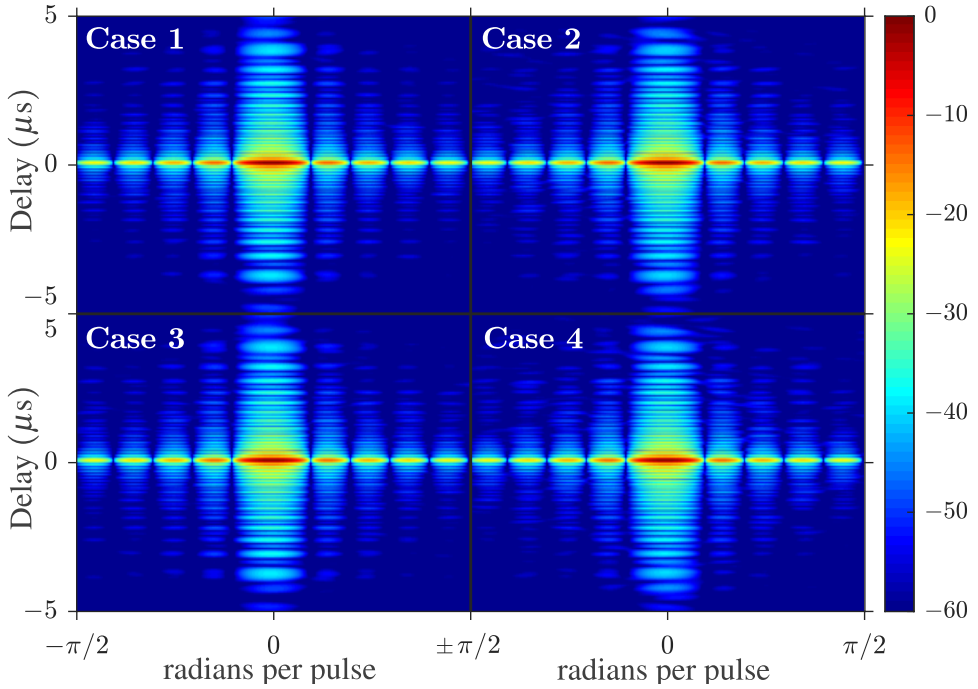

Figure 4.52: Range-Doppler response for radar beam directions for the four cases. ©2017 IEEE

apparent in directions other than the radar and communication directions. This power corresponds to the additional orthogonal power needed to realize a set of constant amplitude waveforms. Also note that the placement of the energy is dependent on the orientation of the radar and communication beams, and for case 2 is symmetric to the actual communication direction.

The average emitted power versus θ and fast-time for cases 3 and 4 are shown in Figures 4.50 and 4.51, respectively. The almost two-fold increase in percent orthogonal power for these cases is apparent as the additional power in other directions is noticeably higher than in the previous cases. For the cases involving the SRRC shaping filter, the amplitude modulation induced by the filters requires more power in the orthogonal complement directions (compared to the RECT cases) to realize a set of constant amplitude waveforms.

Now consider the cross-correlation of the signal captured in the direction of each radar beam with the intended up-chirped LFM radar waveform. The SNR of the radar beam prior to filtering was determined to be 33.16 dB. For each case, the 20 pulses are captured in the direction of the radar beam and then Doppler processed (see Figure 4.52). Each response resembles the typical range-Doppler point spread function of an LFM. For all four cases, the range sidelobes cohere at

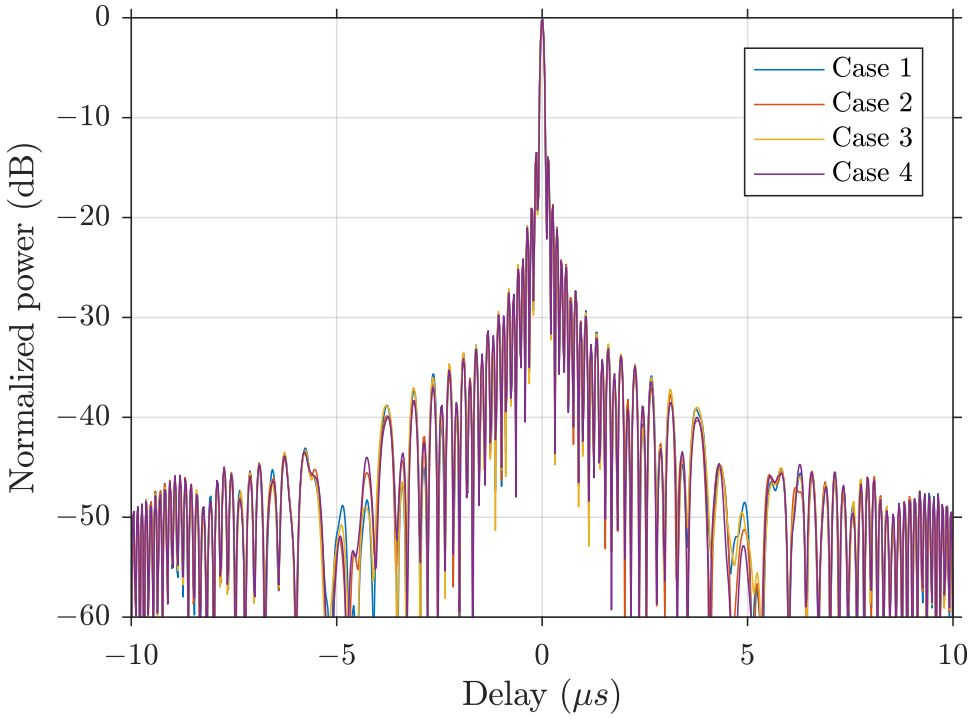

Figure 4.53: Zero-Doppler cut for radar beam directions for case 1 (blue), case 2 (red), case 3 (yellow), and case 4 (purple). ©2017 IEEE

zero Doppler indicating that the sidelobe structures are consistent over the 20 pulses. The zero Doppler cut of each case is likewise shown in Figure 4.53, where the sidelobe structure is nearly identical over the four cases and is very close to what is expected for the autocorrelation of an LFM waveform.

The signal emitted in the communication direction $\theta_c = 30°$ was captured and determined to have an average SNR of 21.13 dB (12.03 dB less than the radar signal, 0.97 dB different from the design specification of 13 dB). For each case the communication signal was demodulated using a Maximum-Likelihood estimator [47] and compared against the known bit sequence that was transmitted. Recall that cases 1 and 2 involved a total of 4000 bits while cases 3 and 4 involved 3600 bits. For cases 1, 2, and 4, zero bit errors were found, while 2 bit errors occurred for case 3.

A communication scatter plot for each case is shown in Figure 4.54. Note that case 2 (RECT shaping filter; $\theta_r = 0°$) produced the tightest grouping while case 3 produced the broadest grouping. A tighter grouping is associated with a better estimate of the true symbol value. For such a high SNR (21.13 dB), the inconsistent area covered by the bit groupings among the 4 cases

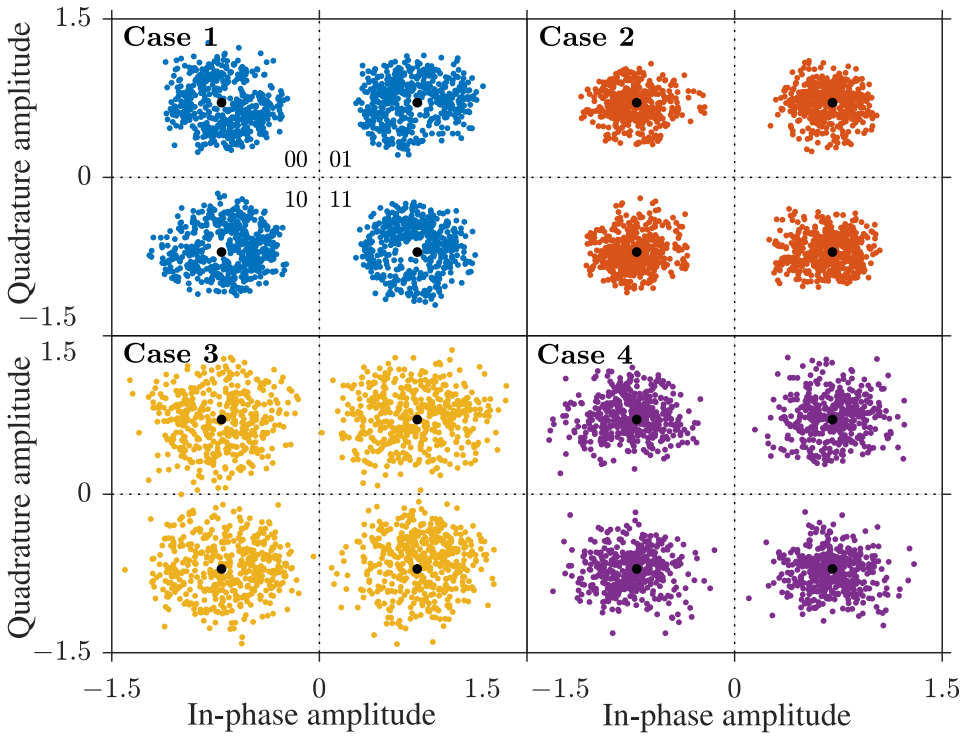

Figure 4.54: Constellation scatter plot for case 1 (blue), case 2 (red), case 3 (yellow), and case 4 (purple). ©2017 IEEE

indicates that interference in the communications direction is causing a wider spread among the bits compared to a case with only noise present. This interference is likely caused by errors in the transmit model used during optimization [24].

The convex hull of the demodulated symbols with the associated true constellation value for each is depicted in Figure 4.55. Note that the two bit errors for case 3 (yellow) are discernible in the '01' and '11' quadrants. It is also observed that the groupings for the RECT cases (1-blue and 2-red) are more consistent than the SRRC cases (3-yellow and 4-purple). This result is likely due to the communication signal in cases 3 and 4 being more sensitive to transmit model errors due to the resulting amplitude modulation from the SRRC shaping filter. Also, the groupings for the cases having radar direction $\theta_r = -15°$ (1-blue and 3-yellow) cover a larger area than the cases having radar direction $\theta_r = 0°$ (2-red and 4-purple). The disparity between these results indicates that the transmit model (steering vector) used for the radar direction $\theta_r = 0°$ better approximates the actual transmitter effects.

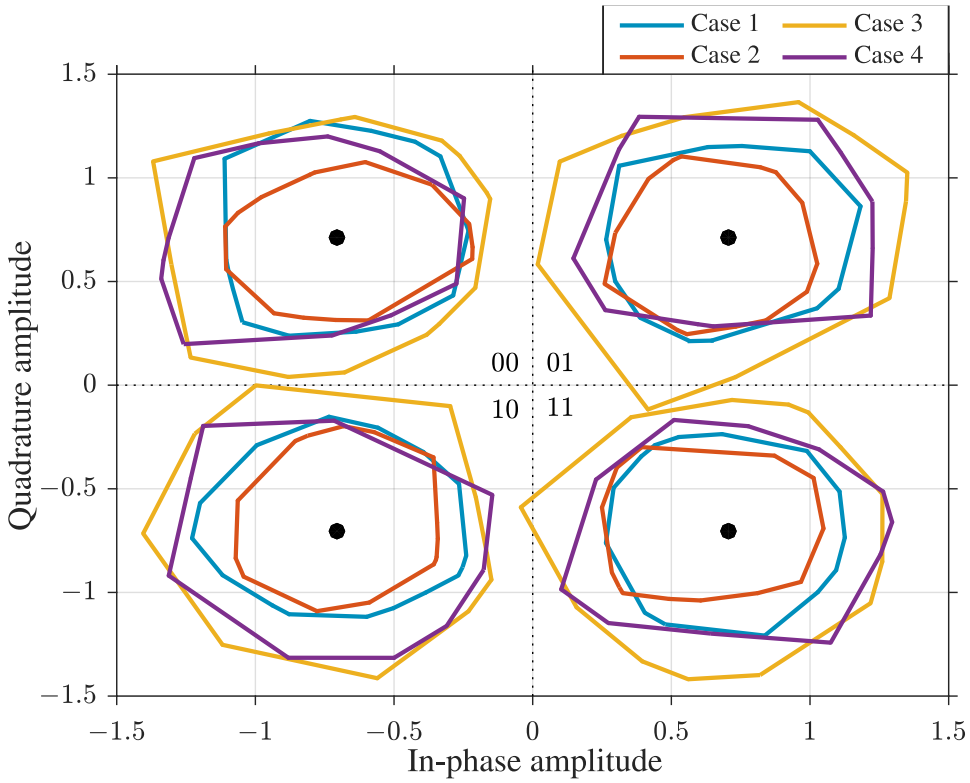

Figure 4.55: Convex hull of demodulated symbols with associated constellation symbol for case 1 (blue), case 2 (red), case 3 (yellow), and case 4 (purple). ©2017 IEEE

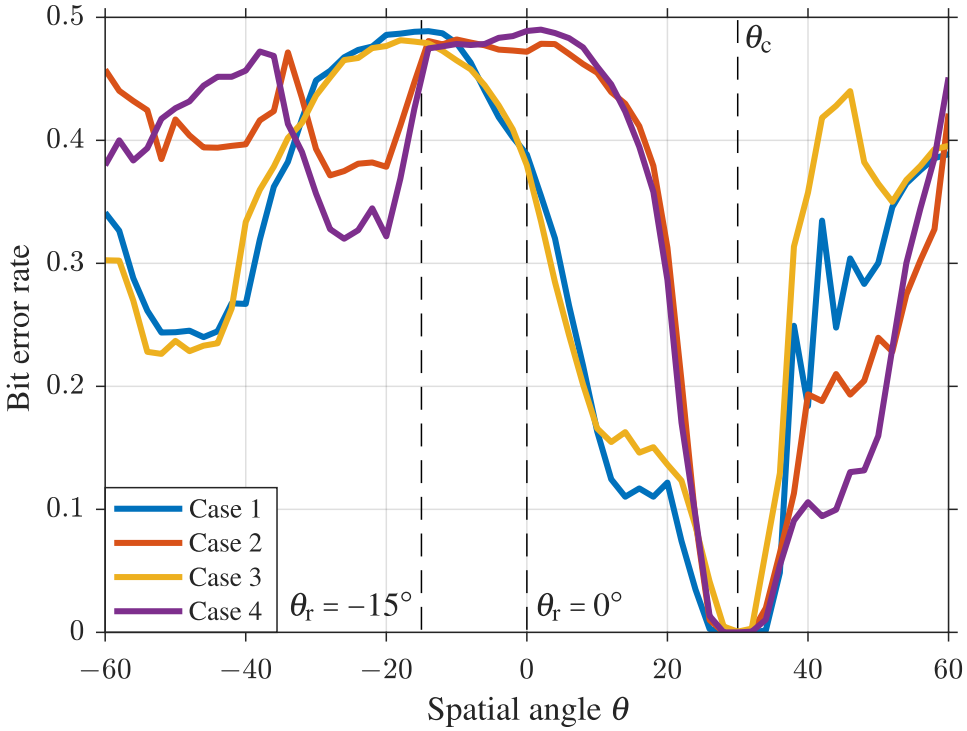

Figure 4.56: Bit error rate versus spatial angle for case 1 (blue), case 2 (red), case 3 (yellow), and case 4 (purple). ©2017 IEEE

It is also interesting to examine the structure of the fast-time signal in other spatial directions. Specifically, consider the impact of applying the communication ML estimator [47] to the signal captured from different directions. Comparing the results to the known bit sequences (and phase rotating as needed to assess the minimum possible bit error) as a function of angle produces the angle-dependent measured bit error rates (BER) shown in Figure 4.56 for the four test cases. In the intended communication direction of $\theta_c = 30°$ the previous good results are observed: for cases 1, 2 and 4 have no bit errors (BER = 0) while case 3 yields BER = 5.5×10^{-4} (2 errors out of 3600 bits). However, for other spatial angles, the BER increases significantly because the fast-time signals in those directions does not possess the expected communication signal structure. Note that the worst possible BER is 0.5 which is the expected value of BER for truly random bit estimates. The BER plots are shown in a linear scale instead of the traditional logarithmic scale as the curve shows more detail in angles away from the communications direction and to prevent the plots at $\theta = 30°$ from decreasing to minus infinity. Note cases possessing the same radar/communication spatial

separation (cases 1 and 3 for $\theta_r = -15°$ and cases 2 and 4 for $\theta_r = 0°$) also realize similar BER responses. The “dips" at $\theta = -50°$ (cases 1 and 3) and $\theta = -25°$ (cases 2 and 4) could be a result of multipath as the tests were not administered in an anechoic chamber.

4.3.6 Summary

The iterative optimization method of generating constant amplitude physically realizable waveforms that emit simultaneous radar and communications beams introduced in [24] and experimentally validated in [25] was further explored in this section. Particular attention is paid to power efficiency, through consideration of the average directed power (ADP) derived from a simple amplifier model, and how the orthogonal energy manifests itself in both space and frequency. It was found that the converged constant amplitude solutions generated using the FFRED algorithm produce waveforms can have as high as a 50% increase in ADP compared to the minimum-norm solution. It was also discovered that a constant amplitude communications signal resulted in a higher power efficiency as compared to a communications signal that requires amplitude modulation (e.g. SRRC-filtered QPSK). How the orthogonal power manifests itself under different scenarios was illustrated by observing the average spatial beampatterns and maximum spectral content. The communications performance was evaluated via a bit error rate evaluation simulated under different communications directions and power levels. It was found that the relative power level of the communications controls the “coherence beamwidth” at which the communications link can be achieved and that the method of symbol estimation can control the BER of signals emitted in directions away from the desired communications direction. The FFRED optimized emissions were experimentally tested using the AFRL four-channel BEEMER testbed and were found to provide satisfactory results even in this dimensionality constrained scenario.

4.4 Conclusions

The combination of waveform diversity and spatial diversity is realized in the the fully digital array radar (DAR) [20], which utilizes independent waveform generation at the element level to achieve multiple simultaneous functions. With the emergence of new digital array technology [22], the DAR is a future trend in array research which brings with it high-dimensional emission design capabilities to achieve multiple functions simultaneous and/or a MIMO/ubiquitous radar capability [20, 142]. In this chapter, three different examples spatially-diverse waveform design capabilities were presented with particular attention paid to attributes that are robust to deleterious effects within the radar. All waveforms in this section are designed/optimized to be constant amplitude and spectral contained, common characteristics of FM waveforms that are known to limit the performance degradation caused by high power amplifiers. Also, in Section 4.2 the invisible space was considered in the formation of wideband spatially-diverse emissions where the size of the reactive region in dependent on frequency.

Chapter 5

Descent Optimization Methods for Continuous-time, Frequency-Modulated Waveforms

Frequency modulated (FM) radar waveforms have been in use for more than 50 years [153] and come in many different forms [38, 50, 51, 57–59, 130, 154, 154–160] (see [3, 5] for further details). Such waveforms are particularly attractive because they are inherently constant amplitude (though additional tapering may be applied) and are well-contained spectrally, thus making them amenable to implementation in high-power radar transmitters (as discussed in Chapter 2). A considerable portion of traditional FM waveform design relies on the principle of stationary phase (POSP) [5, 50, 51, 57] where, given a prescribed amplitude envelope, the phase function of an FM waveform that approximates a desired spectral shape can be determined. This approximation becomes more accurate as the time-bandwidth product increases. By leveraging the power spectrum / autocorrelation Fourier pair, the power spectrum shape is thus chosen to correspond to an autocorrelation with low sidelobes. Here, the notion of FM waveform design is explored from an optimization perspective.

In Section 5.1 a continuous-time frequency-modulated waveform framework denoted as the Coded Frequency Modulated (CFM) waveform is defined. The phase function of the CFM waveform is defined using a weighted finite sum of predetermined basis functions. Therefore,

A portion of the text and figures in Chapter 5 are taken from "Nonlinear conjugate gradient optimization of polyphase-coded FM radar waveforms" by McCormick et al. printed in *2017 IEEE Radar Conference Proceedings* in May 2017, ©2011 IEEE. Another portion of the text and figures in Chapter 5 are taken from "Gradient-based Coded-FM Waveform Design using Legendre Polynomials" by McCormick et al. printed in *2017 IET International Conference on Radar Systems Proceedings* in October 2017, ©2017 IET.

the CFM waveform is parameterized using a discrete set of parameters thus lending itself to gradient-based optimization methods [161, 162]. Gradient descent optimization has previously been examined (e.g. [128, 163–167] to address various attributes of radar code design). Such methods have likewise been applied to design the ambiguity function adaptively for target matched illumination [168]. However, to the author's knowledge, the work presented in this chapter, along with the corresponding publications [161,162], are the first instances of continuous-time waveform optimization using gradient-based methods.

Generally speaking, the determination of a radar waveform's "goodness" is primarily determined via some measure of the properties of the waveform's autocorrelation (matched filter response) [3]. Specifically, we generally wish to minimize the sidelobes for a given mainlobe width. Typical metrics associated with the quality of a waveform autocorrelation function are the integrated-sidelobe level (ISL) which is the ratio of sidelobe to mainlobe energy, and peak-sidelobe level (PSL) which is the ratio of peak sidelobe level to maximum overall correlation level. Here, a generalized integrated sidelobe (GISL) metric for FM waveforms is introduced to encapsulates both the ISL and PSL metrics into one metric by taking the q-norm ratio of the autocorrelation sidelobes to the autocorrelation mainlobe, where $q = 2$ corresponds to ISL and $q \to \infty$ corresponds to PSL. In this chapter is it shown that by leveraging the relationship between the pulse compression ratio and time-bandwidth product from (2.69), the time-bandwidth product of the optimized waveform can be effectively set without explicit shaping of the waveform spectrum through determination of the corresponding normalized peak-to-null mainlobe width $\Delta\tau/T$ of the autocorrelation and application within the GISL metric.

In Section 5.2, the optimization of a specific type of CFM waveform denoted as polyphase-coded FM (PCFM) is demonstrated using nonlinear conjugate gradient descent [38, 79, 161]. The notion of waveform design degrees of freedom is addressed within the context of both sampled bandwidth (via the receiver sampling rate) and 3 dB resolution bandwidth. When the sampled bandwidth is larger than the resolution bandwidth, additional degrees of freedom corresponding to the spectral roll-off region become available for use in waveform optimization. Utilizing this extra

dimensionality we show that the possible optimized autocorrelation is largely independent of the waveform time-bandwidth product, which is itself defined using resolution bandwidth.

In Section 5.3, a novel waveform optimization function is proposed for use in the GISL metric that encapsulates both the continuous-time nature of the CFM waveform and the discrete-time nature of the pulse compression receive filter in an attempt to incorporate real-world effects into the optimization. The sidelobes of the modified correlation function are lowered using a Quasi-Newton method to minimize the GISL metric for a CFM waveform defined using the Legendre polynomial basis. This basis is shown to require a fraction of the basis functions needed to represent a waveform with low sidelobe level as compared to the PCFM basis. A experimental loopback[1] capture of the optimized waveforms reveal a slight distortion in very low power sidelobe levels (~ -80 dB) which is found to be caused by transmitter and receiver distortions that are ignored within the modified correlation function.

In Section 5.4, *system specific* waveform optimization is explored through estimation of the transmitter and receiver distortion via a linear model for three different loopback hardware configurations: 1) single RF cable, 2) a single amplifier (not in saturation), and 3) two cascaded amplifiers with one in saturation. The linear model is incorporated into the modified correlation function from Section 5.3 to compensate for the distortion and achieve a better prediction of the correlation response. The optimized waveforms are shown to match the expected responses (via the estimated linear model) to a high degree and achieve a lower overall sidelobe level response than what was previously shown in Section 5.3 using the Legendre polynomial basis set and the same waveform parameters.

5.1 Evaluation of Coded FM Waveforms

The coded frequency modulated (CFM) waveform model is a continuous-time waveform definition that is parameterized using a discrete, finite sequence of values. By defining the ambiguity function

[1] A loopback capture is performed by directly connecting the waveform generator to the radar receiver. The RF chain can include different layers of reality into the testing (e.g. all RF components in chain, a direct connection between the generator and ADC) to observe the behavior of the RF distortion of the components.

and discrete-time autocorrelation of these waveforms we can construct a waveform metric denoted Generalized Integrated Sidelobe Level (GISL) that encompasses both the peak sidelobe level (PSL) and the integrated sidelobe level (ISL) which are common waveform evaluation metrics. In doing so, a peak-to-null mainlobe width must be defined to partition the correlation mainlobe from that of the sidelobes.

5.1.1 Coded Frequency Modulated Waveforms

Recall from Section 2.1.1 that the complex-baseband FM waveform can be represented as

$$s(t) = u(t)e^{j\psi(t)}, \tag{5.1}$$

where $u(t)$ is the positive, real-valued, amplitude envelope and $\psi(t)$ is the continuous phase function. For pulsewidth T, define $u(t)$ over the interval $t \in [0, T]$ (zero outside these limits), therefore $\psi(t)$ must also be defined over this interval. In general, the coded FM (CFM) phase function $\psi(t)$ can be represented as a weighted sum of N_p continuous-time basis functions as

$$\psi(t; \mathbf{x}_\mathrm{w}) = \sum_{n=0}^{N_\mathrm{p}-1} \alpha_n h_n(t), \tag{5.2}$$

where $h_n(t)$ is the nth basis function, α_n is its corresponding real-valued weighting, and $\mathbf{x}_\mathrm{w} = \begin{bmatrix} \alpha_0 & \alpha_1 & \cdots & \alpha_{N_\mathrm{p}-1} \end{bmatrix}^T$ is an $N_\mathrm{p} \times 1$ vector containing the parameters. The collection of N_p basis functions $h_n(t)$ for $n \in \{0, 1, \ldots, N_\mathrm{p} - 1\}$ can be expressed as the basis function set $\mathcal{B}$ defined as

$$\mathcal{B} = \{h_0(t), h_1(t), \ldots, h_{N_\mathrm{p}-1}(t)\}. \tag{5.3}$$

For a given amplitude envelope $u(t)$ and set of basis functions $\mathcal{B}$, the FM waveform is completely parameterized by the N_p parameters contained in $\mathbf{x}_\mathrm{w}$. The parameterization is akin to the polyphase-coded FM (PCFM) definition discussed in Section 2.1.2.4. In fact, the CFM definition is a generalized waveform model for which PCFM is a particular basis.

5.1.2 Generalized Integrated Sidelobe Level

A generalized integrated sidelobe level (GISL) metric is defined that encompasses both the PSL metric from (2.64) and ISL metric from (2.65) into one by taking the q-norm ratio of the autocorrelation sidelobes to the autocorrelation mainlobe as

$$\mathcal{J}_{\mathrm{c}}(\mathbf{x}_{\mathrm{w}};q)=\left(\frac{\displaystyle\int_{-T}^{-\Delta\tau}|\chi_{\mathrm{a}}(\tau)|^{q}dt+\int_{\Delta\tau}^{T}|\chi_{\mathrm{a}}(\tau)|^{q}dt}{\displaystyle\int_{-\Delta\tau}^{\Delta\tau}|\chi_{\mathrm{a}}(\tau)|^{q}dt}\right)^{1/q} \tag{5.4}$$

where q is a positive integer. The exponent q dictates the particular sidelobe metric used, with $q=2$ corresponding to ISL and $q\to\infty$ to PSL. A similar metric to (5.25) has also recently been proposed for the design of phase codes [165, 166].

Observe that, for $q\in\{2,3,4,\dots\}$, the metric in (5.4) is a continuous function of the length-N_{p} parameter vector $\mathbf{x}_{\mathrm{w}}$. As such, gradient-based optimization methods (e.g. nonlinear conjugate gradient [161], quasi-Newton method, etc.) can be implemented to minimize this metric [79]. The variability of the cost function in (5.4) with norm q can drastically change the autocorrelation properties of a resulting (iteratively) optimized waveform given the same waveform initialization. Of course, it should be noted that the gradient of $\mathcal{J}_{\mathrm{a}}(\mathbf{x}_{\mathrm{w}};\xi,q\to\infty)$ is discontinuous, and thus gradient-based PSL optimization can only be approximated for q large. A q-norm of $q\in\{5,6,7\}$ has been found to retain both ISL and PSL properties.

The discretized version of (5.4) uses the discrete-time autocorrelation from (2.204) and is likewise

$$\mathcal{J}_{\mathrm{d}}(\mathbf{x}_{\mathrm{w}};q)=\left(\frac{2\displaystyle\sum_{\ell=\Lambda}^{N-1}|r[\ell]|^{q}}{\displaystyle\sum_{\ell=-\Lambda+1}^{\Lambda-1}|r[\ell]|^{q}}\right)^{1/q}, \tag{5.5}$$

where $\Lambda=\lceil f_{\mathrm{s}}\Delta\tau\rceil=\lceil\kappa\rceil$ is the discrete peak-to-null mainlobe sample width for $\lceil\bullet\rceil$ the ceiling operation. Note that the outer exponent $(\bullet)^{1/q}$ in (5.4) and (5.5) is the reason why the general

metric becomes PSL when $q \to \infty$. However, from a numerical standpoint very large values of q can be problematic. When more modest values are employed (e.g. $5 \leq q \leq 7$ has been found to work well) the $(\bullet)^{1/q}$ operation can be omitted since is does not affect the minimums in the cost function, though it is kept here for completeness. Similar metrics have also recently been used for optimization of phase codes [165, 166]. The discrete sequence parameterization of the CFM waveform coupled with the GISL metric to measure the quality of the waveform provide a foundation for continuous-time waveform optimization via gradient-based methods.

In Section 2.1.4 it was shown that the peak-to-null mainlobe width $\Delta\tau$ is related to the 3 dB bandwidth as $\Delta\tau \approx 1/B_{3\text{dB}}$ via (2.67) which can be used to find an approximate relationship between the time-bandwidth product and the pulse compression ratio, $T/\Delta\tau \approx BT$ from (2.69). Therefore, within the optimization process the relative peak-to-null mainlobe width $\Delta\tau/T$ is set to the inverse of the desired time-bandwidth product $\Delta\tau/T = 1/[BT]_{\text{desired}}$ which effectively sets the time-bandwidth of the waveform without explicitly shaping the spectral content. For the discretized cost function $\mathcal{J}_{\text{d}}(\mathbf{x}_{\text{w}};q)$, the same relationship can be implemented however in a discrete form. The normalized discrete peak-to-null width for $r[\ell]$ is Λ/N. Because Λ is an integer, the achievable time-bandwidth products using (5.5) are limited to integer divisions of N (i.e. $BT \in \{N, N/2, N/3, \dots\}$).

5.2 Optimization of CFM waveforms with Polyphase-Coded FM Basis via Nonlinear Conjugate Gradient Descent

The polyphase-coded FM (PCFM) basis for CFM is well established in the literature [38, 44, 62, 157, 169, 170] denoted simply as the PCFM waveform. The coded-FM framework is the result of a generalization of PCFM which was previously developed using continuous phase modulation (CPM) framework used in communications to produce constant modulus signals (see Section 2.1.2.4 for more information). The optimization of PCFM waveforms has been considered in the past using a greedy-search algorithm to minimize a combination PSL, ISL, and frequency template

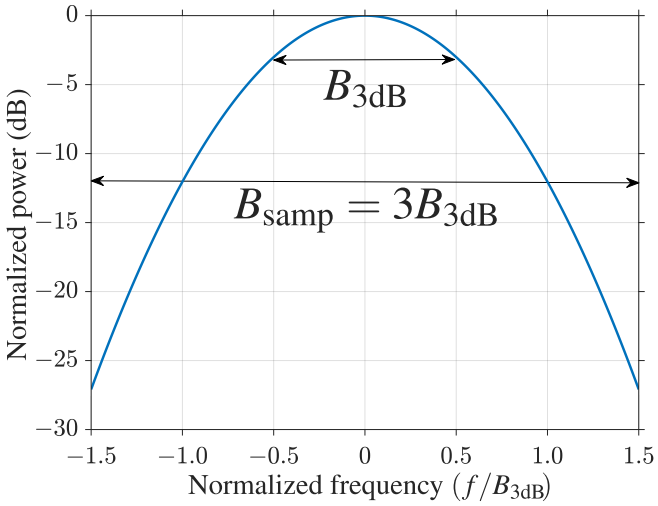

Figure 5.1: Comparison of resolution bandwidth $B_{3\text{dB}}$ and sampled bandwidth B_{samp} for Gaussian power spectrum with over-sampling $\kappa = 3$. ©2017 IEEE

error (FTE) metrics [44]. A main drawback of the greedy search algorithm used in [44] is only a single parameter α_n can be updated each iteration which restricts the amount that the cost function can reduce per iteration. Here, a nonlinear conjugate gradient method (NLCG) is implemented to minimize the GISL metric by updating the entirety of the parameter vector $\mathbf{x}_{\text{w}}$ each iteration.

As discussed in Section 2.1.3, it is known that a pulsed waveform such as in (5.1), having finite time support on $[0,T]$, corresponds to a theoretically infinite bandwidth. As such, it is not theoretically possible to achieve Nyquist sampling. However, because FM waveforms possess good spectral containment (i.e. acceptable roll-off), the amount of energy outside the sampled frequency content can be made small by over-sampling the digital matched filter with respect to the 3 dB resolution bandwidth. Denote $B_{3\text{dB}}$ as the 3 dB *resolution bandwidth* associated with the time-bandwidth product, BT, and $B_{\text{samp}} = f_{\text{s}} = \kappa B_{3\text{dB}}$ as the *sampled bandwidth* for over-sampling factor $\kappa \geq 1$. Figure 5.1 illustrates the sampled bandwidth versus the resolution bandwidth for a Gaussian power spectrum with over-sampling $\kappa = 3$.

For $B_{3\text{dB}}$ and T the pulse duration, the time-bandwidth product BT is generally viewed as a determining factor in how low the autocorrelation sidelobes can be driven. For example, length-N Barker codes, along with their polyphase counterpart, possess the property that the PSL does not exceed $1/N$ [5], where N also closely approximates BT. Likewise, in [58] it is stated that

for hyperbolic FM (HFM) waveforms the bound on PSL is $-20\log_{10}(B_{\mathrm{a}}T) - 3$ dB albeit for the analytical bandwidth B_{a} in place of the 3 dB bandwidth. In this section, it is shown that it is actually the receiver *sampled bandwidth* that determines the general sidelobe floor for the autocorrelation of a waveform. For FM waveforms, the sampled bandwidth provides additional degrees-of-freedom for waveform design (as long as an appropriate spectral roll-off is also maintained). While such over-sampling incurs a higher computational cost for pulse compression, it is known to remediate some of the degradation that may occur from range straddling effects [81]. Further, by designing the waveform with knowledge of the degree of over-sampling, and thus the discrete length of the digital pulse compression filter, the minimum PSL from (2.205) (Section 2.4.3) for that given filter length can be achieved.

5.2.1 Polyphase-coded FM basis definition

PCFM waveforms as discussed in Section 2.1.2.4 are defined via the continuous phase modulation implementation [151] via Figure 2.10. Here the PCFM waveform is discussed in terms of a basis used in the CFM framework defined in (5.1) and (5.2). The basis set $\mathcal{B}$ from (5.3) for PCFM is comprised of basis functions defined by the expression

$$h_n(t) = \int_0^t w_{\mathrm{p}}(\zeta - nT_{\mathrm{p}})d\zeta \tag{5.6}$$

for $n \in \{0,\ldots,N_{\mathrm{p}}-1\}$ and defined over $t \in [0,T]$. Recall from Section 2.1.2.4 that $w_{\mathrm{p}}(t)$ is a rectangular function which is defined to be nonzero over the interval $t \in (0,T_{\mathrm{p}}]$ with an amplitude of $1/T_{\mathrm{p}}$ where $T_{\mathrm{p}} = T/N_{\mathrm{p}}$. Therefore the set $\mathcal{B}$ for the PCFM basis is defined as

$$\mathcal{B}_{\mathrm{PCFM}} = \left\{ \int_0^t w_{\mathrm{p}}(\zeta)d\zeta, \int_0^t w_{\mathrm{p}}(\zeta - T_{\mathrm{p}})d\zeta, \ldots, \int_0^t w_{\mathrm{p}}(\zeta - (N_{\mathrm{p}}-1)T_{\mathrm{p}})d\zeta \right\}. \tag{5.7}$$

An illustration of the nth PCFM basis function is shown in Figure 2.11.

A summation of scaled PCFM basis functions results in a piecewise linear phase function $\psi(t)$.

As the the number of basis functions/parameters N_p increases (thus increasing the dimensionality of code vector $\mathbf{x}_\mathrm{w}$) the ramp transition time T_p decreases which results in finer control over the continuous transition of phase within the waveform. It is generally thought that the time-bandwidth product BT of a waveform corresponds to the available design degrees of freedom for a waveform. However, such as was demonstrated using the notion of "over-coding" in [157], the spectral roll-off region can be used as a source of additional degrees of freedom without changing the resolution bandwidth or significantly altering the spectral containment. In that situation, the number of code values N_p can be made to exceed BT significantly to give further lowering of the autocorrelation sidelobe level. In fact, the maximum degrees of freedom correspond to $B_\mathrm{samp}T$ which is the length N of the matched filter used on receive.

5.2.2 Waveform optimization via nonlinear conjugate gradient descent

The cost function used for optimization of CFM waveforms using the PCFM basis is the discrete version of the GISL metric from (5.5) which considers only the discrete-time autocorrelation (2.204). Thus, the optimization problem can be stated as:

$$\underset{\mathbf{x}_\mathrm{w}}{\text{minimize}} \quad \mathcal{J}_\mathrm{d}(\mathbf{x}_\mathrm{w}; q), \tag{5.8}$$

which can be readily minimized using the gradient of $\mathcal{J}_\mathrm{d}(\mathbf{x}_\mathrm{w}; q)$. Here, the nonlinear conjugate gradient method is used which is an iterative scheme that descends onto a stationary point of a given objective function. The conjugate gradient method (both linear and nonlinear versions) converge faster than steepest descent and do not require the calculation/estimation of the Hessian as would be necessary for quadratic model techniques such as Newton's method [79]. Here, the modified Hestenes-Stiefel NLCG method using a line search satisfying the strong Wolfe conditions [79] for step-size determination is implemented to optimize the vector $\mathbf{x}_\mathrm{w}$ that parameterizes the CFM waveform.

5.2.2.1 Gradient Calculation

The gradient with respect to the real-valued parameter vector $\mathbf{x}_\mathrm{w}$ is composed of the partial derivatives

$$\nabla = \left[\begin{array}{cccc} \dfrac{\partial}{\partial \alpha_0} & \dfrac{\partial}{\partial \alpha_1} & \cdots & \dfrac{\partial}{\partial \alpha_{N_\mathrm{p}-1}} \end{array} \right]^T. \tag{5.9}$$

Application of the nth partial derivative from (5.9) (for $n \in \{0, \ldots, N_\mathrm{p}-1\}$) to the GISL cost function in (5.5) yields

$$\frac{\partial \mathcal{J}_\mathrm{d}(\mathbf{x}_\mathrm{w}; q)}{\partial \alpha_n} = \left(\frac{2 \sum\limits_{\ell=\Lambda}^{N-1} |r[\ell]|^q}{\sum\limits_{\ell=-\Lambda+1}^{\Lambda-1} |r[\ell]|^q} \right)^{1/q} \left[\frac{\sum\limits_{\ell=\Lambda}^{N-1} |r[\ell]|^q \Re\left\{ \dfrac{a_n[\ell] + a_n^*[-\ell]}{r[\ell]} \right\}}{\sum\limits_{\ell=\Lambda}^{N-1} |r[\ell]|^q} - \frac{\sum\limits_{\ell=-\Lambda+1}^{\Lambda-1} |r[\ell]|^q \Re\left\{ \dfrac{a_n[\ell] + a_n^*[-\ell]}{r[\ell]} \right\}}{\sum\limits_{\ell=-\Lambda+1}^{\Lambda-1} |r[\ell]|^q} \right] \tag{5.10}$$

where $\Re\{\bullet\}$ extracts the real value and

$$a_n[\ell] = \frac{-j}{N} \sum_{i=0}^{N-1} h_n(iT_\mathrm{s} + \xi) s^*(iT_\mathrm{s} + \xi)\, s\big((i+\ell)T_\mathrm{s} + \xi\big). \tag{5.11}$$

A derivation of (5.10) is provided in Appendix A.10. Recall from Section 2.4.2 that $\xi \in [0, T_\mathrm{s}]$ is a subsample offset chosen during discretization of the waveform $s(t)$ for matched filtering. For the results in Section 5.2, the subsample shift is chosen as $\xi = T_\mathrm{s}$. The N_p partial derivatives in (5.10) are collected into the $N_\mathrm{p} \times 1$ gradient vector $\nabla \mathcal{J}_\mathrm{d}(\mathbf{x}_\mathrm{w}; q)$ that is used in the NLCG formulation.

5.2.2.2 Nonlinear Conjugate Gradient Descent

The nonlinear variant of the conjugate gradient is a generalization of the linear conjugate gradient method that is known to converge faster than steepest descent while only requiring the memory storage of a few vectors. The general form of the update of vector $\mathbf{x}_\mathrm{w}$ at iteration i is

$$\mathbf{x}_{\mathrm{w},i+1} = \mathbf{x}_{\mathrm{w},i} + \mu_i \mathbf{p}_i \tag{5.12}$$

for direction $\mathbf{p}_i$ and step-size μ_i. For NLCG, the direction $\mathbf{p}_i$ is initialized to the gradient descent direction $\mathbf{p}_0 = -\nabla \mathcal{J}_{\mathrm{d}}(\mathbf{x}_{\mathrm{w},0}; q)$ and is updated as

$$\mathbf{p}_i = \begin{cases} -\nabla \mathcal{J}_{\mathrm{d},0} & \text{when } i = 0 \\ -\nabla \mathcal{J}_{\mathrm{d},i} + \beta_i \mathbf{p}_{i-1} & \text{otherwise} \end{cases} \tag{5.13}$$

where $\nabla \mathcal{J}_{\mathrm{d},i} = \nabla \mathcal{J}_{\mathrm{d}}(\mathbf{x}_{\mathrm{w},i}; q)$ and β_i is a scalar chosen such that a conjugacy condition holds [171] (assuming exact line search). There are various adaptations to NLCG that have been proposed involving adaptation of the parameter β_i. Here we choose the modified Hestenes-Stiefel method [79] of

$$\beta_i = \beta_i^{\mathrm{HS+}} = \max\{\beta_i^{\mathrm{HS}}, 0\} \tag{5.14}$$

where

$$\beta_i^{\mathrm{HS}} = \frac{-\nabla \mathcal{J}_{\mathrm{d},i}^T \left(\nabla \mathcal{J}_{\mathrm{d},i} - \nabla \mathcal{J}_{\mathrm{d},i-1} \right)}{\left(\nabla \mathcal{J}_{\mathrm{d},i} - \nabla \mathcal{J}_{\mathrm{d},i-1} \right)^T \mathbf{p}_{i-1}} \tag{5.15}$$

which has a built in reset stage where the direction $\mathbf{p}_i$ reverts back to the negative of the gradient when $\beta_i^{\mathrm{HS}} < 0$.

The Hestenes-Stiefel method has been proven to be robust and ensure local convergence for general nonlinear cost functions that are continuously differentiable if the step sizes μ_i satisfy the strong Wolfe conditions [79, 171]. Specifically, the strong Wolfe conditions are the *sufficient decrease condition*

$$\mathcal{J}_{\mathrm{d}}\left(\mathbf{x}_{\mathrm{w},i} + \mu_i \mathbf{p}_i; q\right) \leq \mathcal{J}_{\mathrm{d}}\left(\mathbf{x}_{\mathrm{w},i}; q\right) + c_1 \mu_i \nabla \mathcal{J}_{\mathrm{d}}(\mathbf{x}_{\mathrm{w},i}; q)^T \mathbf{p}_i \tag{5.16}$$

and the *curvature condition*

$$\left| \nabla \mathcal{J}_{\mathrm{d}}(\mathbf{x}_{\mathrm{w},i} + \mu_i \mathbf{p}_i; q)^T \mathbf{p}_i \right| \leq c_2 \left| \nabla \mathcal{J}_{\mathrm{d}}(\mathbf{x}_{\mathrm{w},i}; q)^T \mathbf{p}_i \right| \tag{5.17}$$

for $0 < c_1 < c_2 < 1$. Here the values $c_1 = 10^{-3}$ and $c_2 = 0.1$ are used. The step size μ_i is determined using a Bisection method with a Wolfe condition check between each step [79].

The algorithm is terminated when the 2-norm of the step direction is approximately zero $\|\mathbf{p}_i\|_2$ indicating $\mathbf{x}_{\mathrm{w},i}$ is located at a stationary point of $\mathcal{J}(\mathbf{x}_{\mathrm{w},i}; q)$. Therefore, the vector $\mathbf{x}_{\mathrm{w},\star} = \mathbf{x}_{\mathrm{w},i}$ is returned as the locally optimal solution. The NLCG procedure for optimizing CFM waveform using the PCFM basis is shown in Algorithm 5.1.

Algorithm 5.1 Nonlinear conjugate gradient descent using modified Hestenes-Stiefel method

Initialize: BT, κ, N_{p}, q, $\mathbf{x}_{\mathrm{w},0}$, $\mathcal{B} = \mathcal{B}_{\mathrm{PCFM}}$, $\mathbf{p}_0 = -\nabla\mathcal{J}_{\mathrm{d},0}$, $c_1 = 10^{-3}$, $c_2 = 0.1$, and $i = 0$
repeat
  Choose μ_{i} that satisfies (5.16) and (5.17)
  $\mathbf{x}_{\mathrm{w},i+1} = \mathbf{x}_{\mathrm{w},i} + \mu_i \mathbf{p}_i$
  $i = i + 1$
  Calculate $\nabla\mathcal{J}_{\mathrm{d},i}$ via (5.10)
  Calculate β_i^{HS} via (5.15)
  $\beta_i = \max\{\beta_i^{\mathrm{HS}}, 0\}$
  $\mathbf{p}_i = -\nabla\mathcal{J}_{\mathrm{d},i} + \beta_i \mathbf{p}_{i-1}$
until $\|\mathbf{p}_i\|_2 \approx 0$
$\mathbf{x}_{\mathrm{w},\star} = \mathbf{x}_{\mathrm{w},i}$
return $\mathbf{x}_{\mathrm{w},\star}$

5.2.3 Optimized CFM waveforms using the PCFM basis

To understand how the exponent parameter q in (5.5) affects the optimization, a rectangular envelope (for $u(t)$) CFM waveform of time-bandwidth product $BT = 128$ with over-sampling $\kappa = 4$ is optimized for each of the integer exponent values $q \in \{2, 4, 7\}$. The length of the discretized waveform is $N = 4BT = 512$. The number of PCFM basis functions is also set to $N_{\mathrm{p}} = BT = 128$. The NLCG method was initialized with an approximation of the linear-frequency modulated (LFM) waveform[2] of the same time-bandwidth, BT.

Figure 5.2 shows the converged CFM waveform autocorrelations for $q \in \{2, 4, 7\}$. The $q = 2$ (ISL) case does not prioritize minimizing the energy close to the mainlobe and falls into a local

[2]Because the phase function using the PCFM basis is piecewise linear, the quadratic phase function of an LFM is approximated.

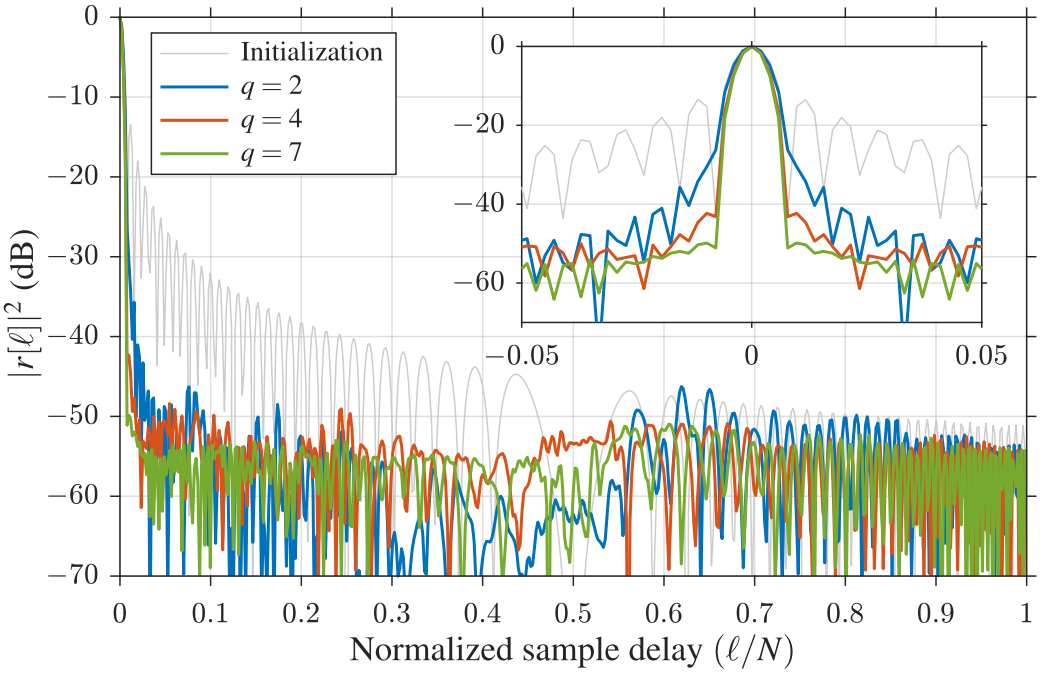

Figure 5.2: Optimized discrete autocorrelation responses $|r[\ell]|^2$ from (2.204) versus normalized sample delay (ℓ/N) for CFM waveforms with PCFM basis of $BT = N_p = 128$ and $\kappa = 4$ using $q = 2$ (blue), $q = 4$ (red), and $q = 7$ (yellow) cost function norms with LFM initialization in gray. ©2017 IEEE

minimum with relatively high PSL. Both the $q = 4$ and $q = 7$ cases improve on this characteristic. It was observed (though not included here) that autocorrelation responses for $q > 7$ change only marginally from the $q = 7$ case. For this particular initialization and set of parameters the $q = 7$ case produced the best autocorrelation response and thus is used for the remainder of Section 5.2.

Figure 5.3 shows the autocorrelation of two optimized CFM waveforms with $BT = 128$ over-sampled by $\kappa = 4$ ($N = 512$) both having a rectangular envelope $u(t)$ of duration T. To demonstrate how the optimization performance improves with increased degrees of freedom, the CFM parameter vector $\mathbf{x}_w$ is optimized for lengths $N_p = BT = 128$ and $N_p = 2BT = 256$, where the latter represents over-coding by 2 [157]. The $N_p = 256$ case has converged to a sidelobe level that is approximately 4 dB lower than the $N_p = 128$ case. The doubling of the degrees of freedom has also allowed the PSL of the $N_p = 256$ case, which is −52 dB (near mainlobe), to get within 2.19 dB of the theoretical $\text{PSL}_{\text{RECT-bound}}$ limit of −54.19 dB (from (2.205)). Figure 5.4 shows the power spectra of these two cases along with the LFM initialization for the entire sampled bandwidth. Note that

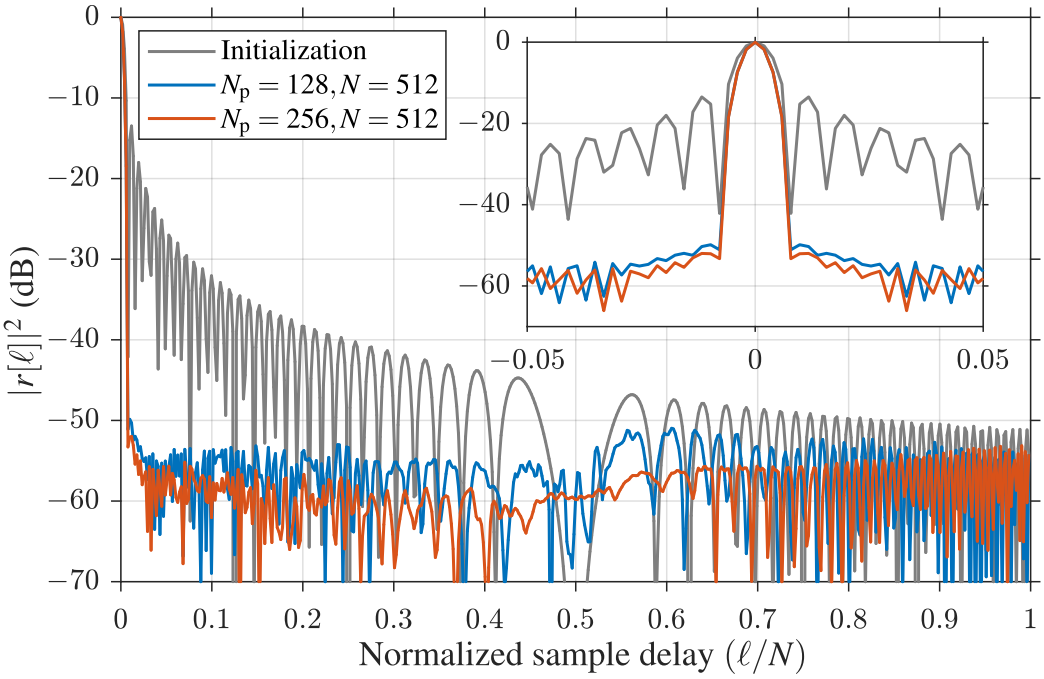

Figure 5.3: Optimized discrete autocorrelation responses $|r[\ell]|^2$ from (2.204) versus normalized sample delay (ℓ/N) for CFM waveforms with a PCFM basis of $BT = 128$ and $N = 4BT = 512$ using $N_p = 128$ (blue) and $N_p = 256$ (red) parameters with LFM initialization in gray. ©2017 IEEE

by approximating $BT \approx N/\Lambda = 512/4 = 128$ we have successfully set the desired bandwidth B_{3dB} at the half-power point of the spectrum.

Now consider the case of a fixed code dimensionality of $N_p = 256$ for use with a discretized matched filter length of $N = 512$ while the time-bandwidth product is varied over $BT \in \{32, 64, 128, 256\}$[3]. These cases correspond to respective over-coding factors of $\{8, 4, 2, 1\}$ [157]. Likewise, the associated over-sampling factors are $\kappa \in \{16, 8, 4, 2\}$. It is assumed that these waveforms have a rectangular envelope $u(t)$ of pulse duration T, such that a fixed N corresponds to a fixed sampled bandwidth B_{samp}. Thus the different BT values correspond to a change in the waveform resolution bandwidth B_{3dB}. This comparison therefore demonstrates how much of an effect BT has on the autocorrelation of an optimized waveform.

For each case, the optimization is initialized with an PCFM-approximated LFM waveform of the same BT, Figure 5.5 shows the resulting power spectra after the algorithm has converged. It is interesting to note that, despite there being no explicit spectral shaping performed, each frequency

[3]Recall that for $\mathcal{J}_d(\mathbf{x}_w; q)$, the time-bandwidth product can only be set to integer divisions of N (Section 5.1.2).

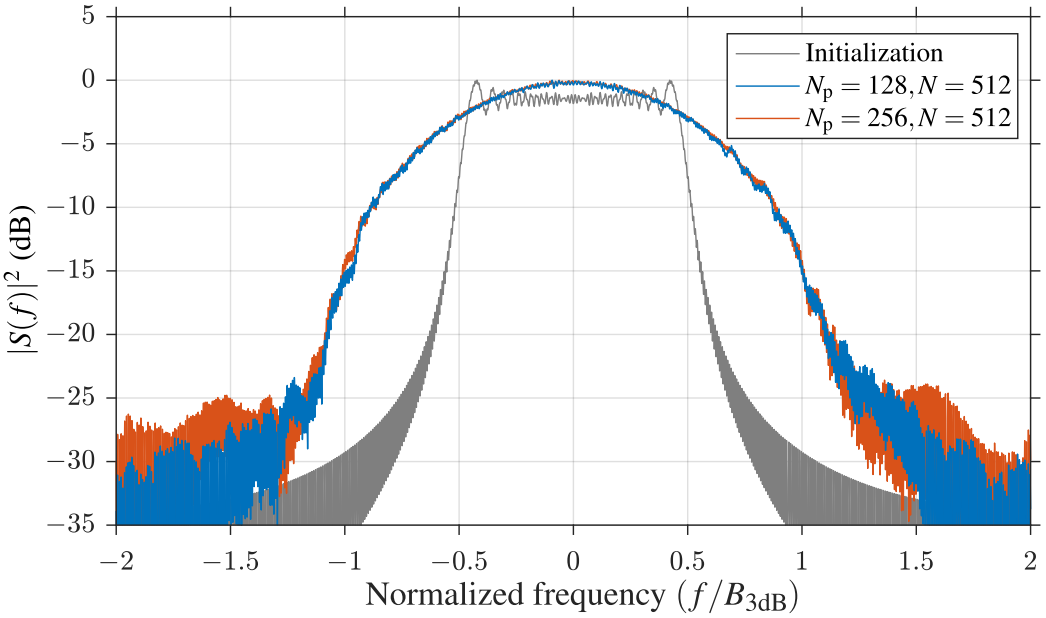

Figure 5.4: Optimized power spectra $|S(f)|^2$ from (2.10) versus normalized frequency (f/B_{3dB}) for CFM waveforms with a PCFM basis of $BT = 128$ and $N = 4BT = 512$ using $N_p = 128$ (blue) and $N_p = 256$ (red) parameters with LFM initialization in gray. ©2017 IEEE

response resembles a Gaussian shape which is known to correspond to low range sidelobes [44, 57, 59, 130]. Since each case has the same B_{samp}, the observed spectral content for each is dependent of the associated BT.

Figure 5.6 shows the autocorrelations after convergence for the different BT cases. Notice that as BT decreases (and thus the amount of over-coding increases), the sidelobe level also decreases. The associated increase in mainlobe width and sidelobe reduction is similar to the response obtained by frequency tapering, albeit without the associated SNR loss. Figure 5.7 provides a close-up of the outer autocorrelation values, along with the sampled PSL bound for rectangular envelope $u(t)$ (from (2.205)) which for these cases is $(-20\log_{10}(512) = -54.19$ dB$)$. The $BT = 128$ and $BT = 256$ cases realize PSL values of -52 dB (near mainlobe) and -52.74 dB, respectively (2.19 dB and 1.45 dB above the bound). The PSL values for the $BT = 64$ and $BT = 32$ cases actually equals the bound at the autocorrelation edge and have much lower sidelobes at every other delay within the sidelobe region. These examples demonstrate that it is the sampled bandwidth B_{samp} of the matched filter that determines the lower bound on PSL and not the 3 dB bandwidth of the waveform B_{3dB}. Put another way, the combination of over-coding the waveform

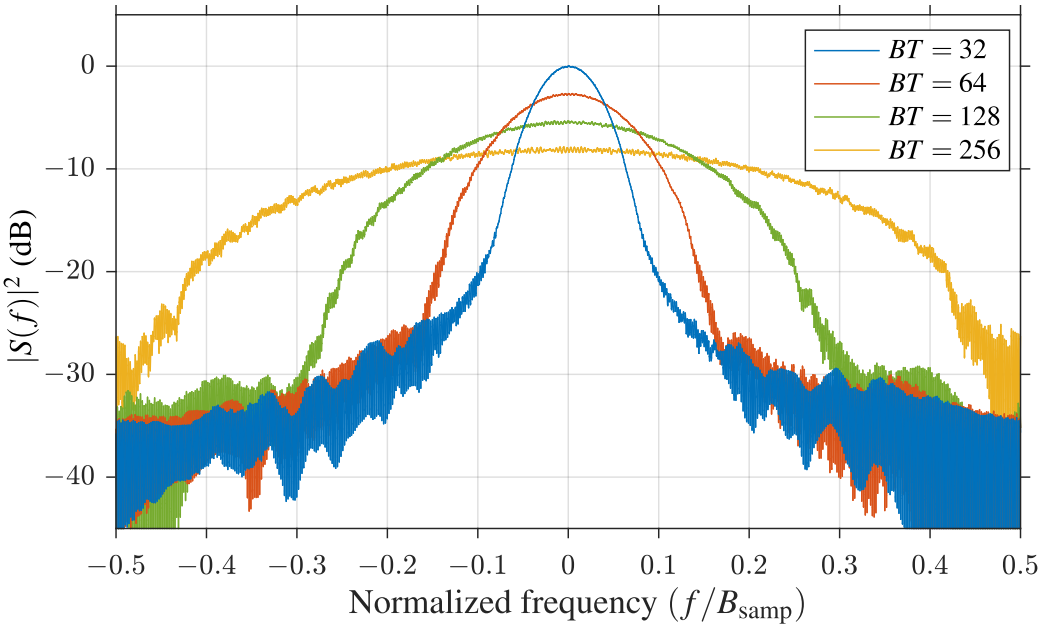

Figure 5.5: Optimized power spectra $|S(f)|^2$ from (2.10) versus normalized frequency (f/B_{samp}) for CFM waveforms with a PCFM basis of $N_{\text{p}} = 256$ and $N = 512$ with $BT = 32$ (blue), $BT = 64$ (red), $BT = 128$ (green), and $BT = 256$ (yellow). ©2017 IEEE

$(N_{\text{p}} > BT)$ and over-sampling the matched filter can facilitate substantial reductions in sidelobe levels through finer control of the spectral roll-off.

Finally, Figure 5.8 shows the instantaneous time-frequency relationships for these four waveforms with different time-bandwidths. Generally speaking, each realizes the familiar "sideways-S" curve that is associated with low autocorrelation sidelobes [50, 51, 57]. The additional small perturbations observed in Figure 5.8 are not random but arise from the optimization process (similar behavior has been observed for other FM waveform optimization approaches [38, 157, 158]). The analytical time-bandwidths $B_{\text{a}}T$ for $BT \in \{32, 64, 128, 256\}$ are $B_{\text{a}}T \in \{226.2, 243.9, 297.1, 424.1\}$. The flaring of the instantaneous frequencies at the beginning and ends of the waveform result in an inflated analytical time-bandwidth $B_{\text{a}}T$ compared to BT.

5.3 Optimization of CFM waveforms with Legendre Basis

The phase function model via (5.2) is now constructed using an alternate basis $\mathcal{B}$ from (5.3) which is comprised of different orders of Legendre polynomials. As an example, it is demonstrated that

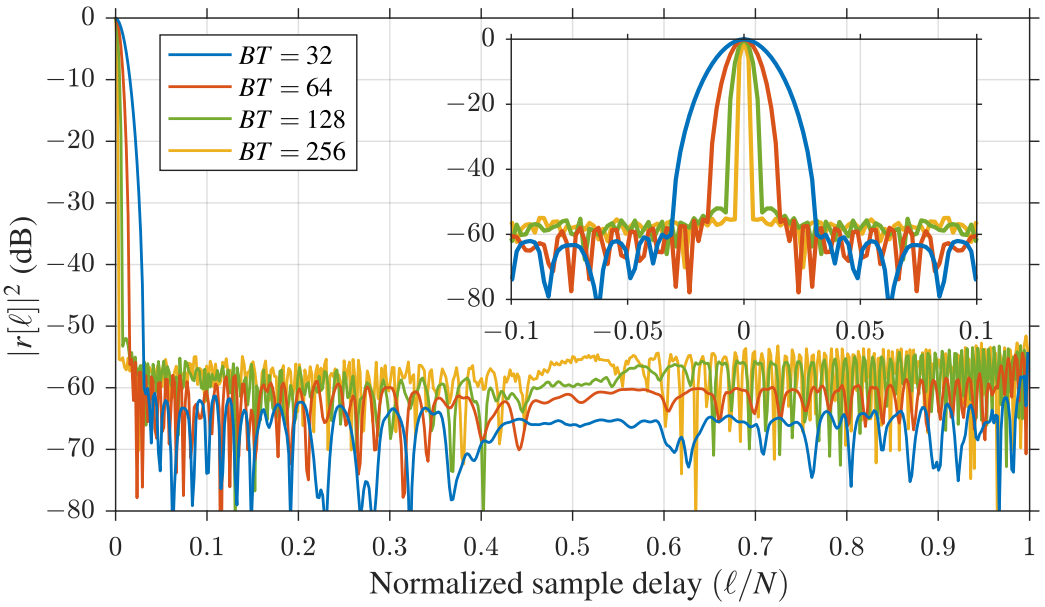

Figure 5.6: Optimized discrete autocorrelation responses $|r[\ell]|^2$ from (2.204) versus normalized sample delay (ℓ/N) for CFM waveforms with a PCFM basis using $N_p = 256$ and $N = 512$ with $BT = 32$ (blue), $BT = 64$ (red), $BT = 128$ (green), and $BT = 256$ (yellow). ©2017 IEEE

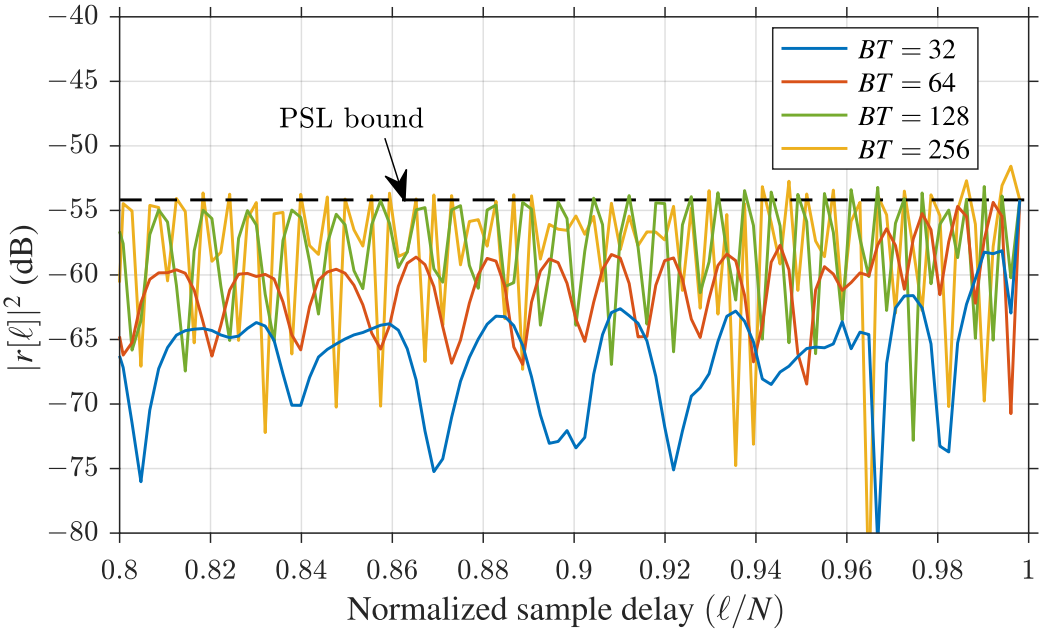

Figure 5.7: Close-up optimized discrete autocorrelation responses $|r[\ell]|^2$ from (2.204) versus normalized sample delay (ℓ/N) for CFM waveforms with a PCFM basis using $N_p = 256$ and $N = 512$ with $BT = 32$ (blue), $BT = 64$ (red), $BT = 128$ (green), and $BT = 256$ (yellow). ©2017 IEEE

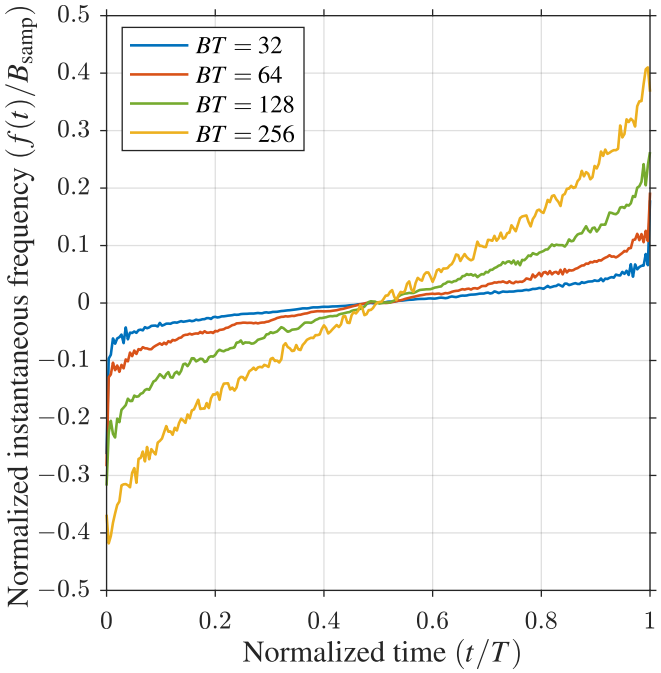

Figure 5.8: Normalized instantaneous frequency $(f(t)/B_{\text{samp}})$ from (2.20) versus normalized time (t/T) for CFM waveforms with a PCFM basis using $N_{\text{p}} = 256$ and $N = 512$ with $BT = 32$ (blue), $BT = 64$ (red), $BT = 128$ (green), and $BT = 256$ (yellow). ©2017 IEEE

for waveforms of time-bandwidth less than 1024, only a small number of these polynomials (less than 12) are needed to produce a waveform with low autocorrelation sidelobes (with diminishing returns thereafter).

As further examples, two waveforms are optimized for experimental loopback testing using the CFM Legendre polynomial model: one with a rectangular amplitude envelope and the other with a Tukey envelope. The loopback correlation response agrees with the theoretical response in the rectangular case but deviates in Tukey case due to hardware distortion. The distortion was estimated and applied to the waveform model to produce a correlation response resembling that of the loopback test.

5.3.1 Legendre Polynomial Basis

Another natural basis for the phase function defined in (5.2) is a polynomial basis. Furthermore, it is advantageous to select functions that are orthogonal over a certain interval to avoid highly

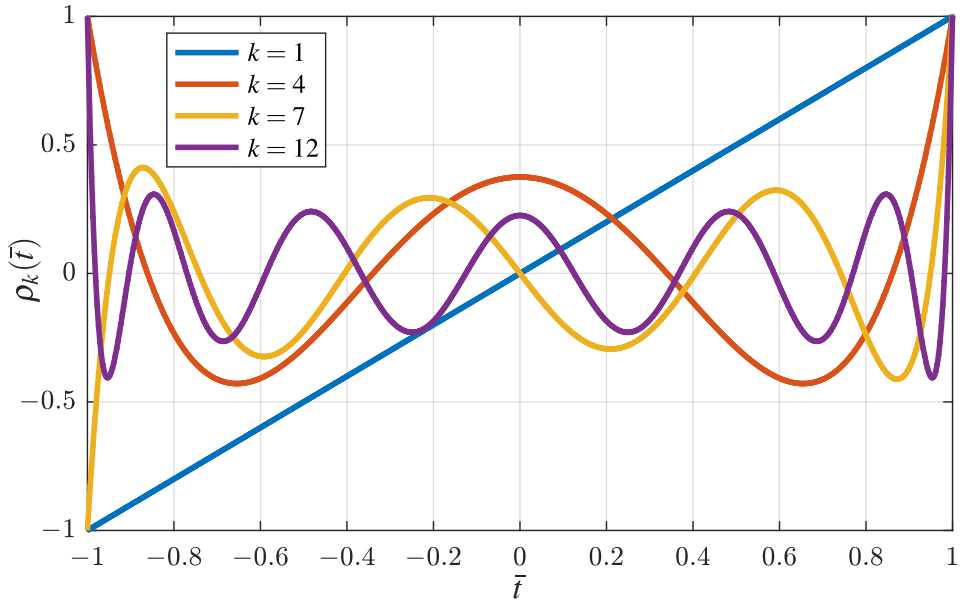

Figure 5.9: Sampling of Legendre polynomial functions $\rho_v(\bar{t})$ for $v \in \{1,4,7,12\}$. ©2017 IET

correlated basis functions. Thus we consider Legendre polynomial functions which are orthogonal over $\bar{t} \in [-1,1]$, where the kth polynomial is defined as [172]

$$\rho_k(\bar{t}) = \frac{1}{2^k} \sum_{i=0}^{k} \binom{k}{i}^2 (\bar{t}-1)^{k-i} (\bar{t}+1)^i \tag{5.18}$$

For example, Figure 5.9 depicts the Legendre polynomial functions for $k \in \{1,4,7,12\}$. Since the Legendre polynomial functions are orthogonal over $\bar{t} \in [-1,1]$ each parameter α_n corresponds to a unique basis function $h_n(t)$.

Note that even values of k produce even (symmetric) functions, while odd values produce odd (antisymmetric) functions. Thus we shall limit attention to the even symmetric functions $k \in \{2,4,6,\dots\}$ as they yield symmetric frequency responses (given that $u(t)$ is also symmetric). Therefore the CFM basis functions are set as

$$h_n(t) = \rho_{2(n+1)}\left(\frac{2t}{T} - 1\right) \tag{5.19}$$

for $n \in \{0,1,\dots,N_\mathrm{p}-1\}$. Thus the set $\mathcal{B}$ for this Legendre basis is defined as

$$\mathcal{B}_{\text{Leg}} = \left\{ \rho_2\left(\frac{2t}{T} - 1\right), \rho_4\left(\frac{2t}{T} - 1\right), \ldots, \rho_{2N_\text{p}}\left(\frac{2t}{T} - 1\right) \right\}. \tag{5.20}$$

Note that the $k = 0$ Legendre polynomial is excluded as it only contributes a phase shift to the phase function $\psi(t)$.

5.3.2 Continuous Correlation of Digital Filter

Although the continuous autocorrelation response from (2.62) is widely used in practice, the expression does not capture the interaction of the continuous-time waveform that is physically emitted by the transmitter with the digital (and thus discrete-time) pulse compression filter on receive, though the ideal response can be well approximated if the receiver sampling rate is much higher than the waveform 3 dB bandwidth [38, 81]. With rapid advances in diverse waveform design and generation [3], this interaction is becoming increasingly more common.

To address this limitation, we propose the alternative correlation function

$$\tilde{r}(\tau;\xi) = \frac{1}{\|\mathbf{s}(\xi)\|_2^2} \int_0^T \tilde{s}^*(t-\tau;\xi) s(t) dt, \tag{5.21}$$

where

$$\tilde{s}(t;\xi) = \sum_{n=0}^{N-1} s(nT_\text{s} + \xi)\delta\big(t - (nT_\text{s} + \xi)\big) \tag{5.22}$$

is a train of N weighted impulses at time instants $nT_s + \xi$ for $n \in \{0, 1, \ldots, N-1\}$. The impulses represent the length-N discretized waveform $\mathbf{s}$ from (2.172) used to create the matched filter which is a function of the subsample shift $\xi \in [0, T_\text{s}]$ where the nth sample of $\mathbf{s}$ is defined as $s[n] = s(nT_\text{s} + \xi)$ (Section 2.4.2). Here, the dependence on ξ is made explicit in the discretized waveform as $\mathbf{s}(\xi) = [s(\xi) \;\; s(T_\text{s} + \xi) \cdots s((N-1)T_\text{s} + \xi)]^T$.

An illustration of the amplitudes of $s(t)$ and $\tilde{s}(t;\xi)$ is shown in Figure 5.10. Correlating the waveform $s(t)$ with the weighted impulse train $\tilde{s}(t;\xi)$ naturally accounts for the continuous nature

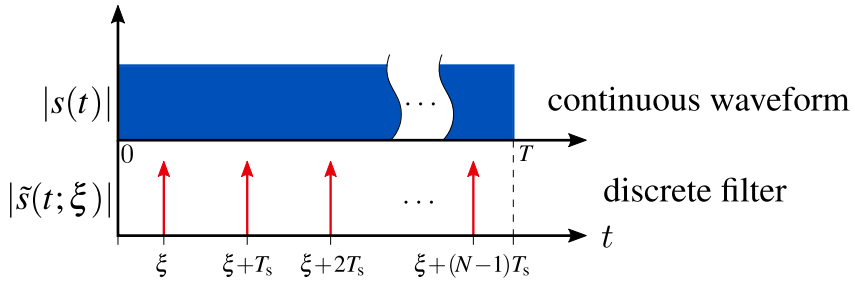

Figure 5.10: Signal amplitude structures for continuous waveform $|s(t)|$ and discrete filter $|\tilde{s}(t;\xi)|$.

of the physical radar emissions and the subsequent digital filtering in the radar receiver. The particular delay values $\tau = \ell T_s$ for discrete index $\ell \in \{0, \pm 1, \ldots, \pm(N-1)\}$ of the correlation function $\tilde{r}(\tau)$ are equivalent to the discrete-time autocorrelation of $\mathbf{s}(\xi)$ from (2.204) as

$$\tilde{r}(\ell T_s; \xi) = r[\ell] = \frac{1}{\|\mathbf{s}(\xi)\|_2^2} \sum_{n=0}^{N-1} s^*\big((n-\ell)T_s + \xi\big) s\,(nT_s + \xi)\,. \tag{5.23}$$

All other delays $\tau \notin \{0, \pm T_s, \ldots, \pm(N-1)T_s\}$ for $-T < \tau < T$ correspond to range straddling conditions that can elicit mismatch loss [56] and possibly sidelobe degradation [38, 81] (Section 2.4.3). Thus, for range straddled subsample shift $\varrho \in \left[-\frac{T_s}{2}, \frac{T_s}{2}\right]$ and straddled cross-correlation response $r[\ell; \varrho]$ from (2.206), the relationship in (5.23) becomes

$$\tilde{r}(\ell T_s + \varrho; \xi) = r[\ell; \varrho] = \frac{1}{\|\mathbf{s}(\xi)\|_2^2} \sum_{n=0}^{N-1} s^*\big((n-\ell)T_s + \xi\big) s\,(nT_s + \xi + \varrho)\,. \tag{5.24}$$

By defining the waveform/filter correlation using (5.21) so that these range straddling effects are included in the optimization process, subsequent evaluation of the range sidelobes via metrics such as peak sidelobe level (PSL) or integrated sidelobe level (ISL) inherently address the finite degrees of freedom of the receive filter.

5.3.3 Waveform Optimization via Quasi-Newton Method

As long as the function $\tilde{s}(t;\xi)$ is discretized at a rate sufficiently greater than the 3 dB bandwidth, the mainlobe of the modified correlation function $\tilde{r}(\tau;\xi)$ remains similar to that of the continuous autocorrelation function $\chi_a(\tau)$. Therefore, the relationship $\Delta\tau/T \approx 1/[BT]_{\text{desired}}$ (discussed in

Section 5.1.2) can still be leveraged to approximate a desired time-bandwidth product. Thus, the continuous GISL metric from (5.4) can be redefined using the modified correlation function (5.21) as

$$\mathcal{J}_{\mathrm{a}}(\mathbf{x}_{\mathrm{w}};\xi,q) = \left(\frac{\displaystyle\int_{\Delta\tau}^{T} |\tilde{r}(\tau;\xi)|^q \, d\tau + \int_{-T}^{-\Delta\tau} |\tilde{r}(\tau;\xi)|^q \, d\tau}{\displaystyle\int_{-\Delta\tau}^{\Delta\tau} |\tilde{r}(\tau;\xi)|^q \, d\tau} \right)^{\frac{1}{q}}. \tag{5.25}$$

Thus the optimization problem is stated as

$$\underset{\mathbf{x}_{\mathrm{w}}}{\text{minimize}} \quad \mathcal{J}_{\mathrm{a}}(\mathbf{x}_{\mathrm{w}};\xi,q). \tag{5.26}$$

A quasi-Newton gradient descent method with a Broyden-Fletcher-Goldfarb-Shanno (BFGS) Hessian approximation update is used to minimize (5.25) [79]. The Hessian (denoted as $\nabla^2\mathcal{J}_{\mathrm{a}}(\mathbf{x}_{\mathrm{w}};\xi,q)$) and gradient of the cost function $\nabla\mathcal{J}_{\mathrm{a}}(\mathbf{x}_{\mathrm{w}};\xi,q)$ provides a quadratic model of the cost function around a point defined by parameter vector $\mathbf{x}_{\mathrm{w}}$. The second-order model provides faster convergence (as compared to NLCG from Section 5.2) at the expense of higher per iteration computational cost [79]. The method follows the same line-search based update from (5.12) where the step direction on iteration i is defined as

$$\mathbf{p}_i = -\mathbf{B}_i^{-1} \nabla\mathcal{J}_{\mathrm{a}}(\mathbf{x}_{\mathrm{w},i};\xi,q) \tag{5.27}$$

where $\mathbf{B}_i$ is the BFGS approximation to the $N_{\mathrm{p}} \times N_{\mathrm{p}}$ Hessian of the cost function $\nabla^2\mathcal{J}_{\mathrm{a}}(\mathbf{x}_{\mathrm{w}};\xi,q)$ where

$$\nabla^2 = \begin{bmatrix} \frac{\partial^2}{\partial\alpha_1\partial\alpha_1} & \cdots & \frac{\partial^2}{\partial\alpha_1\partial\alpha_{N_{\mathrm{p}}}} \\ \vdots & \ddots & \vdots \\ \frac{\partial^2}{\partial\alpha_{N_{\mathrm{p}}}\partial\alpha_1} & \cdots & \frac{\partial^2}{\partial\alpha_{N_{\mathrm{p}}}\partial\alpha_{N_{\mathrm{p}}}} \end{bmatrix} \tag{5.28}$$

is the Hessian matrix. The BFGS update to $\mathbf{B}_i^{-1}$ at iteration $i+1$ is

$$\mathbf{B}_{i+1}^{-1} = \left(\mathbf{I}_{N_\mathrm{p}} - \frac{1}{\mathbf{p}_i^T\mathbf{h}_i}\mathbf{p}_i\mathbf{h}_i^T\right)\mathbf{B}_i^{-1}\left(\mathbf{I}_{N_\mathrm{p}} - \frac{1}{\mathbf{p}_i^T\mathbf{h}_i}\mathbf{h}_i\mathbf{p}_i^T\right) + \frac{\mu_i}{\mathbf{p}_i^T\mathbf{h}_i}\mathbf{p}_i\mathbf{p}_i^T \tag{5.29}$$

where

$$\mathbf{h}_i = \nabla\mathcal{J}_\mathrm{a}(\mathbf{x}_{\mathrm{w},i+1};\xi,q) - \nabla\mathcal{J}_\mathrm{a}(\mathbf{x}_{\mathrm{w},i};\xi,q) \tag{5.30}$$

is the difference between successive cost function gradients. The gradient of (5.25) is found via a finite-difference approximation where the derivative with respect to α_n can be approximated as

$$\frac{\partial\mathcal{J}_\mathrm{a}(\mathbf{x}_{\mathrm{w},i};\xi,q)}{\partial\alpha_n} \approx \frac{\mathcal{J}_\mathrm{a}(\mathbf{x}_\mathrm{w}+\epsilon\mathbf{e}_n;\xi,q) - \mathcal{J}_\mathrm{a}(\mathbf{x}_\mathrm{w};\xi,q)}{\epsilon} \tag{5.31}$$

where ϵ is a very small positive number and $\mathbf{e}_n$ is the nth coordinate vector which is defined as a vector of zeros except for a one in the nth entry. The step size μ_i is chosen to satisfy the Wolfe conditions from (5.16) and (5.17) which guarantees convergence for BFGS quasi-Newton [79]. An overview of the quasi-Newton optimization of CFM waveforms using a Legendre basis is detailed in Algorithm 5.2.

Algorithm 5.2 Quasi-Newton method using BFGS Hessian approximation

Initialize: BT, κ, q, N_p, $\mathbf{x}_{\mathrm{w},0}$, $\mathcal{B} = \mathcal{B}_\mathrm{Leg}$, $\mathbf{p}_0 = -\nabla\mathcal{J}_\mathrm{a}(\mathbf{x}_{\mathrm{w},0};q)$, $\mathbf{B}_0^{-1} = \mathbf{I}_{N_\mathrm{p}}$, $c_1 = 10^{-3}$, $c_2 = 0.1$, and $i = 0$
repeat
  Choose μ_i that satisfies (5.16) and (5.17)
  $\mathbf{x}_{\mathrm{w},i+1} = \mathbf{x}_{\mathrm{w},i} + \mu_i\mathbf{p}_i$
  Calculate $\nabla\mathcal{J}_\mathrm{a}(\mathbf{x}_{\mathrm{w},i+1};q)$ via (5.31)
  $\mathbf{h}_i = \nabla\mathcal{J}_\mathrm{a}(\mathbf{x}_{\mathrm{w},i+1};q) - \nabla\mathcal{J}_\mathrm{a}(\mathbf{x}_{\mathrm{w},i};q)$
  Calculate $\mathbf{B}_{i+1}^{-1}$ via (5.29)
  $i = i+1$
  $\mathbf{p}_i = -\mathbf{B}_i^{-1}\nabla\mathcal{J}_\mathrm{a}(\mathbf{x}_{\mathrm{w},i};q)$
until $\|\mathbf{p}_i\|_2 \approx 0$
$\mathbf{x}_{\mathrm{w},\star} = \mathbf{x}_{\mathrm{w},i}$
return $\mathbf{x}_{\mathrm{w},\star}$

As for all gradient-based methods, the algorithm descends onto a locally optimal solution which is not guaranteed to be globally optimal. Therefore the locally optimal solution is highly dependent

on the initialization. As such, an order-recursive nested approach is implemented to ensure the quasi-Newton method is initialized with a waveform that already has good autocorrelation properties.

Define $\mathbf{x}_{\mathrm{w},k}$ as the $k \times 1$ vector stored on the kth iteration of the order-recursive process[4]. These parameters corresponds to the first k basis functions contained in $\mathcal{B}$. The BFGS optimization procedure is initialized with $k \times 1$ vector $\tilde{\mathbf{x}}_{\mathrm{w},0}\big|_{k\times 1} = \mathbf{x}_{\mathrm{w},k}$. After optimization, the converged $k \times 1$ vector $\tilde{\mathbf{x}}_{\mathrm{w},\star}$ is used to define the $(k+1) \times 1$ stored vector $\mathbf{x}_{\mathrm{w},k+1} = [\tilde{\mathbf{x}}_{\mathrm{w},\star}^T \; 0]^T$ which corresponds to the first $k+1$ basis functions in $\mathcal{B}$. This process is repeated until the optimized vector reaches the desired dimensionality, $k = N_{\mathrm{p}}$. This procedure allows the optimization to gradually increase the order of the phase function while achieving an "optimal" lower order initialization for each step. This implementation prevents $\mathbf{x}_{\mathrm{w}}$ from falling into an undesirable local minimum and has been shown to provide better results compared to a full dimensional initialization. The nested order-recursive procedure using BFGS quasi-Newton is detailed in Algorithm 5.3. Figure 5.11 provides an illustration of the order-recursive process where 'optimize' represents the quasi-Newton implementation.

5.3.4 Simulations and Loopback Measurements

It is first useful to determine the optimal offset delay ξ for the receive filter and the sufficient number of basis functions N_{p} as a function of time-bandwidth product, BT. Using this knowledge, two waveforms are then optimized: one with a rectangular amplitude envelope and one with a 10% Tukey tapered envelope. These waveforms are evaluated on hardware in a loopback configuration and their filter responses are compared to the theoretical autocorrelation responses.

5.3.4.1 Sample Offset and Number of Basis Functions

The Algorithm 5.3 is implemented to determine the optimal sample offset ξ, for $\tilde{s}(t;\xi)$ the digital receive filter. The normalized offset is varied from $\xi/T_{\mathrm{s}} = 0$ to $\xi/T_{\mathrm{s}} = 1$, with the remaining

[4]The variable k in this sense pertains to an iteration index and not the polynomial order from (5.18).

Algorithm 5.3 Order recursive optimization of Legendre basis using Quasi-Newton method

Initialize: BT, κ, q, N_p, $\mathbf{x}_{\mathrm{w},1} = 0$, $\mathcal{B} = \mathcal{B}_\mathrm{Leg}$, $c_1 = 10^{-3}$, and $c_2 = 0.1$
for $k = 1, 2, \ldots, N_\mathrm{p}$ **do**
    $\tilde{\mathbf{x}}_{\mathrm{w},0}\big|_{k\times 1} = \mathbf{x}_{\mathrm{w},k}$
    $\tilde{\mathcal{B}} = \mathcal{B}\{1:k\}$ ▷ Choose only first k basis functions
    Calculate $\nabla \mathcal{J}_\mathrm{a}(\tilde{\mathbf{x}}_{\mathrm{w},0}; q)$ via (5.31) using $\tilde{\mathcal{B}}$
    $\mathbf{p}_0 = -\nabla \mathcal{J}_\mathrm{a}(\tilde{\mathbf{x}}_{\mathrm{w},0}; q)$
    $\mathbf{B}_0 = \mathbf{I}_k$
    $i = 0$
    repeat
        Choose μ_i that satisfies (5.16) and (5.17)
        $\tilde{\mathbf{x}}_{\mathrm{w},i+1} = \tilde{\mathbf{x}}_{\mathrm{w},i} + \mu_i \mathbf{p}_i$
        Calculate $\nabla \mathcal{J}_\mathrm{a}(\tilde{\mathbf{x}}_{\mathrm{w},i+1}; q)$ via (5.31) using $\tilde{\mathcal{B}}$
        $\mathbf{h}_i = \nabla \mathcal{J}_\mathrm{a}(\tilde{\mathbf{x}}_{\mathrm{w},i+1}; q) - \nabla \mathcal{J}_\mathrm{a}(\tilde{\mathbf{x}}_{\mathrm{w},i}; q)$
        Calculate $\mathbf{B}_{i+1}$ via (5.29)
        $i = i + 1$
        $\mathbf{p}_i = -\mathbf{B}_i \nabla \mathcal{J}_\mathrm{a}(\tilde{\mathbf{x}}_{\mathrm{w},i}; q)$
    until $\|\mathbf{p}_i\|_2 \approx 0$
    $\tilde{\mathbf{x}}_{\mathrm{w},\star} = \tilde{\mathbf{x}}_{\mathrm{w},i}$
    if $k < N_\mathrm{p}$ **then**
        $\mathbf{x}_{\mathrm{w},k+1} = \begin{bmatrix} \tilde{\mathbf{x}}_{\mathrm{w},\star} \\ 0 \end{bmatrix}$
    end if
end for
$\mathbf{x}_{\mathrm{w},\star} = \tilde{\mathbf{x}}_{\mathrm{w},\star}$
return $\mathbf{x}_{\mathrm{w},\star}$

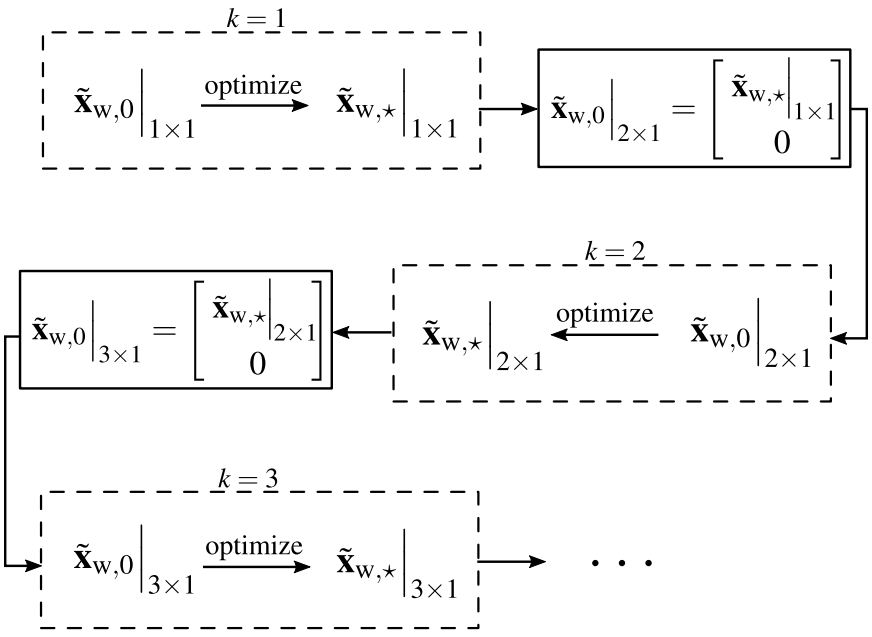

Figure 5.11: Order-recursive optimization process.

quantities set to $BT = 128$, $\kappa = 2$, $N_\mathrm{p} = 32$ basis functions, a rectangular amplitude envelope $u(t)$, and $q = 5$.

Figure 5.12 shows the converged values of $\mathcal{J}_\mathrm{a}(\mathbf{x}_{\mathrm{w},\star}; \xi, q = 5)$ versus normalized sample delay ξ/T_s, where we find that $\xi/T_\mathrm{s} = 0.5$ provides the minimum value. Unsurprisingly, this condition arises because delay $\xi/T_\mathrm{s} = 0.5$ is equidistant (in time) from the extremes of range-straddling that may occur. The subsample offset of $\xi/T_\mathrm{s} = 0.5$ is used for the remainder of Section 5.3 and the cost function dependence on ξ is removed for brevity (i.e. $\mathcal{J}_\mathrm{a}(\mathbf{x}_\mathrm{w}; q)$).

To determine a sufficient number of basis functions to characterize the phase function $\psi(t)$, Figure 5.13 plots the cost function $\mathcal{J}_\mathrm{a}(\mathbf{x}_{\mathrm{w},\star}; q = 5)$ as a function of N_p for the values $BT \in \{64, 128, 256, 512, 1024\}$. As before, $\kappa = 2$ and $u(t)$ has a rectangular envelope. It is observed that for each time-bandwidth product BT there are two regimes: one in which $\mathcal{J}_\mathrm{a}(\mathbf{x}_{\mathrm{w},\star}; q = 5)$ decreases rapidly with increasing N_p and then a 'diminishing return' region where $\mathcal{J}_\mathrm{a}(\mathbf{x}_{\mathrm{w},\star}; q = 5)$ decreases much more slowly with increasing number of parameters. The transition between these regions depends on BT but is found to be between $N_\mathrm{p} = 6$ and $N_\mathrm{p} = 12$ for the cases considered. For the remainder of the optimization scenarios in this section, $N_\mathrm{p} = 32$ basis functions shall be used

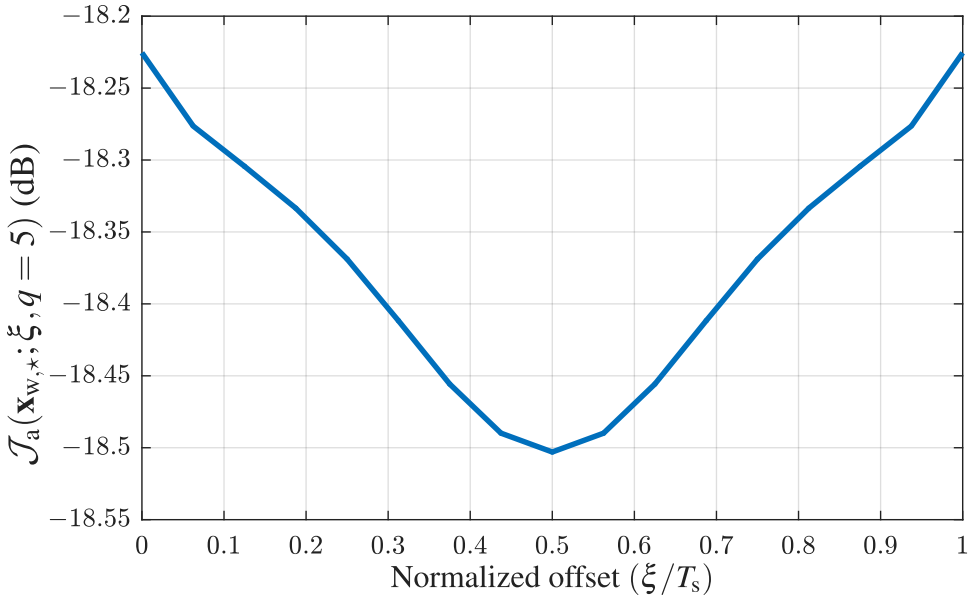

Figure 5.12: Converged values of $\mathcal{J}_a(\mathbf{x}_{w,\star};\xi,q=5)$ versus normalized offset ξ/T_s for CFM waveforms using Legendre basis and rectangular amplitude envelope $u(t)$ with $BT = 128$, $\kappa = 2$, and $N_p = 32$. ©2017 IET

which resides well within the second region.

5.3.4.2 Optimized CFM waveforms using Legendre Basis

Two waveforms of $BT = 200$ are optimized for an over-sampling of $\kappa = 2$ (which is practically achievable for most systems) using $N_p = 32$ Legendre polynomials as basis functions (polynomial order of 64). The first waveform has a rectangular amplitude envelope (labeled OPT-R) and its optimization uses $q = 5$ in (5.25). The second waveform has a 10% Tukey tapered envelope (labeled OPT-T) and its optimization uses $q = 2$ in (5.25), which has been found to produce a lower overall sidelobe level than $q = 5$ for this amplitude taper. Figure 5.14 displays the envelopes $u(t)$ for OPT-R and OPT-T. The Tukey amplitude taper results in a minimum SNR loss of 0.56 dB due to the requirement of operating in the linear region of an amplifier.

Figure 5.15 shows the power spectra of OPT-R (blue) and OPT-T (red) waveforms after convergence with the receiver sampled bandwidth $(f_s = \kappa B_{3dB} = 2B_{3dB})$ indicated by the vertical dashed lines. Note that by setting the relative peak-to-null width $T/\Delta\tau$ in the optimization, we have effectively established the desired 3 dB bandwidth of both the rectangular and Tukey envelope

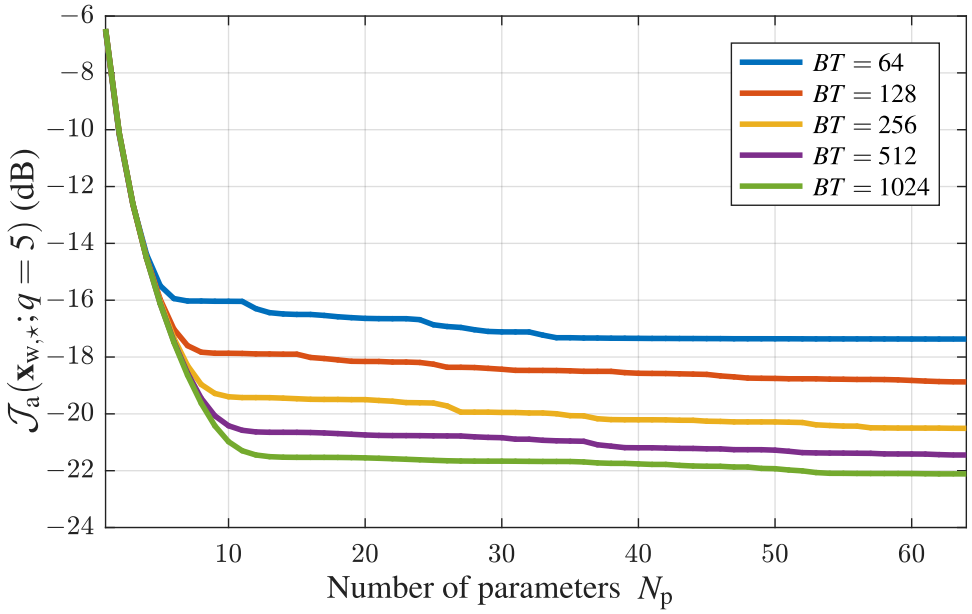

Figure 5.13: Converged values of $\mathcal{J}_{\mathrm{a}}(\mathbf{x}_{\mathrm{w},\star}; q = 5)$ versus N_{p} for CFM waveforms using Legendre basis and rectangular amplitude envelope $u(t)$ with $BT = 64$ (blue), $BT = 128$ (red), $BT = 256$ (yellow), $BT = 512$ (purple), and $BT = 1024$ (green). ©2017 IET

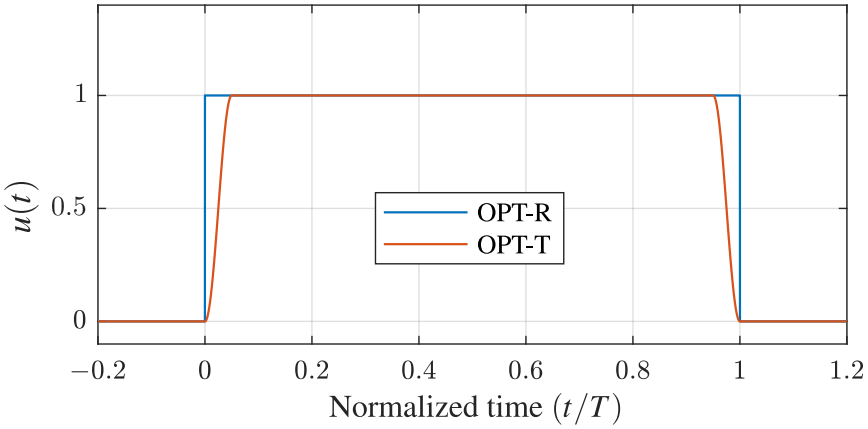

Figure 5.14: Amplitude envelopes $u(t)$ versus normalized time (t/T) for OPT-R (blue) and OPT-T (red).

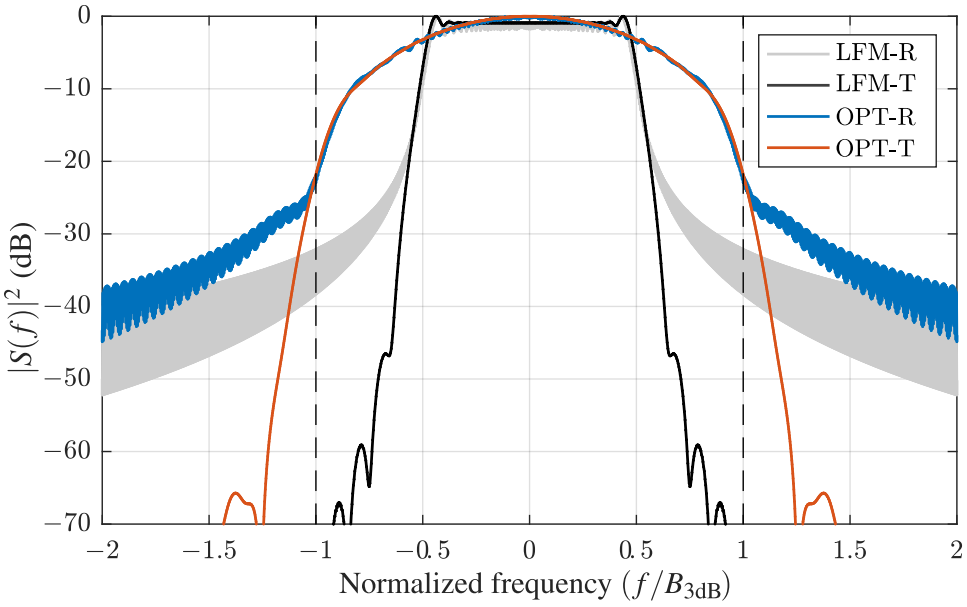

Figure 5.15: Power spectra $|S(f)|^2$ versus normalized frequency $(f/B_{3\text{dB}})$ of LFM-R (gray), LFM-T (black), optimized rectangular envelope waveform OPT-R (blue), and optimized Tukey envelope waveform OPT-T (red) for $BT = 200$, $\kappa = 2$, and $N_\text{p} = 32$. Receiver sampled bandwidth indicated by vertical dashed lines. ©2017 IET

waveforms. While the in-band spectral content of the two optimized waveforms is nearly identical, the Tukey envelope case has a much sharper roll-off. This result is not unexpected since the abrupt on/off transition of the rectangular envelope will exhibit a $\sin(x)/x$ spectral skirt. For comparison, a rectangular-windowed linear FM (LFM-R) and Tukey-windowed linear FM (LFM-T) with similar time-bandwidth products are included. While all the waveforms have similar 3 dB bandwidths, the optimized waveform spectra clearly exhibit some spectral broadening.

Figure 5.16 displays the normalized instantaneous frequencies $f(t)/B_{3\text{dB}}$ for the four waveforms. Both of the optimized waveforms OPT-R and OPT-T take on a "sideways-S" curve (much like Figure 5.8 from Section 5.2) whose general shape is known to produce low sidelobes [50, 51, 57]. However, the flaring of $f(t)$ at the beginning and ends of the optimized waveform pulses is directly linked to the spectral broadening seen in Figure 5.15. The wide span of energy in the frequency domain may not be a desirable effect for some radar applications, but it is found to be necessary to lower sidelobe levels while maintaining a set range resolution.

While the optimization via (5.25) uses the hybrid continuous/discrete autocorrelation of

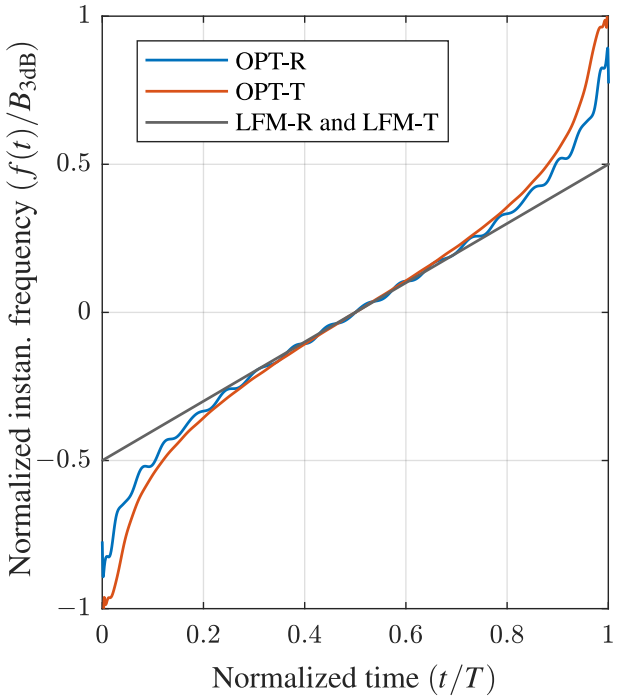

Figure 5.16: Normalized instantaneous frequency $(f(t)/B_{3\text{dB}})$ versus normalized time (t/T) of optimized rectangular envelope waveform OPT-R (blue), optimized Tukey envelope waveform OPT-T (red), and LFM-R/LFM-T (gray) for $BT = 200$, $\kappa = 2$, and $N_\text{p} = 32$.

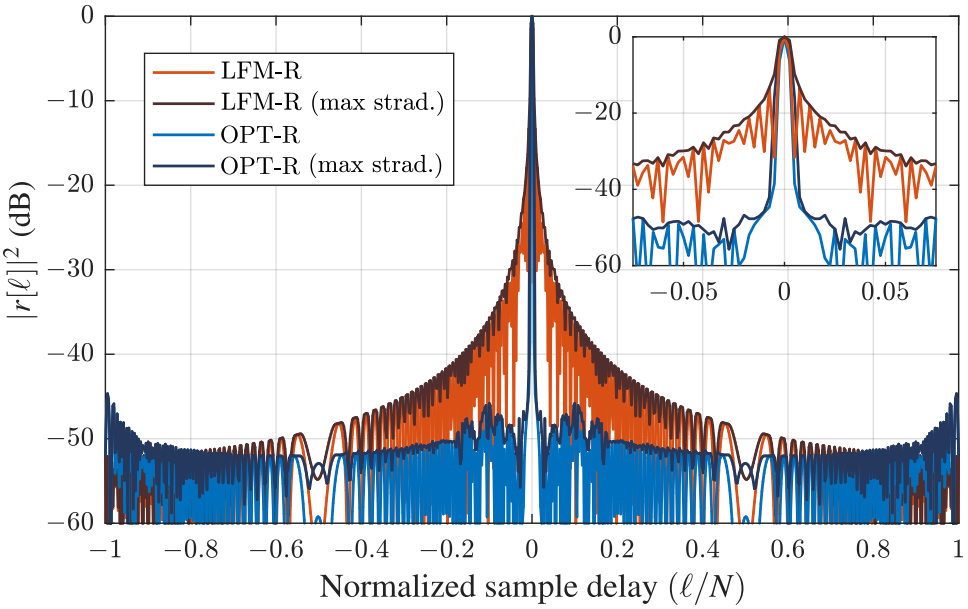

Figure 5.17: Autocorrelation $|r[\ell]|^2$ (in dB) via (5.23) versus normalized sample delay (ℓ/N) of LFM-R (red) and the optimized rectangular envelope waveform OPT-R (blue) for $BT = 200$, $\kappa = 2$, and $N_\text{p} = 32$. Maximum straddled responses in dark blue and dark red, respectively. ©2017 IET

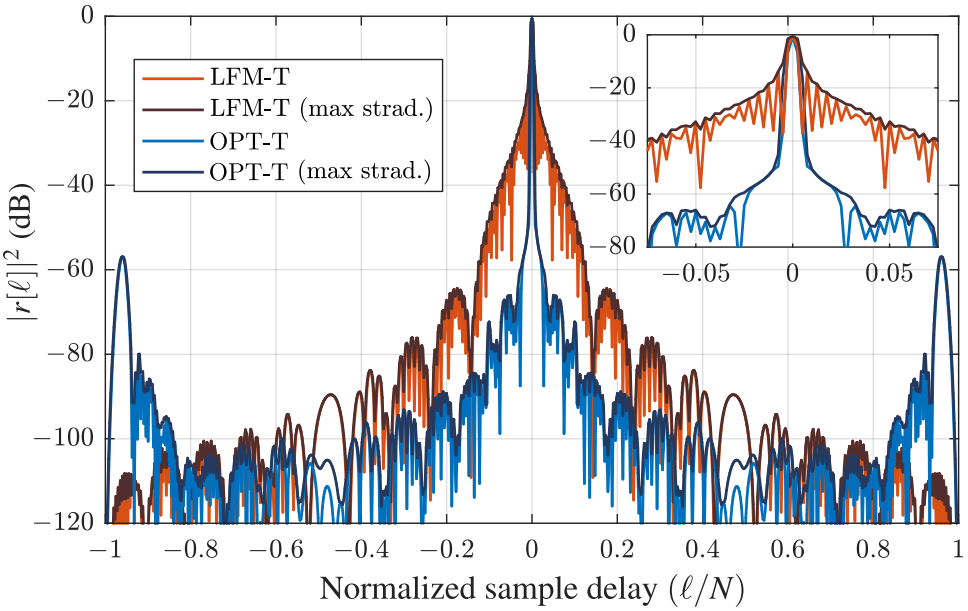

Figure 5.18: Autocorrelation $|r[\ell]|^2$ (in dB) via (5.23) versus normalized sample delay (ℓ/N) of LFM-T (red) and optimized Tukey envelope waveform OPT-T (blue) for $BT = 200$, $\kappa = 2$, and $N_p = 32$. Maximum straddled responses in dark blue and dark red, respectively. ©2017 IET

(5.21) to account for straddling effects, it is easier to depict the final result using the discrete autocorrelation of (5.23). The autocorrelation responses $r[\ell]$ (using (5.23)) are shown in Figure 5.17 for the optimized rectangular envelope waveform OPT-R (blue) and the rectangular-windowed LFM-R (red). The maximum straddled responses from (5.21) are also shown in dark blue and dark red, respectively, which represent the worst-case responses for these waveforms. The maximum straddled case for OPT-R shows that the correlation response isn't sensitive to subsample shifts in the waveform. The maximum PSL of the optimized waveform is −44.75 dB, as compared to −13.36 dB for the LFM-R case.

Figure 5.18 shows the autocorrelation responses $r[\ell]$ (using (5.23)) for the Tukey envelope optimized waveform OPT-T (blue) and the Tukey-windowed LFM-T (red). The maximum straddled responses from (5.21) are likewise shown in dark blue and dark red, respectively. The waveform OPT-T achieves much lower sidelobes compared to the rectangular envelope OPT-R from Figure 5.17 while only incurring 0.56 dB in SNR loss due to the tapering. As compared to the LFM-T response, the energy close to the mainlobe is reduced for OPT-T, though sidelobes of approximately −57 dB are observed at the autocorrelation edges. These peaks have been found to

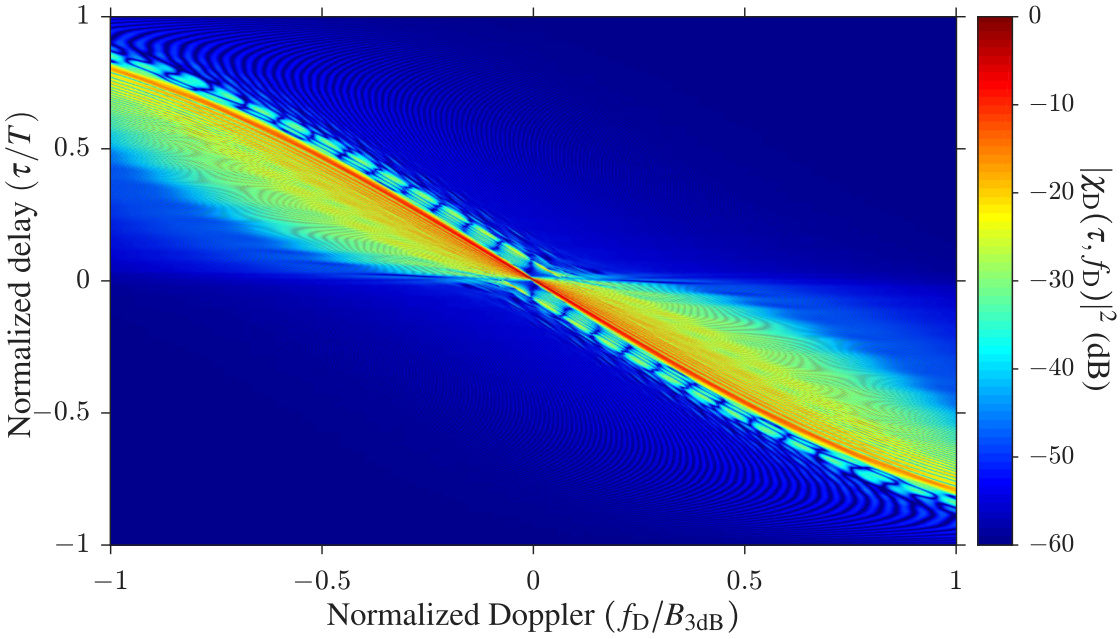

Figure 5.19: Ambiguity function $|\chi_D(\tau, f_D)|^2$ (in dB) via (2.74) versus normalized delay (τ/T) and normalized Doppler (f_D/B_{3dB}) of the optimized rectangular envelope waveform (OPT-R) with $BT = 200$ and $N_p = 32$. ©2017 IET

appear when the 3 dB bandwidth B_{3dB} is near to the sampling rate f_s $(\kappa \leq 2)$ such that a majority of the sampled bandwidth has significant spectral power.

Figures 5.19 through 5.22 depict the ambiguity functions (via (2.74)) for the OPT-R, LFM-R, OPT-T, and LFM-T waveforms, respectively. Both optimized waveforms, OPT-R and OPT-T, exhibit a delay-Doppler ridge similar to that of the LFM waveforms indicating these waveforms are relatively Doppler tolerant. However, off of zero Doppler, the sidelobes in delay for the optimized waveforms increase while the sidelobes for the LFM waveforms remain at a fairly consistent level over all Doppler space. This change in performance is no surprise since the optimization is only minimizing the zero-Doppler sidelobes thus does not penalize the increase in sidelobe level. Future work will investigate a modification to the GISL cost function to include a range of fast-time Doppler frequencies to limit this sidelobe degradation. A further investigation of the effects of fast-time Doppler on nonlinear FM waveforms can be found in [57].

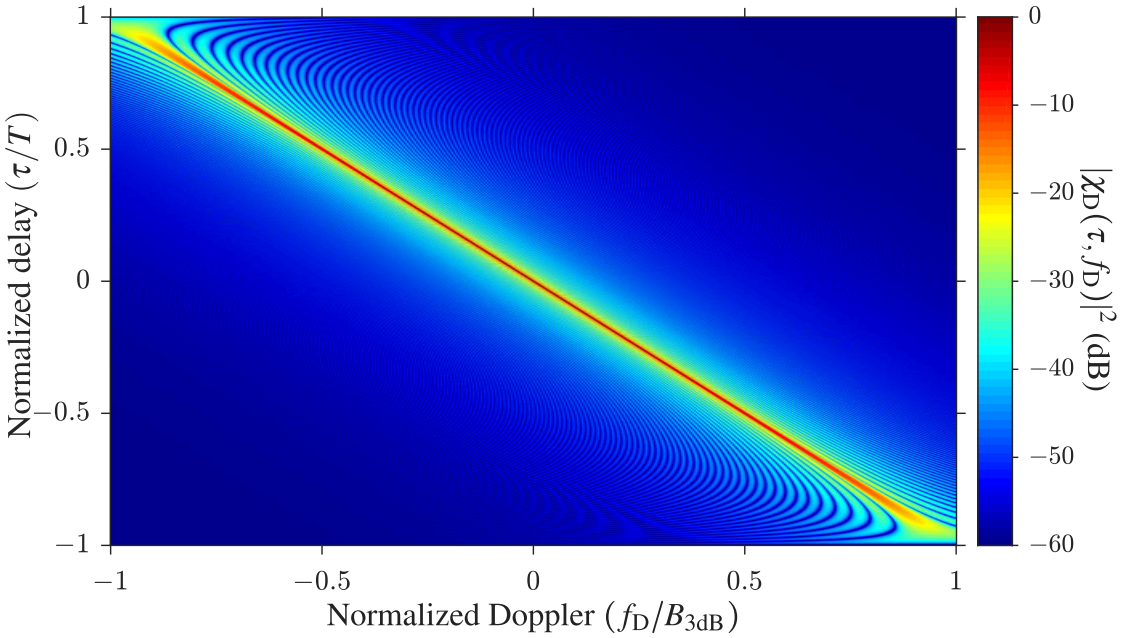

Figure 5.20: Ambiguity function $|\chi_D(\tau, f_D)|^2$ (in dB) via (2.74) versus normalized delay (τ/T) and normalized Doppler (f_D/B_{3dB}) of the LFM with rectangular envelope (LFM-R) with $BT = 200$.

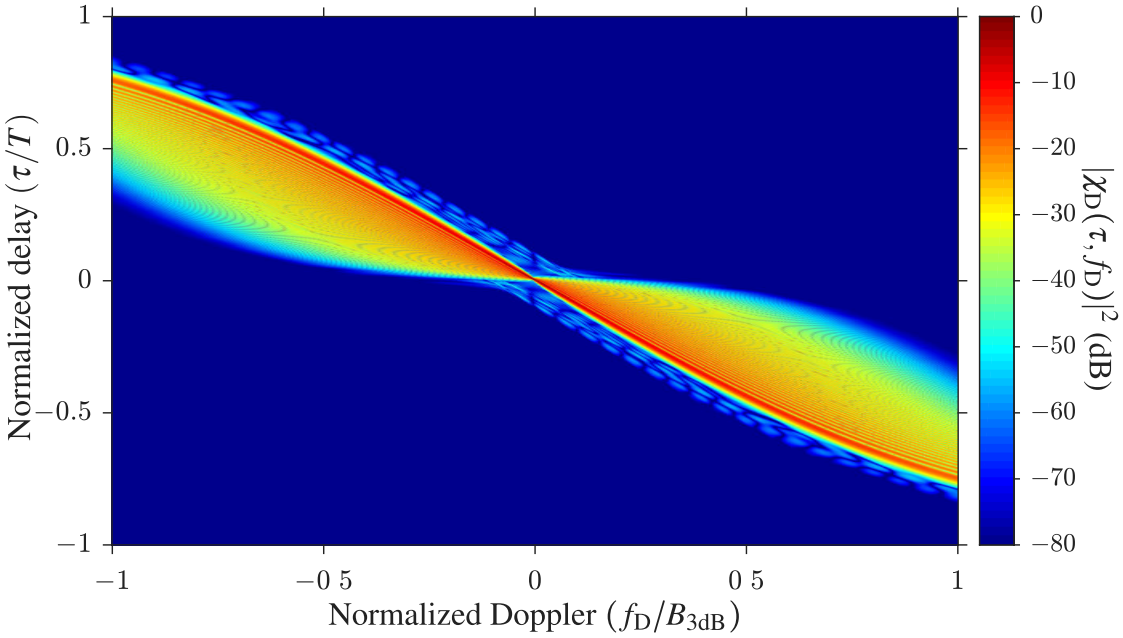

Figure 5.21: Ambiguity function $|\chi_D(\tau, f_D)|^2$ (in dB) via (2.74) versus normalized delay (τ/T) and normalized Doppler (f_D/B_{3dB}) of the optimized Tukey envelope waveform (OPT-T) with $BT = 200$ and $N_p = 32$. ©2017 IET

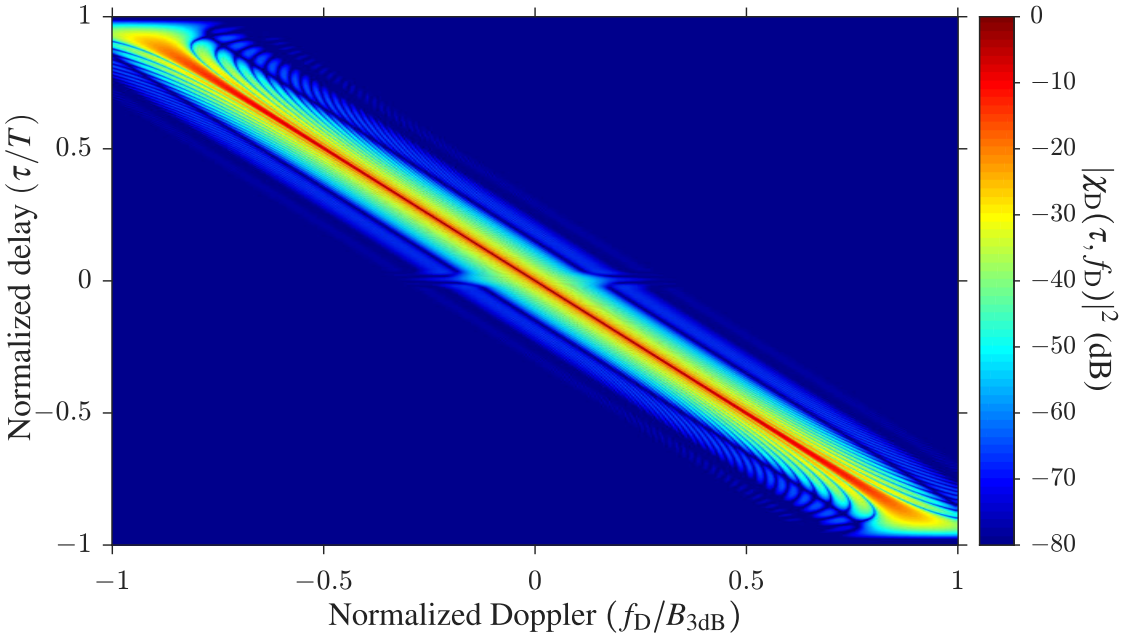

Figure 5.22: Ambiguity function $|\chi_D(\tau, f_D)|^2$ (in dB) via (2.74) versus normalized delay (τ/T) and normalized Doppler (f_D/B_{3dB}) of the LFM with Tukey envelope (LFM-T) with $BT = 200$.

5.3.4.3 Hardware Loopback Measurements

The two optimized waveforms were tested in a loopback configuration using a Tektronix AWG70002A arbitrary waveform generator (10-bit) and a Rohde & Schwarz FSW 26 real-time spectrum analyzer (18-bit) to evaluate the degradation of the waveforms when filtered, sampled, and represented with finite bit-depth. The bandwidth of the waveforms was set at $B_{3dB} = 50$ MHz with a pulse duration of $T = 4$ µs and transmitted at a center frequency of $f_c = 2$ GHz. For $\kappa = 2$ over-sampling the receiver sampling rate was set to $f_s = 100$ MHz.

Figure 5.23 shows the loopback response (red) and the theoretical discrete autocorrelation via (5.23) (blue) for the rectangular envelope waveform OPT-R. The loopback measurement results in 0.0110 dB in mismatch loss due to either straddling or filtering, while the sidelobe responses are nearly identical. Figure 5.24 likewise shows the loopback and theoretical autocorrelation responses for the Tukey-tapered optimized waveform. A mismatch loss of only 0.0076 dB is observed, however the sidelobe response of the loopback data is noticeably different from the lower sidelobes of theoretical response which is due to RF distortion in the loopback configuration. The sidelobe

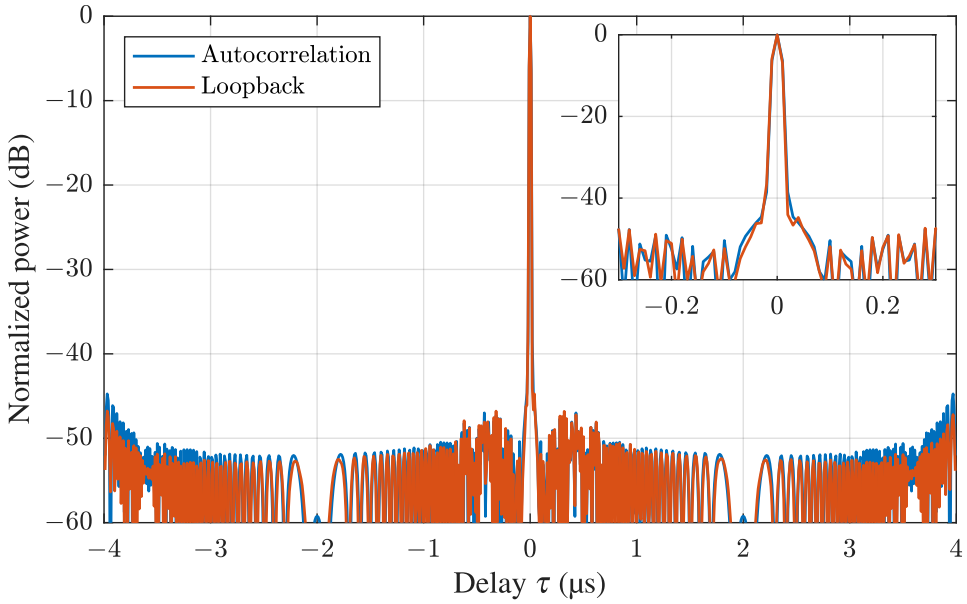

Figure 5.23: Theoretical autocorrelation $|r[\ell]|^2$ (blue) via (5.23) and hardware loopback correlation (red) for the optimized rectangular envelope waveform OPT-R with $B_{3\text{dB}} = 50$ MHz, $T = 4$ μs, $f_s = 100$ MHz $(\kappa = 2)$, and $N_p = 32$. ©2017 IET

degradation is not theorized by any straddling effects as shown in Figure 5.18 and thus must be due to a mismatch in the model used to predict the correlation response. Note that a mismatch of 0.0076 dB indicates that the captured signal is nearly identical to that of the matched filter, though the small difference is enough to alter the theorized correlation response.

To confirm that the discrepancies between the correlation plots in Figure 5.24 are in fact due to the RF distortion, the distortion of the waveform due to up-conversion, down-conversion, linear filtering, and finite bit-depths of the loopback setup is approximated and applied to the continuous-time waveform model in (5.1) for the Tukey envelope optimized waveform OPT-T. The complex baseband waveform $s(t)$ is first up-converted to the passband representation $s_{\text{pb}}(t)$ via (2.1)[5]. The passband signal is then quantized using a 10-bit model to capture the DAC quantization error. A b_{tx}-bit DAC can generate $2^{b_{\text{tx}}}$ unique voltage levels, thus, assuming that the voltage range of $s_{\text{pb}}(t)$ fully fills the dynamic range of the DAC, the quantized passband signal is represented as

[5]An AWG transmit sampling rate of 8 GHz is used to represent the continuous-time signal which, for a center frequency of $f_c = 2$ GHz, is high enough to ignore the distortion effects of the transmit Nyquist zones and sinc-shaped frequency roll-off due to the zero-order hold of the AWG. Therefore, the transmitted continuous-time waveform $s_{\text{pb}}(t)$ (before quantization) can be approximated as an up-converted version of the 'ideal' baseband signal $s(t)$.

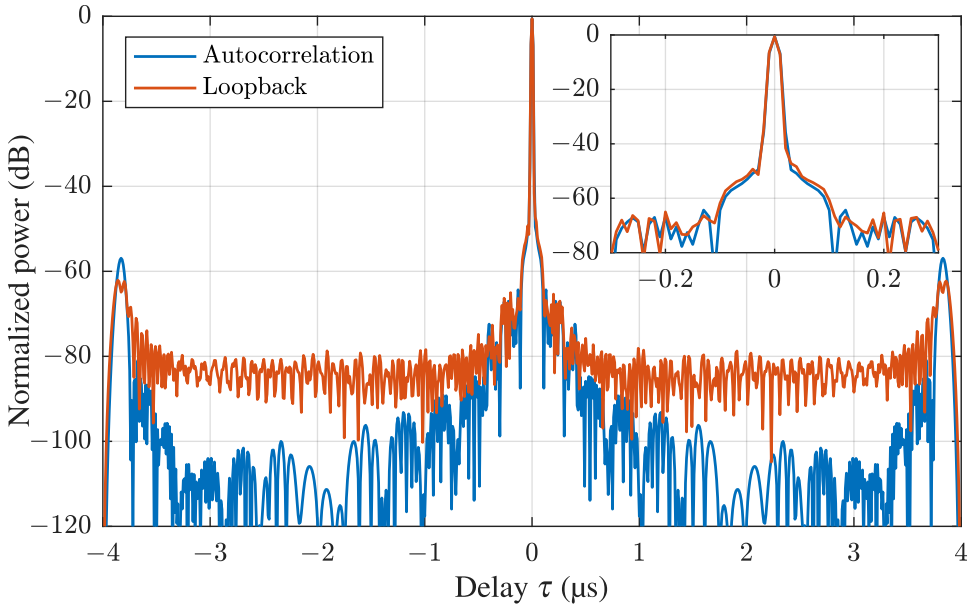

Figure 5.24: Theoretical autocorrelation $|r[\ell]|^2$ (blue) via (5.23) and hardware loopback correlation (red) for the Tukey envelope optimized waveform OPT-T with $B_{3\text{dB}} = 50$ MHz, $T = 4$ μs, $f_\text{s} = 100$ MHz $(\kappa = 2)$, and $N_\text{p} = 32$. ©2017 IET

$$s'_{\text{pb}}(t) = \left\lfloor \frac{s_{\text{pb}}(t)}{\max\limits_t\{s_{\text{pb}}(t)\} - \min\limits_t\{s_{\text{pb}}(t)\}} (2^{b_{\text{tx}}} - 1) \right\rceil \frac{\max\limits_t\{s_{\text{pb}}(t)\} - \min\limits_t\{s_{\text{pb}}(t)\}}{2^{b_{\text{tx}}} - 1}, \tag{5.32}$$

where $\lfloor \bullet \rceil$ rounds to the nearest integer and $b_{\text{tx}} = 10$ bits. The signal from (5.32) is then down-converted into its in-phase and quadrature components via (2.137) and (2.138), low-passed filtered[6], and sampled at 100 MHz which is denoted as the complex baseband sequence, $s'[n]$. Finally, assuming that the sampled voltage range in $s'[n]$ fully fills the b_{rx}-bit ADC dynamic range, the signal is quantized as

$$s''[n] = \left\lfloor \frac{s'[n]}{\max\limits_n\{s'[n]\} - \min\limits_n\{s'[n]\}} (2^{b_{\text{rx}}} - 1) \right\rceil \frac{\max\limits_n\{s'[n]\} - \min\limits_n\{s'[n]\}}{2^{b_{\text{rx}}} - 1}, \tag{5.33}$$

where $b_{\text{rx}} = 18$ bits. The estimated RF distortion process of the ideal signal $s(t)$ using this approximate model is summarized in Figure 5.25.

[6]The down-converted baseband signal is resampled from 8 GHz to 100 MHz using a 100 point, linear-phase, FIR anti-aliasing filter. This filter is generic and is not derived from the true anti-aliasing filter used in the RSA.

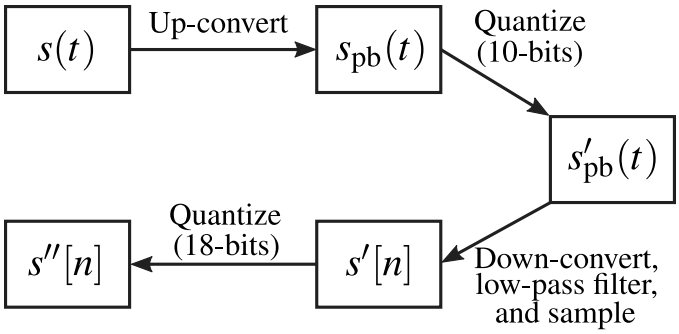

Figure 5.25: Estimated RF distortion model of idealized signal $s(t)$.

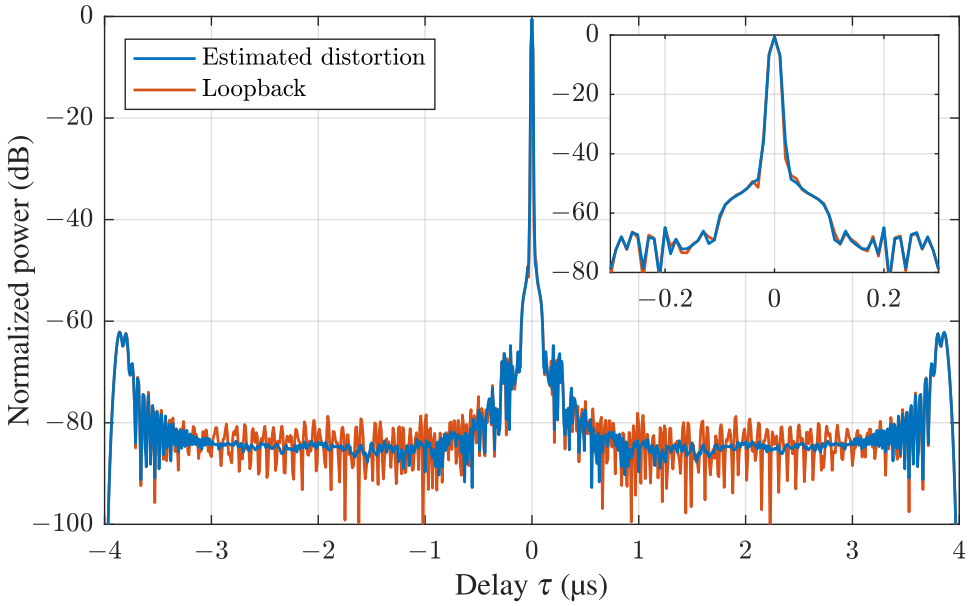

Figure 5.26: Correlation response with estimated loopback distortion (blue) and hardware loopback correlation (red) for the Tukey envelope optimized waveform OPT-T with $B_{3\mathrm{dB}}$ = 50 MHz, T = 4 µs, f_{s} = 100 MHz $(\kappa = 2)$, and N_{p} = 32. ©2017 IET

Figure 5.26 shows the correlation response of the loopback test (red) (same as in Figure 5.24) and the estimated distorted response when correlating the sequence $s''[n]$ with the matched filter $\mathbf{s}(\xi = 0.5)$ (blue). The correlation responses now resemble one another much more closely than was observed in Figure 5.24. In the same manner as the ultra-low sidelobes achieved in [130], this result indicates that more knowledge of the distortion imposed by the RF transmit/receive chain needs to be incorporated into the waveform model to realize the fidelity necessary to achieve the promised performance gains of advanced waveform design and, by extension, waveform diversity [3].

Figure 5.27(a) shows the estimated distorted response as shown in Figure 5.26 with both the

linear filtering and quantization effects. Figure 5.27(b) shows the estimated response when only the linear filtering is applied to the model in Figure 5.25 (no quantization). The fact that both responses maintain a similar sidelobe degradation (as compared to the ideal response in Figure 5.24) shows that the main source of sidelobe distortion is caused by the anti-aliasing filter used prior to sampling on receive. The lack of this filter model in the optimization process limits the fidelity needed to achieve the predicted correlation response. To improve on these results, *system specific* optimization is needed to capture the particular distortion characteristics of the RF chain.

5.4 Incorporation of Hardware Distortion Model into CFM Waveform Optimization

Up to this point the GISL metric is defined using an ideal correlation function derived from the CFM waveform model, (5.1) – (5.3). The properties of the CFM waveform model (with appropriate choice of basis $\mathcal{B}$ and amplitude envelope $u(t)$) allow for the assumption of minimal distortion to the signal structure when passed through the RF chain thus is a *system considerate* waveform design framework. The minimization of these "ideal" metric definitions provides a means to optimize CFM waveforms absent of any knowledge of specific hardware that onto which they would be implemented while still achieving good loopback correlation performance (Section 5.3). However, if the distortion caused by a given RF chain can be characterized, any deleterious effects to the correlation response can be mitigated (if not improved upon) through optimization, thus presenting a method for *system specific* emission/waveform development.

The optimization of radar waveforms with knowledge of transmit hardware effects has been considered in the past in [62,63,173,174] using a greedy-search waveform optimization scheme to minimize either the waveform PSL or ISL. Here, the GISL metric is redefined using a correlation function which incorporates a distortion model derived from three different RF loopback chain configurations with varying degrees of nonlinearity. The updated "model-in-the-loop" GISL metric is then minimized using the BFGS quasi-Newton approach which has the benefit of updating the

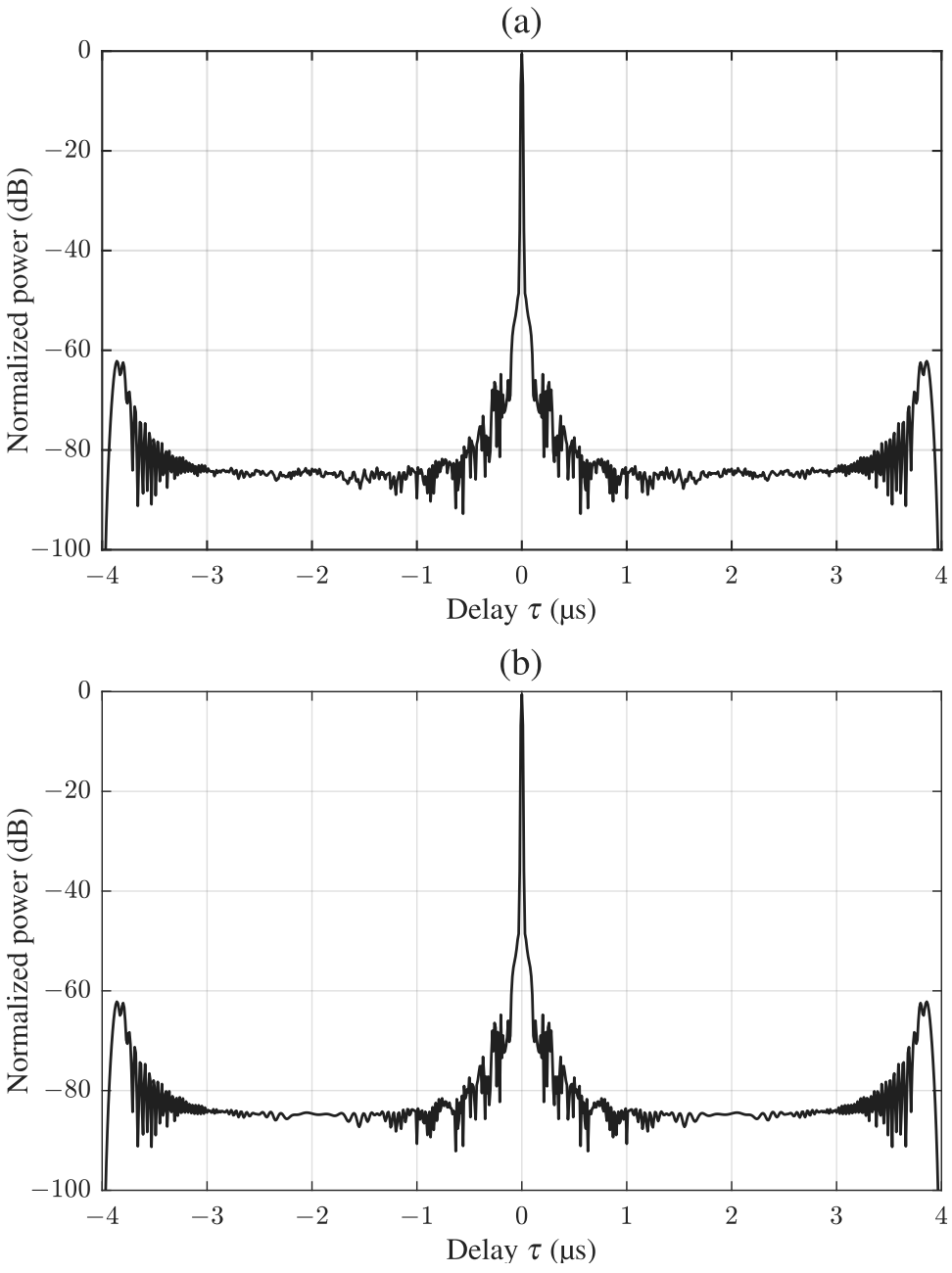

Figure 5.27: Estimated distortion of correlation response using: (a) Both linear filtering and quantization errors and (b) only linear filtering.

entirety of the code vector $\mathbf{x}_{\mathrm{w}}$ per iteration as opposed to the greedy approach from [62,63,173,174] which is limited to an update of a small number of values in $\mathbf{x}_{\mathrm{w}}$ due to massive computation requirements of combinatorial evaluations of the cost function.

In Section 2.2.2 different distortion models were introduced including: the *ideal* model, which models the forward voltage on the transmit chain as a scalar of the analytical waveform $S_{\mathrm{pb}}(f)$; the *linear-only* model, which models the distortion caused by the transmit chain as a linear filter that alters the signal structure; and *nonlinear* distortion modeling techniques, such as Weiner-Hammerstein [68]. Here, the linear model of three different loopback configurations of increasing nonlinearity are estimated and included in the GISL metric so that the distortion is accounted for in the waveform optimization process. Note that this technique is reminiscent of waveform predistortion, where an inverse model of the RF distortion is applied to the waveform such that the desired response is seen after the distortion occurs. However, predistortion typically alters the modulus of the waveform thus may not be admissible in some systems. Here the waveform is designed with the distortion model "in-the-loop" thus inherently accounting for the RF distortion without requiring predistortion.

The hardware distortion model for the three loopback configurations is estimated using time-shifted impulse transmit excitations that effectively increase the sampling rate of the transmit model beyond that of the receiver sampling rate (more details in Section 5.4.2). The distortion model allows for the prediction of the waveform structure at the receiver which is then used to generate the modified correlation function from (5.21). The bandlimiting caused by the model produces a loss in waveform energy outside the bandwidth of the receiver anti-aliasing filter. Typically a constraint would be needed (thus requiring a constrained optimization algorithm) to limit this loss, however by using the Legendre basis and order-recursive structure discussed in Section 5.3, this constraint is not needed as the waveforms remain spectrally-contained thus limiting the loss due to filtering.

Once optimized, the CFM waveforms are captured in a loopback setting using the same RF chains that were modeled to compare the theoretical responses to the captured signal. It is found

that the linear distortion models are an effective means to predict the signal structure at the receiver even when significant transmitter nonlinearities are present (multiple amplifiers, one in saturation)[7]. Furthermore, the idealized OPT-R and OPT-T correlation responses (Figures 5.17 and 5.18) are improved upon using the same waveform framework ($BT = 100,\ \kappa = 2,\ N_\mathrm{p} = 32$) by leveraging the inherent pulse-shaping caused by the RF bandlimiting.

5.4.1 Model-in-the-loop Cost Function Formulation

The configuration that is considered here is a loopback mode where the transmit chain is directly connected to the receive chain. Therefore, the only hardware components not characterized in this setup are the transmit/receive antennas. In this configuration, the distortion and filter for both the transmit and receive chains are characterized using a single complex-baseband filter model $W_\mathrm{L}(f)$, which can be defined as the combination of the transmit linear distortion response $W_\mathrm{tx}(f)$ from (2.112), and the receive distortion response $W_\mathrm{rx}(f)$ from (2.140) as

$$W_\mathrm{L}(f) = W_\mathrm{tx}(f + f_\mathrm{c})W_\mathrm{rx}(f). \tag{5.34}$$

Recall that the transmit filter $W_\mathrm{tx}(f)$ is defined at passband while the receive filter $W_\mathrm{rx}(f)$ is defined at baseband. Assume that the filter $W_\mathrm{L}(f)$ is peak normalized (in frequency) such that no frequency component is amplified, thus the distorted received complex-baseband response can be ideally modeled as the noiseless signal

$$S_\mathrm{L}(f) = \sqrt{2}S_\mathrm{pb}(f + f_\mathrm{c})W_\mathrm{L}(f). \tag{5.35}$$

The $\sqrt{2}$ ensures that $S_\mathrm{L}(f)$ and $S(f)$ have similar scaling thus can be directly compared. By estimating $W_\mathrm{L}(f)$, the expected distortion caused by the RF components can be included in the GISL metric. In the time domain $S_\mathrm{L}(f)$ is represented as

[7]Both amplifiers that are used are class A, solid-state amps designed to run in the linear region of gain curve. To avoid damage the saturated amplifier was amplified only 1 dB past its 1 dB compression point, but was still found to produce significant nonlinearities

$$s_{\mathrm{L}}(t) = \sqrt{2}\int_{-\infty}^{\infty} s_{\mathrm{pb}}(\zeta)e^{-j2\pi f_c\zeta}w_{\mathrm{L}}(t-\zeta)d\zeta, \tag{5.36}$$

where $W_{\mathrm{L}}(f) = \mathcal{F}\{w_{\mathrm{L}}(f)\}$. The loss associated with filtering out-of-band spectral content in $s(t)$ can be defined as

$$\mathcal{L}_{\mathrm{L}}\ (\mathrm{dB}) = 10\log_{10}\left\{\|s(t)\|_2^2\right\} - 10\log_{10}\left\{\|s_{\mathrm{L}}(t)\|_2^2\right\}. \tag{5.37}$$

Note that (5.37) is a coarse estimate of the absolute loss caused by the filtering process as the peak-normalization of $W_{\mathrm{L}}(f)$ is an ad-hoc method for comparing $s_{\mathrm{L}}(t)$ and $s(t)$. Though (5.37) is sufficient in characterizing the relative losses due changing the waveform throughout the optimization process.

In the Sections 5.2 and 5.3, the ideal waveform $s(t)$ was sampled to construct the match filter. However, because is ideal response $s(t)$ is altered as it traverses through the RF chain, the filter defined using this method would no longer be matched to the expected response. Therefore, the expected receive signal $s_{\mathrm{L}}(t)$ is sampled (as in (5.22)) for the matched filter. Assuming the filter $w_{\mathrm{L}}(t)$ has an impulse response duration of T_{L} over the interval $t \in [0, T_{\mathrm{L}}]$, the signal $s_{\mathrm{L}}(t)$ is of duration $T + T_{\mathrm{L}}$ and the number of samples kept for the matched filter is $N_{\mathrm{L}} = \lfloor f_{\mathrm{s}} \cdot (T + T_{\mathrm{L}}) \rfloor$. Thus define the complex-weighted impulse train corresponding to the matched filter as

$$\tilde{s}_{\mathrm{L}}(t;\xi) = \sum_{n=0}^{N_{\mathrm{L}}-1} s_{\mathrm{L}}(nT_{\mathrm{s}} + \xi)\delta(t - (nT_{\mathrm{s}} + \xi)), \tag{5.38}$$

for $\xi \in [0, T_{\mathrm{s}}]$, the subsample shift. Thus modified correlation response (similar to (5.21)) for use in the GISL metric is

$$\tilde{r}_{\mathrm{L}}(\tau;\xi) = \frac{1}{\|\mathbf{s}_{\mathrm{L}}(\xi)\|_2^2}\int_0^{\infty} \tilde{s}_{\mathrm{L}}^*(t-\tau;\xi)s_{\mathrm{L}}(t)dt, \tag{5.39}$$

where $\mathbf{s}_{\mathrm{L}}(\xi) = \begin{bmatrix} s_{\mathrm{L}}(\xi) & s_{\mathrm{L}}(T_{\mathrm{s}} + \xi) & \cdots & s_{\mathrm{L}}((N_{\mathrm{L}} - 1)T_{\mathrm{s}} + \xi) \end{bmatrix}^T$ is the discretized form of the matched filter. The updated GISL metric containing the linear model of the of the combined transmit and

receive chains from (5.34) is

$$\mathcal{J}_{\mathrm{L}}(\mathbf{x}_{\mathrm{w}};\xi,q)=\left(\frac{\displaystyle\int_{\Delta\tau}^{T}|\tilde{r}_{\mathrm{L}}(\tau;\xi)|^{q}\,d\tau+\int_{-T}^{-\Delta\tau}|\tilde{r}_{\mathrm{L}}(\tau;\xi)|^{q}\,d\tau}{\displaystyle\int_{-\Delta\tau}^{\Delta\tau}|\tilde{r}_{\mathrm{L}}(\tau;\xi)|^{q}\,d\tau}\right)^{\frac{1}{q}}. \tag{5.40}$$

Note that due to the inclusion of the distortion model, the cost function (5.40) contains a lossy model of the waveform. It is possible that the optimization problem would need to be reformulated to account for this loss by incorporating an inequality constraint into the design to limit the loss $\mathcal{L}_{\mathrm{L}}$ from (5.37), thus necessitating the use of constrained optimization algorithms such as sequential quadratic programming or nonlinear interior point methods [79]. However, the results presented in this section did not require a constraint as the loss never exceeds 0.23 dB after optimization relative to the loss of the corresponding LFM benchmark case.

5.4.2 Hardware Distortion Model Estimation

The waveforms are generated using a Tektronix AWG70002A arbitrary waveform generator (AWG) and received using the IQ mode of a Rohde and Schwarz FSW 26 real-time spectrum analyzer (RSA) which down-converts the passband signal to complex baseband. The approximate linear model was estimated for three different hardware configurations (with increasing nonlinearity): case 1) the AWG and RSA are directly connected, case 2) an amplifier is placed in the RF chain, and case 3) two amplifiers are placed in loop with one driven into saturation. Figure 5.28 displays the three hardware configurations and Table 5.1 has a detailed list of every component used in the hardware loopback tests. Attenuators were used to control the power level of the signal throughout the chain to ensure that no damage was caused to any component.

The linear frequency response of any systems can be estimated via multiple difference methods including an impulse, swept spectrum, or least-squares (LS) or minimum mean-square error (MMSE) techniques. Here, the impulse response is estimated via an impulse generated via the AWG and captured at the RSA. This method gives the most direct estimate of the filter $w_{\mathrm{L}}(t)$ as

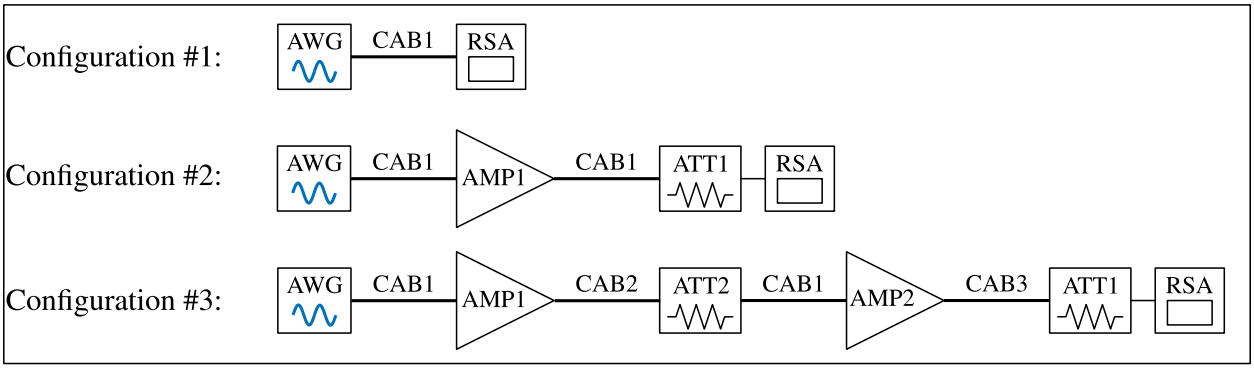

Figure 5.28: Three hardware configurations with varying nonlinearity. The response distortion of which is estimated for model-in-the-loop CFM waveform optimization.

Table 5.1: Component list used in loopback testing.

Tag	**Description**
AWG	Tektronix AWG70002A arbitrary waveform generator
RSA	Rohde & Schwarz FSW 26 real-time spectrum analyzer
CAB1	Pasternack PE300-36 cable (3 ft.)
CAB2	Minicircuits 086-12SM+ cable (12 in.)
CAB3	Pasternack PE300-72 cable (6 ft.)
AMP1	Mini-circuits TVA-82-213 wideband amp
AMP2	Mini-circuits ZHL-42W+ medium-HPA
ATT1	Minicircuits 20 dB attenuator
ATT2	JFW 50BR-008 variable attenuator (set to 22 dB)

the order of the filter does not need to be chosen.

For an ideal impulse response, the complex baseband, continuous-time signal incident on the in-phase and quadrature chains of the RSA (ignoring propagation delays) is approximately equal to the filter $w_{\mathrm{L}}(t)$,

$$\begin{aligned} y(t) &\approx \int_{-\infty}^{\infty} \delta(\zeta) e^{-j2\pi f_{\mathrm{c}}\zeta} w_{\mathrm{L}}(t-\zeta) d\zeta \\ &\approx w_{\mathrm{L}}(t). \end{aligned} \tag{5.41}$$

For a sampling period of T_{s}, assume the RSA samples at the time instants $\{0, T_{\mathrm{s}}, 2T_{\mathrm{s}}, \dots\}$ thus the distortion filter is estimated at the time instants, $\{w_{\mathrm{L}}(0), w_{\mathrm{L}}(T_{\mathrm{s}}), w_{\mathrm{L}}(2T_{\mathrm{s}}), \dots\}$. By shifting[8] the generated impulse by some amount t_{d} where $0 \le t_{\mathrm{d}} < T_{\mathrm{s}}$, complex baseband, continuous-time signal incident on the in-phase and quadrature chains of the RSA is now approximated as

$$\begin{aligned} y(t) &\approx \int_{-\infty}^{\infty} \delta(\zeta + t_{\mathrm{d}}) e^{-j2\pi f_{\mathrm{c}}\zeta} w_{\mathrm{L}}(t-\zeta) d\zeta \\ &\approx w_{\mathrm{L}}(t + t_{\mathrm{d}}) e^{j2\pi f_{\mathrm{c}} t_{\mathrm{d}}}. \end{aligned} \tag{5.42}$$

Thus by sampling at time instants $\{0, T_{\mathrm{s}}, 2T_{\mathrm{s}}, \dots\}$, the distortion filter is sampled at the points $\{w_{\mathrm{L}}(t_{\mathrm{d}}), w_{\mathrm{L}}(T_{\mathrm{s}} + t_{\mathrm{d}}), w_{\mathrm{L}}(2T_{\mathrm{s}} + t_{\mathrm{d}}), \dots\}$. Note that the additional phase shift $e^{j2\pi f_{\mathrm{c}} t_{\mathrm{d}}}$ must be accounted for when forming the estimate of the distortion filter. We would like to achieve the highest fidelity linear distortion model to incorporate as much reality into the optimization process. Therefore this method of shifting the transmit signal to sample different points within $w_{\mathrm{L}}(t)$ is leveraged to achieve a highly sampled version of the distortion model $w_{\mathrm{L}}(t)$.

The finest duration the transmit signal can be shifted in the AWG is 40 ps = $\frac{1}{25\ \mathrm{GS/s}}$, where 25 GS/s is the maximum transmit sampling rate of the AWG thus is the granularity of the filter estimate for this experiment. Here, the system parameters are the same as loopback specifications discussed

[8]Note that this shift may not be possible for some transmit scenarios (e.g. many software-defined radios (SDRs) operate at transmit sample rates equal to the receiver sampling rate and utilize DAC filtering and analog up-conversion). However the Tektronix AWG70002A has a transmit sampling rate up to 25 GHz thus is high enough to approximate "continuous time" for the operating frequencies that are considered.

in Section 5.3: center frequency $f_c = 2$ GHz and receiver sampling rate of $f_s = 100$ MHz. Thus, a distortion filter model estimated at a sampling rate of 25 GHz is essentially "continuous" for all intents and purposes. Note that it is possible that the distortion filter model could be estimated at a much lower sampling rate, though here it was maximized to provide that highest degree of sensitivity to the filter model.

Define $M_L = \frac{f_{s,tx}}{f_s}$ as the ratio of the transmit sampling rate $f_{s,tx}$ and the receiver sampling rate f_s. Therefore M_L shifted impulses are needed to represent the distortion model at the higher sampling rate. An impulse train containing the shifted impulses can be constructed as

$$s_{imp}(t) = \sum_{m=0}^{M_L-1} \delta\big(t - m\cdot(T_{sep} - T_{s,tx})\big) \tag{5.43}$$

where $T_{s,tx}$ is the transmitter sampling period and $T_{sep} > T_L$ is the separation between the delta functions (without the $T_{s,tx}$ shift). Note that T_{sep} is chosen such that $f_s T_{sep}$ is an integer so that the received signal $y(t)$ is sampled at the points pertaining to the distortion filter model $\{w_L(0), w_L(T_{s,tx}), w_L(2T_{s,tx}), \dots\}$.

The complex-baseband, signal incident on the receiver is then approximated as the summation

$$\begin{aligned} y(t) &\approx \int_{-\infty}^{\infty} s_{imp}(\zeta) e^{-j2\pi f_c \zeta} w_L(t-\zeta) d\zeta \\ &\approx \sum_{m=0}^{M_L-1} w_L\big(t - m(T_{sep} - T_{s,tx})\big) e^{-j2\pi f_c m(T_{sep}-T_{s,tx})} \end{aligned} \tag{5.44}$$

where the interval

$$y\big(mT_{sep} \le t \le (m+1)T_{sep}\big) \approx w_L\big(t - m(T_{sep} - T_{s,tx})\big) e^{-j2\pi f_c m(T_{sep}-T_{s,tx})} \tag{5.45}$$

corresponds to the mth time and phase shifted distortion model for $m \in \{0, 1, \dots, M_L - 1\}$. Sampling $y(t)$ at the points $\{0, T_s, 2T_s, \dots\}$, the filter estimate $\hat{w}(t)$ sampled at $f_{s,tx} = 25$ GHz can be constructed as

$$\hat{w}_{\mathrm{L}}(mT_{\mathrm{s,tx}} + nT_{\mathrm{s}}) = y(nT_{\mathrm{s}} + mT_{\mathrm{sep}})e^{j2\pi f_{\mathrm{c}} m(T_{\mathrm{sep}} - T_{\mathrm{s,tx}})} \tag{5.46}$$

for $m \in \{0, 1, \ldots, M_{\mathrm{L}} - 1\}$ and $n \in \{0, 1, \ldots, N_{\mathrm{L}} - 1\}$. Thus the estimate of the discretized distortion filter samples are collected as $\left\{\hat{w}_{\mathrm{L}}(0), \hat{w}_{\mathrm{L}}(T_{\mathrm{s,tx}}), \ldots, \hat{w}_{\mathrm{L}}(T_{\mathrm{s}}), \hat{w}_{\mathrm{L}}(T_{\mathrm{s}} + T_{\mathrm{s,tx}}), \ldots, \hat{w}_{\mathrm{L}}(T_{\mathrm{L}} - T_{\mathrm{s,tx}})\right\}$ which is used to approximate continuous time in the cost function (5.40).

Note that the "impulse" used to estimate the filter $w_{\mathrm{L}}(t)$ is a rectangular pulse of a 40 ps duration which places a slight sinc-shape on top of the estimated filter spectrum. However, over the receive band that is considered (f_{c} = 2 GHz and f_{s} = 100 MHz), the response varies only 0.0086 dB due to the additional sinc envelope thus is considered negligible and ignored. For each loopback scenario, the impulse response was coherently integrated using 2000 trials due to the low amount of energy present for this estimation method. Figure 5.29 shows the baseband frequency response $W_{\mathrm{L}}(f)$ for each of the three configurations introduced in Figure 5.28.

5.4.3 Model-in-the-loop Waveform Optimization via Quasi-Newton Method

The minimization of cost function $J_{\mathrm{L}}(\mathbf{x}_{\mathrm{w}}; \xi, q)$ from (5.40) is different than that of Sections 5.2 and 5.3 as the distortion filter model is included in the formation of the correlation function $\tilde{r}_{\mathrm{L}}(\tau; \xi)$. Thus, depending on the algorithm and initialization, the parameters $\mathbf{x}_{\mathrm{w}}$ could enter regions of the cost function surface that correspond to undesirable losses ($\mathcal{L}_{\mathrm{L}}$ in (5.37)) due to the filtering process. In other words, the waveform could have significant out of band energy that gets filtered out in loopback. There are two methods of avoiding these regions of the cost function surface: 1) by constraining the optimization problem such that these regions are not possible to converge on, or 2) by optimizing the waveform in an unconstrained manner but choose an initialization, waveform model, and optimization method that naturally do not not place significant energy out of band. It has been found that if the Legendre basis used for the CFM model and $\mathcal{J}_{\mathrm{L}}(\mathbf{x}_{\mathrm{w}}; \xi, q)$ is minimized via BFGS quasi-Newton descent in an unconstrained formulation then the converged solutions do not exhibit significant losses.

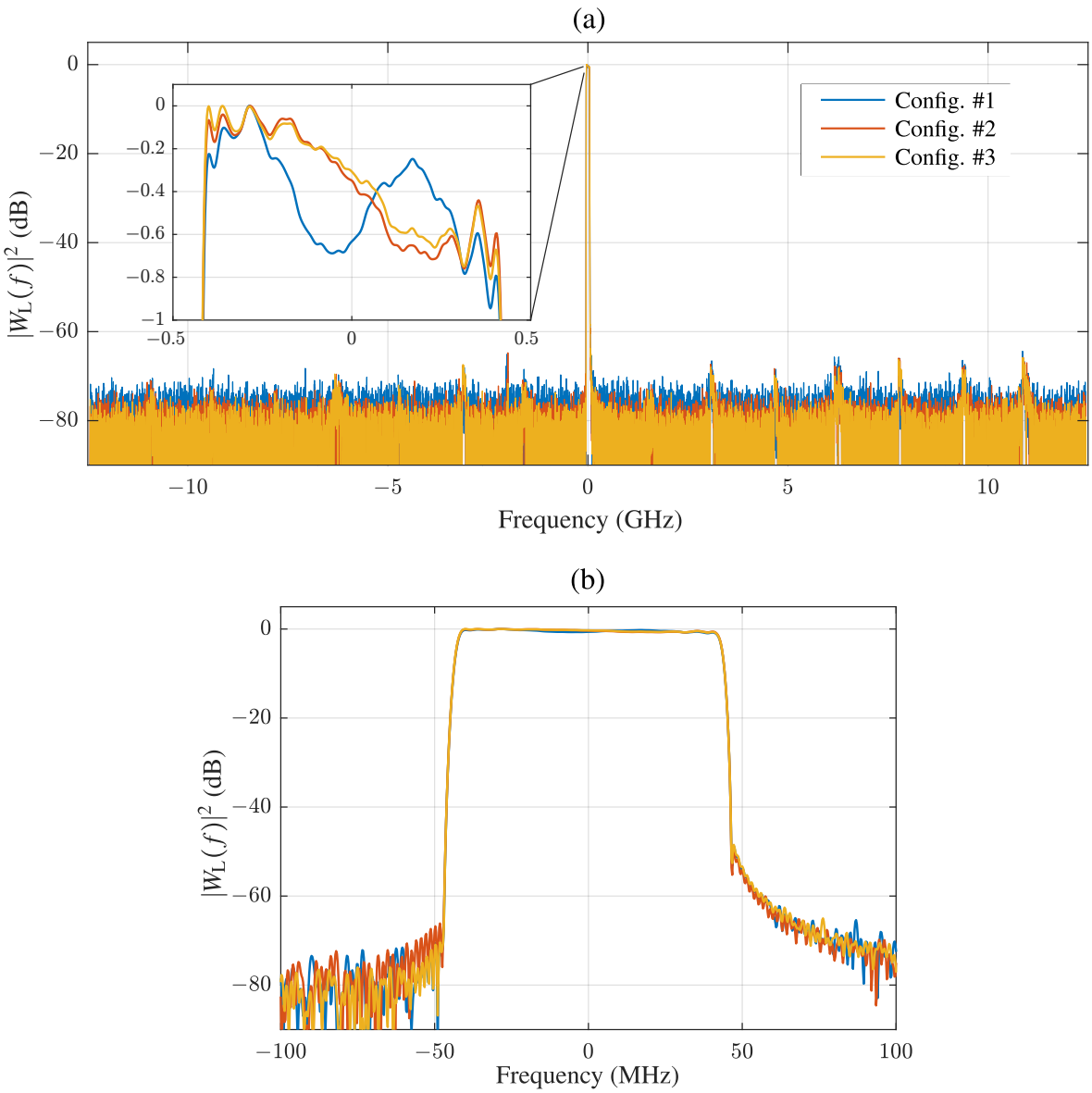

Figure 5.29: Estimated hardware frequency response of configuration 1 (blue), configuration 2 (red), and configuration 3 (yellow) for (a) full-band with detailed inset and (b) view of filter roll-off.

Just as in Section 5.3, two waveforms are optimized for each loopback configuration: one with a rectangular envelope (OPT-R) and one with a Tukey envelope (OPT-T) (see Figure 5.14). The waveforms are optimized for a time-bandwidth of $BT = 100$ and receiver over-sampling factor $\kappa = 2$. Thus for a receiver sampling rate of $f_s = 100$ MHz, the 3 dB bandwidth of the waveforms is $B_{3dB} = 50$ MHz and the pulse duration is $T = 2\mu s$. The order-recursive optimization process illustrated in Figure 5.11 with BFGS quasi-Newton method (Algorithm 5.3) was implemented using the Legendre polynomial basis and terminated after the coefficients for $N_p = 32$ polynomials are optimized (order 64 polynomial). The gradients of the cost function $\mathcal{J}_L(\mathbf{x}_w; \xi, q)$ were calculated using the finite-difference method from (5.31). The cost function norm q was set to be the ISL of the modified correlation function $(q = 2)$ as it was found to produce to best results for this scenario, and the subsample shift ξ is again chosen to be $0.5T_s$. These parameters are deliberately chosen such that they are similar to those of Section 5.3 such that the results can be compared to illustrate the improvement in performance when incorporating a system model into the design[9]

Figure 5.30 shows the value of the cost function $\mathcal{J}_L(\mathbf{x}_w; \xi = 0.5T_s, q = 2)$ per iteration for (a) OPT-R and (b) OPT-T and RF configuration #1 (top row), configuration #2 (middle row), and configuration #3 (bottom row). The black dots represent an increase of the polynomial order within the order-recursive process. The cost function value for the OPT-T waveform decreases very little after $N_p = 10$ Legendre polynomials. This effect is likely due to the Tukey envelope not requiring the higher order polynomials to achieve a low sidelobe level whereas the OPT-R waveform utilizes these polynomials to achieve a higher fidelity phase function at the beginning at ends of the waveform. Also of note is that configurations #2 and #3 achieve a lower cost function value for both the OPT-R and OPT-T waveforms mostly likely caused by the differences in the frequency responses (see Figure 5.29).

The loss $\mathcal{L}_L$ (dB) from (5.37) was calculated for all three hardware configurations and both OPT-R and OPT-T waveforms. However, because the loss is a coarse estimate of the actual, the

[9]The difference between the waveforms optimized in Section 5.3 and the waveforms optimization in Section 5.4 is the reduction in pulse duration from 4 μs to 2 μs thus halving the time-bandwidth product to $BT = 100$.

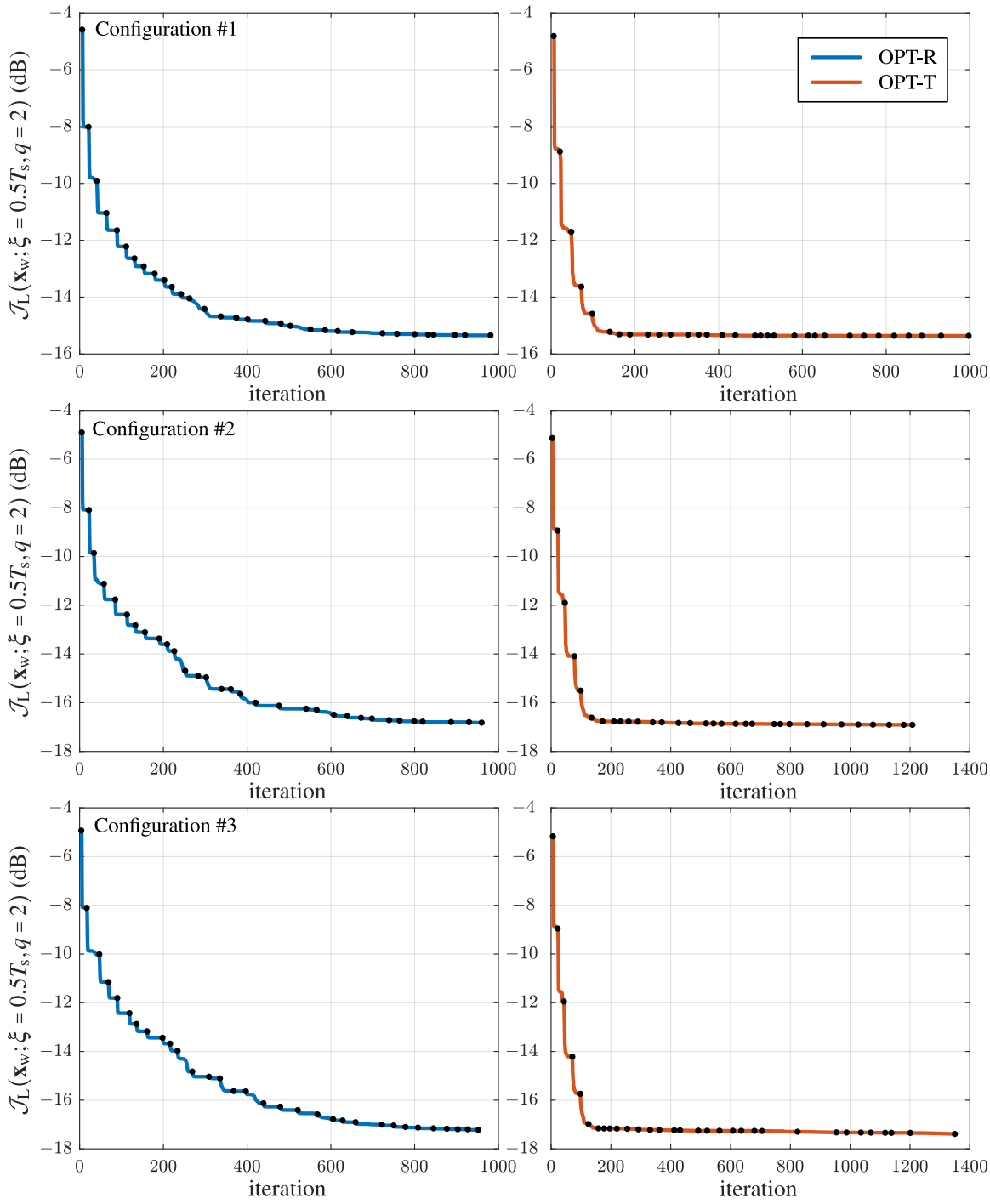

Figure 5.30: Cost $\mathcal{J}_{\mathrm{L}}(\mathbf{x}_{\mathrm{w}};\xi = 0.5T_{\mathrm{s}},q = 2)$ (in dB) for OPT-R (blue) and OPT-T (red) and RF configuration #1 (top row), configuration #2 (middle row), and configuration #3 (bottom row). Black dots indicate an increase in Legendre polynomial order using the order-recursive optimization structure.

Table 5.2: Table of loss ratio between LFM-R and OPT-R and loss ratio between LFM-T and OPT-T

	OPT-R	OPT-T
Configuration #1	0.1134 dB	0.0671 dB
Configuration #2	0.0986 dB	0.1371 dB
Configuration #3	0.1001 dB	0.2232 dB

losses for the OPT-R and OPT-T cases are calculated relative to the losses for LFM waveforms with the corresponding amplitude envelope. The LFM cases represent one of the more spectrally contained and ubiquitous waveform cases thus the loss relative to the loss of the LFM waveform is a meaningful quantity. The losses of the OPT-R and OPT-T cases relative to their respective LFM cases is shown in Table 5.2. While all of the optimized waveforms do increase in loss compared to their LFM counterparts, the maximum loss is 0.2232 dB for OPT-T in configuration #3 which is only a 5% energy loss compared to the LFM-T case. Note that if the loss is ever of concern, a constraint can be implemented which would require the use of constrained nonlinear optimization techniques [79].

The normalized instantaneous frequency versus time for both the OPT-R (blue) and OPT-T (red) waveforms and configuration #1 (top), configuration #2 (middle), and configuration #3 (bottom) are shown in Figure 5.31. The OPT-R waveform has a familiar "sideways-S" curve shape for that has been noted in previous sections for all three configurations. However, the OPT-T waveform has an interesting response where the frequency content at the edges of the pulse traverse rapidly throughout the band of the waveform. Recall that at these points the envelope of the waveform is in the rise/fall regions of the Tukey shape thus these regions may not have much of an effect on the correlation response.

Figure 5.32 shows the spectral content of the OPT-R (blue) and OPT-T (red) waveforms for all three RF configurations using the swept mode of the RSA. A majority of the spurious signals and harmonics are labeled. In configuration #1, the harmonics of the fundamental are subdued with the second harmonic at −50 dB down from the fundamental. A spurious tone occurs in the AWG at $f_{\text{s,tx}}/2$ that causes images to occur at 10.5 and 14.5 GHz. The nonlinear behavior in configurations

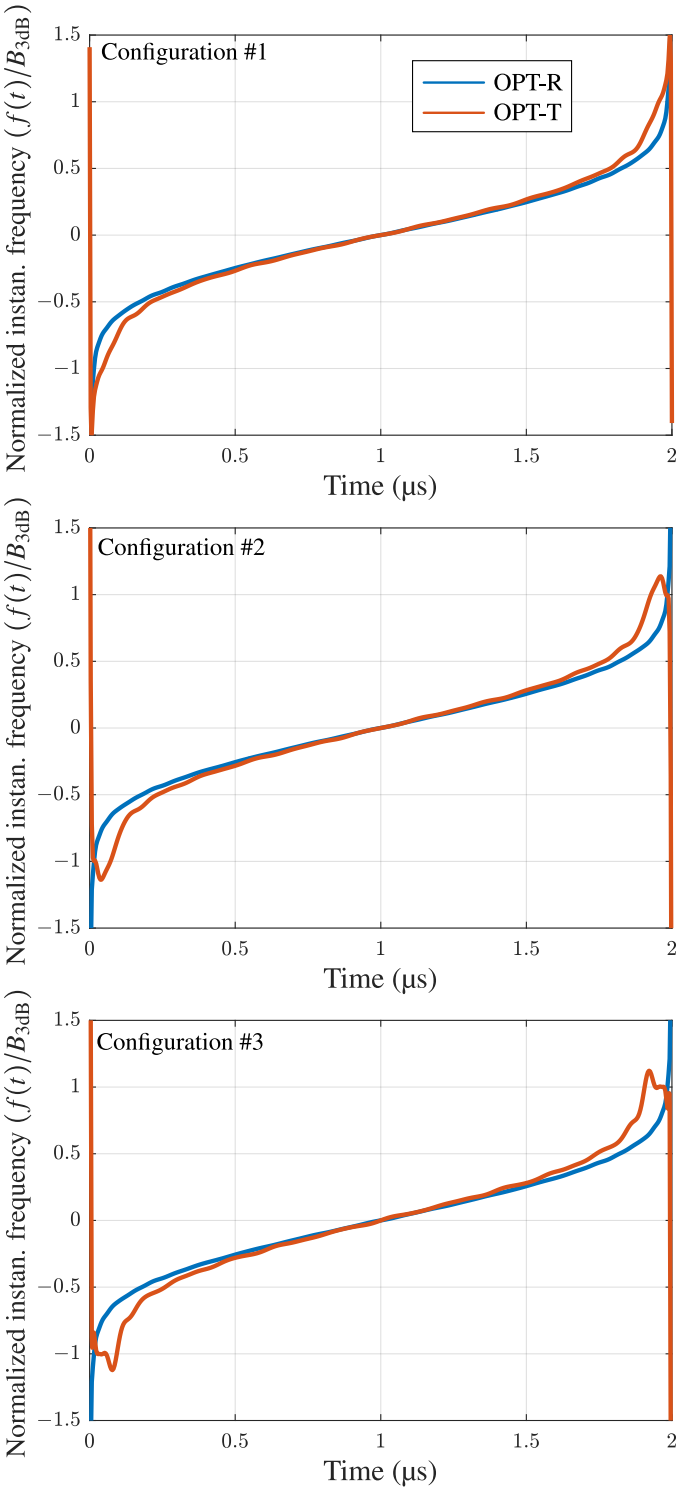

Figure 5.31: Normalized instantaneous frequency $(f(t)/B_{3\text{dB}})$ vs. time (in μs) of optimized waveforms OPT-R (blue) and OPT-T (red) for RF chain in configuration #1 (top), configuration #2 (middle), and configuration #3 (bottom).

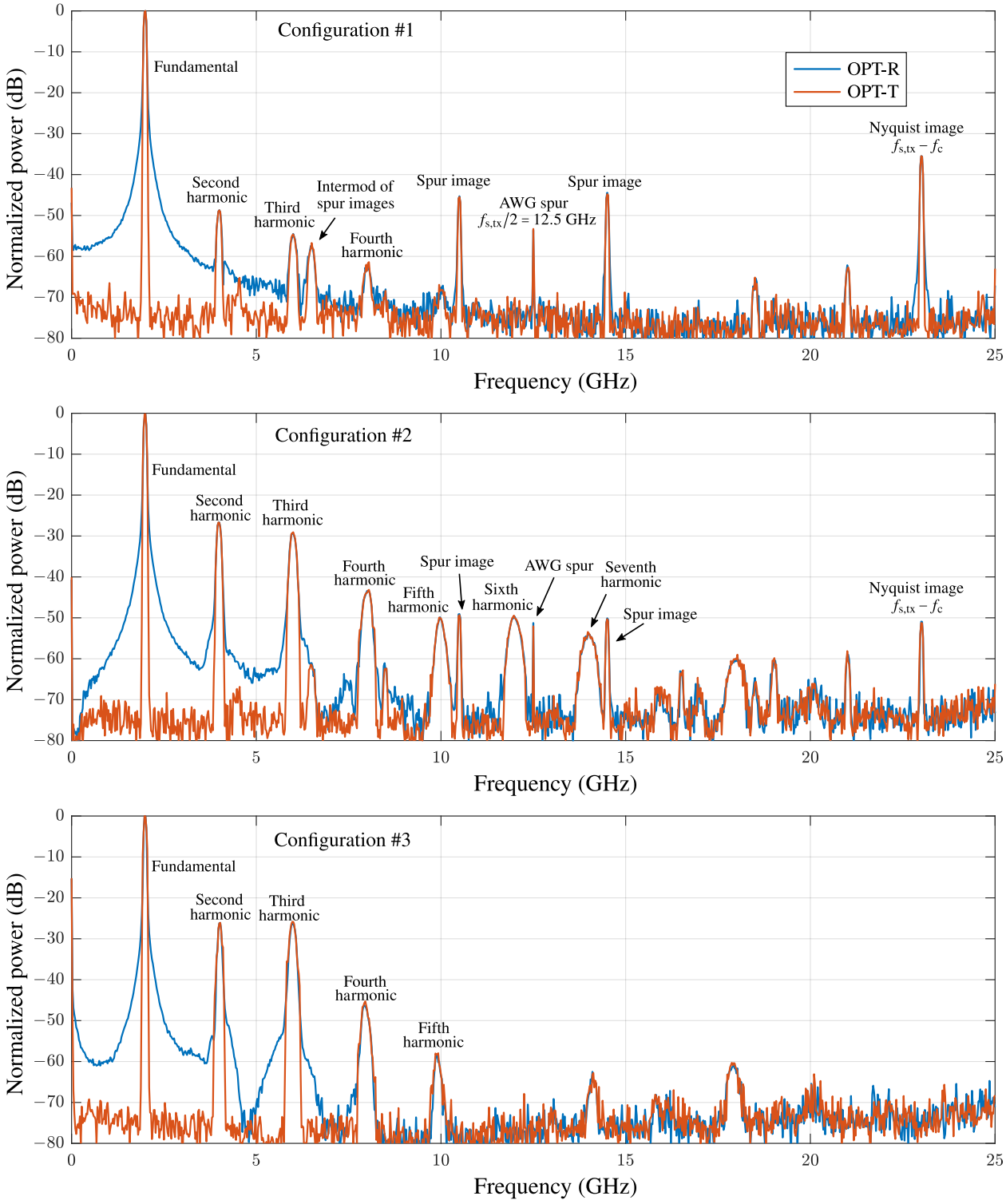

Figure 5.32: Spectral content (before down-conversion and anti-aliasing filter) of OPT-R transmission (blue) and OPT-T transmission for RF chain in configuration #1 (top), configuration #2 (middle), and configuration #3 (bottom) captured using swept mode of RSA.

#2 and #3 is apparent in the increase in harmonic power level. The TVA-82-213 wideband amp has a frequency response up to 27 GHz thus retains a majority of the nonlinear artifacts at the RSA for configuration #2. The ZHL-42W+ amplifier has a specified operating frequency up to 4 GHz thus filters out a majority of the higher frequency nonlinear responses for configuration #3. Note that the OPT-T waveform does have a non-uniform time envelope though spectral response does not exhibit spectral regrowth when put through multiple amplifier stages. This result is due to the Tukey envelope structure which is inherently robust to spectral regrowth effects. Thus, it can be assumed that the signal structure of the in-band content does not change significantly due to the saturated amplifier (see Section 2.2.2.2).

Figures 5.33 through 5.35 show the theoretical envelope responses of the (a) OPT-R and (c) OPT-T waveforms using the estimated linear model $w_{\mathrm{L}}(t)$, and the actual loopback captures of the of the (b) OPT-R and (d) OPT-T waveforms for all three configurations, respectively. Recall that the OPT-R waveform is generated as a constant amplitude waveform and the OPT-T waveform is generated with only a Tukey taper, therefore the envelope distortion seen in Figures 5.33 – 5.35 is solely caused by RF components. For all three configurations, the linear model well approximates the captured loopback response of the three configurations.

Table 5.3: Angle $\left|\cos\bar{\theta}\right|^2$ between $s_{\mathrm{L}}(t)$ and $y(t)$ and also $s(t)$ and $y(t)$

	OPT-R		OPT-T	
	$s(t)$	$s_{\mathrm{L}}(t)$	$s(t)$	$s_{\mathrm{L}}(t)$
Configuration #1	0.9794	0.9995	0.9884	0.9995
Configuration #2	0.9787	0.9999	0.9713	0.9999
Configuration #3	0.9779	0.9997	0.9520	0.9994

The squared-cosine angle is defined as a scaled inner product between two signals that measure the signal correlation/similarity. The inner product takes into account the analytical energies contained in both signals to normalized the result such that it lies between 0 (orthognal) and 1 (maximum) (only occurs if the signals are scaled replicas of the same signal). Define the squared-cosine angle (denoted $\left|\cos\bar{\theta}\right|^2$) between two arbitrary, finite energy signals $a(t)$ and $b(t)$ as

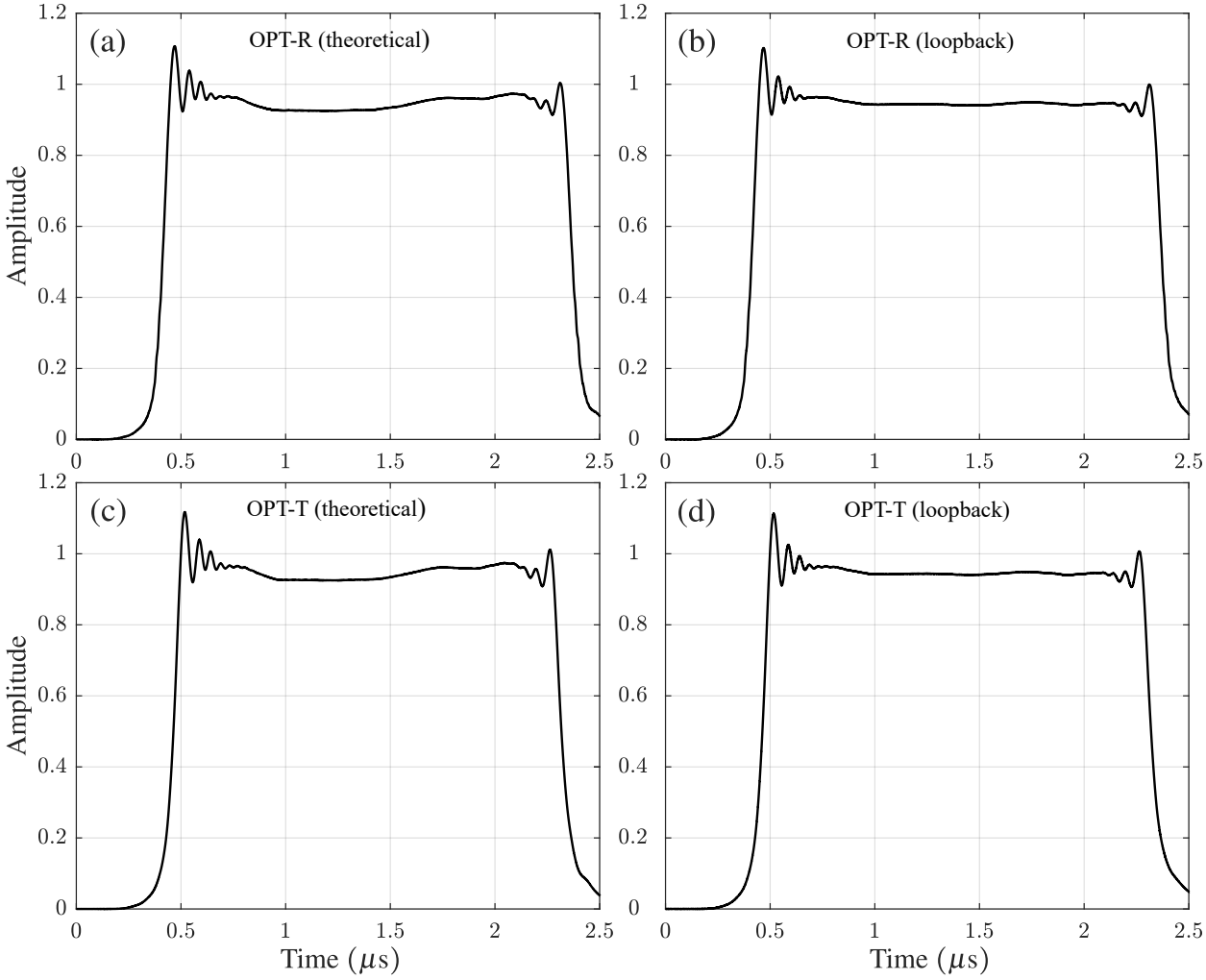

Figure 5.33: Amplitude envelopes for RF chain in **configuration #1**: (a) the theoretical OPT-R response using distortion model, (b) the loopback captured OPT-R response, (c) the theoretical OPT-T response using distortion model, and (d) the loopback captured OPT-T response.

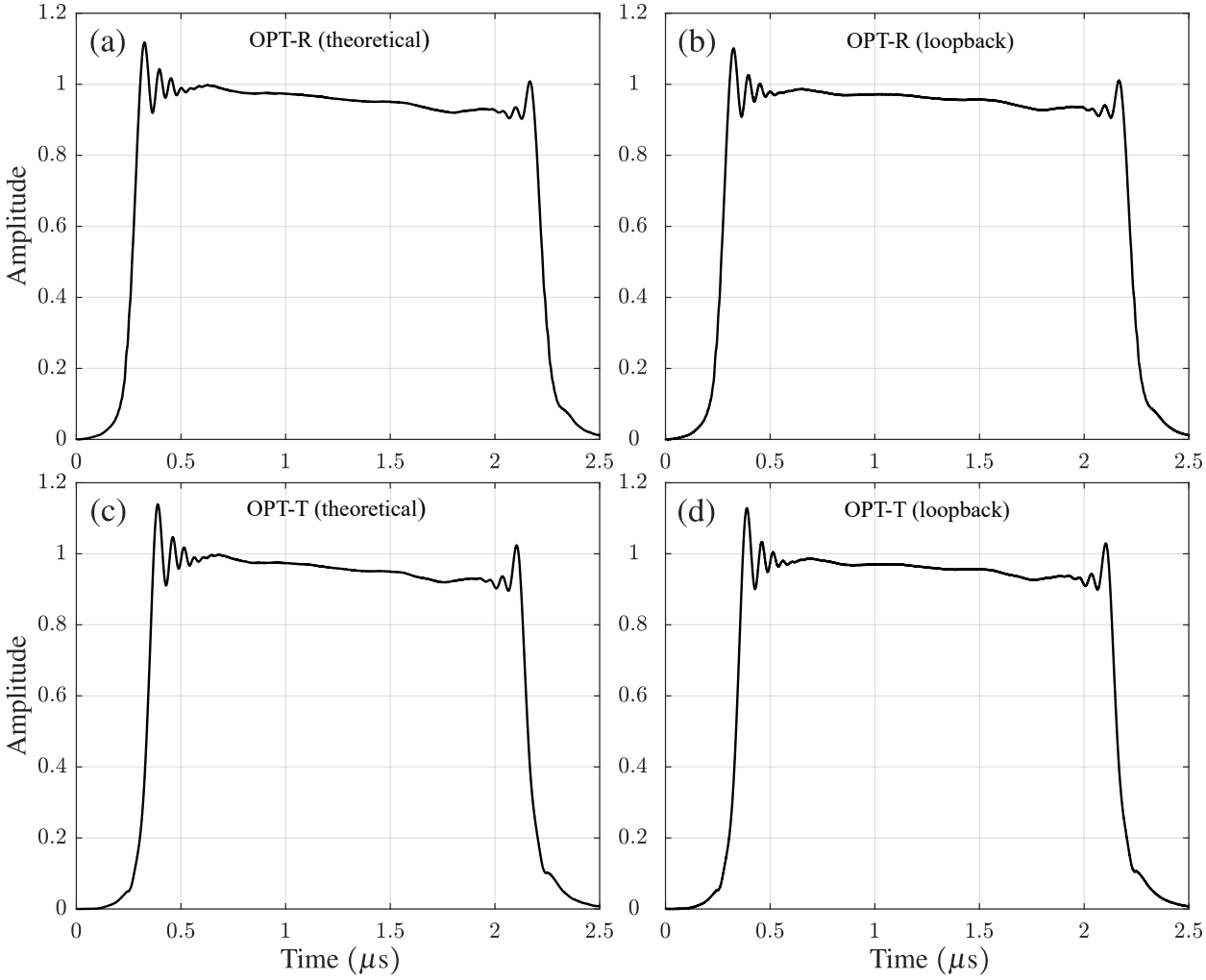

Figure 5.34: Amplitude envelopes for RF chain in **configuration #2**: (a) the theoretical OPT-R response using distortion model, (b) the loopback captured OPT-R response, (c) the theoretical OPT-T response using distortion model, and (d) the loopback captured OPT-T response.

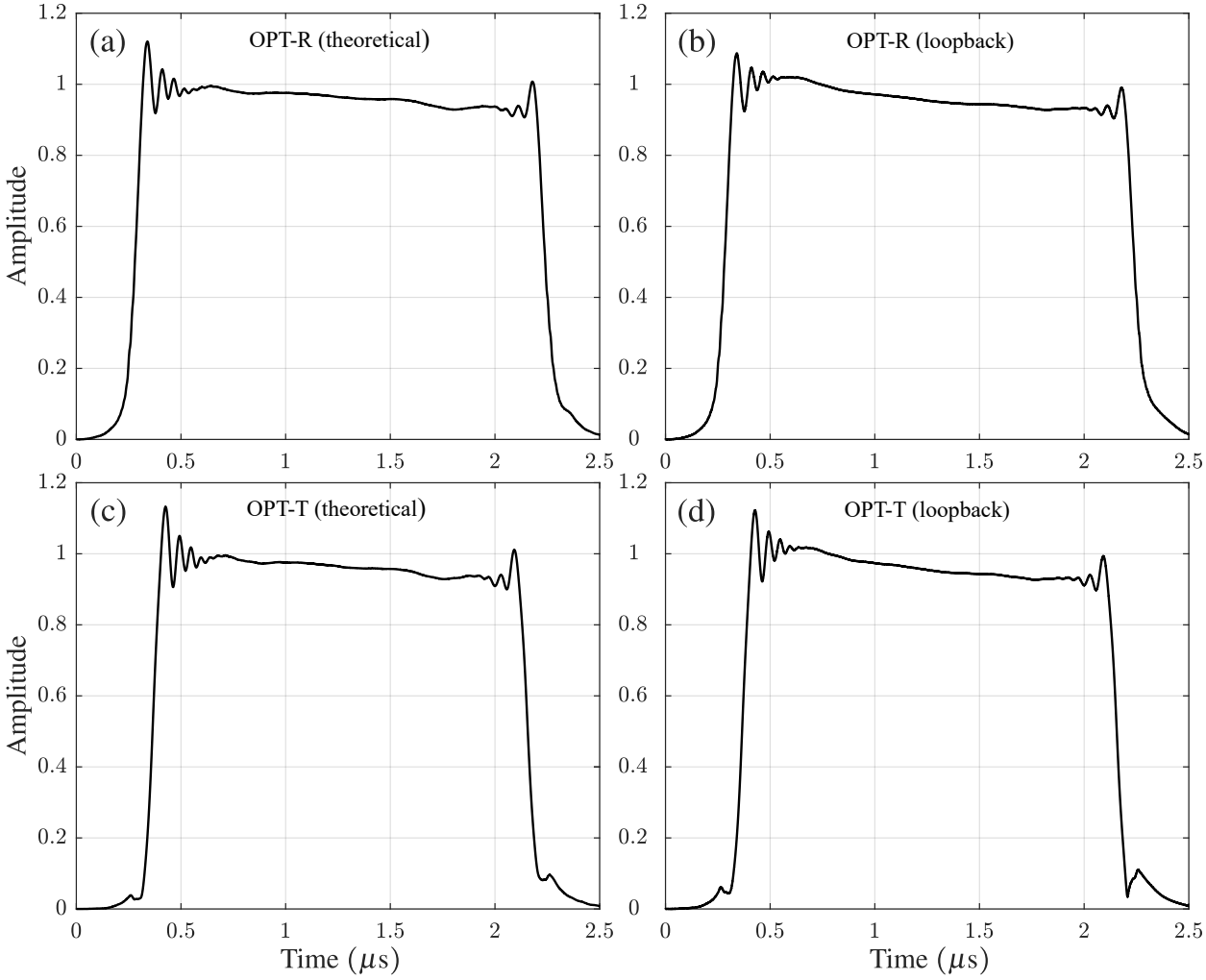

Figure 5.35: Amplitude envelopes for RF chain in **configuration #3**: (a) the theoretical OPT-R response using distortion model, (b) the loopback captured OPT-R response, (c) the theoretical OPT-T response using distortion model, and (d) the loopback captured OPT-T response.

$$\left|\cos\bar{\theta}\right|^2 = \frac{1}{\|a(t)\|_2^2\|b(t)\|_2^2}\left|\int_{-\infty}^{\infty} a^*(t)b(t)dt\right|^2. \tag{5.47}$$

This expression can be used to quantify the quality of the model estimation $s_{\mathrm{L}}(t)$ relative to the loopback capture $y(t)$ for both OPT-R and OPT-T and all configurations. Modifying the expression in (5.47) to find the maximum correlation between $s_{\mathrm{L}}(t)$ and $y(t)$ yields the expression

$$\left|\cos\bar{\theta}\right|^2 = \frac{1}{\|s_{\mathrm{L}}(t)\|_2^2\|y(t)\|_2^2}\max_{\tau}\left\{\left|\int_{-\infty}^{\infty} s_{\mathrm{L}}^*(t-\tau)y(t)dt\right|^2\right\}. \tag{5.48}$$

Note it is assumed that the receive signal $y(t)$ is cropped to exclude any noise outside of the duration $s_{\mathrm{L}}(t)$. Table 5.3 shows that squared-cosine angle between the estimated response $s_{\mathrm{L}}(t)$ and the receive data $y(t)$. Also included in the results is the squared-cosine angle between the waveform model $s(t)$ (i.e. what is loaded on the AWG) and the receive signal $y(t)$. Recall that the square-cosine angle has a maximum of unity only when both signals are scaled copies of one another. The match to $y(t)$ for $s_{\mathrm{L}}(t)$ is within 0.06% of a perfect match for all tested configurations while the waveform $s(t)$ matches approximately 97.5% on average. A match of 97.5% does not result in a significant mismatch loss, however differences between the two signals can affect the expected sidelobe response of the correlation function. In Section 5.3.4.3, the loopback correlation sidelobes deviated from the expected sidelobe response for the OPT-T waveform (Figure 5.24). The small mismatch in square-cosine angle is precisely the reason for the difference in sidelobe response between the theoretical and loopback correlation functions. However by incorporating a model of the distortion a higher fidelity model of the expected signal can be evaluated during optimization.

Figures 5.36 through 5.38 show the power spectrums of the optimized waveform for OPT-R, (a) $|S(f)|^2$ (before application of model) and (b) $|S_{\mathrm{L}}(f)|^2$ (after application of model), and for OPT-T, (c) $|S(f)|^2$ (before application of model) and (d) $|S_{\mathrm{L}}(f)|^2$ (after application of model) for all three hardware configurations. The vertical lines indicate the sampling window of the RSA. The OPT-R waveforms for all three configurations provided a similar smooth "Gaussian-like" spectral shape.

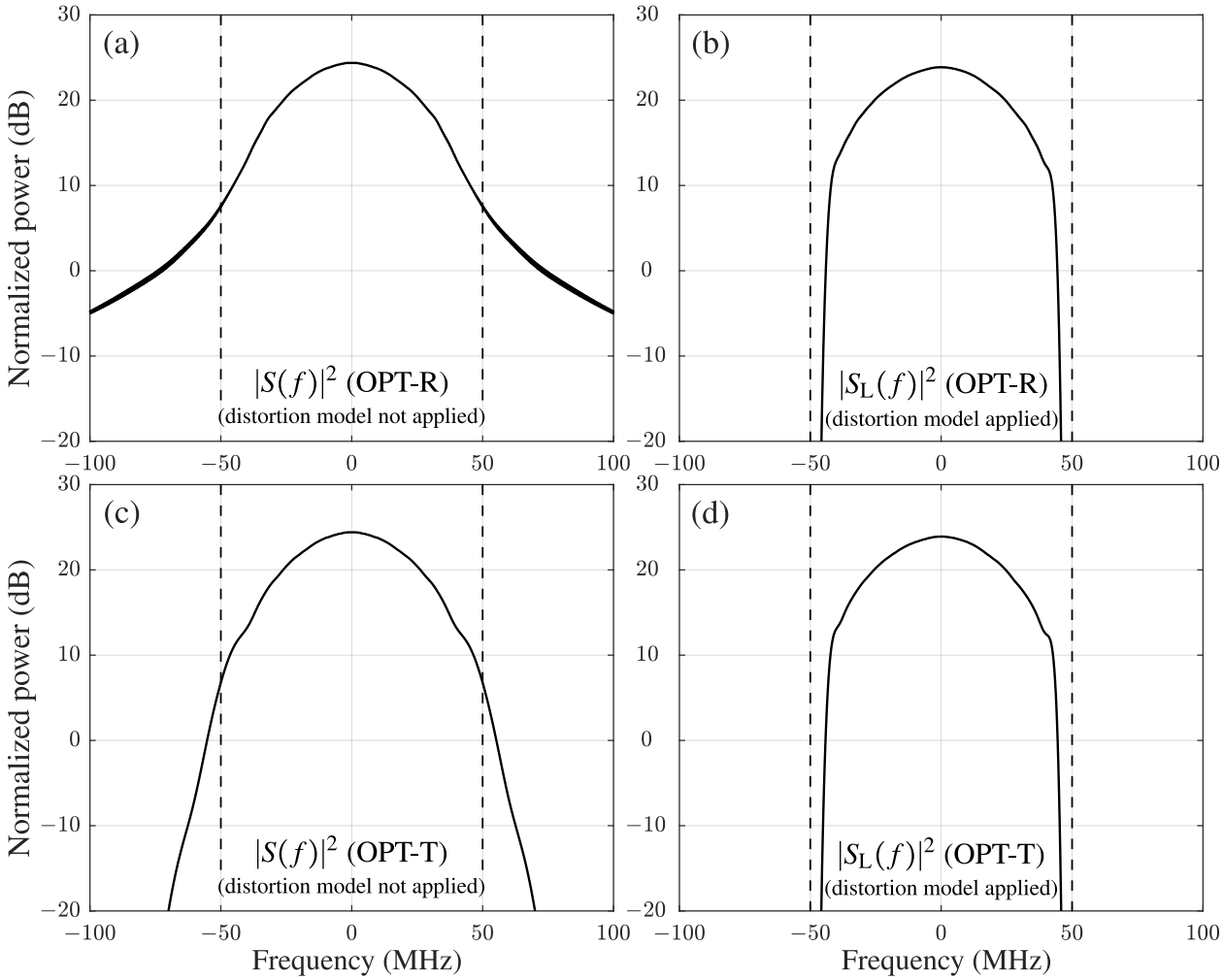

Figure 5.36: Spectral content of OPT-R waveform (a) $|S(f)|^2$ (model not applied) and (b) $|S_{\mathrm{L}}(f)|^2$ (model applied) and spectral content of OPT-T waveform (c) $|S(f)|^2$ (model not applied) and (d) $|S_{\mathrm{L}}(f)|^2$ (model applied) in loopback **configuration #1**. Sampled window indicated by the vertical dashed lines.

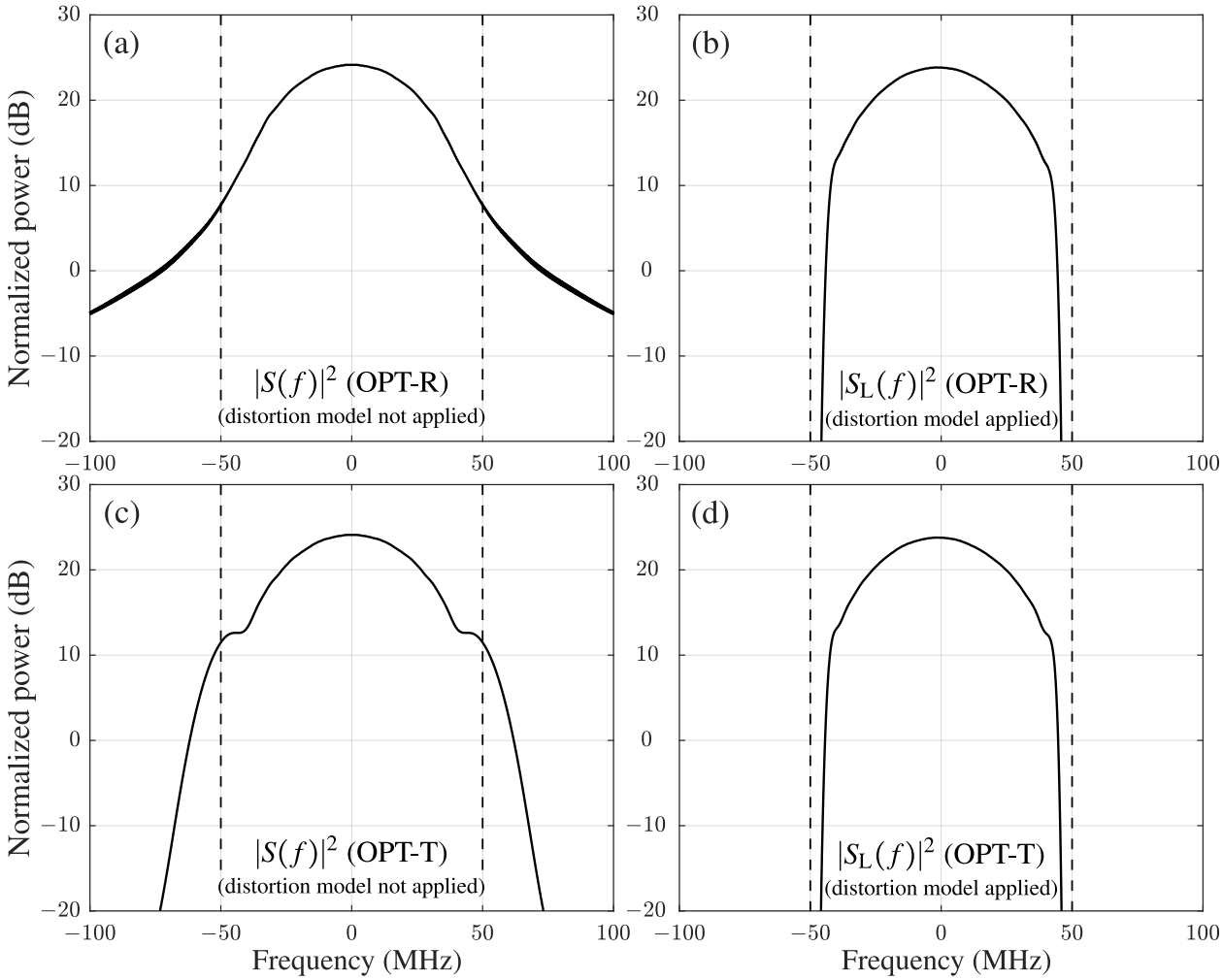

Figure 5.37: Spectral content of OPT-R waveform (a) $|S(f)|^2$ (model not applied) and (b) $|S_{\mathrm{L}}(f)|^2$ (model applied) and spectral content of OPT-T waveform (c) $|S(f)|^2$ (model not applied) and (d) $|S_{\mathrm{L}}(f)|^2$ (model applied) in loopback **configuration #2**. Sampled window indicated by the vertical dashed lines.

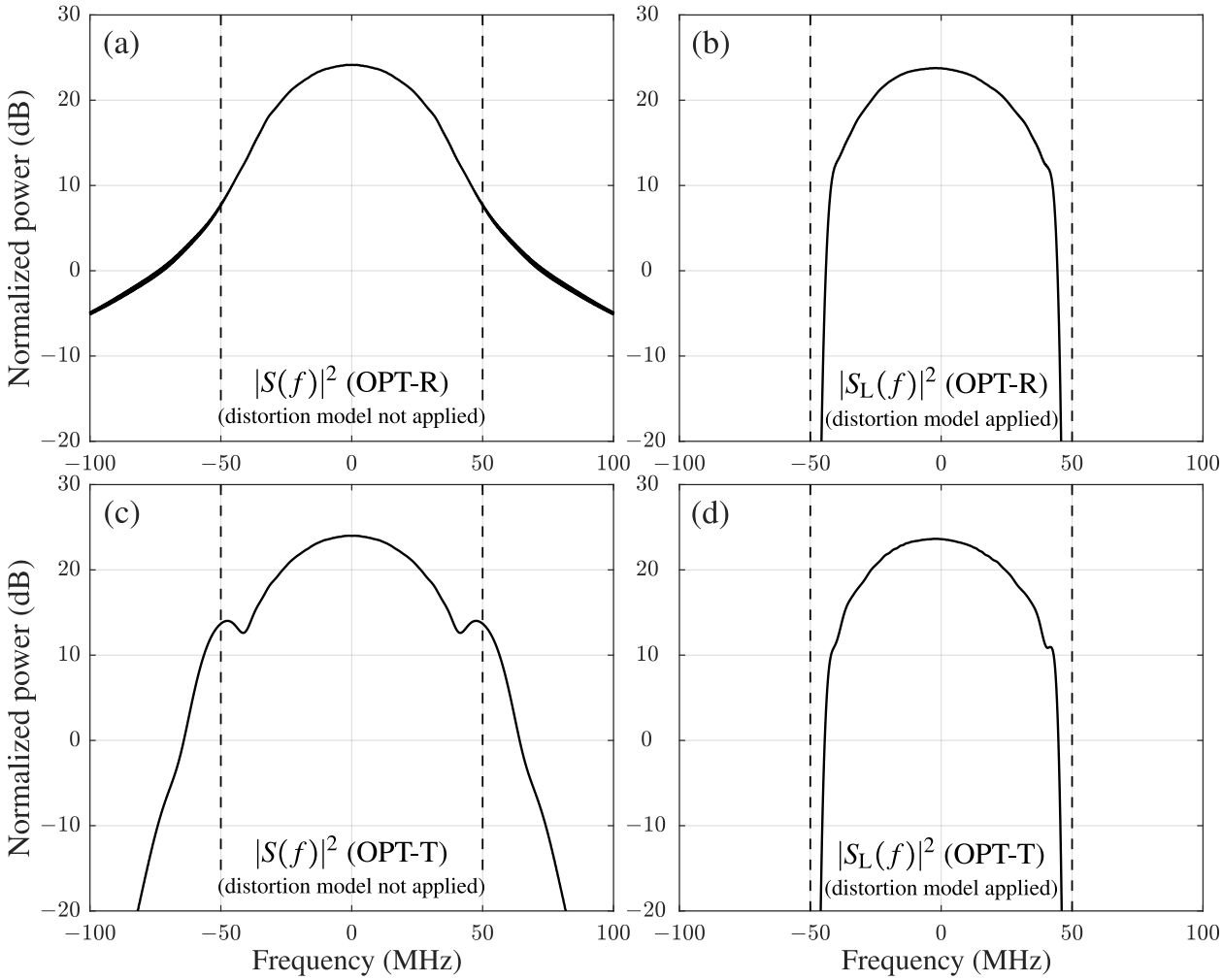

Figure 5.38: Spectral content of OPT-R waveform (a) $|S(f)|^2$ (model not applied) and (b) $|S_{\mathrm{L}}(f)|^2$ (model applied) and spectral content of OPT-T waveform (c) $|S(f)|^2$ (model not applied) and (d) $|S_{\mathrm{L}}(f)|^2$ (model applied) in loopback **configuration #3**. Sampled window indicated by the vertical dashed lines.

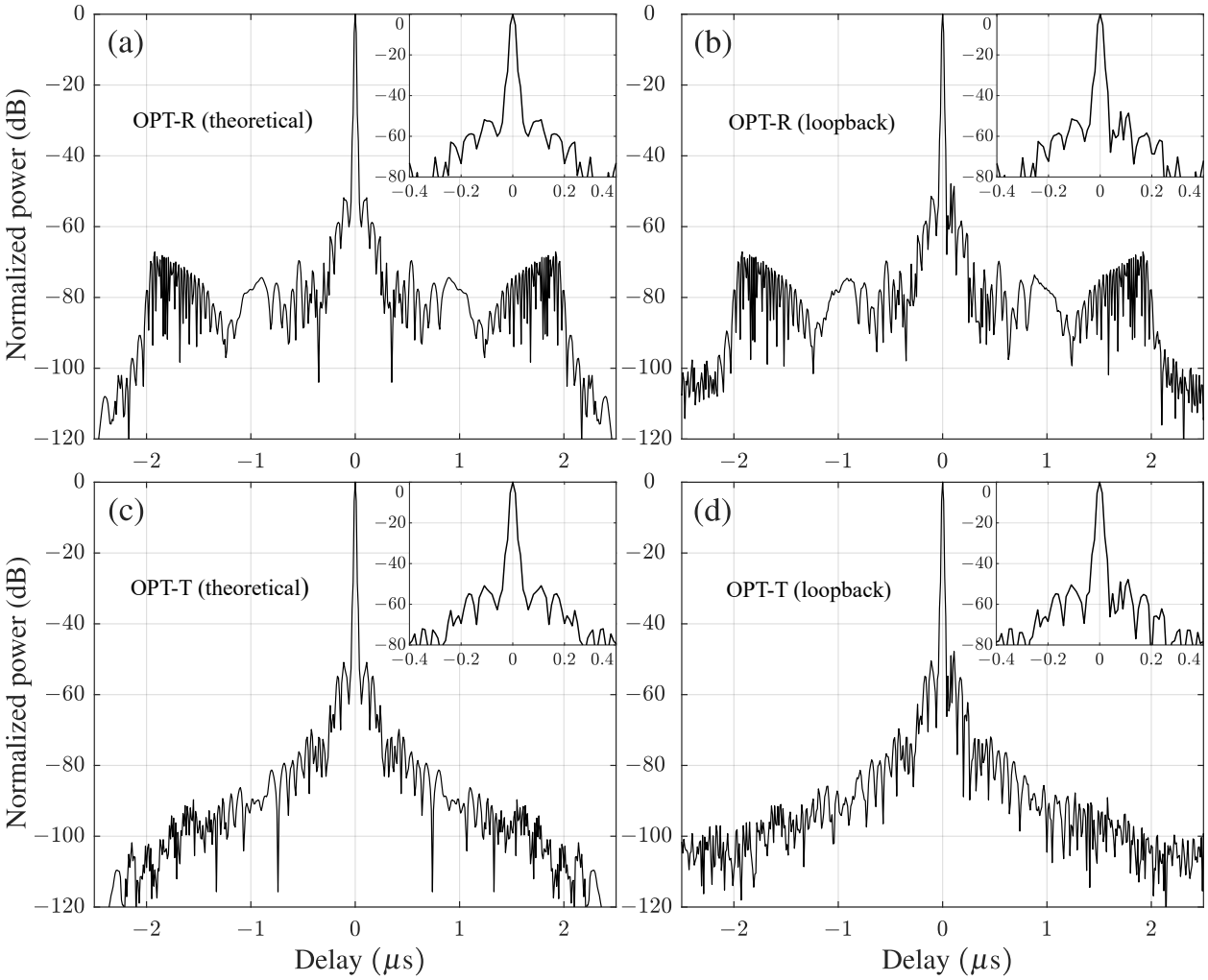

Figure 5.39: Correlation responses in **configuration #1** of (a) the theoretical OPT-R autocorrelation using distortion model, (b) the OPT-R loopback correlation, (c) the theoretical OPT-T autocorrelation using distortion model, and (d) the OPT-T loopback correlation.

The OPT-T waveforms seem to have more control over the spectrum near the $f = \pm\frac{f_s}{2}$ boundary thus place energy near the edges of the band to achieve a lower cost function value (and thus lower correlation sidelobes) by accounting for the filter roll-off. Note that while this is technically energy that is being filtered out, recall that from Table 5.2 the loss never exceeded 0.2232 dB compared to the corresponding LFM benchmark cases.

The expected autocorrelation and loopback cross-correlation responses for both the OPT-R and OPT-T waveform for the three hardware configurations are shown in Figures 5.39 through 5.41, respectively. Recall that the waveform parameters chosen in this section are similar

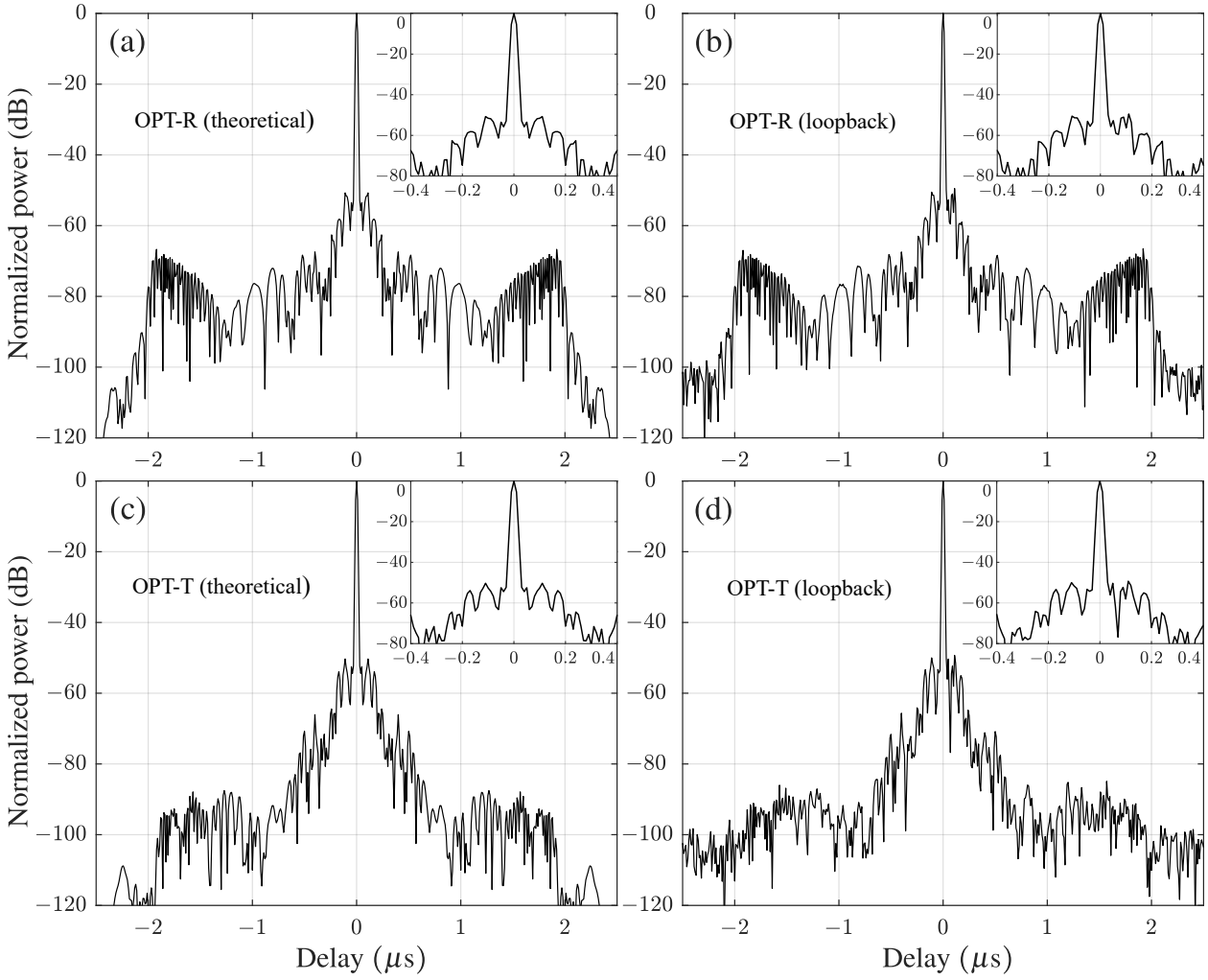

Figure 5.40: Correlation responses in **configuration #2** of (a) the theoretical OPT-R autocorrelation using distortion model, (b) the OPT-R loopback correlation, (c) the theoretical OPT-T autocorrelation using distortion model, and (d) the OPT-T loopback correlation.

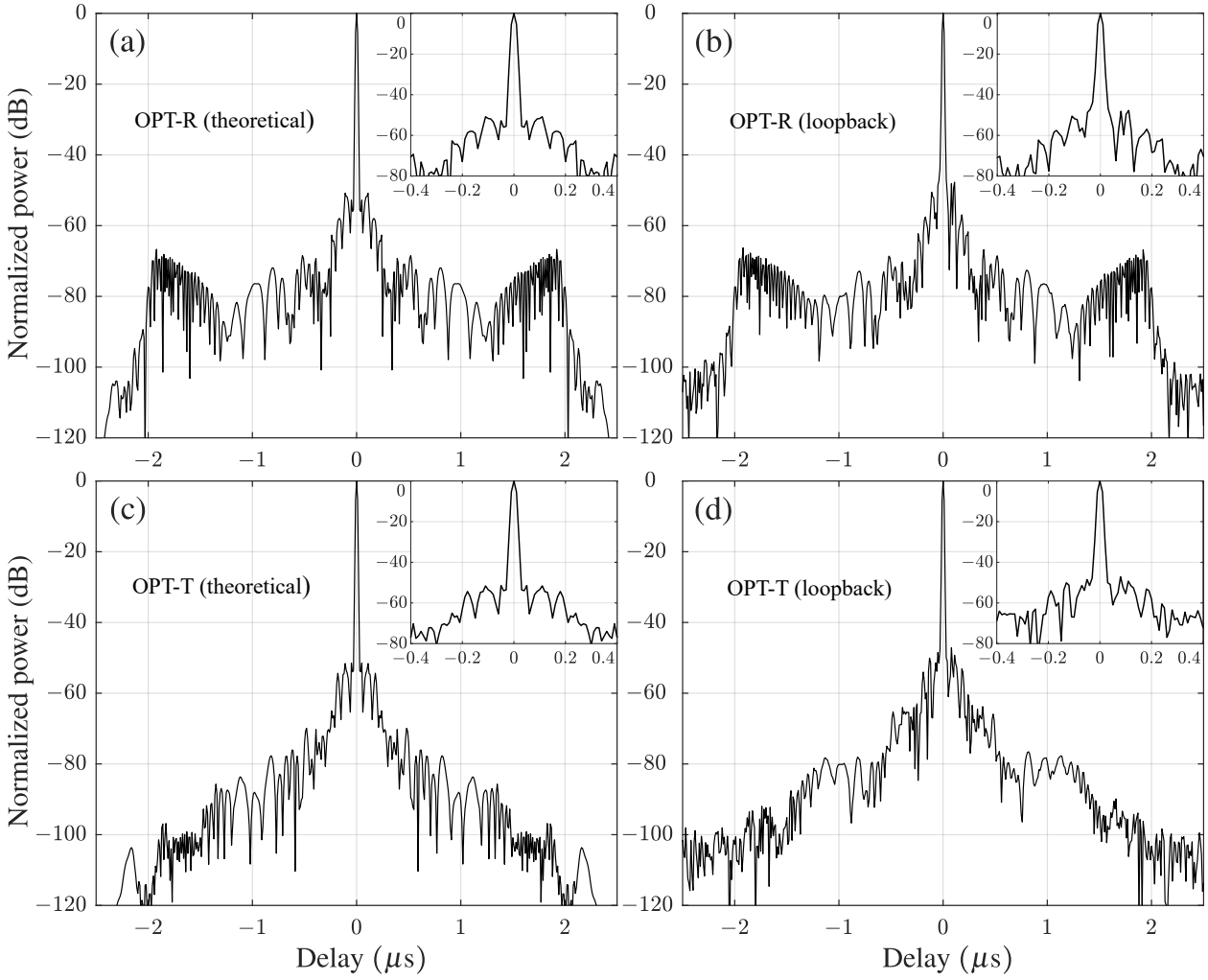

Figure 5.41: Correlation responses in **configuration #3** of (a) the theoretical OPT-R autocorrelation using distortion model, (b) the OPT-R loopback correlation, (c) the theoretical OPT-T autocorrelation using distortion model, and (d) the OPT-T loopback correlation.

as those chosen in Section 5.3 (half the time-bandwidth product). Comparing the theoretical responses in Figures 5.39 through 5.41 ((a) for OPT-R and (c) for OPT-T) to the theoretical responses in Figures 5.17 and 5.18 from Section 5.3, the overall sidelobe levels are lower for the waveforms optimized incorporating the hardware knowledge into the optimization with half the waveform dimensionality. The OPT-R waveforms have a lower over all sidelobe floor and the OPT-T waveforms no longer have the large lobes at the edges of the autocorrelation function. Therefore, for these three hardware configurations, the system knowledge incorporated into the cost function is leveraged during the optimization to produce better performing waveform (in terms of autocorrelation). The loopback captures of the OPT-R and OPT-T waveforms (respectively shown in (b) and (d)) closely match that of the expect correlations at points close to -100 dB below the peak of the response for all three configurations. The estimated linear model, which provided a $> 99\%$ match between the expected and actual loopback captures, exhibits extreme levels of sensitivity in waveform design to achieve predictable sidelobe responses at these low power levels.

The same method used to emulate a higher sampling rate at the receiver during the linear distortion estimation was used to synthetically increase the sampling rate of the loopback capture of both waveforms and all three loopback correlations. This increased sampling rate allows for creation of the modified correlation function from (5.39) using the loopback captured results to compare against the predicted modified correlation function used during the optimization. Figures (5.42) through (5.44) show the (a) expected (using $w_{\mathrm{L}}(t)$) and (b) loopback OPT-R modified correlation function as well as the (c) expected and (d) loopback OPT-T modified correlation function for the three different hardware configurations, respectively. Recall that this modified correlation function includes all straddled responses of the waveforms including the autocorrelation response. The base of the mainlobe for both theoretical correlation functions in Figure 5.42 bubbles outward at approximately -35 dB. This effect is not seen in the same responses for configurations #2 and #3 which might be the reason for the lower converged cost function value from (5.30) in these two scenarios . This difference is likely tied to the disparity in the

distortion filter frequency responses in Figure 5.29 where configuration #1 has a slightly different response over the passband of the filter. The modified correlation responses using the captured loopback signal match well to the expected responses for configurations #1 and #2 (Figures 5.42 and 5.43), however a slight degradation between the expected and actual correlation responses can be seen for configuration #3 (Figure 5.44). This result is likely due to nonlinear distortion effects caused by the saturated amplifier that cannot be modeled using the linear distortion model. For larger nonlinear distortions caused by highly nonlinear but more efficient class B or class C HPAs, a more sophisticated model must be used to fully characterize the effects of RF distortion (see Section 2.2.2 for more information on nonlinear HPA distortion).

5.5 Summary and Conclusions

The coded frequency modulated (CFM) waveform model is a continuous-time waveform definition whose phase function $\psi(t)$ can be represented as a weighted sum of N_p continuous-time basis functions. Therefore, the CFM waveform is parameterized using a discrete set of parameters thus lending itself to gradient-based optimization methods [161, 162]. To the author's knowledge, the work presented in this chapter, along with the corresponding publications [161, 162], are the first instances of continuous-time waveform optimization using gradient-based methods.

A generalized integrated sidelobe (GISL) metric for FM waveforms is introduced that encapsulates both the ISL and PSL metrics into one metric by taking the q-norm ratio of the autocorrelation sidelobes to the autocorrelation mainlobe, where $q = 2$ corresponds to ISL and $q \to \infty$ corresponds to PSL. It is shown that by leveraging the relationship between the pulse compression ratio and time-bandwidth product from (2.69), the time-bandwidth product of the optimized waveform can be effectively set without explicit shaping of the waveform spectrum through determination of the corresponding normalized peak-to-null mainlobe width $\Delta\tau/T$ of the autocorrelation and application within the GISL metric.

In Section 5.2, nonlinear conjugate gradient descent was used to minmize the GISL metric according to the PCFM basis described in Section 2.1.2.4 [38]. It was found that the autocorrelation

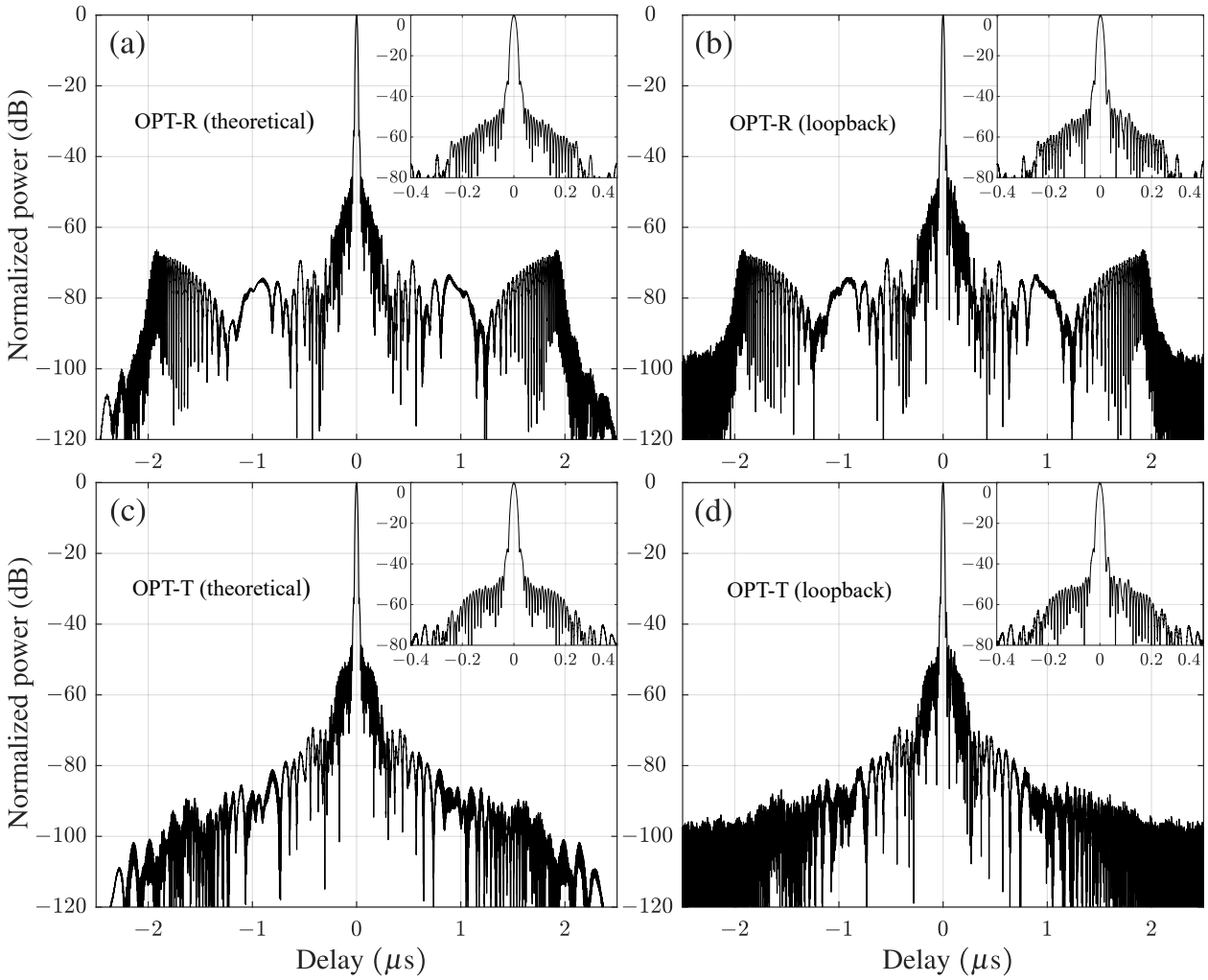

Figure 5.42: Modified correlation responses (includes straddling) in **configuration #1** of (a) the theoretical OPT-R correlation using distortion model, (b) the OPT-R loopback correlation, (c) the theoretical OPT-T correlation using distortion model, and (d) the OPT-T loopback correlation. The dark areas are fine oscillations in the correlation response.

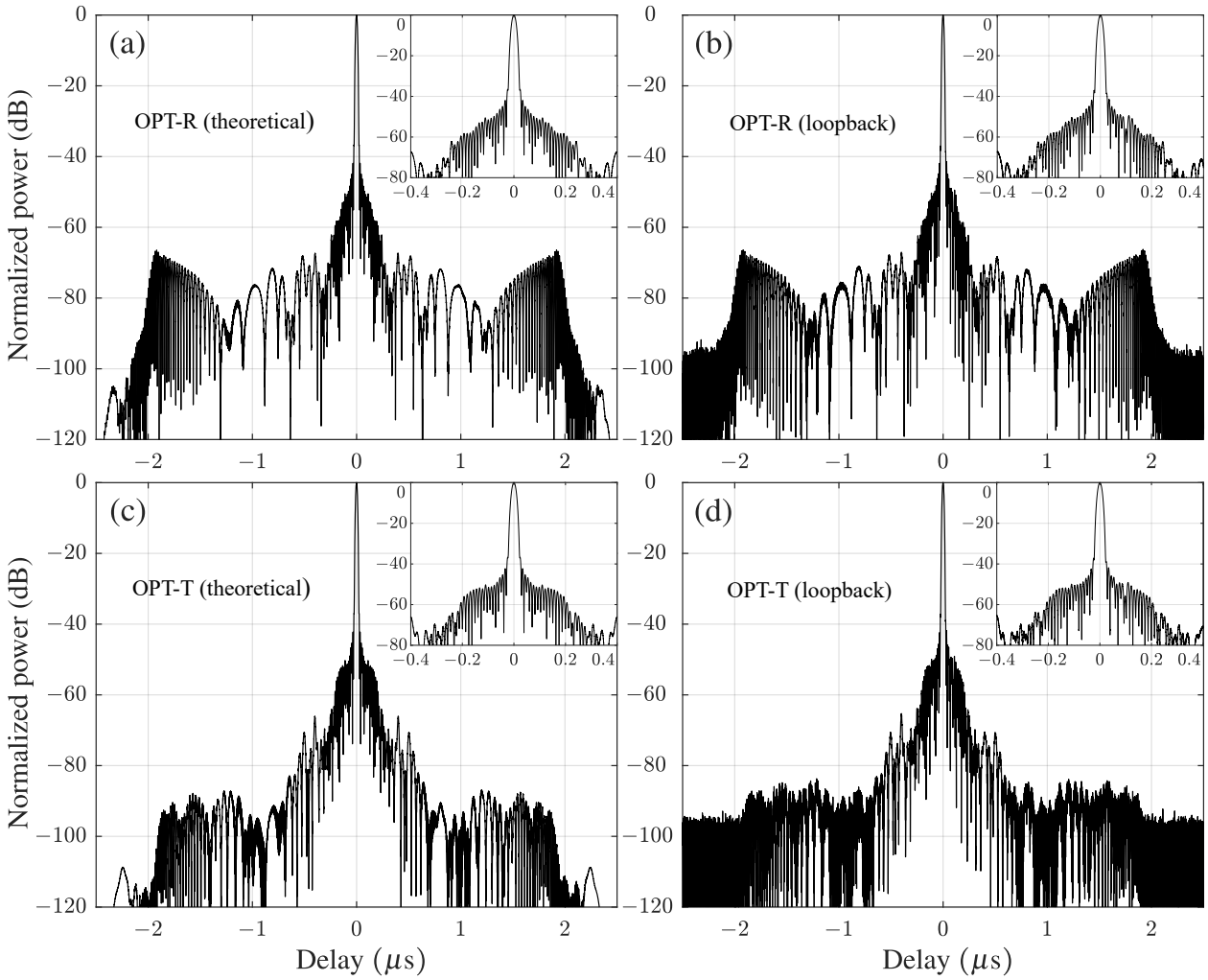

Figure 5.43: Modified correlation responses (includes straddling) in **configuration #2** of (a) the theoretical OPT-R correlation using distortion model, (b) the OPT-R loopback correlation, (c) the theoretical OPT-T correlation using distortion model, and (d) the OPT-T loopback correlation. The dark areas are fine oscillations in the correlation response.

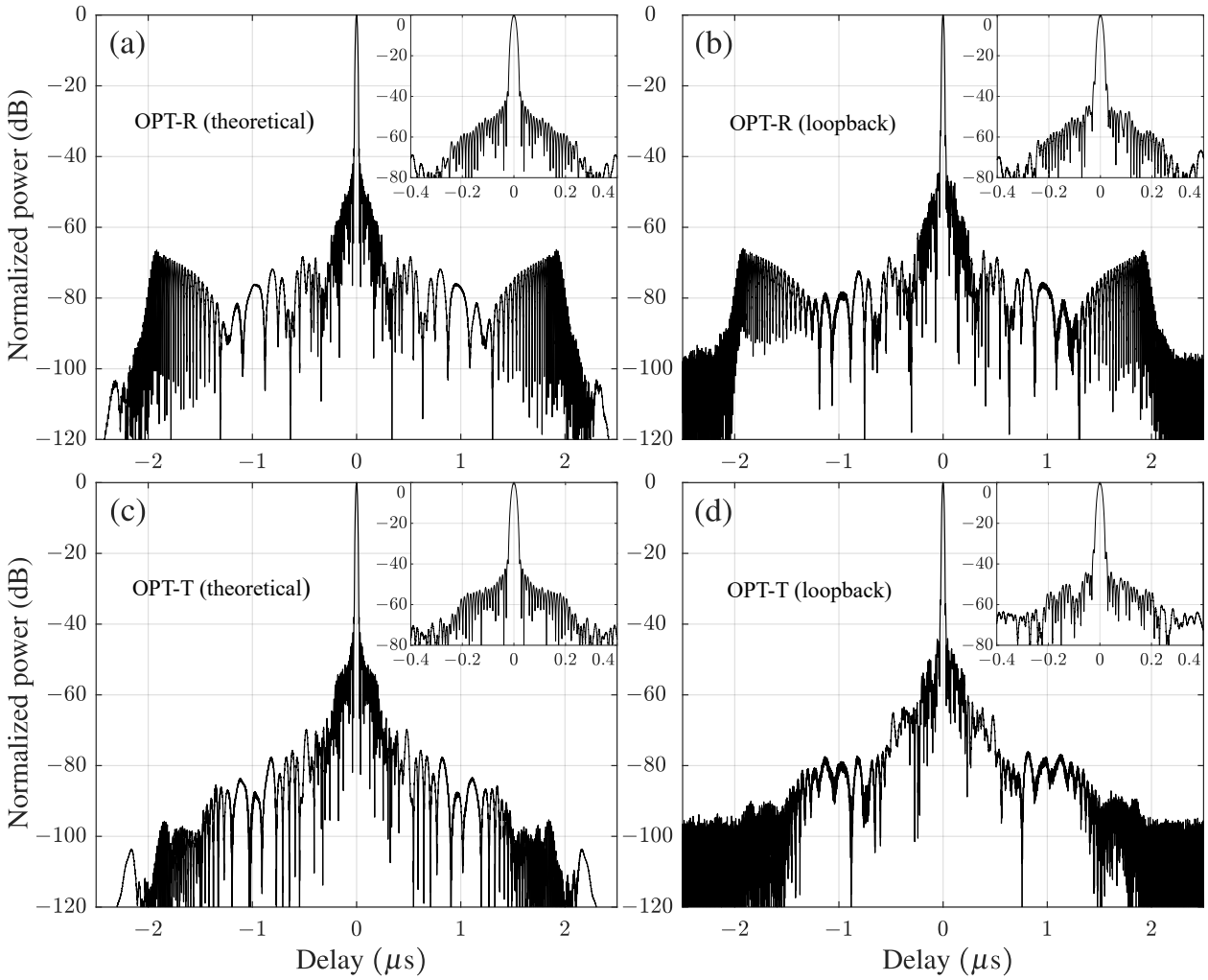

Figure 5.44: Modified correlation responses (includes straddling) in **configuration #3** of (a) the theoretical OPT-R correlation using distortion model, (b) the OPT-R loopback correlation, (c) the theoretical OPT-T correlation using distortion model, and (d) the OPT-T loopback correlation. The dark areas are fine oscillations in the correlation response.

of the optimized FM waveform is largely independent of the time-bandwidth product. Instead, the sampled bandwidth of the receiver matched filter dictates the achievable PSL. Further, how close one can get to this PSL bound appears to be related to the ratio of the sampled bandwidth (sampling freuqency) to 3 dB bandwidth of the CFM waveform.

In Section 5.3, the design of Legendre-polynomial coded waveforms with rectangular (OPT-R) and Tukey (OPT-T) tapers were demonstrated using quasi-Newton method optimization. A correlation function was also defined that allows this optimization to account for range straddling effects. It was found that the orthogonal nature of Legendre polynomials facilitates the design of waveforms with quite low sidelobe levels with a small number of code values. Experimental loopback measurements demonstrated the efficacy of this design procedure for both rectangular-envelope and Tukey-envelope optimized waveforms. Below -80 dB it was observed that the distortion of the RF test equipment limited the fidelity of the ideal CFM model.

In Section 5.4, a *system specific* design problem was considered by estimating three different loopback configurations (with increase nonlinearity) using a linear model which was subsequently introduced into the GISL cost function to account for the linear distortion effects of the RF chain within the waveform design process. The optimized OPT-R and OPT-T waveforms leveraged the hardware distortion of the three configurations to lower the overall sidelobe levels of the correlation response compared to the optimized cases from Section 5.3. It was found that the linear model (for these three hardware configurations) provided a high fidelity prediction of the distorted response. The predicted loopback signal structure matches within 0.06% of the captured loopback signal resulting in a match of the expected and actual correlation sidelobe level close to -100 dB down from the peak correlation. The linear model matched worst with the hardware configuration that included the saturated amplifier (though still provided a low sidelobe response). In the future, more sophisticated modeling (i.e. nonlinear distortion estimation) will be used as an attempt to improve the signal prediction capabilities for highly nonlinear systems.

Chapter 6

Conclusions and Future Work

The technologies of the arbitrary waveform generator and digital array provide unprecedented high-fidelity control over the waveform signal structure. This precise command of waveform and emission design unlocks the capabilities to execute simultaneous multiple functions or improve performance of existing radar modes thus demonstrating the need for new flexible and high-performing waveforms and emission modes that can take advantage of these technologies. A high-fidelity design of a waveform (or waveforms) can be distorted when implemented on a high powered system with many linear and nonlinear distortions. These deleterious system effects (e.g. bandlimiting, HPA distortions) limit the achievable performance that is possible with arbitrary waveform technology thus must also be considered during the design. By constraining the waveform model to be constant amplitude and spectrally contained (i.e. FM), the performance degradation can be minimized as was shown in Chapter 2. Therefore, the designed/optimized FM waveform can be implemented without implementation of a system model or resorting to predistortion (which would affect the modulus of the signal).

The fully digital array radar (DAR) grants the ability to realize spatially-diverse emissions that have the flexibility to operate in different modes relative to the traditional phased array. These modes include but are not limited to: performing multiple simultaneous (spatially-separated) functions that do not have the scheduling/timing constraints of traditional multifunction arrays, ubiquitous radar modes that illuminate over a longer CPI (finer Doppler resolution), flexibility in pulse-to-pulse transmit modes, and improved single pulse spatial coverage, spatial resolution, and spatial ambiguity [20,28,142]. To analyze the improved spatial resolution and reduced ambiguities for a spatially-diverse emission, the angle-delay ambiguity function is derived in Section 3.1.3.2.

For narrowband transmission, the ambiguity function can be decomposed into two functions: the beam factor and the diversity factor. The beam factor illustrates the spatial response of the isolated receive array while the diversity factor illustrates the improvement to both resolution and ambiguity afforded by the spatially-diverse emission.

In Chapter 3, a mutual coupling analysis of a dipole uniform linear array is provided for both scanning and spatially-diverse transmissions. The mutual coupling effects for spatially-diverse radar applications is not well researched thus the work presented in this chapter serves as illustration of the reflected/coupled energy one could expect given different transmission modes and dipole array configurations (i.e. half-wavelength spacing and quarter wavelength spacing). It is also shown that the qualitative aspects of mutual coupling for scanning arrays (e.g. reflection/coupling of energy at endfire and the invisible space) can also be applied to that of a spatially-diverse transmission. Energy that is contained within the invisible space for ULAs with $d < \frac{\lambda}{2}$ is shown to almost entirely reflect/coupling back into the array. This understanding was derived using the analytical dipole mutual impedance model and, much like the constant amplitude and spectral containment for waveforms, provides a qualitative metric for spatially diverse emissions that is based on the geometry of the array and irrespective to the elemental pattern. The qualitative conclusion was then used to derived a novel quantitative metric via the *Fractional Reactive Power* (FRP) that characterizes the amount energy in the invisible space for arrays with $d < \frac{\lambda}{2}$. This metric can be used as a substitute for emission design/optimization when the array scattering parameters are not known/provided.

Using the knowledge and background offered by Chapters 2 and 3, three novel spatially-diverse emission design/optimization methods are introduced in Chapter 4 that are designed differently to perform well in certain missions and achieve some (if not all) of the new potential modes offered by the DAR described above. In Section 4.1, an FM framework was introduced called Spatial Modulation that provides the waveform/emission designer with the capability to form highly directive spatially-diverse transmission while achieving improved single pulse spatial coverage and target spatial resolution/ambiguities. In a limiting case, the framework allows for the emission

to revert back to a standard phased array beamforming mode if SNR needs to be maximized. In Section 4.2, a wideband spatially-diverse optimization algorithm is derived to produce emission with arbitrary space-frequency energy allocation[1]. The flexible framework allows for realization of different emission modes including but not limited to: multiple highly focused beams (e.g. for simultaneous target tracking), a single wide beam (e.g. for a ubiquitous or SAR mode), or any combination thereof (e.g. a single focused beam along with a wide beam). The variability of the spatial beampattern allows for a continuously varying power allocation of the different functions as opposed to traditional multifunction arrays that have discrete power allocation (pulse-by-pulse). This property gives a more straight forward power assignment based on priority level of the radar functions. The limitation of the approach in Section 4.2 is that the emission structure (in time) cannot be precisely controlled, but only approximated via a desired spectral shape. However, in Section 4.3 an optimization method is derived to simultaneously emit radar and communications beams with full control over the directionally emitted signals. The null space of desired transmit directions is used to supplement the set of waveforms such that the results are constant amplitude. A novel metric known as the *Average Directed Power* (ADP) metric is introduced to evaluate the efficiency of the emission considering the null space energy. These emission design/optimization frameworks are unique as they achieve spatially diverse transmission while considering practical transmitter effects, though more work can be done into incorporating more system specific distortions into the presented algorithms.

In Chapter 5, single FM waveform design is approached from an optimization perspective as opposed to traditional methods such as the principle of stationary phase [50]. The CFM framework provides a unique phase function structure that is comprised of a weighted sum of (finite) basis functions. A cost function containing this waveform structure can be minimized via gradient techniques by differentiating with respect to the basis function weights. To the author's knowledge, this is the first instance of FM waveform optimization using gradient-based methods. To further incorporate knowledge of the sampling process, a novel modified correlation function is introduced

[1]This optimization framework can also be implemented for narrowband transmission

that merges both the continuous nature of the waveform and the sampling of the ADC to inherently include straddled waveform responses within the function. The metric used for optimization is a generalization of the traditional ISL and PSL waveform metric defined as the *Generalized Integrated Sidelobe Level* (GISL) that takes the q-norm ratio of the correlation sidelobes to the correlation mainlobe. It is shown through optimization and experimental verification that there are limitations to fidelity using the idealized CFM waveform model due to uncompensated system effects. In Section 5.4, a system specific optimization method is considered by incorporating a linear model of three different loopback hardware configurations into the GISL metric using the modified correlation function. It is shown that by leveraging the "natural tapering" effects of the RF hardware, the correlation function can be drastically improved compared to the ideal waveform model. To the author's knowledge, this work represents the first *system specfic* FM waveform optimization method designed to leverage the distortion characteristics of the RF hardware to improve correlation performance.

Future Work The drive into research for more universal radar system architectures that can perform multiple simultaneous tasks with arbitrary waveform capability such as the digital array radar (DAR) provides a rich landscape for waveform/emission design and optimization. The question that this work asks is: *"What can be done at the waveform level to achieve the best performance for waveform and spatially-diverse transmission modes?"* An answer to this question that might appear cyclical is to *optimize the waveform or emission to achieve the best performance for the given situation*. Thus we can reformulate the original question to be, *"What factors prevent the radar waveform or emission from achieving the best performance?"* I would argue that the answer to this question is *incomplete knowledge of the factors that alter the modulation structure of the radar waveform or emission such that the optimality condition of the waveform or emission is degraded.* These factors could range from RF system distortion to atmospheric attenuation over a portion of the band.

The effects of an RF system is (in one shape or another) available to the designer of the

waveform. Whether it be general characteristics of RF distortion "on average" or system specific modeling, some amount of transmitter distortion knowledge can be incorporated into the design of radar waveforms and emissions to improve radar performance. For example, the "on average" modeling might include design constraints such as constant amplitude to spectral containment when operating a transmit HPA in saturation, or constraining the emitted energy to be within the visible space for a spatially-diverse transmission mode. More specific modeling might include incorporating the frequency-dependent active element patterns into the design of a spatially diverse emission, or forming a high fidelity model of the linear and nonlinear distortions caused by the RF chains. These two schools of thought can be defined as *system considerate* and *system specific* modeling, respectively. The only example of system specific modeling presented in this work was in Section 5.4 where the effects of three different hardware configurations are estimated using a linear model. In future work, the areas of nonlinear hardware distortion modeling will be explored for the purpose of system specific waveform and emission optimization.

As an expansion to the presented work, another research area of interest is *sensitivity* of the waveform model versus *fidelity* of the optimized result. How do we optimize the waveform to not only have high fidelity and performance but also make it robust to errors within (or changes that might occur to) the system model used for optimization. For example, a high PAPR waveform applied to a nonlinear amplifier model operating in the knee of the amplifier gain curve would experience significant compression, thus the optimality of the result is highly dependent on the accuracy of the system model. Conversely, a constant amplitude waveform applied to a HPA operating in saturation is much less effected by model errors and may not even need the amplifier model (i.e. *system considerate* modeling). Thus there are two factors that are of consequence: the *accuracy* of the RF systems model and the *volatility* of the waveform model. An example of a highly volatile waveform is one that is optimized to have wide bandwidth and high PAPR. If the waveform is to be operated near the compression region of the amplifier, the demand for model accuracy becomes significant. This topic is related to sensitivity analysis from optimization theory [79, 146], thus can be possibly applied to a characterization of sensitivity in radar performance

in the presence of model errors or changing systems conditions. The radar performance analysis could also include different "degrees of model reality" which could range from a simple hard limiter single amplifier RF systems modeling to cascaded amplification stages modeled using nested Volterra series models with amplifier memory effects.

References

[1] M. Wicks, E. Mokole, S.D. Blunt, R.S. Schneible, and V.J. Amuso, *Principles of waveform diversity and design*. The Institution of Engineering and Technology, 2010.

[2] S. Pillai, K.Y. Li, I. Selesnick, and B. Himed, *Waveform Diversity: Theory & Applications*. McGraw Hill Professional, 2011.

[3] S.D. Blunt and E.L. Mokole, "Overview of radar waveform diversity," *IEEE Aerospace and Electronics Systems Magazine*, vol. 31, no. 11, pp. 2–42, Nov. 2016.

[4] F. Gini, A. De Maio, and L. Patton, eds., *Waveform design and diversity for advanced radar systems*. IET, 2012.

[5] N. Levanon and E. Mozeson, *Radar signals*. John Wiley & Sons, 2004.

[6] H. Griffiths, S. Blunt, L. Cohen, and L. Savy, "Challenge problems in spectrum engineering and waveform diversity," *IEEE Radar Conference*, Apr. 2013.

[7] J.M. Peha, "Approaches to spectrum sharing," *IEEE Communications Magazine*, vol. 43, no. 2, pp. 10–12, Feb. 2005.

[8] H. Griffiths, L. Cohen, S. Watts, E. Mokole, C. Baker, M. Wicks, and S. Blunt, "Radar spectrum engineering and management: technical and regulatory issues," *Proceedings of the IEEE*, vol. 103, no. 1, pp. 85–102, Jan. 2015.

[9] H. Deng and B. Himed, "Interference mitigation processing for spectrum-sharing between radar and wireless communications systems," *IEEE Transactions on Aerospace and Electronic Systems*, vol. 49, no. 3, pp. 1911–1919, Jul. 2013.

[10] G. Meager, R.A. Romero, and Z. Staples, "Estimation and cancellation of high powered radar interference for communication signal collection," *IEEE Radar Conference*, May 2016.

[11] C. Sturm and W. Wiesbeck, "Waveform design and signal processing aspects for fusion of wireless communications and radar sensing," *Proceedings of the IEEE*, vol. 99, no. 7, pp. 1236–1259, Jul. 2011.

[12] R.A. Romero and K.D. Shepherd, "Friendly spectrally shaped radar waveform with legacy communication systems for shared access and spectrum management," *IEEE Access*, vol. 3, pp. 1541–1554, 2015.

[13] J.T. Johnson, C.J. Baker, H. Wang, L. Ye, and C. Zhang, "Assessing the potential for spectrum sharing between communications and radar systems in the L-band portion of the RF spectrum allocated to radar," *International Conference on Electromagnetics in Advanced Applications*, Aug. 2014.

[14] P. Antonik, M.C. Wicks, H.D. Griffiths, and C.J. Baker, "Frequency diverse array radars," *IEEE Radar Conference*, Apr. 2006.

[15] P.F. Sammartino, C.J. Baker, and H.D. Griffiths, "Frequency diverse MIMO techniques for radar," *IEEE Transactions on Aerospace and Electronic Systems*, vol. 49, no. 1, pp. 201–222, Jan. 2013.

[16] E. Fishler, A. Haimovich, R. Blum, D. Chizhik, L. Cimini, and R. Valenzuela, "MIMO radar: An idea whose time has come," *IEEE Radar Conference*. IEEE, 2004.

[17] D.R. Fuhrmann and G.S. Antonio, "Transmit beamforming for MIMO radar systems using signal cross-correlation," *IEEE Transactions on Aerospace and Electronic Systems*, vol. 44, no. 1, pp. 171–186, Jan. 2008.

[18] F. Daum and J. Huang, "MIMO radar: Snake oil or good idea?" *IEEE Aerospace and Electronics Systems Magazine*, vol. 24, no. 5, pp. 8–12, May 2009.

[19] G. Krieger, "MIMO-SAR: Opportunities and pitfalls," *IEEE Transactions on Geoscience and Remote Sensing*, vol. 52, no. 5, pp. 2628–2645, May 2014.

[20] D.J. Rabideau and P.A. Parker, "Ubiquitous MIMO multifunction digital array radar... and the role of time-energy management in radar," MIT Lincoln Lab, Tech. Rep., 2004.

[21] J. Li and P. Stoica, *MIMO radar signal processing*. John Wiley & Sons, 2008.

[22] J.S. Herd and M.D. Conway, "The evolution to modern phased array architectures," *Proceedings of the IEEE*, vol. 104, no. 3, pp. 519–529, Mar. 2016.

[23] S.H. Talisa, K.W. O'Haver, T.M. Comberiate, M.D. Sharp, and O.F. Somerlock, "Benefits of digital phased array radars," *Proceedings of the IEEE*, vol. 104, no. 3, pp. 530–543, Mar. 2016.

[24] P.M. McCormick, S.D. Blunt, and J.G. Metcalf, "Simultaneous radar and communications emission from a common aperture, part I: theory," *IEEE Radar Conference*, May 2017.

[25] P.M. McCormick, A.J. Duly, B. Ravenscroft, J.G. Metcalf, and S.D. Blunt, "Simultaneous radar and communications emission from a common aperture, part II: experimentation," *IEEE Radar Conference*, May 2017.

[26] S. Sabatini and M. Tarantino, *Multifunction array radar - System design and analysis*.Artech House, 1994.

[27] S.L.C. Miranda, C.J. Baker, K. Woodbridge, and H.D. Griffiths, "Comparison of scheduling algorithms for multifunction radar," *IET Radar, Sonar Navigation*, vol. 1, no. 6, pp. 414–424, Dec. 2007.

[28] D.J. Rabideau and P. Parker, "Ubiquitous MIMO multifunction digital array radar," *The Asilomar Conference on Signals, Systems, and Computers*, vol. 1, Nov. 2003.

[29] S. Haykin, Y. Xue, and P. Setoodeh, "Cognitive radar: Step toward bridging the gap between neuroscience and engineering," *Proceedings of the IEEE*, vol. 100, no. 11, pp. 3102–3130, Nov. 2012.

[30] B. Cordill, J. Metcalf, S.A. Seguin, D. Chatterjee, and S.D. Blunt, "The impact of mutual coupling on MIMO radar emissions," *International Conference on Electromagnetics in Advanced Applications*, Sep. 2011.

[31] Z. Dunn, M. Yeary, C. Fulton, and N. Goodman, "Memory polynomial model for digital predistortion of broadband solid-state radar amplifiers," *IEEE Radar Conference*, May 2015.

[32] ——, "Wideband digital predistortion of solid-state radar amplifiers," *IEEE Transactions on Aerospace and Electronic Systems*, vol. 52, no. 5, pp. 2452–2466, Oct. 2016.

[33] Z. Dunn, M. Yeary, C. Fulton, and R. Rincon, "Impedance-dependent wideband digital predistortion of solid-state radar amplifiers," *IEEE Transactions on Aerospace and Electronic Systems*, vol. 53, no. 5, pp. 2290–2303, Oct. 2017.

[34] S.C. Cripps, *Advanced techniques in RF power amplifier design*. Artech House, 2002.

[35] P. Gardner, "Feedforward amplifiers," in *Encyclopedia of RF and Microwave Engineering*, K. Chang, Ed. John Wiley & Sons, 2003, pp. 1439–1448.

[36] S.C. Cripps, *RF Power Amplifiers For Wireless Communications Steve*.Artech House, 2006.

[37] Z. El-Khatib, L. MacEachern, and S.A. Mahmoud, "Modulation schemes effect on RF power amplifier nonlinearity and RFPA linearization techniques," in *Distributed CMOS Bidirectional Amplifiers: Broadbanding and Linearization Techniques*. Springer Science & Business Media, 2012, pp. 7–28.

[38] S.D. Blunt, M. Cook, J. Jakabosky, J. de Graaf, and E. Perrins, "Polyphase-coded FM (PCFM) radar waveforms, part I: implementation," *IEEE Transactions on Aerospace and Electronic Systems*, vol. 50, no. 3, pp. 2218–2229, Jul. 2014.

[39] M.S. Davis, *MIMO radar*, W.L. Melvin and J.A. Scheer, eds. SciTech Publishing, 2013.

[40] K.W. Forsythe and D.W. Bliss, "MIMO radar: concepts performance enhancements, and applications," in *MIMO radar signal processing*, J. Li and P. Stoica, eds. John Wiley & Sons, 2008.

[41] R.C. Hansen, *Phased array antennas*. John Wiley & Sons, 2009.

[42] G.J. Frazer, Y.I. Abramovich, and B.A. Johnson, "Spatially waveform diverse radar: Perspectives for high frequency OTHR," *IEEE Radar Conference*, Apr. 2007.

[43] B.A. Hansen, G.J. Frazer, and Y.I. Abramovich, "15.2 future othr transmitter sub-systems," in *Principles of Waveform Diversity and Design*, M.C. Wicks, E.L. Mokole, S.D. Blunt, R.S. Schneible, and V.J. Amuso, eds. SciTech Publishing, 2010.

[44] S.D. Blunt, J. Jakabosky, M. Cook, J. Stiles, S. Seguin, and E.L. Mokole, "Polyphase-coded FM (PCFM) radar waveforms, part II: optimization," *IEEE Transactions on Aerospace and Electronic Systems*, vol. 50, no. 3, pp. 2230–2241, Jul. 2014.

[45] A. Papoulis, *Fourier integral and its applications.[The]*. McGraw-Hill Book Co., Inc., Interscience Publishers, 1960.

[46] T.K.S. Moon and C. Wynn, *Mathematical methods and algorithms for signal processing*. Pearson, 2000, no. 621.39: 51 MON.

[47] J.G. Proakis, "Digital communications," *McGraw-Hill, New York, 5th ed.*, 2008.

[48] N. DoC, "Manual of regulations and procedures for federal radio frequency management," *NTIA*, 2015.

[49] J.R. Klauder, A.C. Price, S. Darlington, and W.J. Albersheim, "The theory and design of chirp radars," *The Bell System Technical Journal*, vol. 39, no. 4, pp. 745–808, Jul. 1960.

[50] E. Fowle, "The design of FM pulse compression signals," *IEEE Transactions on Information Theory*, vol. 10, no. 1, pp. 61–67, Jan. 1964.

[51] C.E. Cook, "A class of nonlinear FM pulse compression signals," *Proceedings of the IEEE*, vol. 52, no. 11, pp. 1369–1371, Nov. 1964.

[52] *IRIG Standard 106–00: Telemetry Standards, Range Commanders Council Telemetry Group*, Range Commanders Council, White Sands, Missle Range, New Mexico.

[53] *Bandwidth-Efficient Modulations: Summary of Definitions, Implementation, and Performance*, Report Concerning Space Data System Standards, Informational Report CCSDS 413.0-G-2.

[54] *Specifications of the Bluetooth System*, Bluetooth Special Interest Group, ver. 1.2, Nov. 2003.

[55] W. Melvin and J. Scheer, *Principles of modern radar: radar applications*. SciTech Pub., 2014.

[56] M.A. Richards, J. Scheer, W.A. Holm *et al.*, *Principles of modern radar: basic principles*. SciTech Pub., 2010.

[57] J.A. Johnston and A.C. Fairhead, "Waveform design and Doppler sensitivity analysis for nonlinear FM chirp pulses," *Communications, Radar and Signal Processing, IEE Proceedings F*, vol. 133, no. 2, pp. 163–175, Apr. 1986.

[58] T. Collins and P. Atkins, "Nonlinear frequency modulation chirps for active sonar," *IEE Proceedings - Radar, Sonar and Navigation*, vol. 146, no. 6, pp. 312–316, Dec. 1999.

[59] J. Jakabosky, S.D. Blunt, and B. Himed, "Spectral-shape optimized FM noise radar for pulse agility," *IEEE Radar Conference*, May 2016.

[60] ——, "Waveform design and receive processing for nonrecurrent nonlinear FMCW radar," *IEEE Radar Conference*, May 2015.

[61] J. Jakabosky, S.D. Blunt, and A. Martone, "Incorporating hopped spectral gaps into nonrecurrent nonlinear FMCW radar emissions," *2015 IEEE 6th International Workshop on Computational Advances in Multi-Sensor Adaptive Processing (CAMSAP)*, Dec. 2015.

[62] J. Jakabosky, S.D. Blunt, M.R. Cook, J. Stiles, and S.A. Seguin, "Transmitter-in-the-loop optimization of physical radar emissions," *IEEE Radar Conference*, May 2012.

[63] J. Jakabosky, L. Ryan, and S.D. Blunt, "Transmitter-in-the-loop optimization of distorted ofdm radar emissions," *IEEE Radar Conference*, Apr. 2013.

[64] J.C. Pedro, "Intermodulation," in *Encyclopedia of RF and Microwave Engineering*, K. Chang, Ed. John Wiley & Sons, 2003, pp. 2189–2215.

[65] A.S. Gilmour, *Klystrons, traveling wave tubes, magnetrons, crossed-field amplifiers, and gyrotrons*. Artech House, 2011.

[66] J.C. Pedro and N.B. Carvalho, *Intermodulation distortion in microwave and wireless circuits*. Artech House, 2002.

[67] J.P. Martins, P.M. Cabral, N.B. Carvalho, and J.C. Pedro, "A metric for the quantification of memory effects in power amplifiers," *IEEE Transactions on Microwave Theory and Techniques*, vol. 54, no. 12, pp. 4432–4439, Dec. 2006.

[68] M. Ibnkahla, "Analytical and adaptive modeling of nonlinear high power amplifiers," in *Encyclopedia of RF and Microwave Engineering*, K. Chang, Ed. John Wiley & Sons, 2003, pp. 127–137.

[69] N. air systems command and N. air warfare center, *Electronic warfare and radar systems engineering handbook*. Naval air warfare center, 2013.

[70] R. Raich and G.T. Zhou, "On the modeling of memory nonlinear effects of power amplifiers for communication applications," *IEEE 10th Digital Signal Processing Workshop*, Oct. 2002.

[71] P. Colantonio, F. Giannini, and E. Limiti, "Microwave power amplifiers," in *Encyclopedia of RF and Microwave Engineering*, K. Chang, Ed. John Wiley & Sons, 2003, pp. 2871–2906.

[72] C. Baylis, L. Wang, M. Moldovan, J. Martin, H. Miller, L. Cohen, and J.D. Graaf, "Designing transmitters for spectral conformity: power amplifier design issues and strategies," *IET Radar, Sonar Navigation*, vol. 5, no. 6, pp. 681–685, Jul. 2011.

[73] C.A. Balanis, *Antenna theory: analysis and design*. John Wiley & Sons, 2005, vol. 1.

[74] K.S. Shanmugan and A.M. Breipohl, *Random signals: detection, estimation, and data analysis*. John Wiley & Sons, 1988.

[75] B.R. Mahafza and A. Elsherbeni, *MATLAB simulations for radar systems design*.CRC press, 2004.

[76] M.I. Skolnik, *Radar handbook, Second Edition*. McGraw-Hill Book Co., 1990.

[77] W.L. Melvin and J.A. Scheer, *Principles of modern radar: advanced techniques*. SciTech Publishing, 2013.

[78] G.W. Stimson, *Introduction to airborne radar*. SciTech Pub., 1998.

[79] J. Nocedal and S. Wright, *Numerical Optimization*. Springer Science & Business Media, 2006.

[80] M.A. Richards, *Fundamentals of radar signal processing*. Tata McGraw-Hill Education, 2005.

[81] D. Henke, P. McCormick, S.D. Blunt, and T. Higgins, "Practical aspects of optimal mismatch filtering and adaptive pulse compression for FM waveforms," *IEEE Radar Conference*, May 2015.

[82] M. Labitt, "Obtaining low sidelobes using non-linear FM pulse compression," MIT Lincoln Laboratory, Tech. Rep., 1994.

[83] D.F. Kelley and W.L. Stutzman, "Array antenna pattern modeling methods that include mutual coupling effects," *IEEE Transactions on Antennas and Propagation*, vol. 41, no. 12, pp. 1625–1632, Dec. 1993.

[84] W.L. Stutzman and G.A. Thiele, *Antenna theory and design*. John Wiley & Sons, 2012.

[85] H. Holter and H. Steyskal, "On the size requirement for finite phased-array models," *IEEE Transactions on Antennas and Propagation*, vol. 50, no. 6, pp. 836–840, Jun. 2002.

[86] D.W. Bliss and K.W. Forsythe, "Multiple-input multiple-output (MIMO) radar and imaging: degrees of freedom and resolution," *The Asilomar Conference on Signals, Systems, and Computers*, vol. 1, Nov. 2003.

[87] H.L. Van Trees, *Optimum array processing: Part IV of detection, estimation, and modulation*. John Wiley & Sons, 2002.

[88] G.S. Antonio, D.R. Fuhrmann, and F.C. Robey, "Generalized MIMO radar ambiguity functions," in *MIMO radar signal processing*, J. Li and P. Stoica, eds. John Wiley & Sons, 2008.

[89] G.S. Antonio and D.R. Fuhrmann, "Beampattern synthesis for wideband MIMO radar systems," *IEEE Intl. Workshop on Computational Advances in Multi-Sensor Adaptive Processings.*, Dec. 2005.

[90] P.M. McCormick, S.D. Blunt, and J.G. Metcalf, "Wideband MIMO frequency modulated emission design with space-frequency nulling," *IEEE Journal of Selected Topics in Signal Processing*, vol. 11, no. 2, pp. 363–378, Mar. 2017.

[91] ——, "Joint spectrum/beampattern design of wideband FM MIMO radar emissions," *IEEE Radar Conference*, May 2016.

[92] S.D. Blunt, P. McCormick, T. Higgins, and M. Rangaswamy, "Physical emission of spatially-modulated radar," *IET Radar, Sonar Navigation*, vol. 8, no. 9, pp. 1234–1246, 2014.

[93] J.L. Allen and B. Diamond, "Mutual coupling in array antennas," DTIC Document, Tech. Rep., 1966.

[94] E. Magill and H. Wheeler, "Wide-angle impedance matching of a planar array antenna by a dielectric sheet," *IEEE Transactions on Antennas and Propagation*, vol. 14, no. 1, pp. 49–53, Jan. 1966.

[95] R.J. Mailloux, *Phased array antenna handbook*. Artech House, 2005, vol. 2.

[96] P. Munk, "On arrays that maintain superior CP and constant scan impedance for large scan angles," *IEEE Transactions on Antennas and Propagation*, vol. 51, no. 2, pp. 322–330, Feb. 2003.

[97] I.S. Merrill, *Radar handbook*. John Wiley & Sons, 1990.

[98] B.A. Munk, *Finite antenna arrays and FSS*. John Wiley & Sons, 2003.

[99] D.M. Pozar, *Microwave engineering (2nd edition)*. John Wiley & Sons, 1999.

[100] H. Wheeler, "The grating-lobe series for the impedance variation in a planar phased-array antenna," *IEEE Transactions on Antennas and Propagation*, vol. 14, no. 6, pp. 707–714, Nov. 1966.

[101] J. Allen, "Gain and impedance variation in scanned dipole arrays," *IRE Transactions on Antennas and Propagation*, vol. 10, no. 5, pp. 566–572, Sep. 1962.

[102] J.A. Kasemodel, C.C. Chen, and J.L. Volakis, "Wideband planar array with integrated feed and matching network for wide-angle scanning," *IEEE Transactions on Antennas and Propagation*, vol. 61, no. 9, pp. 4528–4537, Sep. 2013.

[103] Y.T. Lo, S.W. Lee, and Q.H. Lee, "Optimization of directivity and signal-to-noise ratio of an arbitrary antenna array," *Proceedings of the IEEE*, vol. 54, no. 8, pp. 1033–1045, Aug. 1966.

[104] M. Uzsoky and L. Solymar, "Theory of super-directive linear arrays," *Acta Physica Academiae Scientiarum Hungaricae*, vol. 6, no. 2, pp. 185–205, 1956.

[105] R.C. Hansen, "Linear arrays," in *The handbook of antenna design, vol. 2*, A.W. Rudge, K. Milne, A.D. Oliver, and P. Knight, eds. IET, 1982, pp. 1–140.

[106] D.P. Scholnik and W.M. Dorsey, "Transmit pattern synthesis for uniform circular arrays with active reflection constraints," *IEEE Radar Conference*, May 2017.

[107] L. Savy and M. Lesturgie, "Coupling effects in MIMO phased array," *IEEE Radar Conference*, May 2016.

[108] D.M. Pozar, "A relation between the active input impedance and the active element pattern of a phased array," *IEEE Transactions on Antennas and Propagation*, vol. 51, no. 9, pp. 2486–2489, Sep. 2003.

[109] S.D. Blunt, P. McCormick, T. Higgins, and M. Rangaswamy, "Spatially-modulated radar waveforms inspired by fixational eye movement," *IEEE Radar Conference*, May 2014.

[110] T.C. Mealey and A.J. Duly, "BEEMER: A firmware-tuned, software-defined MIMO radar testbed," *2016 IEEE International Symposium on Phased Array Systems and Technology (PAST)*, Oct. 2016.

[111] P. Antonik, M.C. Wicks, H.D. Griffiths, and C.J. Baker, "Range dependent beamforming using element level waveform diversity," *International Waveform Diversity and Design Conference*, 2006.

[112] P. Baizert, T.B. Hale, M.A. Temple, and M.C. Wicks, "Forward-looking radar gmti benefits using a linear frequency diverse array," *Electronics Letters*, vol. 42, no. 22, pp. 1311–1312, Oct. 2006.

[113] M. Secmen, S. Demir, A. Hizal, and T. Eker, "Frequency diverse array antenna with periodic time modulated pattern in range and angle," *IEEE Radar Conference*, Apr. 2007.

[114] T. Higgins and S.D. Blunt, "Analysis of range-angle coupled beamforming with frequency-diverse chirps," *International Waveform Diversity and Design Conference*, Feb. 2009.

[115] M. Rolfs, "Microsaccades: small steps on a long way," *Vision research*, vol. 49, no. 20, pp. 2415–2441, 2009.

[116] E. Ahissar and A. Arieli, "Seeing via miniature eye movements: a dynamic hypothesis for vision," *Frontiers in computational neuroscience*, vol. 6, 2012.

[117] J. Cui, M. Wilke, N.K. Logothetis, D.A. Leopold, and H. Liang, "Visibility states modulate microsaccade rate and direction," *Vision research*, vol. 49, no. 2, pp. 228–236, 2009.

[118] S. Ahmed, J.S. Thompson, Y.R. Petillot, and B. Mulgrew, "Unconstrained synthesis of covariance matrix for MIMO radar transmit beampattern," *IEEE Transactions on Signal Processing*, vol. 59, no. 8, pp. 3837–3849, Aug. 2011.

[119] P. Stoica, J. Li, and X. Zhu, "Waveform synthesis for diversity-based transmit beampattern design," *IEEE Transactions on Signal Processing*, vol. 56, no. 6, pp. 2593–2598, Jun. 2008.

[120] D.P. Scholnik and J.O. Coleman, "Optimal design of wideband array patterns," *IEEE International Radar Conference*, May 2000.

[121] ——, "Optimal array-pattern synthesis for wideband digital transmit arrays," *IEEE Journal of Selected Topics in Signal Processing*, vol. 1, no. 4, pp. 660–677, Dec. 2007.

[122] H. He, P. Stoica, and J. Li, "Wideband MIMO systems: Signal design for transmit beampattern synthesis," *IEEE Transactions on Signal Processing*, vol. 59, no. 2, pp. 618–628, Feb. 2011.

[123] R.W. Gerchberg, "A practical algorithm for the determination of phase from image and diffraction plane pictures," *Optik*, vol. 35, p. 237, 1972.

[124] A. Levi and H. Stark, "Image restoration by the method of generalized projections with application to restoration from magnitude," *IEEE Conference on Acoustics, Speech, & Signal Processing*, vol. 9, Mar. 1984.

[125] H.H. Bauschke and J.M. Borwein, "On projection algorithms for solving convex feasibility problems," *SIAM review*, vol. 38, no. 3, pp. 367–426, 1996.

[126] O.M. Bucci, G. Franceschetti, G. Mazzarella, and G. Panariello, "Intersection approach to array pattern synthesis," *IEE Proceedings H - Microwaves, Antennas and Propagation*, vol. 137, no. 6, pp. 349–357, Dec. 1990.

[127] J.R. Fienup, "Phase retrieval algorithms: a comparison," *Applied Optics*, vol. 21, no. 15, pp. 2758–2769, 1982.

[128] L.K. Patton and B.D. Rigling, "Phase retrieval for radar waveform optimization," *IEEE Transactions on Aerospace and Electronic Systems*, vol. 48, no. 4, pp. 3287–3302, Oct. 2012.

[129] T. Higgins, T. Webster, and A.K. Shackelford, "Mitigating interference via spatial and spectral nulling," *IET Radar, Sonar Navigation*, vol. 8, no. 2, pp. 84–93, Feb. 2014.

[130] J. Jakabosky, S.D. Blunt, and T. Higgins, "Ultra-low sidelobe waveform design via spectral shaping and linc transmit architecture," *IEEE Radar Conference*, May 2015.

[131] B. Munk, T. Kornbau, and R. Fulton, "Scan independent phased arrays," *Radio Science*, vol. 14, no. 6, pp. 979–990, 1979.

[132] G. Laughlin, E. Byron, and T. Cheston, "Very wide-band phased-array antenna," *IEEE Transactions on Antennas and Propagation*, vol. 20, no. 6, pp. 699–704, Nov. 1972.

[133] R.J. Mailloux, "Impedance matching for wide angle and wideband radiation," in *Phased array antenna handbook*. Artech House, 2005, vol. 2.

[134] G.H. Knittel, A. Hessel, and A.A. Oliner, "Element pattern nulls in phased arrays and their relation to guided waves," *Proceedings of the IEEE*, vol. 56, no. 11, pp. 1822–1836, Nov. 1968.

[135] D. Rhodes, "On the stored energy of planar apertures," *IEEE Transactions on Antennas and Propagation*, vol. 14, no. 6, pp. 676–683, Nov. 1966.

[136] G.C. Tavik, C.L. Hilterbrick, J.B. Evins, J.J. Alter, J.G. Crnkovich, J.W. de Graaf, W. Habicht, G.P. Hrin, S.A. Lessin, D.C. Wu, and S.M. Hagewood, "The advanced multifunction RF concept," *IEEE Transactions on Microwave Theory and Techniques*, vol. 53, no. 3, pp. 1009–1020, Mar. 2005.

[137] S. Smith, *Digital signal processing: a practical guide for engineers and scientists*. Newnes, 2003.

[138] J.D. Taylor, *Introduction to Ultra-Wideband Radar Systems*. CRC press, 1994.

[139] I.W. Selesnick, S.U. Pillai, and R. Zheng, "An iterative algorithm for the construction of notched chirp signals," *IEEE Radar Conference*, May 2010.

[140] I.W. Selesnick and S.U. Pillai, "Chirp-like transmit waveforms with multiple frequency-notches," *IEEE Radar Conference*, May 2011.

[141] J. Jakabosky, B. Ravenscroft, S.D. Blunt, and A. Martone, "Gapped spectrum shaping for tandem-hopped radar/communications cognitive sensing," *IEEE Radar Conference*, May 2016.

[142] M. Skolnik, "Opportunities in radar-2002," *Electronics Communication Engineering Journal*, vol. 14, no. 6, pp. 263–272, Dec. 2002.

[143] S.D. Blunt and K. Gerlach, "Adaptive pulse compression," *IEEE Radar Conference*, Apr. 2004.

[144] B. Friedlander, "On transmit beamforming for MIMO radar," *IEEE Transactions on Aerospace and Electronic Systems*, vol. 48, no. 4, pp. 3376–3388, Oct. 2012.

[145] O. Aldayel, V. Monga, and M. Rangaswamy, "Tractable MIMO beampattern design under constant modulus waveform constraint," *IEEE Radar Conference*, May 2016.

[146] S. Boyd and L. Vandenberghe, *Convex Optimization*. Cambridge University Press, 2004.

[147] J.L. Walker, *Handbook of RF and microwave power amplifiers*.Cambridge, UK: Cambridge University Press, 2011.

[148] D. Youla, "Generalized image restoration by the method of alternating orthogonal projections," *IEEE Transactions on Circuits and Systems*, vol. 25, no. 9, pp. 694–702, Sep. 1978.

[149] D.C. Youla and H. Webb, "Image restoration by the method of convex projections, Part 1: Theory," *IEEE Transactions on Medical Imaging*, vol. 1, no. 2, pp. 81–94, Oct. 1982.

[150] H.H. Bauschke, P.L. Combettes, and D.R. Luke, "Phase retrieval, error reduction algorithm, and Fienup variants: a view from convex optimization," *JOSA A*, vol. 19, no. 7, pp. 1334–1345, 2002.

[151] J.B. Anderson, T. Aulin, and C.E. Sundberg, *Digital Phase Modulation*.Springer Science & Business Media, 1986.

[152] A. Viterbi, "Error bounds for convolutional codes and an asymptotically optimum decoding algorithm," *IEEE Transactions on Information Theory*, vol. 13, no. 2, pp. 260–269, Apr. 1967.

[153] J.R. Klauder, A.C. Price, S. Darlington, and W.J. Albersheim, "The theory and design of chirp radars," *The Bell System Technical Journal*, vol. 39, no. 4, pp. 745–808, Jul. 1960.

[154] A.W. Doerry, *Generating nonlinear FM chirp waveforms for radar*. United States. Department of Energy, Sandia Report, SAND2006-5856, Sep. 2006.

[155] I. Gladkova, "Design of frequency modulated waveforms via the Zak transform," *IEEE Transactions on Aerospace and Electronic Systems*, vol. 40, no. 1, pp. 355–359, Jan. 2004.

[156] E.D. Witte and H.D. Griffiths, "Improved ultra-low range sidelobe pulse compression waveform design," *Electronics Letters*, vol. 40, no. 22, pp. 1448–1450, Oct. 2004.

[157] J. Jakabosky, S.D. Blunt, and B. Himed, "Optimization of "over-coded" radar waveforms," *IEEE Radar Conference*, May 2014.

[158] P.S. Tan, J. Jakabosky, J.M. Stiles, and S.D. Blunt, "On higher-order representations of polyphase-coded FM radar waveforms," *IEEE Radar Conference*, May 2015.

[159] J.M. Kurdzo, B.L. Cheong, R.D. Palmer, and G. Zhang, "Optimized NLFM pulse compression waveforms for high-sensitivity radar observations," *IEEE International Radar Conference*, Oct. 2014.

[160] D.A. Hague, "Transmit waveform design using multi-tone sinusoidal frequency modulation," *IEEE Radar Conference*, May 2017.

[161] P.M. McCormick and S.D. Blunt, "Nonlinear conjugate gradient optimization of polyphase-coded FM radar waveforms," *IEEE Radar Conference*, May 2017.

[162] ——, "Gradient-based coded-FM waveform design using Legendre polynomials," *IET International Radar Conference*, Oct. 2017.

[163] L. Li, H. Yang, G. Cui, L. Kong, and X. Yang, "Efficient phase-modulated waveform design for active sensing systems," *IEEE Radar Conference*, May 2014.

[164] P. Setlur and M. Rangaswamy, "Projected gradient waveform design for fully adaptive radar STAP," *IEEE Radar Conference*, May 2015.

[165] B. O'Donnell and J.M. Baden, "Fast gradient descent for multi-objective waveform design," *IEEE Radar Conference*, May 2016.

[166] J. Song, P. Babu, and D.P. Palomar, "Sequence design to minimize the weighted integrated and peak sidelobe levels," *IEEE Transactions on Signal Processing*, vol. 64, no. 8, pp. 2051–2064, Apr. 2016.

[167] U. Tan, C. Adnet, O. Rabaste, F. Arlery, J.P. Ovarlez, and J.P. Guyvarch, "Phase code optimization for coherent MIMO radar via a gradient descent," *IEEE Radar Conference*, May 2016.

[168] B.J. Skinner, J.P. Donohoe, and F.M. Ingels, "Gradient descent method for designing optimum radar signals," *IEEE International Radar Conference*, May 1995.

[169] S. Blunt, M. Cook, E. Perrins, and J. de Graaf, "CPM-based radar waveforms for efficiently bandlimiting a transmitted spectrum," *IEEE Radar Conference*, May 2009.

[170] J. Jakabosky, P. Anglin, M.R. Cook, S.D. Blunt, and J. Stiles, "Non-linear FM waveform design using marginal fisher's information within the CPM framework," *IEEE Radar Conference*, May 2011.

[171] W.W. Hager and H. Zhang, "A survey of nonlinear conjugate gradient methods," *Pacific journal of Optimization*, vol. 2, no. 1, pp. 35–58, 2006.

[172] M. Abramowitz and I.A. Stegun, *Handbook of mathematical functions: with formulas, graphs, and mathematical tables*. Courier Corporation, 1964, vol. 55.

[173] S.A. Seguin, J. Jakabosky, and S.D. Blunt, "Hardware-in-the-loop radar waveform optimization using radiated emissions," *2013 IEEE International Symposium on Electromagnetic Compatibility*, Aug. 2013.

[174] S.A. Seguin, J. Jakabosky, B.D. Cordill, and S.D. Blunt, "Phased array antenna model-in-the-loop radar waveform optimization," *IEEE International Conference on Microwaves, Communications, Antennas, and Electronics Systems*, Oct. 2013.

Appendix A

Derivations

A.1 Proof of total emitted energy relationship: (2.124)

Using (2.123) and (2.124), the total emitted energy can be written as

$$\mathcal{E}_{\text{tx}} = \frac{1}{4\pi Z_0} \int_{-\infty}^{\infty} \int_{0}^{2\pi} \int_{-\pi/2}^{\pi/2} \left(F(t,\theta,\varphi) * V^{+}(t) \right)^2 \cos\theta \, d\theta \, d\varphi \, dt. \tag{A.1}$$

Expanding the convolution into integral form, (A.1) becomes

$$\mathcal{E}_{\text{tx}} = \frac{1}{4\pi Z_0} \int_{-\infty}^{\infty} \int_{0}^{2\pi} \int_{-\pi/2}^{\pi/2} \int_{-\infty}^{\infty} \int_{-\infty}^{\infty} F(t',\theta,\varphi) V^{+}(t-t') F(t'',\theta,\varphi) V^{+}(t-t'') dt' dt'' \cos\theta \, d\theta \, d\varphi \, dt. \tag{A.2}$$

The only variable now dependent on t are the voltages $V^{+}(t-t')$ and $V^{+}(t-t'')$, thus the integrals can be reorganized as

$$\mathcal{E}_{\text{tx}} = \frac{1}{4\pi Z_0} \int_{0}^{2\pi} \int_{-\pi/2}^{\pi/2} \int_{-\infty}^{\infty} \int_{-\infty}^{\infty} \left(\int_{-\infty}^{\infty} V^{+}(t-t') V^{+}(t-t'') dt \right) F(t',\theta,\varphi) F(t'',\theta,\varphi) dt' dt'' \cos\theta \, d\theta \, d\varphi. \tag{A.3}$$

The expression inside of the parenthesis can be expressed in the frequency domain as

$$\int_{-\infty}^{\infty} V^{+}(t-t') V^{+}(t-t'') dt = \int_{-\infty}^{\infty} |V^{+}(f)|^2 e^{j2\pi f t'} e^{-j2\pi f t''} df. \tag{A.4}$$

Plugging this expression into (A.3) and reordering the integrals yields

$$\mathcal{E}_{\text{tx}} = \frac{1}{4\pi Z_0} \int_{-\infty}^{\infty} \int_{0}^{2\pi} \int_{-\pi/2}^{\pi/2} |V^+(f)|^2 \int_{-\infty}^{\infty} F(t', \theta, \varphi) e^{j2\pi f t'} dt' \int_{-\infty}^{\infty} F(t'', \theta, \varphi) e^{-j2\pi f t''} dt'' \cos\theta d\theta d\varphi df. \tag{A.5}$$

Note that the integrals of the antenna pattern equal

$$F^*(f, \theta, \varphi) = \int_{-\infty}^{\infty} F(t', \theta, \varphi) e^{j2\pi f t'} dt' \tag{A.6}$$

and

$$F(f, \theta, \varphi) = \int_{-\infty}^{\infty} F(t'', \theta, \varphi) e^{-j2\pi f t''} dt''. \tag{A.7}$$

Thus, (A.5) can be written as

$$\mathcal{E}_{\text{tx}} = \frac{1}{4\pi Z_0} \int_{-\infty}^{\infty} |V^+(f)|^2 \int_{0}^{2\pi} \int_{-\pi/2}^{\pi/2} |F(f, \theta, \varphi)|^2 \cos\theta d\theta d\varphi df. \tag{A.8}$$

A.2 Proof of down-conversion: (2.137) and (2.138)

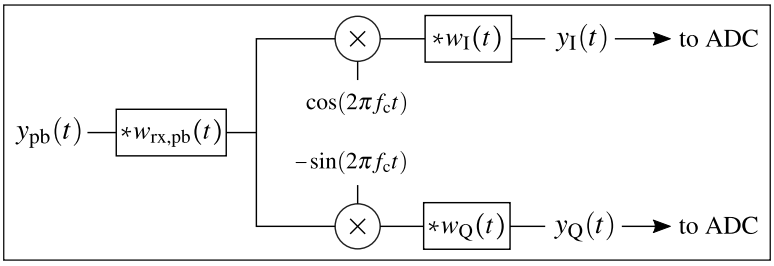

Figure A.1: Simplified receiver model for analog down-conversion.

Figure A.1 shows the receiver down-conversion process. Assume no distortion of the passband signal $y_{\text{pb}}(t)$ before mixing ($w_{\text{rx,pb}}(t) = \delta(t)$) and is equal to the transmitted passband waveform $s_{\text{pb}}(t)$ absent of any noise:

$$\begin{aligned} y_{\mathrm{pb}}(t) &= s_{\mathrm{pb}}(t) \\ &= \sqrt{2}s_{\mathrm{I}}(t)\cos(2\pi f_{\mathrm{c}}t) - \sqrt{2}s_{\mathrm{Q}}(t)\sin(2\pi f_{\mathrm{c}}t). \end{aligned} \tag{A.9}$$

Therefore, after down-conversion and low-pass filtering the continuous baseband signal $y(t) = y_{\mathrm{I}}(t) + jy_{\mathrm{Q}}(t)$ should be equal to the baseband waveform $s(t) = s_{\mathrm{I}}(t) + js_{\mathrm{Q}}(t)$, thus $y_{\mathrm{I}}(t) = s_{\mathrm{I}}(t)$ and $y_{\mathrm{Q}}(t) = s_{\mathrm{Q}}(t)$.

Using the model in (A.9), the signal exiting the top mixer in Figure A.1 can be represented as

$$\begin{aligned} y_{\mathrm{pb}}(t)\cos(2\pi f_{\mathrm{c}}t) &= \left(\sqrt{2}s_{\mathrm{I}}(t)\cos(2\pi f_{\mathrm{c}}t) - \sqrt{2}s_{\mathrm{Q}}(t)\sin(2\pi f_{\mathrm{c}}t)\right)\cos(2\pi f_{\mathrm{c}}t) \\ &= \sqrt{2}s_{\mathrm{I}}(t)\cos^2(2\pi f_{\mathrm{c}}t) - \sqrt{2}s_{\mathrm{Q}}(t)\sin(2\pi f_{\mathrm{c}}t)\cos(2\pi f_{\mathrm{c}}t). \end{aligned} \tag{A.10}$$

Using the trigonometric identities

$$\sin\theta\cos\theta = \frac{1}{2}\sin(2\theta) \tag{A.11}$$

and

$$\cos^2\theta = \frac{1}{2}\left(1+\cos(2\theta)\right), \tag{A.12}$$

the form in (A.10) can be rewritten as

$$\begin{aligned} y_{\mathrm{pb}}(t)\cos(2\pi f_{\mathrm{c}}t) &= \tfrac{\sqrt{2}}{2}s_{\mathrm{I}}(t)\left(1+\cos(4\pi f_{\mathrm{c}}t)\right) - \tfrac{\sqrt{2}}{2}s_{\mathrm{Q}}(t)\sin(4\pi f_{\mathrm{c}}t) \\ &= \tfrac{\sqrt{2}}{2}\left(s_{\mathrm{I}}(t) + s_{\mathrm{I}}(t)\cos(4\pi f_{\mathrm{c}}t) - s_{\mathrm{Q}}(t)\sin(4\pi f_{\mathrm{c}}t)\right). \end{aligned} \tag{A.13}$$

This signal is then sent through the filter $w_{\mathrm{I}}(t)$ which includes a low-pass filtering operation that filters out the higher frequency terms. For analysis purposes, assume $w_{\mathrm{I}}(t)$ is a perfect brickwall low-pass filter with amplitude of $\sqrt{2}$ (for scaling purposes) thus the output of the convolution leaves only the baseband component $s_{\mathrm{I}}(t)$. Therefore, the in-phase component $y_{\mathrm{I}}(t)$ is

$$\begin{aligned} y_{\mathrm{I}}(t) &= y_{\mathrm{pb}}(t)\cos(2\pi f_{\mathrm{c}}t) * w_{\mathrm{I}}(t) \\ &= \tfrac{\sqrt{2}}{2}\left(s_{\mathrm{I}}(t) + s_{\mathrm{I}}(t)\cos(4\pi f_{\mathrm{c}}t) - s_{\mathrm{Q}}(t)\sin(4\pi f_{\mathrm{c}}t)\right) * w_{\mathrm{I}}(t) \\ &= s_{\mathrm{I}}(t). \end{aligned} \tag{A.14}$$

Likewise, the signal exiting the bottom mixer in Figure A.1 can be represented as

$$\begin{aligned} -y_{\mathrm{pb}}(t)\sin(2\pi f_{\mathrm{c}}t) &= -\left(\sqrt{2}s_{\mathrm{I}}(t)\cos(2\pi f_{\mathrm{c}}t) - \sqrt{2}s_{\mathrm{Q}}(t)\sin(2\pi f_{\mathrm{c}}t)\right)\sin(2\pi f_{\mathrm{c}}t) \\ &= -\sqrt{2}s_{\mathrm{I}}(t)\sin(2\pi f_{\mathrm{c}}t)\cos(2\pi f_{\mathrm{c}}t) + \sqrt{2}s_{\mathrm{Q}}(t)\sin^2(2\pi f_{\mathrm{c}}t). \end{aligned} \tag{A.15}$$

Using (A.11) and the trigonometric identity

$$\sin^2\theta = \frac{1}{2}(1 - \cos(2\theta)), \tag{A.16}$$

the form in (A.15) can be expressed as

$$\begin{aligned} -y_{\mathrm{pb}}(t)\sin(2\pi f_{\mathrm{c}}t) &= -\tfrac{\sqrt{2}}{2}s_{\mathrm{I}}(t)\sin(4\pi f_{\mathrm{c}}t) + \tfrac{\sqrt{2}}{2}s_{\mathrm{Q}}(t)(1 - \cos(4\pi f_{\mathrm{c}}t)) \\ &= \tfrac{\sqrt{2}}{2}\left(s_{\mathrm{Q}}(t) - s_{\mathrm{Q}}(t)\cos(4\pi f_{\mathrm{c}}t) - s_{\mathrm{I}}(t)\sin(4\pi f_{\mathrm{c}}t)\right). \end{aligned} \tag{A.17}$$

Again, assume the filter $w_{\mathrm{Q}}(t)$ is a perfect brick wall low-pass filter with amplitude $\sqrt{2}$ to remove the higher frequency components leaving only the quadrature baseband signal component

$$\begin{aligned} y_{\mathrm{Q}}(t) &= -\sqrt{2}y_{\mathrm{pb}}(t)\sin(2\pi f_{\mathrm{c}}t) * w_{\mathrm{Q}}(t) \\ &= \tfrac{\sqrt{2}}{2}\left(s_{\mathrm{Q}}(t) - s_{\mathrm{Q}}(t)\cos(4\pi f_{\mathrm{c}}t) - s_{\mathrm{I}}(t)\sin(4\pi f_{\mathrm{c}}t)\right) * w_{\mathrm{Q}}(t) \\ &= s_{\mathrm{Q}}(t). \end{aligned} \tag{A.18}$$

A.3 Derivation of receiver distortion model: (2.140)

Applying the passband filter $w_{\mathrm{pb,rx}}(t)$ to $y_{\mathrm{pb}}(t)$ in the frequency domain yields the signal temporarily defined as

$$A_{\mathrm{pb}}(f) = Y_{\mathrm{pb}}(f) W_{\mathrm{pb,rx}}(f). \tag{A.19}$$

The spectrums of the LO tones are defined as impulses in the frequency domain as,

$$\mathcal{F}\{\cos(2\pi f_{\mathrm{c}} t)\} = \tfrac{1}{2}\big(\delta(f - f_{\mathrm{c}}) + \delta(f + f_{\mathrm{c}})\big) \tag{A.20}$$

and

$$\mathcal{F}\{-\sin(2\pi f_{\mathrm{c}} t)\} = j\tfrac{1}{2}\big(\delta(f - f_{\mathrm{c}}) - \delta(f + f_{\mathrm{c}})\big). \tag{A.21}$$

The output of the in-phase and quadrature mixer stages, denoted $A_{\mathrm{I}}(f)$ and $A_{\mathrm{Q}}(f)$, respectively, are defined by the convolution of $A_{\mathrm{pb}}(f)$ with the respective LO spectrums resulting in

$$A_{\mathrm{I}}(f) = \tfrac{1}{2}\big(A_{\mathrm{pb}}(f - f_{\mathrm{c}}) + A_{\mathrm{pb}}(f + f_{\mathrm{c}})\big) \tag{A.22}$$

and

$$A_{\mathrm{Q}}(f) = j\tfrac{1}{2}\big(A_{\mathrm{pb}}(f - f_{\mathrm{c}}) - A_{\mathrm{pb}}(f + f_{\mathrm{c}})\big). \tag{A.23}$$

Thus, the spectral content of the in-phase and quadrature signal components ($Y_{\mathrm{I}}(f)$ and $Y_{\mathrm{Q}}(f)$) are found by applying the filters $W_{\mathrm{I}}(f)$ and $W_{\mathrm{Q}}(f)$ to their respective signals $A_{\mathrm{I}}(f)$ and $A_{\mathrm{Q}}(f)$ as

$$Y_{\mathrm{I}}(f) = \tfrac{1}{2} W_{\mathrm{I}}(f)\big(A_{\mathrm{pb}}(f - f_{\mathrm{c}}) + A_{\mathrm{pb}}(f + f_{\mathrm{c}})\big) \tag{A.24}$$

and

$$Y_{\mathrm{Q}}(f) = j\tfrac{1}{2} W_{\mathrm{Q}}(f)\big(A_{\mathrm{pb}}(f - f_{\mathrm{c}}) - A_{\mathrm{pb}}(f + f_{\mathrm{c}})\big). \tag{A.25}$$

The frequency content of complex signal $y(t)$ (denoted $Y(f)$) is found via the complex combination

$$\begin{aligned} Y(f) &= Y_{\mathrm{I}}(f) + jY_{\mathrm{Q}}(f) \\ &= \tfrac{1}{2}W_{\mathrm{I}}(f)\big(A_{\mathrm{pb}}(f-f_{\mathrm{c}}) + A_{\mathrm{pb}}(f+f_{\mathrm{c}})\big) - \tfrac{1}{2}W_{\mathrm{Q}}(f)\big(A_{\mathrm{pb}}(f-f_{\mathrm{c}}) - A_{\mathrm{pb}}(f+f_{\mathrm{c}})\big) \\ &= \tfrac{1}{2}A_{\mathrm{pb}}(f-f_{\mathrm{c}})\big(W_{\mathrm{I}}(f) - W_{\mathrm{Q}}(f)\big) + \tfrac{1}{2}A_{\mathrm{pb}}(f+f_{\mathrm{c}})\big(W_{\mathrm{I}}(f) + W_{\mathrm{Q}}(f)\big). \end{aligned} \tag{A.26}$$

Inserting the form of (A.19) yields the expression

$$Y(f) = \tfrac{1}{2}Y_{\mathrm{pb}}(f-f_{\mathrm{c}})W_{\mathrm{pb,rx}}(f-f_{\mathrm{c}})\big(W_{\mathrm{I}}(f) - W_{\mathrm{Q}}(f)\big) + \tfrac{1}{2}Y_{\mathrm{pb}}(f+f_{\mathrm{c}})W_{\mathrm{pb,rx}}(f+f_{\mathrm{c}})\big(W_{\mathrm{I}}(f) + W_{\mathrm{Q}}(f)\big). \tag{A.27}$$

The filters $W_{\mathrm{I}}(f)$ and $W_{\mathrm{Q}}(f)$ are designed to be low-pass filters that are very similar in frequency response (to prevent an imbalanced distortion effect), thus the difference $W_{\mathrm{I}}(f) - W_{\mathrm{Q}}(f)$ is assumed to be very small. Furthermore, the passband filter $W_{\mathrm{pb,rx}}(f)$ can be assumed to have bandpass filtering to reduce out-of-band signal content. The shifted version of this filter $W_{\mathrm{pb,rx}}(f-f_{\mathrm{c}})$ places the center of the filter at $2f_{\mathrm{c}}$. Given these properties the product between $W_{\mathrm{pb,rx}}(f-f_{\mathrm{c}})$ and $W_{\mathrm{I}}(f) - W_{\mathrm{Q}}(f)$ is assumed negligible,

$$W_{\mathrm{pb,rx}}(f-f_{\mathrm{c}})\big(W_{\mathrm{I}}(f) - W_{\mathrm{Q}}(f)\big) \approx 0. \tag{A.28}$$

Therefore, (A.27) can be represented as

$$\begin{aligned} Y(f) &= \tfrac{1}{2}Y_{\mathrm{pb}}(f+f_{\mathrm{c}})W_{\mathrm{pb,rx}}(f)\big(W_{\mathrm{I}}(f) + W_{\mathrm{Q}}(f)\big) \\ &= Y_{\mathrm{pb}}(f+f_{\mathrm{c}})W_{\mathrm{rx}}(f), \end{aligned} \tag{A.29}$$

where

$$W_{\mathrm{rx}}(f) = \tfrac{1}{2}W_{\mathrm{pb,rx}}(f+f_{\mathrm{c}})\big(W_{\mathrm{I}}(f) + W_{\mathrm{Q}}(f)\big) \tag{A.30}$$

is the comprehensive receive filter that encapsulates both intentional filtering effects (i.e. bandpass

and low-pass filtering) and unintentional linear distortion. Note that the inverse Fourier transform of $W_{\mathrm{rx}}(f)$ is complex valued due to the frequency shift in $W_{\mathrm{pb,rx}}(f+f_{\mathrm{c}})$.

A.4 Proof of relationship between (3.16) and (3.19)

The expression of $g_{\mathrm{pb}}(t,\theta)$ from (3.16) can be derived through up-conversion (see (2.1)) of the signal $g(t,\theta)$,

$$g_{\mathrm{pb}}(t,\theta) = \sqrt{2}\Re\{g(t,\theta)\exp(j2\pi f_{\mathrm{c}}t)\}. \tag{A.31}$$

Inserting the expression from (3.19) into (A.31) yields

$$\begin{aligned} g_{\mathrm{pb}}(t,\theta) &= \sqrt{2}\Re\left\{\sum_m s_m\big(t+m\Delta t(\theta)\big)\exp\big(j2\pi f_{\mathrm{c}}m\Delta t(\theta)\big)\exp(j2\pi f_{\mathrm{c}}t)\right\} \\ &= \sum_m \sqrt{2}\Re\left\{s_m\big(t+m\Delta t(\theta)\big)\exp\Big(j2\pi f_{\mathrm{c}}\cdot\big(t+m\Delta t(\theta)\big)\Big)\right\}. \end{aligned} \tag{A.32}$$

Substituting $\zeta_m = t + m\Delta t(\theta)$ for the time variable and using the up-conversion definition from (2.1), (A.32) reduces to

$$\begin{aligned} g_{\mathrm{pb}}\big(\zeta_m - m\Delta t(\theta),\theta\big) &= \sum_m \sqrt{2}\Re\{s_m(\zeta_m)\exp(jm2\pi f_{\mathrm{c}}\zeta_m)\} \\ &= \sum_m s_{\mathrm{pb},m}(\zeta_m). \end{aligned} \tag{A.33}$$

Inserting the definition of ζ_m back into the expression yields

$$g_{\mathrm{pb}}(t,\theta) = \sum_m s_{\mathrm{pb},m}\big(t+m\Delta t(\theta)\big), \tag{A.34}$$

which is the definition of $g_{\mathrm{pb}}(t,\theta)$ from (3.16).

A.5 Proof of equivalence between traditional MIMO processing and the angle-dependent processing in Section 3.1.2

The traditional method of receive processing a MIMO transmission is by filtering each received signal $y_k(t)\forall k$ by each waveform $s_m(t)\forall m$ prior to receive beamforming. If the matched filter estimate from (3.52) can be rewritten in terms of the waveforms $s_m(t)\forall m$ (where the waveforms are correlated with each received signal $y_k(t)\forall k$ *prior* to receive beamforming) the equivalence is shown. For this proof, a ULA of M elements is assumed to both transmit and receive for $m,k \in \left\{-\frac{M-1}{2},\ldots,\frac{M-1}{2}\right\}$ where the center of the array is at $m=0$ which may or may not contain an element.

Recall the angle-dependent matched filtering operation from (3.52) expressed as

$$\hat{x}_{\mathrm{MF}}(\tau,\vartheta) = \left(M\left\|g(t,\vartheta)\right\|_2^2 \sum_m \left\|s_m(t)\right\|_2^2\right)^{-\frac{1}{2}} \int_{-\infty}^{\infty} g^*(t-\tau,\vartheta)y(t,\vartheta)dt. \tag{A.35}$$

Realizing the scaling term $\left(M\left\|g(t,\vartheta)\right\|_2^2 \sum_m \left\|s_m(t)\right\|_2^2\right)^{-\frac{1}{2}}$ is just a normalization of each angle-dependent filter, it can be applied at anytime during the estimation process. Thus rewrite (A.35) as

$$\hat{x}_{\mathrm{MF}}(\tau,\vartheta) = \gamma(\vartheta) \int_{-\infty}^{\infty} g^*(t-\tau,\vartheta)y(t,\vartheta)dt, \tag{A.36}$$

where

$$\gamma(\vartheta) = \left(\frac{1}{M}\left\|g(t,\vartheta)\right\|_2^2 \sum_m \left\|s_m(t)\right\|_2^2\right)^{-\frac{1}{2}}. \tag{A.37}$$

Inserting the relationships of the narrowband time-varying array factor $g(t,\theta)$ (from (3.32)) and the narrowband beamformed receive signal $y(t,\vartheta)$ (from (3.40)) into (A.36) yields

$$\begin{aligned}\hat{x}_{\mathrm{MF}}(\tau,\vartheta) &= \frac{\gamma(\vartheta)}{M^2}\int_{-\infty}^{\infty}\sum_m s_m^*(t-\tau)e^{-jm\phi(\vartheta)}\sum_k y_k(t)e^{-jk\phi(\vartheta)}dt \\ &= \frac{\gamma(\vartheta)}{M^2}\sum_m\sum_k e^{-j(k+m)\phi(\vartheta)}\int_{-\infty}^{\infty} s_m^*(t-\tau)y_k(t)dt,\end{aligned} \tag{A.38}$$

where

$$\gamma(\vartheta) = \left(\frac{1}{M}\Big\|\sum_m s_m(t)e^{j\phi(\vartheta)}\Big\|_2^2\sum_m\big\|s_m(t)\big\|_2^2\right)^{-\frac{1}{2}}. \tag{A.39}$$

Note that (A.38) applies the cross-correlation prior to beamforming thus proving that the method of processing spatially-diverse emissions discussed in Section 3.1.2 is equivalent to the traditional MIMO processing without virtual array tapering.

A.6 Time-domain equivalents for (3.65) – (3.78)

Taking the inverse Fourier transform of the frequency dependent scattering parameters yields the real-valued scattering filter,

$$\mathcal{S}_{mk}(t) = \mathcal{F}^{-1}\big\{\mathcal{S}_{mk}(f)\big\}. \tag{A.40}$$

Thus the time-domain representation of the backward traveling wave on the mth element is found via a summation of convolutions,

$$V_m^-(t) = \sum_k \mathcal{S}_{mk}(t) * V_k^+(t), \tag{A.41}$$

for $k \in \left\{-\frac{M-1}{2},\ldots,\frac{M-1}{2}\right\}$. The voltage and current at the terminals of the matching network for the mth element are found via the summation of the forward voltage $V_m^+(t)$ and the backward voltage $V_m^-(t)$ as

$$V_m'(t) = V_m^+(t) + \sum_k \mathcal{S}_{mk}(t) * V_k^+(t). \tag{A.42}$$

and

$$\begin{aligned} I_m'(t) &= \frac{V_m^+(t) - V_m^-(t)}{Z_0} \\ &= \frac{V_m^+(t)}{Z_0} - \frac{1}{Z_0}\sum_k \mathcal{S}_{mk}(t) * V_k^+(t), \end{aligned} \tag{A.43}$$

respectively. Similar to the scattering matrix, the (m,k)th index of the impedance matrix $\boldsymbol{Z}'(f)$ from (3.63) can be expressed in the time domain via the inverse Fourier transform as

$$Z_{mk}'(t) = \mathcal{F}^{-1}\{Z_{mk}'(f)\}. \tag{A.44}$$

Thus (A.42) can be expressed in terms of (A.43) and (A.44) as

$$V_m'(t) = \sum_k Z_{mk}'(t) * I_k'(t). \tag{A.45}$$

From Parseval's identity (and assuming finite energy) the net energy flow crossing the mth antenna element for a single pulse is similar to that in Section 3.2.1,

$$\begin{aligned} \mathcal{E}_{\mathrm{tx},m} &= \mathcal{E}_{\mathrm{tx},m}^+ - \mathcal{E}_{\mathrm{tx},m}^- \\ &= \frac{\|V_m^+(t)\|_2^2 - \|V_m^-(t)\|_2^2}{Z_0}, \end{aligned} \tag{A.46}$$

where

$$\mathcal{E}_{\mathrm{tx},m}^+ = \frac{\left\|V_m^+(t)\right\|_2^2}{Z_0} \tag{A.47}$$

and

$$\mathcal{E}_{\mathrm{tx},m}^- = \frac{\left\|V_m^-(t)\right\|_2^2}{Z_0} \tag{A.48}$$

are the incident and reflected/coupled energies, respectively. Likewise, the integrated reflection coefficient for the mth element from (3.77) can expressed as

$$\Gamma_m^{\mathrm{a}} = \frac{\|V_m^-(t)\|_2}{\|V_m^+(t)\|_2}, \tag{A.49}$$

and the total integrated reflection coefficient from (3.78) can be expressed as

$$\Gamma^{\mathrm{a}} = \left(\frac{\sum_m \|V_m^-(t)\|_2^2}{\sum_m \|V_m^+(t)\|_2^2} \right)^{\frac{1}{2}}. \tag{A.50}$$

A.7 Beamlet constraint: (4.32)

We want to constrain the available beamlet directions in Θ such that the mainlobe of each beamlet is contained entirely within the visible domain (for in-band frequencies). The peak-to-null beamwidth $[\Delta\bar{\mathrm{u}}(f)]_{\text{p-n}}$ in $\bar{\mathrm{u}} = \sin\theta$ space from (3.58) is generalized as a function of frequency f as [87]

$$[\Delta\bar{\mathrm{u}}(f)]_{\text{p-n}} = \frac{c}{Mfd}. \tag{A.51}$$

Inserting the representation of d from (4.9) into (A.51) yields

$$[\Delta\bar{\mathrm{u}}(f)]_{\text{p-n}} = \frac{2f_{\mathrm{E}}}{Mf}. \tag{A.52}$$

The widest beamwidth for in-band frequencies according to the 98% bandwidth occurs at $f = f_{\mathrm{c}} - B_{98\%}/2$. Therefore the maximum peak-to-null beamwidth for in-band frequencies is

$$\begin{aligned} \left[\Delta\bar{\mathrm{u}}_{\max}\right]_{\text{p-n}} &= \frac{2f_{\mathrm{E}}}{M \cdot \left(f_{\mathrm{c}} - \frac{B_{98\%}}{2}\right)} \\ &= \frac{2f_{\mathrm{E}}/f_{\mathrm{c}}}{M \cdot \left(1 - \frac{[\%\mathrm{BW}]_{98\%}}{2}\right)}. \end{aligned} \tag{A.53}$$

Bounding Θ such that each mainlobe within the set avoids the invisible domain for all in-band

frequencies is thus

$$|\sin\theta_p| \le 1 - [\Delta\bar{\mathrm{u}}_{\max}]_{\text{p-n}} = 1 - \frac{2f_{\mathrm{E}}/f_{\mathrm{c}}}{M\cdot\left(1-\frac{[\%\mathrm{BW}]_{98\%}}{2}\right)}. \tag{A.54}$$

for $p \in \{0,1,\ldots,P_{\mathrm{B}}-1\}$.

A.8 Minimization of (4.76)

Ignoring the iteration dependence i, the minimization problem of (4.76) can be rewritten as the cost function $\mathcal{J}$ using a $2\times N$ Lagrange multiplier matrix $\tilde{\Lambda}$ as

$$\mathcal{J} = \left\|\tilde{\mathbf{S}}_i - \mathbf{S}_i\right\|_F^2 + \Re\left\{\mathrm{Tr}\left\{\left(\mathbf{C}^H\tilde{\mathbf{S}}_i - \mathbf{G}\right)^H\tilde{\Lambda}\right\}\right\} \tag{A.55}$$

where $\mathrm{Tr}\{\bullet\}$ is the trace operation. The cost function in (A.55) has the equivalent form

$$\mathcal{J} = \sum_{n=0}^{N-1}\|\tilde{\mathbf{a}}_n - \mathbf{a}_n\|_2^2 + \Re\left\{\left(\mathbf{C}^H\mathbf{a}_n - \mathbf{b}_n\right)^H\boldsymbol{\lambda}_n\right\}, \tag{A.56}$$

where $\tilde{\mathbf{a}}_n$, $\mathbf{a}_n$, $\mathbf{b}_n$, and $\boldsymbol{\lambda}_n$ are the nth columns of $\tilde{\mathbf{S}}$, $\mathbf{S}$, $\mathbf{G}$, and $\tilde{\Lambda}$, respectively. The form in (A.56) is minimized when each term in the summation is minimized. Thus (A.56) can be represented as a summation of cost functions as $\mathcal{J} = \sum_{n=0}^{N-1}\mathcal{J}_n$ where the nth cost function is expressed as

$$\mathcal{J}_n = \|\tilde{\mathbf{a}}_n - \mathbf{a}_n\|_2^2 + \Re\left\{\left(\mathbf{C}^H\mathbf{a}_n - \mathbf{b}_n\right)^H\boldsymbol{\lambda}_n\right\}. \tag{A.57}$$

The gradient of (A.57) with respect to $\tilde{\mathbf{a}}_n^*$ yields

$$\nabla_{\tilde{\mathbf{a}}_n^*}\mathcal{J}_n = \tilde{\mathbf{a}}_n - \mathbf{a}_n + \mathbf{C}\boldsymbol{\lambda}_n. \tag{A.58}$$

Setting equal to zero and solving for $\tilde{\mathbf{a}}_n$ produces

$$\tilde{\mathbf{a}}_n = \mathbf{a}_n - \mathbf{C}\boldsymbol{\lambda}_n. \tag{A.59}$$

By multiplying each side by $\mathbf{C}^H$ and substituting $\mathbf{b}_n$ for $\mathbf{C}^H\tilde{\mathbf{a}}_n$, the Lagrange multiplier vector $\boldsymbol{\lambda}_n$ can be solved as

$$\boldsymbol{\lambda}_n = (\mathbf{C}^H\mathbf{C})^{-1}(\mathbf{C}^H\mathbf{a}_n - \mathbf{b}_n). \tag{A.60}$$

Plugging (A.60) into (A.59) yields the form

$$\tilde{\mathbf{a}}_n = \mathbf{P}_\perp\mathbf{a}_n + \mathbf{a}_{\star,n}, \tag{A.61}$$

where $\mathbf{a}_{\star,n} = \mathbf{C}(\mathbf{C}^H\mathbf{C})^{-1}\mathbf{b}_n$ is the nth column of $\mathbf{S}_\star$ and $\mathbf{P}_\perp$ is defined in (4.78). Assembling the N column vectors, the entire $M \times N$ waveform matrix $\tilde{\mathbf{S}}$ is expressed as

$$\tilde{\mathbf{S}} = \mathbf{P}_\perp\mathbf{S} + \mathbf{S}_\star. \tag{A.62}$$

A.9 Minimization of (4.79)

Ignoring the iteration index i, the minimization problem can be expressed in an equivalent vectorized form as

$$\begin{aligned} &\underset{\mathbf{a}}{\text{minimize}} \quad \|\mathbf{a} - \tilde{\mathbf{a}}\|_2^2 \\ &\text{subject to} \quad |a_k| = \gamma \quad \text{for} \quad k = 0, \ldots, MN-1, \end{aligned} \tag{A.63}$$

where $\mathbf{a} = \text{vec}\{\mathbf{S}\}$ and $\tilde{\mathbf{a}} = \text{vec}\{\tilde{\mathbf{S}}\}$. The constant amplitude constraint can be removed by enforcing the waveform model

$$\mathbf{a} = \gamma\exp(j\boldsymbol{\psi}), \tag{A.64}$$

where $\boldsymbol{\psi}$ is an $MN \times 1$ vector of phase values and γ is the positive real-valued amplitude. Thus (A.63) can be rewritten as the minimization of cost function

$$\mathcal{J} = \|\gamma \exp(j\boldsymbol{\psi}) - \tilde{\mathbf{a}}\|_2^2 \tag{A.65}$$

with respect to $\boldsymbol{\psi}$. The gradient of (A.65) with respect to $\boldsymbol{\psi}$ is

$$\nabla_{\boldsymbol{\psi}} \mathcal{J} = j\gamma\big(\tilde{\mathbf{a}} \odot \exp(-j\boldsymbol{\psi})\big) - j\gamma\big(\tilde{\mathbf{a}}^* \odot \exp(j\boldsymbol{\psi})\big) = 0, \tag{A.66}$$

where $\odot$ is the Hadamard product. Solving for $\boldsymbol{\psi}$ yields

$$\boldsymbol{\psi} = \angle \tilde{\mathbf{a}}. \tag{A.67}$$

Note that this expression for $\boldsymbol{\psi}$ is valid for all positive real-values of γ. Thus, the closed-form solution to (4.79) is represented as

$$\mathbf{S} = \gamma \exp(j \angle \tilde{\mathbf{S}}). \tag{A.68}$$

A.10 Derivation of gradient: (5.10)

Using the expression for the cost function from (5.5) we can apply the chain rule multiple times with respect to parameter α_n for $n \in \{0, 1, \ldots, N_\mathrm{p} - 1\}$ to get the derivative in the form:

$$
\begin{aligned}
\frac{\partial \mathcal{J}_{\mathrm{d}}(\mathbf{x}_{\mathrm{w}};q)}{\partial \alpha_n} &= \frac{1}{q}\frac{\partial}{\partial \alpha_n}\left(\frac{2\sum_{\ell=\Lambda}^{N-1}|r[\ell]|^q}{\sum_{\ell=-\Lambda+1}^{\Lambda-1}|r[\ell]|^q}\right)^{\frac{1}{q}} \\
&= \frac{1}{q}\left(\frac{2\sum_{\ell=\Lambda}^{N-1}|r[\ell]|^q}{\sum_{\ell=-\Lambda+1}^{\Lambda-1}|r[\ell]|^q}\right)^{\frac{1}{q}-1}\frac{\partial}{\partial \alpha_n}\left(\frac{2\sum_{\ell=\Lambda}^{N-1}|r[\ell]|^q}{\sum_{\ell=-\Lambda+1}^{\Lambda-1}|r[\ell]|^q}\right) \\
&= \frac{1}{q}\left(\frac{2\sum_{\ell=\Lambda}^{N-1}|r[\ell]|^q}{\sum_{\ell=-\Lambda+1}^{\Lambda-1}|r[\ell]|^q}\right)^{\frac{1}{q}-1}\left(\frac{2\sum_{\ell=\Lambda}^{N-1}\frac{\partial}{\partial \alpha_n}|r[\ell]|^q}{\sum_{\ell=-\Lambda+1}^{\Lambda-1}|r[\ell]|^q} - \frac{2\sum_{\ell=\Lambda}^{N-1}|r[\ell]|^q}{\left(\sum_{\ell=-\Lambda+1}^{\Lambda-1}|r[\ell]|^q\right)^2}\sum_{\ell=-\Lambda+1}^{\Lambda-1}\frac{\partial}{\partial \alpha_n}|r[\ell]|^q\right) \\
&= \frac{1}{q}\left(\frac{2\sum_{\ell=\Lambda}^{N-1}|r[\ell]|^q}{\sum_{\ell=-\Lambda+1}^{\Lambda-1}|r[\ell]|^q}\right)^{\frac{1}{q}}\left(\frac{\sum_{\ell=\Lambda}^{N-1}\frac{\partial}{\partial \alpha_n}|r[\ell]|^q}{\sum_{\ell=\Lambda}^{N-1}|r[\ell]|^q} - \frac{\sum_{\ell=-\Lambda+1}^{\Lambda-1}\frac{\partial}{\partial \alpha_n}|r[\ell]|^q}{\sum_{\ell=-\Lambda+1}^{\Lambda-1}|r[\ell]|^q}\right)
\end{aligned}
\tag{A.69}
$$

The derivative of $|r[\ell]|^q$ with respect to α_n can now be found independently from the form above as:

$$
\begin{aligned}
\frac{\partial |r[\ell]|^q}{\partial \alpha_n} &= \frac{\partial}{\partial \alpha_n}\left(r[\ell]r^*[\ell]\right)^{q/2} \\
&= \frac{q}{2}|r[\ell]|^{q-2}\left(r[\ell]\frac{\partial r^*[\ell]}{\partial \alpha_n} + \frac{\partial r[\ell]}{\partial \alpha_n}r^*[\ell]\right) \\
&= \frac{q}{2}|r[\ell]|^{q}\left(\frac{1}{r^*[\ell]}\frac{\partial r^*[\ell]}{\partial \alpha_n} + \frac{\partial r[\ell]}{\partial \alpha_n}\frac{1}{r[\ell]}\right) \\
&= q|r[\ell]|^q\,\Re\left\{\frac{1}{r[\ell]}\frac{\partial r[\ell]}{\partial \alpha_n}\right\}
\end{aligned}
\tag{A.70}
$$

The derivative of discrete autocorrelation $r[\ell]$ (from (2.204)) with respect to α_n is:

$$\begin{aligned}\frac{\partial r[\ell]}{\partial \alpha_n} &= \frac{\partial}{\partial \alpha_n}\frac{1}{N}\sum_{i=0}^{N-1} s^*\left(iT_\mathrm{s}+\xi\right) s\Big(\left(i+\ell\right)T_\mathrm{s}+\xi\Big) \\ &= \frac{1}{N}\sum_{i=0}^{N-1}\frac{\partial s^*\left(iT_\mathrm{s}+\xi\right)}{\partial \alpha_n} s\Big(\left(i+\ell\right)T_\mathrm{s}+\xi\Big) + \frac{1}{N}\sum_{i=0}^{N-1} s^*\left(iT_\mathrm{s}+\xi\right)\frac{\partial s\Big(\left(i+\ell\right)T_\mathrm{s}+\xi\Big)}{\partial \alpha_n} \\ &= \frac{1}{N}\sum_{i=0}^{N-1}\frac{\partial s^*\left(iT_\mathrm{s}+\xi\right)}{\partial \alpha_n} s\Big(\left(i+\ell\right)T_\mathrm{s}+\xi\Big) + \frac{1}{N}\sum_{i=0}^{N-1}\frac{\partial s\left(iT_\mathrm{s}+\xi\right)}{\partial \alpha_n} s^*\Big(\left(i-\ell\right)T_\mathrm{s}+\xi\Big) \\ &= a_n[\ell] + a_n^*[-\ell]\end{aligned} \tag{A.71}$$

where

$$a_n[\ell] = \frac{1}{N}\sum_{i=0}^{N-1}\frac{\partial s^*\left(iT_\mathrm{s}+\xi\right)}{\partial \alpha_n} s\Big(\left(i+\ell\right)T_\mathrm{s}+\xi\Big). \tag{A.72}$$

Therefore, the derivative of $\mathcal{J}_\mathrm{d}(\mathbf{x}_\mathrm{w};q)$ with respect to α_n can be written as

$$\frac{\partial \mathcal{J}_\mathrm{d}(\mathbf{x}_\mathrm{w};q)}{\partial \alpha_n} = \left(\frac{2\sum\limits_{\ell=\Lambda}^{N-1}|r[\ell]|^q}{\sum\limits_{\ell=-\Lambda+1}^{\Lambda-1}|r[\ell]|^q}\right)^{\frac{1}{q}}\left[\frac{\sum\limits_{\ell=\Lambda}^{N-1}|r[\ell]|^q\Re\left\{\dfrac{a_n[\ell]+a_n^*[-\ell]}{r[\ell]}\right\}}{\sum\limits_{\ell=\Lambda}^{N-1}|r[\ell]|^q} - \frac{\sum\limits_{\ell=-\Lambda+1}^{\Lambda-1}|r[\ell]|^q\Re\left\{\dfrac{a_n[\ell]+a_n^*[-\ell]}{r[\ell]}\right\}}{\sum\limits_{\ell=-\Lambda+1}^{\Lambda-1}|r[\ell]|^q}\right] \tag{A.73}$$

where $a_n[\ell]$ is defined using the CFM definition from (5.1) as

$$\begin{aligned}a_n[\ell] &= \frac{1}{N}\sum_{i=0}^{N-1}\frac{\partial s^*\left(iT_\mathrm{s}+\xi\right)}{\partial \alpha_n} s\Big(\left(i+\ell\right)T_\mathrm{s}+\xi\Big) \\ &= \frac{-j}{N}\sum_{i=0}^{N-1} h_n(iT_\mathrm{s}+\xi) s^*\left(iT_\mathrm{s}+\xi\right) s\Big(\left(i+\ell\right)T_\mathrm{s}+\xi\Big).\end{aligned} \tag{A.74}$$

Appendix B

List of Acronyms and Mathematical Notation

B.1 Acronyms

Acronym	Description
ADC	Analog-to-Digital Conversion
AFRL	Air Force Research Lab
AM	Amplitude Modulation
AWG	Arbitrary Waveform Generator
AWGN	Additive White Gaussian Noise
BEEMER	Baseband-digital at Every Element MIMO Experimental Radar
BER	Bit Error Rate
BFGS	Broyden-Fletcher-Goldfarb-Shanno
BPF	Band-Pass Filter
CFM	Coded Frequency Modulation
CPI	Coherent Processing Interval
CPM	Continuous-Phase Modulation
CW	Continuous-Wave
DAC	Digital-to-Analog Conversion
DAR	Digital Array Radar
DDS	Direct Digital Synthesizer
DFT	Discrete Fourier Transform

Acronym	Description
DTFT	Discrete-time Fourier Transform
DSP	Digital Signal Processing
EM	Electromagnetic/Electromagnetism
FDA	Frequency Diverse Array
FFT	Fast-Fourier Transform
FIR	Finite Impulse Response
FRP	Fractional Reactive Power
FM	Frequency Modulation
FMCW	Frequency Modulated Continuous-Wave
GISL	Generalized Integrated Sidelobe Level
HPA	High-Powered Amplifier
IID	Independent and Identically Distributed
ISL	Integrated Sidelobe Level
IMD	Intermodulation Distortion
LFM	Linear Frequency Modulation
LNA	Low-Noise Amplifier
LO	Local Oscillator
LPF	Low-Pass Filter
LSB	Least Significant Bit
LTI	Linear Time-Invariant
MDS	Minimum Detectable Signal
MFAR	Multifunction Array Radar
MTAE	Multiple-Time-Around Echo
NLCG	Nonlinear Conjugate Gradient
NLFM	Nonlinear Frequency Modulation

Acronym	Description
OFDM	Orthogonal Frequency Division Multiplexing
PAE	Power Added Efficiency
PAPR	Peak-to-Average Power Ratio
PCFM	Polyphase-Coded Frequency Modulation
PM	Phase Modulation
POSP	Principle of Stationary Phase
PRF	Pulse Repetition Frequency
PRI	Pulse Repetition Interval
PRO-FM	Pseudo-Random Optimized Frequency Modulation
PSL	Peak Sidelobe Level
QPSK	Quadrature Phase Shift Keying
RF	Radio Frequency
RCS	Radar Cross Section
RSA	Real-time Spectrum Analyzer
RSEC	Radar Spectrum Engineering Criteria
RUWO	Reiterative Uniform Weight Optimization
SAR	Synthetic Aperture Radar
SDR	Software-Defined Radar
SINR	Signal-to-Interference plus Noise Ratio
SNR	Signal-to-Noise Ratio
SRRC	Square-Root Raised-Cosine
T/R	Transmit/Receive
TWT	Traveling Wave Tube
ULA	Uniform Linear Array
UWB	Ultra Wideband

Acronym	Description
VSWR	Voltage Standing Wave Ratio
WAIM	Wide-Angle Impedance Matching
WSS	Wide-Sense Stationary

B.2 Mathematical Notation

Notation	Description
$a(t)$	Continuous function $a(t)$ dependent on variable t
$a[\ell]$	Discrete function $a[\ell]$ at sample ℓ
$a \cdot b$	a multiplied by b; typically used to distinguish multiplication from function when using parentheses/brackets/braces (e.g. $f \cdot (t-\tau)$ and $f(t-\tau)$)
$a(t) * b(t)$	$a(t)$ convolved with $b(t)$
$\max_t \{a(t)\}$	Maximum of $a(t)$ over variable t
$\min_t \{a(t)\}$	Minimum of $a(t)$ over variable t
$E\{a\}$	Expected value of a
$\mathcal{F}\{a(t)\}$	Fourier transform of continuous signal $a(t)$
$\mathcal{F}^{-1}\{A(f)\}$	Inverse Fourier transform of continuous spectrum $A(f)$
$\lfloor a \rceil$	Rounds a (real-valued) to nearest integer
$\lfloor a \rfloor$	Rounds to nearest integer less than a (real-valued)
$\lceil a \rceil$	Rounds to nearest integer greater than a (real-valued)
$\exp(a)$	$\exp(a) = e^a$;
a^*	Complex-conjugation
a (dB)	a in decibels (i.e. a (dB) $= 10\log_{10}\{a\}$)
$a \propto b$	a is proportional to b
$a \approx b$	a is approximate to b
$a = b$	a is equal to b
$a \triangleq b$	a is defined to be equal to b
$\sim a$	Similar to a
$a_n \forall n$	a_n for all n
$a \to b$	a approaches b
$a(t) \overset{\mathcal{F}}{\longleftrightarrow} A(f)$	$a(t)$ and $A(f)$ are a Fourier transform pair

Notation	Description
$\Re\{a\}$	Extracts the real value of a
$\Im\{a\}$	Extracts the imaginary value of a
$\angle a$	Extract phase of a
$\lvert a\rvert$	Magnitude of a
$\text{sgn}\{a\}$	Sign of a; $+1$ for $a > 0$ and -1 for $a < 0$
$\frac{d}{da}$	Derivative with respect to a
$\frac{\partial}{\partial a}$	Partial derivative with respect to a
$\mathbf{a}^T$	Transposition of vector $\mathbf{a}$
$\mathbf{a}^H$	Hermitian transpose of vector $\mathbf{a}$; equivalent to $(\mathbf{a}^*)^T$
$\{a, b\}$	Set containing a and b
$[a\ b]^T$	2×1 column vector containing a and b
$\text{Tr}\{\mathbf{A}\}$	Trace of square matrix $\mathbf{A}$
$\mathbf{a} \odot \mathbf{b}$	Hadamard product of vectors $\mathbf{a}$ and $\mathbf{b}$